Thermo-Hydro-Mechanical Processes in the Nearfield around a HLW Repository in Argillaceous Formations

Volume I
Laboratory Investigations

Thermo-Hydro-Mechanical Processes in the Nearfield around a HLW Repository in Argillaceous Formations

Volume I
Laboratory Investigations

May 2007 to May 2013

Chun-Liang Zhang
Oliver Czaikowski
Tilmann Rothfuchs
Klaus Wieczorek

June 2013

Foreword

Deep disposal of heat-emitting high-level radioactive waste (HLW) in clay formations will inevitably induce thermo-hydro-mechanical-chemical disturbances to the host rock and engineered barriers over very long periods of time. The responses and resulting property changes of the natural and engineered barriers are to be well understood, characterized, and predicted for assessing the long-term performance and safety of the repositories.

In accordance with the R&D programme defined by the German Federal Ministry of Economics and Technology (BMWi), GRS has intensively performed site-independent research work on argillaceous rocks during the last decade. Most of the investigations have been carried out on the Callovo-Oxfordian argillite and the Opalinus clay by participation in international research projects conducted at the underground research laboratories at Bure in France (MHM-URL) and Mont-Terri in Switzerland (MT-URL). The THM-TON project, which was funded by BMWi under contract number 02E10377, investigated the THM behaviours of the clay host rock and clay-based backfill/sealing materials with laboratory tests, in situ experiments and numerical modelling.

The clay rocks were experimentally studied with respect to the following THM behaviour:

- Short-term deformation, damage and induced permeability change, which will be produced by excavation of a repository;

- Long-term deformation, which controls the closure process of the repository openings and the integrity of the geological and engineered barriers;

- Swelling capability, which may dominate the long-term sealing process of the damaged zone surrounding the openings when water arrives;

- Self-sealing of fractures in the damaged zone, which is presently one of the highest concerns in the assessment of the long-term performance and safety of the repository because it has direct impact on the hydraulics and mechanics in the nearfield;

- Thermal impact on the hydro-mechanical behaviour and the integrity of the natural host rock and engineered barriers.

Excavated claystone and claystone-bentonite mixtures were characterized as backfill and sealing materials with regard to the barrier functions in repositories:

- Compaction behaviour of the backfill/sealing materials, which controls the interactions with support linings and the surrounding rock, and also determines the evolution of the backfill porosity and hydraulic conductivity;

- Permeability in relation with porosity, which controls the fluid transport and thus the hydraulic long-term barrier function of the backfill;

- Water retention capacity, which influences the water saturation process and storage, water/gas two-phase flow, and buildup of swelling pressure in the backfill and seals;

- Swelling pressure in compacted claystone-bentonite mixtures is required for sealing of possibly remaining gaps within the seals and seal/rock interfaces and for supporting the surrounding rock against damage propagation;

- Thermal conductivity of buffer surrounding HLW containers, which controls the heat transfer and temperature distribution in the multi-barrier-system.

In the frame of the Mine-By (MB) experiment in the MT-URL, the hydro-mechanical responses of the Opalinus clay to the excavation of the gallery G08 was monitored with measurement of porewater pressure in the surrounding rock. Additionally, the long-term deformation of a borehole and the porewater pressure in the surrounding rock (DM-A experiment) were also measured.

The coupled hydro-mechanical processes in the Opalinus clay during the in situ experiments were simulated using the finite element programme CODE_BRIGHT developed by the Technical University of Catalonia (UPC) in Barcelona. In addition to that, the coupled thermo-hydro-mechanical processes occurring in the Callovo-Oxfordian argillite during a heating experiment conducted by ANDRA at the MHM-URL were also modelled.

The most important results and conclusions from the laboratory investigations on the clay rocks and clay-based backfill/sealing materials are summarized in this volume, while the in situ experiments and the numerical modelling work are reported in a second volume.

Table of contents

Appendix

1   Introduction

All over the world, clay formations are being investigated as host medium for geologic disposal of radioactive waste because of their favourable properties, such as very low hydraulic conductivity against fluid transport, good sorption capacity for retardation of radionuclides, and high potential of self-sealing of fractures. The construction of a repository, the disposal of heat-emitting high-level radioactive waste (HLW), the backfilling and sealing of the remaining voids, however, will inevitably induce mechanical (M), hydraulic (H), thermal (T) and chemical (C) disturbances to the host formation and the engineered barrier system (EBS) over very long periods of time during the operation and post-closure phases of the repository. The responses and resulting property changes of the clay host rock and engineered barriers are to be well understood, characterized, and predicted for assessing the long-term performance and safety of the repository.

1.1   THM processes in the nearfield of a HLW repository

According to the French and Swiss disposal concepts designed by ANDRA /AND 05/ and NAGRA /NAG 02/ respectively, the potential repositories will be located in the over-consolidated Callovo-Oxfordian and Opalinus argillaceous formations at depths of 500 to 650 m below the ground surface. The corresponding lithostatic stress is in a range of 12 to 18 MPa. The highly-indurated clay rocks are initially saturated with formation water. The designed thermal load from HLW is limited below 90 °C in the host rock. The repository openings will be backfilled and sealed with suitable materials. The main functions of the EBS are to stabilize the repository structures and to prevent release of radionuclides into the biosphere. The design of the repository systems is site dependent. During the repository operation and post-closure phases, complex THMC coupled processes will take place in the natural and engineered barriers. Key processes in the nearfield around a HLW disposal borehole are schematically illustrated in Fig. 1.1 for the operation and post-closure phases. The processes affect the properties of the host rock and the EBS.

1.1.1   Key processes during the operation phase

The operation phase is initiated with excavation of the access shafts, drifts and boreholes and lasts until the closure of a repository. Excavation leads to a redistribution of

the rock stress and the porewater pressure around the openings, particularly to a sharp gradient of the pore pressure and a high concentration of the deviatoric stress near the opening walls after relief of the radial stress component. This results in micro- and macro-fractures in the surrounding rock where the damage and failure criteria of the rock are violated. According to /DAV 03/, /TSA 05/, the perturbed area may be divided into two zones: excavation damaged zone (EDZ) and disturbed zone (EdZ). The hydraulic conductivity of the EDZ near the opening walls may increase by several orders of magnitude up to the point where the barrier function of the host rock with respect to radionuclide migration will be affected. The EdZ outside the EDZ will be disturbed but less damaged without significant changes in flow and transport properties. Convergence of the openings and damage intensity and extent of the EDZ/EdZ are mainly dependent on the mechanical properties of the rock mass, depth of the excavation or local stress state, applied excavation technology, opening size and geometry, and support measures (shotcrete, bolting, steel arches, concrete lining, etc.). The rock deformation and damage develop with time. Moreover, the anisotropic nature of the sedimentary clay rocks and the anisotropic stress state has also considerable influences on the development of the EDZ/EdZ.
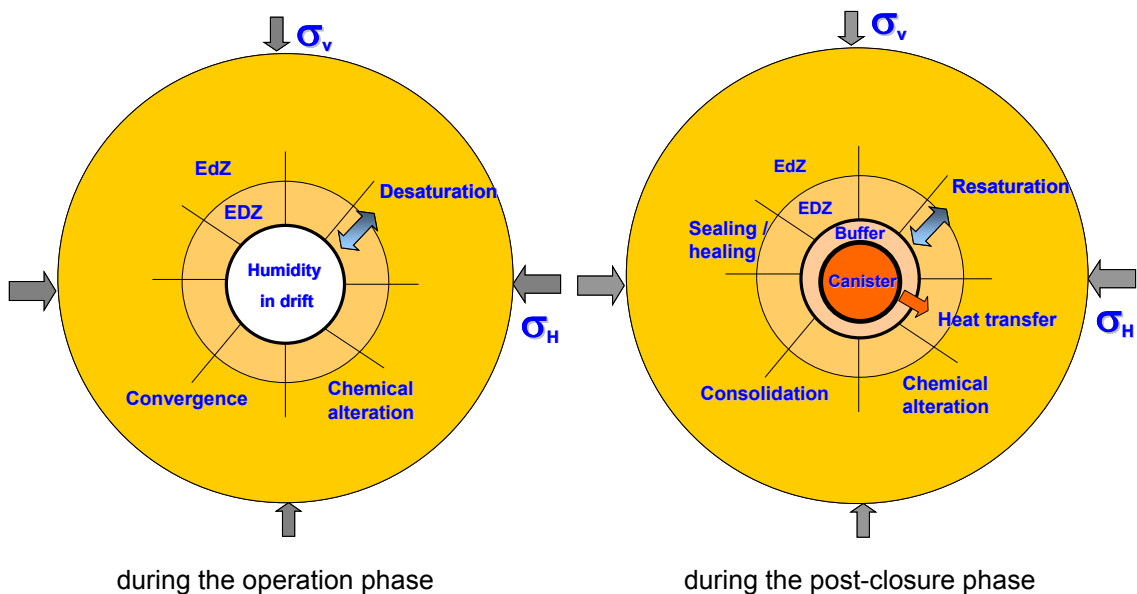

Fig. 1.1   Coupled THM processes in the nearfield around a HLW disposal borehole

The repository openings in deep clay formations normally need to be supported to limit the convergence and the EDZ propagation. The rock-support interaction leads to buildup of back-pressure against the rock deformation and damage. During the opera-

tion phase, the openings will be ventilated. The relatively low humidity of the circulating air will cause desaturation of the surrounding rock. Desaturation in turn gives rise to capillary forces and hence an increase in cohesion and strengthening of the rock mass, while at the same time the release of bound porewater results in collapse of the pore structure and generates microcracks propagating along bedding planes mainly. As stress-bearing element, the release of bound porewater also causes a change in the stress state in the rock mass.

After emplacement of HLW containers and backfilling of the disposal cells decay heat from the waste is transferred away through the buffer to the nearfield rock and then to the farfield. Heating will induce complex THMC processes in the EBS and the host rock. Heating accelerates the rheological deformation of the rock into the openings. For openings supported by rigid linings, a high pressure may build up on the linings. A sufficient thermal resistance of the linings is needed. Heating will cause a transient buildup of excess porewater pressure in the saturated nearfield, reducing the local effective mean stress. In the extreme case when the local minimum principal stress is exceeded, rock fracturing may occur. At high temperatures, the porewater in the buffer and the surrounding rock will evaporate and become more mobile, so that the water migration in liquid and gas phase will be accelerated. Additionally, heating may also affect the properties of the buffer and rock materials, such as transition of clay minerals, alteration of swelling capacity, thermally-induced consolidation and hence increase in stiffness and strength. In spite of these effects the barrier functions of the natural and engineered barriers have to be kept up.

Finally, the boreholes, drifts and shafts will be sealed with plugs consisting of compacted clay-based mixtures and concrete to prevent access of groundwater to the repository and releases of radionuclides via drifts and shafts. Certain degrees of mechanical stiffness and strength, swelling capability during wetting, and low hydraulic conductivity of the seals/plugs enhance the sealing and healing process of the surrounding EDZ/EdZ and hence provide a water-tight sealing system. The whole operation phase could last for a period of time in the order of 100 years /BOC 10/.

1.1.2 Key processes during the post-closure phase

After closing the repository, the THMC processes in the EBS and the host rock will continue. The support system of the openings will degrade gradually. Under effects of wa-

ter pressure gradients in the saturated rock and suction potentials in the unsaturated backfill, the formation water will move toward the backfilled openings, resulting in a re-saturation process in the EDZ and the backfill. With increasing water content, clay minerals in the clay rock and the clay-based backfill tend to swelling. The pre-existing fractures in the EDZ and the large pores in the backfill will be sealed and swelling pressure may build up, mainly depending on the amount of expansive clay minerals, water saturation, and density or porosity of the backfill/seal materials and the host rock. Additionally, wetting also results in weakening of the clay rock and accelerates the rock creep deformation into the backfilled openings. The hydro-mechanical processes and the interactions between the backfill, the support lining, the EDZ, and the farfield rock, enhance the consolidation of the EDZ and the porous backfill materials and thus the confining function of the whole multi-barrier-system. In the nearfield around HLW containers, thermal impact on the processes is one of the most important concerns for the long-term safety assessment of a repository. Thermally-accelerated rock deformation and porewater migration may enhance the compaction of the EDZ and the backfill. With time, the heated rock and backfill are cooling down to the original rock temperature. The hydro-mechanical processes will become slower and tend to a new steady state. Establishment of a new equilibrium in a repository will take a very long time of tens of thousands of years.

Water resaturation may cause long-term geochemical processes in the nearfield involving EDZ, buffer, waste containers, and other support/lining materials. Dissolution of chemical species, their transport, and precipitation may occur, creating potentially a "geochemical damage zone – GDZ" /TSA 12/.

Degradation and corrosion of the metallic components and containers will produce gas. Gas may migrate preferably through the porous backfill, the re-sealed EDZ, and the interfaces between them. Gas migration may be controlled by advection-diffusion of dissolved gas, two-phase flow, dilatancy-controlled flow, and flow in macroscopic tensile fractures /MAR 08/, /BOC 10/, /FOR 13/. The last gas migration mechanism is only possible when the gas pressure becomes sufficiently high to generate fractures. Nevertheless, the gas production and migration has to be verified so that the integrity of the multi-barrier system is not impaired.

Generally, progressive closure of repositories in clay formations is to be expected due to creep of the surrounding host rock. Consolidation of both the EDZ and the backfill will lead to permanent confinement of the radioactive waste from the biosphere.

1.2 Research programme and objectives

For the last two decades, the feasibility of the disposal concepts has been intensively investigated in the Underground Research Laboratories (URLs) in the Callovo-Oxfordian argillite at Meuse-/Haute-Marne in France (MHM-URL) and in the Opalinus clay at Mont-Terri in Switzerland (MT-URL). The most important scientific activities are the investigations of the THMC properties and processes of the natural and engineered barriers by large/full-scale experiments under realistic repository conditions. The in situ experiments are supported by laboratory tests on samples for providing robust database for the host rock and the backfill/seal. On the basis of the knowledge from the experiments, constitutive models and computing codes have being developed for prediction of the coupled processes in the multi-barrier system. Results of the investigations serve as input for the long-term safety assessments of the potential repositories. GRS has participated in a great number of the international research projects in accordance with the German R&D programme /BMW 07/.

Following "Dossier 2005" /AND 05/, in which the most important outcomes of ANDRA's programme during the time period from 1999 to 2005 are summarized and evaluated, ANDRA launched a new geomechanical laboratory programme (called GL-programme) in early 2007 /AND 06/, /DEL 09/, /LEB 10/. The general objective of this programme is to provide more comprehensive and realistic models of the repository behaviour for the operation and the post-closure periods. It was divided into the following sub-objectives.

For the operating phase:

- Quantification of the efficiency of support bolts from excavation through to possible removal of lining, taking anchor and rock behaviour into account;

- Characterization of hydro-mechanical disturbance resulting from excavation and their evolution until the end of the operation phase;

- Characterization of the effects of the rheological deformation of the clay host rock (creep, micro-mechanisms, constitutive models);

- Determination of the conceptual model of the EDZ around the openings;

- Modelling of damage and rupture location (intensity and extent of the EDZ).

For the post-closure phase:

- Description of various physical and chemical processes of deformation taking hydrological conditions into account;

- Evaluation of the macroscopic deformation rate on the basis of the various deformation mechanisms;

- Clarification of relationships between long-term deformation and damage;

- Quantification of the thermal effects on rock behaviour;

- Quantification of mechanical and hydraulic sealing of the EDZ.

For the interactions between the host rock and EBS components:

- Characterisation of the swelling and transport properties and nonsaturated hydromechanical properties of compacted claystone backfill under consideration of effects of cementitious water and backfill installation techniques;

- Specification of the geotechnical properties of the backfill under consideration of effects of alkaline disturbance and long-term rock behaviour;

- Model prediction of the long-term performance of a drift in the potential repository involving the major phenomena of rock-plug interaction, alkaline disturbance, effects on fluid transport, and impact on the long-term safety.

As a partner, GRS has contributed to the ANDRA's GL-programme with the THM-TON research project funded by the German Federal Ministry of Economics and Technology (BMWi) under contract 02E10377 /THM 07/. At that time, a mine-by experiment was also foreseen to be conducted by excavation of a new gallery G08 in the MT-URL to investigate hydro-mechanical responses of the Opalinus clay to excavation /TD 06/.

The first part of the THM-TON programme was carried out from May 2007 to May 2013 with laboratory experiments, in situ measurements and numerical modelling covering most of the objectives mentioned above:

- Laboratory investigations on the Callovo-Oxfordian and Opalinus clay rocks

    − Examination of effective stress and swelling pressure in indurated clay rock by taking bound porewater into account

- Short-term deformation, damage and induced permeability change in the clay host rock, which will be produced by excavation of a repository

- Long-term deformation of the clay host rock, which controls the closure process of the repository openings and the integrity of the geological and engineered barriers

- Swelling capability of the clay host rock, which may dominate the sealing process of the EDZ when water flows through

- Recovery and self-sealing of fractures in the clay host rock, which is one of the most concerns in the assessment of the long-term performance and safety of the repository

- Thermal impact on the hydro-mechanical behaviour and the integrity of the clay host rock

- Laboratory investigations on excavated claystone and claystone-bentonite mixtures as backfill/sealing material

  - Compaction behaviour of claystone backfill, which controls the mechanical interactions with support linings (if existing) and the surrounding rock, and in turn determines the evolution of the backfill porosity and hydraulic conductivity

  - Permeability in relation with porosity, which dominates the fluid transport and thus the barrier function of the backfill/seal

  - Water retention and saturation, which determines the water saturation process, water storage capacity, water/gas two-phase flow, and buildup of swelling pressure in clay-based backfill/ seal

  - Swelling pressure in compacted claystone-bentonite mixtures as seal material, which is required for sealing of possibly remaining gaps within the seals and seal/rock interfaces and for supporting the surrounding rock against damage propagation

  - Thermal conductivity of buffer surrounding HLW containers, which controls the heat transfer and temperature distribution in the multi-barrier-system

- In situ investigation of hydro-mechanical responses of the Opalinus clay to the excavation of the gallery G08 within the mine-by (MB) experiment in the MT-URL

- Monitoring of long-term deformation of a borehole in the Opalinus clay at MT-URL (DM-A experiment)

- Numerical modelling and analysis of coupled hydro-mechanical processes in the Opalinus clay rock during the MB and DM-A experiments performed at MT-URL and coupled THM processes in the Callovo-Oxfordian argillite during the TED heating experiments conducted at MHM-URL.

Since September 2012, the THM-TON project has been merged into the EC DOPAS project – Full Scale Demonstration of Plugs and Seals /DOP 12/, to continue the investigations on the excavated claystone aggregate as backfill material and compacted claystone-bentonite mixtures as seal material.

In this report, main results obtained during the first project period (05.2007 – 05.2013) are presented. In Volume I, laboratory experiments and results obtained on the clay rocks and claystone-based backfill/seal mixtures are presented and discussed, while the in situ experiments and the accompanying numerical modelling work are reported in Volume II.

The experimental and theoretical studies of the THM behaviour of the clay rocks include examination of effective stress in highly-consolidated natural clays, short-term deformation and damage, long-term creep behaviour, response to moisture change, thermal effects, and self-sealing of damaged claystone. These will be illustrated in Chapter 2. Following that, the geotechnical characterizations of the excavated claystone and claystone-bentonite mixtures as backfill/seal material are shown in Chapter 3, including compaction behaviour, permeability to gas or water in relation with compacted porosity, water retention and resaturation, swelling capacity, and thermal properties. The most important results and conclusions will be summarized in Chapter 4.

2 Clay host rock

2.1 Examination of stress concept

Up to now argillaceous rocks and compact clays are generally treated as conventional porous media, in which porewater is assumed to be freely migrating and physico-chemical interactions of water with clay are not explicitly taken into account. However, in natural argillaceous rocks, a considerable fraction of the porewater is adsorbed on the internal and external surfaces of clay particles due to physico-chemical interactions, and thus stress between clay particles must be transferred through the adsorbed porewater rather than directly via solid-to-solid grain contacts. So the important question arises whether the conventional views to the nature of effective stress are applicable to argillaceous rocks and compact clays. The conventional Terzaghi's effective stress defined as the interparticle stress due to direct solid-to-solid contacts between particles has been more theoretically examined for swelling clays such as compacted bentonite, for instance by Mitchell /MIT 76/, Horseman et al. /HOR 96/, Rodwell et al. /ROD 99/, Sridharan /SRI 02/ and Yong et al. /YON 12/. It is recognized that the effective stress in compacted water-saturated clays is partly or even fully transferred by the adsorbed porewater between clay particles. For argillaceous rocks with less expansive clay minerals but more non-clay mineral components, however, the definition of effective stress is still unclear and is currently under debate. Recently, our laboratory experiments have provided strong evidence for the significant role of bound porewater as a load-bearing element in argillaceous rock /ZHA 07b/, /ZHA 10a/, /ZHA 10b/. This fundamental issue will be investigated here theoretically and experimentally in order to highlight the important role of the bound porewater in a dense clay-water system, to improve the understanding of such a system and to increase confidence in models for strongly coupled thermo-hydro-mechanical-chemical processes in argillaceous formations that host radioactive waste repositories and other engineering constructions. It begins with a brief overview of the typical microstructures of the highly-indurated Callovo-Oxfordian and Opalinus clay rocks, both being investigated as potential host rocks for repositories. On the basis of the microstructure, a stress concept will be derived for argillaceous rocks and then validated by laboratory experiments specially designed and performed on the clay rocks.

2.1.1   Microstructure and porewater

The current state of an argillaceous formation results from its specific geological history over hundreds of millions of years, beginning with deposition and aggregation of fine-grained particles in sea water, followed by sedimentation and consolidation with a concurrent expelling of porewater, development of diagenetic bonds between mineral particles, and eventually erosion and uplift. The typical microstructure and the state of porewater in the Callovo-Oxfordian argillite (COX) at Bure in France /AND 05/ and the Opalinus clay (OPA) at Mont Terri in Switzerland /MAZ 08/, /BOC 10/ are illustrated schematically in Fig. 2.1 and Fig. 2.2. Both clay rocks have been over-consolidated to low porosities of 14 – 18 %. The COX argillite contains 25 – 55 % clay minerals, 20 – 38 % carbonates and 20 – 30 % quartz, while the OPA clay has higher clay content (58 – 76 %), less carbonates (6 – 24 %) and quartz (5 – 28 %). Note that both clay rocks do not contain significant quantities of expansive clay minerals such as smectite: 13 – 23 % in the COX argillite /TOU 07/ and 5 – 20 % in the OPA clay /PEA 03/.
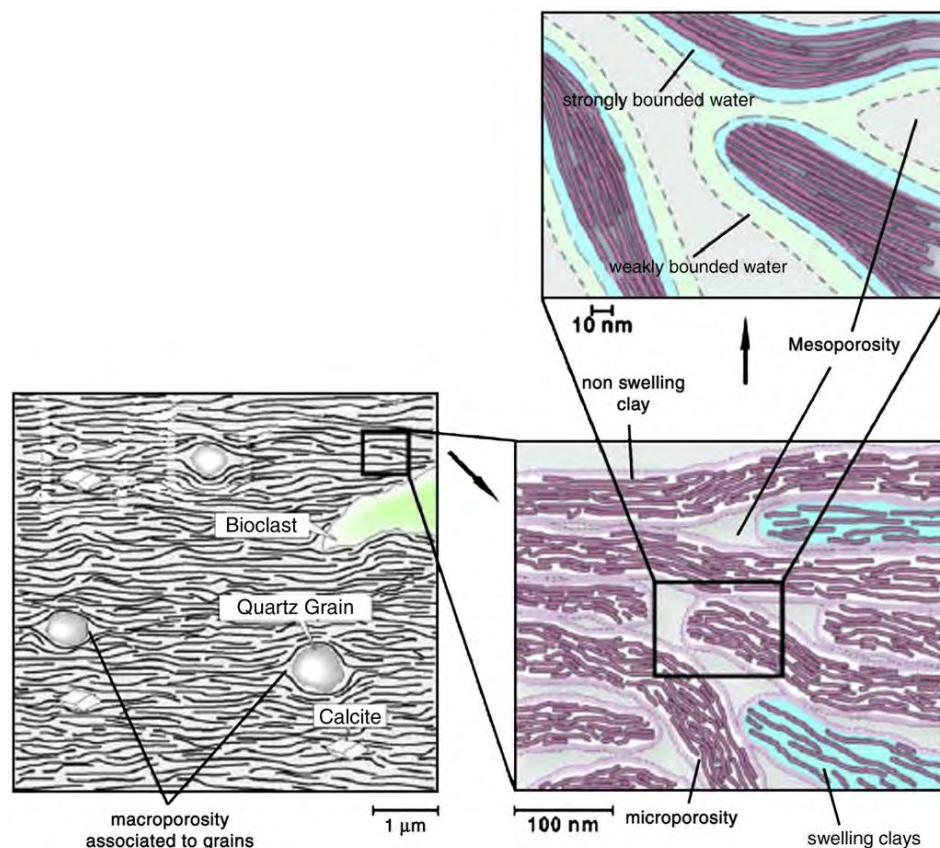

Fig. 2.1   Schematic sketch of microstructure of the Callovo-Oxfordian argillite
   /AND 05/
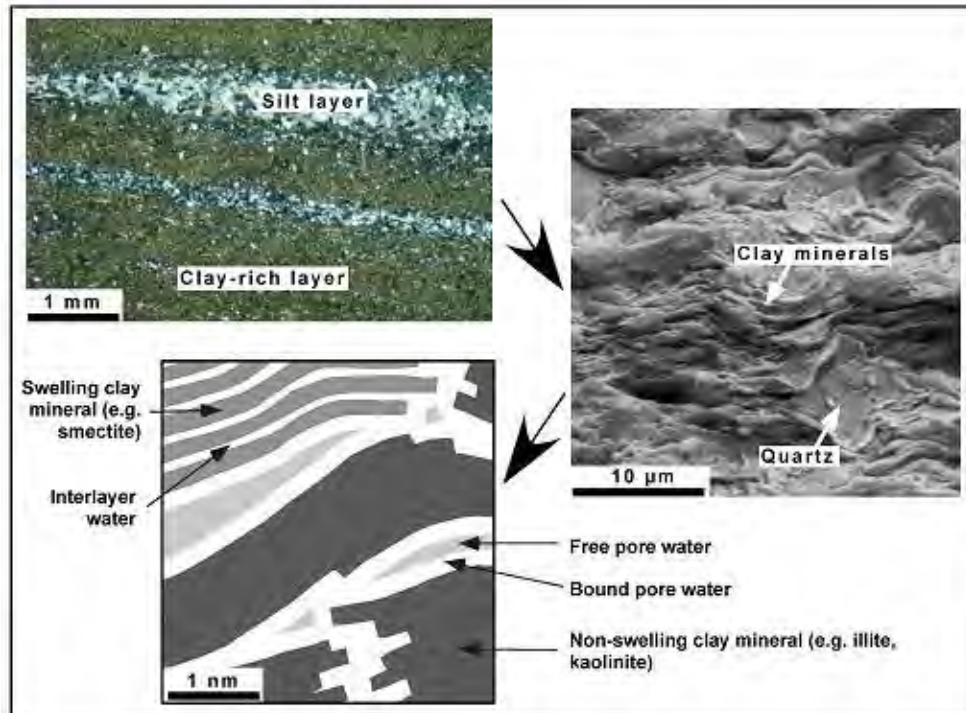
Fig. 2.2 Schematic sketch of microstructure of the Opalinus clay according to /MAZ 08/ and /BOC 10/

Argillaceous rocks have a clayey matrix embedding other mineral particles (quartz, calcite, and others). The clayey matrix consists of clay particles with strongly adsorbed interlayer water within the sheet structures and with strongly to weakly adsorbed water at the external surfaces. Large pores are filled with water that can freely migrate. The pore sizes in clay rocks mainly range from nano-scale (< 2 nm) in between the parallel platelets of the clay particles to micro- and meso-scale (2 – 50 nm) between solid particles. Fig. 2.3 shows the pore size distributions of the COX argillite /AND 05/ and OPA clay /KEL 11/. The fraction of the pores smaller than 20 nm amounts to about 60 – 80 % and the fraction of macro-pores (> 50 nm) is less than 10 % for both clay rocks. The thickness of the adsorbed water-film between clay particles is the most important factor governing the state and properties of the clay rock. For porosities of 12 – 21 % and specific surfaces of 20 – 160 m^{2}g^{-1}, an average water-film thickness of 0.6 to 10 nm has been calculated /ROD 99/. There is experimental evidence that water in micro-pores smaller than 7 – 8 nm is bound to the surface of the clay particles /HOR 96/. Comparison with the calculated water-film thicknesses indicates that the porewater in the COX and OPA clays with porosities of 14 – 18 % is predominantly bound by these surface forces.
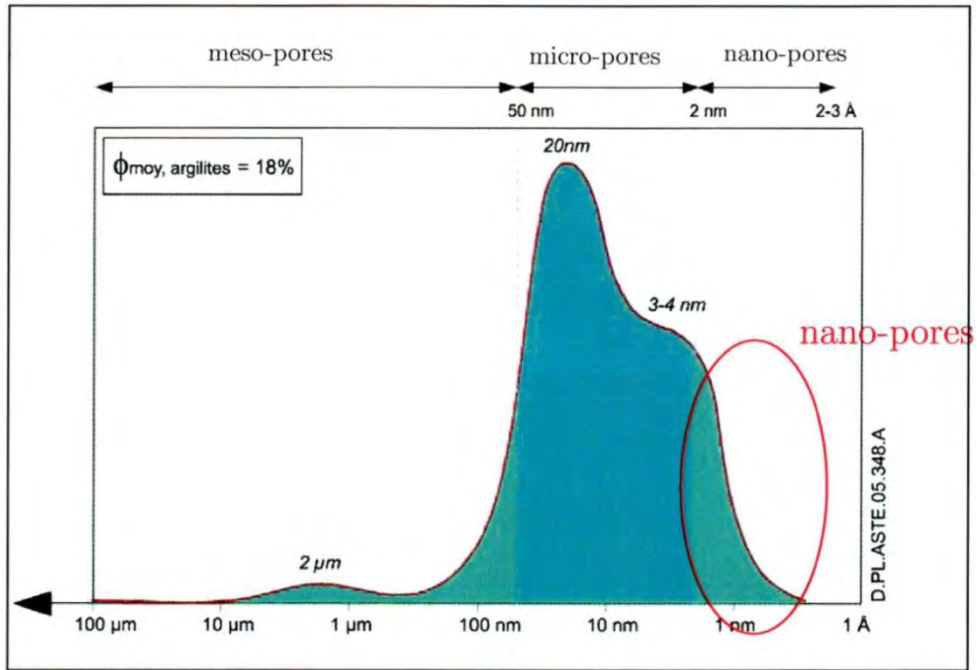
COX argillite
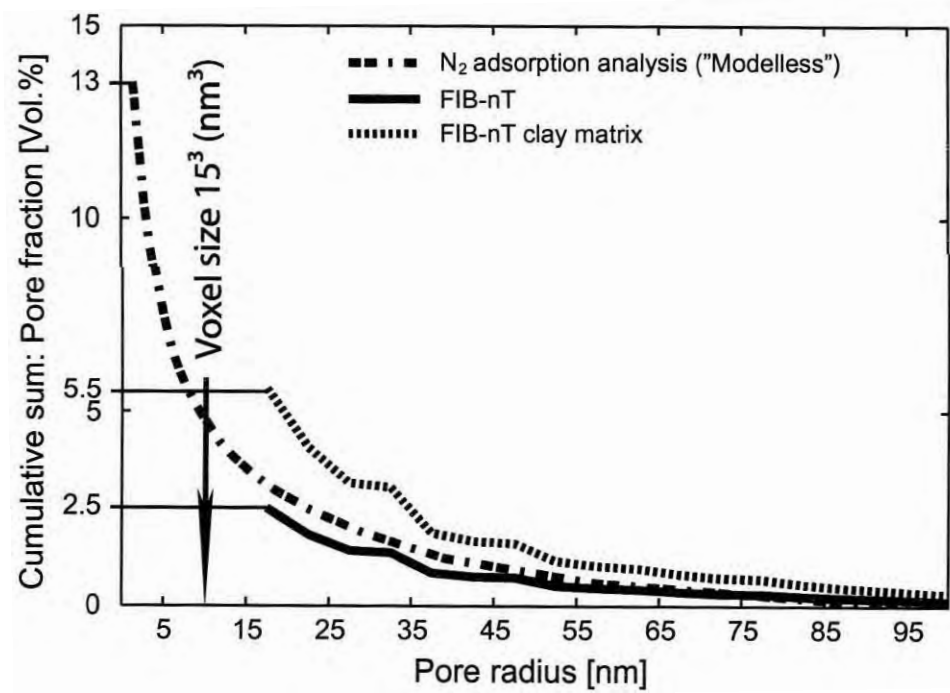
OPA clay

Fig. 2.3 Pore size distributions of the Callovo-Oxfordian argillite /AND 05/ and the Opalinus clay /KEL 11/

2.1.2 Effective stress and swelling pressure

Consider a representative volume of a saturated clay rock that is subject to compressive boundary stresses (σ_v/σ_h = vertical/horizontal stress) and immersed in an aqueous solution at the pressure p_w as schematically illustrated in Fig. 2.4. The external liquid is assumed to be chemically in equilibrium with the sample. The liquid pressure is transferred to the porous clay-water system and is equivalent to the pressure in large pores occupied by free bulk water. Clay particles including interlayer water are taken as microstructural units since the water molecules in the interlayer are strongly adsorbed within the sheet structures and immobile under usually encountered pressure gradients. The clay particles are connected through the double-layers. Under external mechanical compression the particles are squeezed together so that the bound water-films can touch and overlap each other, resulting in a repulsive force between them. The contacts of clay particle with an accessory mineral (carbonate, quartz and others) or of two accessory minerals can be considered to be a solid-to-solid contact.
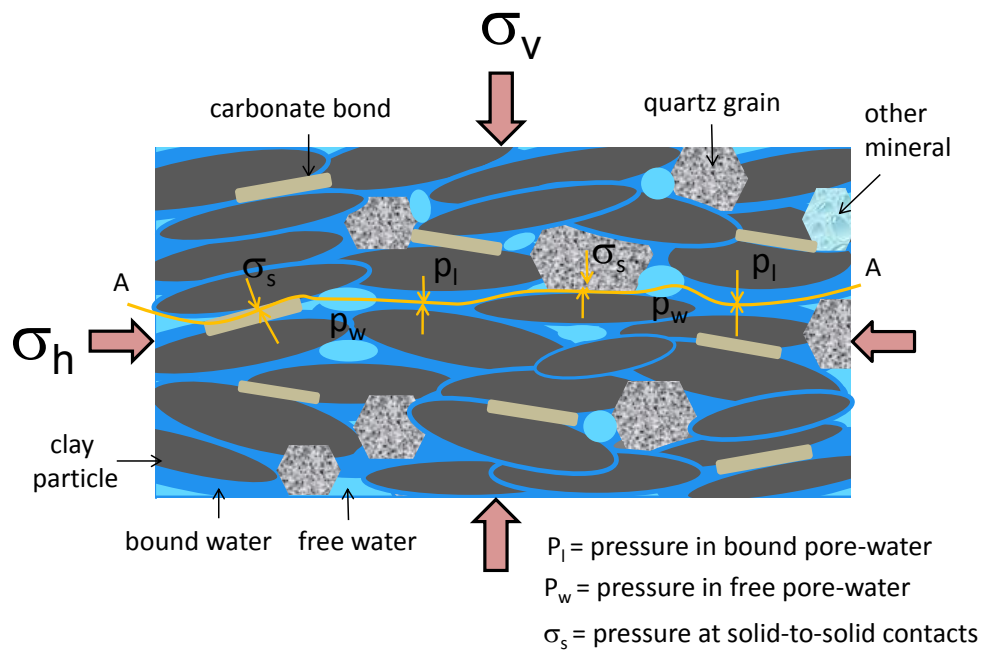

Fig. 2.4 Stress state in a representative volume of a saturated clay mass

Since the stress conditions at contact areas, rather than within particles, are of primary concern in a stress analysis of the porous clay-water system, a wavy surface that passes through contact areas between particles is of interest. Any wavy plane A-A can be selected in the clay sample, passing partly through the bound water-film between clay particles, partly through solid-solid contact area between mineral grains, and partly

through the large pores occupied by free water. At equilibrium, there must be a balance among all forces on the wavy surface, namely the interparticle forces at the solid-solid contacts as well as the pressure in the bound water-film and in the free porewater, and the external load. Equilibrium requires that

$$\sigma_t A = \sigma_{is} A_s + p_l A_l + p_w A_w \tag{2.1}$$

where

$\sigma_t A$ = the total normal force externally applied on the surface A,

$\sigma_{is} A_s$ = the total normal force acting on the solid-solid contact area A_s with the local total stress σ_{is},

$p_l A_l$ = the total normal repulsive force acting in the water-film section A_l between clay particles with the local total pressure p_l,

$p_w A_w$ = the pressure p_w acting on the surface A_w in the large pores occupied by free water.

Analogously, an equilibrium equation for the interparticle shear forces at the wavy plane should be the same formulation as (2.1).

The pressure p_l acting in the interparticle bound porewater consists of two components: the pressure p_w transmitted from the free water in large pores and the local net disjoining pressure π_D contributed from electrostatic double-layer interactions, structural forces, van der Waal's forces, and from any other identified physico-chemical mechanisms /MIT 76/, /HOR 96/, /YON 12/:

$$p_l = \pi_D + p_w \tag{2.2}$$

The local total stress σ_{is} acting on the solid-solid contact area is the sum of the porewater pressure p_w and the net local contact stress σ_{is}'

$$\sigma_{is} = \sigma_{is}' + p_w \tag{2.3}$$

Substituting Eqns. (2.2) and (2.3) into Eqn. (2.1), the equilibrium equation becomes

$$\sigma_t A = (\sigma_{is}' + p_w) A_s + (\pi_D + p_w) A_l + p_w A_w$$

or

$$\sigma_t A = \sigma_{is}' A_s + \pi_D A_l + p_w A \tag{2.4}$$

Division of all terms by A converts the forces to stresses per unit area of cross section

$$\sigma_t = \sigma'_{is} \frac{A_s}{A} + \pi_D \frac{A_l}{A} + p_w \frac{A}{A}$$

or

$$\sigma_t = \sigma'_{is} \alpha_s + \pi_D \alpha_l + p_w$$

$$\sigma_t = \sigma_s + \sigma_l + p_w \tag{2.5}$$

where the term $\sigma_s = \sigma'_{is} \alpha_s$; $\alpha_s = A_s/A$ represents the average net force across solid-solid contact area divided by the total cross sectional area, and $\sigma_l = \pi_D \alpha_l$ with $\alpha_l = A_l/A$ is the average net repulsive force acting in the bound water-film area divided by the total cross section. The interparticle force divided by the total area is the average interparticle stress or the effective stress in common soil/rock mechanics usage:

$$\sigma_{eff} = \sigma_t - p_w = \sigma_s + \sigma_l \tag{2.6}$$

This effective stress concept clearly suggests that the interparticle or effective stress in a compact clay-water system consists of two parts: one acting at solid-solid contact area and another one in interparticle bound porewater.

Horseman et al. /HOR 96/ argue that the average disjoining pressure over the mid-planes of water-films between particles, $\sigma_l = \pi_D \alpha_l$, is equivalent to the measurable swelling pressure acting on the walls of a rigid permeable box containing the clay sample. In clay-rich and less cemented materials, the effect of solid-solid contacts between particles disappears resulting in $\alpha_s = A_s/A \to 0$ and $\sigma_s = \sigma'_{is} \to 0$. Thus the effective stress is carried by the bound porewater and is equivalent to the swelling pressure, $\sigma_{eff} = \pi_D \alpha_l$. Conversely, if a clay sample contains large amounts of non-clay particles and/or strongly cemented particles, the effect of bound water is negligible, $\alpha_l = A_l/A \to 0$, and $\sigma_l = \pi_D \alpha_l \to 0$, and thus the externally applied load will be transferred through the solid-solid grain contacts, $\sigma_{eff} = \sigma_s$. This puts the meaning of the conventional Terzaghi's effective stress into perspective /TER 96/.

If the chemical equilibrium in the clay-water system is perturbed, for instance by exposing it to pure water, an osmotic potential or pressure π_O will be established between the porewater and external water. So the total pressure acting in the interparticle bound porewater (2.2) becomes

$$p_l = \pi + p_w = \pi_D + \pi_0 + p_w \tag{2.7}$$

This local water pressure in narrow pores at equilibrium with an external aqueous solution exceeds the pressure in the external reservoir or in the large pores by $(\pi_D + \pi_0)$. This local pore pressure should be a threshold entry pressure for advective transport into the narrow pore space. Correspondingly, the swelling pressure of the saturated clay increases to

$$\sigma_l = \pi\alpha_l = (\pi_D + \pi_0)\alpha_l \tag{2.8}$$

The fraction parameter α_l should be equivalent to the relative effective degree of saturation S_e of the interparticle bound porewater

$$\alpha_l = S_e = \frac{S_b - S_r}{S_s - S_r} = \frac{(S_l - S_0) - S_r}{(1 - S_0) - S_r} \tag{2.9}$$

where S_l, S_0, S_b are the degrees of saturation of total, free, and bound porewater, respectively; $S_b = S_l - S_0$ represents the sum of the interparticle and interlayer water saturation; $S_s = 1 - S_0$ is the full saturation with bound porewater S_b and $S_s = 1$ as $S_0 = 0$; S_r is the residual saturation of the remaining water in the interlayer and adsorbed on the external surfaces as the clay particles are disconnected; and $S_b - S_r$ is the effective saturation of the interparticle bound porewater. Fig. 2.5 illustrates schematically the definition of the water saturation degrees in a clay sample.
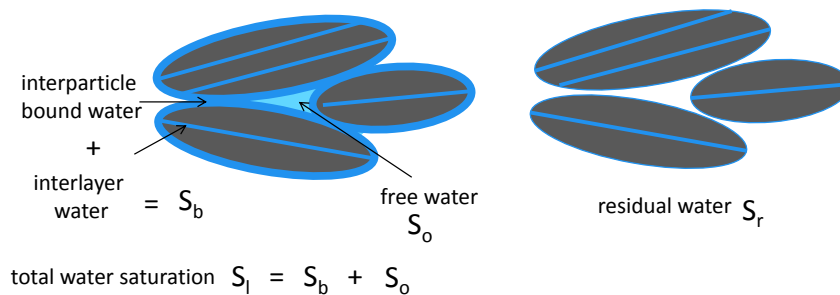
Fig. 2.5   Saturation of total, free, interlayer and interparticle bound porewater in saturated state, and residual porewater after desaturation to disconnection between clay particles

Substituting eq. (2.9) into (2.8), a linear relationship of swelling pressure to effective saturation of bound porewater is obtained

$$\sigma_l \;=\; \pi \cdot S_e \;=\; \pi \cdot \left(\frac{S_l - S_0 - S_r}{1 - S_0 - S_r}\right) \tag{2.10}$$

In a saturated clay-water medium where $S_b = S_s = 1 - S_o$ and $S_e = 1$, the swelling pressure is equal to the average disjoining pressure $\sigma_l = \pi$. When the clay is desaturated to $S_b < S_r$ or $(S_l - S_o) < (1 - S_o)$, the fraction of the effective bound porewater reduces, hence the swelling pressure decreases and tends to zero as the neighbouring clay particles are fully disconnected, $S_l \rightarrow S_r$. Resaturation on the contrary leads to a recovery of the water saturation and the swelling pressure, $\sigma_l \rightarrow \pi$ as $S_l \rightarrow 1$, $S_b \rightarrow S_s$. If no free water exists in argillaceous rocks and highly compacted clays so that $S_0 = 0$, equation (2.10) becomes

$$\sigma_l \;=\; \pi \cdot \left(\frac{S_l - S_r}{1 - S_r}\right) \tag{2.11}$$

It is straightforward to obtain the dependence of the effective stress upon the water saturation by substituting eq. (2.10) into (2.6)

$$\sigma_{eff} \;=\; \sigma_s + \pi \cdot S_e \;=\; \sigma_s + \pi \cdot \left(\frac{S_l - S_0 - S_r}{1 - S_0 - S_r}\right) \tag{2.12}$$

and for $S_0 = 0$,

$$\sigma_{eff} \;=\; \sigma_s + \pi \cdot S_e \;=\; \sigma_s + \pi \cdot \left(\frac{S_l - S_r}{1 - S_r}\right) \tag{2.13}$$

The water saturation of a clay rock is controlled by the suction, which is related to the relative humidity in the pore atmosphere /FRE 93/

$$s \;=\; \frac{RT}{v_{wo}\,\omega_v} \ln\left(\frac{p_{va}}{p_{vp}}\right) \;=\; -\frac{RT}{v_{wo}\omega_v} \ln(RH) \tag{2.14}$$

where s is the matric suction, T the absolute temperature, R the gas constant, v_{wo} the specific volume of water or the inverse of density of water, ω_v the molecular mass of water vapour, p_{va} the partial vapour pressure of porewater, p_{vp} the vapour pressure of pure water, and $RH = p_{va}/p_{vp}$ the relative humidity.

The water saturation S_l at a given humidity RH can be determined by measurements of water content w, water density ρ_w, dry density of the clay ρ_d, and porosity $\emptyset$

$$S_l = \frac{\rho_d w}{\rho_w \, \emptyset} \qquad (2.15)$$

The relationship of water saturation and suction at equilibrium is usually called "water retention curve". It is often mathematically described by the approach of van Genuchten /VAN 80/

$$S_l = \left[1 + \left(\frac{S}{P} \right)^{\frac{1}{1-\beta}} \right]^{-\beta} \qquad (2.16)$$

where P and β are the material parameters.

The stress concept derived above provides a reasonable view to the nature of the effective stress in argillaceous rocks and forms the fundamental basis for studying the coupled hydro-mechanical behaviour. However, it needs to be validated by experiments under various conditions.

2.1.3 Experimental observations

Various kinds of laboratory experiments were designed and carried out on the COX and OPA argillaceous rocks to investigate responses of argillaceous rocks to moisture change, to determine their swelling capabilities, and particularly to validate the newly derived stress concept for natural clays. The stress state and hydrometric conditions in the nearfield around a repository are taken into account in the tests. The host rock in the nearfield is subject to biaxial or even axial stress conditions due to the relief of the radial stress component. It is also affected by the ventilation of air with varying humidity, backfilling with unsaturated materials, and water flow from the farfield. Major experimental findings will be presented as follows.

2.1.3.1 Stress response to humidity change

The so-called uniaxial swelling test method was developed for the investigation of the stress response to humidity changes. Fig. 2.6 illustrates the test setup. A cylindrical

clay sample of 40 mm diameter and 40 mm length is axially pre-loaded and then fixed at unconfined lateral condition in a desiccator. Air with varying humidity is circulated around the peripheral surface of the sample. Response of the axial stress to humidity change is monitored by a pressure sensor installed at the bottom, while free strain in radial direction is recorded by two LVDT displacement transducers positioned opposite-ly at the mid-height of the sample. Variations of water content or saturation are meas-ured on an accompanying sample in the desiccator. It is also possible to measure the axial swelling pressure in volume-constraint condition, where the sample is inserted in a rigid porous cylinder through which migration of water vapour and fluid is allowed.

The test programme and the basic charateristics of the COX and OPA samples are summarized in Tab. A.1. All the samples were extracted from boreholes drilled horizontally or parallelly to the bedding planes. The results of axial stress and radial strain measured on axially-fixed and laterally-unconstraint samples as well as the data of water content and free swelling strain recorded on unconfined samples are plotted in Fig. A.1 to Fig. A.8 for each test in correspondence with the applied air humidity.

Fig. 2.7 shows the typical response of the uniaxial stress to humidity change observed on several COX samples. They were axially pre-loaded to different levels of $\sigma_a = 3$ to 16 MPa while no lateral stress was applied, $\sigma_r = 0$, and then axially fixed, $\Delta\varepsilon_a = 0$.

- Firstly, the more or less desaturated samples were wetted at 100 % air humidity for several days (except for the sample depicted in Fig. 2.7c). As a result, the axial stress increased by 1 – 4 MPa up to 11 – 17 MPa respectively and then decreased slightly due to moisture-induced softening of the material under unconfined lateral condition. The peak stresses are coincident with the uniaxial strength values of 10 – 14 MPa obtained on the fully water-saturated and "over-saturated" COX sam-ples (w = 7.4 – 7.7 %) in conventional uniaxial compression tests (cf. Fig. 2.56).

- Secondly, the samples were dried by stepwise decreasing humidity down to $RH \approx 10$ %, causing loss of the adsorbed porewater. As a consequence the stress decreased nearly to zero, $\sigma_a = 0 - 0.5$ MPa, except for one sample with a high carbonate content of ~30 % (Fig. 2.7d). This suggests that the residual stress carried by solid-solid grain contacts is negligibly small for the COX samples, $\sigma_s = \sigma'_{is}\alpha_s \approx 0$.

a. axial-fixed/lateral-unconstraint   b. volume-constraint

c. testing system
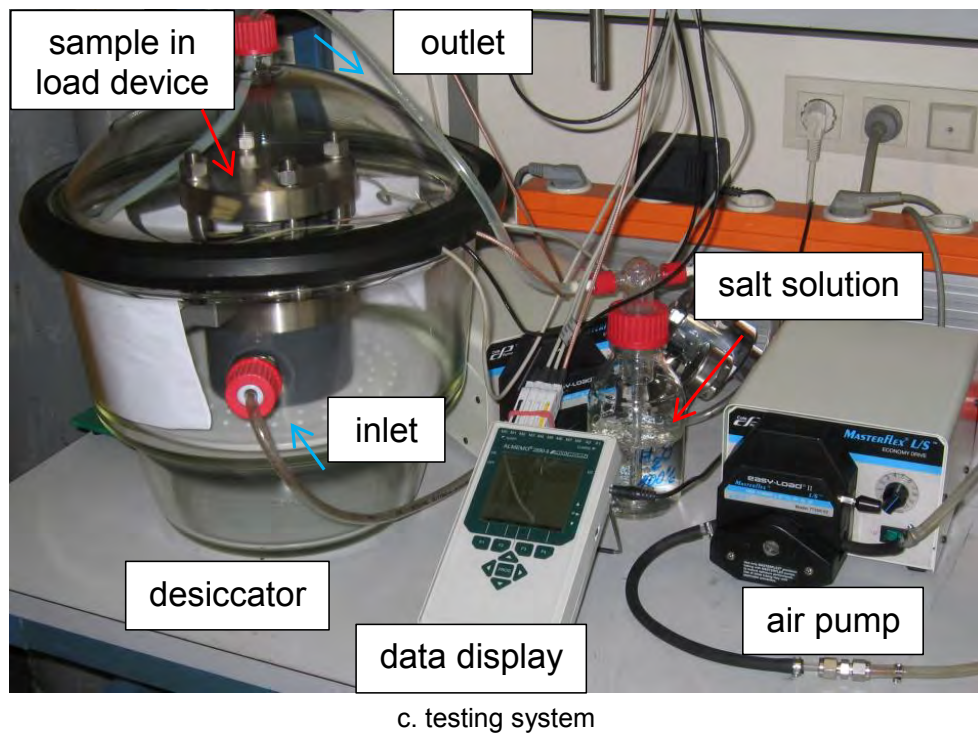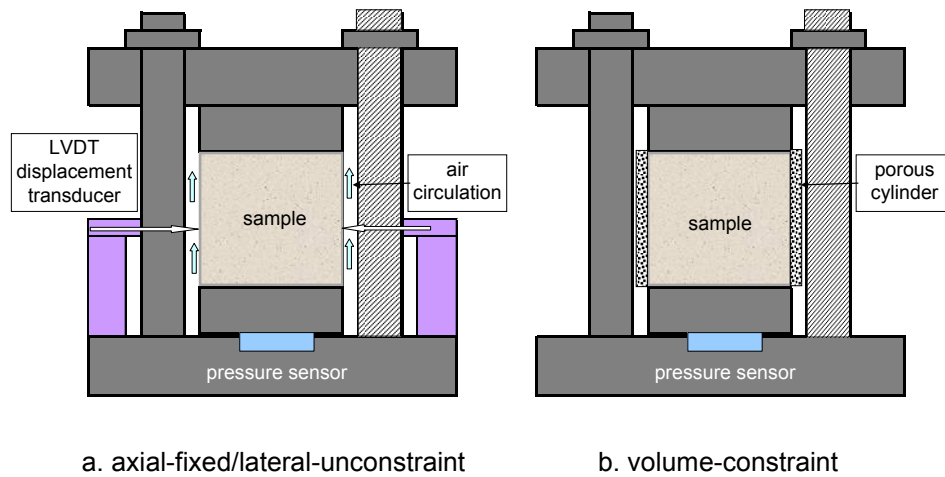
**Fig. 2.6**   Setup of a suction-controlled uniaxial swelling test on claystone

- Increasing the humidity at the sample surface again let the water molecules re-enter the pores, being adsorbed on internal and external surfaces of the clay parti-cles, form double-layers overlapping in narrow pores and buildup repulsive forces against the rigid confinement in axial direction. The maximum pressure buildup at RH = 95 – 100 % was quite high at 10 – 11 MPa. The high swelling pressure com-ponent in the effective stress strongly suggests that the interparticle bound porewa-ter plays the most important role in the transfer of effective stress in dense clay-water media. Note that the recorded swelling pressures are in the same magnitude as the lithostatic pressure at the location where the samples had been taken from,

at the -490 m level of the MHM-URL: the major horizontal stress there amounts to $\sigma_H \approx 16\,\text{MPa}$, the vertical and the minor horizontal stress to $\sigma_v \approx \sigma_h \approx 12.5\,\text{MPa}$ /AND 05/. However, the deviatoric stresses carried by the bound porewater in the samples ($\Delta\sigma = \sigma_a$ *at* $\sigma_r = 0$) are much higher than the original in situ deviatoric stress of $\Delta\sigma = \sigma_H - \sigma_h \approx 3.5\,\text{MPa}$.
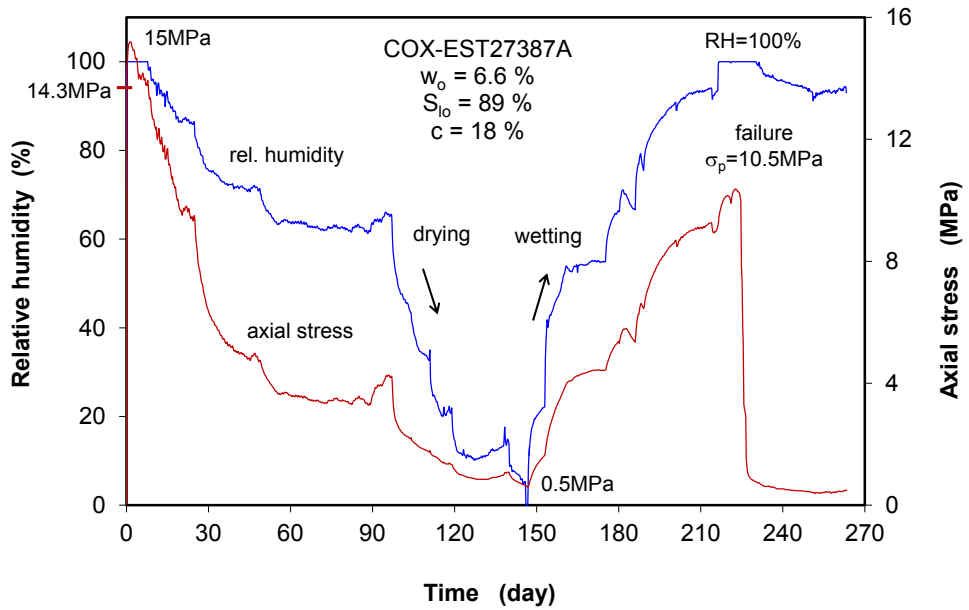
(a) pre-loaded at 14.3 MPa
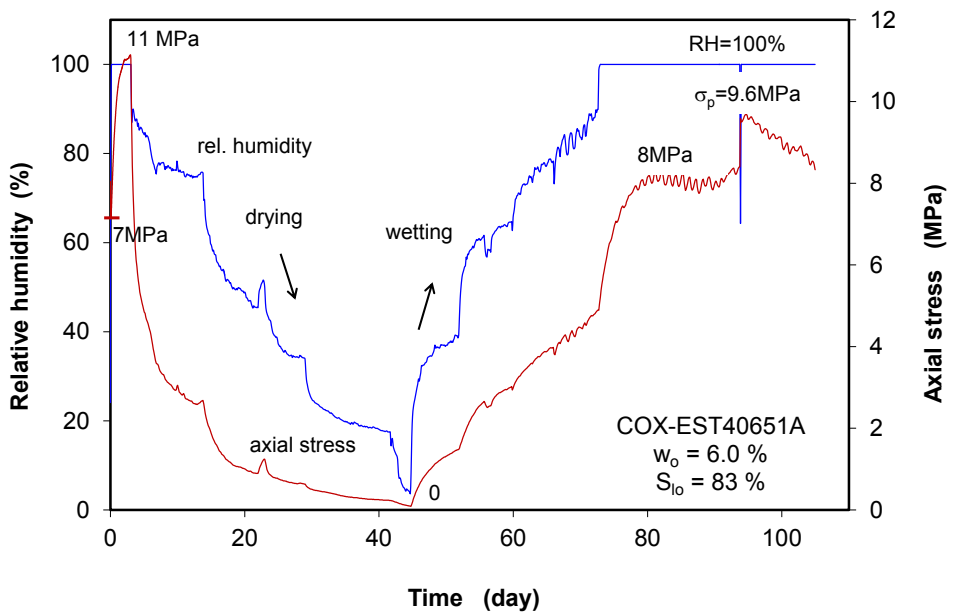
(b) pre-loaded at 7 MPa
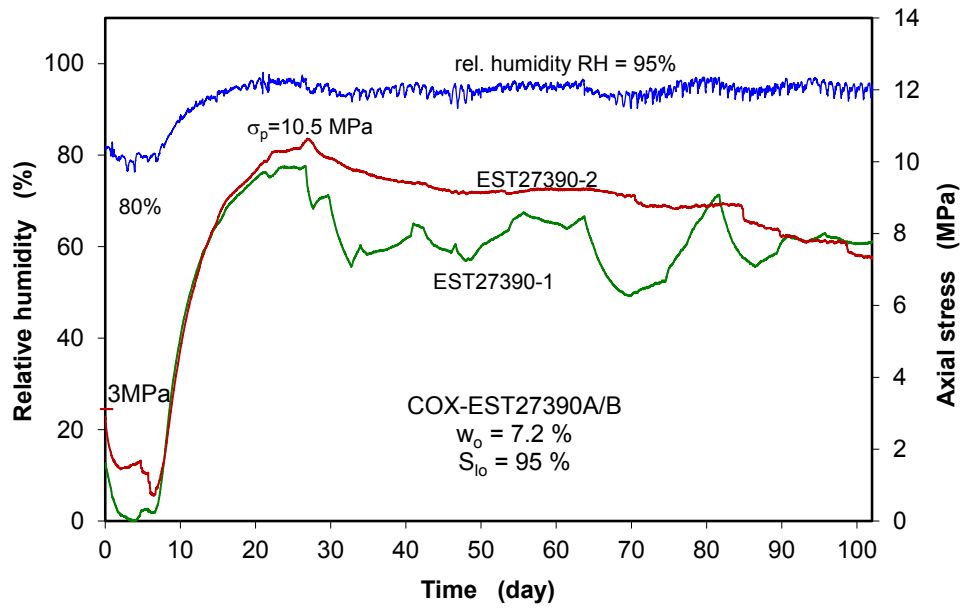
(c) pre-loaded at 2/3 MPa
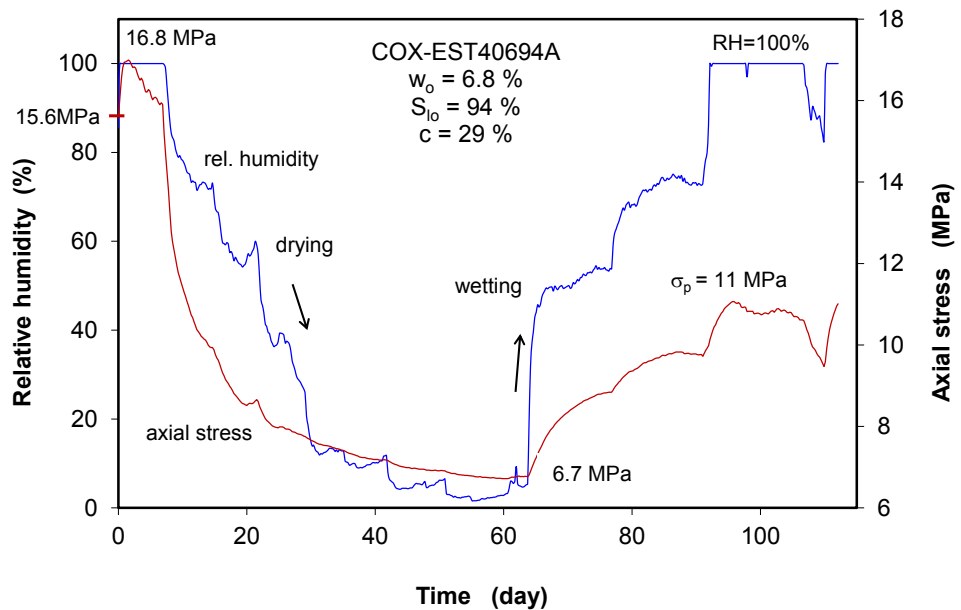
(d) pre-loaded at 15.6 MPa

Fig. 2.7   Response of axial stress to humidity change observed on COX samples at different pre-loads

The same stress response was also observed on OPA samples with a high clay content of ~65 % and a low carbonate content of ~8 % (see Fig. 2.8). A very low residual stress of 0.5 MPa was recorded after drying at $RH \approx 10$ %. The maximum axial stress was measured to be 4.5 – 5.5 MPa after full resaturation, thus falling also into the range of the

intermediate and major principal stresses $\sigma_2 = 4 - 5$ MPa and $\sigma_1 = 6 - 7$ MPa at the sampling locations in the ULR at Mont Terri /BOS 03/.
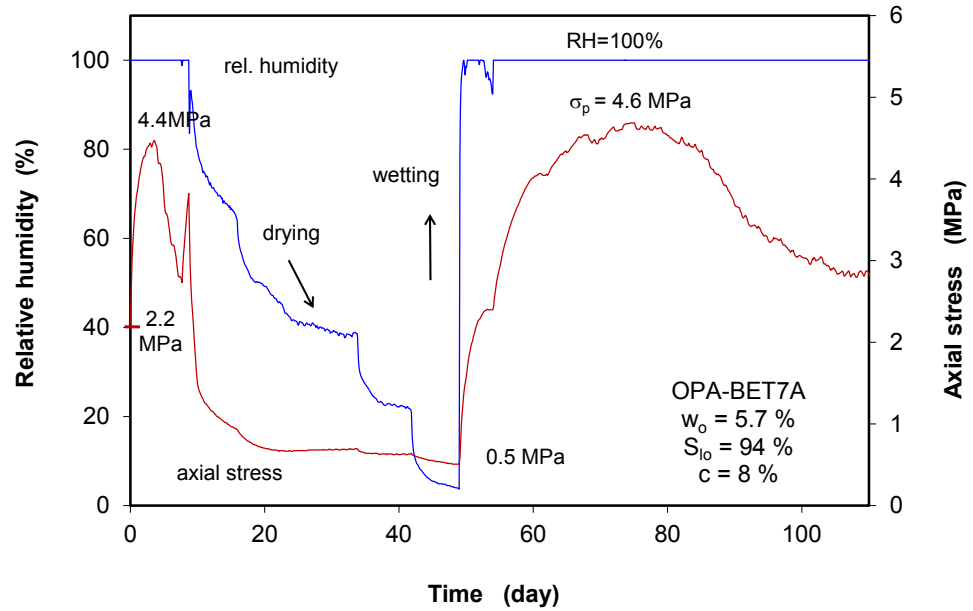
(a) high initial saturation
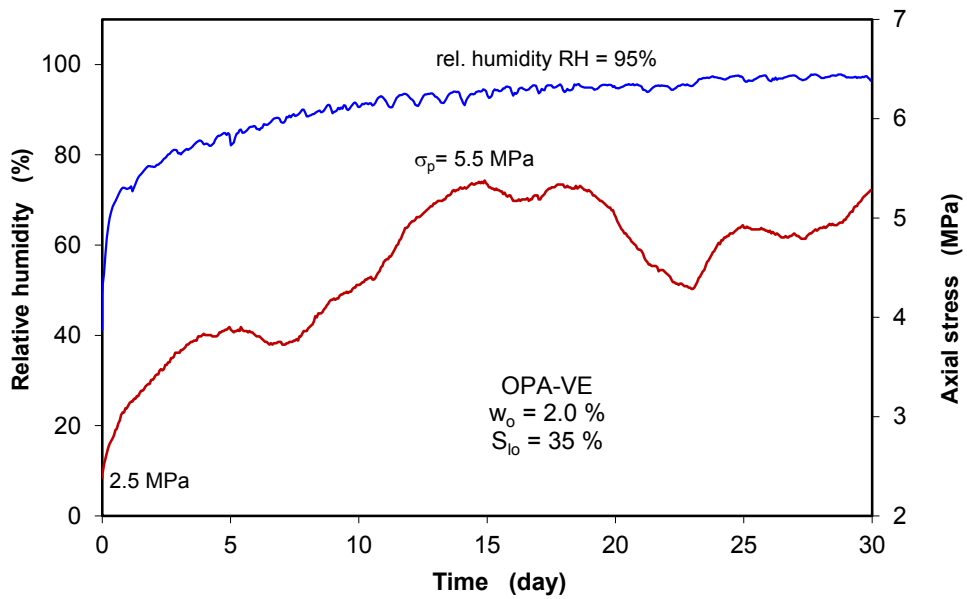
(b) low initial saturation

Fig. 2.8 Response of axial stress to humidity change observed on OPA samples at different initial water saturation degrees

In order to determine the swelling capability of heated argillaceous rocks, three COX samples were pre-heated at 100 to 120 °C and dried out. They were resaturated at in-

creased humidity levels from RH = 15 % to 100 % over 5 – 8 months. During this time the water content increased to 8 – 10 % and a significant stress increase from the pre-loads of 1 – 2.5 MPa to the maximum levels of 4.5 – 5 MPa was observed (Fig. 2.9). This result indicates a high swelling potential of the COX clay rock after heating up to 120 °C.
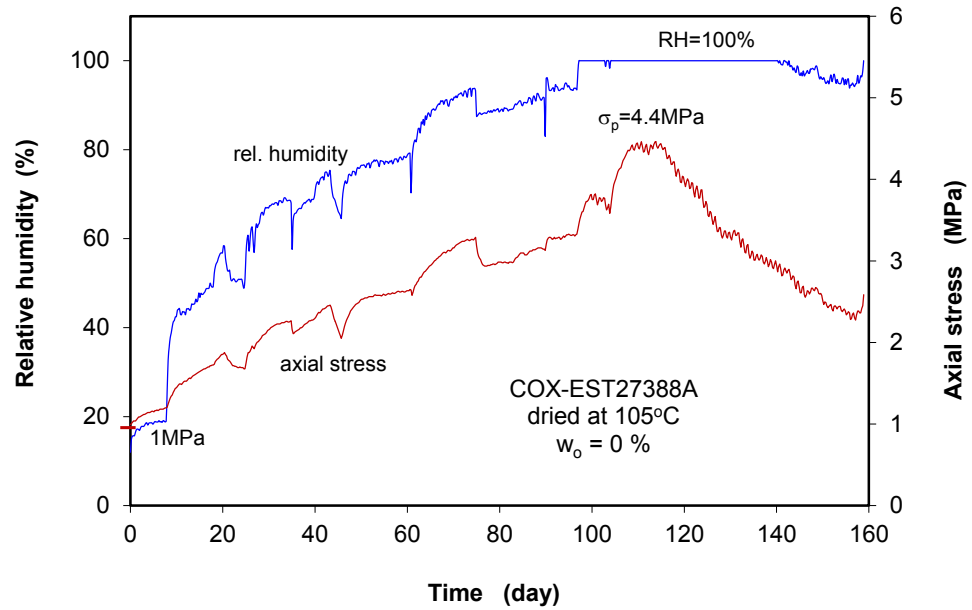
(a) pre-heated at T = 105 °C
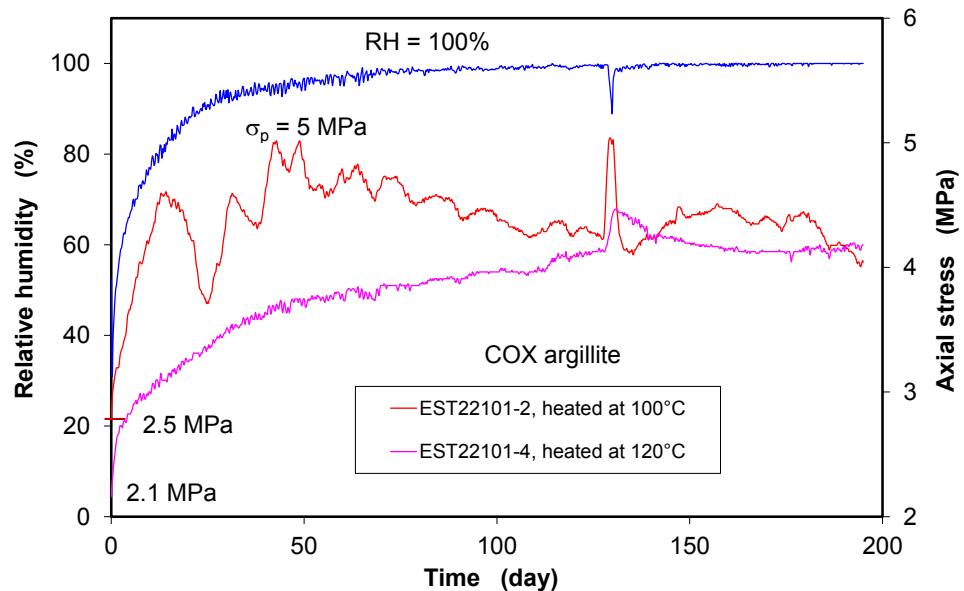
(b) pre-heated at T = 100 °C/120 °C

Fig. 2.9   Response of axial stress to humidity change observed on COX samples heated at 100 °C – 120 °C

Generally, the observed phenomenon of stress relief by drying and stress increase by wetting reflects that the interparticle bound porewater in the clay rocks supports the externally applied loads as high as the lithostatic stresses. Since the studied clay rocks do not contain significant quantities of expansive clay minerals, the high swelling pressures should be developed between the external surfaces of densely-packed clay particles by mechanisms which are similar to those operating during interlayer swelling /HOR 96/. Additionally, the buildup of the uniaxial swelling pressure without lateral confinement confirms the tensor expression of the effective stress in dense clay-water media. Horseman et al. /HOR 96/ and Rodwell et al. /ROD 99/ have already indicated that the stresses in the water-film between the clay platelets must be described by a second-rank tensor.

Furthermore, the test data are used to check the approaches for effective stress and swelling pressure as a function of water saturation (eqns. (2.10) – (2.13)) that were proposed for argillaceous rocks. Firstly, the matric suction can be calculated from the humidity values applied during the tests using eq. (2.14). Secondly, according to eq. (2.15) the degree of water saturation at a given suction is a function of water content and porosity which have been determined from the accompanying samples. The dependency of suction on water saturation – the water retention curve – can be described by the Van Genuchten model (eq. (2.16)).

Fig. 2.10 shows the water retention curves established by neglecting the small differences from wetting and drying paths. The associated parameter values are determined to be P = 50 MPa and β = 0.5 for the COX argillite and P = 23 MPa and β = 0.4 for the OPA clay. Most of the samples were almost or fully saturated at vanishing suction ($s \approx 0$). The long saturation tests previously performed over 8 months /ZHA 10a/, /ZHA 10b/ showed that the unconfined claystones are able to take up a great amount of water of up to 10 – 18 % at $s \approx 0$, more than that of 7.0 – 7.5 % in the naturally-confined and saturated rock mass. This suggests that most (if not all) of the porewater in the very dense clay rocks is adsorbed strongly on the mineral surfaces and weakly far from there. So it is reasonable to assume that the saturation of free porewater is negligible small, $S_o \approx 0$, and hence $S_l \approx S_b$ in eqns. (2.10) and (2.12). Therefore, equation (2.11) for swelling pressure and equation (2.13) for effective stress may be applicable for the clay rocks.
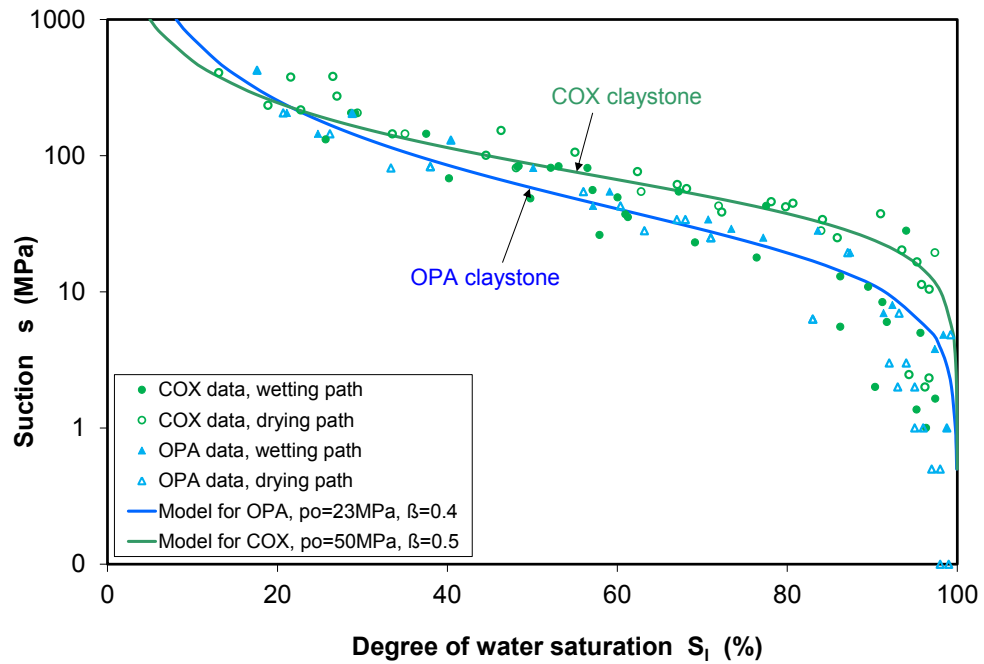
Fig. 2.10 Water retention curves of the COX and OPA claystones

The data of axial stress depicted in Fig. 2.7 – Fig. 2.9 are plotted versus the associated water saturation in Fig. 2.11 for the COX samples, in Fig. 2.12 for the OPA samples, and in Fig. 2.13 for the pre-heated COX samples. The following common features of the stress-saturation curves can be found:

- The pre-applied axial stress of σ_o = 11 – 14.5 MPa at COX samples (Fig. 2.11) and 4.5 MPa at an OPA sample (Fig. 2.12) decreases with desaturation during drying. The stress decrease is relatively fast in the beginning down to a saturation degree of $S_l \approx 80$ % and then continues slowly to a minimum residual stress of S_s = 0 – 0.5 MPa at a residual saturation degree of S_r = 15 – 20 %, below which no stress changes occur. The observed residual water saturation agrees well with the fraction of the nano-pores (< 2 nm) in the COX clay rock (cf. Fig. 2.3), suggesting that the remaining water resides mainly in the interlayer space of the clay particles and has no effect on the stress transfer mainly through the interparticle bound pore water. However, two exceptions were observed, a high residual saturation of S_r = 85 % at a low pre-load of 2 MPa (Fig. 2.11c) and a high residual stress of $S_s \approx 7$ MPa at a strongly-cemented COX sample (Fig. 2.11b).

- The subsequent resaturation leads to a stress increase up to a value σ_{ls} at full saturation (S_l = 100 %). The increase of the stress with water saturation is almost linear within the whole range from residual saturation S_r to full saturation S_l = 100 %.

26

The maximum swelling pressure at full saturation might correspond to the average disjoining pressure π_D in eq. (2.8), which is determined by the difference between σ_{ls} and σ_s, $\pi_D = \sigma_{ls} - \sigma_s$. The disjoining pressure π_D is marked in the stress – saturation curves for the samples providing values of π_D = 4 – 9 MPa for the COX (Fig. 2.11), $\pi_D \approx 2$ MPa for the OPA (Fig. 2.12), and $\pi_D \approx 2$ MPa for the COX samples heated up to 100 °C – 120 °C (Fig. 2.13). The variation of the axial stress σ_a with water saturation S_l is quite linear for all the samples and therefore can be well reproduced by the stress equation (2.13) by introducing π_D instead of π and using the determined parameters of σ_s at S_r and σ_{ls} at S_l = 100 %. This is also adequate for the drying part in a range of $S_r < S_l < 80$ %.

- Interesting is that even after recovery of the fully saturated state, the stress still increases with more water uptake to a maximum value of σ_p σ_p = 9.5 – 10.5 MPa corresponding to the uniaxial strength of ~10 MPa obtained on the "over-saturated" sample with w = 7.7 % (cf. Fig. 2.568). The swelling pressure building up after water saturation is here estimated by $\pi_O = \sigma_p - \rho_{ls}$: π_O = 0.5 – 4.5 MPa for the COX (Fig. 2.11), π_O = 1 – 2 MPa for the OPA (Fig. 2.12), and π_O = 0.2 – 1 MPa for the pre-heated COX samples (Fig. 2.13).

- The total swelling pressure π is the sum of π_O developing with water saturation and π_O with more water uptake after saturation. It amounts to π = 9 – 11 MPa for the COX claystone, π = 3 – 4 MPa for OPA claystone (Fig. 2.12), and π = 2 – 3 MPa for the pre-heated COX claystone (Fig. 2.13).

Based on these observations the effective stress is divided into three parts: a) the residual stress σ_s acting at solid-solid contact area, b) the saturation dependent swelling pressure $\pi_D(S_l)$ acting in the interparticle bound porewater, and c) the swelling pressure $\pi_O(w)$ depending on the additional water uptake in saturated state which might be mainly attributed to the osmotic effect. The stress equation (2.13) may be rewritten as

$$\sigma_{eff} = \sigma_s + \pi_D S_e + \pi_O(\Delta w) = \sigma_s + \pi_D \left(\frac{S_l - S_r}{1 - S_r} \right) + \pi_O(\Delta w) \tag{2.17}$$

where Δw is the increase of water content after full saturation.
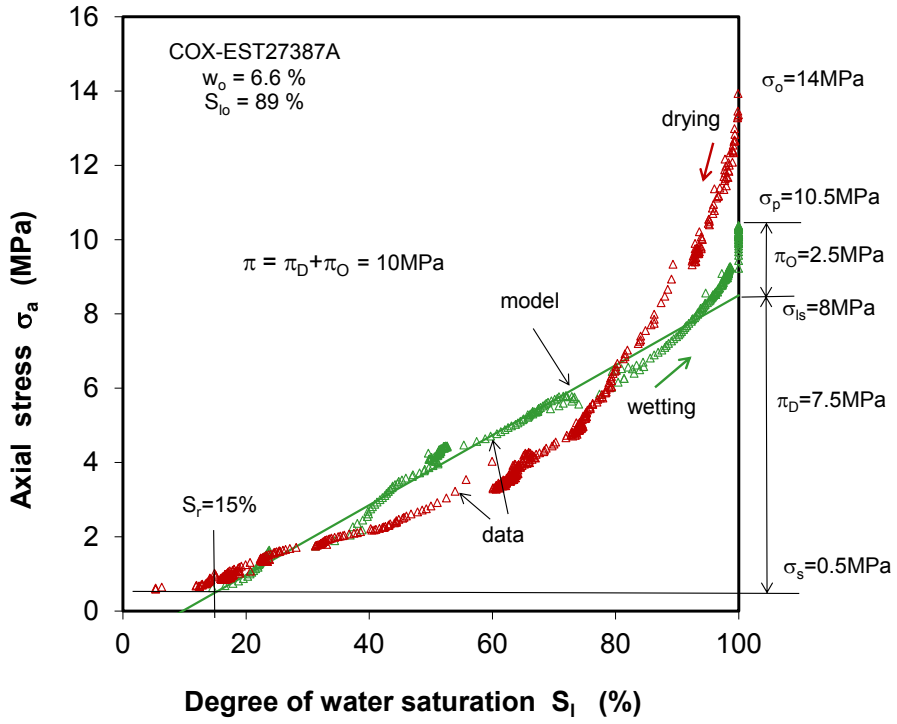
(a) sample EST27387A
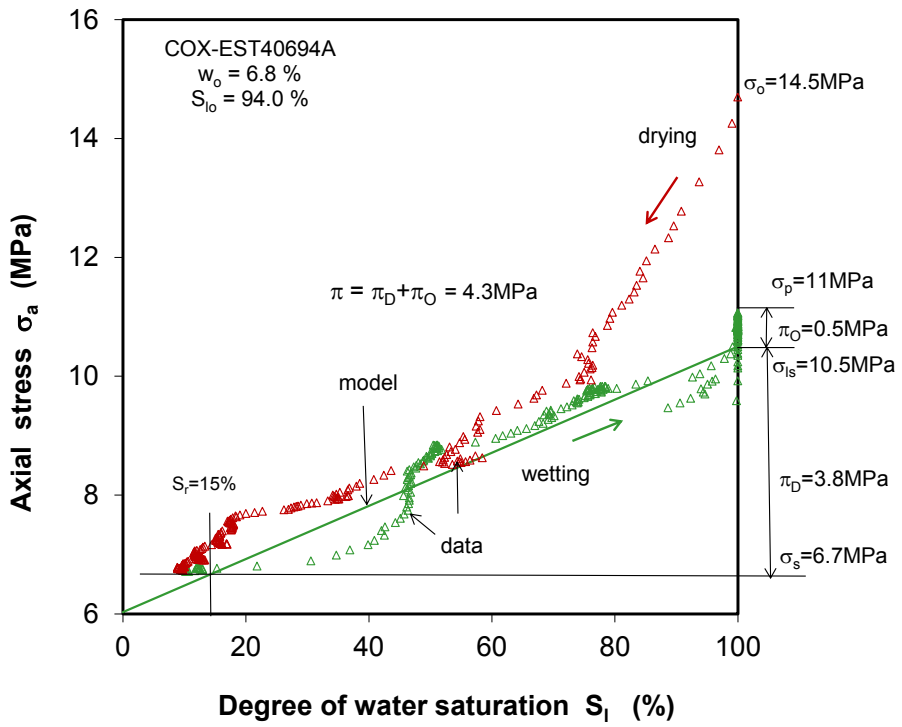

(b) sample EST40694A
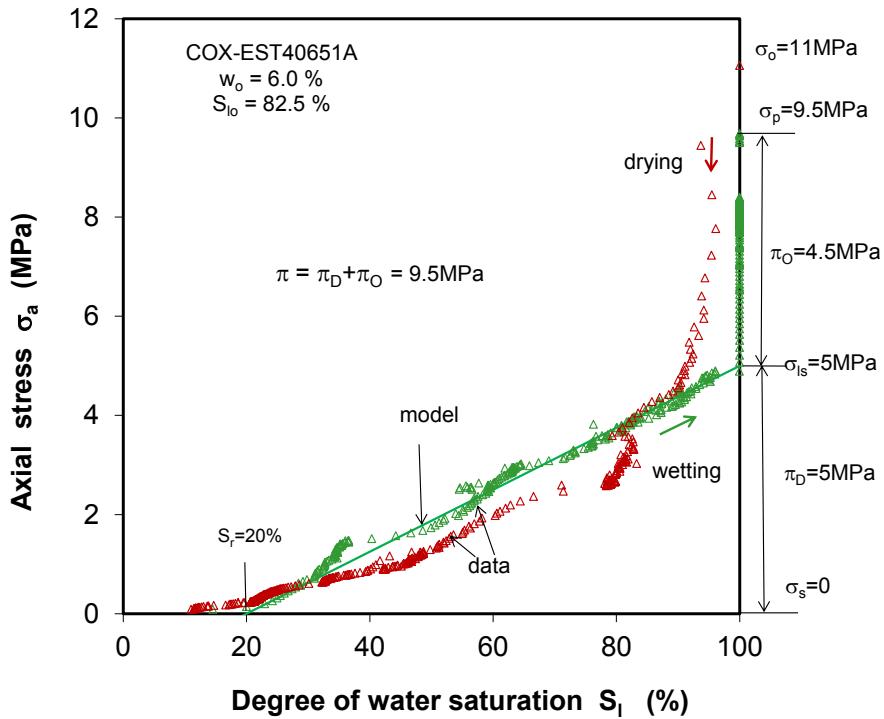
(c)　sample EST40651A
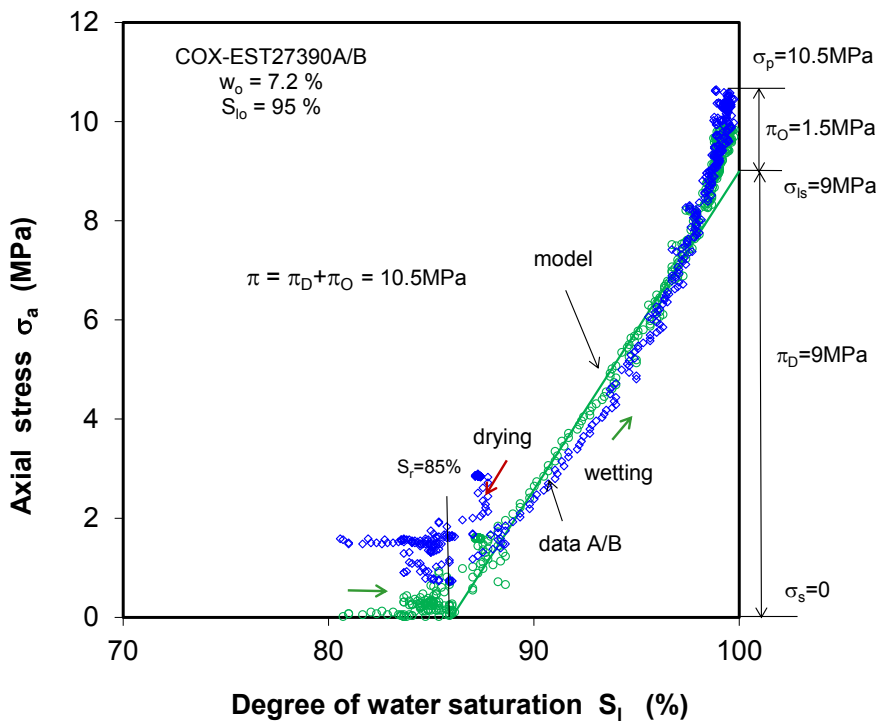
(d)　samples EST27390A/B

Fig. 2.11　Axial stress and swelling pressure of COX samples as function of water saturation
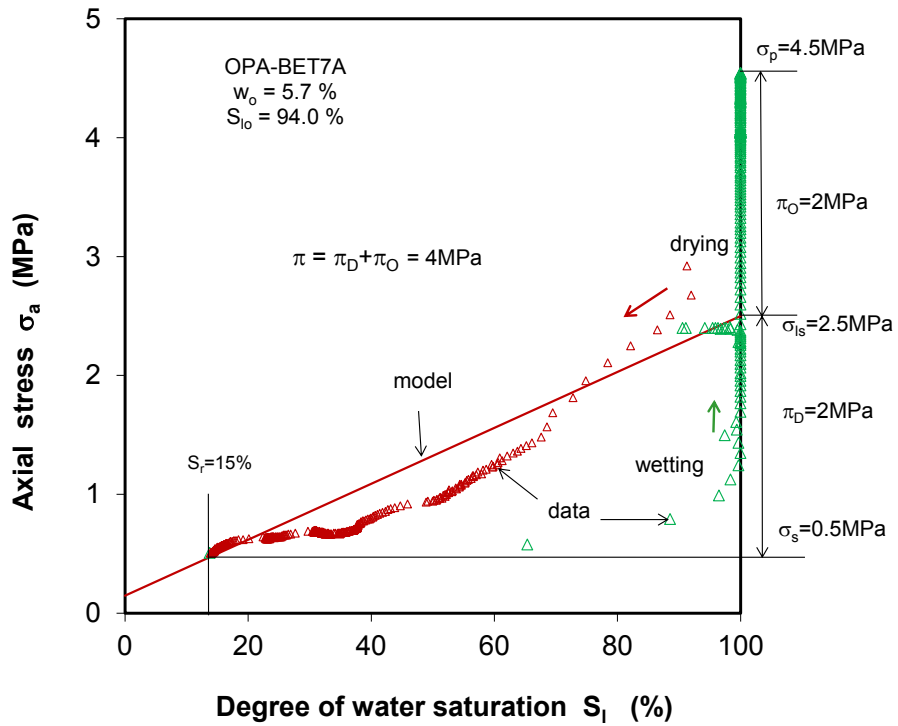
(a)   sample OPA-BET7A
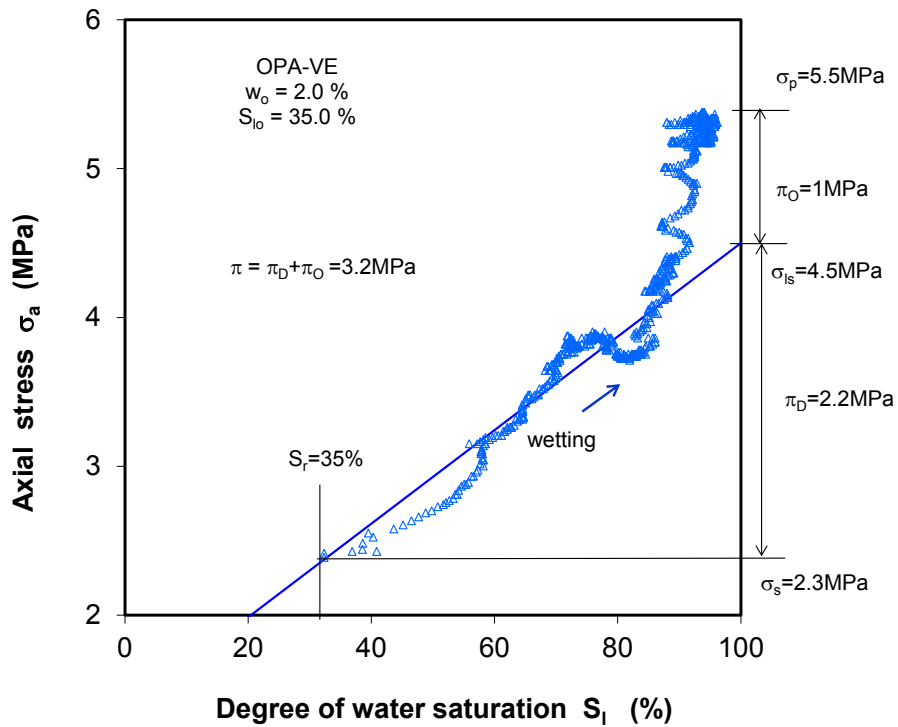
(b)   sample OPA-VE

Fig. 2.12   Axial stress and swelling pressure of OPA samples as function of water saturation

(a) sample EST27388A pre-heated at 105 °C

(b) sample EST22101A pre-heated at 120 °C

Fig. 2.13 Axial stress and swelling pressure of heated COX samples as function of water saturation

2.1.3.2 Swelling pressure with liquid water

Swelling pressure of the clay rocks was also examined by wetting the samples with synthetic porewater under various confining conditions.

Two COX samples of 50 mm diameter and 10 mm thickness were tested simultaneously in two oedometer cells. Both had porosities of 15.5 – 16.5 % and water contents of 4.5 – 5.5 %. The first sample was used for the swelling pressure measurement under confined conditions, while the second sample was used for measuring axial free swelling strain at a confined lateral boundary. Fig. 2.14 summarises the evolution of axial swelling pressure of sample A and axial free swelling strain of sample B. The synthetic porewater was introduced into the samples. This resulted in a quick rise of the swelling pressure from 0.8 to 2.5 MPa and a subsequent gradual increase to a maximum of 3.3 MPa, while the free swelling strain increased rapidly up to 6 % after the first contact with water and then gradually up to 7.3 % over 9 months. Even though the synthetic porewater was applied, the osmotic effects are obviously very significant causing the large swelling strain and swelling pressure of the nearly saturated clay rock.
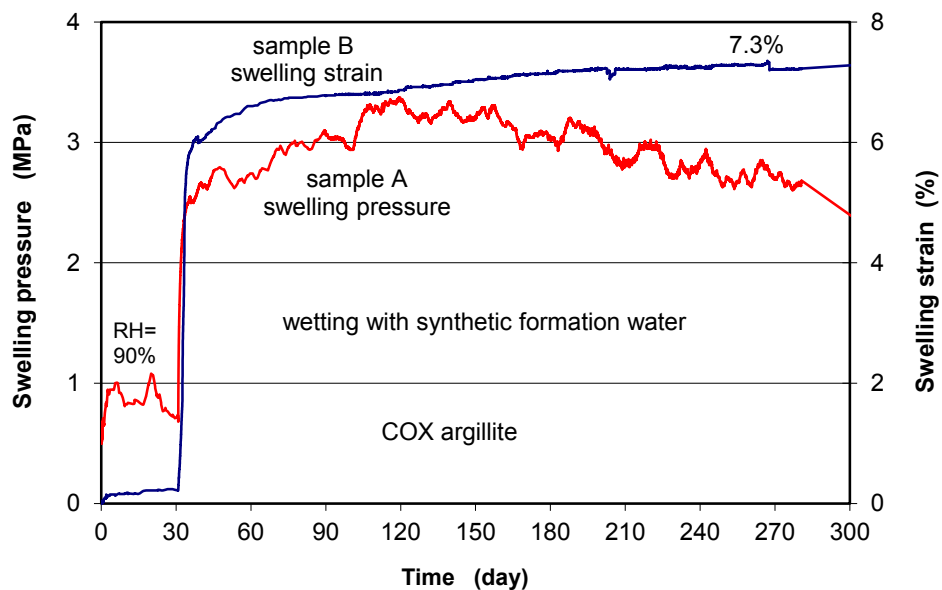
Fig. 2.14   Swelling pressure at constrained volume and free swelling strain of COX claystone by wetting with synthetic porewater

Another test result shown in Fig. 2.15 demonstrates the osmotic effects more clearly. The swelling pressure induced by vapour wetting at RH = 100 % reached 2.8 MPa, and the following flooding with the synthetic water increased the swelling pressure up to 3.8 MPa due to the osmotic effects.
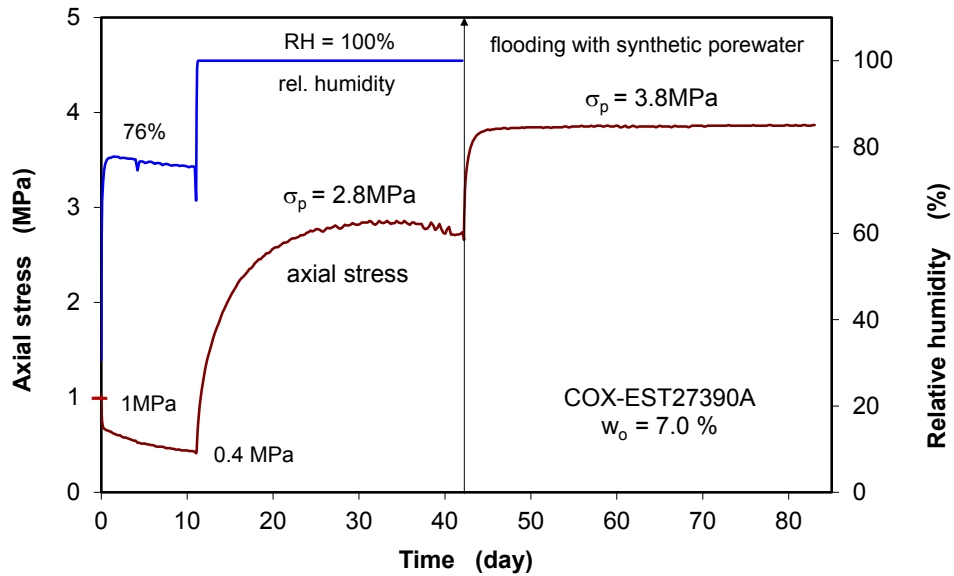
Fig. 2.15   Buildup of swelling pressure of volume-constraint COX claystone by wetting with water vapour and synthetic porewater

However, the so-called swelling test technique under confined condition generally yields relatively low swelling pressures /YON 12/. One reason for this might be that clay minerals close to the clay-water interface expands so quickly and thereby reduces the pore space to such an extent that further water inflow into the constraint samples is strongly impeded. This effect is strongly indicated by measurements for expansive clays /PUS 01/. In this case swelling pressure in the samples would not develop homogenously. Therefore, the so-called consolidation test technique /YON 12/ might be suitable and here applied. The COX sample B fully expanded to a porosity of ~25 % (Fig. 2.14) was reconsolidated to different porosities, at which the required loads were recorded. Fig. 2.16 shows the evolution of the measured axial stress in correspondence to the porosity. Because of problems with fixing strain at the beginning, the stress dropped sharply but then stabilized within several days. During the consolidation, the adsorbed porewater was expelled and the pores were compacted. The remaining bound porewater was then carrying the external load. The stabilized stress at each porosity level is therefore actually equivalent to the swelling pressure or effective stress.
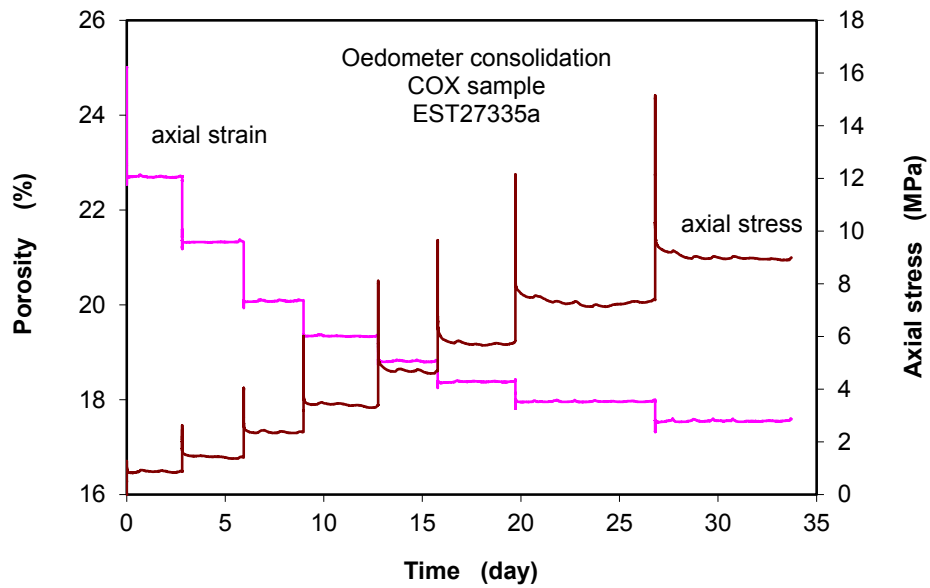
Fig. 2.16   Reconsolidation of a fully saturated and expanded COX sample in oedo-
meter cell

Another evidence for the high swelling pressure is provided by a triaxial swelling test on a COX sample. The original lithostatic stress conditions of σ_1 = 15 MPa/σ_2 = σ_3 = 12 MPa and the external water pressure of p_w = 4.5 MPa were applied to the sample for two months. Fig. 2.17 illustrates the test result. The strain curves show that a continuous expansion rather than compression occurred in axial direction during the injection of the synthetic porewater. It reflects a high swelling pressure that is at least equal to the effective stress of $\sigma_1 - p_w$ = 11.5 MPa in this direction. The supporting capacity of the bound porewater, however, is reduced by elevating the temperature. In drained conditions, the temperature increase causes desorption, mobilisation and expelling of the porewater from the sample, and hence compaction of the pores.
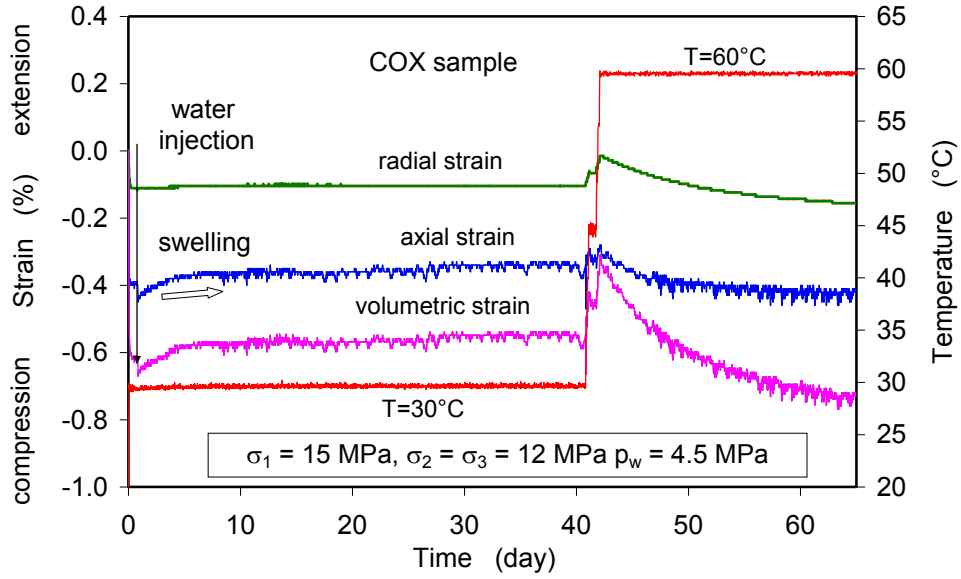
Fig. 2.17 Swelling strains of a COX sample under the high lithostatic confining stresses

Interesting is the comparison of the porosity – load data obtained from the samples and from the geologic evolution of the argillaceous formation at a depth of ~500 m (modified Fig. 2-3 in /BOC 10/), as shown in Fig. 2.18. The porosity obtained on the samples decreased with the applied load from the initial value of 25 % to ~ 16.5 % at the field burial pressure of 12.5 MPa. The porosity – stress curve represents the upper limit of swelling of the clay rock under confining stresses. If the burial pressure relief continues and the external water is still available, the clay rock would expand gradually up to this limit. The porosity reduction with burial pressure increase during the sedimentation period and the porosity increase with burial pressure relief during the uplift process may be approached by an exponential function

$$\emptyset = \emptyset_O \cdot exp(-a\sigma^b) \tag{2.18}$$

where $\emptyset$ is the porosity, $\emptyset_O$ is the maximum porosity at vanishing burial pressure, σ is the effective burial pressure, a and b are the material parameters. The parameters are determined as a = 0.13 and b = 0.45 for the sedimentation path and a = 0.2 and b = 0.46 for the uplift path. The model matches both the porosity – burial pressure curves well, as shown in Fig. 2.18.
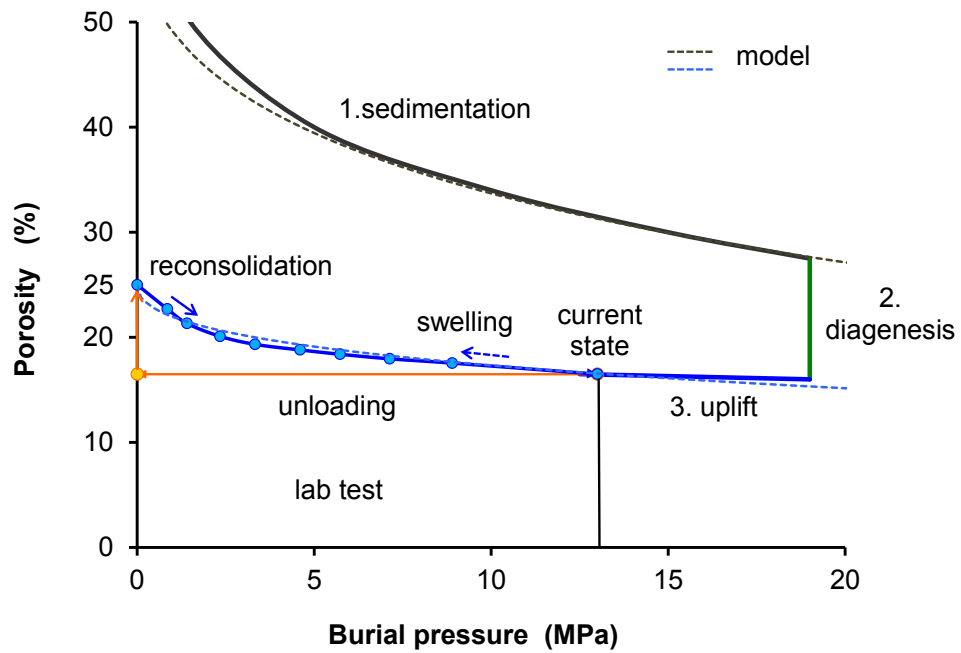
Fig. 2.18 Reconsolidation of COX claystone in lab tests compared with the geologic evolution in terms of porosity versus burial pressure (modified Fig. 2-3 in /BOC 10/)

2.1.4   Conclusions on the stress concept

Effective stress and swelling pressure in argillaceous rocks have been preliminarily examined by theoretical consideration and experimental validation. Based on the microstructures of the studied Callovo-Oxfordian argillite and the Opalinus clay, a stress concept has been derived, which are consistent with the suggestions by Horseman et al. /HOR 96/, Rodwell et al. /ROD 99/, and others. The stress concept suggests that the effective stress in a dense clay-water system is transferred through both interparticle bound porewater in narrow pores and solid-solid contact area between non-clay mineral grains. The disjoining or swelling pressure acting in the interparticle water-films due to physico-chemical interactions exceeds the pressure in large pores occupied by free water. The swelling pressure and the effective stress are related linearly with the effective degree of saturation of bound porewater serving as stress-bearing element.

This stress concept is strongly supported by experimental observations made on the COX and OPA claystones. In uniaxial condition, axial swelling pressure increased with increasing water saturation up to the peak strength of the materials, indicating that the adsorbed porewater is capable of bearing deviatoric stresses. Under the triaxial lithos-

tatic stress conditions, a gradual swelling strain was observed on the samples when contacting with the synthetic porewater, suggesting a high swelling pressure against the applied lithostatic stresses.

This stress concept provides a reasonable view to the nature of the effective stress in argillaceous rocks and may form the fundamental basis for studying the hydro-mechanical properties and processes such as the stress-strain behaviour, time-dependent deformation, moisture effects on the stiffness and strength, water and gas transport, sealing and healing of fractures, thermal and chemical impacts.

It is to be pointed out that this work should be considered very preliminary and more theoretical and experimental investigations are necessary to improve and confirm the proposed stress concept for clay rocks. Particularly, the information of the nano-microscopic structures in the clay rocks, like currently presented at the NEA-CLAYCLUB-Workshop dealing with clay characterisation from nanoscopic to micro-scopic resolution /NEA 11/, will provide new insights for the understanding of the physi-cal mechanisms of the complex processes in clay rocks and clay-based engineered barriers.

2.2   Short-term mechanical-hydraulic behaviour

Excavation of an underground repository leads to a redistribution of the rock stresses, particularly to a high concentration of the deviatoric stress in the surrounding rock after relief of the radial stress component and the porewater pressure. This results in micro- and macro-fractures in the nearfield when the damage and failure criteria of the rock are violated. The hydraulic conductivity of the surrounding rock may increase up to the point where the barrier function with respect to radionuclide migration will be affected. Precise knowledge of the deformation, damage, and permeability increase in the sur-rounding rock is required for the proper design of a repository. Moreover, the character-ization and prediction of the hydro-mechanical coupling processes in the damaged zone are essential for evaluation of the barrier function of the host rock against radio-nuclide migration. Up to now, even though there are data available for the short-term deformation behaviour of argillaceous rocks, a solid database is still needed for devel-opment of constitutive models for damage and induced permeability changes. There-fore, a series of laboratory experiments has been conducted in this project on the COX clay rock. Major results are presented below.

2.2.1 Characterization of samples

Seven cores were extracted from two boreholes TED1201/2 in the TED heater test field and another one from PAC1011. They were drilled horizontally at the -490 m level in the MHM-URL. The axes of the cores are nearly parallel to the bedding plane. After coring, they were immediately confined in T-cells. From the cores cylindrical samples were carefully prepared to a size of 70 mm diameter and 140 mm length. Due to the coring and preparation, microcracks were unavoidably induced mostly along the bedding planes and even grew into few macro-cracks in a few samples (see the pictures in Fig. A.9). The fundamental properties of the samples determined are summarized in Appendix B.1. The water content, dry density and grain density were measured after dried at 105 °C for 48 hours. The porosities ranged from 15.1 % to 18.7 %. The measured water contents of 5.5 % to 7.4 % correspond to the saturation degrees of 75 % to 94 %. The more or less disturbed samples were reconsolidated under confining stress of 15 MPa corresponding to the original lithostatic stress at the sampling depth. This led to closure of the pre-existing cracks. The porosity decreased from an average value of 17.5 % to 16.4 % and the corresponding water saturation increased to ~ 100 % (Appendix B.1). The quality of the reconsolidated samples was significantly improved and closely represented the original natural state of the clay rock.

2.2.2 Testing method

The COX samples were tested in triaxial compression conditions with measurements of deformation, gas permeability, and ultrasonic wave signals. Fig. 2.19 illustrates schematically the assembly of a sample in a triaxial cell. The sample is inserted in a rubber jacket and located between two load pistons, in which piezo-electric P wave transducers were installed at the end faces for ultrasonic wave measurement while thin channels were introduced for gas flow. The annular gap between sample and jacket in the middle section of 2/3 length is sealed with silicon to avoid leakage, while the upper and lower section of 1/6 length each is filled with thin filter sheets. This configuration allows measurement of gas flow through shearing fractures which are inclined to the sample axis and not directly connected to the end faces.
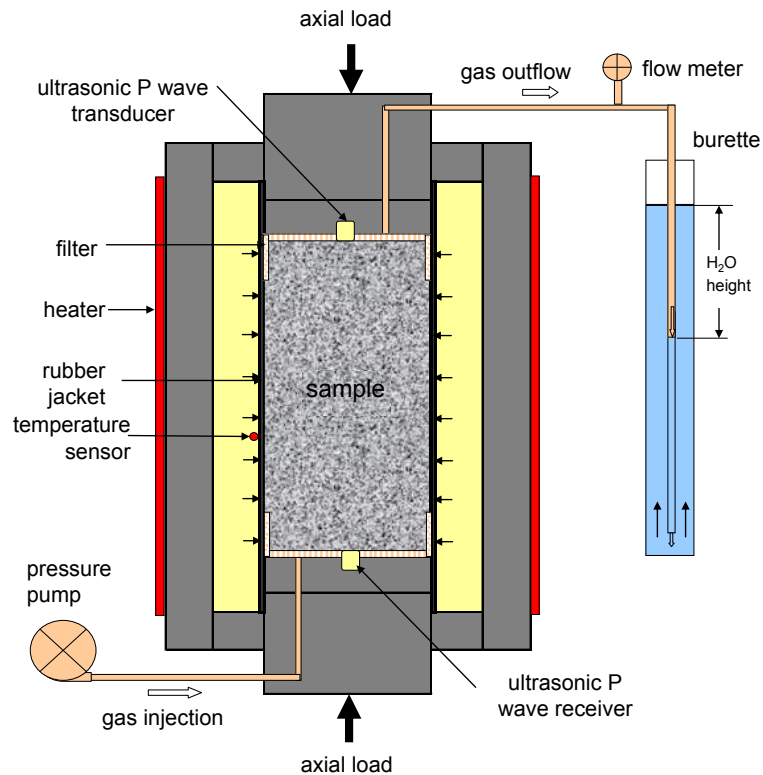
Fig. 2.19   Schematic assembly of a clay sample in triaxial cell with measurements of
deformation, permeability, and ultrasonic wave signals

The samples were firstly reconsolidated at isostatic stress of 15 MPa to close the pre-existing cracks. Following that, the stress was lowered to the desired levels of 1 to 12 MPa, respectively. And then keeping the radial stress constant ($\sigma_2 = \sigma_3$ = const.), axial load was increased by increasing axial strain at a rate of $1 \cdot 10^{-6}\,\mathrm{s^{-1}}$ to failure. During the loading, axial strain ε_1 and volumetric strain ε_v were measured by a LVDT-transducer and a pressure/volume GDS-controller. Radial strain ($\varepsilon_2 = \varepsilon_3$) was then calculated by $\varepsilon_v = \varepsilon_1 + 2\varepsilon_3$. As a useful technique to detect damage evolution in the stressed sample, ultrasonic wave signal amplitude A_p and velocity V_p were recorded. The amplitude is defined here by the ratio of the maximum peak of the ultrasonic pulse to the average value of the background noise. Additionally, damage effect on the hydraulic conductivity was monitored by gas flow. Nitrogen gas was introduced into the bottom at constant pressure of 0.2 MPa and the gas outflow was recorded at the top by means of a burette.

Taking the sealed middle part of the sample into account, the appearance permeability is determined according to Darcy's law

$$K_g = \frac{2q_g\mu_g p_o L_g}{A(p_i^2 - p_o^2)} \tag{2.19}$$

where K_g is the effective gas permeability (m^2), $L_g = 2/3L$ is the effective length of the gas flow measurement (m), A is the cross section of the sample (m^2), q_g is the flow rate of the gas (m^3/s), μ_g is the gas dynamic viscosity (Pa·s), p_o is the atmospheric pressure (Pa), and p_i is the gas injection pressure (Pa).

2.2.3 Isostatic compaction

Fig. 2.20 illustrates typical results of the isostatic compaction of several disturbed samples in terms of volumetric strain, gas permeability, ultrasonic wave amplitude and velocity as function of applied stress. A few samples exhibited macro-cracks on the surfaces in axial direction (Fig. B.10). The isostatic compaction led to closure of the cracks. The volumetric strain – mean stress ($\varepsilon_v - \sigma_m$) curves are non-linear. The porosity decreased from the initial values of ∅ = 17.7 – 18.7 % to ∅ = 16.1 – 16.6 % at 15 MPa. A nearly full water saturation was recovered (Appendix B.1) due to the closure of the cracks.

As a consequence of the fracture closure, the permeability decreased drastically from the initial high values of $K_g = 10^{-13} - 10^{-16}\,m^2$ to very low levels of $10^{-18} - 10^{-20}\,m^2$. The mechanical consolidation was also revealed by the significant increases of the ultrasonic wave amplitude A_p and the velocity V_p. Both the parameters increase with loading. Some jumps of V_p at relatively low confining stresses were recorded. At the confining stress of 15 MPa, the wave velocities recorded on the samples range from 3,270 to 3,370 m/s, slightly higher than the *in situ* observation in the less or undisturbed zone in the MHM-URL /SHA 08/. At constant load, creep consolidation occurred, leading to a significant decrease in permeability and increase in wave velocity (cf. Fig. 2.20d). After unloading, the volume increased slightly and the corresponding permeability decreased too, but much lower than the initial value before unloading. This indicates a pronounced plastic close of the cracks by the previously applied load.
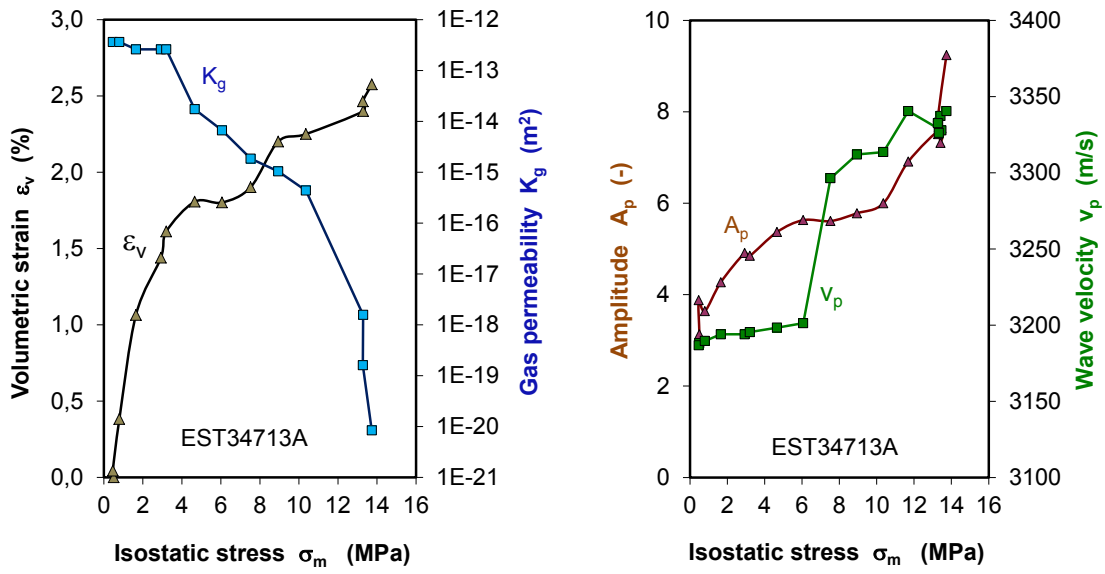
(a) Sample EST34713A: ∅ = 18.7 % → 16.1 %, S_w = 83.5 % → 100.0 %
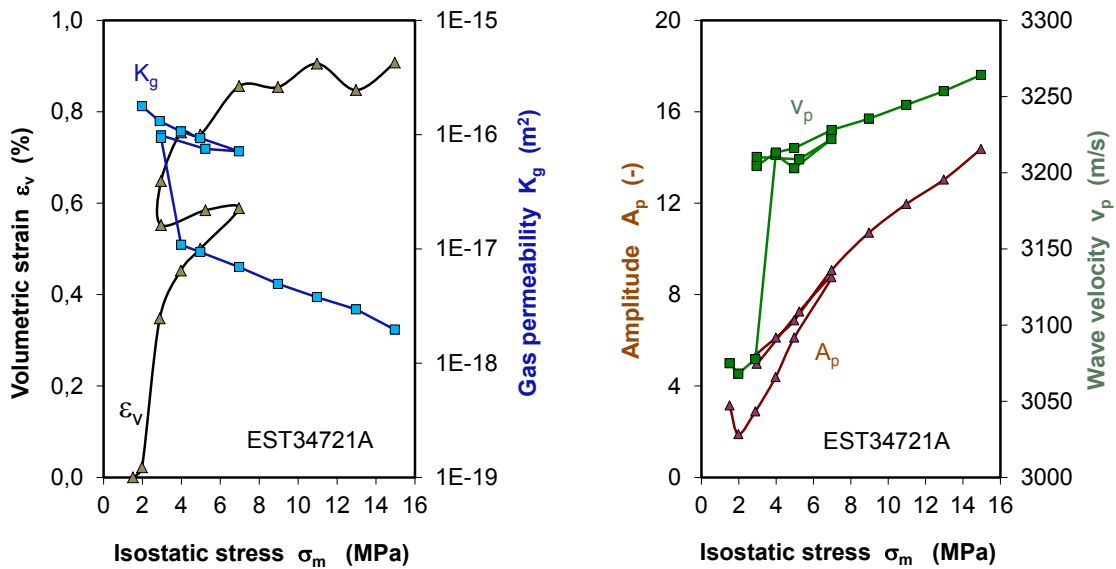
(b) Sample EST34721A: ∅ = 17.7 % → 16.5 %, S_w = 92.6 % → 100.0 %
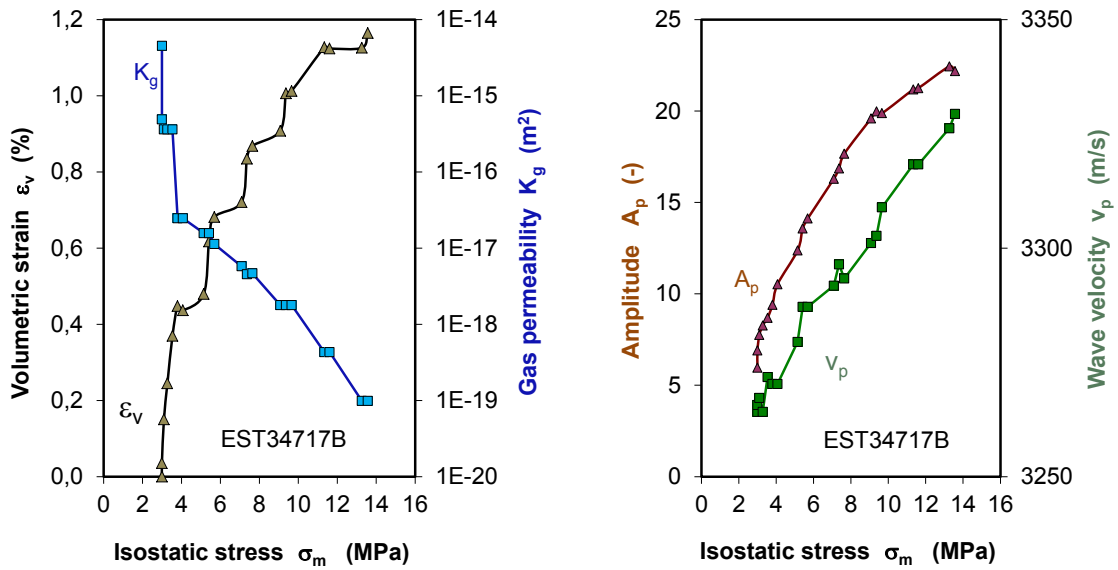
(c) Sample EST34717B: Ø = 18.0 % → 16.6 %, S_w = 91.2 % → 100.0 %
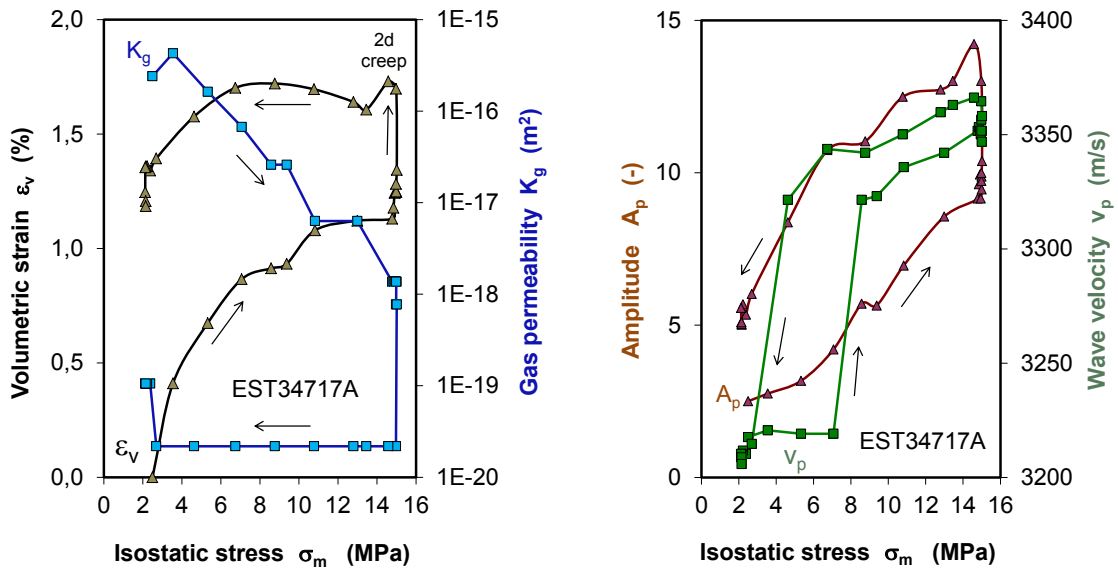
(d) Sample EST34717A: Ø = 17.8 % → 16.6 %, S_w = 92.0 % → 100.0 %

Fig. 2.20   Compaction behaviour of disturbed COX samples in terms of volumetric strain, gas permeability, ultrasonic wave amplitude and velocity as function of applied isostatic stress

2.2.4   Deviatoric stress-strain behaviour

The deviatoric compression of the previously reconsolidated samples was conducted by increasing axial strain at a rate of $1 \cdot 10^{-6} \, \text{s}^{-1}$ at different confining stresses in a range from 1 to 12 MPa. Results of the tests are summarized in Appendix B.2 in terms of axi-

al/radial/volumetric strains, gas permeability, ultrasonic wave amplitude and velocity as function of the increased deviatoric stress ($\Delta\sigma = \sigma_1 - \sigma_3$). Two typical examples at σ_3 = 2 and 5 MPa are shown in Fig. 2.21 and Fig. 2.22 respectively. The stress-strain behaviour and the responses of permeability and ultrasonic wave can be characterised by four subsequent stages similar to that identified for most brittle rocks /MAR 97/:

1. The stress-strain behaviour in the very beginning of the load is non-linear but insignificant because of the reconsolidation effect.

2. Further increase of the deviatoric stress causes a linear elastic compression, which is also perfectly revealed by the evolution of wave amplitude and velocity. The permeability does not change significantly.

3. As the stress reaches a critical value called yield stress σ_Y, a deviation from the linear elastic behaviour appears, not only by the stress-strain curves ($\Delta\sigma - \varepsilon_1$ and $\Delta\sigma - \varepsilon_v$) but also the wave amplitude and velocity curves ($A_p - \varepsilon_1$ and $v_p - \varepsilon_1$). This indicates the initiation of microcracks. Therefore, the yield stress is also referred to as the crack initiation stress or damage initiation threshold. The onset of cracking was initiated at 53 – 67 % of the failure strength σ_F, on average, σ_Y/σ_F = 0.60. During this stage shear cracking dominates the process. Further growth and propagation of the microcracks with increasing the load results in a transition from the volumetric compaction to dilation at stress σ_D, namely dilatant threshold. The dilation occurred at 72 – 93 % of the failure strength, on average, σ_D/σ_F = 0.83. The crack propagation is stable before the dilatant threshold and then becomes unstable after that. This is also reflected by the reduction of the wave amplitude and slowing-down of the wave velocity at the dilatant point. Because there is no macroscopic flow pathways formed yet before the dilatant point, the low permeability remains.

4. When the unstable crack propagation continues with increasing the load, the microcracks tend to be connected forming a fracture network, resulting in failure of the claystone at the peak stress σ_F. Under low confining stresses, the structure rupture is brittle and quite quickly. And in contrast under high confining stresses, the failure is more ductile and slow. The brittle rupture is well reflected by the rapid drop of the wave amplitude and velocity, while during the ductile failure process the variations of the ultrasonic wave signals are slow. As a flow pathway is initiated, the permeability jumps to several orders of magnitude high levels at low confining stresses. This indicates a percolation process. The so-called percolation threshold

was identified mostly at or shortly after the peak stress. Under high confining stresses, the permeability increase is insignificant. This might be due to the high normal stress compressing the shearing fractures closure. After failure, the fractured claystone still has a residual bearing capacity σ_R contributed from the remaining friction resistance between fracture surfaces.

(a) stress-strain

(b) gas permeability

(c) wave amplitude
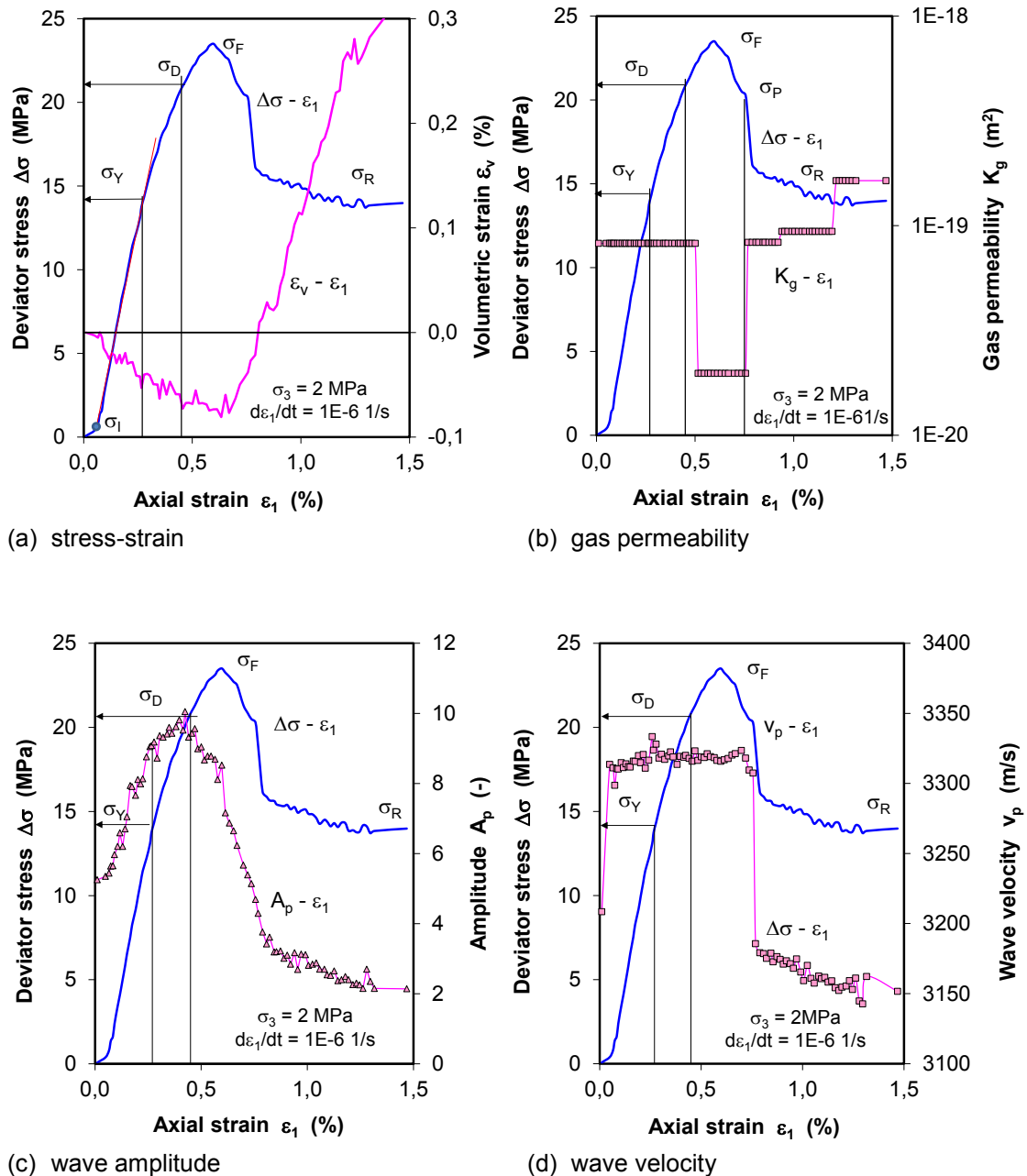
(d) wave velocity

Fig. 2.21   Stress-strain behaviour and responses of gas permeability, wave amplitude and velocity to axial loading at radial confining stress of 2 MPa

(a) stress-strain

(b) gas permeability

(c) wave amplitude
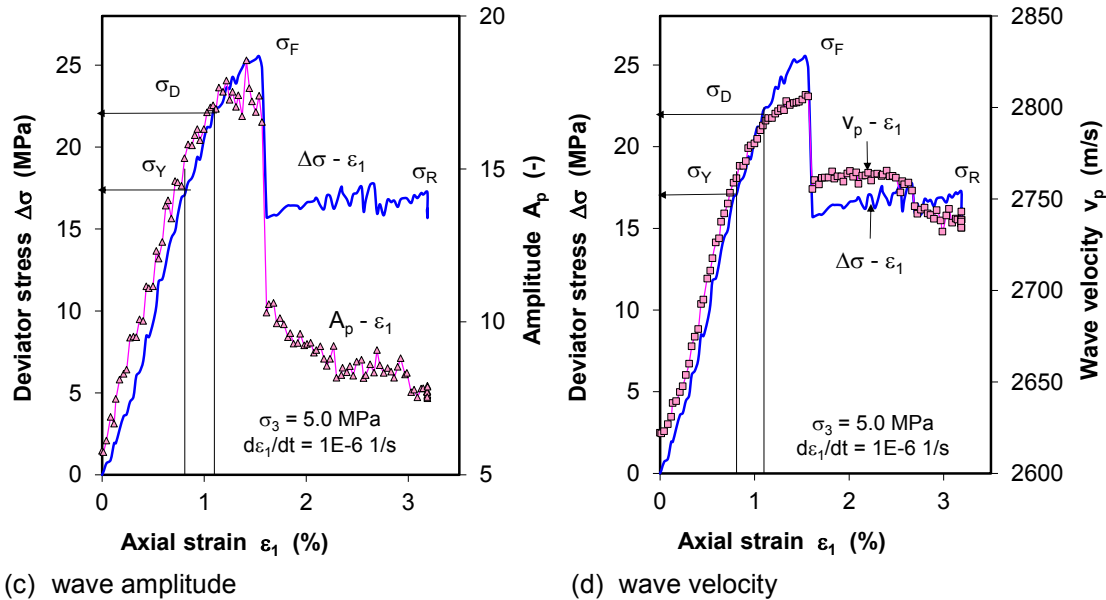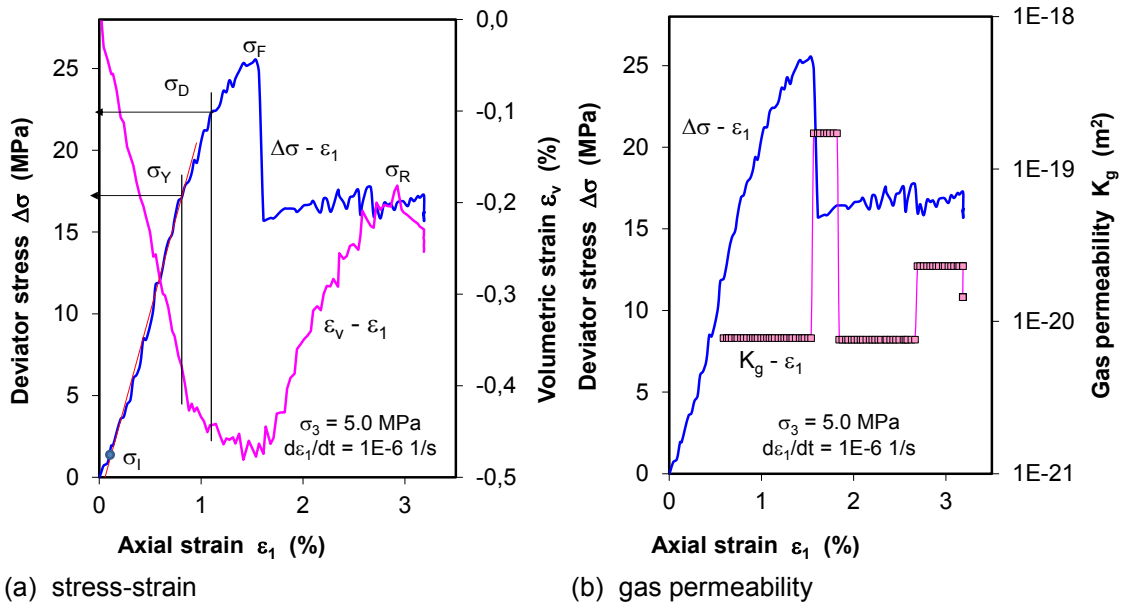
(d) wave velocity

Fig. 2.22   Stress-strain behaviour and responses of gas permeability, wave amplitude and velocity to axial loading at radial confining stress of 5 MPa

From the test data, the elastic parameters are determined by a mean value of Young's modulus E = 4,900 MPa and Poisson ratio ν = 0.3, which agree with E = 4,500 MPa and ν = 0.3 for the rheological zone B' (460 – 515 m) obtained by the others /SU 07/.

The deformation, damage, and damage-induced permeability changes are dependent on the confining stress. Fig. 2.23a summarizes the stress-strain curves obtained at different confining stresses. In comparison, the data previously obtained on the COX

claystone from the main level of the MHM-URL /ZHA 10b/ are represented in Fig. 2.23b. One can recognize from both figures that a) the clay rock becomes from brittle to ductile with increasing the confining stress; b) the higher confining stress, the larger the volumetric compaction and the smaller the dilation; and c) the yield, dilatancy, peak and residual strengths increase with confining stress.
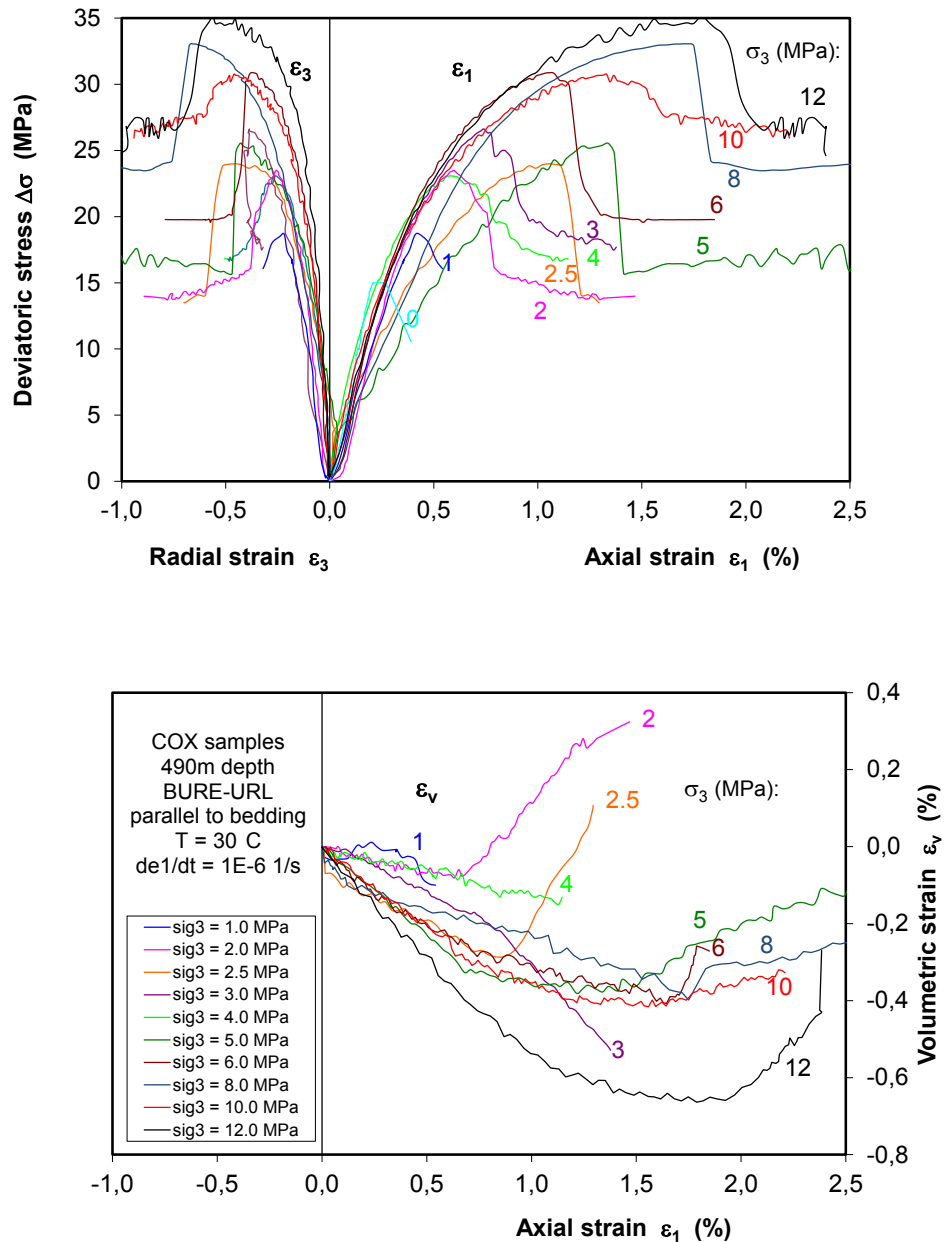
Fig. 2.23 Stress-strain curves obtained on the COX samples at different confining stresses
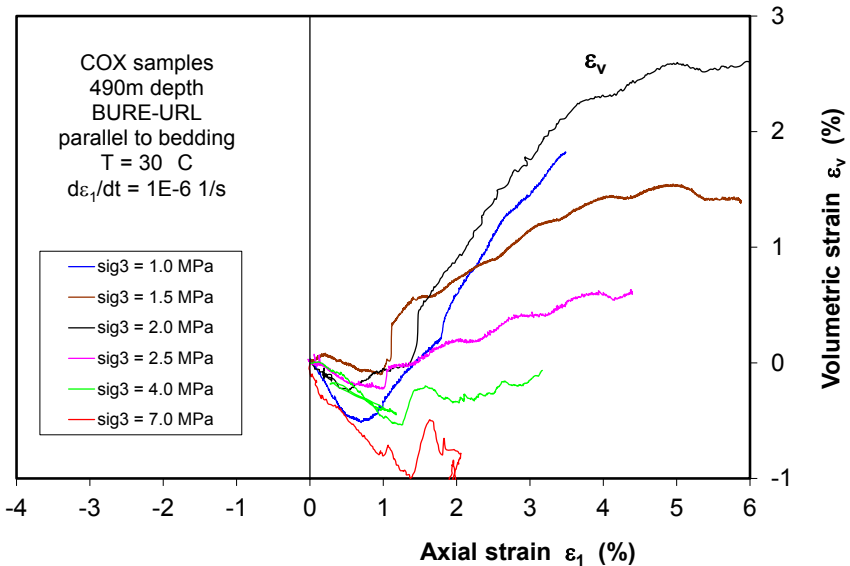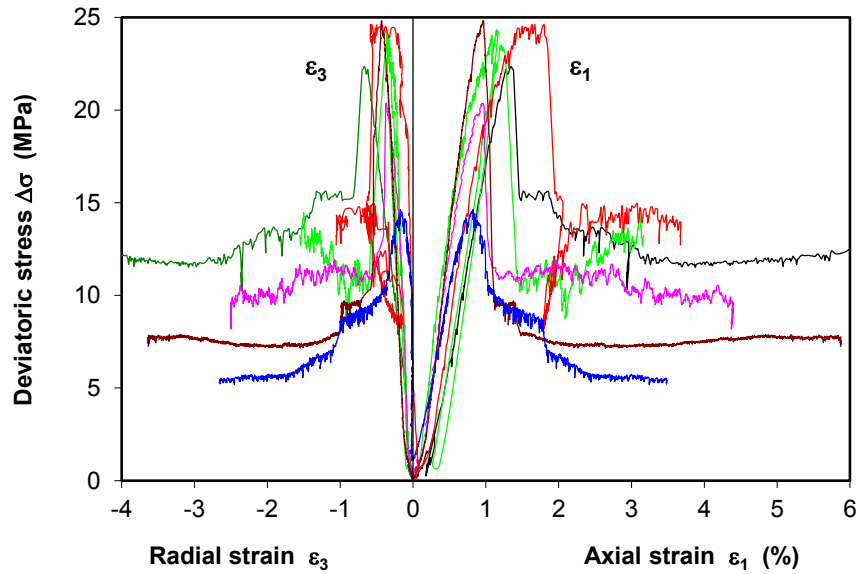
Fig. 2.24 Stress-strain curves previously obtained on the COX samples at different confining stresses /ZHA 10b/

The tested samples were visually inspected. Their pictures are shown in Appendix B.3. The pre-existing cracks which had been more or less parallel to the sample axis became more open after testing. Single or few shear fractures were created and developed obliquely to the direction of axial stress at angles of 25 ° – 35 °. They were intersected. The samples loaded at high confining stresses over 6 MPa showed two major families of shear fractures intersecting at an angle of 40 ° – 50 °. The failure of the claystone at the applied confining stresses of 1 to 12 MPa seems to be governed by shearing. Under unconfined and slightly confined conditions, tensile cracking leads to failure

of the claystone. The tensile strength of the COX claystone was determined using the Brazilian testing method. The tensile stress-strain curves are presented in Appendix B.4. The tensile strengths measured on the COX samples are between 1.2 and 1.7 MPa, lower than that of 2.6 MPa obtained on the claystone in the upper layer with more carbonate component /AND 05/ and /SU 07/.

2.2.5 Damage and failure strengths

The critical values of the yield, dilatant and peak strengths (σ_Y, σ_D, σ_F) are summarized in Appendix B.3. The ratios of the yield and dilatant strengths to the peak one are calculated, indicating a less dependency upon the confining stress. The averaged values are: $R_Y = \sigma_Y/\sigma_F = 0.60 \pm 0.07$ and $R_D = \sigma_D/\sigma_F = 0.83 \pm 0.06$. These observations are comparable with those made previously on COX /ZHA 10b/ and OPA samples /ZHA 07a/, /NAU 07/, /POP 07/. Taken into account the current and previous results /ZHA 10b/ together for the COX claystone at the 490m level of the MHM-URL, average strength ratios are determined at $R_Y = \sigma_Y/\sigma_F = 0.55$ and $R_D = \sigma_D/\sigma_F = 0.75$. As follows, the strength data are evaluated as function of the confining stress σ_3 with regard to three different strength criteria.

Griffith criterion

As commonly known, excavation may lead to occurrence of tensile or extensile stress around underground openings, particularly near the drift walls, resulting tensile fractures. The Griffith theory is widely applied for analysis of tensile ruptures, particularly for brittle, isotropic and elastic materials such as granite. The Griffith criterion represented in /BRA 06/, /WU 10/ is examined here for the COX clay rock:

$$(\sigma_1 - \sigma_3)^2 = 8\sigma_t(\sigma_t + \sigma_3) \qquad \text{if} \quad \sigma_1 - 3\sigma_3 > 0$$

$$\sigma_3 = \sigma_t \qquad \text{if} \quad \sigma_1 - 3\sigma_3 < 0$$

$$\sigma_1 = \sigma_3 + 4\sigma_t + 4\sqrt{\sigma_t(\sigma_t + \sigma_3)} \quad \text{if} \quad \sigma_3 \geq -\sigma_t; 3\sigma_t \leq \sigma_1 \leq 8\sigma_t \qquad (2.20)$$

where σ_t is the uniaxial tensile strength of the un-cracked material. The averaged tensile strength of $\sigma_t = 1.5$ MPa is taken into account for the studied COX claystone. The uniaxial tensile strength of the OPA claystone was determined by others: $\sigma_t = 1.2$ MPa

parallel to bedding and σ_t = 0.6 MPa perpendicular to bedding /BOC 10/, and σ_t = 1.1 – 2.5 MPa /JOB 10/.

Fig. 2.25 shows the comparison of the measured data with the Griffith criterion. It is obvious that the yield strength σ_Y or the crack initiation stress is reasonably predicted by the model. But the dilatant and failure strengths resulting from fracture propagation are significantly underestimated by the model. It is not surprised because the Griffith criterion was initially established for crack initiation of rocks.
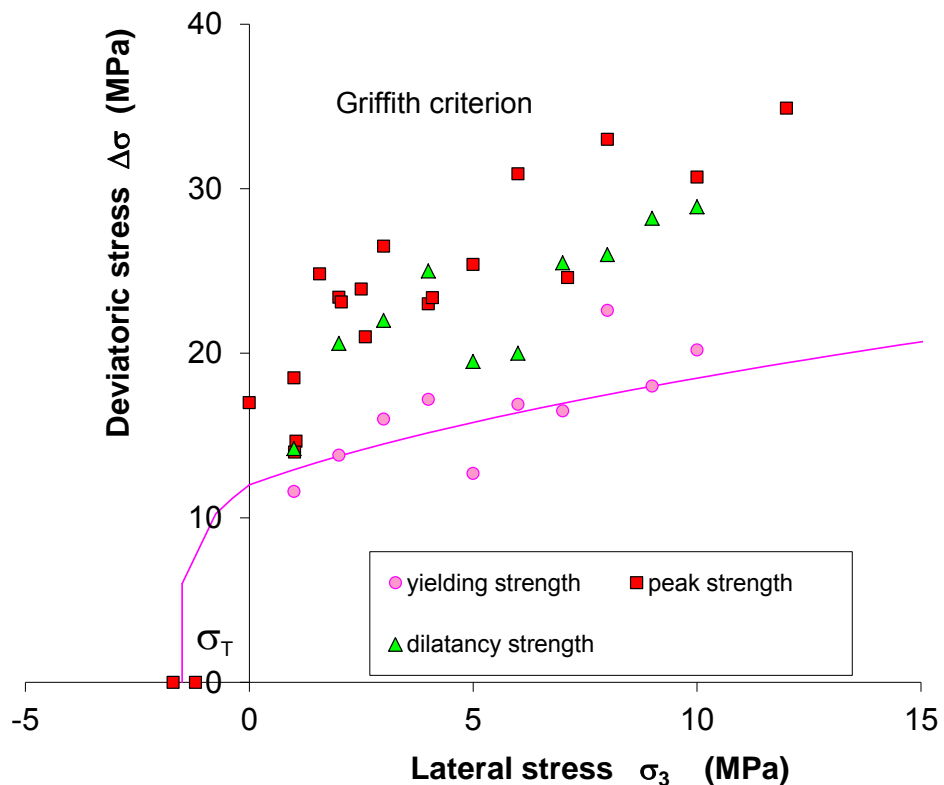
Fig. 2.25   Griffith criterion compared with the yield, dilatant and peak strengths for the COX clay rock

Mohr-Coulomb criterion

The Mohr-Coulomb's shear strength criterion is usually accepted for soils and rocks:

$$\tau = \sigma_n \cdot tan\varphi + c \qquad\qquad\text{(a)}$$

or

$$\sigma_1 = 2 \cdot c \cdot tan\left(45° + \frac{\varphi}{2}\right) + \sigma_3\, tan^2\left(45° + \frac{\varphi}{2}\right) \qquad\qquad\text{(b)}$$

and

$$\beta = 45° - \frac{\varphi}{2} \qquad\qquad\qquad (c) \qquad\qquad (2.21)$$

where τ refers to the shear stress at failure on the failure plane, σ_n is the normal stress on the failure plane, c is the cohesion, φ is the angle of internal friction, and β is the angle of the shear fracture plane to the major stress direction.

Based on the data for the COX claystone, the peak strength parameters are determined: c = 5.0 MPa and φ = 28°. The yield and dilatant envelopes are estimated by using their constant ratios to the peak strength mentioned above (R_Y = σ_Y/σ_F = 0.55; R_D = σ_D/σ_F = 0.75). Fig. 2.26 compares the Mohr-Coulomb's model with the measured data. For the region $\sigma_3 \geq 0$ the Mohr-Coulomb's criterion matches the data well. But it is not adequate for the tensile stress state, $\sigma_3 < 0$. Usually, a tensile cut-off is applied by $\sigma_3 = \sigma_t$ for modelling the tensile stress condition. Additionally, the Mohr-Coulomb's model predicts a shear plane angle of β = 31°, slightly larger than the mean value of β = 29° observed.
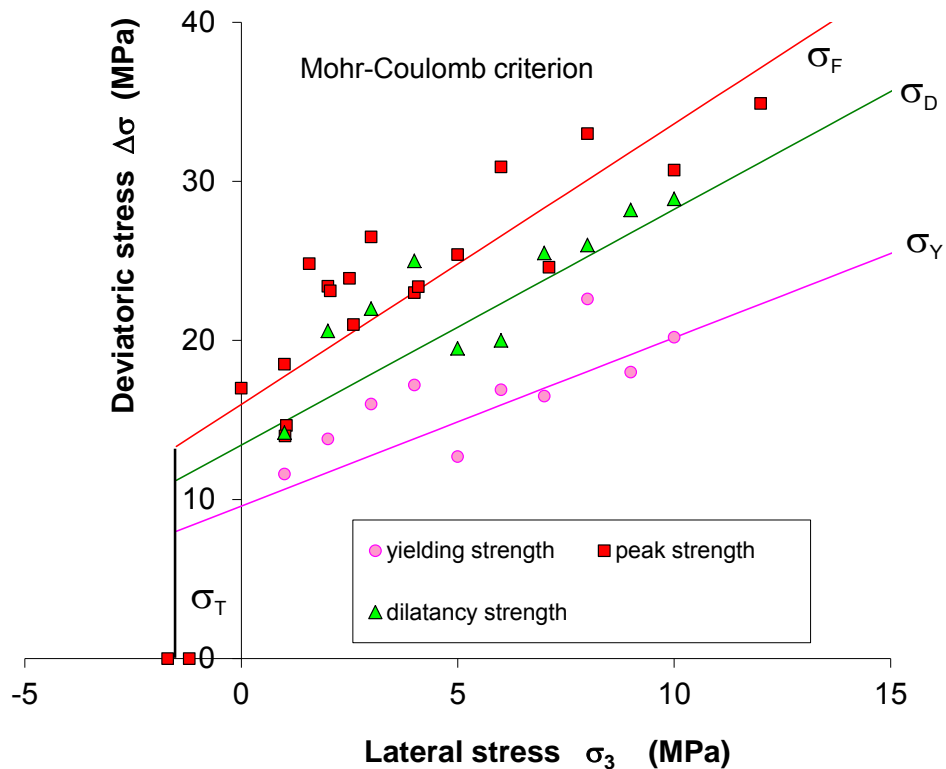
Fig. 2.26 Mohr-Coulomb criterion compared with the yield, dilatant and peak strengths for the COX clay rock

Hoek-Brown criterion

The empirical Hoek-Brown criterion is widely applied for description of the strength behaviour of all kinds of rocks:

$$\Delta\sigma_F = \sigma_{1F} - \sigma_3 = (m \cdot \sigma_c \cdot \sigma_3 + s\sigma_c^2)^{1/2} \tag{2.22}$$

where the uniaxial compression strength σ_c = 14 MPa, the parameter m = 9, and s = 1 are estimated for the peak strength of the COX claystone. Introducing the ratios of $R_Y = \sigma_{1Y}/\sigma_{1F}$ = 0.55 and $R_D = \sigma_{1D}/\sigma_{1F}$ = 0.75 into equation (2.22), one can obtain the yield and dilatant envelopes. The Hoek-Brown model is compared with the measured data in Fig. 2.27. A reasonable agreement is satisfactory for both tensile and compressive regions. For high confining stresses of σ_3 > 10 MPa, the peak strength is somewhat overestimated by the model.
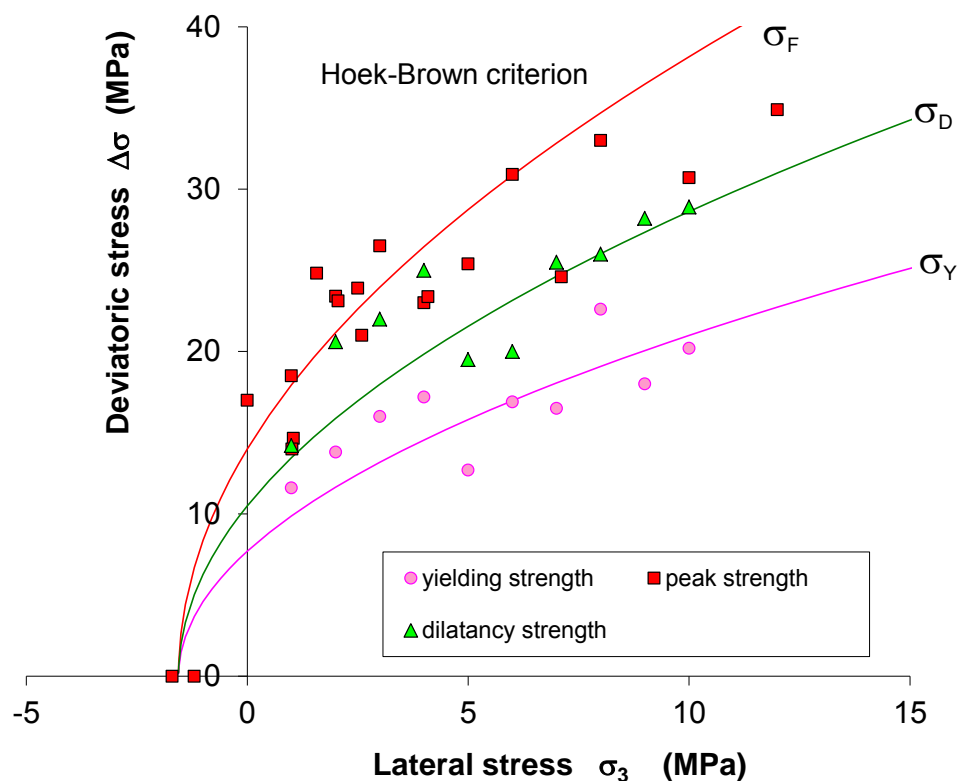
Fig. 2.27   Hoek & Brown's criterion compared with the yield, dilatant, and peak strengths for the COX clay rock

2.2.6 Damage induced permeability

Typical results of permeability change produced by increasing deviatoric stress are illustrated in Fig. 2.28 for confining stresses of 1, 4, 6, and 10 MPa. The data obtained at the other confining stresses are presented in Appendix B.2. Even though the initially disturbed samples had been pre-consolidated at the lithostatic stress of 15 MPa, some closed cracks could be more or less reopened after unloading to the desired confining stresses. The resulting gas permeability ranged between 10^{-19} and 10^{-17} m^2 being relatively high compared with that impermeable intact rock. During the subsequent deviatoric loading within the volume compaction range and even somewhat beyond the dilatancy point, the permeability decreased to a low level of ~10^{-20} m^2. At low confining stresses below 5 MPa, a pronounced increase in permeability occurred before or after the peak failure as a fracture network was established with the fracture propagation. The maximum permeability values of 10^{-16} – 10^{-15} m^2 were observed and maintained relatively constant with further loading and fracturing. Interesting is that almost no permeability increase was observed at the high confining stresses beyond 6 MPa. This indicates that the resulting local normal stresses on the fractures may be high enough to close them.

The permeability changes during the fracturing at the confining stresses of 1 and 4 MPa are depicted again in Fig. 2.29 as function of the radial extensive strain. It is obvious that as the radial extension or fracture opening reaches a threshold, the permeability begins to rising drastically. The maximum permeability is reached within a rather small fracture aperture range. This phenomenon represents a percolation process of crack growth and coalescence forming a fracture network. Further fracture opening leads only to a minor change in permeability.
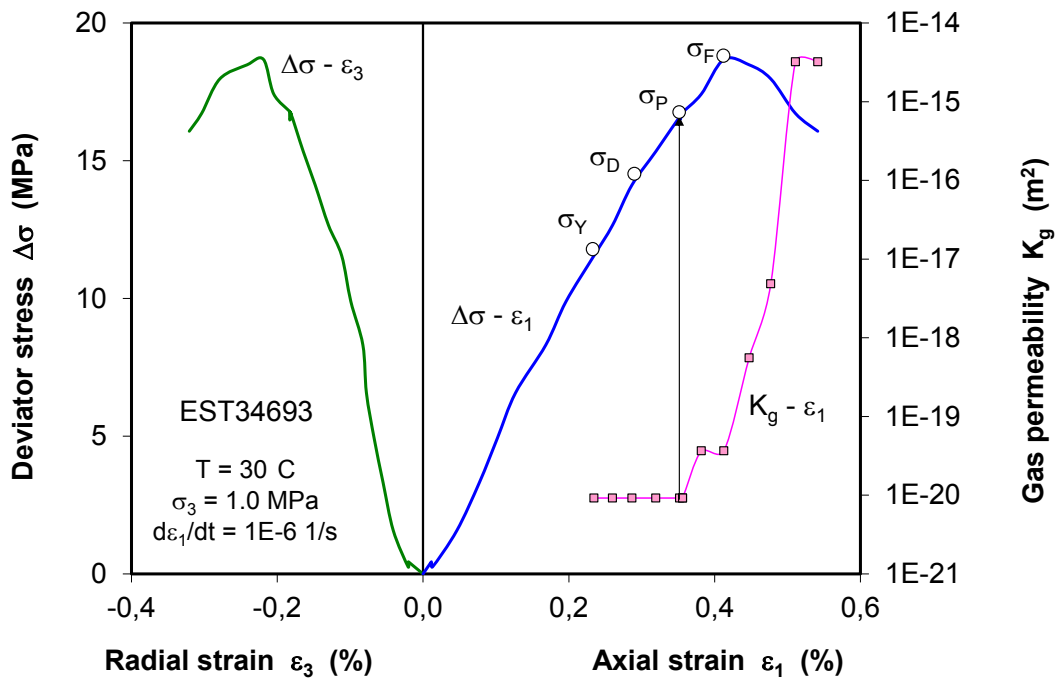
(a) $\sigma_3 = 1.0$ MPa
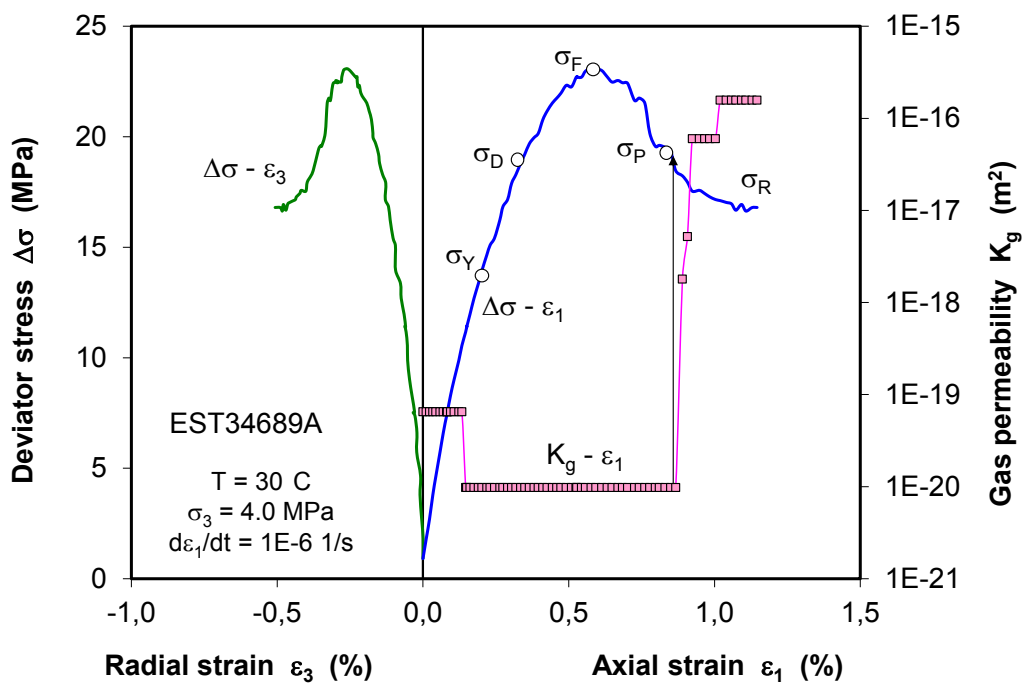
(b) $\sigma_3 = 4.0$ MPa
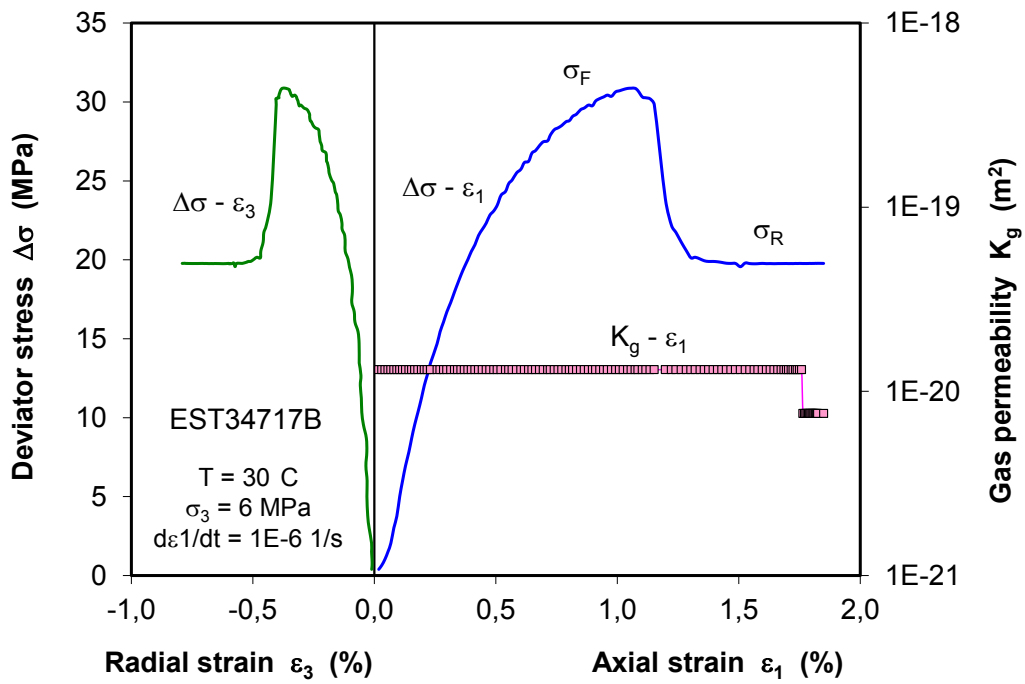
(c) σ_3 = 6.0 MPa
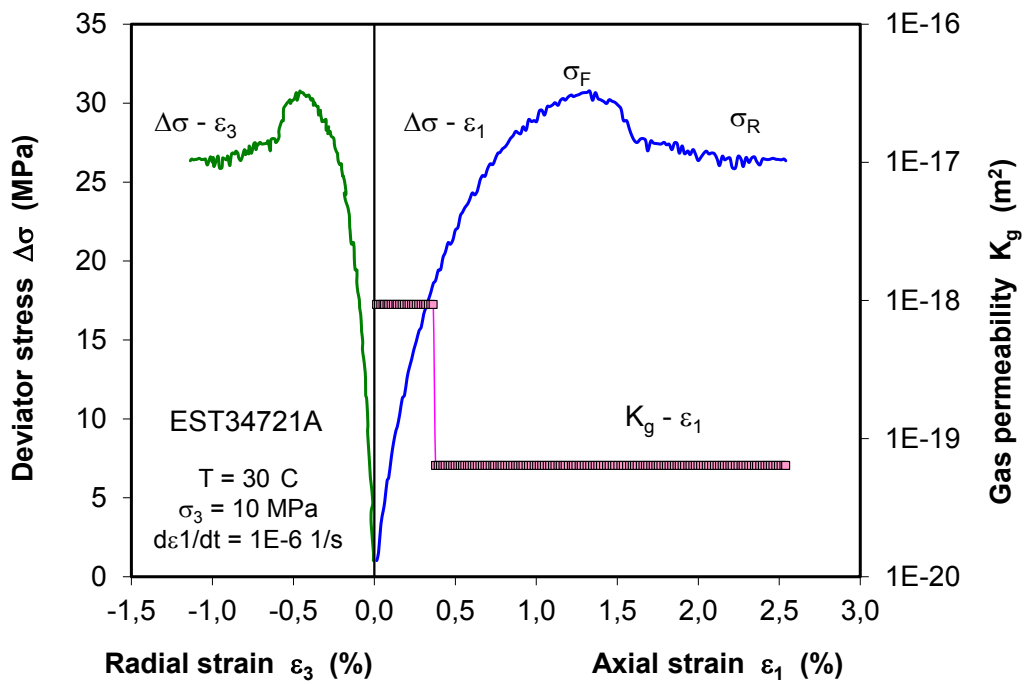
(d) σ_3 = 10.0 MPa

Fig. 2.28   Variation of gas permeability by deviatoric loading at different confining
stresses of 1 to 10 MPa
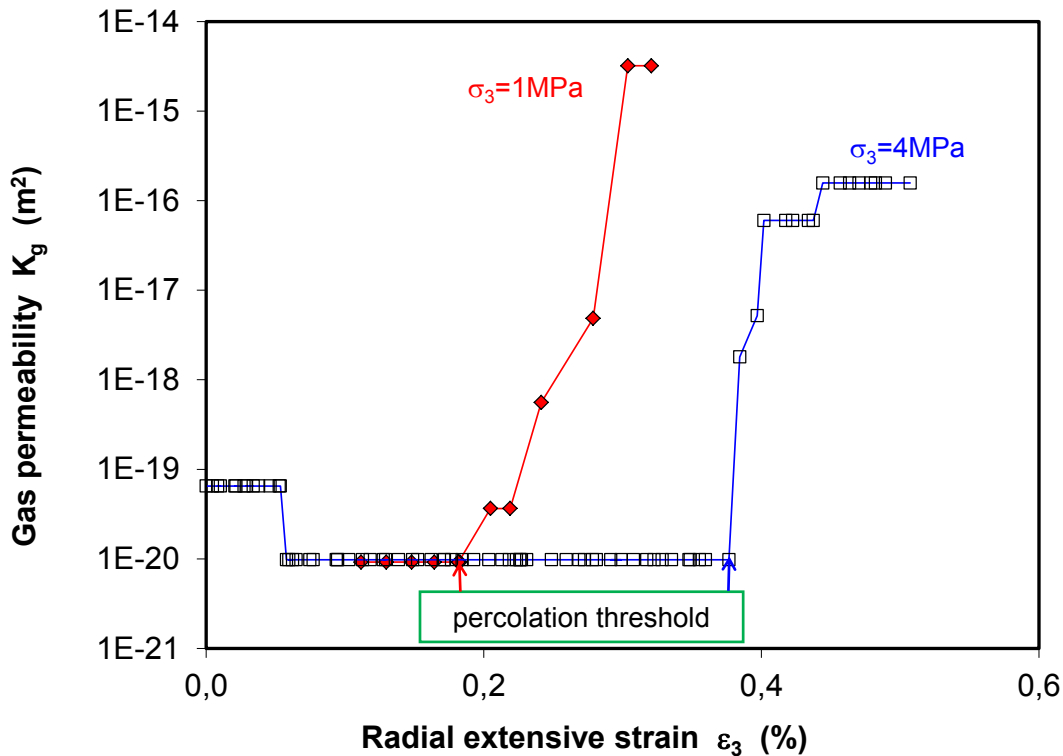
Fig. 2.29 Dependency of gas permeability on the radial extensive strain representing fracture opening at confining stresses of 1 and 4 MPa

2.2.7 Post-failure behaviour

The post-failure behaviour of fractured clay rock was examined on four COX samples (EST34689A, EST34711A, EST34713A/B), which had been broken down by the previous deviatoric loading. A few macro-fractures were developed through the samples mainly in two directions: the pre-existing fractures nearly parallel to the axis along the bedding plane due to coring and the other shear fractures obliquely to the axis at angles of 25° – 35° (see the pictures in Appendix B.3).

In order to obtain extensive information from each sample, multistage testing procedure was applied. The loading began with a low radial stress, at which the axial stress increased at a strain rate of $1 \cdot 10^{-6}$ s^{-1}. When the stress-strain curve became relatively flat or over a peak point, the axial loading was terminated. The next loading step followed at an increased radial stress. This procedure was repeated several times at confining stresses of σ_3 = 1, 2, 4, 8, 12 and 16 MPa. It made possible to determine effects of increasing isostatic and deviatoric stress components on fracture deformation and per-

meability change. Additionally, one can also obtain the shear strength of fractured clay rock.

Fig. 2.30 shows typical results obtained on a fractured COX sample in terms of deviatoric stress-axial strain ($\Delta\sigma$–ε_1), volumetric strain-axial strain (ε_v–ε_1) and gas permeability–axial strain (K_g–ε_1) curves at increased radial stress (σ_3). The results from the other tests are summarized in Appendix B.5. The important conclusions can be drawn from the data:

- The shear deformation of fractured claystone is dominated by irreversible plasticity or slip of fractures with hardening, accompanied by dilatancy at low confining stresses but contrarily by compaction at high confining stresses. Increasing the radial confining stress compacts the fracture apertures and gives the stiffness and strength rising.

- The stress point σ_R, at which the stress-strain curve becomes flat with slight hardening indicates the initiation of fracture shearing and is defined here as the residual strength of fractured claystone. The σ_R-values determined on the fractured samples are comparable with those determined immediately after the rupture of intact samples as shown in Fig. 2.31. The residual strength increases with increasing the minimal confining stress. The strength envelope can be well approached by the Hoek-Brown's criterion with parameters of σ_c = 12 MPa, m = 5 and s = 0. The Mohr-Coulomb's model with zero cohesion (c = 0) and a friction angle of φ = 35° seems to be acceptable for the low confining stress region below 10 MPa. Above that, the shear strength is overestimated by the model.

- The permeability of the fractured claystone is controlled by closure of fractures or volumetric strain, less dependent on the slip of fractures. The high initial permeability of 10^{-13} m^2 decreases largely with increasing minimal confining stress or volume compaction down to 10^{-18} – 10^{-20} m^2 at σ_3 = 16 MPa. The permeability – compaction behaviour is illustrated in Fig. 2.32 for two fractured COX samples.
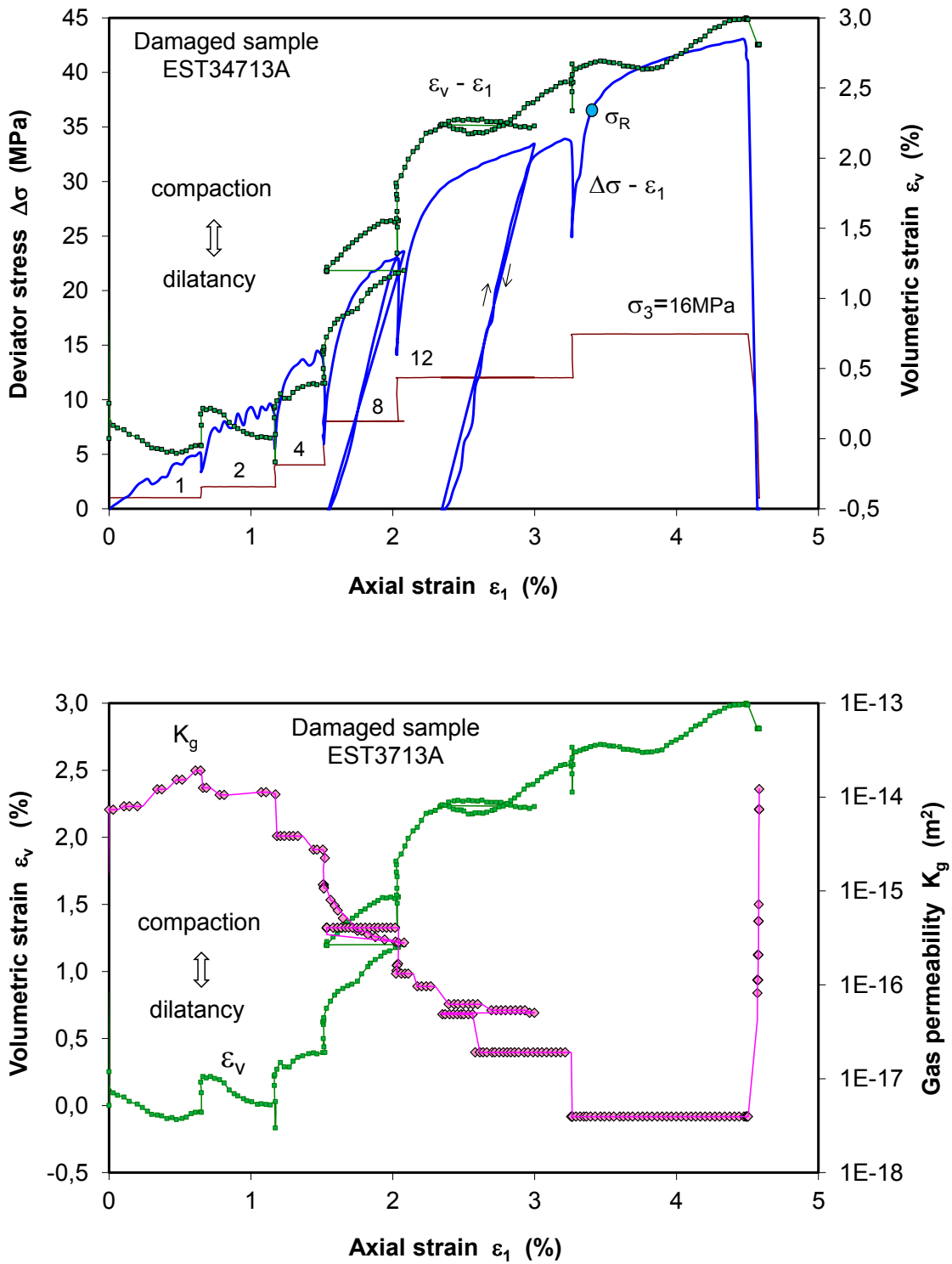
Fig. 2.30 Typical post-failure stress-strain behaviour and permeability response to post-failure deformation of fractured COX claystone
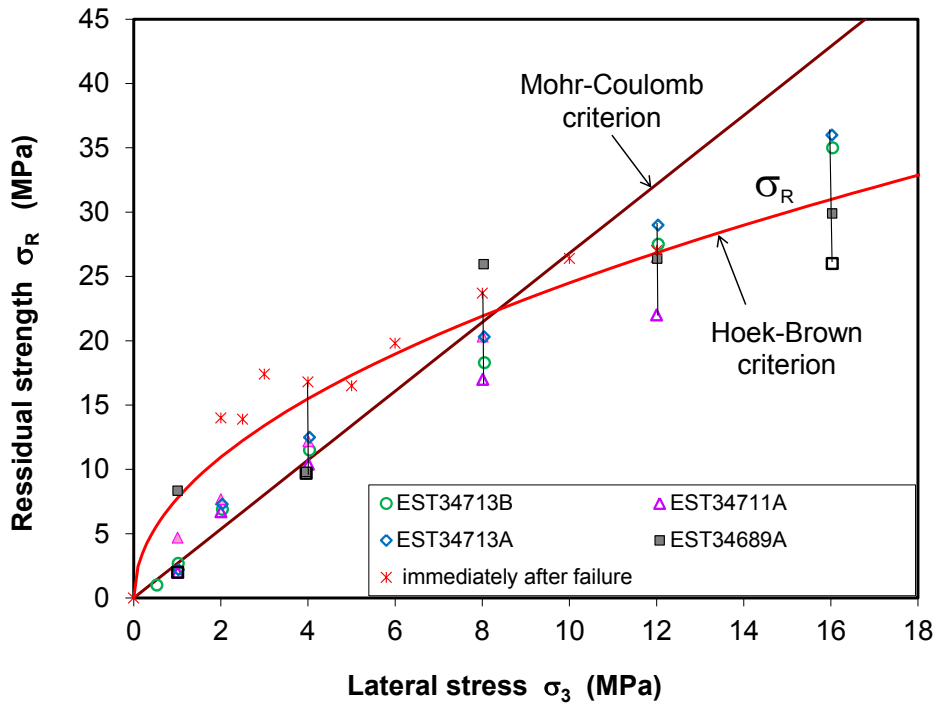
Fig. 2.31 Residual strength behaviour of fractured COX claystone
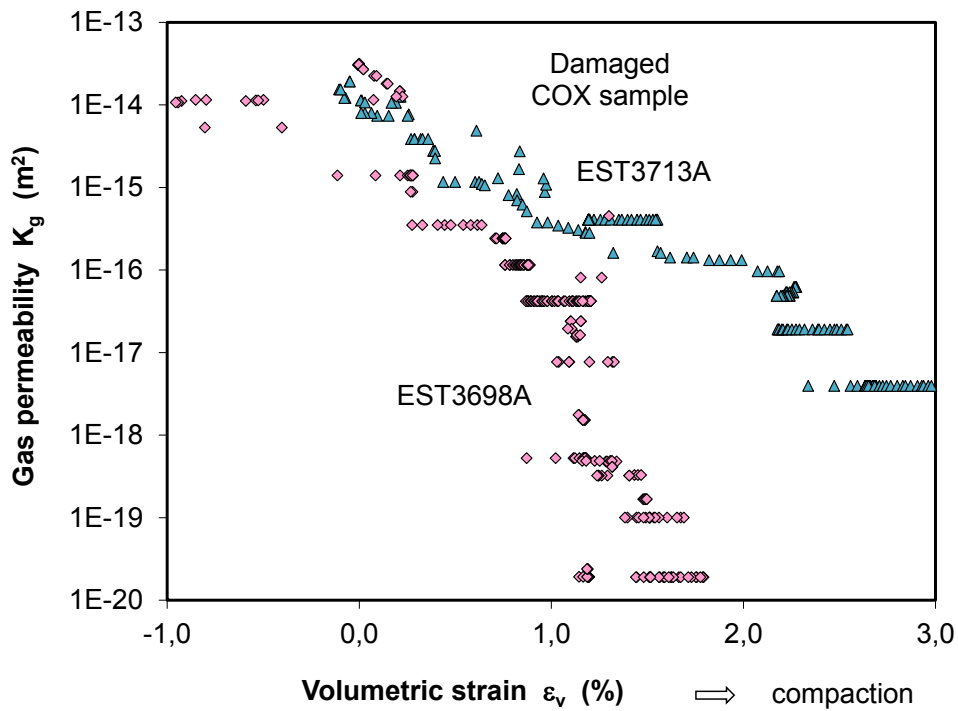
Fig. 2.32 Permeability-compaction behaviour of fractured COX claystone

2.2.8 Conclusions on the short-term hydromechanical behaviour

The short-term hydromechanical behaviour of the COX clay rock was investigated on the samples in triaxial compression tests. The stress-strain behaviour, responses of gas permeability and ultrasonic wave to deformation and damage were determined. The claystone behaves elasto-plastically before failure and can be characterised by the following four subsequent stages:

1. The linear elastic stress-strain behaviour occurs at low stresses below the yield threshold, being ~55 % of the failure strength. Above the yield stress, a deviation from the linearity appears due to the initiation of microcracks.

2. Further growth and propagation of the microcracks with stressing results in a transition from compaction to dilation at the dilatant threshold, being ~75 % of the failure strength. The crack propagation before dilatancy is stable, no macro-fractures occur, and thus no permeability increases before the dilatancy.

3. When the stress increase continues, more opening, propagation and coalescence of the microcracks leads to shear fractures until failure. The failure is brittle at low confining stresses and becomes ductile at high confining stresses. The permeability increases drastically by several orders of magnitude up to about 10^{-14} m^2 shortly before or after the failure under low confining stresses of less than 6 MPa. Above that, the local normal stress component on the shear fracture planes is sufficiently high to seal them and hence the permeability does not increase.

4. Beyond the failure point, the fractured claystone still has a residual bearing capacity due to the remaining friction resistance between fracture surfaces. The slip between fracture planes is dominated by irreversible plasticity accompanied by dilatancy at low confining stresses but contrarily by compaction at high confining stresses. Increasing the confining stress compacts the fracture apertures and gives the stiffness and strength rising. The permeability of the fractured claystone after post-failure is controlled by closure of fractures, less dependent on the shear slip of fractures. The permeability during shearing decreases mainly with increased minimal confining stress from the high values of $10^{-13} - 10^{-14}$ m^2 down to very low levels of $10^{-18} - 10^{-20}$ m^2 at the confining stress of 16 MPa and deviatoric stresses of 30 – 40 MPa.

The evaluation of the well-known Griffith, Mohr-Coulomb, and Hoek-Brown criteria against the experimental data suggests that the Hoek-Brown criterion is more adequate

for the damage, failure and residual strengths of the clay rock over a wide region from tensile to compressive stress state, $\sigma_{1F} = \sigma_3 + (m \cdot \sigma_c \cdot \sigma_3 + s\sigma_c^2)^{1/2}$, with the parameters of σ_c = 14 MPa, m = 9, and s = 1 for the peak strength of the COX clay rock at the 490 m main level of the MHM-URL. Introducing the ratios of $R_Y = \sigma_{1Y}/\sigma_{1F}$ = 0.55 and $R_D = \sigma_{1D}/\sigma_{1F}$ = 0.75 into the equation, one can obtain the yield and dilatant criteria. For the residual strength, the parameter m = 5, and s = 0 are estimated.

To note that it is necessary to consolidate of core samples before testing for minimising effects of pre-existing cracks that have been produced by coring and preparation. The data quality is strongly determined by the quality of the samples, which must be representative for the rock mass.

2.3 Long-term deformation behaviour

Progressive closure of repository openings in clay formations is to be expected due to creep of the surrounding host rock. Consolidation of both the excavation damaged zone and the porous backfill material will lead to permanent isolation of the radioactive waste from the biosphere /BMU 09/. For prediction and assessment of the long-term repository performance, the knowledge of the time-dependent behaviour of the host clay rock is needed.

In order to characterize the time-dependent deformation of the host clay rock, to understand the physical mechanisms, and to develop constitutive models for prediction of the long-term behaviour, comprehensive long-term creep experiments have been carried out by GRS on the COX and the OPA clay rocks since a decade. The previous results are published in GRS project reports and papers /ZHA 02/, /ZHA 04a/, /ZHA 04b/, /ZHA 07a/, /ZHA 10b/. In the tests, relevant repository conditions have been simulated by application of (1) stresses ranging from the initial lithostatic state to stress redistribution after excavation, (2) water contents from saturated to desaturated state, and (3) temperatures from ambient temperature to the designed maximum temperature of 90 °C and higher. The most tests were performed over extremely long time periods of 1 to 7 years. Various aspects have been investigated such as stress dependence of creep, moisture influence, thermal impact, and anisotropy of the clay rocks. In this Chapter, main results of the creep tests performed on the claystones with the natural water contents at ambient temperature are presented and discussed. Effects of moisture and temperature on the creep behaviour of the claystones will be shown in next Chapters 2.4 and 2.5 respectively.

2.3.1 Characterization of samples

Core materials for the creep tests were taken from the COX argillite at the MHM-URL and the OPA clay at the MT-URL. Most of the cores were drilled parallel to the bedding planes. They were prepared to cylindrical samples of diameter/length D/L = 70mm/140mm to 100mm/200mm. Within this project, more than 20 COX and OPA samples were tested in uniaxial and triaxial compression conditions. Due to the coring and preparation, microcracks were unavoidably induced along the bedding planes. The pictures of several samples are shown in Fig. B.10, and the fundamental properties of all the samples are summarized in Tab. C.4. The water content was measured on the rest pieces of 50 – 250 g cut off from the cores. The determined values of water content vary between 5.0 % and 6.3 %, which were adopted for the calculation of dry density, porosity and saturation degree for the creeping samples. The porosities were determined from 14.1 % to 17.3 % for the COX samples and ~14.3 % for the OPA samples. The calculated water saturation degrees range from 73 % to 100 %.

2.3.2 Testing equipment

Uniaxial creep tests were performed in five rigs in air-controlled room. One rig allows five samples being simultaneously tested at the same load up to 500 kN at ambient temperature, while each of the other four rigs allows two samples tested in separated chambers at elevated temperatures in a range of 20 to 200 °C. Fig. 2.33 shows the rig for uniaxial creep tests on five samples. All samples were sealed in rubber jacket and steel platen to avoid loss of pore water during testing. Axial load was applied equally to the five samples by means of an oil balance with accuracy higher than ±0.5 %. Axial deformation of each sample was originally measured by three displacement transducers (LVDT) with an accuracy of ±0.1 mm. The strain measurement was then improved by means of two more precise transducers within a variation of ±0.05 mm which were installed close to each sample and also several strain gauges of higher solution of 10^{-6} were directly glued on some samples for both axial and radial strain.

It is to be pointed out that results of uniaxial creep tests are more applicable to the rock near openings because of the comparability of the stress state sustained in testing samples with that area. The creep behaviour of the host clay rocks in the in situ triaxial stress state was investigated using two triaxial creep rigs with better controlling and measuring systems.
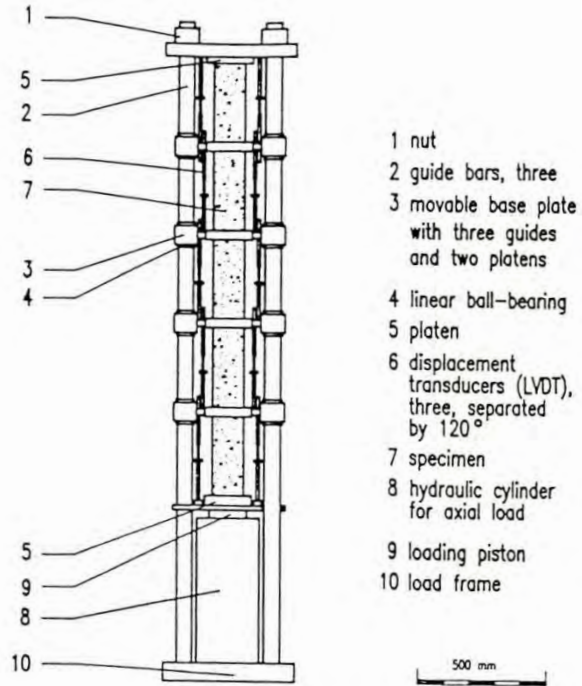
Fig. 2.33   Rig for uniaxial creep tests on five samples one upon another

It is to be pointed out that results of uniaxial creep tests are more applicable to the rock near openings because of the comparability of the stress state sustained in testing samples with that area. The creep behaviour of the host clay rocks in the in situ triaxial stress state was investigated using two triaxial creep rigs with better controlling and measuring systems.

Fig. 2.34 shows a triaxial creep rig allowing testing two samples simultaneously. Two triaxial cells were designed for cylindrical samples with a size of 70 mm diameter and 140 mm length. They are placed in two separated chambers and simultaneously loaded at same axial stress by the oil pressure in the low hydraulic cylinder. The maximum load is 500 kN corresponding to the maximum axial stress of 130 MPa. As a desired load is reached, a syringe pump with higher precision is switched over to keep the applied stress constant with a higher accuracy of better than 0.05 %. The lateral confining stress is applied separately to each sample by using two individual syringe pumps with the same accuracy of 0.05 %. The maximum lateral stress of 20 MPa is allowed. The tests can be carried out at high temperatures up to 200 °C by means of heaters installed inside each chamber. Temperature fluctuations are limited within ±0.2 °C. Axial displacement of each sample is measured by means of a transducer LVDT outside the cell and of two strain gauges directly glued on the sample surface, while radial strain is

monitored using other two strain gauges. They are positioned at the middle of each sample. The strain gauges have a higher solution of 10^{-6}.
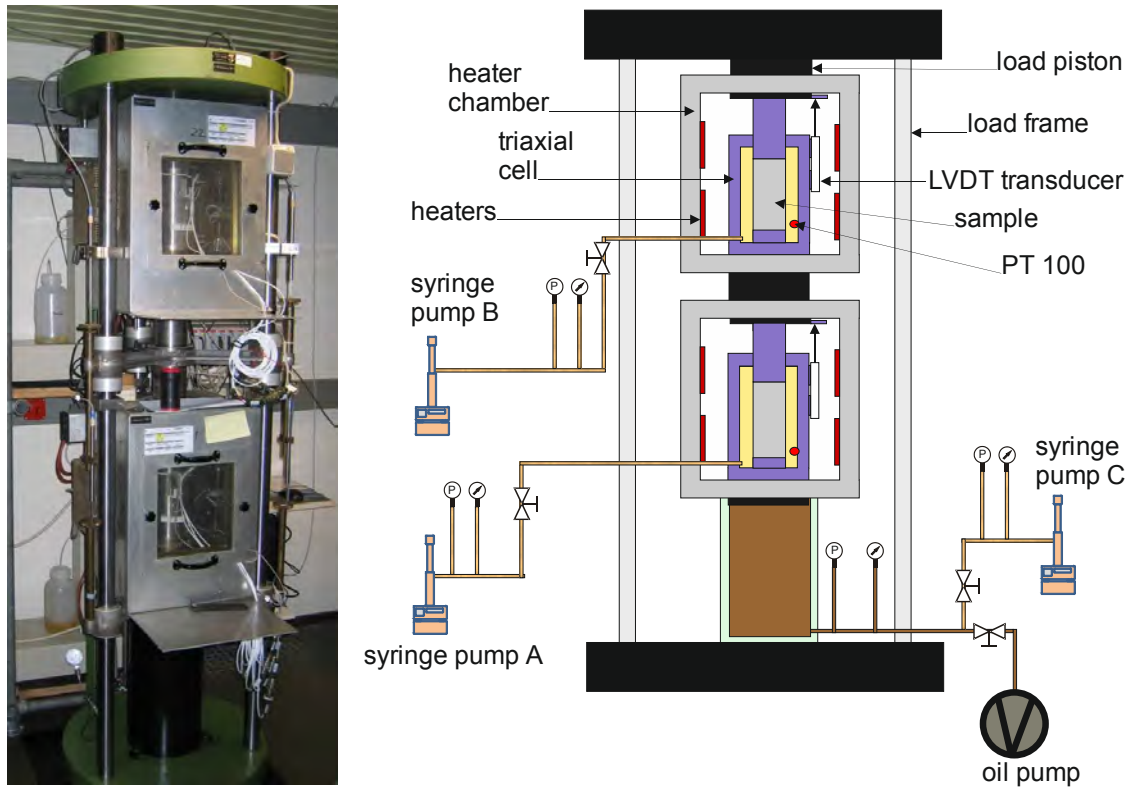
Fig. 2.34   Coupled rig for triaxial creep testing on two samples one upon another

Another triaxial creep apparatus is shown in Fig. 2.35. The triaxial cell allows a maximum axial stress of 70 MPa and a lateral pressure of 50 MPa with an accuracy of better than ±0.02 MPa (< 0.05 % of the maximum). The sample is inserted in a rubber jacket and located between two load pistons. It can be heated by means of a heater mounted outside around the cell up to a temperature of 150 °C within a fluctuation range of ±0.02 °C. While axial deformation is recorded by a LVDT deformation transducer installed inside the cell close to the sample, radial strain can be measured by a circumferential extensometer mounted around the sample outside the jacket. Two strain gauges for respective axial and radial strain are allowed to be glued on the surface at the sample mid-height. In addition to the strain measurements, this apparatus is also equipped with an ultrasonic device and a hydraulic system for detecting damage and sealing of the sample under various mechanical loads. The piezo-electric P and S wave transducers are positioned in the upper and lower pistons. Gas is allowed to be

injected to the bottom at constant pressure and outflow is recorded at the top by means of a burette and a flow meter.
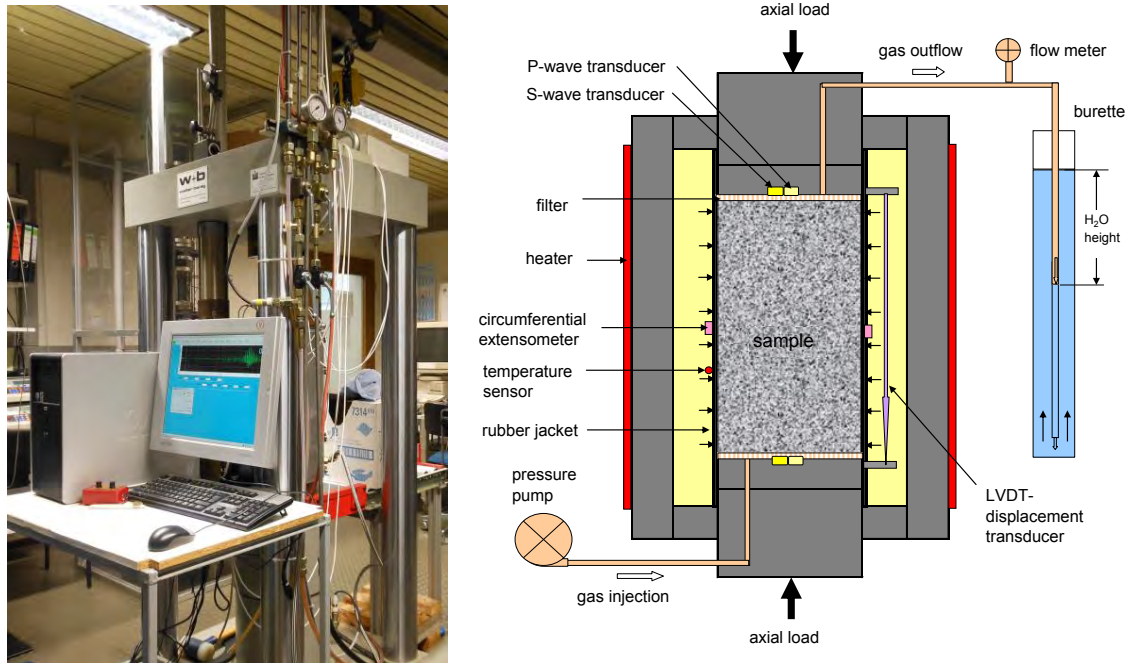
Fig. 2.35   Triaxial testing apparatus for THM coupling experiments on rock samples

2.3.3   Creep under uniaxial loads

The uniaxial creep tests on COX and OPA samples were mostly performed at ambient temperature and under multi-step uniaxial loads from very low levels of 0.3 – 1.0 MPa to rupture. Most of the tests lasted over exceptionally long time periods of 1 to 7.7 years with each step duration of 4 to 18 months. Totally, 13 samples were tested in five groups. Uniaxial strain-time curves measured on 5 COX and 3 OPA samples in groups 1 to 4 are illustrated in Appendix C.2.

Results of the other long-term creep tests on five COX samples are presented in Fig. 2.36. Sample EST25321 from a horizontal borehole TER1101 was axially loaded parallel to bedding while the others from a vertical borehole REP2206 were loaded perpendicular to bedding. The remaining water contents are between 5.3 % and 5.7 %, corresponding to water saturation degrees of 80 – 90 %. The tests focused on investigating influences of load level, load path, and load direction with respect to the bedding plane. The axial stress was multiply increased to 4, 7, 10, and 13 MPa in the first phase, then dropped down to 10, 7, and 4 MPa in the second phase, and finally in-

creased again to high levels of 15, 17, 19.5, 21, 22, 28, and 30 MPa. From the long-term creep curves, one can identify the following phenomena.
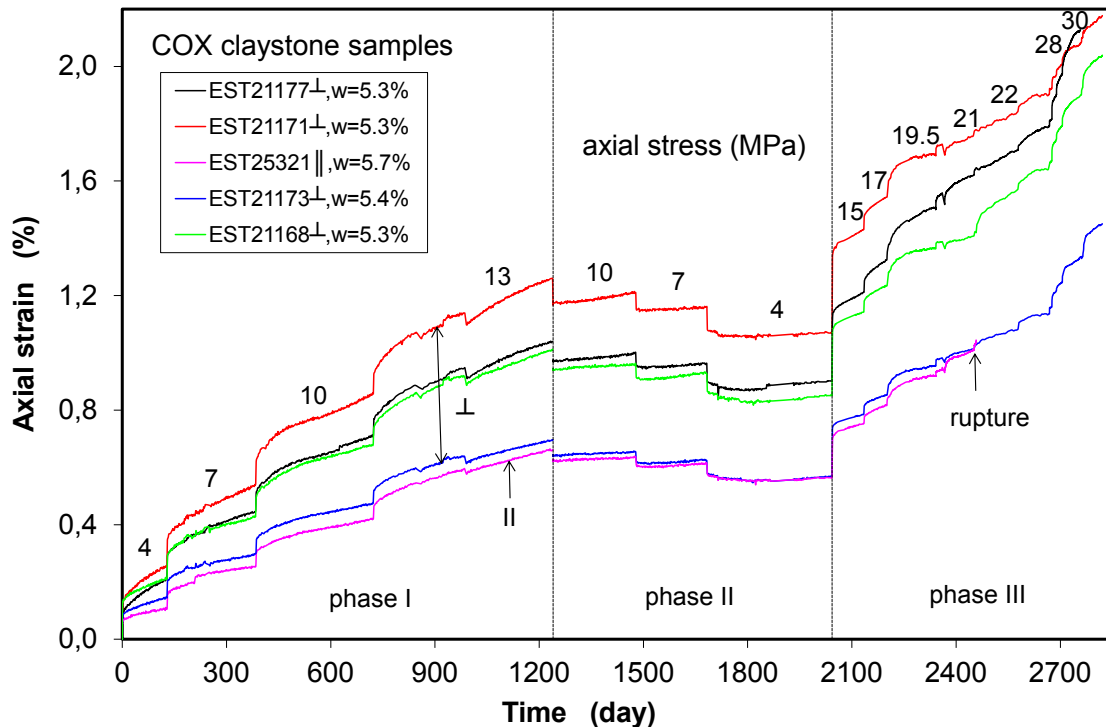
Fig. 2.36   Long-term uniaxial creep behaviour of five COX claystone samples under multi-step loads parallel and perpendicular to bedding plane

The total strains in direction perpendicular to bedding are larger than those in parallel direction, because of the relatively low stiffness in the perpendicular direction. The elastic moduli determined on the four samples in the perpendicular direction vary from $E_\perp$ = 3.5 to 5.6 GPa. The values are lower than that of E_{II} = 6.8 GPa in the parallel direction. However, the strain evolution curves are relatively parallel, suggesting little anisotropy of the viscous deformation in the clay rock. The same conclusion was already drawn from the previous tests on the other COX samples /ZHA 04a/, /ZHA 04b/.

It is interesting to compare the creep curves obtained at the same stress level but reached by different loading paths (loading path in phase I and unloading path in phase II). Fig. 2.37 compares the creep curves obtained at axial load of 7 MPa reached (a) along loading path and (b) along unloading path, while the other creep curves at 10 and 4 MPa reached along loading and unloading paths presented in Fig. C.32 and Fig. C.33 respectively. The creep curves at the same stress but reached along different loading paths show different patterns, indicating that the creep behav-

iour is dependent upon loading path. The creep strain curve at increased load is typically characterized by a transient phase with decreasing rates and a following stationary phase with an asymptotically approached constant rate. In contrast, the creep strain at decreased load evolves firstly backwards with negative rates and then returns with time to positive rates and gradually to steady state. However, the steady-state creep rates of $2 \cdot 10^{-11}$ to $6 \cdot 10^{-11}$ s^{-1} obtained on the five samples at decreased loads are relatively higher than those of $1 \cdot 10^{-11}$ to $2 \cdot 10^{-11}$ s^{-1} at decreased loads (see Fig. 2.35). The difference might be mainly attributed to the effect of over-consolidation resulted from the previously applied high loads, which increases the density and thus the connection number and intensity of interparticle bonds which hinders deformation /MIT 76/, /MIT 92/.

Fig. 2.38 summarizes the steady-state creep rates of the five samples as function of applied stress level and path. The creep rates vary insignificantly with stress in the low range below 20 MPa. Beyond that, the creep rate increases faster. This might be caused by initiation and propagation of microcracks in the samples. The damage-accelerated creep can lead to rupture. Fig. 2.39 shows the typical tertiary creep to rupture observed on sample EST25321 at a high load of 22 MPa. This value is slightly higher than the short-term uniaxial strength (c.f. Fig. 2.27). Another sample EST21177 loaded perpendicular to bedding failed by increasing the load from 28 to 29 MPa. The other three samples deformed gradually with time during the last phase at a higher stress of 30 MPa. No creep rupture occurred. The high load exceeds the uniaxial strength of ~25 MPa in direction perpendicular to bedding /ZHA 10b/. This might be attributed to possible desaturation of the samples over the very long time periods. This issue was examined by measurement of the water contents of the remaining samples. The rest water contents measured are: w_r = 3.01 % for sample EST21171, w_r = 2.48 % for sample EST21173 and w_r = 2.67 % for sample EST21168. That means that the total loss of the porewater over the long duration of 7.7 years is about 2.3 – 2.8 % compared with the initial water content of w_o ≈ 5.3 %. Because the desaturation process during the tests is unclear, possible effects of water content change on the creep deformation cannot be evaluated yet. This issue will be examined later in Section 2.4.

The uniaxial creep was also investigated under extremely low stresses of less than 1.0 MPa to examine whether a threshold exists for onset of creep. Fig. 2.40 shows the measured creep curves. It is obvious that the COX and OPA samples deformed steadily with time, except for one COX sample that originated from the upper zone A with less clay and water contents but more carbonates. Over a transient phase during

66

the first two months, the creep curves are quite linear with constant creep rates. This observation suggests that there is practically no creep limit.
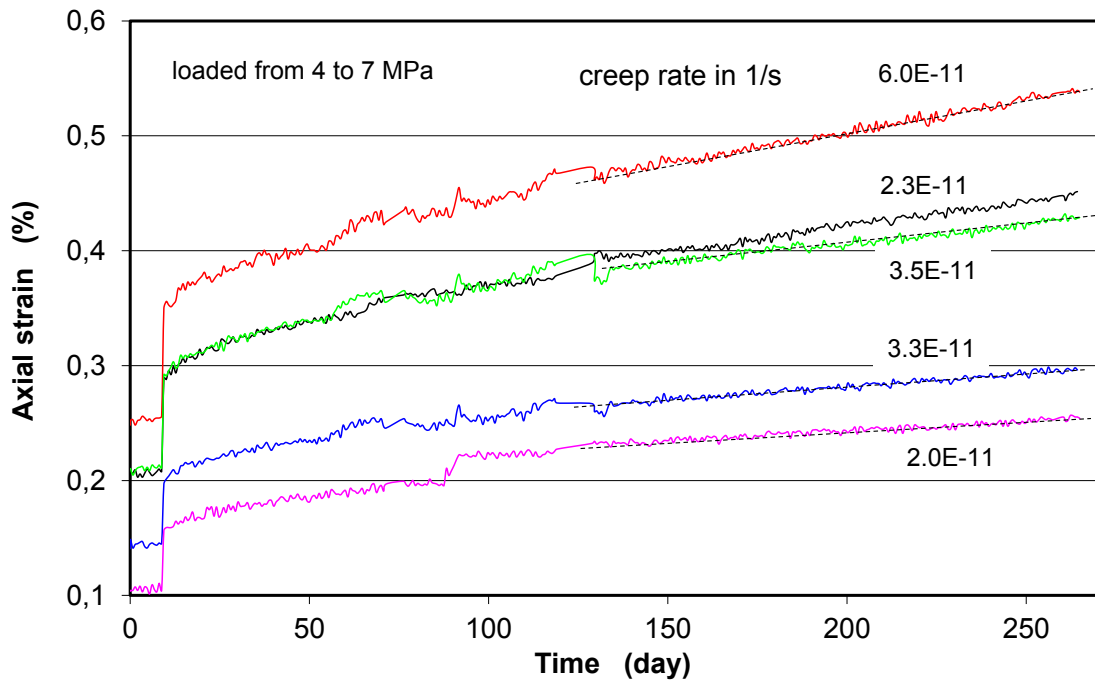
(a) loaded from 4 to 7 MPa
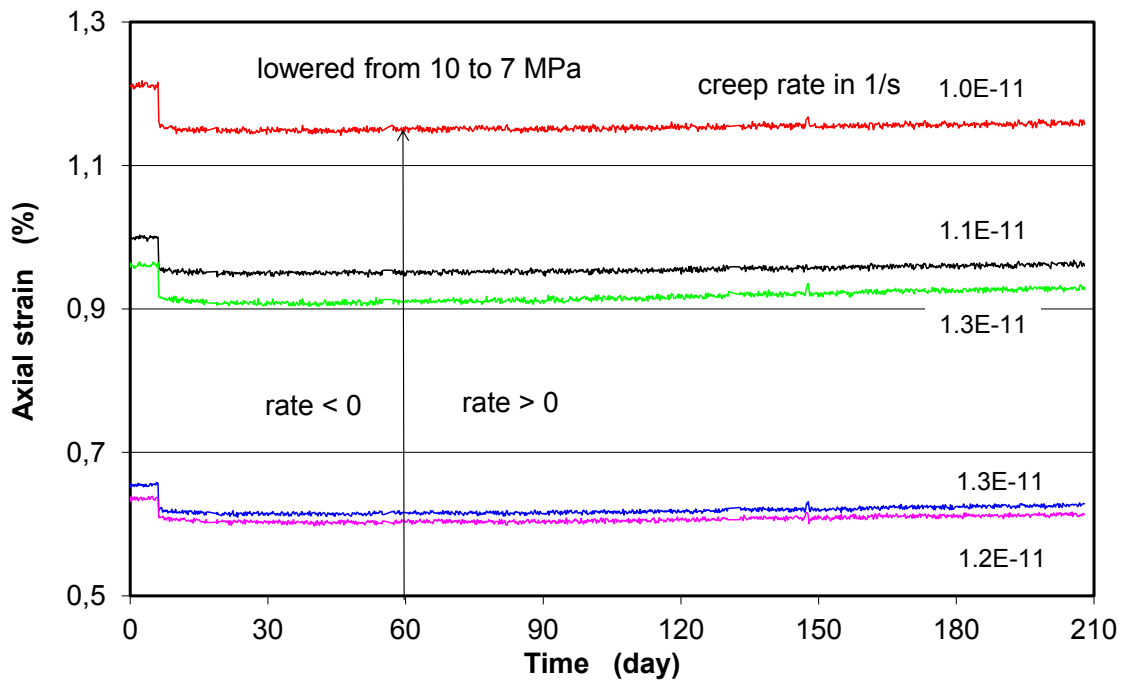
(b) unloaded from 10 to 7 MPa

Fig. 2.37 Comparison of uniaxial creep curves under axial stress of 7 MPa reached by upload and download

67
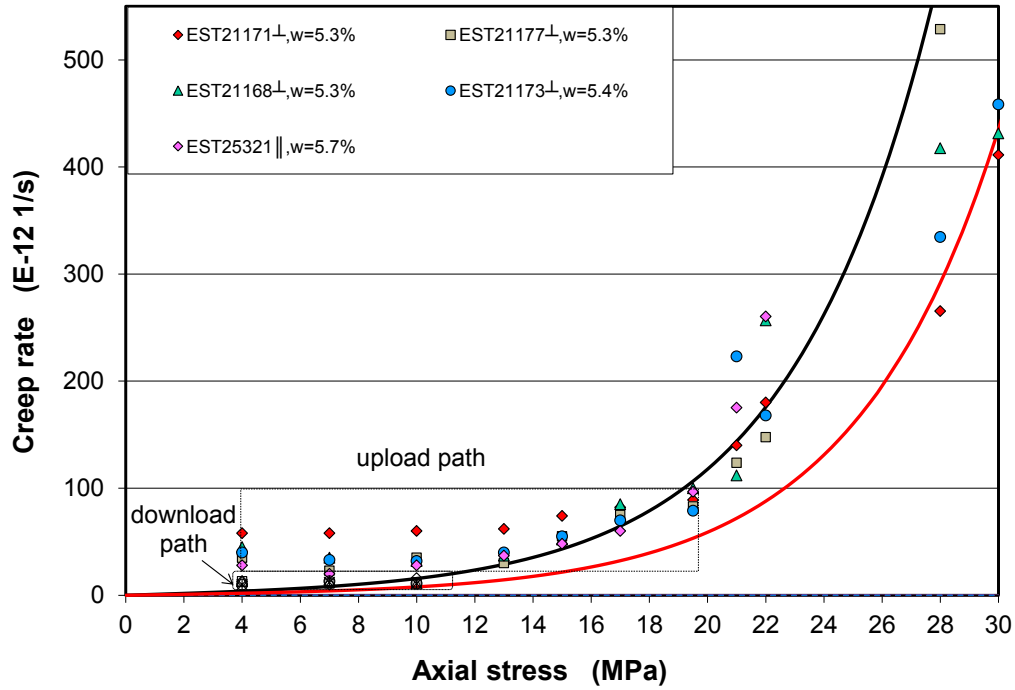
Fig. 2.38 Steady-state creep rates obtained on five COX samples as a function of applied uniaxial loads
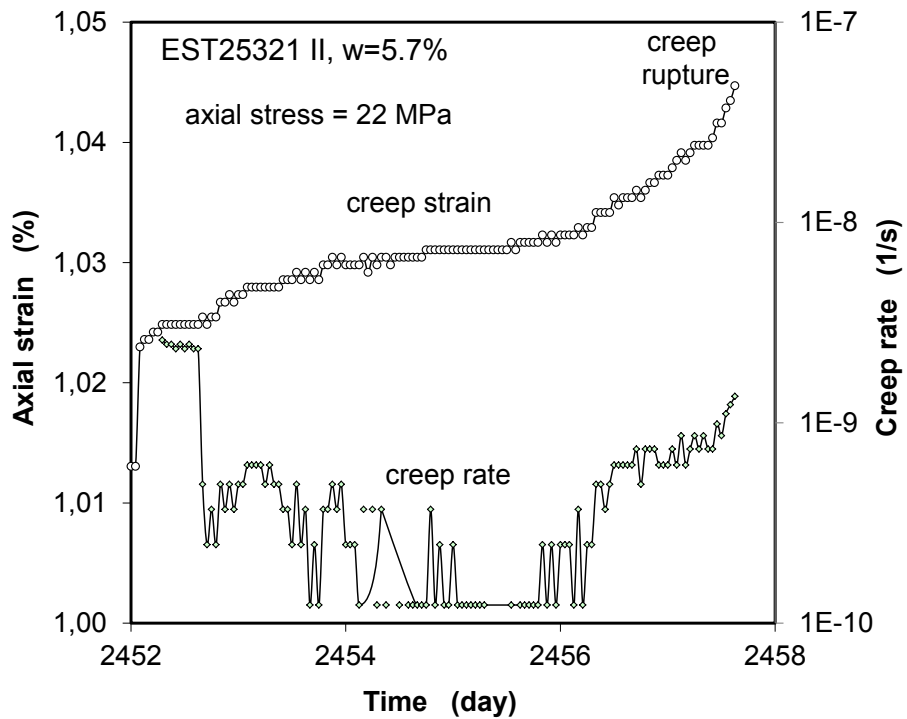
Fig. 2.39 Creep rupture of a COX sample loaded in direction parallel to bedding
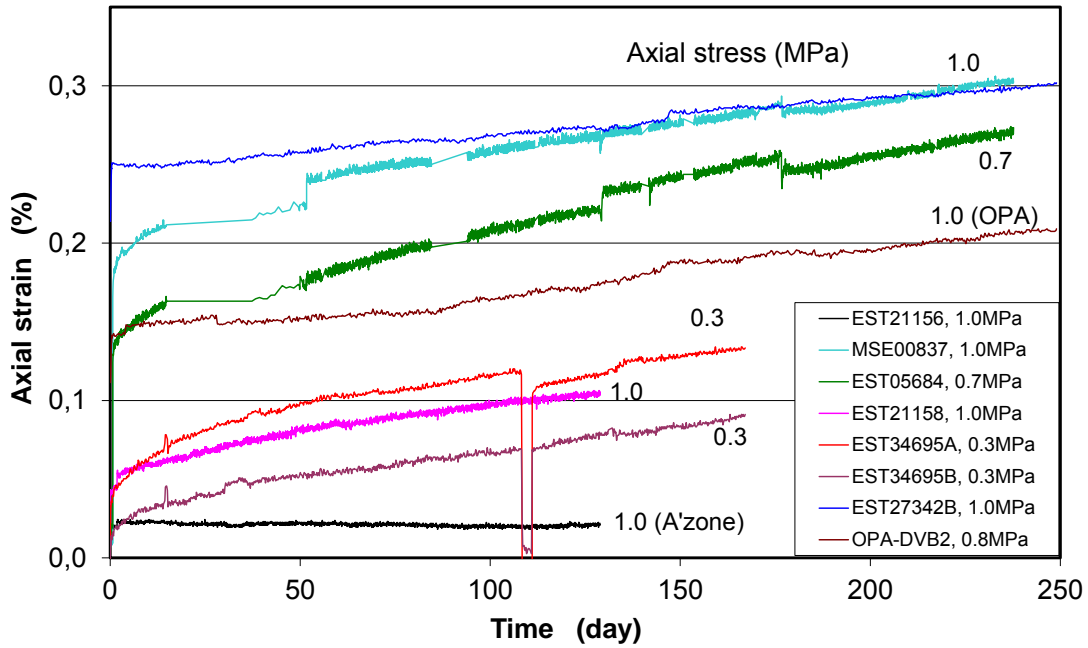
Fig. 2.40   Uniaxial creep curves of COX clay samples under very low axial stresses
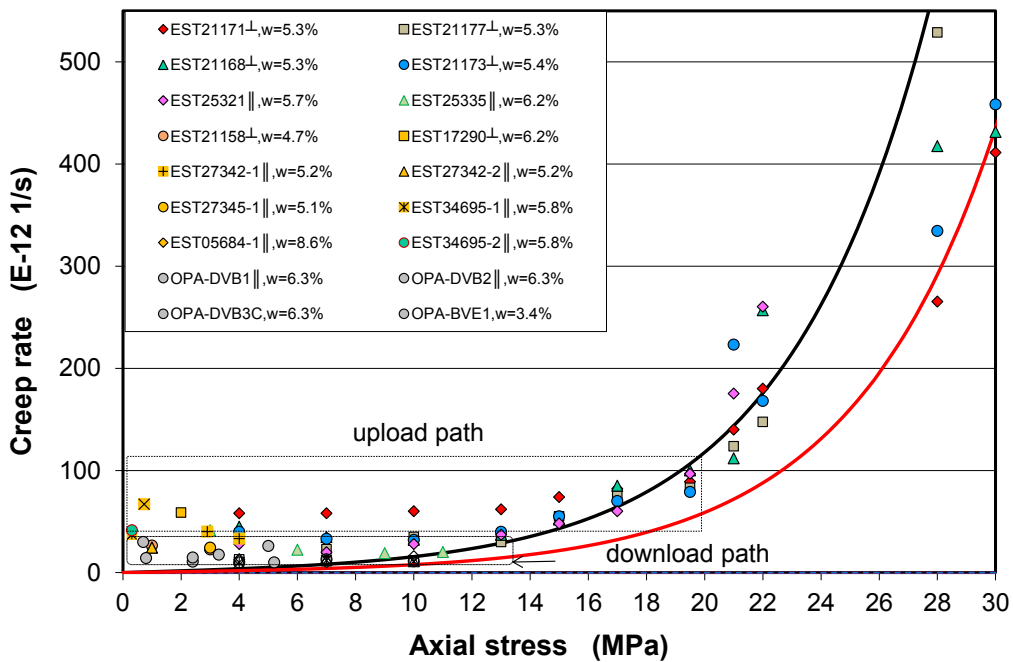
Fig. 2.41   Steady-state creep rates obtained on COX samples under uniaxial loads
ranging from very low to high levels

The steady-state creep rates obtained on both COX and OPA samples at low stresses
of 0.3 to 5.0 MPa are depicted in Fig. 2.41 together with those obtained at high stress-
es. It can be clearly found that the creep rates even at the very low stresses of smaller

than 1 MPa are comparably high in the same range between $2 \cdot 10^{-11}$ and $6 \cdot 10^{-11}$ s^{-1} as determined at the stresses of 5 to 20 MPa. In the stress region below 20 MPa, the creep rate seems to be little dependent or even independent of the stress levels. This phenomenon of the relatively high creep rates and stress independent cannot be reasonably interpreted yet. This needs information of micro-processes in the clay-water-system during the deformation. Moreover, the creep rates of both the studied clay-stones are comparable.

2.3.4   Creep under triaxial loads

In order to better approach the *in situ* stress states in the rock mass, triaxial creep tests have been conducted. An additional advantage of triaxial tests is the possibility of re-consolidating samples prior to the testing for removing the pre-existing microcracks and providing reliable data.

Fig. 2.42 presents results of a triaxial creep test on COX sample EST34737 extracted from a horizontal borehole in the TED test field in the MHM-URL. The sample was prepared to a cylinder of 70 m diameter and 140 mm length. It had an initial porosity of 17.3 % and water content of 7.1 %. On the sample surface, a few microcracks can be visually identified along the bedding plane parallel to the sample axis (see the picture in Fig. 2.42a). For measurements of axial and radial strain, two groups of strain gauges were attached on the sample surface at the middle length. The gauge strips for the lateral strain measurement were positioned perpendicular and parallel to the bedding plane respectively, while the other two were parallel to the bedding for the axial strain measurement. Additionally, a displacement transducer LVDT was also used for the axial strain measurement along the whole sample length. This test aimed to examine the creep behaviour of the claystone under the lithostatic stress state. The stress conditions applied to the sample and the strain responses are shown in Fig. 2.42b. The testing temperature was controlled at 25.5±0.1 °C.

The sample was firstly reconsolidated by increasing the confining stresses up to σ_1/σ_3 = 18.3/18.0 MPa, resulting a decrease in porosity to a rest value of 15.5 % and full water saturation. The radial compression perpendicular to bedding ($\varepsilon_{r\text{-DMS2}}$) was relatively larger than $\varepsilon_{r\text{-DMS1}}$ parallel to bedding, while the axial strain values are also local dependence. The axial strain measured along the whole sample length by means of LDVT is larger than those local values. Regardless of the local dependence of the

measured strains, the creep behaviour of the sample is illustrated in Fig. 2.43 in terms of averaged axial strain $\varepsilon_a = (\varepsilon_{a-DMS1} + \varepsilon_{a-DMS2} + \varepsilon_{a-LDVT})/3$, radial strain $\varepsilon_r = (\varepsilon_{r-DMS1} + \varepsilon_{r-DMS2})/2$ and volumetric strain $\varepsilon_v = \varepsilon_a + 2\varepsilon_r$ with time. The steady-state creep rates determined within the last stationary intervals are marked too.
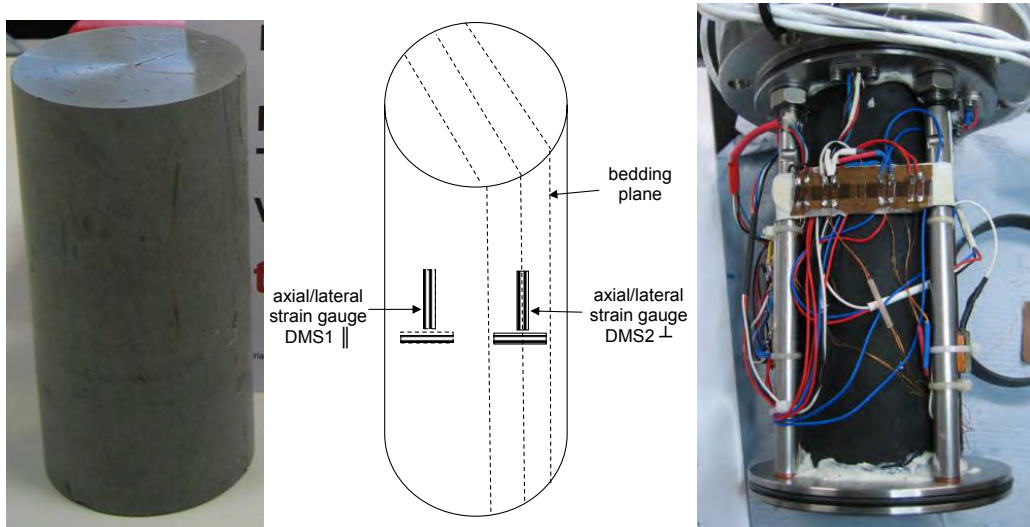
(a) prepared COX sample and positions of used stain gauges
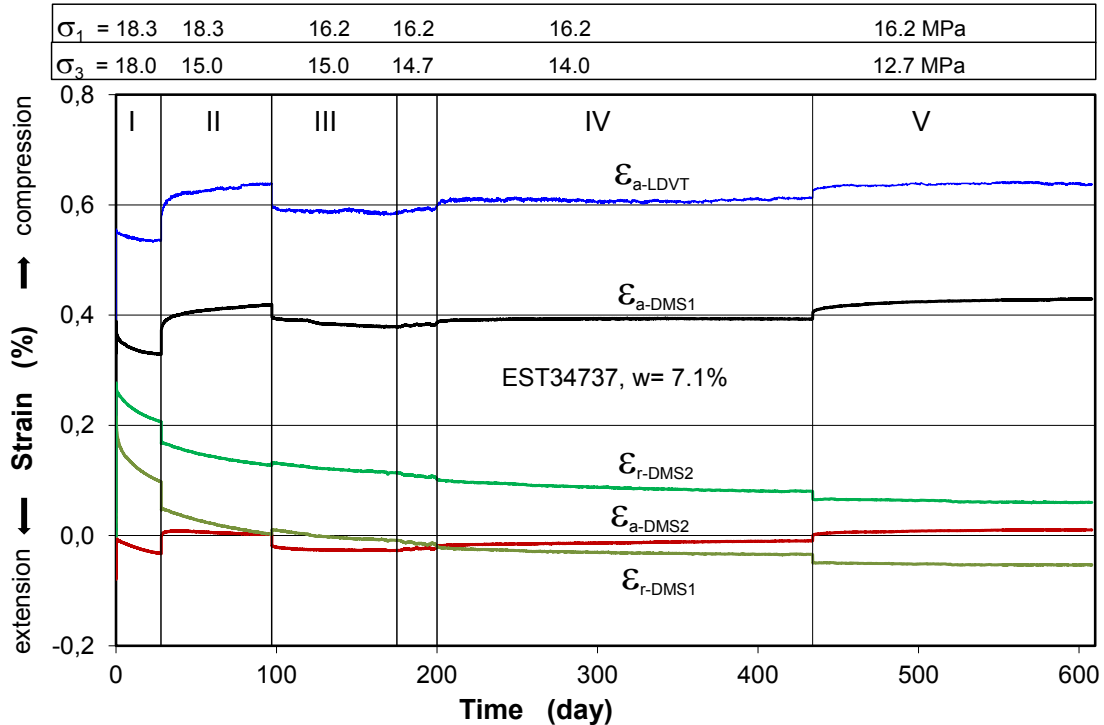
(b) evolution of measured strains

Fig. 2.42 Measurement of axial and radial strains during a triaxial creep test on COX sample under the lithostatic stress conditions

71

| σ_1 = 18.3 | 18.3 | 16.2 | 16.2 | 16.2 | 16.2 MPa |
| σ_3 = 18.0 | 15.0 | 15.0 | 14.7 | 14.0 | 12.7 MPa |
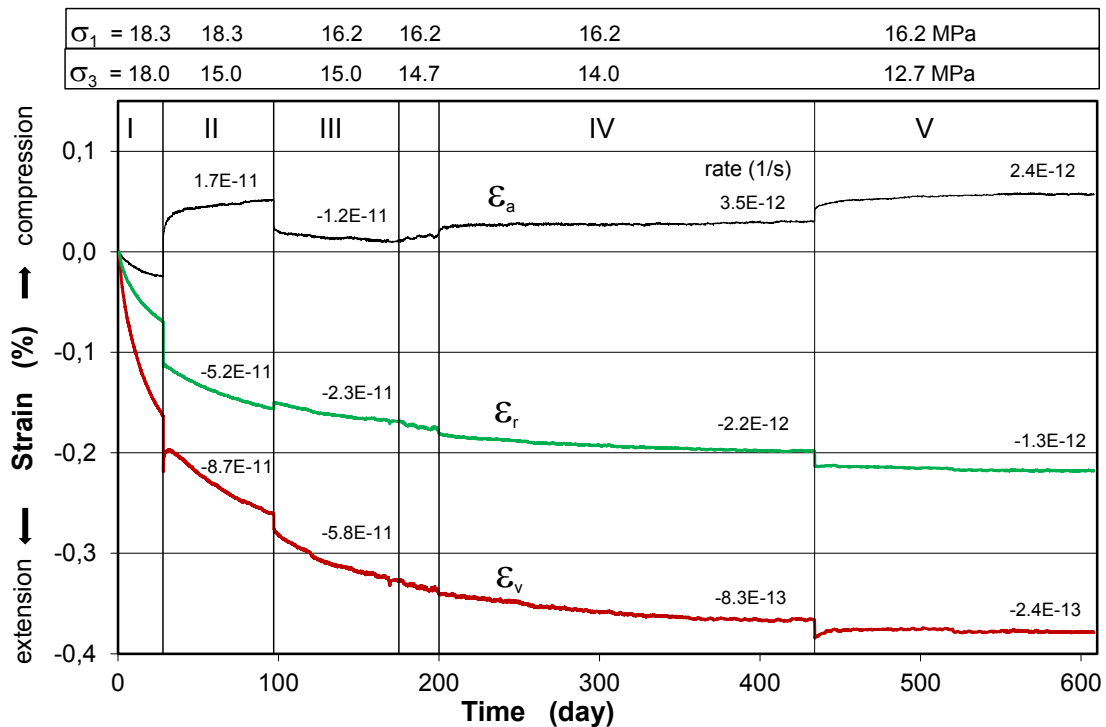
Fig. 2.43 Triaxial creep behaviour of the COX claystone under the lithostatic stress conditions

The creep curves in Fig. 2.43 show that:

1. At the high quasi-isostatic stress of σ_1/σ_3 = 18.3/18.0 MPa, a gradual extension in all directions took place rather than compression. The volume expansion reached at 0.16 % over a month. This unexpected phenomenon is differing from that consolidation process commonly observed on other types of saturated porous soils and rocks. It seems to be difficult to reasonably explain the "abnormal" process in the saturated claystone by application of the conventional porous medium theories.

2. The first creep phase was conducted at decreased radial stress of σ_3 = 15.0 MPa by keeping σ_1 = 18.3 MPa. The drop of radial stress produced a gradual radial extension ($\dot{\varepsilon}_r$ < 0) and axial compression ($\dot{\varepsilon}_a$ > 0). Under effect of the deviatoric stress, the axial and radial strains continued with time from a transient phase to a quasi-steady state. The magnitude of the radial expansion rate of $\dot{\varepsilon}_r$ = -5.2·10⁻¹¹ s⁻¹ determined is faster than the axial compression rate $\dot{\varepsilon}_a$ = 1.7·10⁻¹¹ s⁻¹, leading to a volumetric dilation with a rate of $\dot{\varepsilon}_V$ = -8.7·10⁻¹¹ s⁻¹. Because of the high confining stress and the very low deviatoric stress of $\sigma_1 - \sigma_3$ = 18.3 – 15.0 = 3.3 MPa, much below the onset stress of damage-induced dilatancy mentioned before in Section 2.2.4 – 2.2.5, the progressive dilation during the creep is not induced by initia-

72

tion and propagation of microcracks, but probably due to the expansion of over-lapped bound-water-films between clay particles after stress relief.

3. The subsequent drop of axial stress σ_1 to 16.2 MPa at σ_3 = 15.0 MPa caused an elastic recovery shortly, followed by a gradual extension in axial and radial direction ($\dot{\varepsilon}_a$ < 0, $\dot{\varepsilon}_r$ < 0) over 3 months. Following that, the lateral confining stress dropped slightly down to ~14.7 MPa due to a short-term failure of the testing system. The relative increase in deviatoric stress caused a gradual compression in axial direction over a month.

4. After adjusting the radial stress of σ_3 = 14.0 MPa at σ_1 = 16.2 MPa, a longer creep phase followed over 8 months. Axial compressive and radial extensive strains evolved steadily with time. Because the radial expansion was still faster than the axial compression, the corresponding volume dilation continued. Within the last two months, the steady-state creep rates were determined at $\dot{\varepsilon}_a$ = 3.5·10^{-12} s^{-1}, $\dot{\varepsilon}_r$ = -2.2·10^{-12} s^{-1}, and $\dot{\varepsilon}_v$ = -8.3·10^{-13} s^{-1}.

5. Keeping σ_1 = 16.2 MPa, the lateral stress was lowered to σ_3 = 12.7 MPa, corresponding to the anisotropic rock stress state at a depth of 500 m at the MHM-URL /AND 05/, namely the vertical and minor horizontal stress $\sigma_V \approx \sigma_h$ = 12.5 MPa and the major horizontal stress $\sigma_H \approx 1.3\,\sigma_h$ = 16.2 MPa. It is obvious that the axial compressive and radial extensive strains continued progressively over 6 months. The steady-state creep rates were determined within the last two months: $\dot{\varepsilon}_a$ = 2.4·10^{-12} s^{-1}, $\dot{\varepsilon}_r$ = -1.3·10^{-12} s^{-1}, and $\dot{\varepsilon}_v$ = -2.4·10^{-13} s^{-1}. The values are comparable with those before at a slightly higher deviatoric stress of $\sigma_1 - \sigma_3$ = 2.2 MPa.

There are also more similar results of triaxial creep tests performed on COX and OPA samples under high confining stresses but low deviatoric components of σ₁ = 15.3 MPa and σ₃ = 14, 13, 12 MPa, as shown in Fig. C.36 and /ZHA 10b/. All the experimental observations suggest that there is practically no creep limit for the saturated clay rocks.

Another triaxial test aimed at investigating influences of confining stress and loading path on creep of claystone. COX sample EST34678 was prepared to a size of D/L = 100/190 mm and used for the test. The sample was characterized with an initial porosity of 15.6 %, water content of 5.9 %, and saturation degree of 90 %. After preparation, a few microcracks appeared on the surface nearly parallel to the sample axis as the sample pictures show in Fig. 2.44. In order to avoid effects of the microcracks, the sample was pre-consolidated at isostatic stress of 15 MPa over 20 days, decreasing

the porosity to 14.7 % and hence increasing the water saturation to 97 % near the full saturation. The sample was instrumented with a displacement transducer and an extensometer chain for axial and radial strain measurement respectively, and moreover, two strain gauges were glued on the surface for local strain measurement.
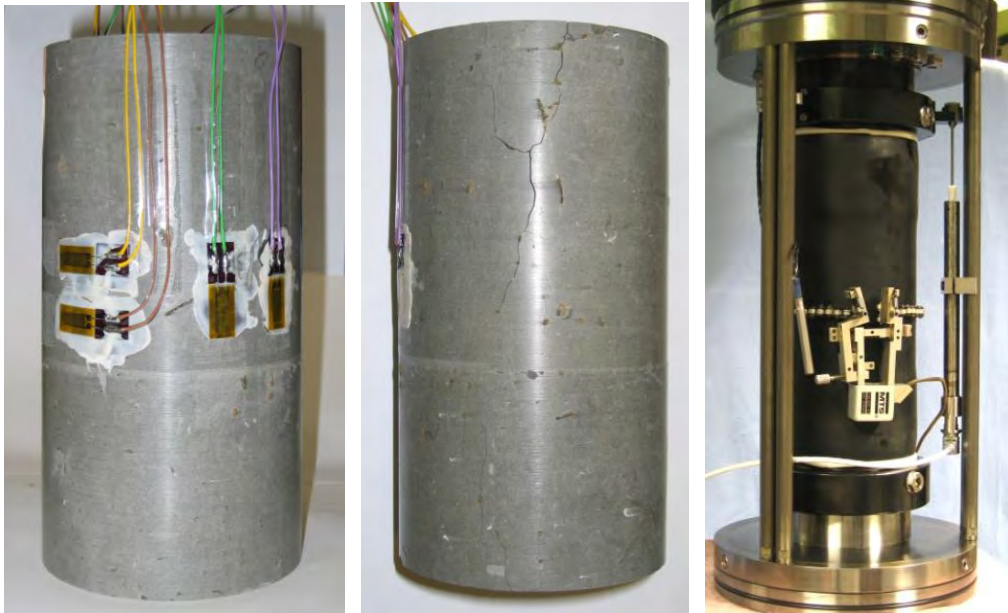
Fig. 2.44 Pictures of a prepared COX sample and instrumentation for strain measurements during triaxial creep testing

Fig. 2.45a illustrates the evolution of applied axial and radial stresses and well-controlled temperature of 24.9 ± 0.02 °C. Following the first consolidation phase, the creep test was performed by (1) keeping the axial stress σ_1 = 15 MPa constant and dropping the radial stress stepwise down to σ_3 = 5, 8, 5, 3, 2, 1, and 0.5 MPa; (2) increasing σ_1 to 17.0, 17.5 and 18.5 MPa at σ_3 = 0.5 MPa; (3) increasing σ_3 to 1, 2, 3 MPa and (4) back to 1 and 0.5 MPa at σ_1 = 18.5 MPa. Each creep phase lasted for 2 to 4 months. The loading path is represented in $\Delta\sigma - \sigma_3$ diagram in Fig. 2.45b in comparison with the damage and failure boundaries determined from the short-term tests. It is obvious that the applied loads cover the compression and dilatancy regions.
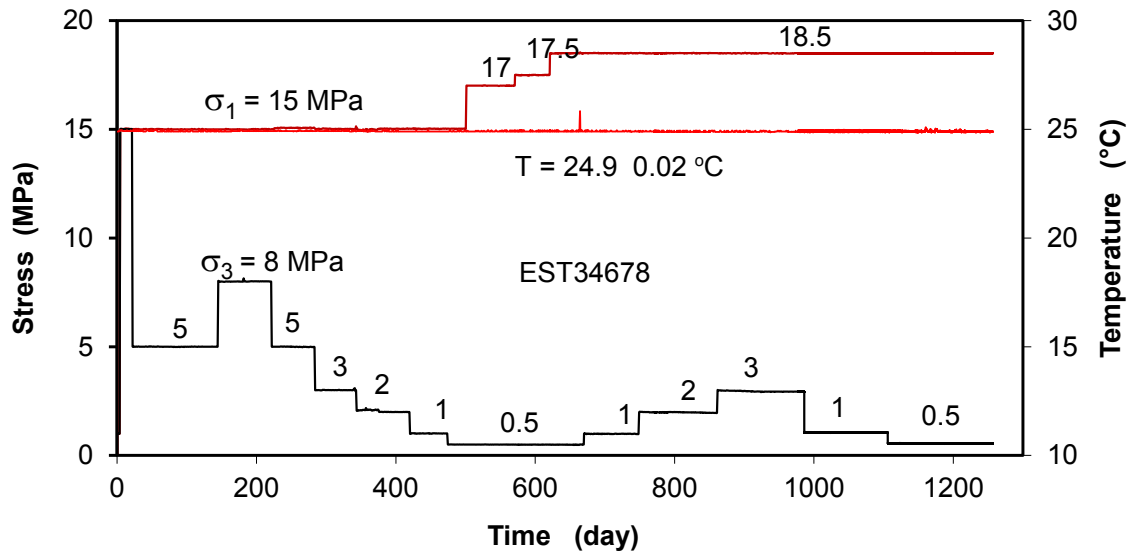
(a) applied stress and temperature conditions
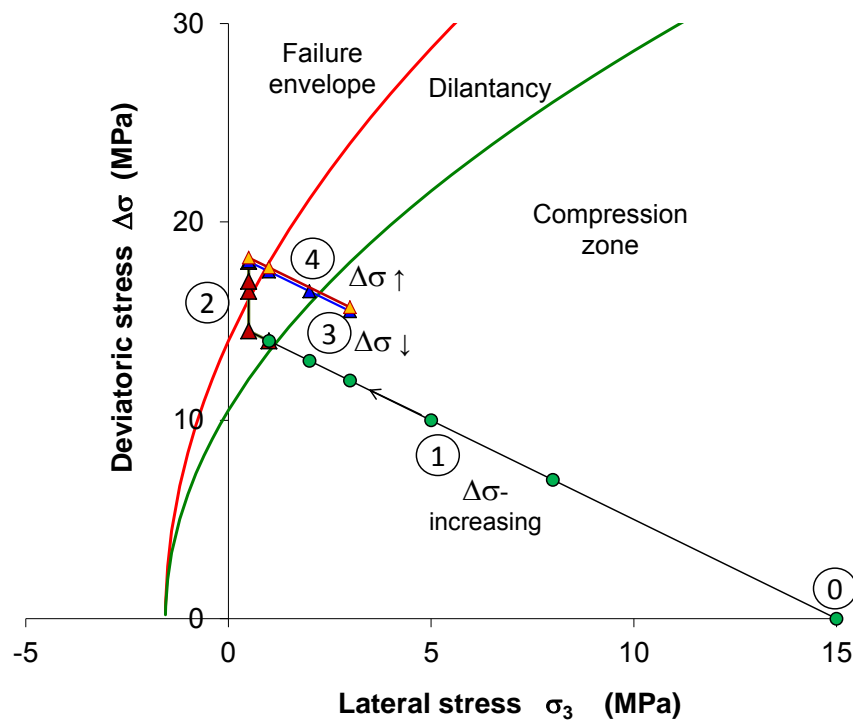
(b) comparison between applied loads and damage boundary

Fig. 2.45   Applied multi-step loads and comparison with the damage boundary

Fig. 2.46 presents the axial, radial and calculated volumetric strains (ε_a, ε_r, ε_v) in correspondence to the applied axial and lateral stresses (σ_1, σ_3). The steady-state creep rates determined within the last time intervals of 1 to 2 months are illustrated in

Fig. 2.47 as a function of applied deviatoric stress. From the data, the following phenomena can be recognized:

- The first drop of the radial stress from σ_3 = 15 to 5 MPa at σ_1 = 15 MPa caused a temporary radial expansion ($\Delta\varepsilon_r$ < 0), but then a rapid turn over to a progressive compression with time. The radial compression might be attributed to the closure of the remaining microcracks parallel to the sample axis.

- The subsequent increase of σ_3 to 8 MPa produced a temporal radial compression ($\Delta\varepsilon_r$ > 0) and extension in axial direction ($\Delta\varepsilon_a$ < 0). While the radial compression continued steadily, the axial strain turned over from temporal extension to gradual compression with time but at very low rates.

- The following successive drops of σ_3 produced the same evolution pattern of axial compression and radial extension in each phase, however, with increased strain rates at higher deviatoric stresses. At the stress difference of $\sigma_1 - \sigma_3$ = 15 – 1 MPa slightly above the dilatancy boundary (Fig. 2.45b), the volume began to increase with time indicating onset of dilatancy. The volumetric strain rate became negative at that point (Fig. 2.47). The coincidence of the dilatancy thresholds observed at the long and short-term tests suggests no or less time-dependence of the damage onset.

- Further decrease of the radial stress to σ_3 = 0.5 MPa and increase of the axial stress to σ_1 = 17, 17.5 and 18.5 MPa accelerated creep significantly. The radial extension is faster than the axial compression, giving dilatancy or damage rising. It seemed that the damage is dominated reopening of the compressed microcracks and/or by initiation of new microcracks.

- The damaged sample was reconsolidated by increasing the radial stress to σ_3 = 1, 2 and 3 MPa at σ_1 = 18.5 MPa. After a short compression, the radial strain turned over to a continual extension in each phase, whereas the axial strain contrarily turned over from a short extension to a gradual compression. The evolution of dilatancy was largely decelerated and almost terminated at σ_3 ≥ 2 MPa and σ_1 = 18.5 MPa. The magnitude of strain rates at each increased radial stress is lower than that at decreased radial stress (cf. Fig. 2.47).

- During the last phase after reducing radial stress from σ_3 = 3 MPa to 1 and 0.5 MPa, the creep rate increased again with dilatancy evolution, but slightly lower than before at the same stress state. This loading path dependence indicates the effect of strain hardening.
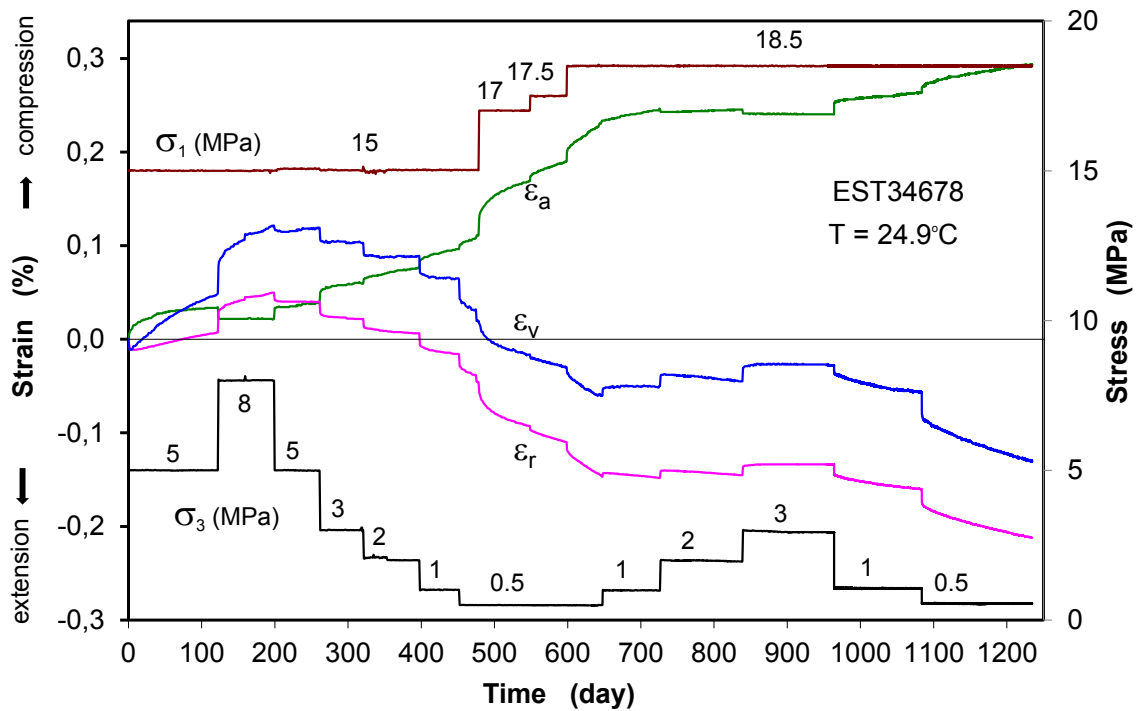
Fig. 2.46 Evolution of axial, radial and volume strains under multi-step triaxial loads
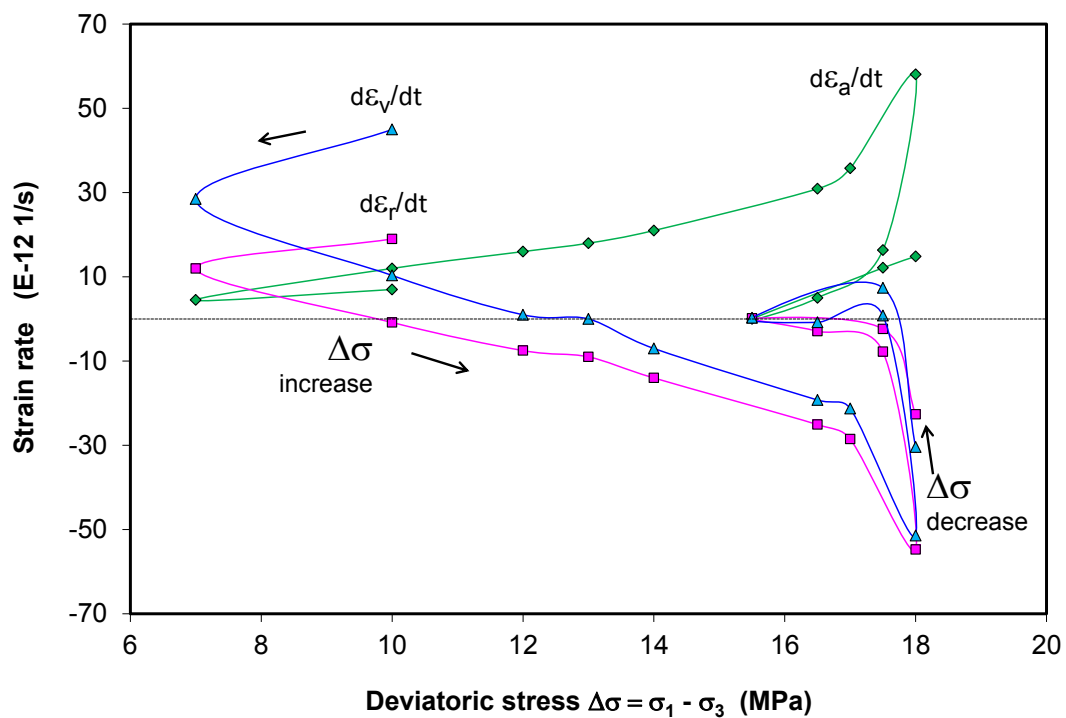
Fig. 2.47 Steady-state creep rates as a function of applied deviatoric stress

The axial steady-state creep rates obtained on COX and OPA samples under triaxial loads are plotted together in Fig. 2.48 as a function of applied deviatoric stress. It can

be clearly seen that a) the creep rates of both claystones are closely coincident; b) the variation of creep rate with stress is insignificant in the region below the damage boundary at $\Delta\sigma$ = 13 – 15 MPa; c) above the damage boundary, creep is accelerated due to the propagation of microcracks; and d) the creep rates after decreasing deviatoric stress are lower than those after increasing the stress before, indicating hardening effects.
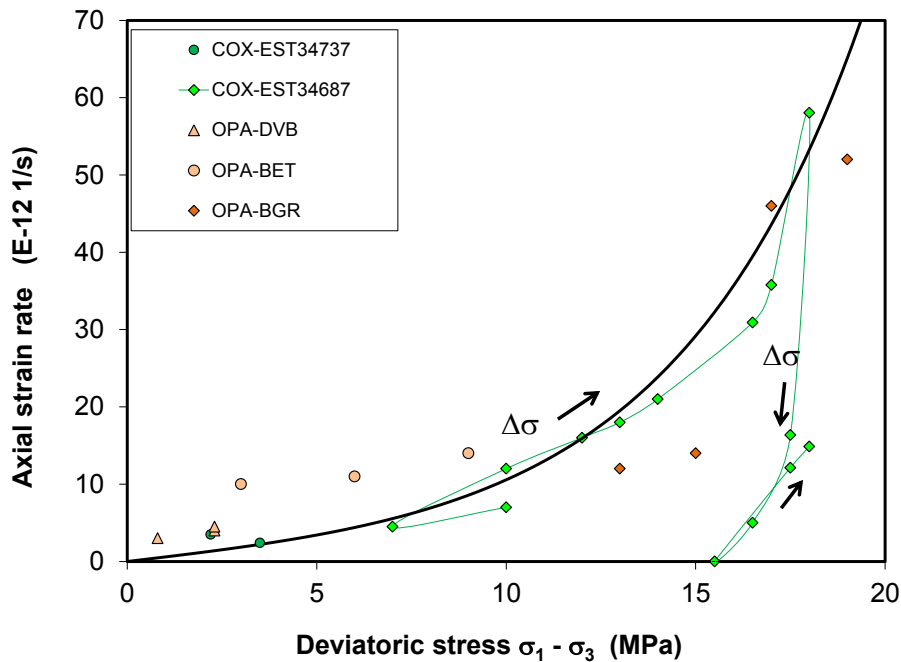
Fig. 2.48   Relationship of axial steady-state creep rate with deviatoric stress

2.3.5   Creep model

Mitchell /MIT 76/, /MIT 96/ has derived a constitutive equation for creep of clay soils through thermodynamically analysis of soil flow by application of the absolute reaction-rate theory. The flow rate is considered as resulting from the successful operation of "flow units", where the strain carrier moves by overcoming an energy barrier with the help of the applied stress and thermal agitation. Fig. 2.49 shows schematically the potential energy-displacement relationship for the movement of a flow unit from curve A to B by application of a shear force f. The number of flow units is assumed to correspond to the number of interparticle bonds, to which belong not only solid but also liquid bonds between particles. The particle movements mainly involve slips and ruptures at

interparticle contacts rather than particle breakage. The shear strain rate $\dot{\varepsilon}$ is expressed

$$\dot{\varepsilon} = 2X\frac{kT}{h} \exp\left(\frac{-\Delta F}{RT}\right) \sinh\left(\frac{\sigma\lambda}{4SkT}\right) \tag{2.23}$$

where

T = absolute temperature (K), k = Boltzmann's constant ($1.38 \cdot 10^{-23}$ JK^{-1}),
h = Planck's constant ($6.626 \cdot 10^{-34}$ Js), R = universal gas constant (8.3143 Jmol^{-1}K^{-1}),
ΔF = activation energy, λ = distance between successive equilibrium positions,
S = flow units per unit area, X = a function of the proportion of successful barrier crossings,
$\sigma = \frac{1}{\sqrt{2}}\sqrt{(\sigma_1 - \sigma_2)^2 + (\sigma_2 - \sigma_3)^2 + (\sigma_3 - \sigma_1)^2}$ = shear stress,
$\dot{\varepsilon} = \frac{\sqrt{2}}{3}\sqrt{(\dot{\varepsilon}_1 - \dot{\varepsilon}_2)^2 + (\dot{\varepsilon}_2 - \dot{\varepsilon}_3)^2 + (\dot{\varepsilon}_3 - \dot{\varepsilon}_1)^2}$ = shear strain rate
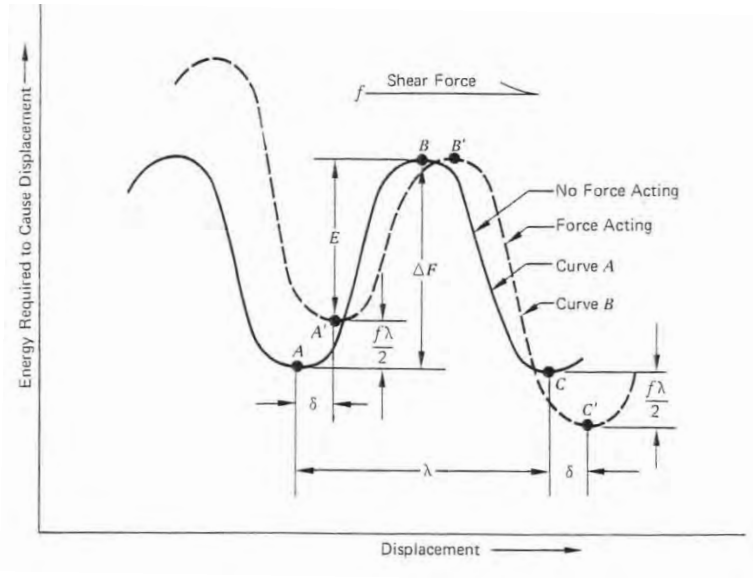
Fig. 2.49   Representation of energy barriers separating equilibrium positions (from /MIT 76/, /MIT 92/)

Presuming $A = 2X(kT/h)$ and $\alpha = \lambda/4SkT$ being constant for the over-consolidated clay rocks and a temperature range from ambient temperature to 100 °C, and introducing Q as the activation energy instead of ΔF, equation (2.23) may be simplified to

$$\dot{\varepsilon} = A \exp\left(-\frac{Q}{RT}\right) \sinh(\alpha\sigma) \tag{2.24}$$

If $\alpha\sigma < 1$, then $\sinh(\alpha\sigma) \approx \alpha\sigma$, and the strain rate is directly proportional to σ

$$\dot{\varepsilon} = A \exp\left(-\frac{Q}{RT}\right)(\alpha\sigma) \tag{2.25}$$

This is the case for ordinary Newtonian fluid flow and diffusion. According to Rutter /RUT 83/, the linear stress/strain rate relation implicates that the time-dependent deformation of water-saturated claystones is controlled by diffusive mass transfer or pressure solution processes in interfaces between grains. One of the required conditions for admitting diffusive transport is the existence of interparticle water-films which must be so strongly adsorbed onto grain surfaces that it is not squeezed out and able to support shear stress. As demonstrated earlier in Section 2.1.3, the large amounts of the pore water in the studied claystones are strongly adsorbed between clay particles and capable of sustaining high shear stresses up to the material strength.

For most deformation problems of soils and rocks, $\alpha\sigma > 1$, so then $\sinh(\alpha\sigma) \approx 1/2 \exp(\alpha\sigma)$, and equation (2.24) becomes

$$\dot{\varepsilon} = \frac{A}{2}\exp\left(-\frac{Q}{RT}\right) \cdot \exp(\alpha\sigma) \qquad (2.26)$$

Based on the data of steady-state creep rates obtained from the triaxial tests on the water-saturated COX samples, the parameters are preliminarily established: A = $2.5 \cdot 10^{-4}\,s^{-1}$, α = 0.2 MPa^{-1}, and Q = 45 kJmol^{-1}. The parameter Q is determined from the triaxial creep tests on COX samples at elevated temperatures, which will be presented later in Section 2.5.

Fig. 2.50 compares the creep equations (2.24), (2.25), and (2.26) with the test data obtained at the ambient temperature of 25 °C. At low stresses below ~10 MPa, the linear stress/rate equation (2.25) matches the data well, suggesting that the creep of the water-saturated COX claystone in the low stress region is dominated by diffusive mass transfer of adsorbed porewater or pressure solution processes in interfaces between grains. At high stresses, the creep rate increases faster than linearly, which may point to increasing contributions from slips and ruptures at interparticle contacts through water-films. Accumulation of the micro-ruptures between particles results in development of micro-fractures to failure. The comparison shows clearly that both the hyperbolic sine equation (2.24) and exponential equation (2.26) match the data excellently for the whole tested stress region without distinguishing the creep mechanism. They are differing only slightly from each other in the very low stress area below ~3 MPa. The hyperbolic sine model is justified for null stress. Because the creep rates obtained on the OPA samples are relatively higher than those of the COX samples, the models underestimate the steady-state creep rates for the OPA claystone.
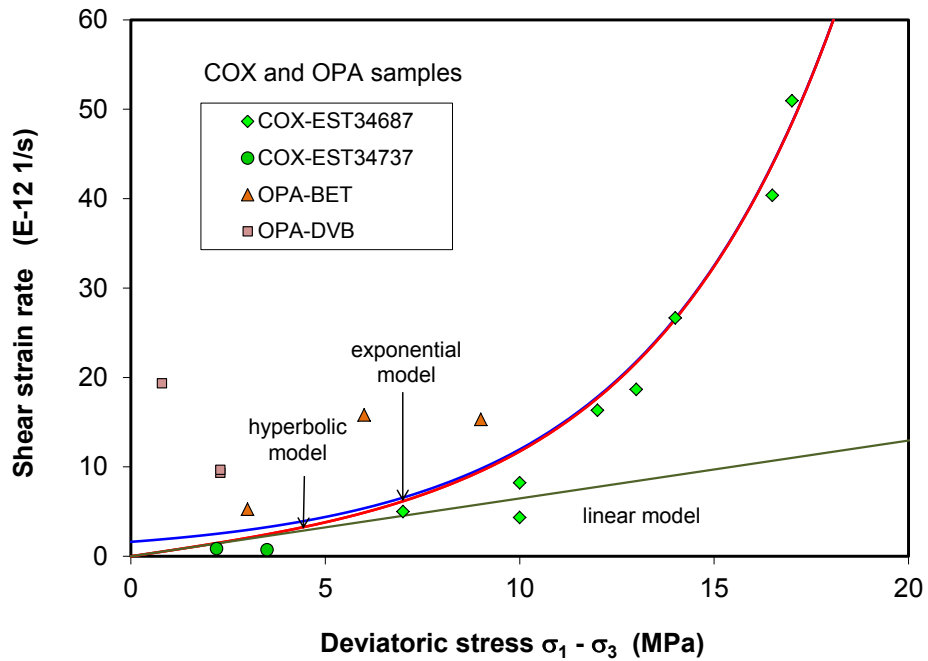
Fig. 2.50 Relationship of shear steady-state creep rate with deviatoric stress for water-saturated COX and OPA claystones

The hyperbolic sine model is applied for fitting the axial creep rate data obtained in uniaxial tests in Fig. 2.38 and Fig. 2.41 with a factor = 2/3 (lower red curve) and 4/3 (upper black curve). They cover the data for the whole applied stress range. But in the low stress region the creep rates obtained along the upload path are slightly underestimated by the model. In contrast, the axial creep rates along the unload path in triaxial tests cannot be captured by the model as shown in Fig. 2.48. This might be due to the effects of strain hardening (volumetric change) which is not yet taken into account in the creep equation.

Additionally, the shear creep rates obtained at high temperatures of 25 °C to 110 °C can also be reasonably represented by the models, as shown in Fig. 2.51 comparing the hyperbolic sine equation (2.24) with the data from the tests to be shown in Fig. 2.73 and Fig. 2.74.

It is to be pointed out here that the creep equations derived above are limited to the shear steady-state creep of water-saturated COX claystone. Adequate models for the volumetric creep (consolidation or dilatancy) are to be developed for capturing the effects of loading path or strain hardening.

81
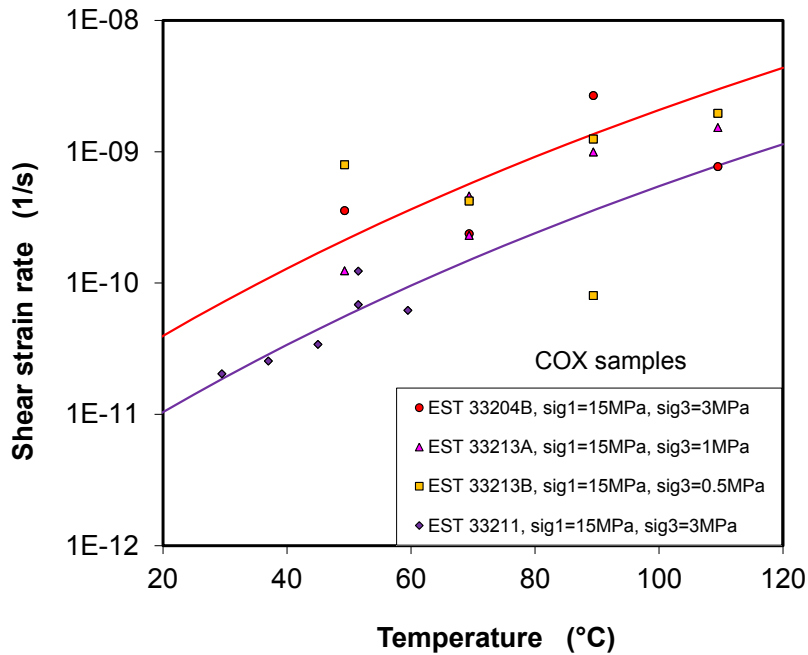
Fig. 2.51   Relationship of shear creep rate with temperature for COX claystone

2.3.6   Conclusions on the creep behaviour

The long-term creep behaviour of the COX and OPA clay rocks has been investigated on the samples under uniaxial and triaxial stresses over extremely long time periods of 1 to 7.7 years. The creep tests focused on the aspects of stress dependence, influence of load path, and anisotropy effect on the creep of the claystones with natural water contents at ambient temperature. The following major conclusions can be drawn:

1. The clay samples creep already under the lithostatic stress states of the rock formations und even at extremely low deviatoric stresses of 0.3 to 1.0 MPa, indicating that there is practically no creep limit in the lab conditions.

2. The creep behaviour is dependent on load path. The creep under increased deviatoric stress is characterized by a transient phase with decreasing rates governed by strain hardening and a following stationary phase with an asymptotically approached constant rate. Under decreased deviatoric stress, creep evolves contrarily from firstly backwards at negative rates with then switching to a steady-state creep at positive rates.

3. In the low stress region below the damage threshold, the creep rate varies insignificantly with stress. Above that, the creep rate increases more significantly. The acceleration of creep suggests the initiation and propagation of microcracks.

82

4. As a first approach, the creep equation derived by Mitchell /MIT 76/, /MIT 92/ has been simplified to a hyperbolic sine equation $\dot{\varepsilon} = A \exp(-Q/RT) \sinh(\alpha\sigma)$ for the stationary shear creep of water-saturated claystone, where $\dot{\varepsilon}$ = steady-state shear creep rate, T = absolute temperature, R = universal gas constant, Q = activation energy, σ = shear stress, A and α = parameters. In the low stress region below 10 MPa, where diffusion processes in adsorbed water-films between solid particles are dominating, the creep rate is linearly related with stress by $\dot{\varepsilon} = A \exp(-Q/RT)(\alpha\sigma)$. For relatively high stresses, the creep rate can be approached by an exponential equation: $\dot{\varepsilon} = A/2 \exp(-Q/RT) \exp(\alpha\sigma)$. The three creep parameters A, α, and Q were preliminarily determined from the triaxial creep tests on the nearly-saturated COX claystone under increased shear stresses: A = $2.5 \cdot 10^{-4} s^{-1}$, α = 0.2 MPa^{-1} and Q = 45 kJmol^{-1}. To note that an additional equation needs to be formulated for the volumetric creep deformation (consolidation or dilatancy) for modelling the complete time-dependent deformation behaviour of the claystone.

5. Total deformation perpendicular to the bedding plane is larger than parallel to bedding due to the difference of the stiffness in both directions. However, pure creep strains and creep rates are not significantly dependent on the loading directions, suggesting a negligible anisotropy effect on creep.

6. Both the studied clay rocks with average clay contents of 40 % to 65 % exhibit quite similar creep behaviour. Low clay content and high carbonate content slow down the creep.

2.4 Response to moisture change

During the operation phase of a repository, the ventilation and the subsequent backfill with unsaturated materials will lead to evaporation and migration of porewater from the surrounding rock. Desaturation gives rise to capillary forces and hence an increase in cohesion and strengthening of the rock mass. On the other hand, it simultaneously increases local tensile stress and the potential for bond failure leading to shrinkage and fissures. The release of bound porewater acting as stress-bearing element will result in change of the stress state in the rock mass. After closing the repository, the previously desaturated clay rock and backfill will be gradually resaturated by water uptake from the saturated farfield. The resaturation will cause swelling of clay minerals in claystone and clay-based backfill and hence building up of swelling pressure against further de-

velopment of rock damage. These hydro-mechanical processes and interactions between rock and backfill enhance the consolidation of the damaged zone as well as the backfill, so that the isolating functions of the multi-barrier-system will be guaranteed.

In order to determine moisture effects on the mechanical behaviour of clay host rock, various kinds of laboratory experiments have been carried out under different conditions within this project. The most important part dealing with stress response to humidity change has been already presented in Chapter 2.1 for the validation of the stress concept newly derived for argillaceous rocks. This Chapter focuses on strain response to humidity change and influence of water content on the stress-strain behaviour.

2.4.1   Free swelling and shrinking

Accompanying the swelling pressure tests presented in Section 2.1.3.1, strain response to humidity change was also measured on COX and OPA samples of 40 mm diameter and 40 mm length in unconfined conditions. Results of the tests on 8 samples are presented in Appendix A.

As a typical example, Fig. 2.52 shows the strain response of an unconfined COX sample to humidity change. The initially unsaturated sample was firstly resaturated at a relative humidity of RH = 100 % for several days. The wetting caused an expansion in all directions to a volume increase of 1.3 %. The swelling in radial direction normal to the bedding plane was relatively larger than the axial swelling parallel to bedding. The subsequent drying phase by decreasing the humidity down to nearly zero removed the porewater out of the pores, resulting in collapse of the pore structure and thus a macroscopic shrinkage of 1.8 % in volume. The shrinkage is also anisotropic with a relatively larger value in radial direction normal to bedding. During the following wetting by elevating the humidity up to 100 % increased the water content and hence the thickness of the water-films between solid particles, yielding a full recovery of the strains. However, the strain – water saturation curves depicted in Fig. 2.52b are different between the drying process and the wetting process. Wetting yields a relatively larger strain. The strain varies significantly in the region of high saturation degrees of higher than ~80 %. Below that, the strain variation is insignificant.
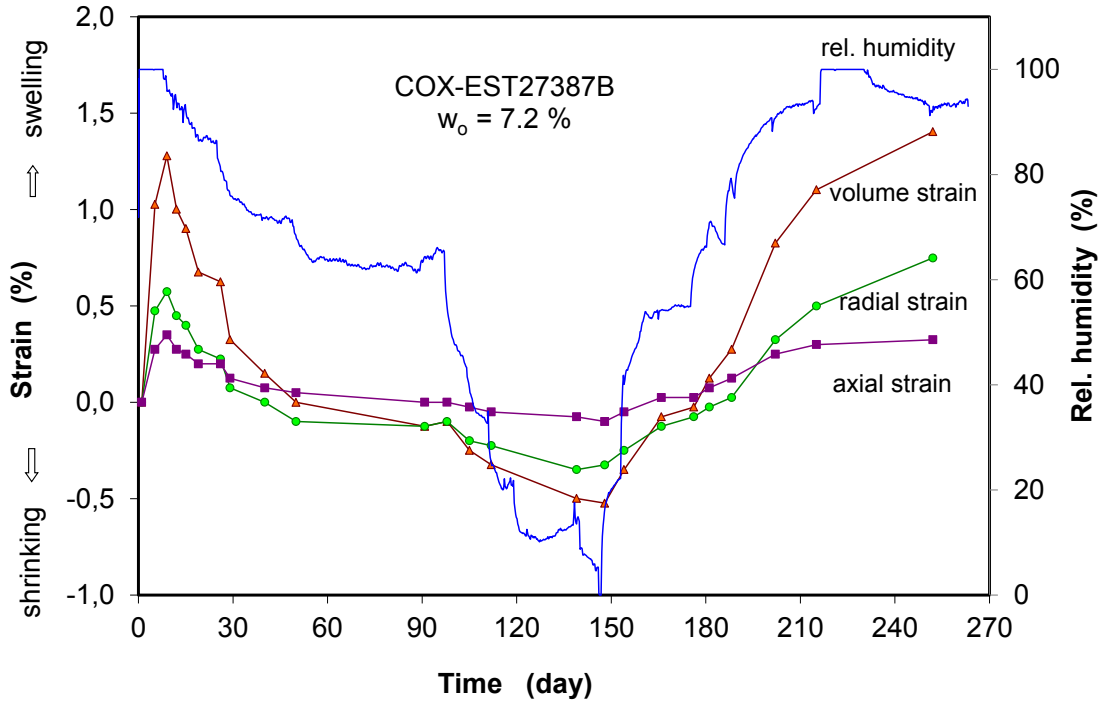
(a) free swelling/shrinking strains
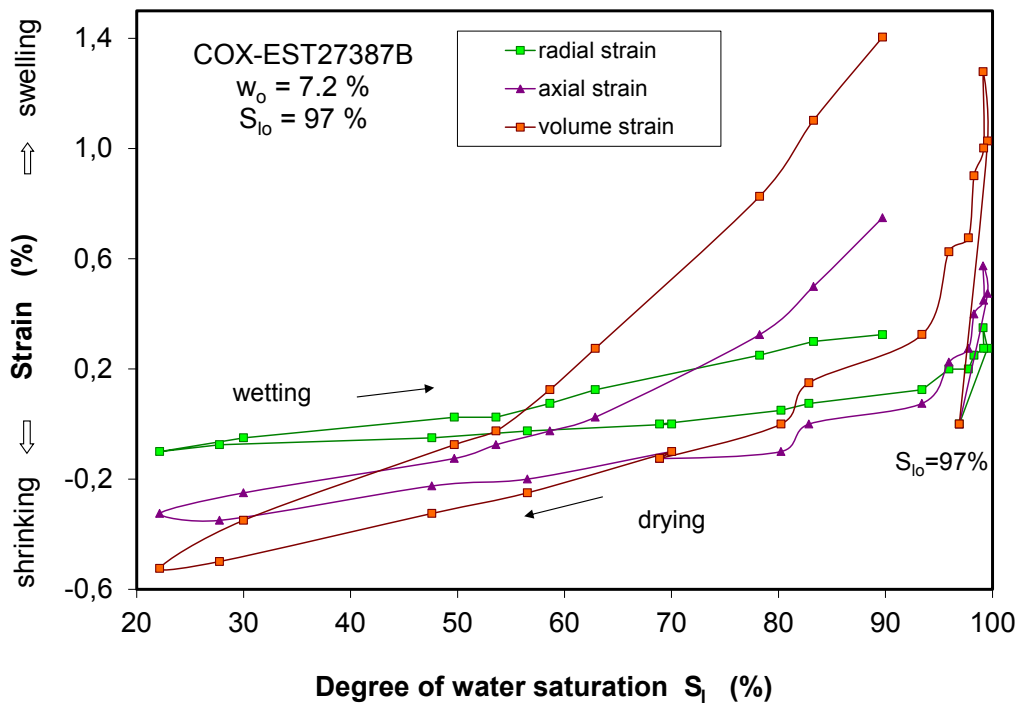
(b) relationship of free swelling strains to water saturation degree

Fig. 2.52   Swelling and shrinking of unconfined COX claystone

The hysteric performance in strain as a result of drying-wetting cycle may be interpreted with help of a schematic illustration of a clay aggregate shown in Fig. 2.53. Drying causes release of adsorbed porewater successively from the large pores, from the nar-

85

row space between clay particles, and from the interlayer within the sheet structure. The release of the bound porewater as bearing element results in collapse of the pore structure and thus a macroscopic shrinkage. Contrary, wetting drives water molecules into the pores. Under the effect of physic-chemical potentials, water molecules are adsorbed on the surface of clay particles. The narrow pores will be firstly filled and expand by taking up more water. The air in some large pores may be enclosed there and even forever when the surrounding narrow pores are fully sealed. Thus, at a same volume, the degree of water saturation by wetting is lower than that by drying. And the strain – water saturation curve from wetting is above that from drying.
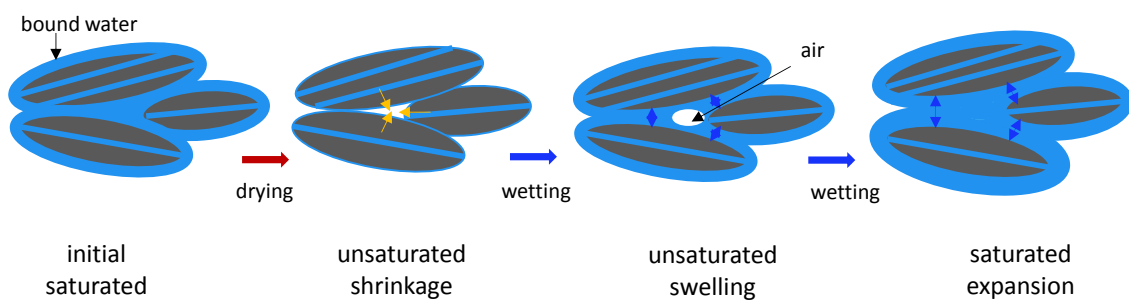
Fig. 2.53   Schematic illustration of hysteric performance in strain as a result of drying-wetting cycle for clay aggregate

Additionally, because of the high water adsorption potentials, the unconfined claystones after unloading can take up great amounts of water up to 10 – 13 %, much more than that of 7 – 8 % in the naturally confined state. The increase in water content can contribute to the volumetric expansion up to 7 – 13 %, as shown in Fig. 2.54 comparing the swelling capacities of the COX and OPA claystones by wetting with water vapour and with synthetic porewater. The OPA claystone with a higher clay content of ~65 % exhibits a larger swelling capacity compared with the COX. As the claystone contacts with the synthetic water, the swelling takes place rapidly. The swelling induced by contact with liquid water is much faster in the beginning and then tends to constant. The final magnitudes of swelling by liquid and vapour are nearly the same.

Moreover, the water uptake also leads to degradation of the inner structures of claystone and even generates fractures along bedding planes as the disjoining pressure in the bound water exceeds the normal compressive stress on the planes and the inner cohesion. The pictures in Appendix A show some fractured samples after wetting with water vapour and synthetic porewater.
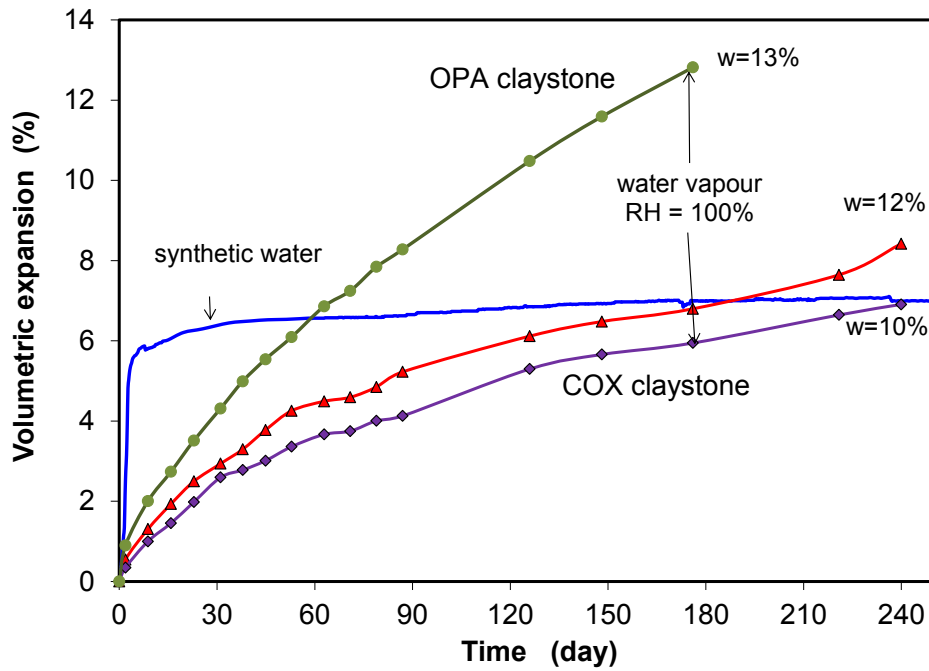
Fig. 2.54   Volumetric expansion of COX and OPA claystones during wetting with water vapour and with synthetic porewater

Another test examined the swelling capacity of pre-heated claystone. Fig. 2.55 shows the free swelling of a COX sample that had been pre-heated at 105 °C and dried out. Wetting by increasing humidity from RH = 15 % to 100 % over 5 months gave rise in the amount of water uptake up to 8.5 %. The resaturation led to a total volume expansion up to ~5 % including the contribution of induced microcracks which might occur as the degree of water saturation was beyond ~75 % where the swelling became faster. This result confirms again the conclusion previously derived in Section 2.1.3 that the preheated claystone still has a significant swelling potential. It implies that the clay host rock near the heat-emitting HLW, even though heated up to 100 °C, can still swell as contacting with water and enhance the sealing process of the disposal system.
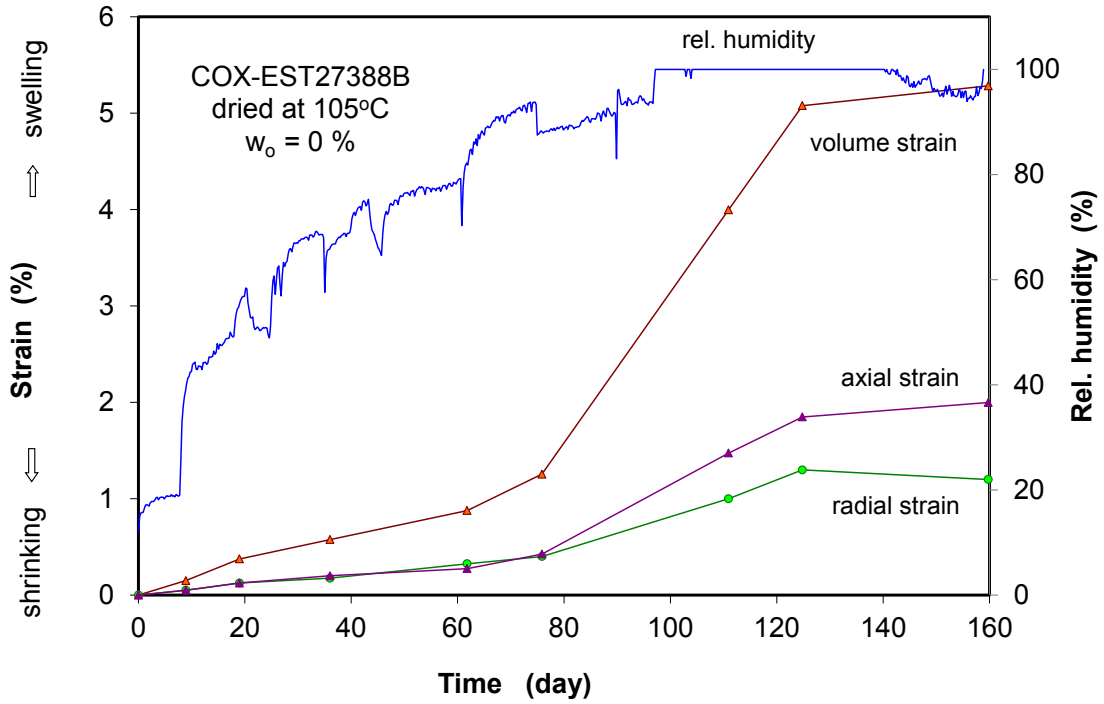
(a) free swelling strains
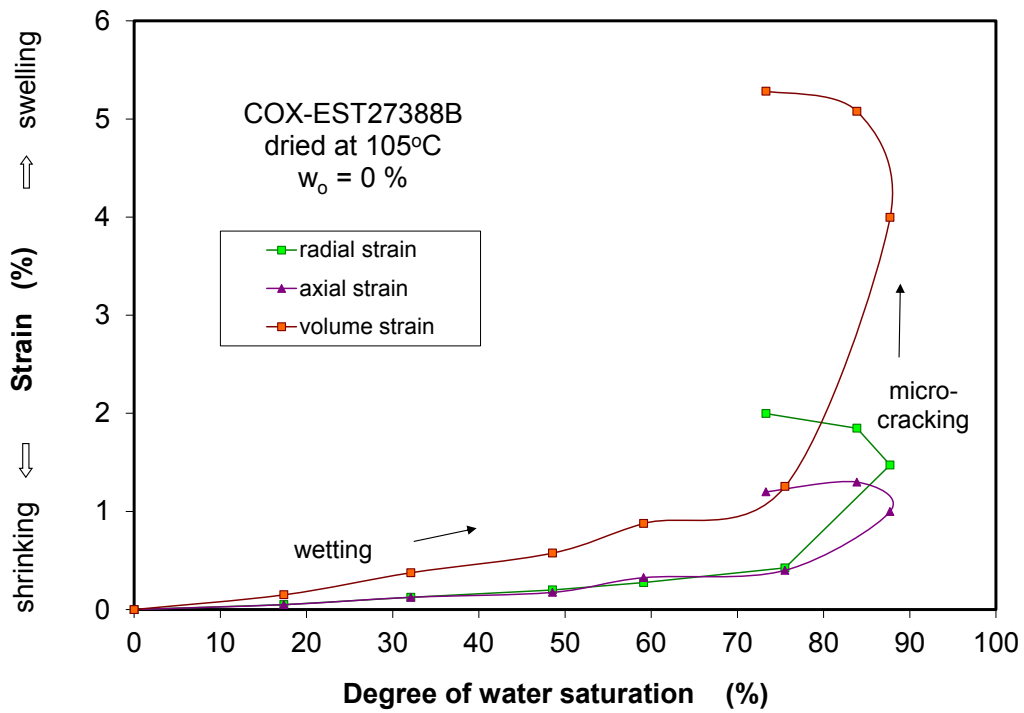
(b) relationship of free swelling strains to water saturation degree

Fig. 2.55 Free swelling of pre-heated COX claystone

2.4.2 Swelling and shrinking under partly-confined conditions

The nearfield close to the opening walls is usually subjected to biaxial and/or uniaxial stresses and affected mostly by humidity changes due to the ventilation and direct contacts with the unsaturated backfill on one side and with the saturated rock mass on the other side. Knowledge about responses of the clay rock in the nearfield to humidity change is of importance for the design of excavation support measures, for the evaluation of the rock stability during the operation phase, and for the prediction of sealing process during the post-closure phase. This issue was experimentally investigated on COX samples under two kinds of partly-confined conditions: a) under constant uniaxial stress and b) under constrained uniaxial strain, both being laterally unconfined.

2.4.2.1 Humidity influence on deformation under constant uniaxial stress

Two COX samples of D78mm/L200mm were axially loaded one upon another in a creep rig at a stress of 3.3 MPa parallel to bedding. It was actually the typical uniaxial creep test. The initial water contents of them were measured at 6.2 % for EST40701 and 7.0 % for EST40646, respectively. The latter sample was highly water-saturated. Under the constant load, axial strain ε_a was monitored by a deformation transducer LVDT along the sample length while radial strain was recorded locally by means of strain gauges glued on two mid-height positions ($\varepsilon_{r0°}$, $\varepsilon_{r90°}$) perpendicular to each other. The samples were sealed in jackets during the first creep phase of 3 months, then exposed to the circulating air at relative humidity RH = 75 % for 4 months, and finally dried at RH = 40 – 20 % for another 4 months. The measured strains are illustrated in Fig. 2.56a, b for each sample in correspondence to the humidity variations. Major findings are:

1. Within the first phase, the samples with constant water contents deformed gradually with a relatively large radial expansion compared to the axial compression. The calculated volumetric strain indicates an evolution of dilatancy to ~0.6 %. The dilatancy could not be induced by initiation and propagation of microcracks at the relatively low stress compared with the dilatancy point of ~15 MPa.

2. As the samples were exposed to the surrounding air of RH = 75 %, the axial strain ceased while the radial expansion was accelerated shortly and then tended to ceasing, except for the uncontrolled failure of the load. Keeping the humidity constant, no or negligible deformation occurred with time. This fining indicates that the

friction resistance between mineral particles increased against further deformation. The sustained stress may be considered as the creep threshold for the partly saturated claystone.
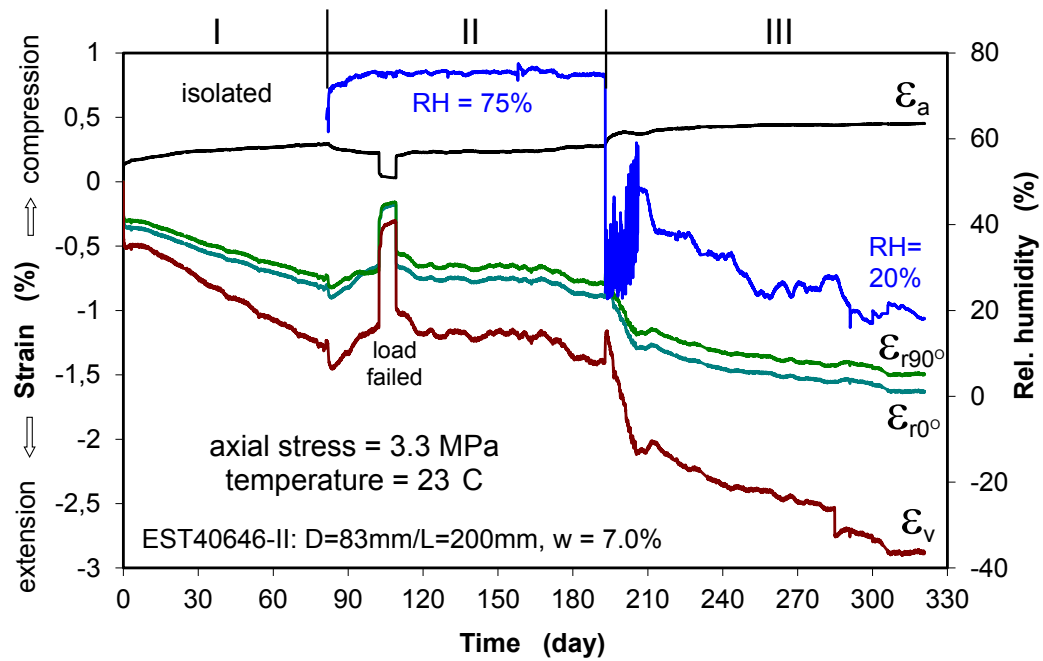
(a) COX sample EST40646
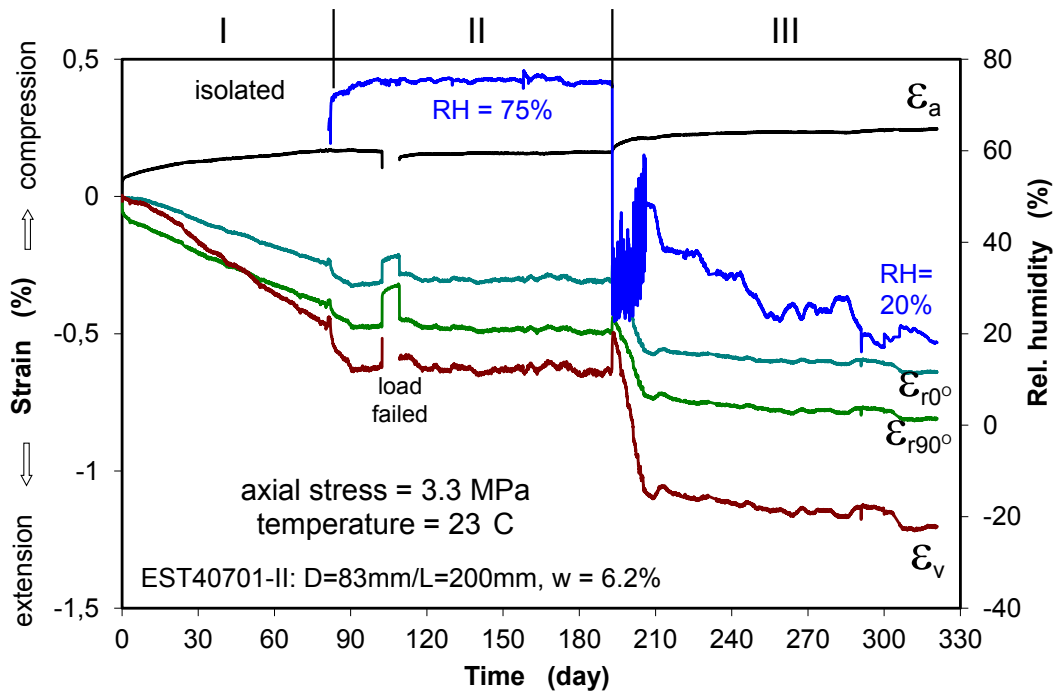
(b) COX sample EST40646

Fig. 2.56 Humidity influence on deformation of COX claystone under axial load

3. Further drying by suddenly dropping the humidity down to RH = 25 % induced a shrinkage in all directions shortly. The following increase in humidity to RH = 60 % led to a gradual radial expansion and axial compression. Drying again to a low humidity of ~20 % caused a gradual compression in loaded axial direction and small radial extension. The time-dependent axial compression is mainly caused by a gradual collapse of air-occupied pores with the desaturation process.

2.4.2.2 Humidity influence on stress/strain under constrained uniaxial strain

A COX sample EST40701 of D40 mm/L40 mm that had been extracted from the same core as the tested sample shown in Fig. 2.56b was firstly loaded to an axial stress of 4.7 MPa parallel to bedding and then fixed at unconfined lateral condition in the same test setup as illustrated in Fig. 2.6a. It was in fact the typical uniaxial stress relaxation test. Under the axially-fixed and laterally-free conditions, variation of the applied axial stress was monitored by a pressure sensor installed at the bottom, while free radial strain was recorded by two LVDT displacement transducers positioned oppositely at the mid-height of the sample. Firstly, the samples was isolated in jackets to prevent loss of the porewater, then wetted by applying high air humidity values of RH = 90 – 100 % for 4 months, and finally dried at decreasing humidity to RH = 50 – 40 % for another 5 months. The applied environment conditions and the responses of axial stress and radial strain are illustrated in Fig. 2.57. The following phenomena can be recognised from the test data:

1. At constant water content and fixed axial strain, the applied axial stress decreased steadily from the initial value of 4.7 MPa to 3.3 MPa over a time period of 52 days, whereas the radial strain varied insignificantly. Within the last time interval of 12 days, the relaxation rate maintained relatively constant at $8.5 \cdot 10^{-13}$ MPa/s. The obvious stress relaxation observed indicates the significance of the time-dependent behaviour of the claystone.

2. Wetting the unsaturated sample resulted in an increase in axial stress to 4.1 MPa at RH ≈ 90 % and then to 4.6 MPa at RH ≈ 100 %, and correspondingly led to free expansion in radial direction up to 0.3 %. When the humidity remained constant, the reached stress and strain did not change much. The stress increase with wetting is actually attributed to the buildup of repulsive forces or swelling pressures in the adsorbed and overlapped water-films in narrow pores between solid particles, as mentioned before in Section 2.1.

3. In contrast, drying caused a release of the adsorbed water from pores, and conse-
    quently, the axial stress (or swelling pressure) being carried by the bound porewa-
    ter decreased and the desaturated pores went to be collapsed leading to shrinkage
    as observed in radial direction.

From all the observations of the stress/strain responses to moisture changes, one can
conclude that the adsorbed porewater in the clay rock acts as stress-bearing element
and dominates the deformation process.
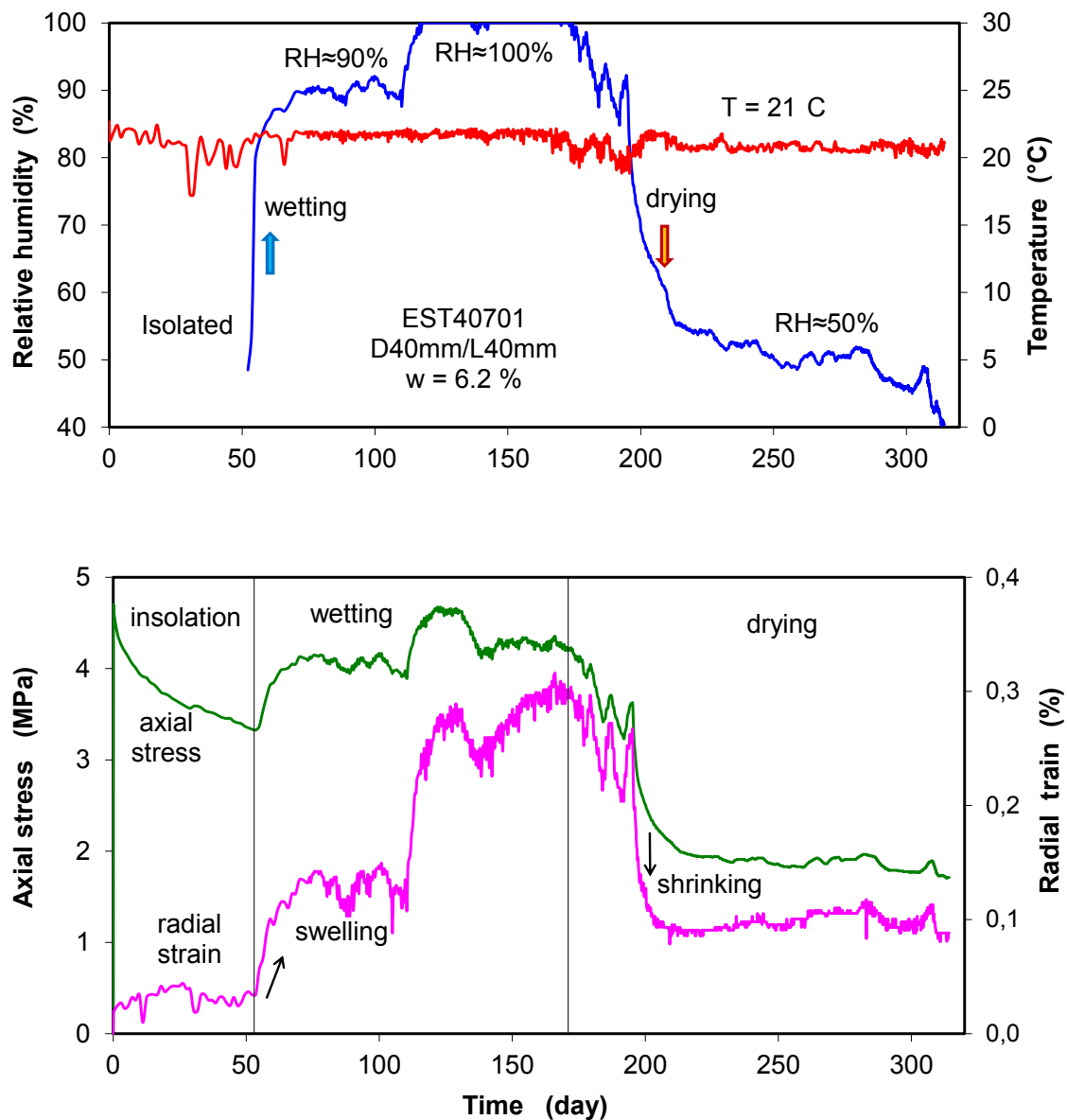
Fig. 2.57   Humidity influence on axial stress and radial strain of COX claystone under
axially-fixed and laterally-unconstrained conditions

2.4.3 Influence of water content on strength

In order to examine influence of water content on the stress-strain and strength behaviour, a set of uniaxial compression tests were carried out on six COX samples with different water contents from w = 1.5 % to 7.7 %. They had been achieved by drying or wetting at various humidity values of RH = 12 % to 100 % over more than a month. The prepared samples were wrapped in thin plastic foil during testing to void possible influence of the surrounding humidity. Axial load was applied to the samples at a rate of 0.2 MPa/min parallel to the bedding plane. Multiple unloading-reloading cycles were performed for determination of the elastic parameters as a function of applied load. Axial deformation was recorded by a LVDT deformation transducer, and lateral strain was measured by a circumferential extensometer chain mounted around the sample at its mid-height. The basic characteristics of the samples and some pictures of the samples before and after testing are given in Appendix D. The measured stress-strain curves of each sample are illustrated in Appendix D.

Fig. 2.58 summarizes the stress-strain curves obtained on the samples. Each sample showed the typical nonlinear elasto-plastic behaviour. The linear elastic behaviour is dominating in the low stress region. The porous material is compacted with increasing the load until the dilatancy point σ_D, at which the volume turns over to increase due to initiation and growth of microcracks. As the microcracks develop so far to forming disconnected macro-fractures, failure occurs at the peak stress σ_F. The elastic parameters, dilatancy and peak strengths are dependent on the water content in claystone.

The values of Young's modulus and Poisson ratio determined from each loading path are illustrated in Fig. 2.59 as function of applied load and water content. It is obvious that a) the elastic stiffness increases with increasing the load but with decreasing water content due to hardening effects of compaction of unsaturated pores; and b) the Poisson's ratio increases with load but decreases more significantly with reduction of water content, indicating that the major direction of the compression of unsaturated pores parallel to the major stress direction. The values of Young's modulus and Poisson ratio determined at 10 MPa are depicted again in Fig. 2.60 as a function of water content. The Young's modulus increases largely from E = 1,200 MPa at w = 7.7 % to E = 4,800 MPa at w = 1.4 %. The Poisson's ratio varies in a range of ν = 0.14 to 0.25 in the region of w = 3 % to 7 %. At high water content of 7.7 %, the ν – value becomes much higher at ν = 0.67 above 0.5, indicating dilatancy and damage.
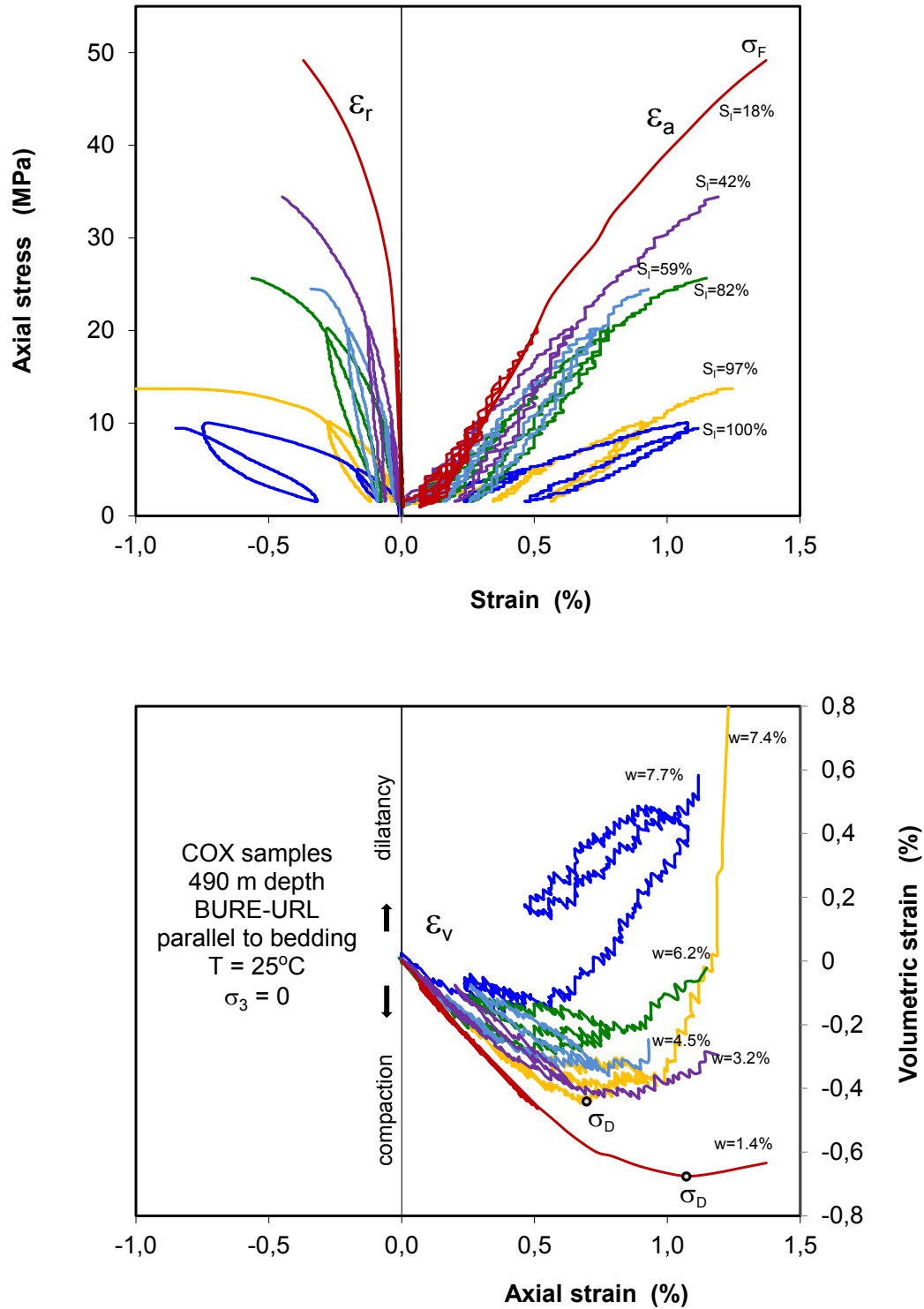
Fig. 2.58   Stress-strain curves obtained from uniaxial compression tests on COX samples with different water contents
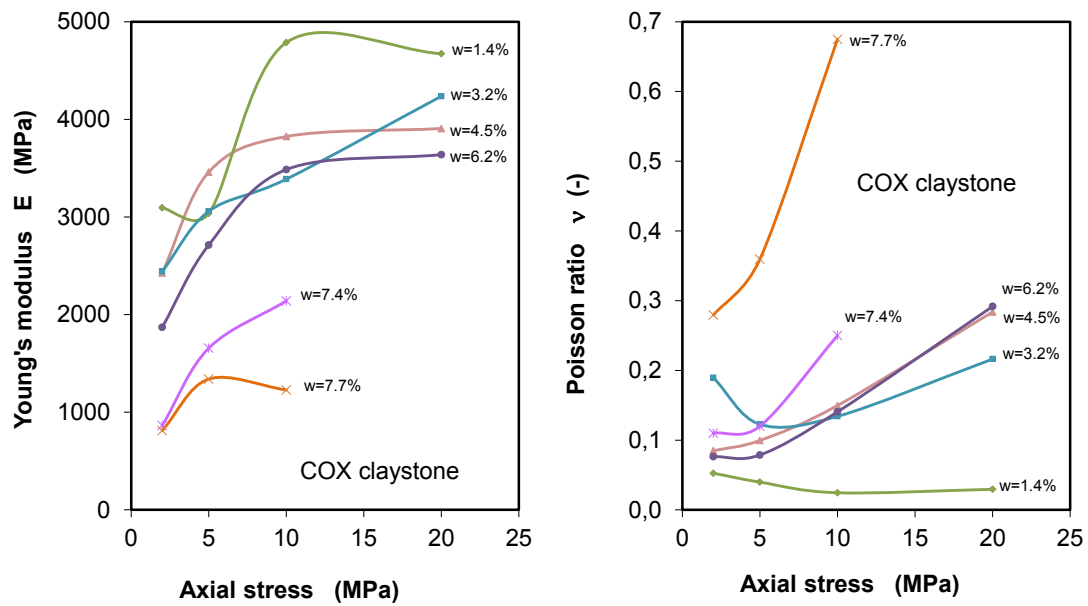
Fig. 2.59   Dependence of elastic parameters on water content and applied load
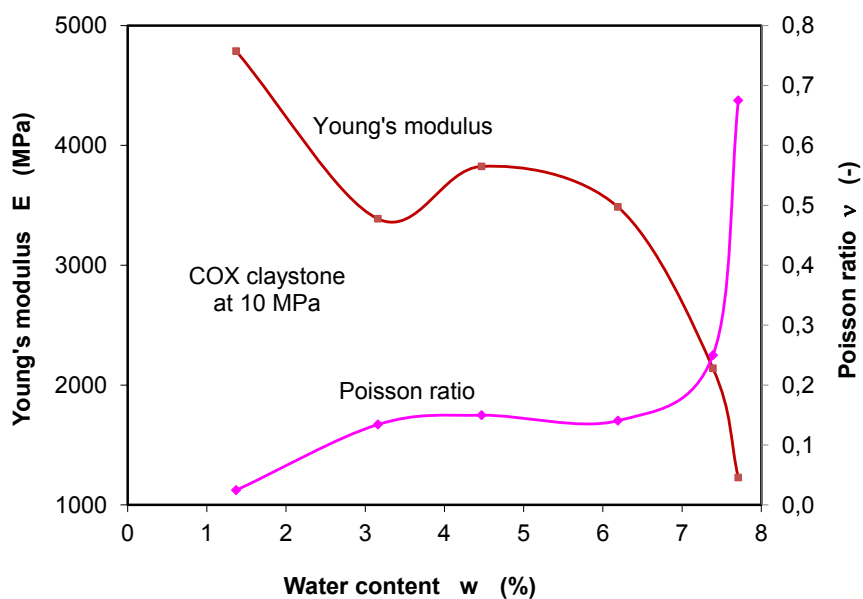
Fig. 2.60   Elastic parameters determined at axial load of 10 MPa as a function of wa-
ter content

The dilatancy and peak strengths (σ_D, σ_F) increase almost linearly with decreasing wa-
ter content, as shown in Fig. 2.61. The uniaxial peak strength of 49 MPa obtained at
w = 1.4 % is nearly 5 times as high as that of 10 MPa at w = 7.7 %. The σ_D/σ_F-ratio is
obtained in a range of 0.5 to 0.6. These values are higher than that mean value

$\sigma_D/\sigma_F = 0.75$ obtained on the same claystone with the natural water content (slightly desaturated) in triaxial compression tests in Section 2.2.5.

Generally, the increase in the stiffness and strength with water desaturation implies that the ventilation with dry air can strengthen the surrounding clay rock and enhance the stability of the underground construction.
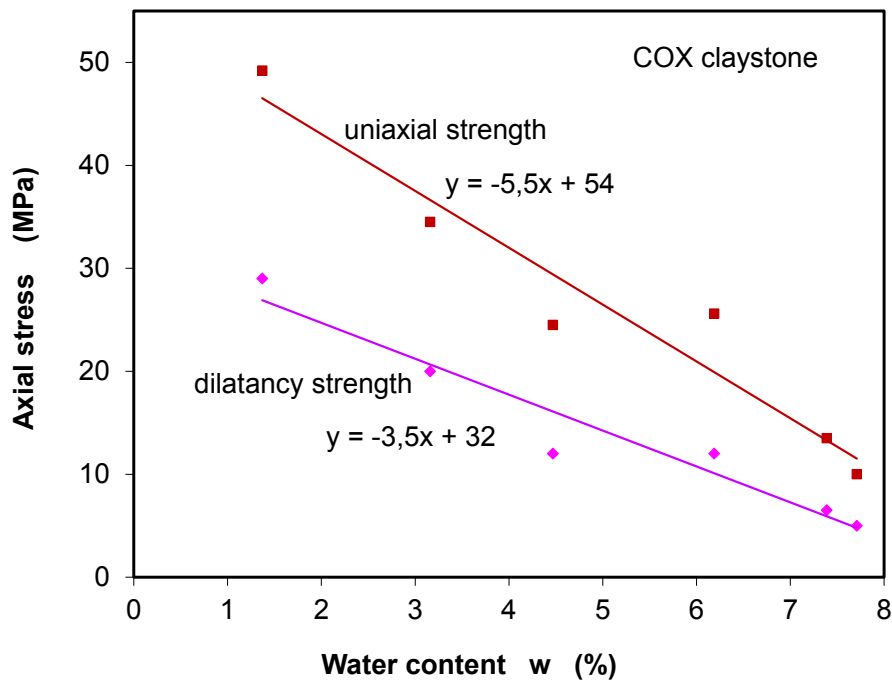
Fig. 2.61   Dilatancy and peak strengths of claystone in relation with water content

2.4.4   Conclusions on the moisture effects

From the laboratory observations on the responses of the COX and OPA claystones to moisture change, it can be concluded that:

- The argillaceous rocks exhibit high adsorption potentials, under which a great amount of water can be taken up from the humid environment to water contents of more than 10 – 13 % in unconstrained conditions, higher than that in the naturally-confined and saturated rock mass. The higher the clay content, the higher is the water adsorption potential.

- The water uptake during wetting enlarges the distance or pore space between solid particles, resulting in swelling up to 7 – 13 % in volume under unconfined and hu-

96

mid conditions. Conversely, drying causes release of porewater, leading to collapse of the pore structure and thus the macroscopic shrinkage to 1 – 2 % without loading. Application of a drying-wetting cycle produces a hysteric strain – water saturation behaviour, i. e. the strain by wetting is larger than that by drying at a same degree of water saturation. The swelling/shrinking strains vary significantly in the saturation degrees above 80 %. Below that, the strain variation is insignificant.

- Because of the sedimentary structure, the swelling/shrinking strain is more significant in direction perpendicular to bedding planes and even fractures appear along the weak planes.

- The adsorbed porewater in such dense claystones are capable of bearing external loads as high as the lithostatic stress and even bearing high deviatoric stresses up to the strength of the material (cf. Section 2.1). The significant influences of drying and wetting on the uniaxial creep and stress relaxation suggest that the adsorbed porewater play the key role in the long-term deformation of claystones.

- The mechanical properties such as elastic stiffness and strength increase strongly with decreasing water content due to the increase in friction resistance between particles in dried conditions. The elastic stiffness, uniaxial dilatancy and failure strength determined at a low water content of ~1.5 % are about 4 – 5 times those after wetting to water content of ~7.5 %.

- Generally, the experimental results imply for practice that a) drying by ventilating dry air can strengthen the surrounding clay rock and enhance the stability of the underground construction; and b) wetting by water uptake from the farfield causes swelling of claystone and sealing of the fractures in the damaged zone.

2.5 Thermal impact

According to the France concept for disposal of HLW in the COX argillaceous formation /AND 05/, the disposal cells are sub-horizontal dead-end tunnels of about 40 m length and 0.7 m diameter. Each tunnel has an inner lining consisting of a thick, low or non-alloy steel tube in which the HLW canisters are inserted. This lining has a thickness ranging of between 25 mm and 40 mm allowing for the possible removal of the canisters for reversibility purposes. Heat released from HLW will dissipate through the buffer and the surrounding rock. The resulting temperature changes may affect the mechanical and hydraulic processes in the surrounding host rock. In order to enhance the

knowledge about thermal impact on the clay rock, ANDRA has conducted two in situ heating experiments called TER and TED at the main level of the MHM-URL /AND 09/. The measurement results from the TER experiment and the THM modelling results made by GRS are already presented in the previous TIMODAZ project report /ZHA 10b/. The TED experiment and its modelling work newly made by GRS within this project will be presented in Volume II of this THM-TON project report. The main objectives of both TER/TED heating experiments were defined to

1. enhance the knowledge about the THM behaviour of the clay rock, particularly thermal impact on EDZ development around HLW boreholes;

2. validate the THM constitutive models and parameters; and

3. provide a solid data base for design of a potential repository as well as for evaluation of the thermal impact on its long-term safety.

Most recently, additional small scale and full scale in situ experiments have been designed and set up in the MHM-URL in order to examine thermal impact on the mechanical stability of the lined tunnels /BUM 12/. While the small scale (1:5) experiments have been performed on steel casing with different thicknesses and tightness specifications in horizontal boreholes (length = 10 m and diameter = 143 mm), a full scale horizontal micro-tunnel of 40 m long and 0.7 m in diameter has been equipped with a 20 mm thick steel casing.

GRS has contributed to the in situ heating experiments with laboratory tests and numerical modelling. The laboratory heating tests emphasised on thermal expansion/contraction under various confining stresses, temperature influences on creep deformation and strength, and thermal impact on the stability of boreholes with inner lining using large core samples. Main results of the tests are presented in the following.

2.5.1 Characterization of samples

Normally-sized rock cores were extracted from TED boreholes drilled horizontally at the -490 m level in the MHM-URL. The axes of the cores are nearly parallel to the bedding plane. After coring, they were immediately confined in T-cells. Most of the samples were prepared to a size of 50 mm diameter and 100 mm length for triaxial creep tests at elevated temperatures of 22 °C to 110 °C. A sample EST34676 of D/L = 98/200 mm was used for the determination of thermal expansion coefficient under isostatic confin-

ing stresses (see Fig. 2.62). Due to the coring and preparation, microcracks were unavoidably induced mostly along the bedding planes and even grew into few macro-cracks in a few samples. Their basic characters and pictures are summarized in Appendix E. The water content, dry density and grain density were measured after dried at 105 °C for 48 hours. The porosities ranged from 14 % to 17 %. The measured water contents of 5.7 % to 7.1 % correspond to the saturation degrees of 82 % to 99 %.
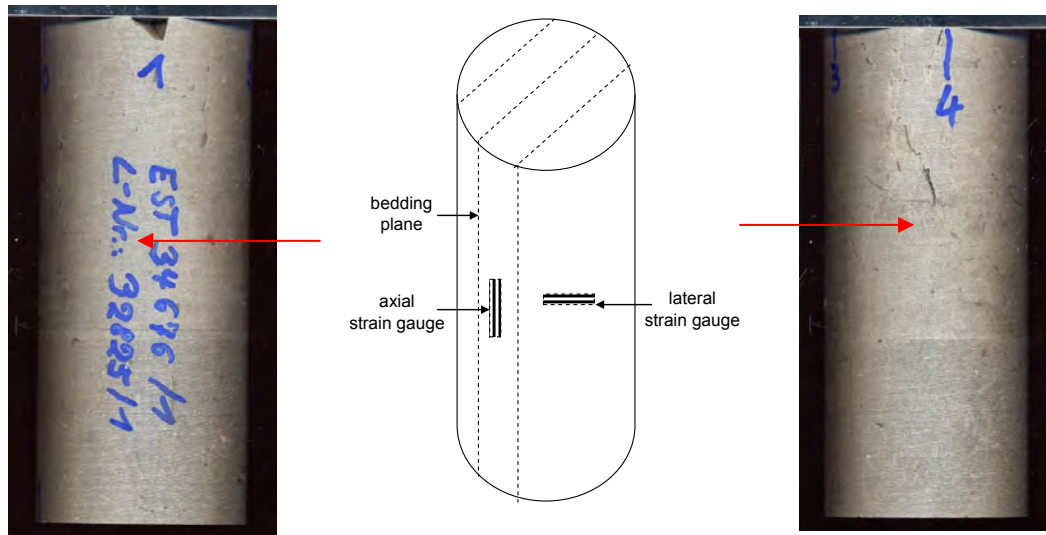
Fig. 2.62   Pictures of a normally-sized COX sample prepared for thermal expansion test and positions of used strain gauges for deformation measurement

Several big cores of 290 mm diameter and ~600 mm length were drilled vertically from the -490 m level of the MHM-URL. The axes of the cores were nearly perpendicular to the bedding planes. Immediately after the extraction of the cores, they were carefully prepared to large hollow cylinders of 280 mm outer diameter, 100 mm inner diameter and length of 520 mm by plane of the surfaces in a lathe and drilling the central bore-hole axially. The basic characteristics and pictures of the cores are summarized in Tab. E.7. The pictures of two prepared hollow cylinders EST45590 and EST45592 are shown in Fig. 2.63. Microfissures oriented along the horizontal bedding planes could be visually recognised on the sample surface. The prepared samples had quite high water saturation at degree of S_w = 90 % at EST45590 and S_w = 97 % at EST45592 respectively-ly.

(a) EST45590 D280/d103/L518mm   (b) EST45592 D280/d103/L520mm

Fig. 2.63   Large COX hollow cylinders prepared for borehole stability tests at high temperatures

2.5.2 Testing methods

2.5.2.1 Thermal tests on normally-sized samples

Thermal tests on normally-sized COX samples were carried out in triaxial apparatus under so-called undrained condition to determine thermal impact on deformation and damage of claystone. In the strict sense, the testing samples that were not fully water-saturated do not fill the requirement of the undrained condition because the porewater may migrate into unsaturated voids. The testing equipment allows a maximum axial and radial load of 50 MPa and a maximum temperature of 200 °C. Fig. 2.64 shows the setup. Axial deformation is recorded by a LVDT deformation transducer mounted inside the cell between the upper and lower loading platen, while a circumferential extensometer chain is mounted around the sample outside the jacket at its mid-height to determine lateral deformation. Heating is accomplished using an electrical heater positioned near the bottom of the cell.
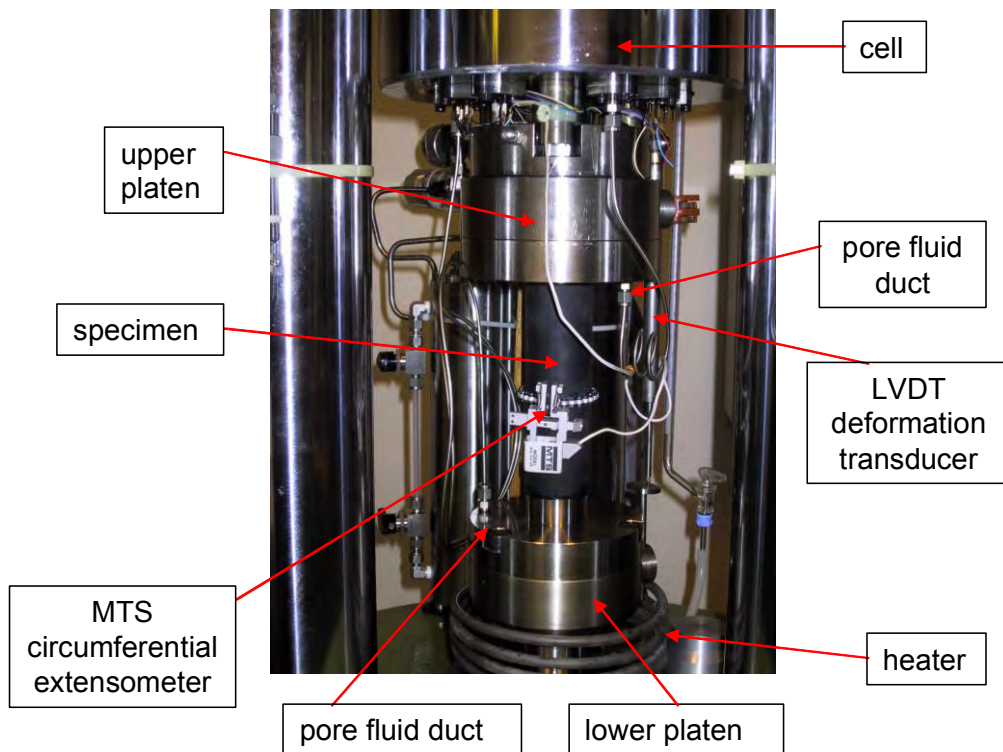
Fig. 2.64 Setup of a GRS triaxial testing apparatus for coupled THM experiments

2.5.2.2 Thermal tests on large hollow cylinders

Heating tests on large COX hollow cylinders aimed at investigating thermal impact on the deformation and damage of the clay rock surrounding HLW boreholes. A big MTS triaxial apparatus at the GRS laboratory was used, which allows application of THM conditions to cylindrical samples of 280 mm diameter and 450 – 700 mm lengths. The testing system permits a maximum lateral confining stress of 50 MPa and axial stress up to 75 MPa, temperature up to 150 °C, and fluid pressure up to 16 MPa. Fig. 2.65 shows a picture of the testing apparatus and the test layout designed for the heating tests on large hollow cylinders. A large hollow cylinder of 280 mm outer diameter and 520 mm length with a central borehole of 100 mm is sealed with an outer rubber jacket, while the borehole is equipped with a heater-packer. The relevant conditions expected in the potential HLW repository are taken into account in the tests, i. e. the lithostatic stresses of 13 to16 MPa at a depth of ~500 m below the ground surface and the de-signed maximum temperature of 90 °C. The borehole convergence can be determined by measuring changes of the oil volume in the packer using a precise syringe pump. The external stress is applied by regulating the axial load and lateral pressure in the cell. Thermal load is applied by means of the heater mounted outside the triaxial cell.

101

The temperature of the sample is monitored by PT100 sensors installed in the borehole and in the cell. Axial strain is measured by a LVDT deformation transducer mounted in the lower piston outside the cell. External radial strain is recorded using two circumferential extensometers installed at the middle and the lower position of ¼ sample length.
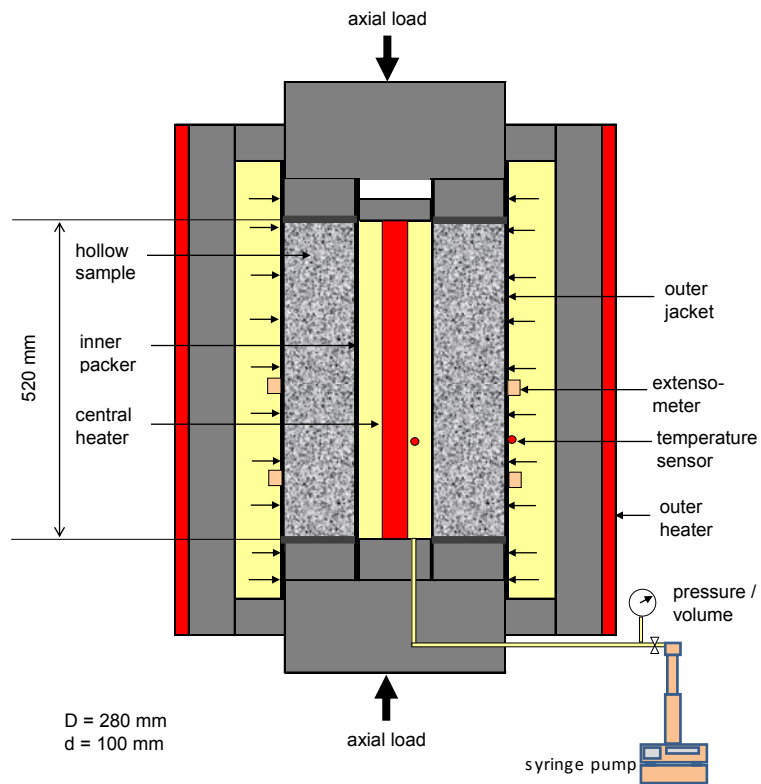
Fig. 2.65 Picture of the big triaxial apparatus and test layout for heating large hollow cylinders

The above mentioned parameters are evaluated according to the following definitions:

Axial stress

$$\sigma_a = \frac{F}{A_{ring}} = \frac{4\,F}{\pi\,(D^2 - d^2)} \tag{2.27}$$

where F = axial force, A_{ring} = cross section of the hollow cylinder, D = outer diameter of the sample, d = diameter of the central borehole.

Outer radial stress on the outer surface σ_R = applied oil pressure in the triaxial cell.

Inner radial stress on the borehole wall σ_r = 0.

Axial strain

$$\varepsilon_a = \frac{\Delta L}{L_0} = \frac{L_0 - L}{L_0} \tag{2.28}$$

where L = length of the sample, L_0 = initial length of the sample.

Outer radial strain

$$\varepsilon_R = \frac{\Delta D}{D_0} = \frac{D_0 - D}{D_0} \tag{2.29}$$

where D = outer diameter of the sample, D_0 = initial outer diameter.

Inner radial strain or borehole convergence

$$\varepsilon_r = \frac{\Delta d}{d_0} = \frac{d_0 - d}{d_0} = 1 - \sqrt{\frac{V_b/L}{V_{b0}/L_0}} \tag{2.30}$$

where d = average diameter of the borehole, d_0 = initial diameter of the borehole, V_b = volume of the borehole, which is determined by measuring the oil volume in the packer, V_{b0} = initial borehole volume.

Volumetric strain

$$\varepsilon_v = \frac{\Delta V}{V_0} = \frac{V_0 - V}{V_0} = 1 - \frac{L(D^2 - d^2)}{L_0(D_0^2 - d_0^2)} \tag{2.31}$$

with the borehole diameter $d = \sqrt{4V_b/\pi L}$.

Before testing, the measurement of the oil volume in the heater-packer for the borehole convergence was calibrated.

2.5.3 Thermal deformation under isostatic stresses

The thermal expansion test was carried out on the sample EST34676 (see Fig. 2.62) under various isostatic stresses and undrained conditions. Two strain gauges were attached on the sample surface at the middle length and nearly parallel to bedding for measurements of axial and lateral strain. The locations were selected where no bedding planes or visual fissures existed. In order to minimize effect of the pre-existing micro-fissures, the sample was pre-consolidated under isostatic stress of 15 MPa comparable to the in situ stress state at the sampling depth of ~490 m. This led to an increase in water saturation up to 96 %. The stressed sample was then heated at a low rate of 1.6 °C/h from the room temperature of 22 °C to 35 °C, 48 °C, 57 °C, 62 °C, 68 °C and then cooled down to the room temperature. Each stage lasted over one to several days, so that it was possible to look at time dependency of the thermal expansion/contraction. The same heating/cooling cycle was repeated under subsequently lowered isostatic stresses of 10, 5 and 1 MPa to examine influence of the confining stress. The measured data are summarized in Appendix E.1. As a typical example, Fig. 2.66 shows the measured strains via time during a heating/cooling cycle at the low stress of 1 MPa. From the data, one can recognize the following phenomena occurred:

1. Each temperature increase generates expansion in all directions. The expansion recorded in axial direction is larger than that in radial direction at all the applied stress levels.

2. The thermal deformation reached at each heating level below ~50 °C does not change significantly with time. Beyond that point, an inverse strain evolves gradually with time. The gradual contraction might be caused by migration of thermally-mobilized porewater into some unsaturated fissures and thus by the resulting compaction of the unsaturated voids.

3. Cooling down leads to a recovery of the thermal expansion. In the saturated state und undrained conditions at 10, 5 and 1 MPa (not during the first phase at 15 MPa), the thermal deformation is reversible.

4. After cooling down, the measured strain curves show a gradual swelling process at all the applied confining stresses from 15 to 1 MPa. Fig. 2.67 illustrates an example of the swelling evolution after cooling down at 23 °C under 5 MPa.
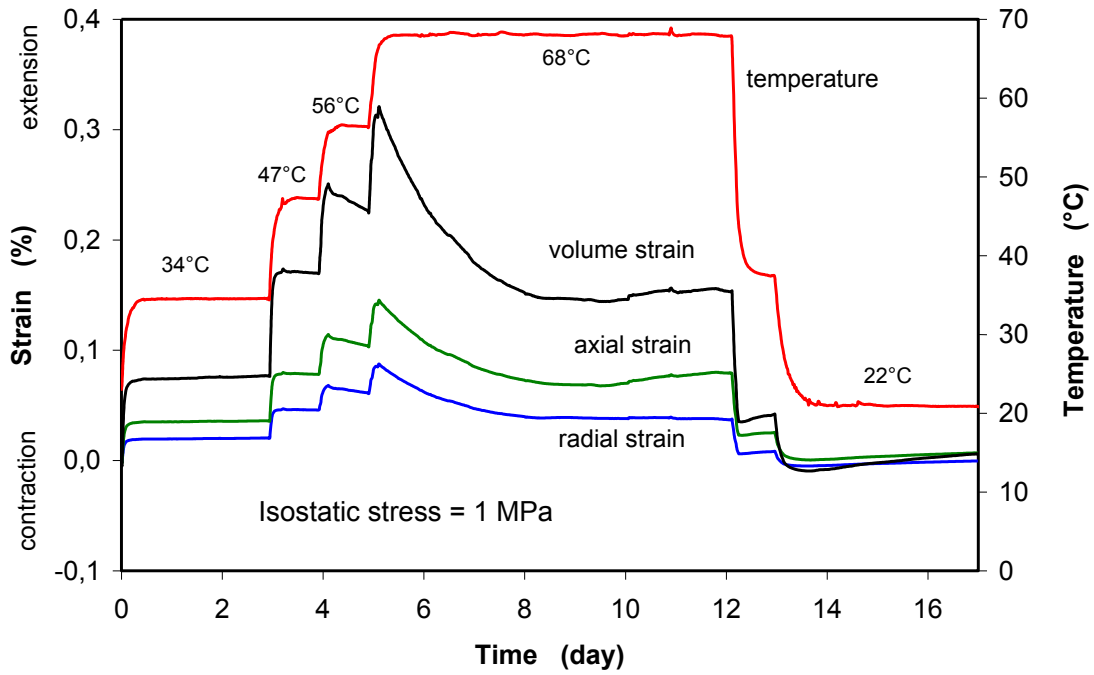
Fig. 2.66 Typical evolution of thermal expansion of COX claystone during heating and cooling cycle at isostatic confining stress of 1 MPa
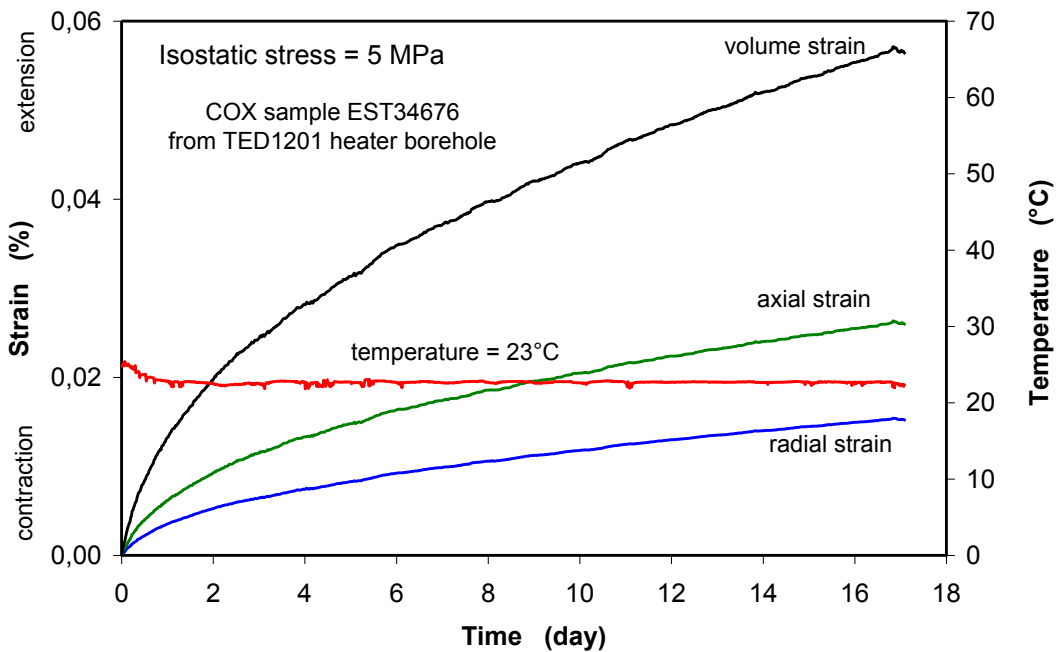
Fig. 2.67 Swelling deformation of COX claystone at confining stress of 5 MPa after cooling down to 23 °C

Fig. 2.68 illustrates the axial, radial and volumetric strains in relation to applied temperature at the confining stress of 1 MPa. The stepwise heating led to a linear increase of the thermal expansion in the beginning of each phase and then a slow departure from

the linearity. The strain – temperature curves obtained during the monotonic cooling phase show a better linearity.

From the slop of each linear part of the strain – temperature curve, the thermal expansion coefficient can be determined. Fig. 2.69 illustrates the data averaged from the axial and radial strain along the heating path. The influences of temperature and confining stress are insignificant. An average value is estimated by $2.9 \cdot 10^{-5}\,°C^{-1}$. If the delay of thermal expansion is taken into account, the coefficient may be determined by the segment spanning the whole test range from $25\,°C$ to $65\,°C$. These expansion coefficients vary between $1.5 \cdot 10^{-5}$ and $2.9 \cdot 10^{-5}\,°C^{-1}$. The mean value is about $2.5 \cdot 10^{-5}\,°C^{-1}$.

For saturated porous medium, the thermal expansion is governed by the expansion of both the solid grains and the pore water. According to /ZHA 07a/, /ZHA 08c/, /ZHA 09a/, /ZHA 10b/, the linear thermal expansion coefficient can be approached by

$$\alpha_m = \alpha_s(1-\phi) + \frac{\alpha_w}{3}\phi \tag{2.32}$$

where ϕ is the porosity, and α_s, α_w, α_m are the expansion coefficients of the solid grains, the pore water, and the saturated rock mass, respectively. The expansion coefficient for clay minerals have a value of $\alpha_s = 2.0 \cdot 10^{-6}\,K^{-1}$ /NOY 00/. The expansion of the pore water in both COX and OPA clay formations were determined on the synthetic waters which were produced by the GRS laboratory according to the chemical components reported in /AND 05/, /PEA 03/. The results are shown in Fig. E.43. The coefficient of the synthetic water is established by $\alpha_w = 4.2 \cdot 10^{-4}\,K^{-1}$ being slightly higher than that of pure water $\alpha_w = 3.4 \cdot 10^{-4}\,K^{-1}$ /UPC 04/.

Using the measured data and according to equation (2.32), the coefficient of the saturated claystone with a porosity of $\phi = 16.5\,\%$ is calculated to $\alpha_m = 2.48 \cdot 10^{-5}\,K^{-1}$, nearly the same as the mean value of $2.5 \cdot 10^{-5}\,K^{-1}$ from the delayed expansion data. The volumetric expansion coefficient is $\alpha_{mv} = 3\alpha_m = 7.43 \cdot 10^{-5}\,K^{-1}$. Using this value, the volumetric expansion of the saturated claystone is calculated and compared with the test data in Fig. 2.70. It can be seen that the theoretical model reasonably agrees with the observation. The model curve is also relatively parallel to the segments of the contraction curves, indicating the applicability of the model to cooling path too. Using the value for pure water, the expansion of the saturated claystone is underestimated. Because the expansion coefficient of the porewater is two orders of magnitude higher than that

of the solid grains, the thermal expansion of saturated clay rocks is mainly dominated by the water expansion.
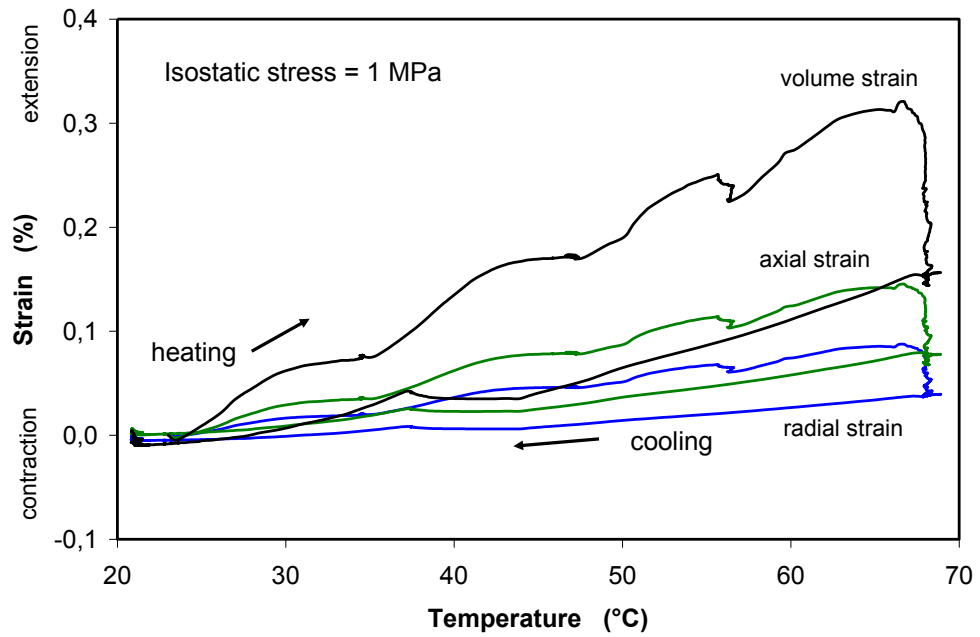
Fig. 2.68   Thermal expansion of COX claystone in dependence of applied temperature at confining stress of 15 MPa
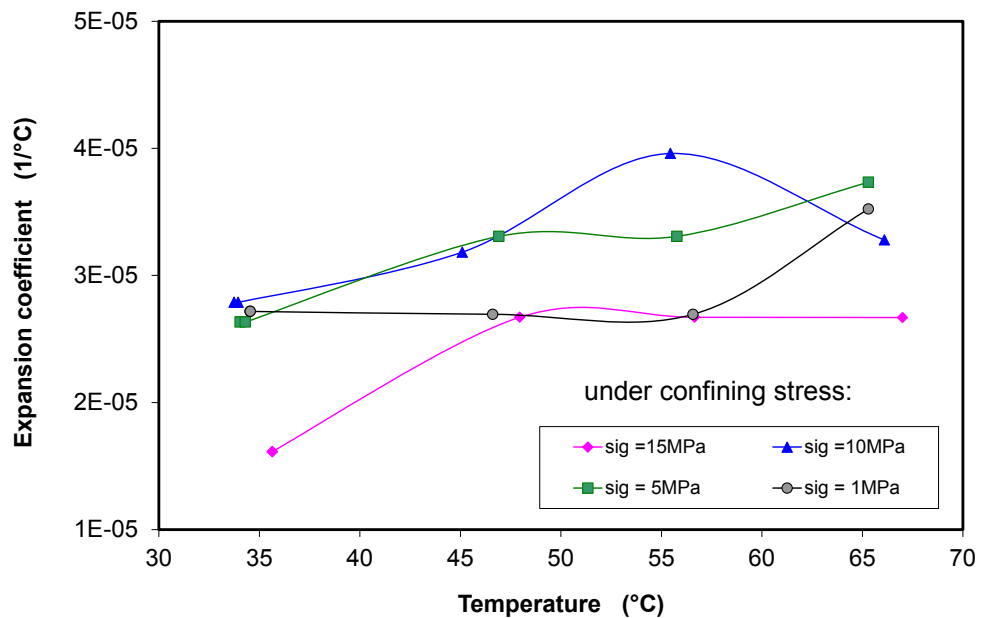
Fig. 2.69   Thermal expansion coefficients determined along heating path
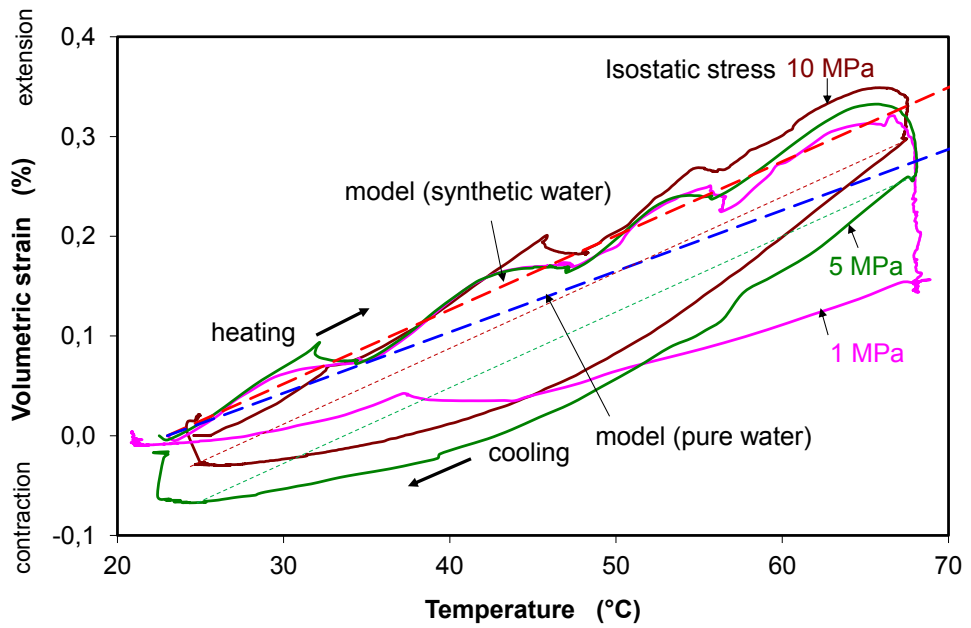
Fig. 2.70   Comparison between calculated and measured volumetric expansion of saturated claystone as a function of temperature

After the test, the sample was dismantled and inspected. Fig. 2.71 shows the pictures after testing. Fissures appeared on the surface, whereby water condensation could be clearly identified. The fissuring might be caused by the relief of the confining stress after dismantling. Under certain confined conditions, fracturing will be constrained.

Fig. 2.71   Micro-fissures appeared on the sample surface after heating test

2.5.4 Thermal deformation under deviatoric stresses

The clay host rock near heat-emitting HLW containers will be mostly impacted by thermal load. The most concern is whether and how the favourable barrier properties of the clay rock will be altered during the thermal period under designed temperatures below 90 °C, particularly EDZ development under thermal loading. This important issue has been investigated under the nearfield conditions expected, where the rock will be disturbed by excavation, desaturated during ventilation, and subjected to high deviatoric stresses and to heating/cooling cycle over several thousands of years. These conditions were simulated in the laboratory experiments.

Fig. 2.72 shows results of uniaxial creep tests on two COX samples under different temperatures between 24 °C and 90 °C. One sample was stressed at a very low load of 0.74 MPa while another one at a high load of 13.8 MPa. They were sealed in rubber jackets to avoid escape of porewater. The temperature was elevated step by step from 24 °C to 28 °C, 40 °C, 50 °C, 60 °C, then decreased down to 40 °C, and finally increased again to 60 °C, 70 °C, 80 °C, 90 °C. The main observations are the following:

- Each temperature rise leads to a short-time expansion followed by gradual compression with time;

- The strain-time curve at each elevated temperature is quite linear, i. e., the temperature increase does not cause a significant transient creep;

- The creep becomes faster, the higher the temperature is increased, as long as no or less porewater escapes;

- In contrast to heating, cooling down results in contraction, but no further creep takes place after cooling from 60 °C down to 40 °C;

- Further increasing the temperature from 40 °C to 60 °C, 70 °C, 80 °C and 90 °C produces a repeat of the short-term expansion and a progressive compression each, but the strain rates are slightly lower than before at the same temperatures;

- The creep rates obtained at the different loads are relatively comparable.
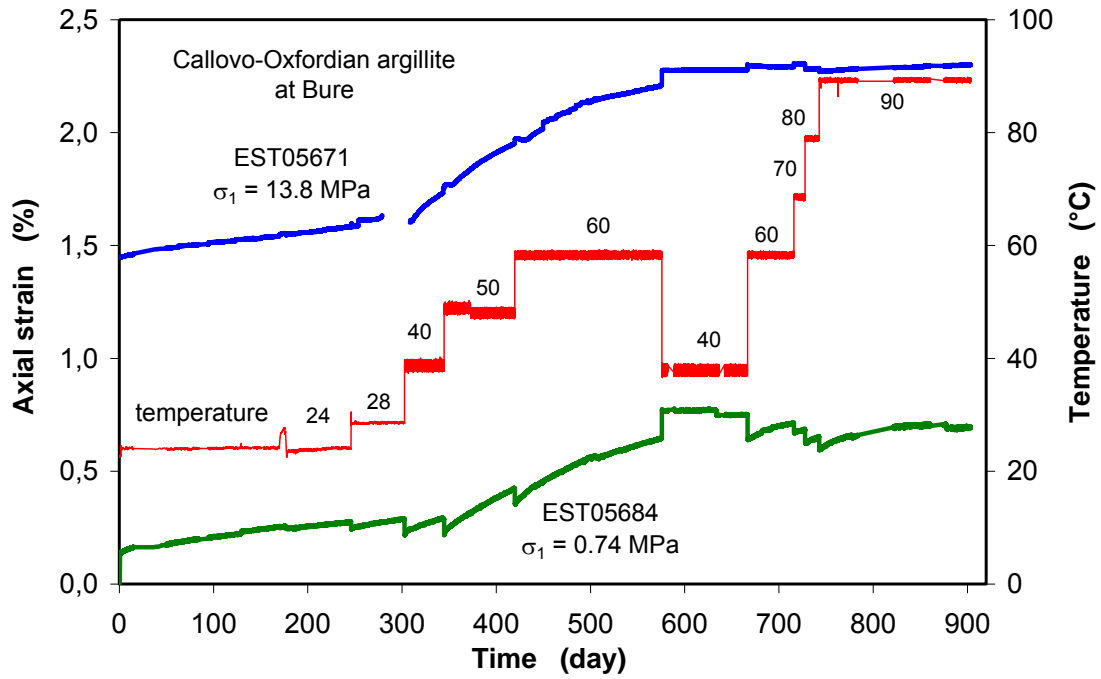
(a) creep curves
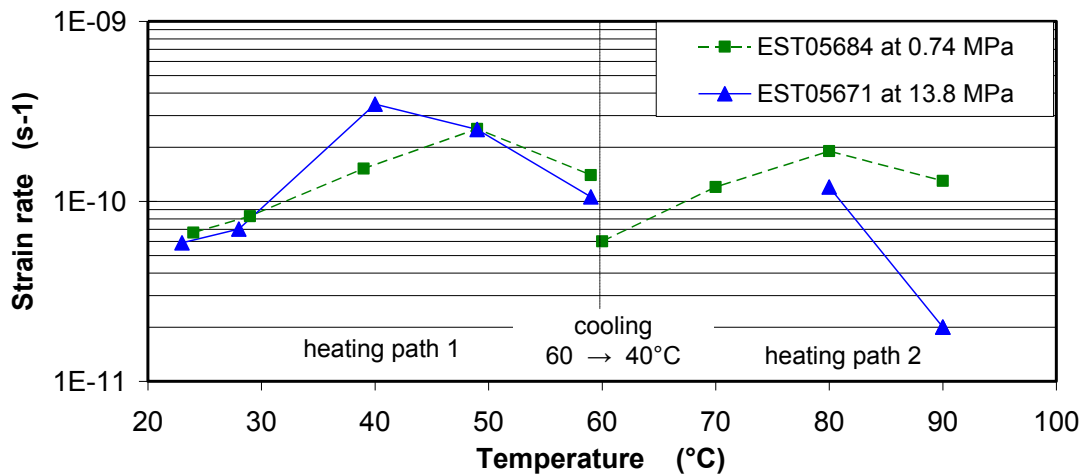
(b) steady-state creep rates

Fig. 2.72   Uniaxial creep behaviour of COX claystone at elevated temperatures

Most of the above conclusions from the uniaxial creep tests are confirmed by the following triaxial creep tests. Fig. 2.73 illustrates axial/radial/volume strain-time curves obtained on several COX samples at a constant axial stress of 15 MPa and different radial stresses of 3, 1, 0.5 MPa, respectively, and at temperatures of 28 °C to 110 °C. In order to gain high degrees of water saturation, the samples were wetted by spraying synthetic porewater upon the surface before installation in the jackets. To minimize effects of the pre-existing microcracks, the samples were firstly consolidated under high isostatic stress of 15 MPa. After consolidation, the radial stress was lowered down to each de-

sired level. Under constant stresses, the temperature was increased stepwise up to the designed levels at a rate of 1 °C/h, kept constant for creep testing, and then decreased stepwise again to the previous levels at the same rate. The strain-time curves obtained on each sample show that:

- Each temperature rise leads to a short-time expansion in radial direction, but only a slight axial compression and, hence, a resultant volume increase;

- The following creep progresses in compression in both axial and radial directions and thus in volume;

- The evolution of the strains with time is quite linear for each elevated temperature below ~90 °C, suggesting no or small thermal transient creep; Above that, the creep slows with time due to some release of thermally-evaporated porewater and the resultant hardening;

- Cooling down results in a short-term radial contraction but negligible axial strain, and at each lowered temperature no or very limited creep appears;

- Heating again (from 30 °C to 60 °C in Fig. 2.73a) produces a repeat of the short-term expansion in radial direction and then a progressive compression in both axial and radial directions, but the strain rates are slightly lower than before at the same temperature;

- Heating/cooling cycles between 30 and 110 °C did not create volumetric dilatancy or damage, but consolidation due to release of some porewater towards the non-perfectly undrained boundary which however is more comparable with the in situ situation;

- Post measurement after testing indicates the porewater loss up to ~2 %, suggesting the non-perfect undrained condition during the tests.

Fig. 2.74 shows the data of axial and radial creep rates obtained during the heating phase. The creep rate increases with temperature in the range below 90 °C, and beyond that, the creep becomes slower because the porewater released more during the tests increasing contact areas between solid particles and hence increasing friction resistance between them. The data of axial and radial creep rate are used for determination of the shear creep rates and the apparent activation energy Q in the Arrhenius equation (2.24), $\dot{\varepsilon} \sim \exp(-Q/RT)$.
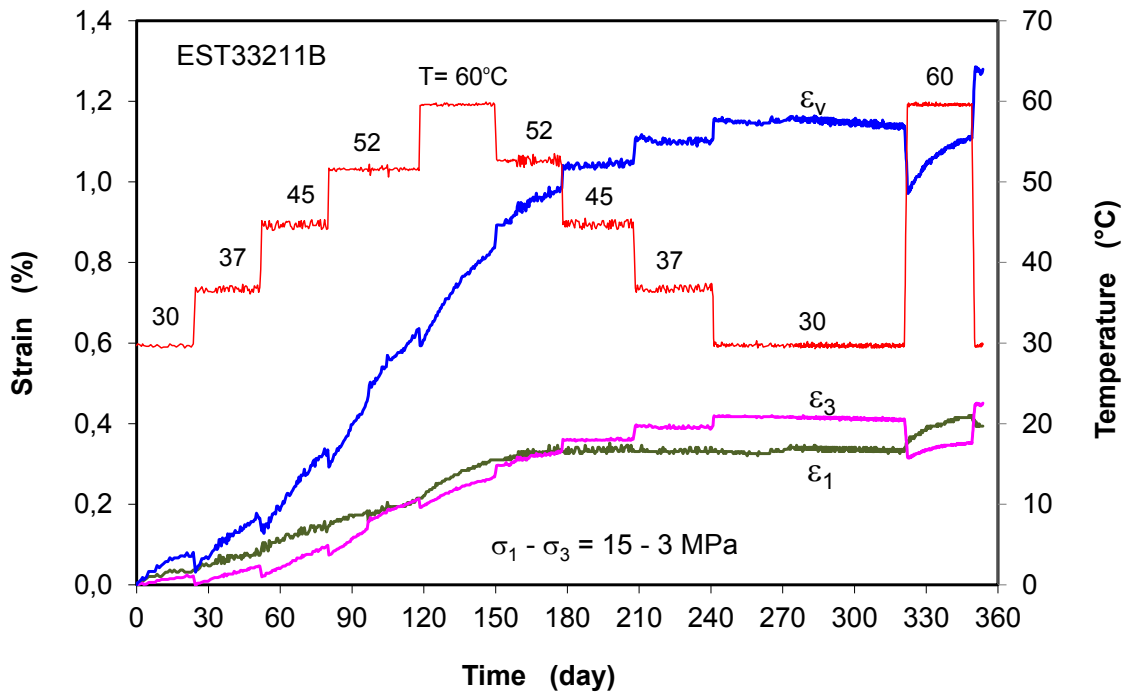
(a) creep test at $\sigma_1 - \sigma_3 = 15 - 3$ MPa and T = 30 °C to 60 °C
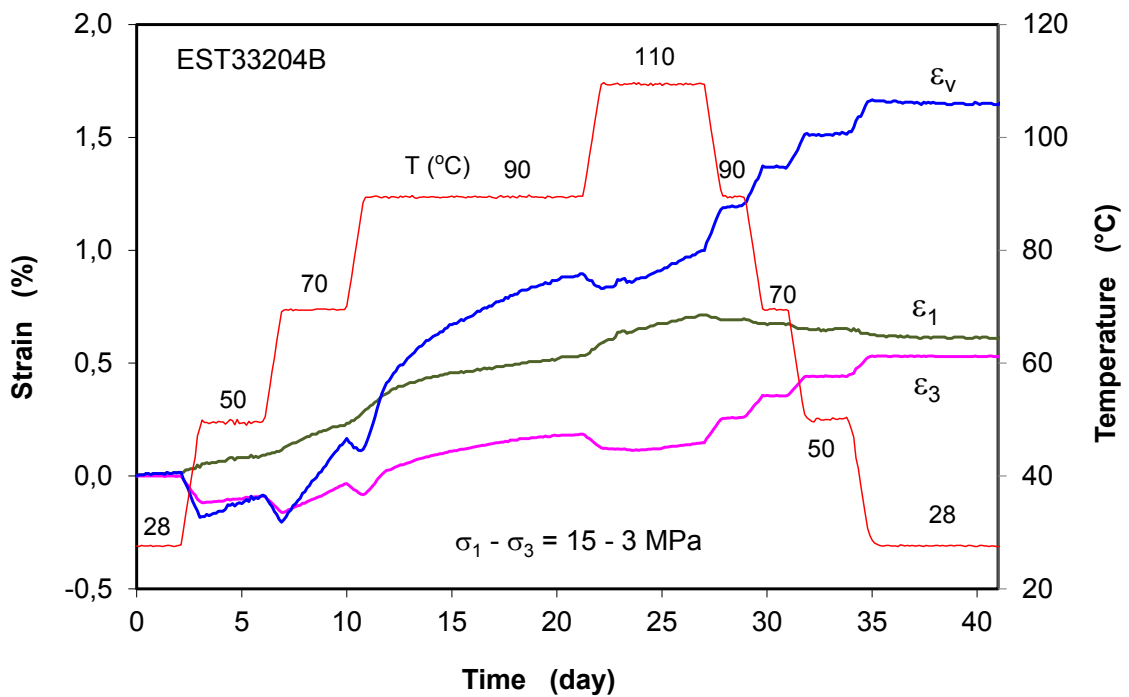
(b) creep test at $\sigma_1 - \sigma_3 = 15 - 3$ MPa and T = 28 °C to 110 °C

112
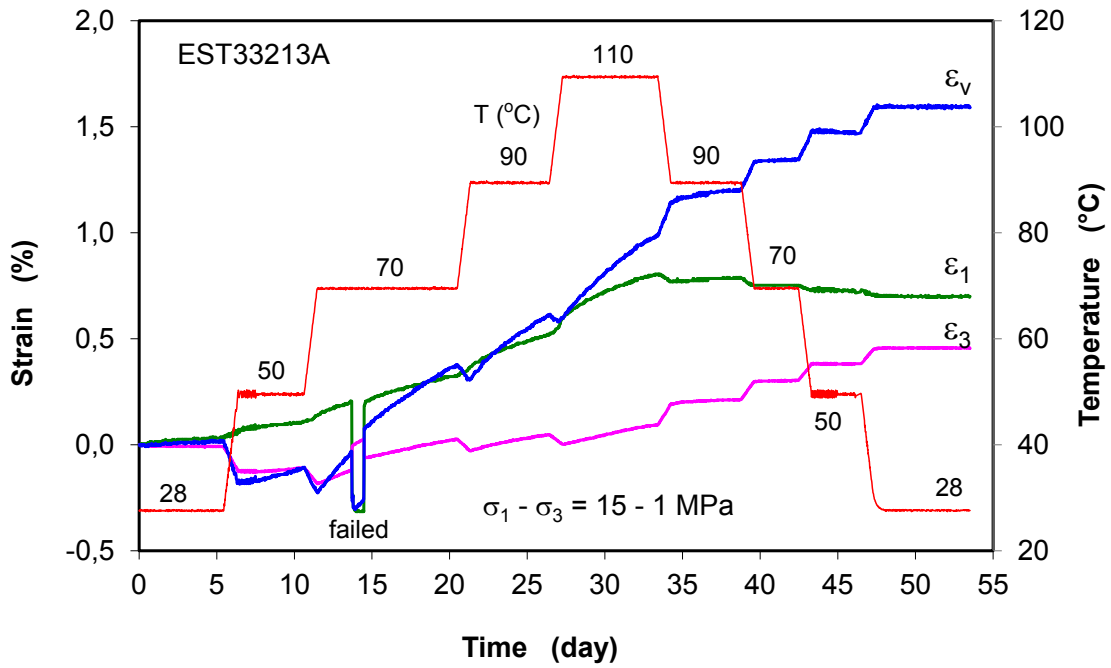
(c) creep test at $\sigma_1 - \sigma_3$ = 15 – 1 MPa and T = 28 °C to 110 °C
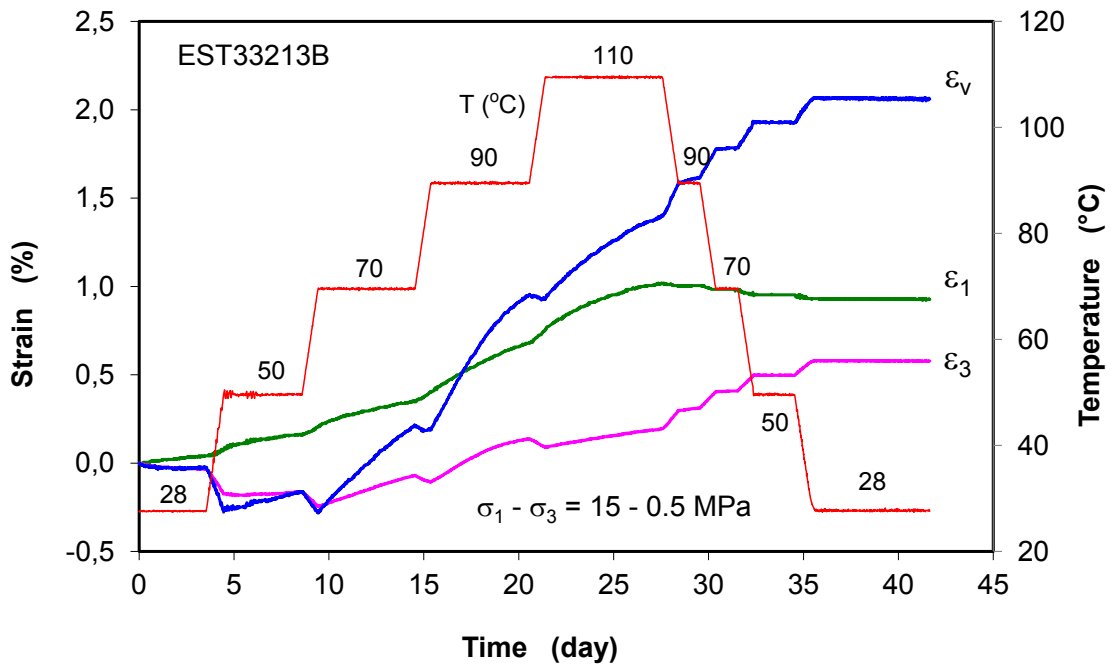
(d) creep test at $\sigma_1 - \sigma_3$ = 15 – 0.5 MPa and T = 28 °C to 110 °C

Fig. 2.73   Triaxial creep behaviour of COX claystone under various triaxial stress
conditions and different temperatures between 30 °C and 110 °C
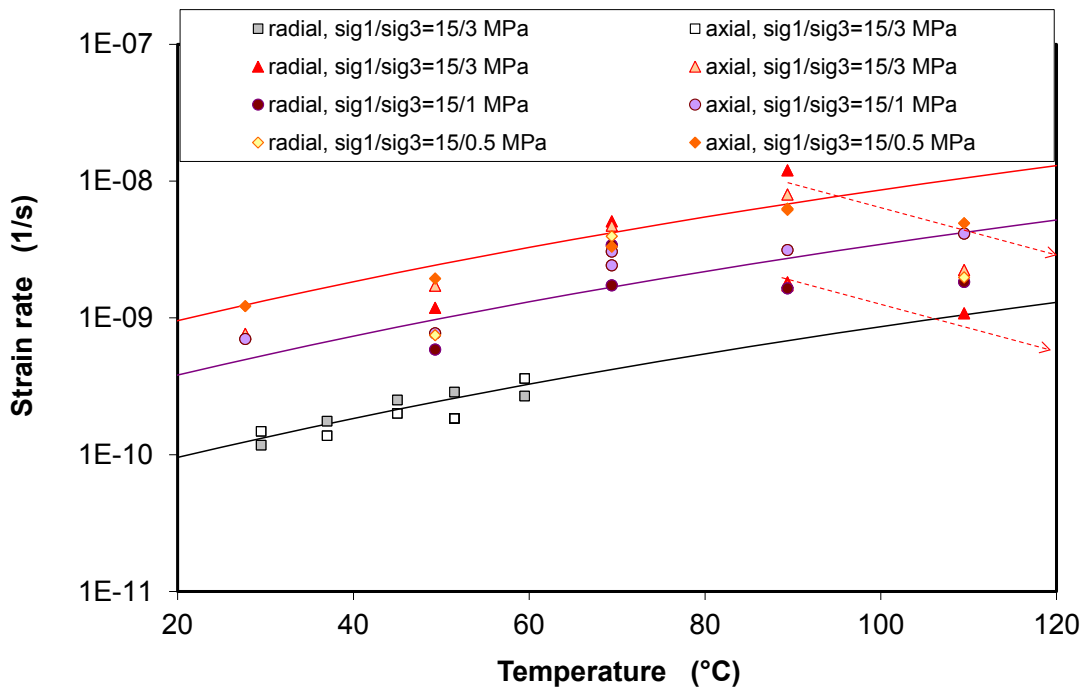
Fig. 2.74   Axial and radial strain rates obtained in triaxial creep tests during the temperature increase phase

2.5.5   Temperature influence on strength

Temperature influences on the stress-strain behaviour and strength of a claystone are differing from saturated to unsaturated state and from drained to undrained conditions. In saturated and undrained conditions, the claystone becomes more ductile and weaker with increasing temperature, as observed in the triaxial compression tests on the Opalinus claystone at temperatures between 20 °C and 116 °C /ZHA 05/, /ZHA 06/, /ZHA 07a/, /ZHA 07c/. At lateral confining stress of σ_3 = 3 MPa, the peak strength reduced by a factor of 4 from 20 MPa at 20 °C down to 5 MPa at 116 °C. The weakness might be mainly caused by thermally-induced over pore pressure, which in turn reduces the effective mean stress. This effect is also revealed by the other tests on the COX claystone /TIM 10/.

In contrast, heating a claystone in undrained condition drives the existing water out of the pores, resulting in consolidation under confining stresses, increasing the inner friction resistance between particles against shearing and hence strengthening the rock. Fig. 2.75 compares the stress-strain curves obtained on COX samples after cooling down from 150 °C and 110 °C to 30 °C during the previous creep tests. Both samples were subjected to a radial stress of 3 MPa and non-perfect undrained conditions during

testing. Both samples showed the typical nonlinear elasto-plastic deformation with volume compaction but without dilatancy until failure.

(a) during heating at T = 150 °C   (b) after heating at T = 110 °C
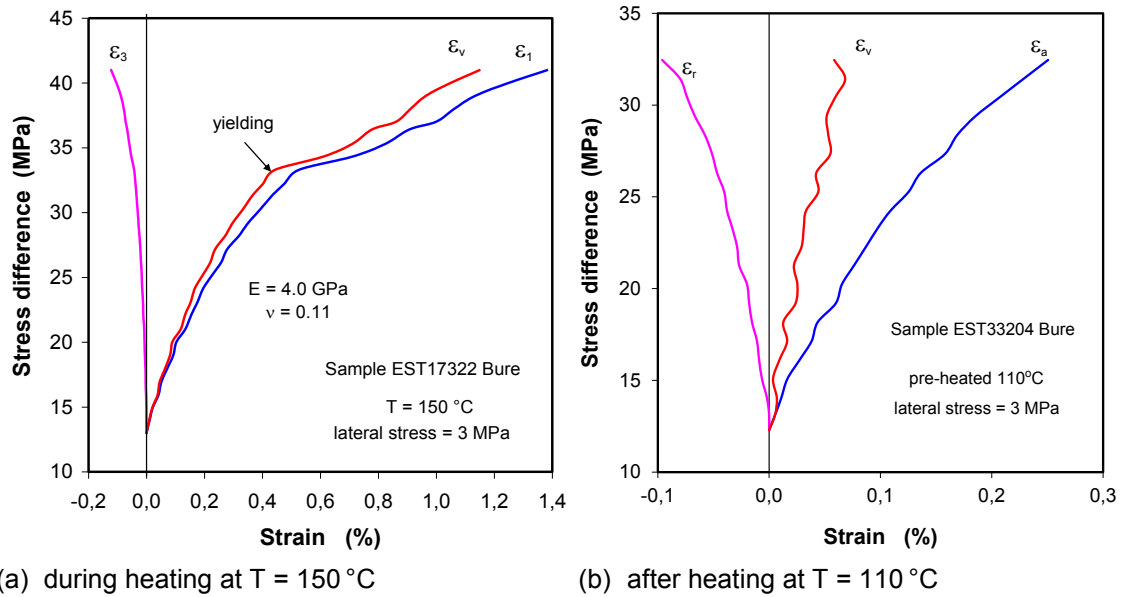
Fig. 2.75   Stress-strain behaviour of COX claystone during and after heating

Fig. 2.76   Temperature influence on the strength of the COX claystone
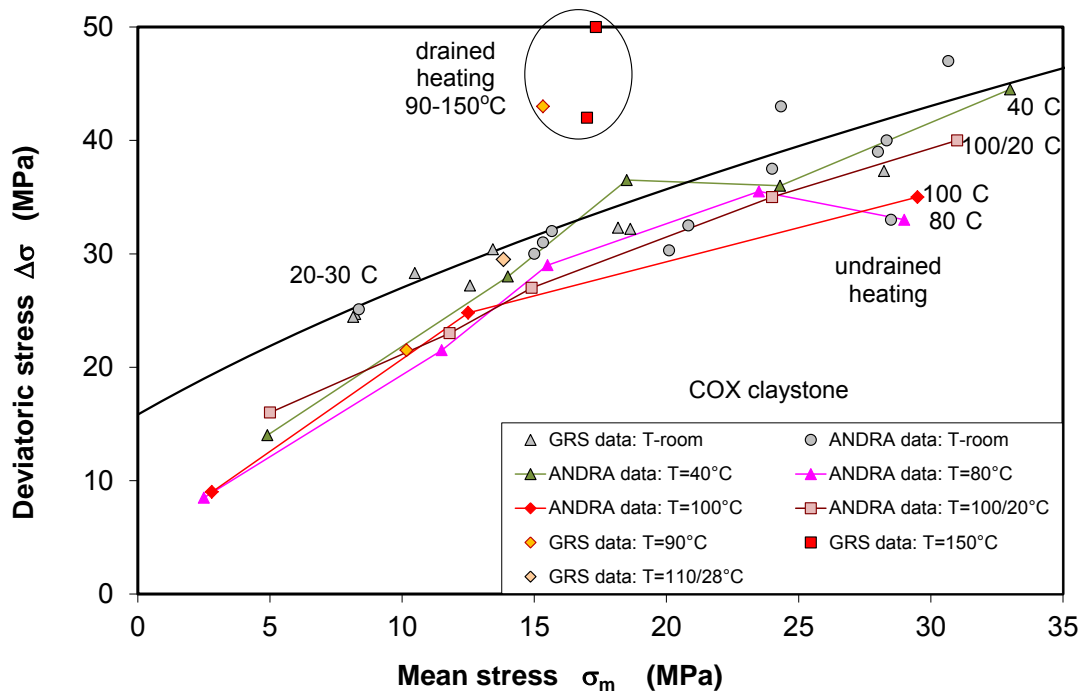
The peak strength values are depicted in Fig. 2.76 in comparison with the strength data previously obtained on the COX claystone at ambient temperature and elevated temperatures of 90 °C – 150 °C in drained condition (GRS-data), and at 40 °C – 100 °C in saturated and undrained conditions (ANDRA-data from /TIM 10/). It can be recognized that the maximum strength is achieved by heating in drained condition, followed by the strength at ambient temperature, and the strength of the saturated claystone in un-drained condition decreases with increasing temperature.

2.5.6 Thermal impact on borehole stability

2.5.6.1 Testing procedure

Thermal impact on the mechanical stability of HLW boreholes was tested with large COX hollow cylinders. The prepared samples are shown in Fig. 2.63 and the designed test layout in Fig. 2.65. The boundary conditions around boreholes in the large clay-stone samples were designed to be simulated with the following stages:

1. Reconsolidation of the disturbed samples is necessary to approach the original state by increasing the external confining stress and the borehole packer-pressure to the in situ stress level of 15 – 16 MPa at the -490 m level of the MHM-URL

2. Borehole excavation is simulated by lowering the borehole pressure to 0.5 MPa;

3. Support of the steel lining is simulated by keeping the borehole volume constant;

4. Thermal load is applied by heating the samples from 30 °C to 50 °C, 70 °C and 90 °C and then cooling down;

5. Dismantling and inspection of the samples after testing.

Obviously, conducting such a very complex experiment is a great challenge. Because of unexpected technical difficulties, the envisaged test programme might not be com-pletely performed.

2.5.6.2   Test results

Test 1 on sample EST45590

Fig. 2.77a illustrates the evolution of applied temperature, axial and radial confining stress, and packer-pressure in the borehole, while the responses of axial strain, outer radial strain, and borehole convergence are presented in Fig. 2.77b. The test started with the application of the initial conditions of T = 26 °C and σ_a = σ_R = σ_r = 1 MPa.

1. Reconsolidation: The large hollow cylinder was compacted by increasing the loads at a rate of 6 MPa/h to a quasi-isotropic stress state of axial stress of σ_a = 16 MPa, outer radial stress and inner borehole pressure of σ_R = σ_r = 15 MPa. The temperature was adjusted at 30 °C. The consolidation phase lasted for 5 days, resulting in compaction of axial strain ε_a = 0.3 %, outer radial strain ε_R = 0.01 %, and borehole divergence ε_r = 1.0 %. The relatively large axial strain was mainly attributed to the closure of the pre-existing microcracks oriented along the horizontal bedding planes. The consolidation increased the water saturation to S_w > 90 % due to the reduction of unsaturated pores and microcracks. The reconsolidated state was defined as the initial conditions of the sample by set up of strains $\varepsilon_a = \varepsilon_R = \varepsilon_r = 0$.

2. Borehole excavation was simulated by reducing the borehole pressure down to σ_r = 0.5 MPa, which resulted in a borehole convergence to ε_r = 0.25 % and the inward strain of the outer surface to $\varepsilon_{R-1/2L}$ = 0.22 % at the middle of the sample. The deformations maintained almost unchanged over 7 days.

3. Heating 1: The "excavated" claystone was heated by increasing the temperature at a rate of 1 °C/h to 50 °C. Correspondingly, the hollow cylinder expanded in all directions shortly. Keeping the elevated temperature, it followed by a gradual borehole convergence ($\Delta\varepsilon_r > 0$) and radial compression ($\Delta\varepsilon_R > 0$) over the first 7 days. Subsequently, the support of the lining was simulated by switching off the oil volume in the inner packer. With the continual convergent creep of the claystone ($\Delta\varepsilon_R > 0$), the contact stress between the rock and the lining rose up to 2 MPa over 8 days. The following removal of the lining simulated by reducing the support stress to σ_r = 0.5 MPa caused a sudden convergence of $\Delta\varepsilon_r$ = 0.4 %.
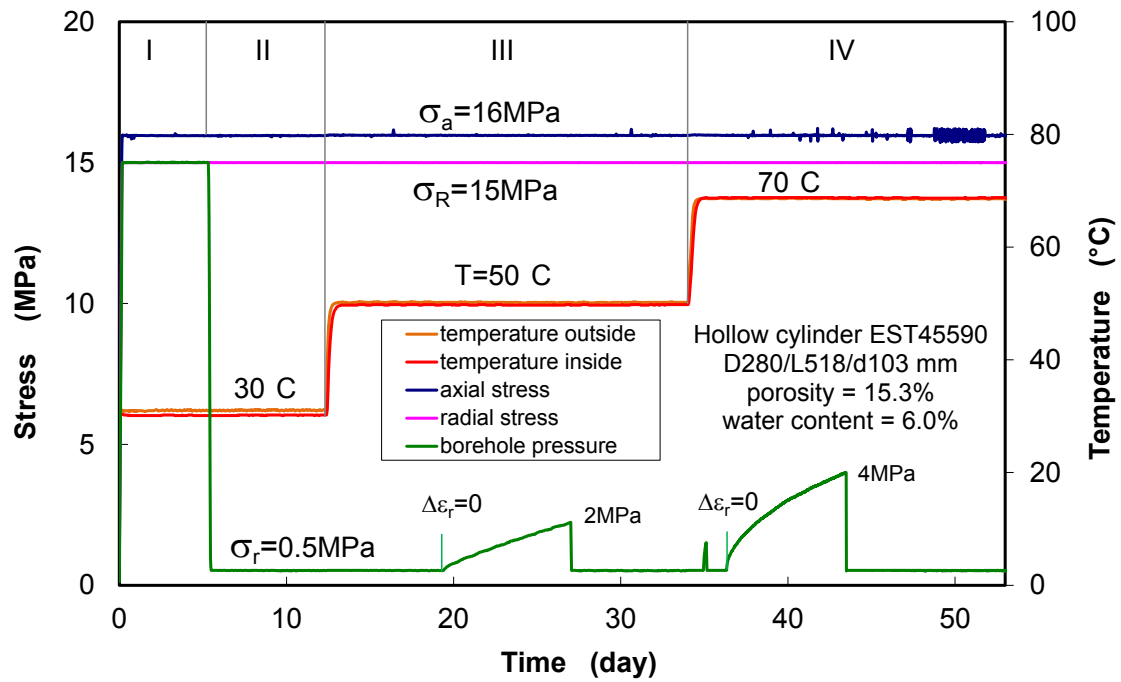
(a) boundary conditions of temperature, external stresses and borehole pressure
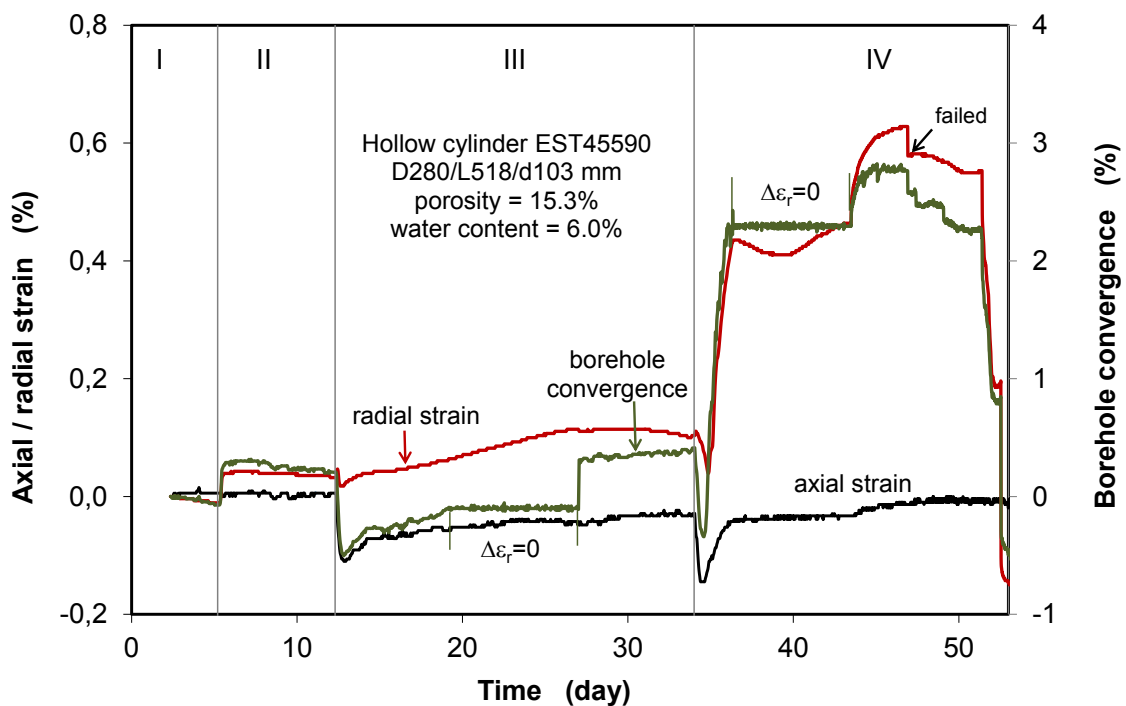
(b) responses of strains and borehole convergence to thermal-mechanical loading

Fig. 2.77 Results of the first heating test on a large COX hollow cylinder EST45590

4. Heating 2: The second heating to 70 °C caused the similar response of the clay-
stone, i. e. a short thermal expansion with increasing the temperature and then fol-
lowed by a large contraction with an outer radial compression of $\Delta\varepsilon_R$ = 0.4 % and

an inner borehole convergence of $\Delta\varepsilon_r$ = 2.4 %. Switching off the inner packer volume led to a gradual buildup of the lining stress against the rock up to 4 MPa after 6 days, being two times that at 50 °C. The subsequent removal of the lining by reducing the support stress caused a sudden convergence. Several days later, it was unfortunately terminated because the outer rubber jacket was damaged at the contact area with the lower piston. The rest water content was determined at 6.0 %, being the same as before. It suggests no water loss during the undrained test.

Test 2 on sample EST45592

Fig. 2.78a illustrates the evolution of applied temperature, axial and radial confining stress, and packer-pressure in the borehole, while the responses of axial strain, outer radial strain, and borehole convergence are presented in Fig. 2.78b. The test started with the application of the initial conditions of T = 26 °C and $\sigma_a = \sigma_R = \sigma_r$ = 1 MPa.

1. Reconsolidation: The large hollow cylinder was compacted by increasing the loads at a rate of 6 MPa/h to a quasi-isotropic stress state of axial stress of σ_a = 16 MPa, outer radial stress and inner borehole pressure of $\sigma_R = \sigma_r$ = 15 MPa. The temperature was adjusted at 30 °C. The consolidation phase lasted for 3 days, resulting in a volumetric compaction of an axial strain ε_a = 0.3 %, an outer radial strain ε_R = 0.26 %, and a borehole divergence ε_r = 2.3 %. The axial and radial strains are quite comparable indicating a negligible anisotropy of the sample. The consolidation increased also the water saturation, i. e. S_w > 97 %. The reconsolidated state was defined as the initial conditions of the sample by set up of zero strains: $\varepsilon_a = \varepsilon_R = \varepsilon_r$ = 0.

2. Borehole excavation was simulated by reducing the borehole pressure down to σ_r = 0.5 MPa. The excavation resulted in a borehole convergence to ε_r = 0.5 %. The outer wall of the cylinder was displaced inwardly to a strain of $\varepsilon_{r-1/2L} \approx \varepsilon_{R-1/4L}$ = 0.4 % at the middle and the low positions. The deformations maintained almost unchanged over 7 days. Following that, it was tried to heating the sample by means of the heater in the packer. But the temperature could only be increased by 1 °C because the bottom of the heater was not thermally isolated. The small temperature change caused a remarkable expansion and contraction of the sample.

3. Damage enlargement: In order to examine damage process, the external stresses were further increased to σ_R = 20 MPa and σ_a = 21 MPa, corresponding to a depth of about 800 m below the ground surface. This resulted in a significant borehole

convergence from ε_r = 0.4 % to 1.0 % and a convergent strain from ε_R = 0.07 % to 0.10 %. Under the constant stress difference of $\sigma_R - \sigma_r$ = 19.5 MPa, the convergent deformation continued with time. The rates of the borehole convergence and the outer radial strain at the middle of the sample are quite high. At 10 days, the deformation rates rose rapidly to a large borehole convergence of ε_r = 2.8 % and an outer radial strain of ε_R = 0.5 %. The shape of the strain evolution is consistent with the typical creep rupture curve (cf. Fig. 2.39), suggesting a damage process around the borehole.

4. Heating: The damaged claystone was additionally heated to 50 °C. This accelerated the damaging process. At the elevated temperature, the borehole convergence and radial compression continued with time. Because the borehole convergence touched the device limit, the heating phase could only be performed for a short term of 5 days.

5. Cooling down followed by reducing the temperature to 30 °C in a day led to a continual convergence. Keeping the lowered temperature for 28 days further, no or negligible deformation was observed.

6. Support of backfill/lining: The impact of backfill/lining support on the damaged zone was simulated by increasing the borehole pressure step-by-step from 0.5 to 2, 8, 12 and 15 MPa for several days in each step. The increase of the back-pressure enlarged the borehole diameter by Δd 1.0 mm ($\Delta \varepsilon_r \approx$ 1.0 %) and the outer diameter extended by $\Delta D \approx$ 0.28 mm ($\Delta \varepsilon_{R-1/2L} \approx \Delta \varepsilon_{R-1/4L} \approx$ 0.1 %). The calculated volume strain of $\Delta \varepsilon_v$ = 0.25 % suggests a recovery of the EDZ due to the backfill effect.

7. Post-testing: Fig. 2.79 shows pictures of the dismantled sample after testing. Multiple fractures were generated and interconnected vertically and horizontally. A large fracture was developed at an angle of ~15° inclined to the sample axial. The determined rest water content of 6.3 % suggests a water loss of 0.8 % compared with the initial value of 7.1 %.
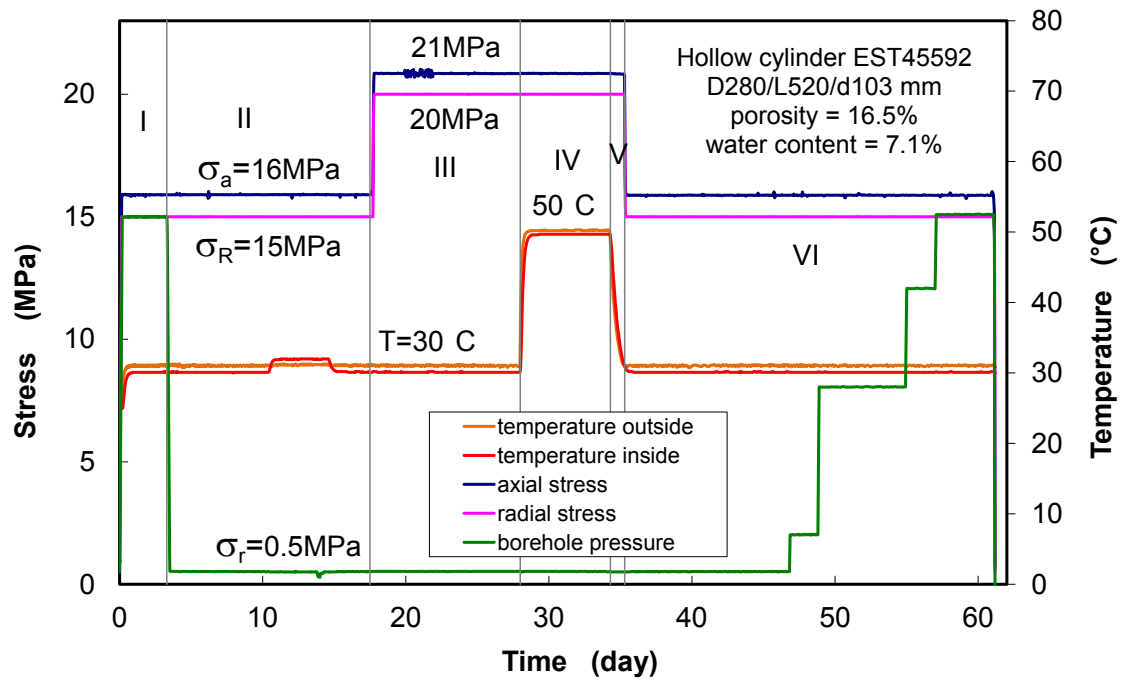
(a) boundary conditions of temperature, external stresses and borehole pressure
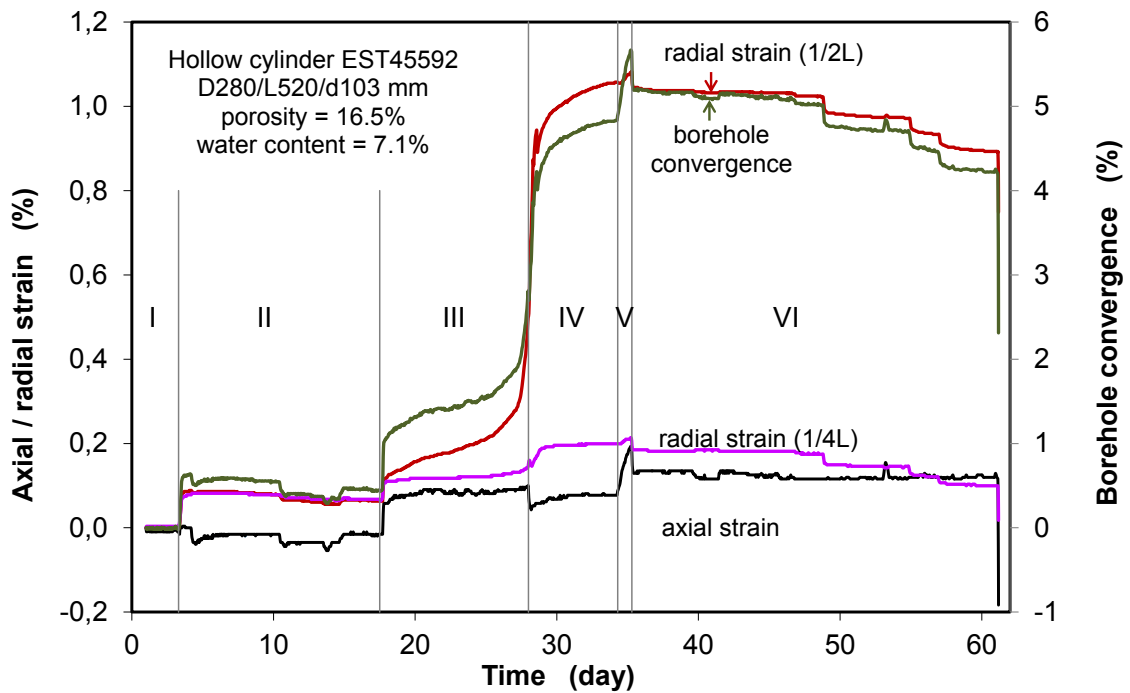
(b) responses of strains and borehole convergence to thermal-mechanical loading

Fig. 2.78 Results of the second heating test on a large COX hollow cylinder EST45592

Fig. 2.79   Pictures of the large hollow cylinder EST45592 damaged after testing

2.5.7   Conclusions on the thermal impact

The thermal impact on the mechanical behaviour of the COX claystone was experimentally studied in respects of thermal expansion and contraction under various confining stresses, temperature influences on creep deformation and strength, and thermal impact on borehole stability. Heating/cooling cycles from the room temperature to the maximum temperatures of 90 °C to 110 °C were applied to the testing samples. The following conclusions can be drawn:

- Under isostatic confining stresses of 1 to 15 MPa and in undrained condition, the water-saturated claystone expands with increasing temperature and contracts with decreasing temperature. The thermal expansion and contraction are reversible and vary with temperature almost linearly. The thermal expansion and contraction are predominantly controlled by the porewater because of its much higher expansion coefficient compared to that of the solid grains. The thermal expansion and contraction coefficients of the COX claystone can be approached by the Zhang's model: $\alpha_m = \alpha_s(1 - \phi) + \alpha_w/3 \cdot \phi$, where α_s = 2.0·10^{-6} K^{-1} is the expansion coefficient of clay minerals, α_w = 4.2·10^{-4} K^{-1} is the expansion coefficient of the porewater, and α_m = 2.48·10^{-5} K^{-1} for a porosity of ϕ = 16.5 %.

- The temperature influence on deformation of the COX clay rock was examined on the samples in triaxial creep tests under high deviatoric stresses of 12 – 15 MPa and at elevated temperatures of 25 °C to 110 °C. In saturated and undrained conditions, the creep at a constant temperature below ~90 °C evolves linearly with time without or less transient phase. The creep is accelerated with temperature. The relationship of the steady-state shear creep rate with temperature can be approached by the Arrhenius equation, $\dot{\varepsilon} \sim \exp(-Q/RT)$, with the apparent activation energy Q = 45 kJmol^{-1} for the COX claystone. In drained conditions, heating leads to mobilisation, evaporation and expulsion of the porewater from the claystone. The release of the porewater results in pore collapse and thus consolidation under confining stresses. The thermal consolidation strengths the clay rock due to the increase in friction resistance between particles against shearing.

- Thermal impact on the mechanical stability of boreholes is significant. In case of the heating tests on large hollow cylinders in undrained conditions, the temperature increase accelerates the borehole convergence and generates thermal stress on the support lining. The magnitude of the load and the stability of the boreholes are dependent on the stiffness of the liner, local contact area between rock and liner, and anisotropic deformation of the rock induced by the anisotropic stress distribution and the bedding structure in the clay rock. For backfilled boreholes, thermally-driven convergent deformation of the clay rock consolidates the porous backfill material and the EDZ, and thus enhances the sealing process and integrity of the natural and engineered barriers. Cooling down has little effects on the borehole stability.

2.6 Self-sealing of fractures

After backfilling and sealing of repositories in argillaceous formations, a recovery process of the EDZ can be expected during the post-closure phase due to combined impact of the progressive deformation of the clay host rock, the increasing resistance of the engineered barriers (buffer, backfill, seals), and the swelling of clay matrix into fracture interstices. For the long-term safety assessment of a repository, various kinds of evidence, deep understanding, quantitative characterisation, and prediction of the self-sealing process of the EDZ are indispensable. Since the previous studies on sealing of clay rocks /ZHA 08a/, /ZHA 08b/, /ZHA 09b/, /ZHA 10c/, more comprehensive investigations have been conducted on COX and OPA clay rocks in this project. According to the Swiss and French disposal concepts /NAG 02/, /AND 05/, the potential repositories will be located in the argillaceous formations at depths of about 500 m and 650 m below

the ground surface. The corresponding lithostatic stress is in a range of 12 MPa to 18 MPa. The maximum thermal load from HLW is designed for 90 °C in the host rocks. The repository openings will be backfilled and sealed with suitable materials to stabilize the integrity of the natural and engineered barrier system and to prevent release of radionuclides into the biosphere. When the formation water migrates in the EDZ, possible chemical reactions may result between porewater, solutes, and fracture surfaces. In consideration of the relevant repository conditions, various kinds of experiments were designed and performed on fractured samples to characterize the self-sealing behaviour of damaged clay rocks under combined mechanical compression, water flow, and thermal loading. The most important results obtained previously by GRS /ZHA 08a/, /ZHA 08b/, /ZHA 09b/, /ZHA 10c/ have contributed to the synthesis report of the NEA Clay Club /BOC 10/: *Self-sealing of fractures in the argillaceous formations in the context of geological disposal of radioactive waste – review and synthesis*. All the data provided experimental evidence for the significant sealing potential of the studied clay rocks. However, they are not sufficiently enough for formulation of constitutive models and quantification of the parameters. The new tests aimed at providing a systematic database for developing advanced constitutive models for sealing of clay rocks.

2.6.1 Sealing of fractures under compression

During the post-closure phase of a repository in clay rock, the EDZ will be gradually compressed by the progressive rock deformation and the increasing support by the backfill/seal. The resulting increase in mean stress or normal stress leads to a gradual closure of fractures in the EDZ and a decrease in permeability. The sealing behaviour of fractures by mechanical compression was investigated on pre-fractured samples of the COX and OPA clay rocks under various load conditions.

2.6.1.1 Testing samples and methods

Testing samples were prepared to cylinders of different sizes in diameter/length D/L = 50/100, 70/140, and 100/200 mm/mm. Due to the coring and preparation, microcracks were generated along the bedding planes and even grew into few macrocracks through some samples, which were used in the sealing test. A large COX sample (D/L = 100/200 mm) was artificially cracked along the length nearly parallel to the bedding by Brazilian tensile test loading. Fig. 2.80 shows the pictures of an artifi-

cially-fractured COX and a naturally-cracked OPA sample, while the other four COX samples (EST34713A, EST34717A-B, EST34721A) are shown in Fig. B.10.

(a) COX sample (D/L = 100/200 mm)
    artificially-fractured

(b) OPA sample (D/L = 100/200 mm)
    naturally-fractured

Fig. 2.80   Pictures of fractured COX and OPA samples for sealing tests

The sealing tests were performed by compressing the fractured samples in a triaxial cell. Fig. 2.80 illustrates the test principle. Two different loading paths were applied: a) isotropic loading by simultaneously increasing axial and radial stress $\sigma_1 = \sigma_2 = \sigma_3$; and b) multi-step deviatoric loading by increasing axial stress σ_1 at stepwise increased radial stress $\sigma_{2-i} = \sigma_{3-i}$ = constant (i-step). The samples were isolated in jackets and then loaded. Radial strain or closure of fractures parallel to the sample axis was measured by a circumferential extensometer chain mounted at the sample mid-height, while axial strain was recorded by a LVDT deformation transducer installed inside the cell between the top and bottom. Additionally, fracture closure was also detected by monitoring changes in wave velocity using an ultrasonic device with piezo-electric P and S wave transducers installed in the upper and lower pistons. Changes in permeability to gas along the fractures were measured by injecting nitrogen gas to the sample bottom at a constant pressure and by recording the outflow at the opposite side using a burette at atmospheric pressure. The permeability is calculated according to Darcy's law for gas (equation (2.19)).
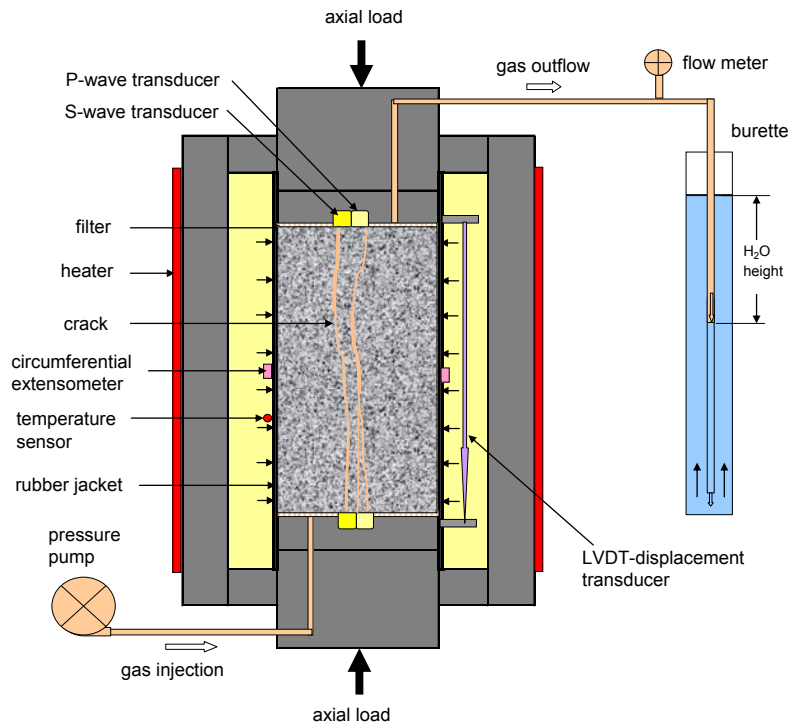
Fig. 2.81 Principle of triaxial sealing tests on fractured samples with measurements of axial/radial deformation, gas permeability and wave velocity

2.6.1.2 Fracture closure and permeability change under isostatic loads

Results obtained during dry gas flowing

Fig. 2.82 shows two examples of the tests on the COX and OPA samples with measurements of axial/radial strain (ε_1 /ϵ_3), gas permeability (K_g), and P wave velocity (v_p) during isotropic loading. The fracture pattern of both samples is shown in Fig. 2.81.

The fractures in the COX sample were artificially made nearly parallel to its axis, whereas the cracks in the OPA sample occurring along the bedding planes are only the result of coring, unconfined storage, and preparation. Both samples were hydrostatically loaded step by step from 1 to 15 MPa. After that, the isostatic stress on the COX sample was lowered down to the initial level of 1 MPa, while only the radial stress normal to the fracture planes in the OPA sample was unloaded to 1 MPa by keeping the axial stress constant. It can be recognized from Fig. 2.82 that

a) the damaged claystone samples under isotropic stress were more largely compressed in the radial direction normal to the fracture planes;
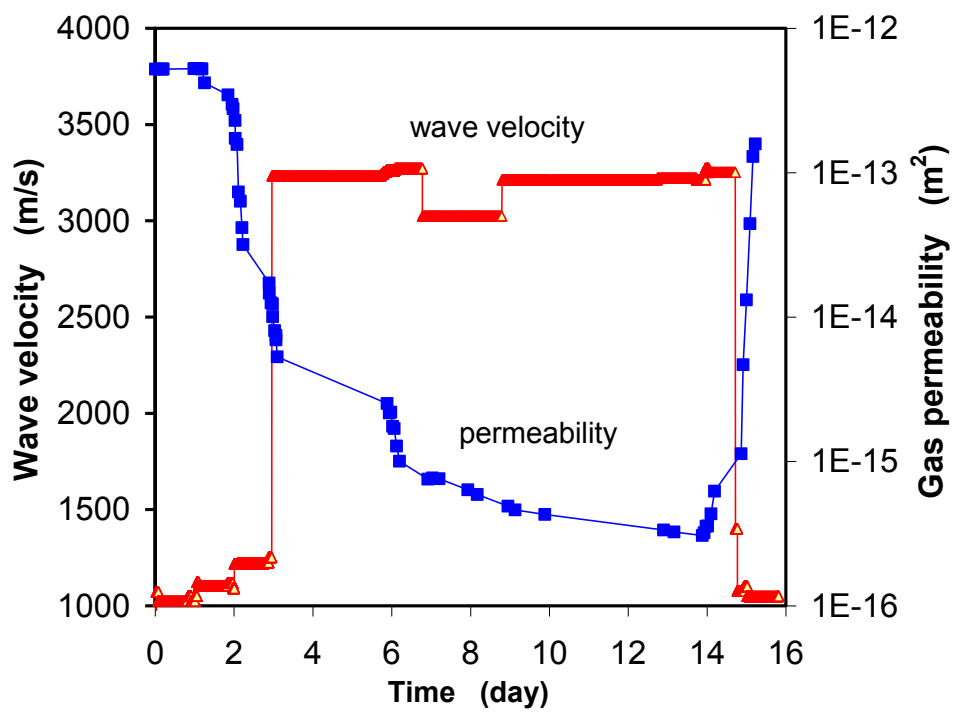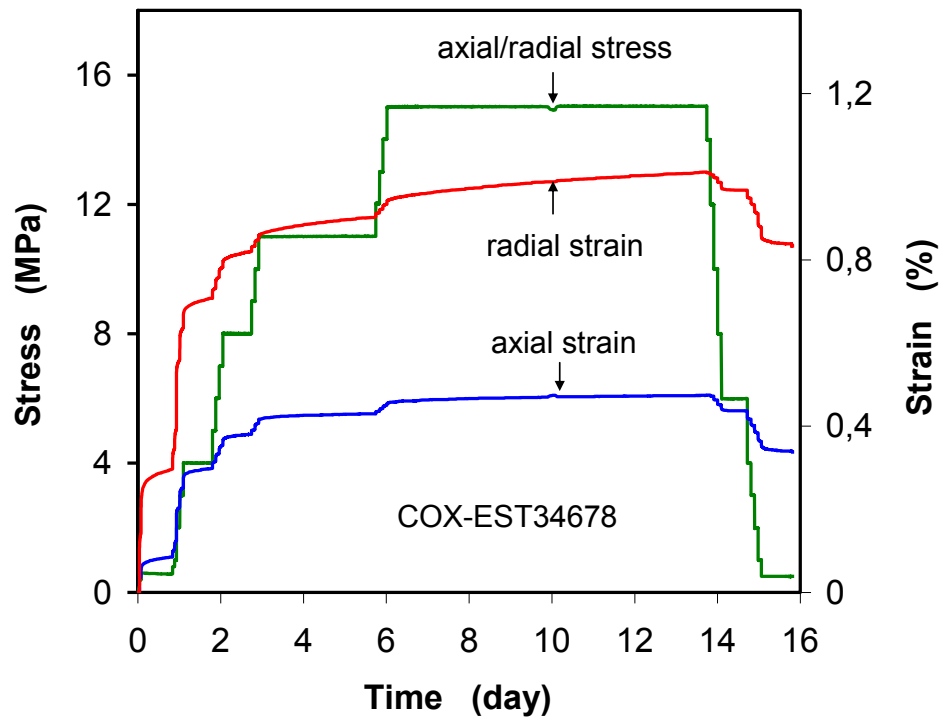
(a) COX sample
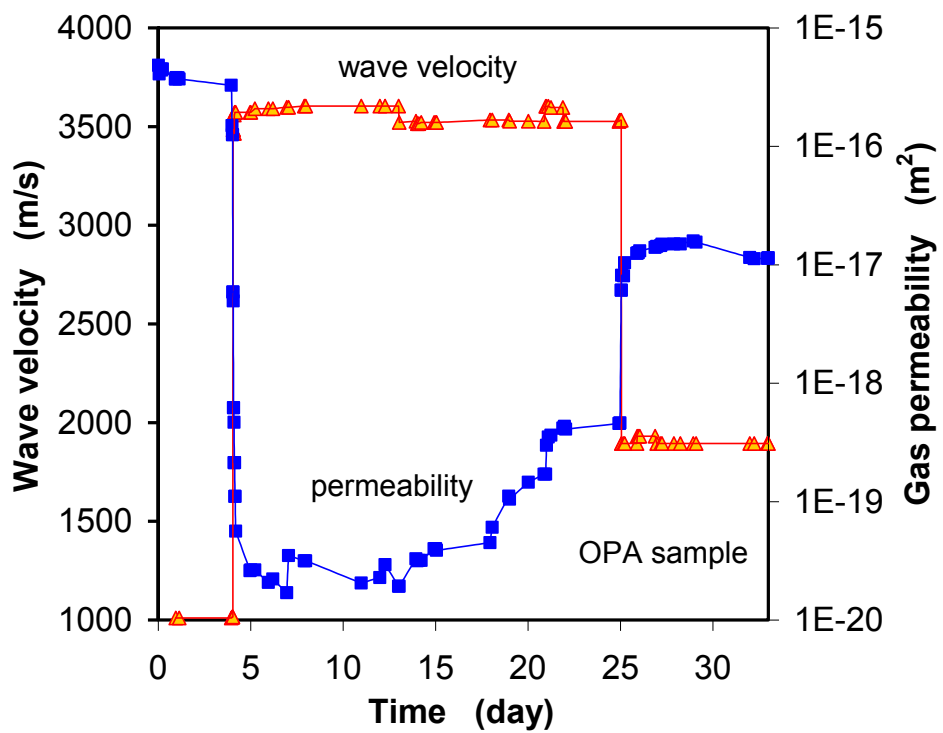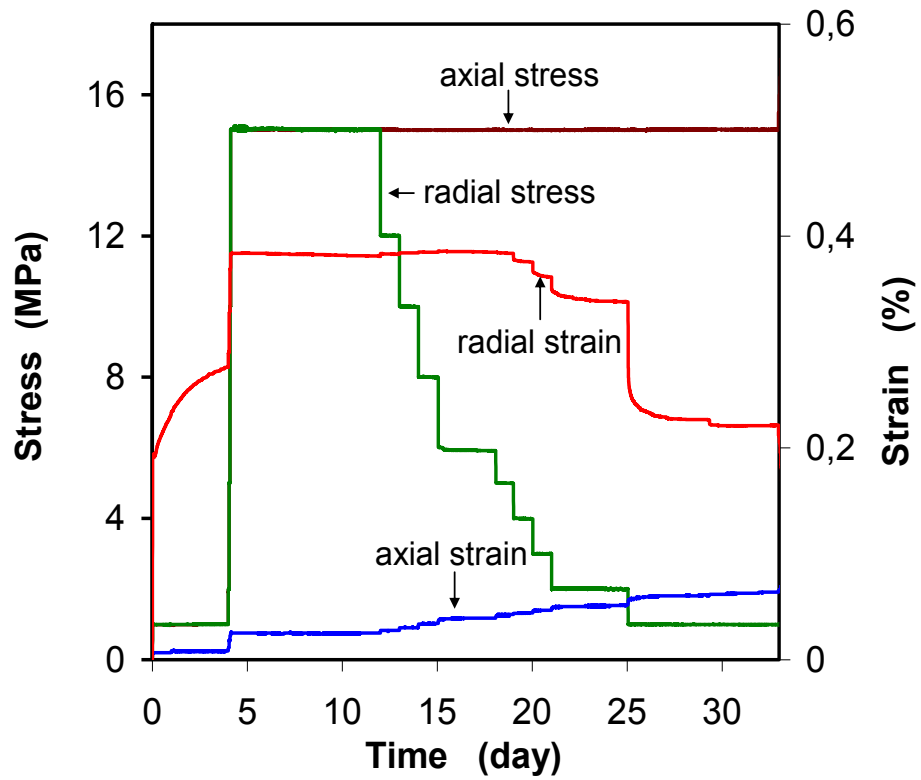
(b) OPA sample

Fig. 2.82 Responses of deformation, gas permeability, and wave velocity of fractured samples to loading and unloading

b) the closure of the fractures was accompanied both by a decrease in permeability parallel to the fracture planes by three to four orders of magnitude (from $10^{-13}\,m^2$ to $10^{-16}\,m^2$ at the heavily fractured COX and from $10^{-16}\,m^2$ to $10^{-20}\,m^2$ at the less damaged OPA sample) and by an increase in wave velocity (from 1000 to 3200 m/s at COX and to 3600 m/s at OPA);

c) the sealing of the fractures at a given load continued progressively with time at lower closure and permeability rates; and

d) unloading either by reducing hydrostatic stress down to 1 MPa at the COX sample or normal stress down to 1 MPa at the fractures in the OPA sample reopened the previously compressed fractures only to small extent ($\Delta\varepsilon_3$ < 0.2 %) but largely increased the permeability by several orders of magnitude, however, still lower than the initial values.

Similar results were obtained on the other four COX samples with single or few cracks. The pictures of the samples are shown in Fig. B.10 and the measured data are presented in Fig. 2.20.

Results obtained during wetted gas flowing

Fig. 2.83 shows results of another test example emphasising upon effects of gas humidity on the sealing of fractures in clay rock. An artificially fractured COX sample EST34692 (D/L = 50/100 mm) was first hydrostatically compacted stepwise from 1 MPa to 20 MPa and then unloaded back to 1 MPa again, whereby dry nitrogen gas was injected into it for permeability measurement. The increase of the confining stress resulted in a large closure of the fractures indicated by the radial strain of ε_3 = 3.5 %, and correspondingly, the permeability along the fractures decreased from $3 \cdot 10^{-13}$ to $1 \cdot 10^{-15}\,m^2$. After that, the unloading reopened the fracture slightly by $\Delta\varepsilon_3 \approx 0.4$ %, leading to a part recovery of the permeability to $2 \cdot 10^{-14}\,m^2$.

Maintaining the lowered confining stress at 1 MPa, the inflowing gas was wetted by adjusting the humidity of RH = 75 %, 85 % and 100 %. Because the sample was previously more or less dried by flowing dry nitrogen, some amount of the moisture in the wetted gas was taken up by the claystone, so that low RH-values of 65 % to 75 % were recorded at the outlet. It can be seen that a swelling process in radial direction normal to the fracture plane developed up to $\Delta\varepsilon_3 \approx 2.0$ % and the permeability decreased gradually from $2 \cdot 10^{-14}$ to $5 \cdot 10^{-16}\,m^2$ over the wetting phase of three months. The exter-

nally observed expansion and permeability reduction implies that the local swelling pressures acting in contact areas between fracture walls are higher than the external confining stress on the one hand, and the fracture voids between the contact areas tend to be filled due to the expansion of the surrounding clay matrix on the other hand.
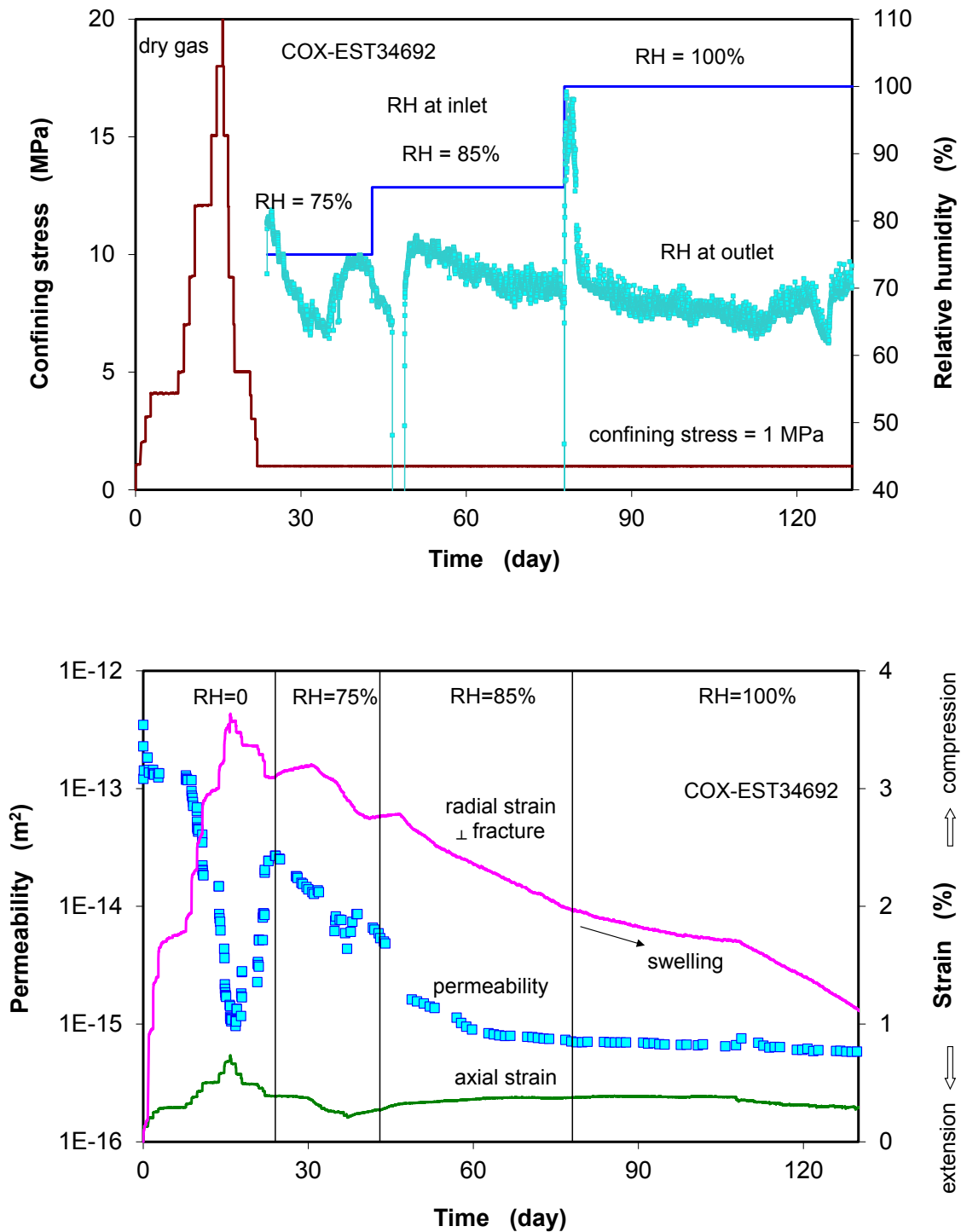
Fig. 2.83   Effects of gas humidity on sealing of fractures in COX claystone

130

Normal stress – fracture closure relationship

The fracture closure is defined here as $\Delta b = \varepsilon_3 D$ by neglecting the deformation of the compact matrix compared with fractures, where D is the diameter of the sample. The measured data of fracture closure at the COX samples are presented in Fig. 2.84a as a function of the applied normal stress (σ_n) for all the samples, whereas some data obtained on other COX samples by Davy et al. /DAV 07/ are represented in Fig. 2.84b together with the data from the tested OPA and COX samples shown in Fig. 2.82. All the $\sigma_n - \Delta b$ curves express the non-linear behaviour, involving the hysteresis cycle by loading/unloading and the permanent plastic deformation. Fracture closure evolves faster at large apertures in the initial loading stage and then closure rates decrease with increasing fracture stiffness at reduced apertures.

The fracture closure can be approached by hyperbolic functions such as those proposed by Goodman /GOO 76/ and Bandis et al. /BAN 83/ or by exponential equations adequately applied for the compaction of porous soils or backfill materials /BOC 10/. Among others, Zhang et al. /ZHA 93/ proposed an exponential model for the compaction of backfill materials which can be analogously applied for the description of the normal stress – fracture closure relation:

$$\Delta b = b_m \left[1 - \exp\left(-\alpha \sigma_n^\beta \right) \right] \tag{2.33}$$

where Δb is the aperture closure, b_m is the possible maximum aperture closure (equal to the initial aperture), σ_n is the normal stress, α and β are constants. If the stress tends to infinity, $\sigma_n \to \infty$, the fractures will be fully closed, $\Delta b \to b_m$.

This model is compared in Fig. 2.84 with the data of fracture closure along the loading path without considering the creep and unloading path. Fitting the data presented in Fig. 2.84a leads to a unique set of the parameters α = 0.3 and β = 0.5 for the COX samples with different initial apertures of b_m = 0.32 – 1.70 mm. A reasonable agreement between the model and the data is achieved. The α and β values also fit the data obtained on other COX samples with small initial apertures of b_m = 0.10 – 0.36 mm /DAV 07/ and the OPA sample with b_m = 0.60 mm, as shown in Fig. 2.64b. The unique parameter set suggests an insignificant influence of the fracture features (amplitude and distribution of the aperture, surface roughness, contact area, etc.) on the fracture compaction behaviour.
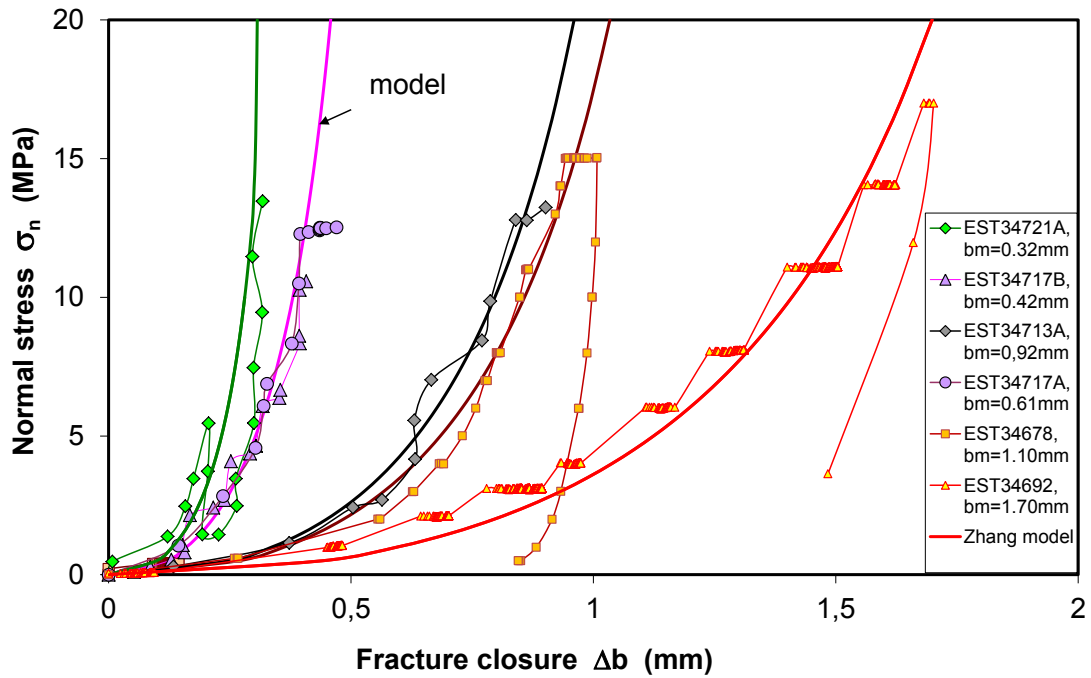
(a) Results from cracked COX samples
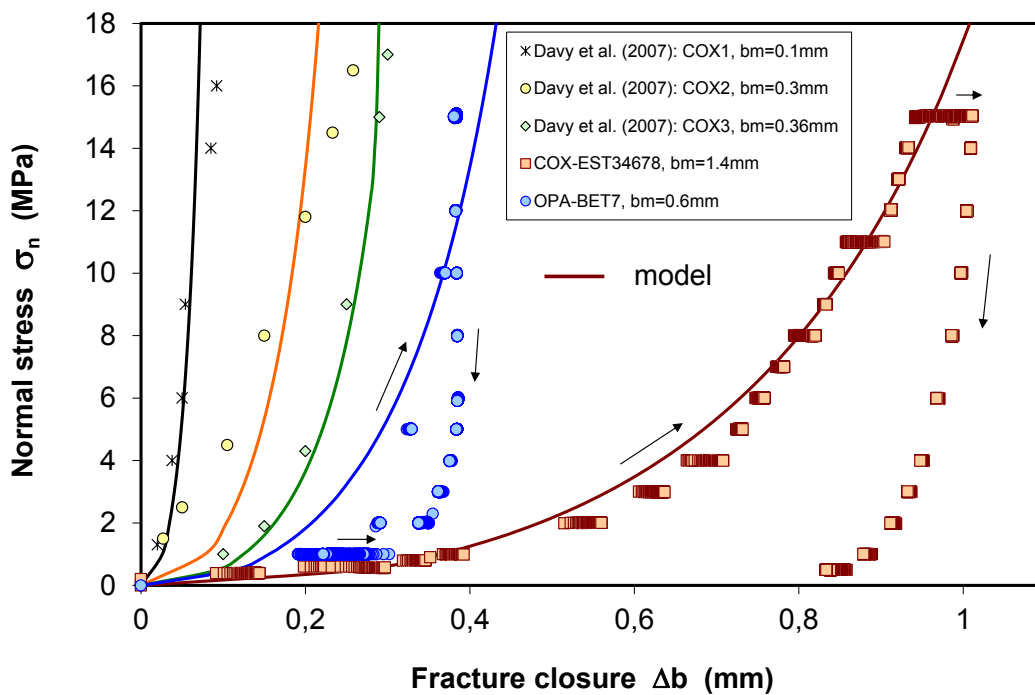
(b) Comparison of the results between COX and OPA samples

Fig. 2.84 Fracture closure – normal stress behaviour of COX and OPA clay rocks

Introducing the fracture normal strain $\varepsilon_n = \Delta b/D$ and the maximum strain $\varepsilon_m = b_m/D$, equation (2.34) can also be straightforward expressed as

$$\varepsilon_n = \varepsilon_m \left[1 - \exp \left(-\alpha \sigma_n^\beta \right) \right] \tag{2.34}$$

This expression may be conveniently implemented in computer codes for calculation of the closure behaviour of the EDZ with multi-fractures. It is also to be noted that this model shall be extended to predict the time dependence of the fracture closure.

Fracture closure – permeability relationship

The closure of fractures is related to the intrinsic permeability in fractured clay rock. The permeability variation with fracture aperture may be approached by the "cubic law" for a set of parallel fractures of equal aperture which are oriented parallel to flow direction /LEE 93/, /OLI 08/, /LEV 10/, /RUT 03/, /RUT 13/. Fig. 2.85 illustrates the schematic model of a fractured rock element with a set of cracks.
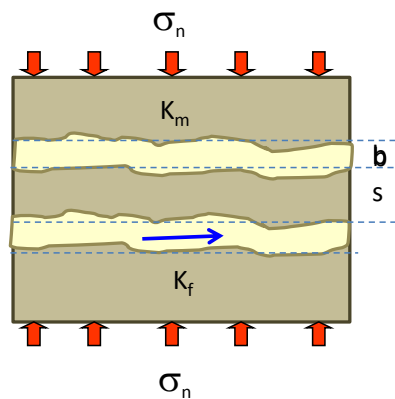
Fig. 2.85   Sketch of a fractured rock element

The permeability of a fractured rock is contributed by the fracture conductivity (K_f) and also increasingly with compaction by that of the porous matrix (K_m) /ZHA 10c/

$$K_g = K_m + K_f = K_m + \frac{Rb^3}{12s} = K_m + \frac{Fb^3}{12} \tag{2.35}$$

with K_m =   matrix permeability of the porous medium (m^2)

$\quad\quad K_f$ =   fracture permeability along the fracture direction (m^2)

$\quad\quad b$ =   average fracture aperture (m), $b = b_m - \Delta b$,

$\quad\quad R$ =   roughness factor (-) of the fracture surfaces,

$\quad\quad s$ =   mean fracture spacing (m),

$\quad\quad F$ = R/s, integrated parameter characterizing the fracture features (m^{-1})

The undisturbed claystones in natural confined conditions are practically impermeable to gas under normally-encountered pressure gradients, i.e. $K_m = 0$ in equation (2.35). Only as a pressure threshold named gas entry/breakthrough pressure is excessed, advective gas transport can occur through generated microfissures. The breakthrough pressure of the intact claystone is quite high up to 10 MPa under confining stresses of 12 – 15 MPa /FOR 13/. Usually, it is difficult and even impossible to precisely identify the fracture parameters R and s or F for a cracked rock element. The parameter F can be determined by fitting the test data. Fitting the data yields different F – values of $1 \cdot 10^{-5}$ to $2 \cdot 10^{-2}$ m^{-1} due to the different fracture features (amplitude and distribution of apertures, surface roughness, contact area, interconnectivity, deformability of asperities, etc.) between samples.

Fig. 2.86 compares the cubic model by application of the F-values with the measured permeability data as function of the fracture aperture decreased by loading. The fracture closure results in a decrease in gas permeability from the initial values of 10^{-16} – 10^{-12} m^2 down to 10^{-20} – 10^{-21} m^2. As the fracture aperture b decreases to null, K_f tends to zero. Actually, the network of fractures may be disconnected and becomes ineffective for gas flow before b reaches zero ($b \geq 0$). The reasonable agreement between the model and the data confirms the validity of the cubic law for the gas flow in fractured claystone.

The relationship of permeability with the fracture aperture can also be illustrated as a function of the normal compressive strain on the fracture surfaces in the rock element (see Fig. 2.87). The cubic law (equation (2.35) can be transformed as

$$K_g = K_m + K_o(\varepsilon_m - \varepsilon_n)^3 \tag{2.36}$$

with $K_o = F \cdot D^3/12$ in m^2, referred as the initial permeability of the fractures before compression at $\varepsilon_n = \varepsilon_m$. A reasonable agreement between the model and the data can be found from the comparison in Fig. 2.87.
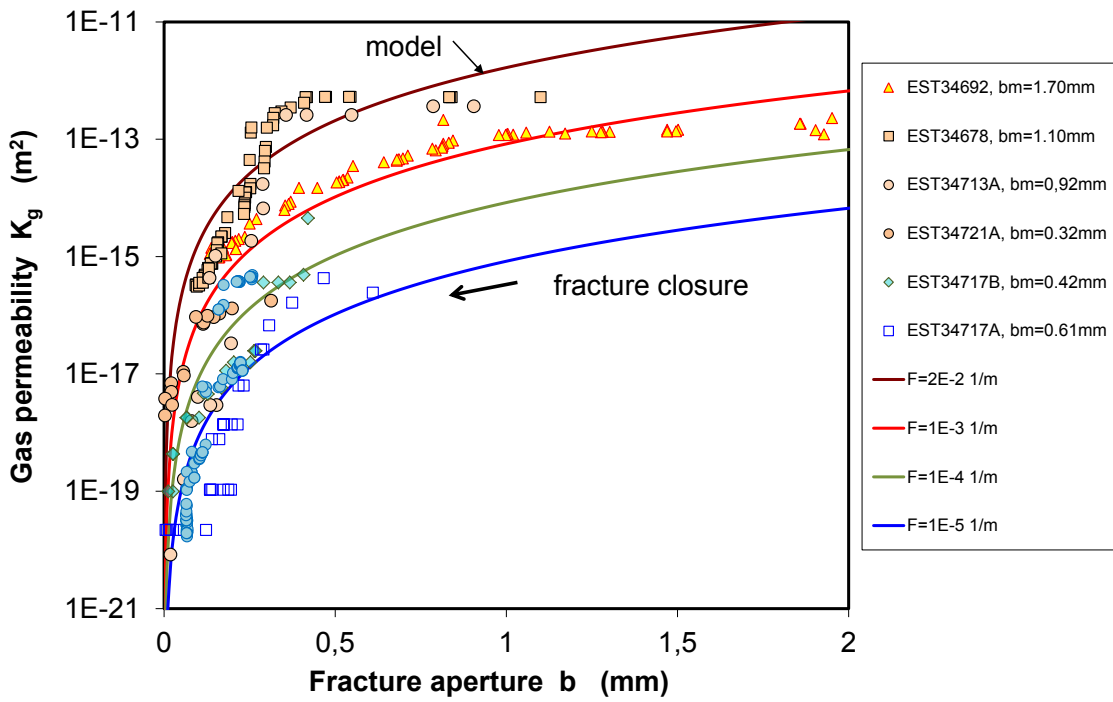
Fig. 2.86   Fracture permeability – aperture relationship of cracked claystone
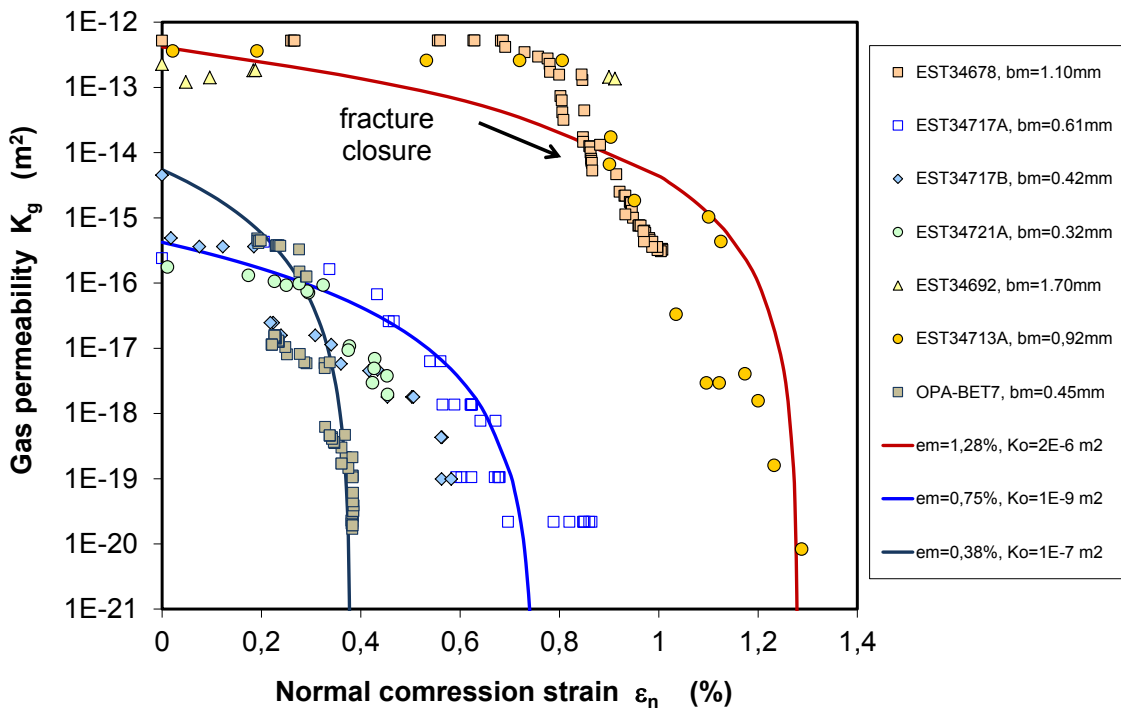
Fig. 2.87   Permeability – normal strain relationship of cracked claystone

2.6.2 Water-enhanced sealing of fractures

During the post-closure phase of a repository, formation water will migrate from the saturated far-field towards the EDZ. As well known, the studied clay rocks have high water adsorption potentials and swelling capabilities (Sections 2.1 and 2.4). The swelling experiments showed that both COX and OPA claystones can take up great amounts of water. These quantities are much higher than the water content in the naturally saturated and loaded state. The increase in water content results in a large volume expansion of up to 10 % in unconstrained conditions and/or high swelling pressures of 5 MPa to 12 MPa at fixed deformation. Moreover, the specific properties of claystones such as wetting-induced plasticity and slaking are additionally contributing to the sealing of fractures.

2.6.2.1 Water permeability of intact clay rock

The water permeability of the intact COX clastone was measured on two cylindrical discs in oedometer cells. They had a diameter of 50 mm and a thickness of 10 mm. The water content was about 5 % and the porosity was measured to ϕ = 15.5 % at sample EST27335a and ϕ = 16.4 % at EST27335b. Fig. 2.88 shows their pictures before testing.

(a) COX-EST27335a (d/l = 50/10 mm)   (b) COX-EST27335b (d/l = 50/10 mm)
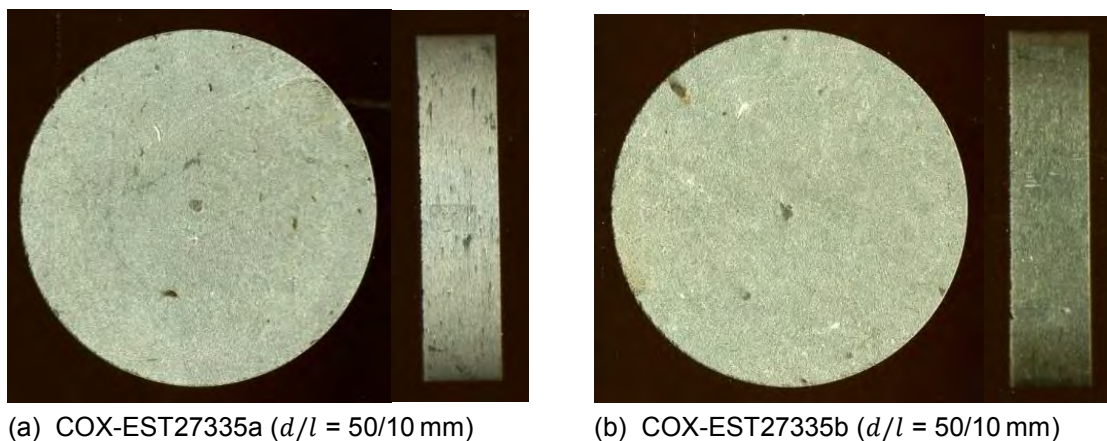
Fig. 2.88 Pictures of intact COX samples for measurement of water permeability

First, the samples were used to examine the swelling capability of the clay rock by measuring free swelling expansion in axial direction on EST27335a and swelling pressure on the volume-constrained sample EST27335b. The results have already been presented in Fig. 2.14 in terms of evolution of free swelling strain and swelling pressure

over a year and discussed in Section 2.1.3.2. The free expanded sample EST27335a was then re-compacted step by step up to 15 MPa over a month. The measured data have been illustrated in Fig. 2.14 and discussed there. A final porosity of ~16.5 % was achieved. Fig. 2.89 shows that the load compressed the clay matrix into the pores of the porous discs at the sample top and bottom.

| (a) top | (b) bottom |
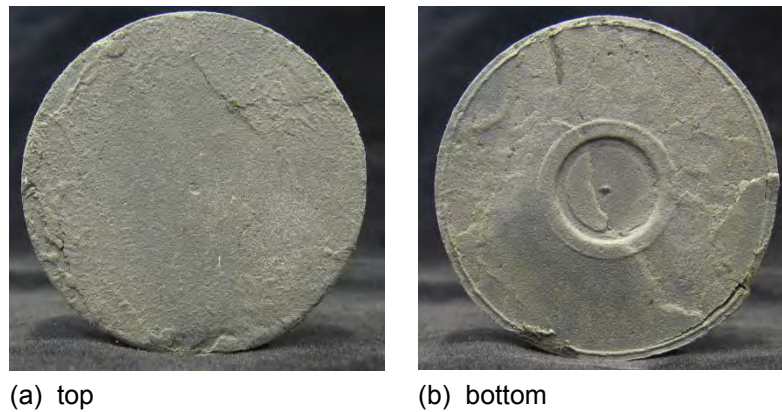
Fig. 2.89   Impression of sintered porous discs on the end faces of an expanded COX sample under load

After consolidation, the volume of sample EST27335a was constrained, while the constraint condition at another sample continued. Water permeability measurement followed at different injection pressures between 0.1 and 2.0 MPa over a total duration of 1.5 years. During steady state water flow at each step over months, the permeability is determined according to Darcy's law for liquid:

$$K_w = \frac{Q_w \cdot \mu_w \cdot L}{A \cdot \Delta p} \tag{2.37}$$

where K_w = water permeability (m^2), Q_w = flow rate of the water (m^3/s), μ_w = dynamic viscosity of the water (Pa·s), and Δp = pressure difference (Pa). The viscosities of the COX and OPA synthetic porewater were determined at different temperatures between 25 °C and 80 °C, as shown in Fig. 2.90.

Fig. 2.91 presents the measured data of water permeability and the response of axial stress during the long-term period of water injection. Very low water permeabilities were determined in a range of $1 \cdot 10^{-20}$ to $6 \cdot 10^{-21}$ m^2 at EST27335a and $5 \cdot 10^{-21}$ to $1 \cdot 10^{-21}$ m^2 at EST27335b under the lowered injection pressure from 2.0 to 1.0, 0.5, 0.25 and 0.1 MPa over 10 months. The minimum permeability of each sample was recorded in the beginning at the lowest injection pressure of 0.1 MPa. However, within the follow-

ing 7 months, no outflow could be detected. A calculation suggests a minimum amount of water outflow of $0.4\,cm^3$ over $1-8$ months for the permeabilities of $1\cdot10^{-20}$ to $1\cdot10^{-21}\,m^2$ as shown in Fig. 2.92. This examination implies that the Darcy's law seems to be not applicable for the intact clay rock under the hydraulic gradients below 1000 m/m. This important conclusion has to be validated with more experiments.
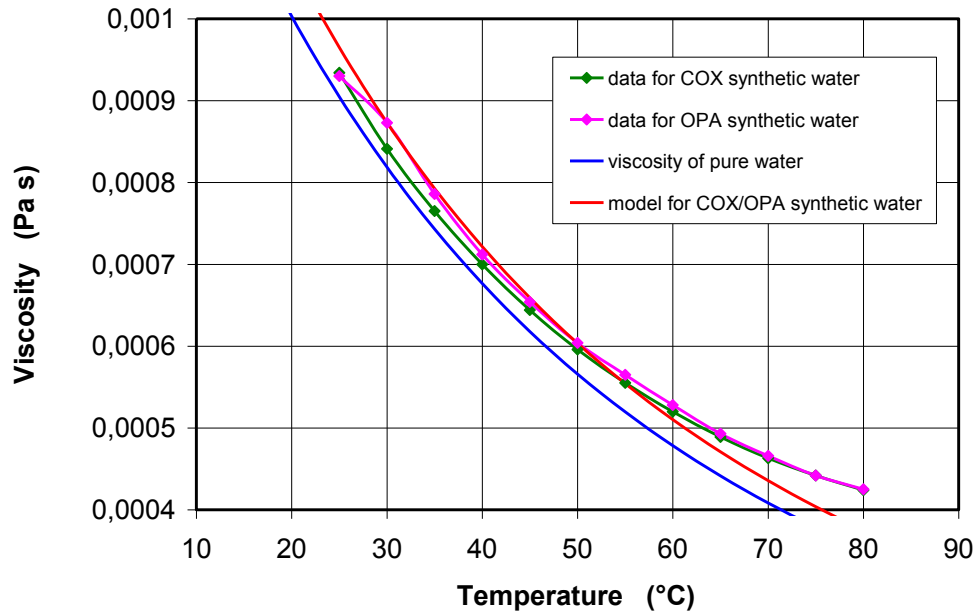
Fig. 2.90   Viscosities of the COX and OPA synthetic water measured at different temperatures
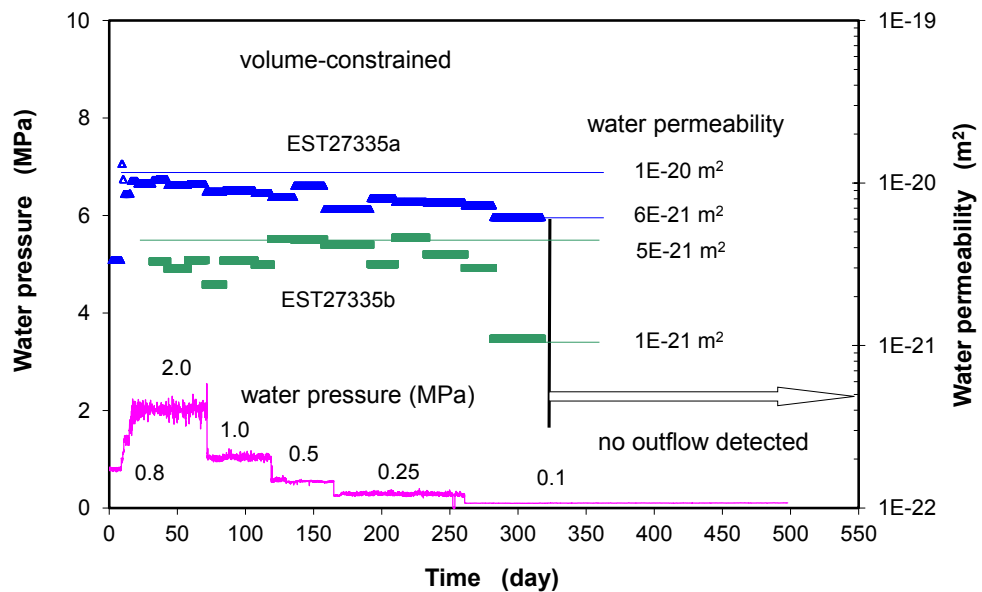
Fig. 2.91   Long-term water permeability of intact COX claystone

138
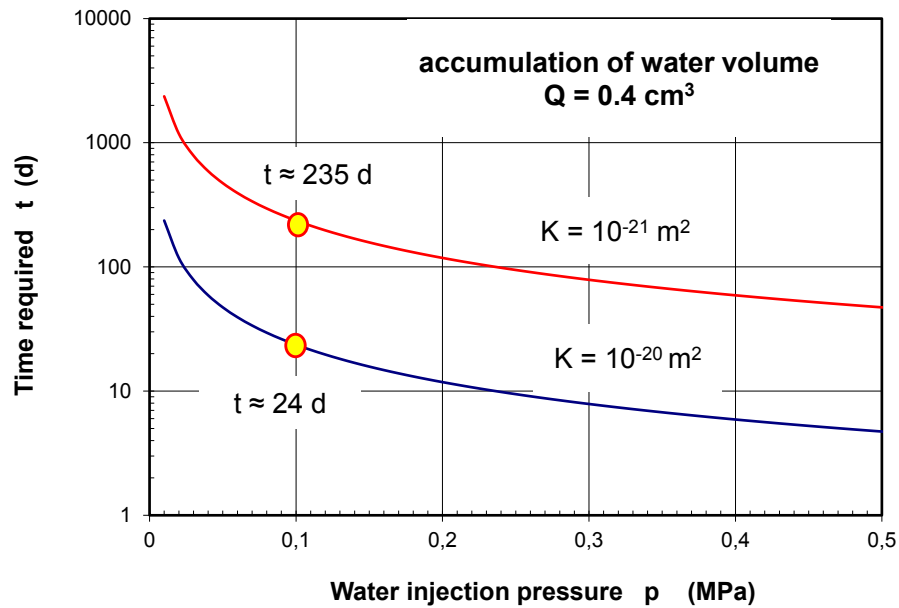
Fig. 2.92 Time required for a water outflow of 0.4 cm^3 through the intact samples

2.6.2.2 Fracture closure and water permeability

The sealing behaviour of fractures in clay rock under mechanical load and water flow conditions was investigated on artificially-cracked COX samples in a triaxial cell. A sample EST21158 (D/L = 50/74 mm) was cracked parallel to the axis. It was hydrostatically loaded stepwise from 1 MPa to 13 MPa and then unloaded to 1 MPa. Before water flowing, the intrinsic permeability of K_g = 1·10^{-13} m^2 was determined by gas flowing at the first load step of 1 MPa. Following that, the synthetic porewater was injected to the fractured sample at a pressure of 0.5 MPa and the water permeability was measured under elevated load levels.

Fig. 2.93 illustrates the combined impact of compression and water flow on the sealing of fractures in the sample. The recorded radial strain normal to the fracture planes shows that each load increase led to an immediate closure of the fractures. Because of the high swelling capability of the clay rock, a gradual expansion of the fractured sample followed at each constant load below 10 MPa rather than a gradual closure. The externally observed expansion indicates high local swelling pressures acting in contacting areas between fracture walls, where the material must expand more into the fracture voids than elsewhere. Additionally, the clay particles in the fracture walls contacting with water become weakening, slaking and filling the voids.

139
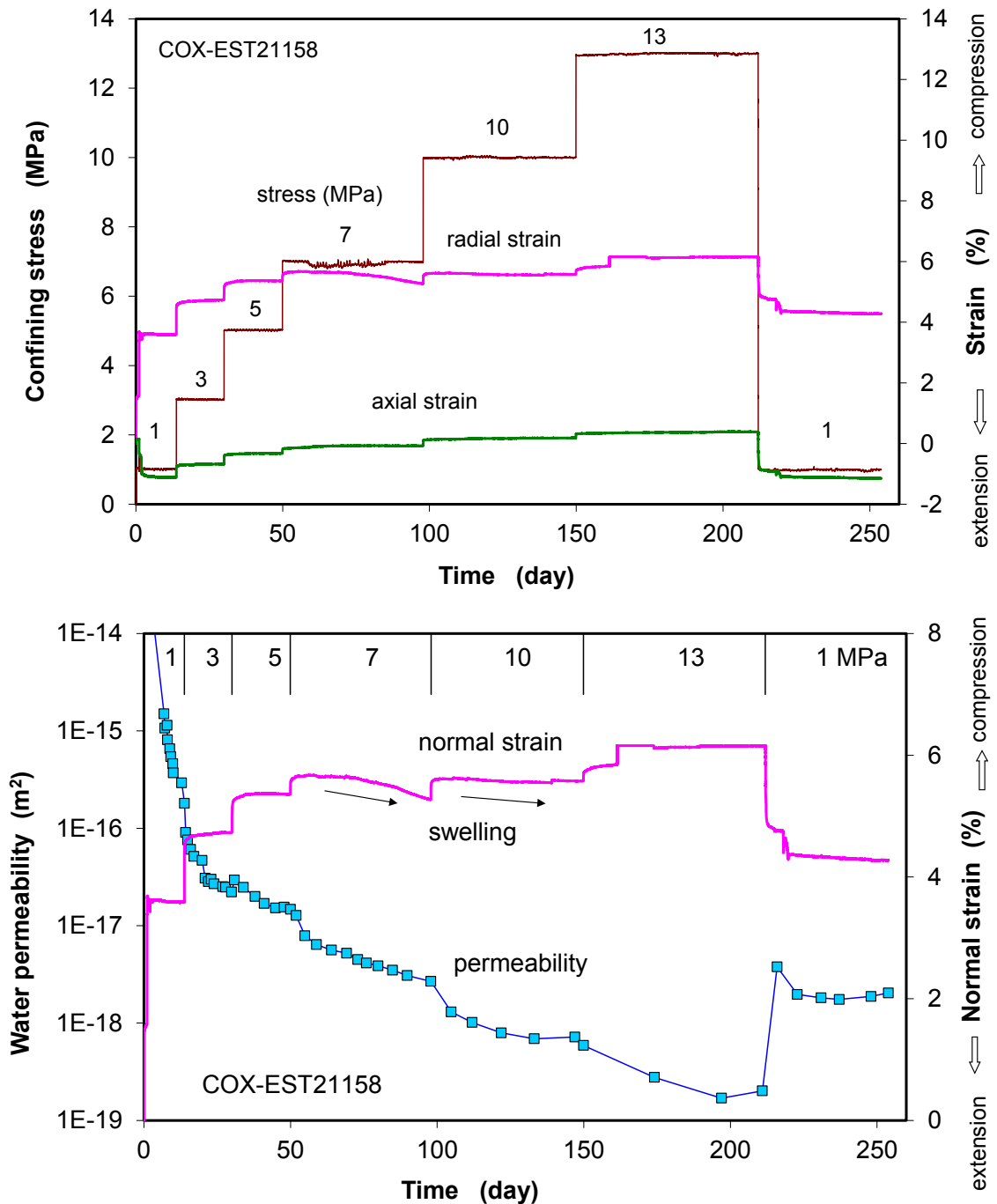
Fig. 2.93 Evolution of normal strain and permeability parallel to fractures in a COX sample during water flowing under different confining stresses

The significance of the water-induced sealing of fractures in the clay rock can also be identified by the evolution of water permeability along the fractures. At the first load step of 1 MPa, the determined water permeability of $K_w = 2 \cdot 10^{-15}\,m^2$ is nearly two orders of magnitude lower than that of $K_g = 1 \cdot 10^{-13}\,m^2$ obtained before with gas. Secondly, the water permeability decreased steadily with time at each elevated confining stress. After stepwise increasing the load to 13 MPa over seven months, a very low

permeability of K_w = $2 \cdot 10^{-19}\,m^2$ was reached, which is close to that of the intact clay rock. Moreover, the reversibility of the fracture sealing was examined in the last phase by unloading the sample to the initial stress of 1 MPa. Even though the sample expanded nearly to the initial level of $\Delta \varepsilon_3 \approx 4\,\%$, the increased permeability of $2 \cdot 10^{-18}\,m^2$ is still three orders of magnitude lower than that initial value of $2 \cdot 10^{-15}\,m^2$ before sealing.

The permanent sealing of fractures by swelling and slaking of clay matrix is clearly visible on the pictures in Fig. 2.94 showing the fractures on the COX sample surface before and after loading and water flowing. Before testing, sharp wall edges of the fractures were observed. After loading and water flowing, the fractures were compacted, the fracture walls became weaker, the sharp edges disappeared, and the interstices were filled with slaked and fine-grained particles. The disappearance of the fractures is a clear evidence of the self-healing, which is defined as "sealing with loss of memory of the pre-healing state" /TSA 05/. The grade of healing depends on the initial intensity of fractures, the content of clay minerals, the confining stress, the duration of consolidation, etc.

(a) before water flowing

(b) after water flowing
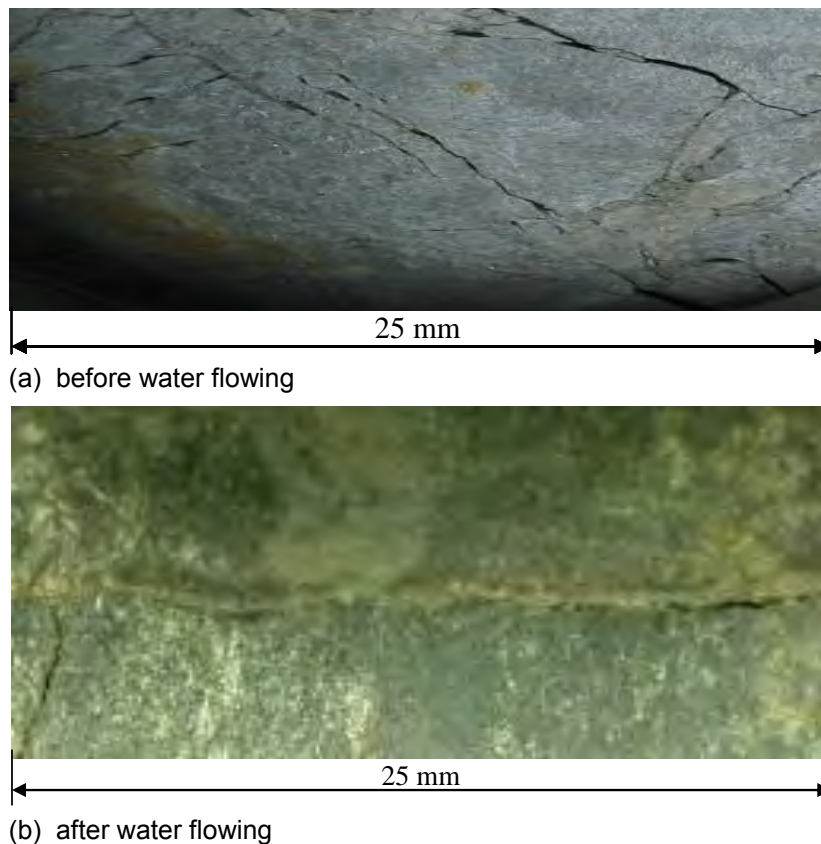
Fig. 2.94 Comparison of fracture patterns on COX sample surface before and after water flowing under varied confining stresses

Fig. 2.95 illustrates results of another sealing test on axially-cracked COX sample EST34692 (D/L = 50/100 mm). In the first phase, the gas permeability along the fractures was measured by flowing of wetted gas as function of confining stress. The results have been presented in Section 2.6.1.2 (Fig. 2.83). In the second phase, the synthetic porewater was injected into the fractures at pressure of 0.5 MPa under the lowered confining stress of 1 MPa. Consequently, the clay matrix at the fracture walls took up water and expanded largely in normal direction up to $\Delta\varepsilon_3$ = 3.7 % on the one hand. And on the other hand, the fracture walls actually expanded more into the fracture voids, so that the intrinsic permeability of the fractures decreased by 1.5 orders of magnitude from K_g = $5 \cdot 10^{-16}$ m² down to K_w = $1 \cdot 10^{-18}$ m². The subsequent increase of the confining stress compressed the fractures leading to a decrease of the permeability down to $2 \cdot 10^{-19}$ m² at 3 MPa and $7 \cdot 10^{-20}$ m² at 6 MPa, very close to that of the intact clay rock.

2.6.2.3   Long-term water permeability of fractures in pre-heated claystone

After the disposal of HLW, the damaged host rock will be heated up and dried. Thus, the clay minerals may change, affecting their swelling capacity and correspondingly the reversibility of the heated EDZ. This issue has been investigated by measurements of water permeability on three cracked COX samples in a set of permeameters. Fig. 2.96 shows pictures of the testing apparatus and the samples (COX 2/3/4, D/L = 50/50 mm). The samples were artificially cracked along the length and then pre-heated up to temperatures of 50 °C, 100 °C and 150 °C, respectively. The intensity of the fractures was different from one sample to another. The samples were hydrostatically compressed at relatively low stresses of 2 to 3.5 MPa and at ambient temperature of 20 °C. Synthetic porewater was flowed through the fractured samples. The water injection pressure was kept at 1 MPa over the first 2 years and then adjusted between 0.1 and 1 MPa in another 1.2 years. From the measurement of the water outflow, the water permeability can be determined according to equation (2.37).
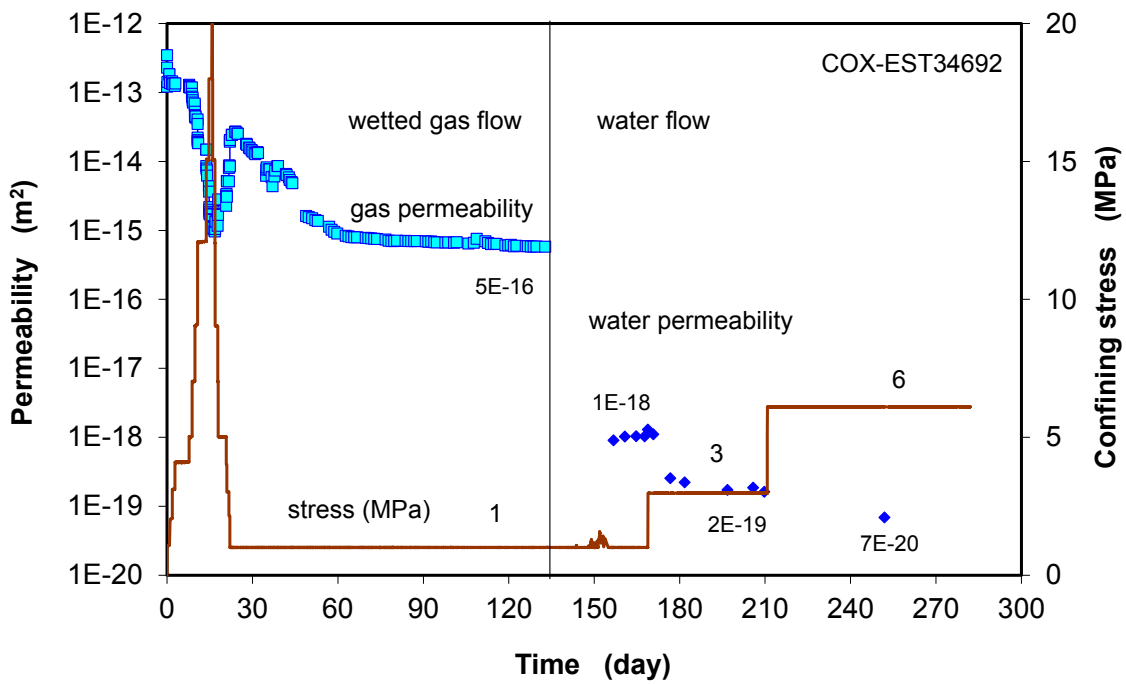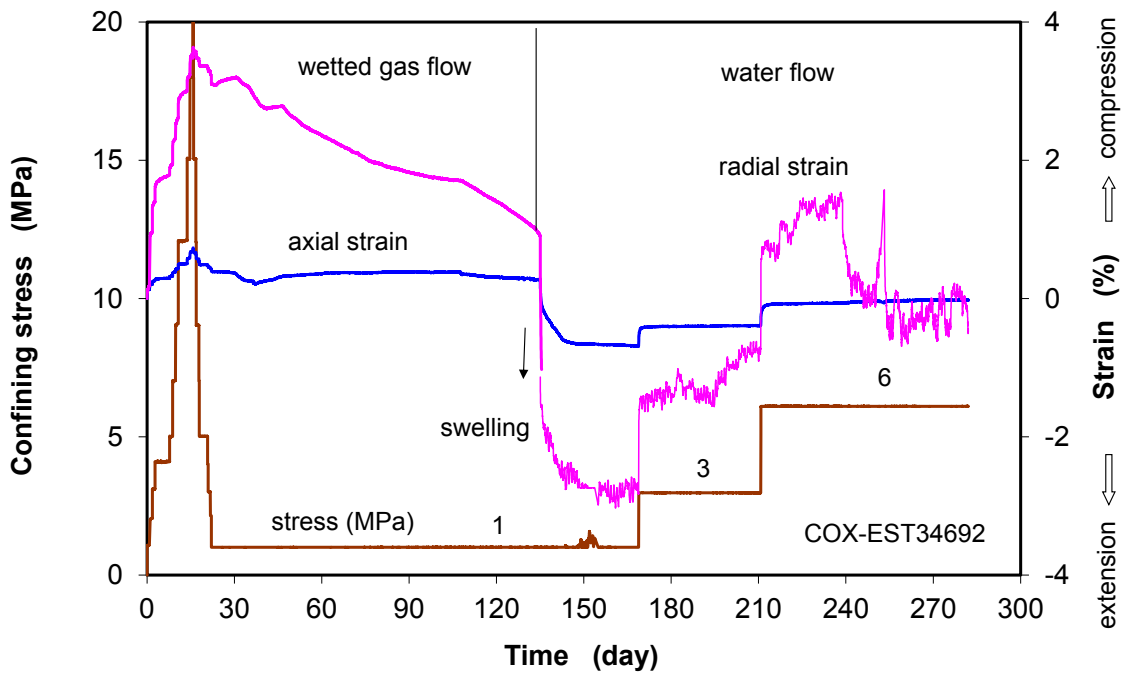
Fig. 2.95 Effects of wetted gas and liquid water on sealing of fractures in claystone

(a) A set of permeameters	(b) Principle

(c) COX 2 heated at 50 °C   (d) COX 3 heated at 100 °C   (e) COX 4 heated at 150 °C
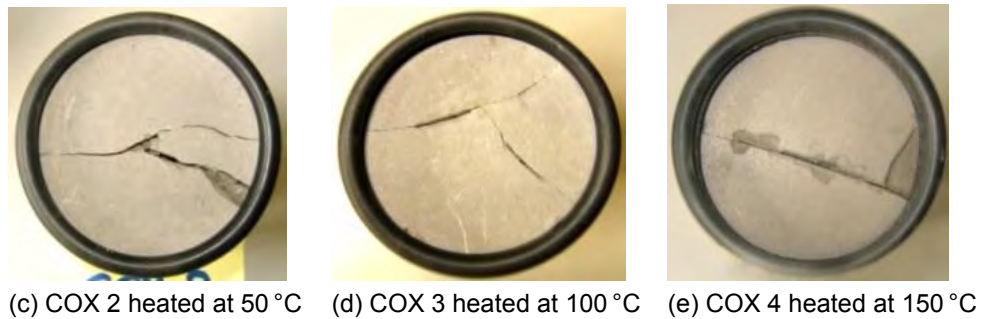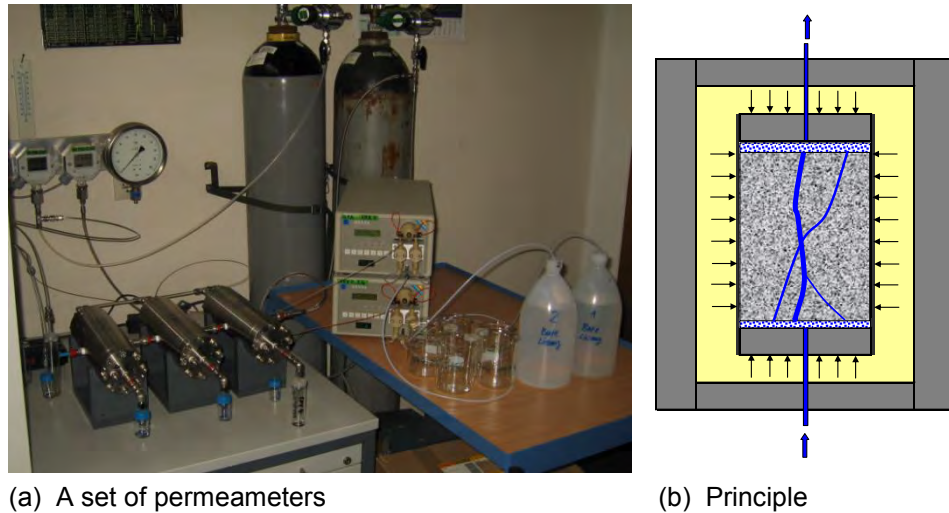
Fig. 2.96   Permeameters for measurements of water permeability of fractured COX samples under different confining stresses

Fig. 2.97 summarizes the permeability data recorded during the test. Before injecting the synthetic porewater, an intrinsic permeability of $K_g = 3 \cdot 10^{-12}\,m^2$ was determined on all samples by gas flowing. The following measurements were performed by injecting the synthetic porewater into the fractured samples at a pressure of 1 MPa and by increasing the confining stress from 2 MPa to 2.5, 3 and 3.5 MPa over a total duration of 2 years. As soon as the water was supplied, the intrinsic permeability dropped immediately by five to seven orders of magnitude from $K_g = 3 \cdot 10^{-12}\,m^2$ down to $K_w = 10^{-17} - 10^{-19}\,m^2$, depending on the fracture intensity of each sample. As discussed above, this drastic drop in permeability is mainly attributed to the water-induced swelling, slaking, and clogging of the fractures. At each load level, the permeability decreased gradually with time. The influence of the confining stress on the permeability variation was not very significant in the testing range. Because of the large differences in fracture intensity from a sample to another, a remarkable effect of the pre-heating treatment could not be identified. But it is clear that the pre-heating up to 150 °C did not hinder the sealing process of the fractures in the claystone. Another important observation is that within

144

2 years, the permeability of the fractured samples decreased to the very low level of $3 \cdot 10^{-20}$ – $7 \cdot 10^{-21}$ m^2 as the same as that of the intact clay rock (cf. Fig. 2.91). The strong sealing of the fractured claystone is completed within a very short time compared with the long repository post-closure phase of tens of thousands of years.
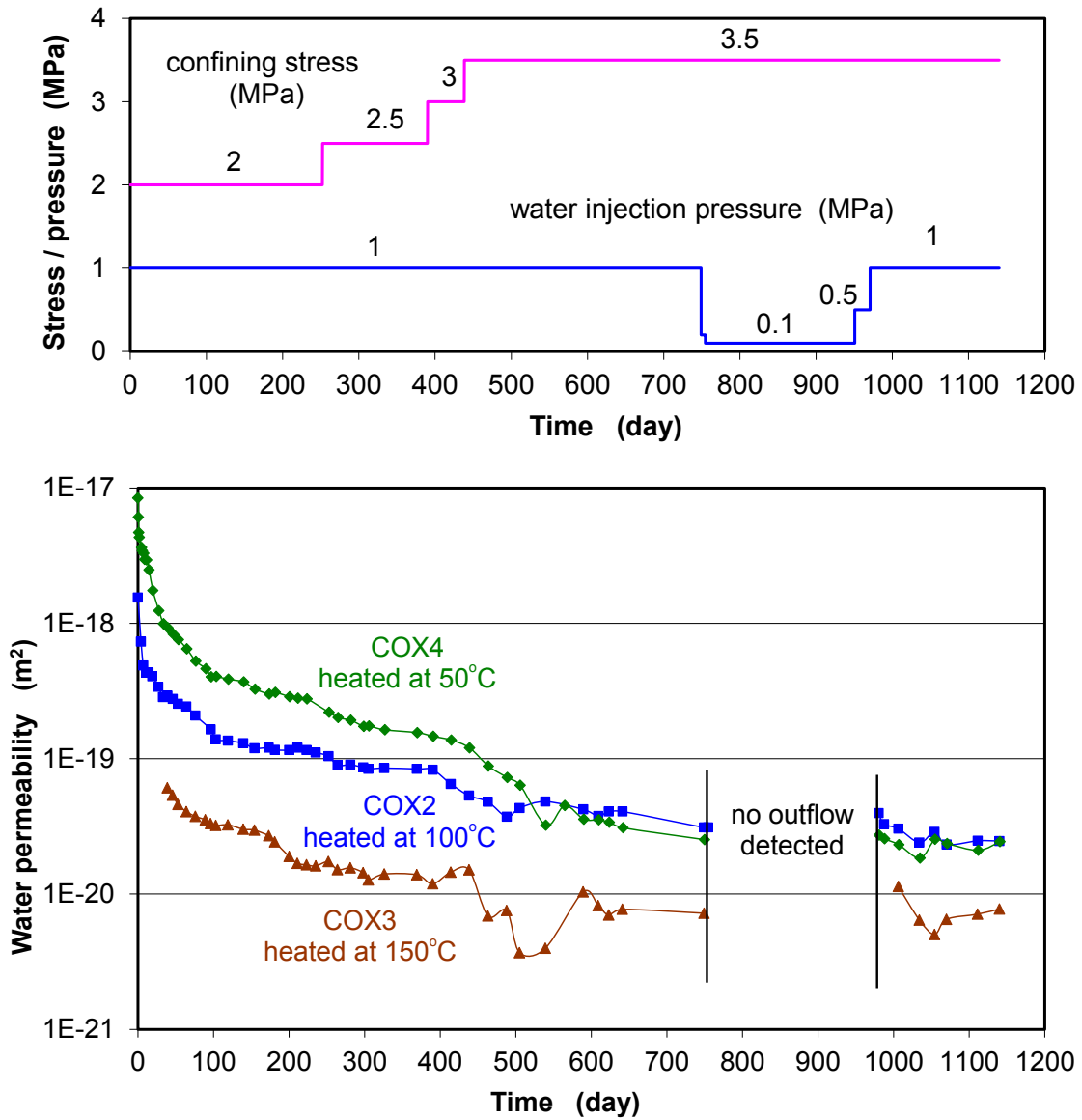
Fig. 2.97 Long-term evolution of the water permeability of fractured and pre-heated COX samples under different confining stresses

In order to examine possible hydraulic threshold for Darcy's flow in the resealed clay rock, the water injection pressure was reduced down to p_w = 0.1 MPa over 8 months. The corresponding pressure gradient across the sample length of 50 mm is 200 m/m. If Darcy flow took place in the resealed samples of low permeabilities of $3 \cdot 10^{-20}$ to

$7 \cdot 10^{-21}$ m², a detectable water outflow of 0.5 cm³, should be accumulated at the end of the measuring duration of 8 months, as calculated in Fig. 2.98. This examination suggests that the Darcy's law might be not applicable for the highly resealed claystone under the hydraulic gradients below 200 m/m. This important issue has to be validated with more experiments.

Subsequently, the water injection pressure was increased to the same high level of 1 MPa as before, at which the water outflow became measurable. The water permeability values determined again are the same as those before and represent the stabilisation of the sealing process at the confining stress of 3.5 MPa.
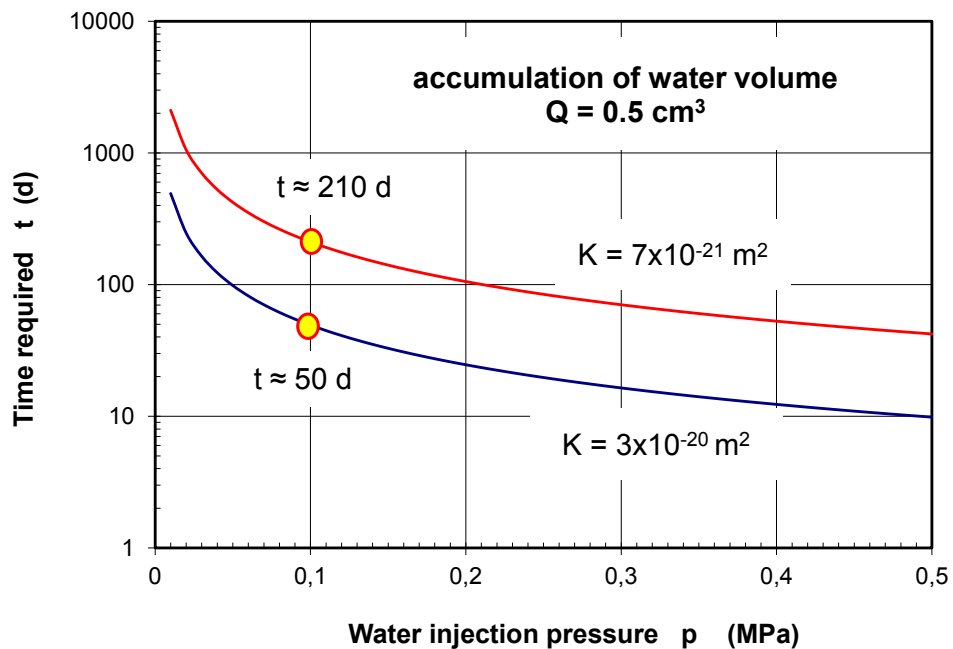
Fig. 2.98   Time required for a water outflow of 0.5 cm³ through the resealed samples

2.6.3   Thermal impact on the sealing of fractures

Heat released from HLW is dissipated through the buffer and the surrounding rock. The resulting temperature change may affect the development of the EDZ. The thermal impact on the sealing of fractures was investigated by heating cracked COX and OPA samples under constant confining stress and water injection pressure.

2.6.3.1 Fracture closure and water permeability during thermal loading

A triaxial sealing test was performed on an axially-cracked COX sample (D/L = 50 /100 mm) under an axial stress of 2.5 MPa and a radial stress of 2.0 MPa. The synthetic porewater was introduced into the fractured sample at inlet pressure of 0.5 MPa while the outlet was kept atmospheric. The sample was heated stepwise from 27 °C to 40 °C, 60 °C, 75 °C, 90 °C and then cooled down to 60 °C and 30 °C, whereby radial strain normal and axial strain parallel to the fracture planes and water permeability in axial direction parallel to the fractures were measured. In the calculation of water permeability according to Equation (2.37), the viscosities of the synthetic porewater at different temperatures were taken into account (see Fig. 2.90).

Fig. 2.99 shows the evolution of measured radial/axial strains and water permeability in correspondence with the applied temperatures. Within the first 6 days before water injection at 27 °C, the damaged sample was only slightly compacted even in the radial direction normal to the fractures planes. As the synthetic porewater was introduced to the bottom at stepwise elevated pressures up to 0.5 MPa, the wetted area at the bottom expanded quickly causing a large swelling in axial direction firstly and then followed by radial swelling too. The fracture walls expanded into the fracture apertures and decreased the permeability. The tendency of the permeability reduction was not significantly affected by elevating temperature up to 40 °C. Over 60 °C, the swelling effect disappeared and the fractures became more closure at elevated temperatures. But the permeability increased slightly from $5 \cdot 10^{-19}$ at 40 °C to $7 \cdot 10^{-19}$ m^2 at 60 °C – 75 °C, and $1 \cdot 10^{-18}$ m^2 at 90 °C. In contrast, cooling down caused fracture compaction and permeability reduction down to $3 \cdot 10^{-19}$ m^2 at 30 °C.
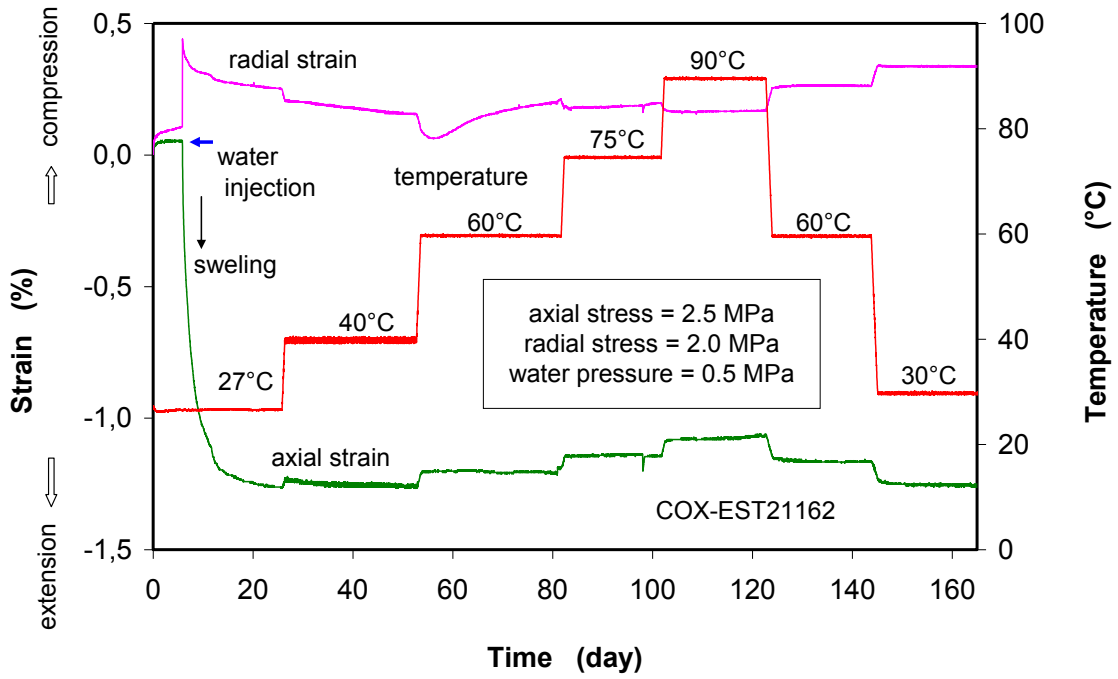
(a) radial strain normal and axial strain parallel to fracture planes
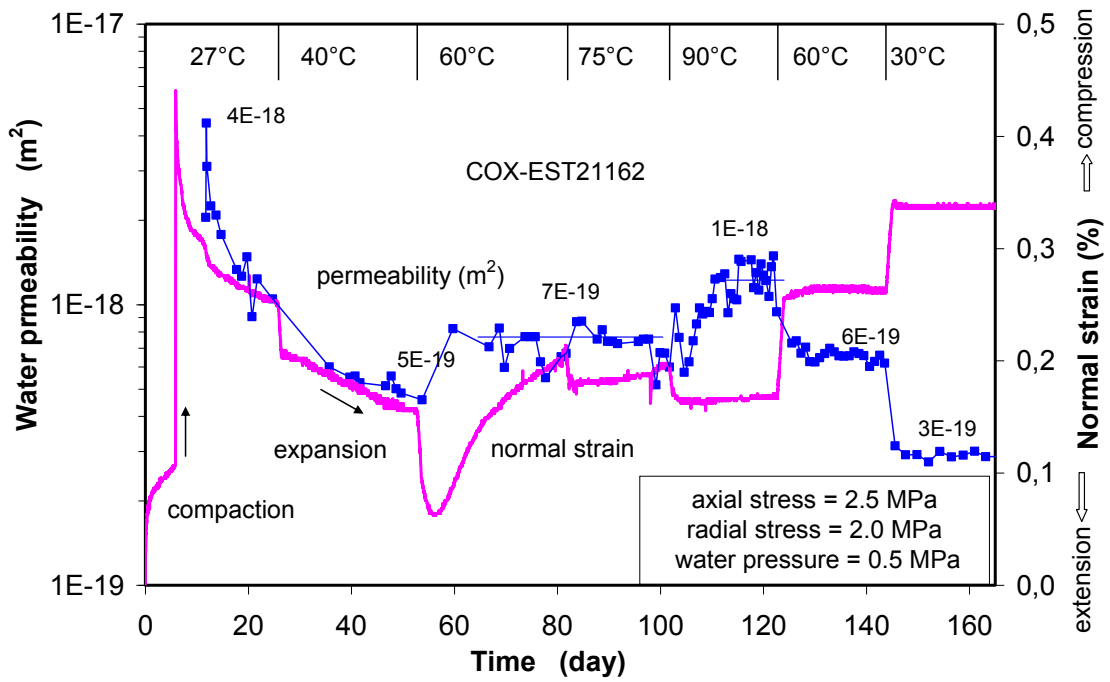
(b) water permeability of fractures in correspondence with normal strain

Fig. 2.99   Thermal effects on closure and water permeability of fractures in claystone

2.6.3.2 Long-term water permeability of fractures during thermal loading

Additional tests to investigate thermal impact on the sealing of fractures in clay rock were performed by long-term measurements of water permeability of axially-cracked COX and OPA samples (D/L = 50/50 mm) at temperatures between 20 °C and 90 °C. Pictures of these samples are shown in Fig. 2.100. They were hydrostatically confined in permeameter cells in an oven under a stress of 2 MPa und flowed with the synthetic porewater through the fractures at inlet pressure of 1 MPa within the first 2 years and then at 0.1 and 1 MPa during the last 1.2 years. The viscosities of the flowing water at the applied temperatures were taken for the calculation of the intrinsic permeabilities according to equation (2.37).

COX 1

OPA   Permeameter cells in oven
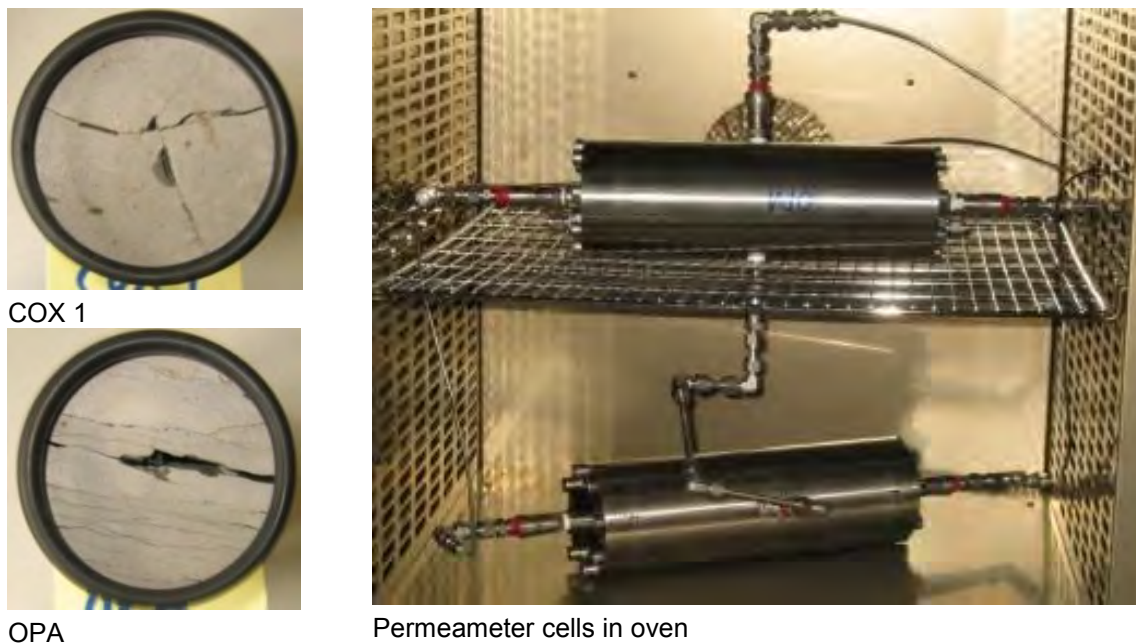
Fig. 2.100 Permeameters for measurements of water permeability of fractured COX and OPA clay samples at elevated temperatures

Fig. 2.101 summarises the measured data. Again, the water-induced swelling effect on the hydraulic sealing of fractures is evident during the first stage at 20 °C. The permeability decreased from $1 \cdot 10^{-15}$ to $3 \cdot 10^{-18}$ m^2 at OPA and from $1 \cdot 10^{-17}$ to $5 \cdot 10^{-19}$ m^2 at COX sample. Subsequently, the rates of permeability reduction, however, are less affected by the temperature increase up to 60 °C. Further heating up to 90 °C and also cooling down to 60 °C had no effect on the permeability reached before. The second cooling-down phase to 20 °C, however, induced a relatively significant decrease in permeability from $6 \cdot 10^{-19}$ to $3 \cdot 10^{-19}$ m^2 and from $4 \cdot 10^{-19}$ to $1 \cdot 10^{-19}$ m^2 for the OPA and COX samples,

respectively. At 20 °C, the water injection pressure was decreased to 0.1 MPa to 8 months, during which no outflow of water could be detected as the same as the observations on the other samples (Fig. 2.97). If the Darcy's flow is true for both the clay samples with permeabilities of $1 \cdot 10^{-19}$ to $3 \cdot 10^{-19}$ m^2, an amount of water volume of 10 cm^3 should be accumulated at the outlet under the hydraulic gradient of 200 m/m over the measuring periods of 8 months. The following increase of the water pressure to 1 MPa again made the permeability measurable. The values determined seem to be slightly higher than that before at the same conditions.
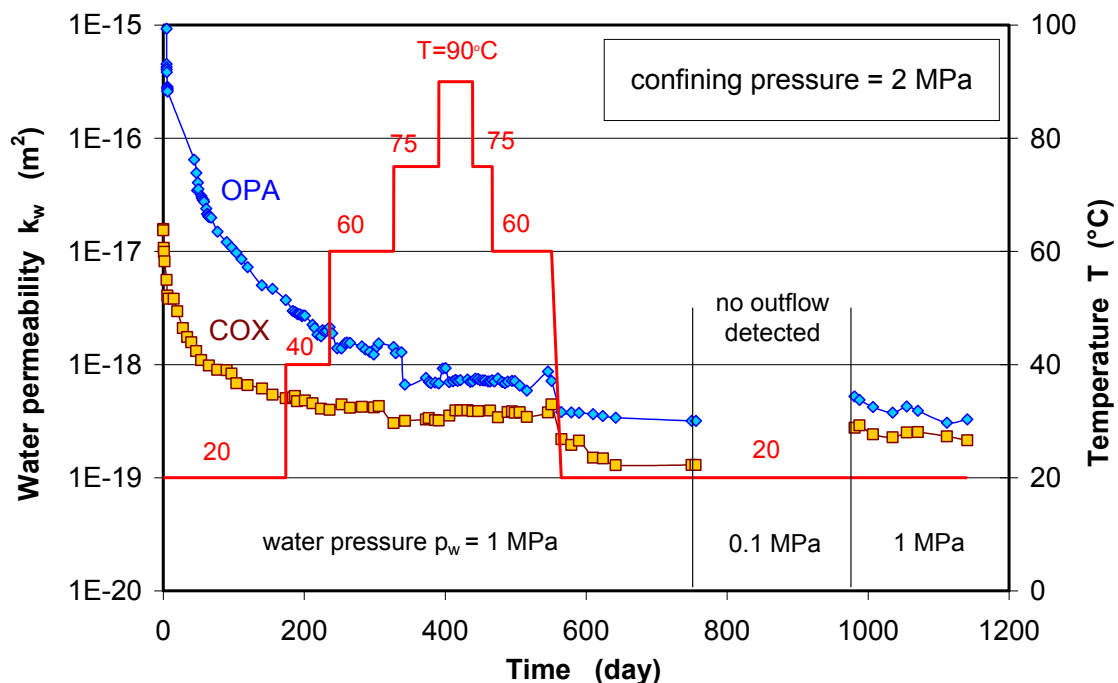
Fig. 2.101 Long-term measurements of water permeability on fractured COX and OPA samples at different temperatures

Fig. 2.102 depicts the last data of water permeability within each phase as function of applied temperature. It is obvious that the water permeability of the fractured claystones decreases more or less with increasing temperature and drops down further after cooling. So an important conclusion can be drawn: thermal loading up to the maximum temperature of 90 °C designed for repositories in clay rocks has no negative effects on the sealing process of fractures in the EDZ. However, because the hydraulic conductivity k depends both on the structure of fractures and pores in the material and the thermally-induced changes in viscosity μ and density ρ of the porewater, the relatively constant intrinsic permeability K suggests an enhanced hydraulic conductivity

during heating due to the decrease of water viscosity, according to the relationship between these parameters $k = K\rho g/\mu$ (g = gravity).
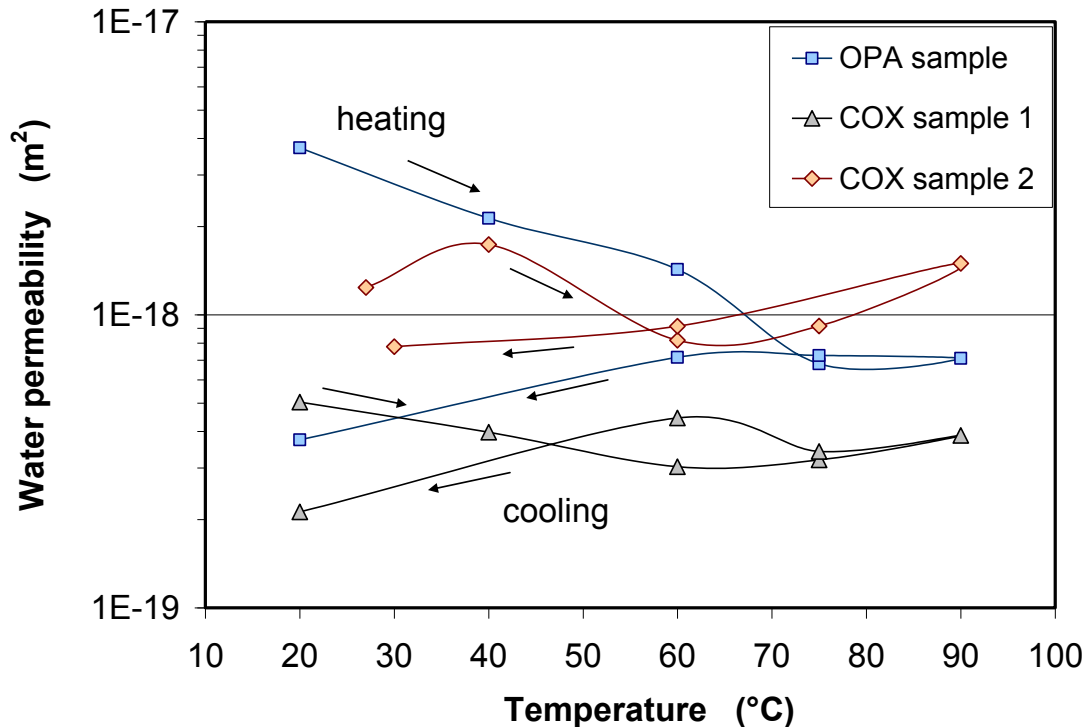
Fig. 2.102 Dependency of water permeability of fractured claystone on temperature

2.6.4 Conclusions on the sealing of fractures

Various laboratory sealing experiments were carried out on strongly cracked samples from the COX and OPA argillaceous formations under relevant repository conditions. The fractured samples were compacted and flowed through with gas or synthetic porewater under triaxial stresses and elevated temperatures. The sealing behaviour of the fractured claystones was detected by deformation, permeability, and wave velocity measurements. From the experiments, the following conclusions can be drawn:

- The fracture aperture decreases non-linearly with increasing normal confining stress. It can be approached by an exponential equation: $\Delta b = b_m \left[1 - \exp\left(-\alpha\sigma_n^\beta\right)\right]$, where σ_n is the normal stress, Δb is the aperture closure, b_m is the initial aperture of individual sample (b_m = 0.1 – 1.7 mm for the tested samples), the parameters α = 0.3 and β = 0.5 are estimated for the damaged claystones. If the stress tends to infinity, $\sigma_n \to \infty$, the fractures will be fully closed, $\Delta b \to b_m$.

- The decrease in fracture permeability is related to the average aperture by a cubic law: $K_f = K_m + Fb^3/12$, where K_m is the gas permeability of the intact claystone ($K_m = 0$), b is the average fracture aperture, and the parameter F characterizes the fracture features and varies in a range of $1 \cdot 10^{-5} - 2 \cdot 10^{-2}$ m^{-1} for the tested samples. As the fracture aperture b decreases to null, K_f tends to zero.

- Wetting by water flow through fractures induces swelling and slaking of the clay matrix, filling and clogging of the interstices, and a drastic decrease in permeability by three to seven orders of magnitude compared with the data obtained by gas flow. At a hydraulic gradient of 200 m/m, no outflow of water could be detected through the resealed samples with very low water permeabilities of 10^{-19} to 10^{-21} m^2 over 8 months. It seemed that the Darcy's flow might not take place in the highly compacted clay rock.

- Heating from 20 °C to 90 °C has no remarkable impact on the water permeability of fractures, while cooling down again decreases the permeability slightly. The thermally-induced changes in hydraulic conductivity are mainly attributed to the variations of water viscosity and density.

- Under the relevant repository conditions (confining stresses of 2 MPa to 13 MPa, temperatures of 20 °C – 90 °C, gas and water flow), the intrinsic permeability of the fractured claystones decreases significantly to very low levels of 10^{-19} to 10^{-21} m^2, which corresponds to intact clay rock, within very short periods of months to years compared with the long repository post-closure phase of tens of thousands of years.

- All the laboratory observations suggest the high sealing potentials of the studied argillaceous rocks. Prediction and assessment of the long-term sealing performance of the damaged zone around the repository openings need adequate constitutive models and computing codes. Respective model development and modelling work will be started in the near future.

3 Claystone-based backfill and sealing materials

3.1 Objectives

The disposal concepts developed by many countries for repositories in clay formations are based on the principle of a multi-barrier system which comprises the natural geological barriers provided by the host rock including its surroundings as well as an engineered barrier system (EBS). After emplacement of the containers for radioactive waste, the disposal boreholes, drifts and shafts must be backfilled and sealed with suitable materials to prevent a release of radionuclides from the repository that can eventually do harm to the biosphere. The geotechnical properties of each EBS component are to be specified with regard to their intended function. As a result of the EC ESDRED project /ESD 04/, these functional requirements are identified with respect to the barrier functions of the buffer around HLW containers in clay formations. In most concepts, bentonite-based materials are chosen for filling the disposal boreholes. For instance, in the Swiss concept /NAG 02/ emplacement of the containers on compacted bentonite blocks that are positioned on the drift floor and subsequent backfilling of the remaining space with granular bentonite (Fig. 3.1) is envisaged. However, according to the French concept /AND 05/, the drifts will be backfilled with excavated claystone and sealed with a swelling clay core confined between concrete plugs (Fig. 3.2).

Crushed claystone produced by excavation of repository openings may be a favourable alternative to bentonite as a backfill and sealing material, because of its many advantages such as chemical-mineralogical compatibility with the host rock, availability in sufficient amounts, low costs of material preparation and transport, and no or at least less occupancy of the ground surface with the excavated tailings. The raw aggregate with coarse grains is considered to be used for backfilling the repository openings and, mixed with bentonite, for sealing boreholes, drifts, and shafts.

An experimental programme has been conducted to characterize the geotechnical properties of the excavated Callovo-Oxfordian claystone (COX) and the compacted claystone-bentonite mixtures under relevant repository conditions with regard to the following properties:

- Compaction behaviour of the backfill material, which controls the mechanical interactions of buffer and backfill with support linings (if existing) and with the surrounding rock and which also governs the evolution of backfill porosity;

153

- Permeability as a function of porosity, which is a key parameter for modelling fluid flow and radionuclide transport in the backfill and sealing;

- Water retention as a function of saturation, which determines the water saturation process as well as storage capacity and which in turn influences the mechanical behaviour and the thermal conductivity of the backfill and sealing;

- Swelling capacity of the sealing material, which is required for closing possibly remaining gaps between the seals and the rock and for supporting the surrounding rock against damage propagation;

- Thermal conductivity of the buffer material around the waste containers, which controls heat transfer and temperature distribution in the multi-barrier system.

Main results of the investigations are presented in this report.
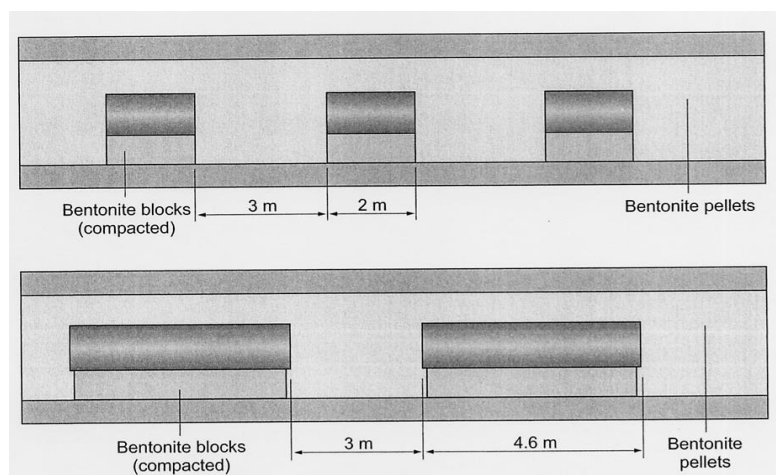
Fig. 3.1   NAGRA concept for backfilling and sealing of disposal drifts /NAG 02/
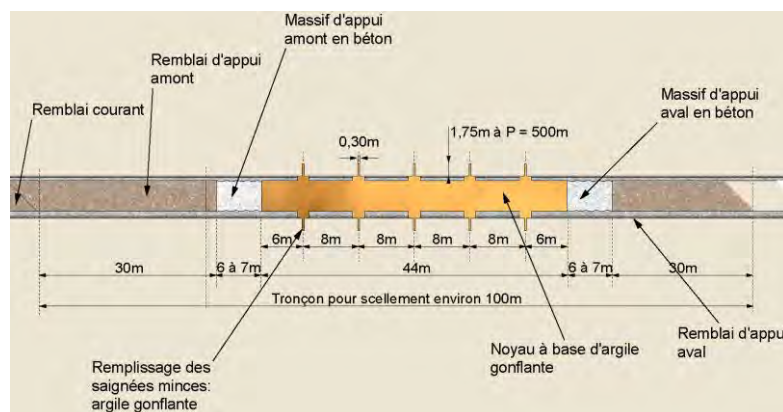
Fig. 3.2   ANDRA concept for backfilling and sealing of access drifts /AND 05/

3.2   Testing materials

The crushed claystone investigated here was produced by drift excavation in the Callovo-Oxfordian argillaceous formation at the main level of 490 m below ground level in the MHM-URL. The initially saturated material with a water content of ~7.4 % was somewhat desaturated to residual values of 4 % to 5 % due to exposure to air after excavation. It would be convenient to use the excavated material immediately for backfilling the repository openings without any further treatment. Therefore, the raw aggregate with grain sizes of less than 32 mm was investigated. Considering that coarse grains may be further crushed and/or segregated during transport and backfilling, smaller grains with diameters of d < 20 mm and d < 10 mm were also prepared for testing by sieving the raw material correspondingly. Fig. 3.3 shows a photo of the material pre-compacted by hand stamping. The grain size distributions of the tested materials are depicted in Fig. 3.4. Additionally, fine-grained claystone powder with grain sizes of d < 0.5 mm was mixed with the expansive MX80 bentonite of the same maximum grain size. The claystone-bentonite ratio was varied to provide different mixtures. The produced mixtures are considered to be typical for the use as buffer, backfill or seals in disposal boreholes, drifts and shafts. The grains of the COX powder have about the same size as in other investigations e. g. /DEN 10/, /TAN 10a/, /TAN 11/. The MX80 bentonite from Wyoming in the USA has been worldwide extensively investigated as a reference buffer material in form of granulated mass and/or compacted blocks, particularly for sealing HLW disposal boreholes in granite. MX80 is a highly expansive Na-bentonite containing 75 % montmorillonite, 15 % quartz and 10 % other minerals /KAR 08/, /LIU 10/. The delivered MX80 bentonite is relatively dry with a water content of w = 9.6 %. The grain density of MX80 bentonite is 2.78 g/m^3.

Fig. 3.3   Photo of the crushed claystone with grains d < 32 mm after hand stamping
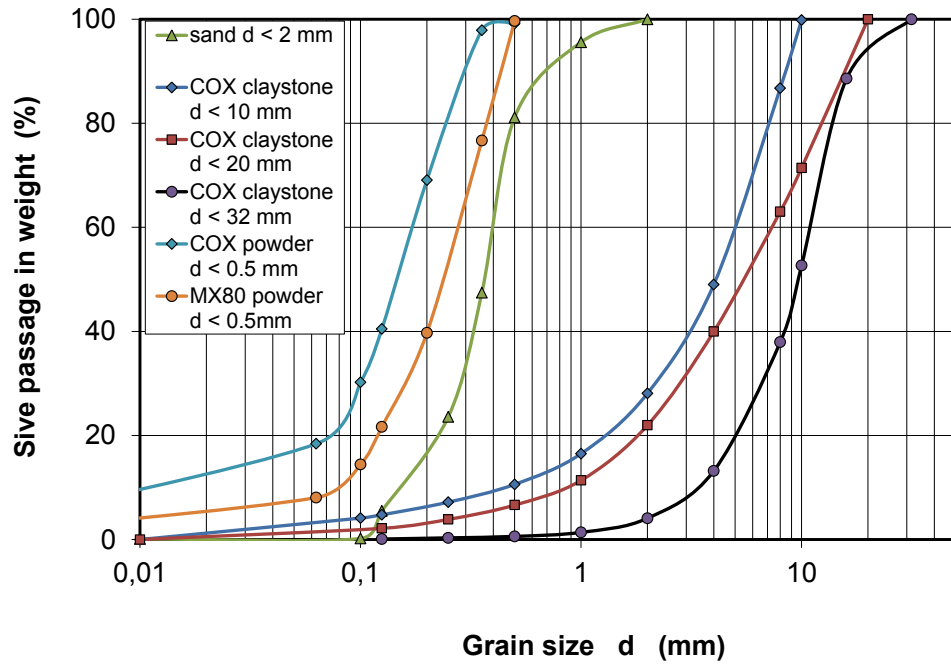
Fig. 3.4   Grain size distributions of crushed claystone and other materials

3.3   Compaction and permeability of crushed claystone backfill

After installation the backfill material in underground openings will be compacted under effects of the convergent deformation of the surrounding clay rock. Consequently, resistance of the backfill against these deformations increases, limiting damage propagation of the surrounding rock. At the same time porosity and permeability of the backfill decrease which increases the effectiveness of the barrier against groundwater flow. To quantify these processes the compaction and permeability behaviour of crushed claystone backfill was investigated experimentally.

3.3.1   Sample preparation and testing method

Coarse claystone aggregates with grain sizes of $d < 32$ mm and $d < 20$ mm were tested. The partly saturated material was wetted by spraying it with synthetic COX clay water and then mixed in a mixing drum to a homogeneous aggregate. The water contents of the samples varied between $w = 6.6$ % and 7.8 %, comparable to the water content found in situ. The aggregate was filled in a rubber jacket of 280 mm diameter in 7 layers of 100 mm height each. Each layer was compacted by application of different measures such as stamping by hand (Fig. 3.5a), by application of a vibrator (Fig. 3.5b),

or compression by load piston (Fig. 3.5c). Initial dry densities of ρ_d = 1.45 g/cm³ were achieved by vibration, ρ_d = 1.60 g/cm³ by stamping, and ρ_d = 1.82 g/cm³ by mechanical compression at 1 MPa. The resulting properties of the prepared samples are compiled in Tab. 3.1.

(a) stamp　　　　　　　　　　　(b) vibrator　　　　　　　　　　　(c) load piston
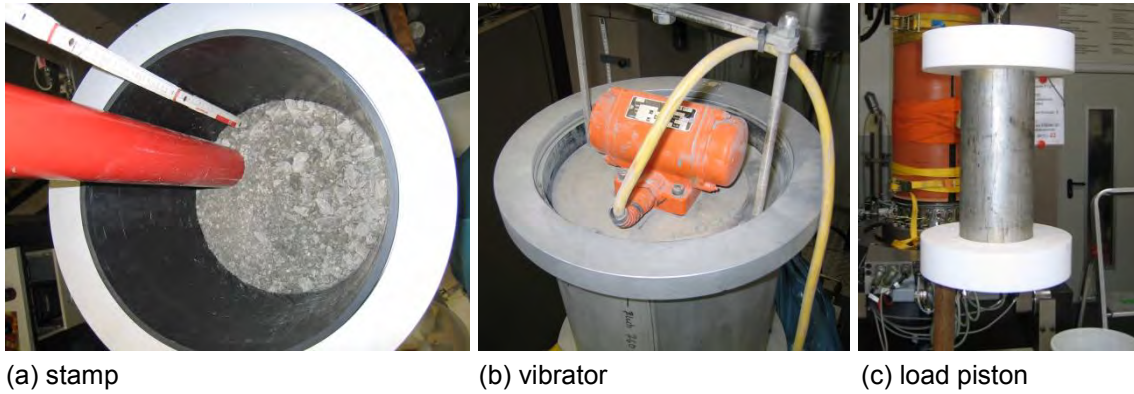
Fig. 3.5　　Photos of preparation of large backfill samples

Tab. 3.1　　Properties of the initial state of prepared backfill samples

Initial state	Sample 1	Sample 2	Sample 3	Sample 4
Pre-consolidation by	stamping	compression	compression	vibration
Grain size d (mm)	< 20	< 32	< 32	< 32
Diameter D_o (mm)	281.4	262.5	282.2	273.4
Height H_o (mm)	637.6	661.5	644,4	680.6
Mass G (kg)	68.24	69.44	78.54	62.01
Dry density ρ_d (g/cm³)	1.595	1.819	1.826	1.456
Water content w (%)	7.82	6.62	6.62	6.62
Porosity ϕ_o (%)	40.9	32.6	32.4	46.1

The prepared samples were installed in a triaxial cell (cf. Fig. 3.6), which allows compaction of large samples up to 280 mm diameter and 700 mm length under controlled thermo-hydraulic conditions. The upper limits of applicable stresses for this sample size are the maximum lateral stress σ_{r-max} = 50 MPa and the maximum axial stress σ_{a-max} = 75 MPa. Maximum temperature is T_{max} = 150 °C and the maximum pore fluid pressure p_{max} = 15 MPa. Axial strain is measured by a LVDT deformation transducer mounted to the lower piston outside the cell, while radial strain is recorded by two circumferential extensometers, one at midheight and one at ¼ of the sample length from the bottom. From the axial and radial deformation, the resulting volume change is cal-

culated. The permeability is measured in axial direction by injecting nitrogen gas at a constant injection pressure. In order to achieve sufficiently high flow rates at low porosities. The gas pressure was adjusted from 0.2 to 8.0 bars with decreasing porosities.
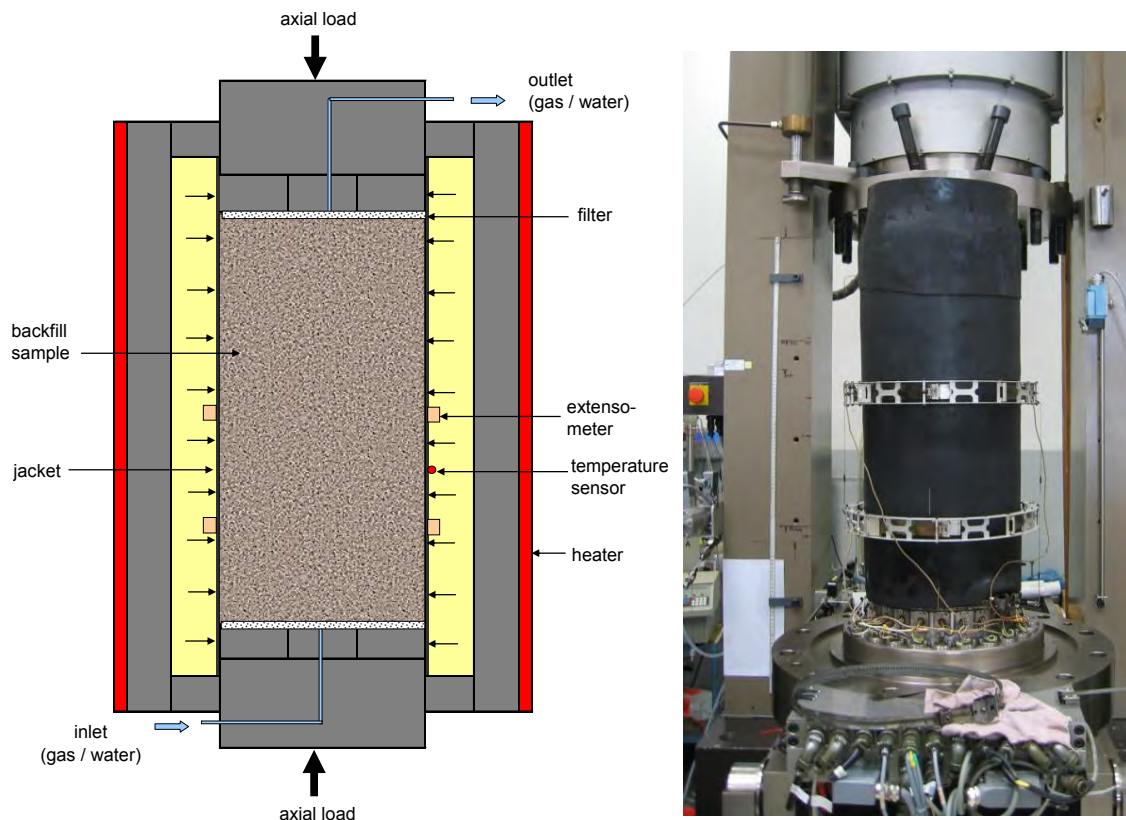
Fig. 3.6   Schematic of coupled compaction-permeability tests on backfill material

The samples were compacted along different loading paths. The load was also kept constant at several levels to examine time dependence of the compaction (creep compaction). Additionally, the strength of a compacted sample was determined under confining stresses from 2 to 7 MPa.

The test data were evaluated according to the following definitions:

- radial stress σ_r oil pressure in cell

- axial stress $\sigma_a = \frac{F - \sigma_r(A_0 - A)}{A}$

  F = axial force
  A_0 = initial sample cross section
  A = current sample cross section

- mean stress $\sigma_m = (\sigma_a + 2\sigma_r)/3$

- differential stress $\quad \Delta\sigma = (\sigma_a - \sigma_r)$

- axial strain $\quad\quad\quad \varepsilon_a = (H_o - H)/H_o$

  H = height of the sample, H_o = initial height

- radial strain $\quad\quad\quad \varepsilon_r = (D_o - D)/D_o$

  D = sample diameter, D_o = initial diameter

- volumetric strain $\quad \varepsilon_v = (V_o - V)/V_o$

  V = sample volume, V_o = initial volume

- bulk modulus $\quad\quad K = \Delta\sigma_m/\Delta\varepsilon_v \quad\quad\quad$ determined from the unloading path

- Yong's modulus $\quad E = \Delta(\sigma_a - \sigma_r)/\Delta\varepsilon_a \quad$ determined from the loading path

- Poisson's ratio $\quad\quad v = -\varepsilon_r/\varepsilon \quad\quad\quad\quad\quad$ determined from the loading path

- Porosity $\quad\quad\quad\quad \phi = 1 - (\rho/\rho_s)$

  ρ = bulk density, ρ_s = grain density

- gas permeability after Darcy's law

$$K_g = 2\mu\,\frac{p_a \cdot Q}{p_{in}^2 - p_a^2}\cdot\frac{H}{A}$$

μ = 1.74·10-5 Pa·s dynamic viscosity of gas,
p_a = atmospheric pressure,
p_{in} = injection pressure,
Q = flow rate of gas,
H/A = height/cross section of the sample.

3.3.2 Results

Six samples were investigated. However, only three tests were successfully conducted while the other three failed at the very beginning due to damage of the rubber jackets by sharp edges of coarse grains. Results of the successful tests are discussed below.

Sample 1 was compacted under a continually increasing lateral stress at a rate of 0.5 MPa/h and under a fixed axial strain of $\Delta\varepsilon_a = 0$. This loading path is similar to the compression conditions of the backfill in long boreholes and drifts. Fig. 3.7 shows the test results in terms of time evolution of axial and radial stresses (σ_a and σ_r), axial, radial and volumetric strains (ε_a, ε_r and ε_v), radial strain rate ($\dot\varepsilon_r$) as well as the porosity-mean-stress-relation ($\phi-\sigma_m$), and the permeability-porosity-relation ($K_g-\phi$). At $\Delta\varepsilon_a = 0$,

the radial stress was stepwise increased from 0.5 to 1, 4 and 6 MPa, resulting in an increase of the axial stress to $\Delta\sigma_a$ = 0.1 – 0.4 MPa. Each phase of constant stress lasted between 8 to 14 days, during which the radial strain ε_r and/or the volumetric compression ($\varepsilon_r = \varepsilon_v$ at $\Delta\varepsilon_a = 0$) increased further with time (Fig. 3.7a). The initial compaction rates in the beginning of each phase are relatively comparable at $\dot{\varepsilon}_r \approx 8 \cdot 10^{8} \, s^{-1}$. The compaction rate $\dot{\varepsilon}_r$ at σ_r = 1 MPa decreased down to $5 \cdot 10^{-10} \, s^{-1}$ over a period of Δt = 6 d, to $\dot{\varepsilon}_r = 9 \cdot 10^{-10} \, s^{-1}$ at σ_r = 4 MPa over Δt = 14 d, and to $\dot{\varepsilon}_r = 1 \cdot 10^{-9} \, s^{-1}$ at σ_r = 6 MPa over Δt = 10 d (Fig. 3.7b), respectively.
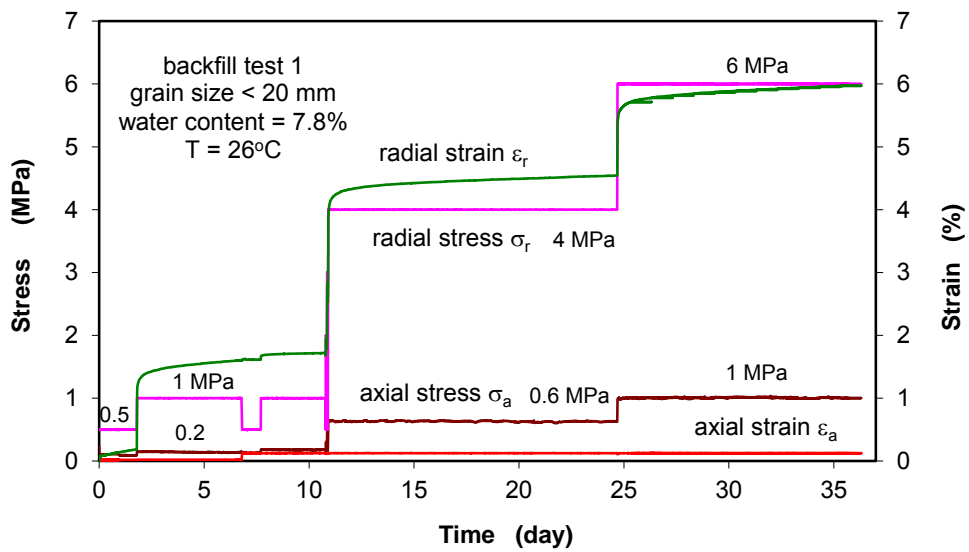
(a) Evolution of stresses and strains
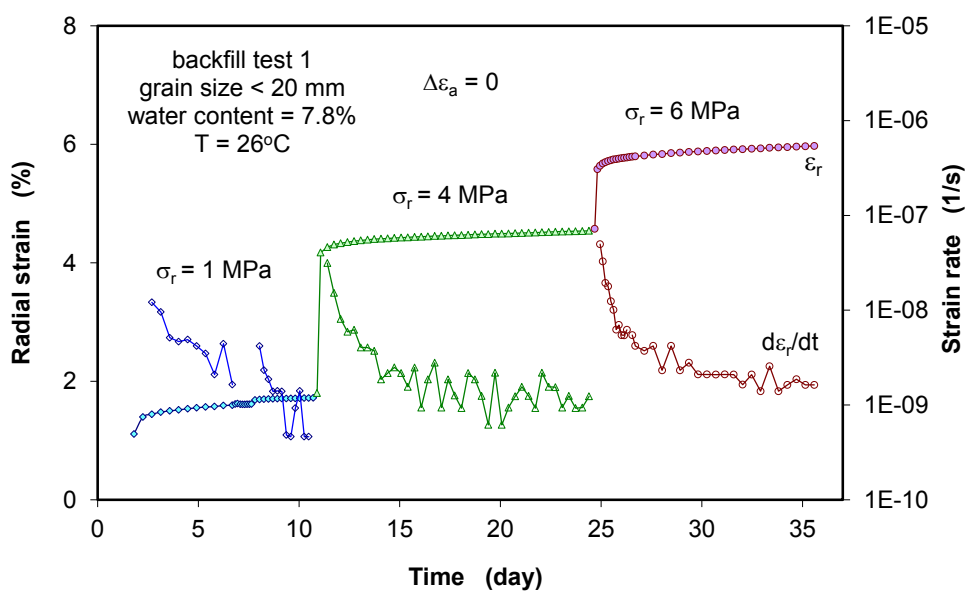
(b) Radial strain and strain rate
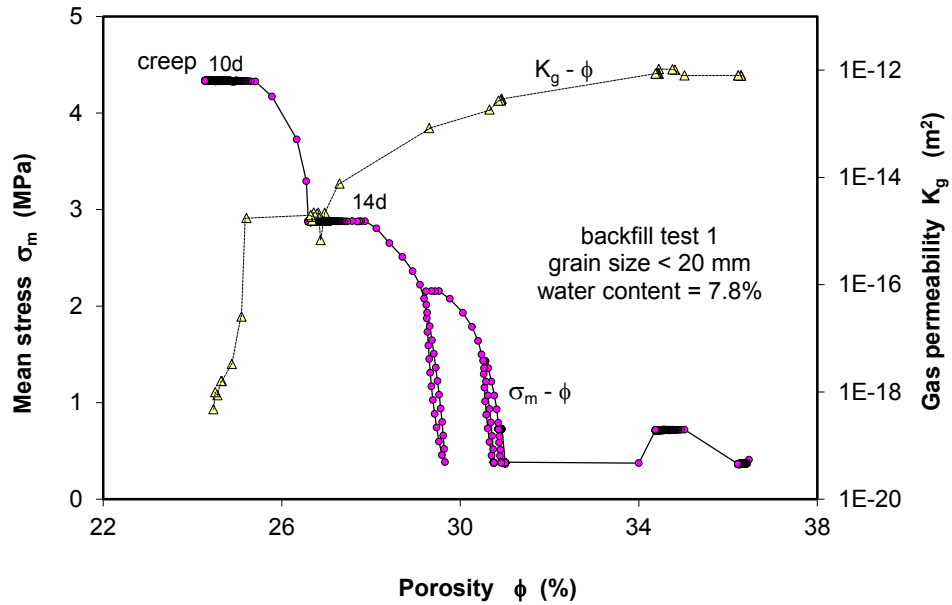
(c) Mean stress-porosity-permeability relation

Fig. 3.7 Results of the compaction and permeability test on clay backfill sample 1

At the same time the porosity was reduced with increasing compressive stress and with time, which was dominated by the irreversible visco-plastic deformation as shown by the $\sigma_m - \phi$ curve in Fig. 3.7c. The reversible elastic strain is relatively small as indicated by several loading/unloading cycles. Furthermore, the porosity reduction led to a significant decrease in permeability from the initial value of ~10^{-12} m^2 at ϕ = 34 – 37 % down to $5 \cdot 10^{-19}$ m^2 at ϕ = 24.5 % (Fig. 3.7c). A sharp reduction in permeability occurred in the low porosity range below ϕ = 26 %.

Sample 2 was quasi-hydrostatically compacted by increasing axial and lateral stress stepwise up to the levels of σ_a/σ_r = 1.1/0.5, 3.0/2.0, 10.5/8.0, 15.7/13.0, 19.5/16.0 and 3.5/2.0 MPa. Each phase at constant stress lasted for several days or weeks. The applied axial/radial stress (σ_a/σ_r) and the response of axial/radial/volumetric strain ($\varepsilon_a/\varepsilon_r/\varepsilon_v$) are depicted as a function of the test duration in Fig. 3.8a, while the variation of volume strain rate ($\dot{\varepsilon}_r$) with time is shown in Fig. 3.8b, and the relationships of porosity to mean stress ($\phi - \sigma_m$) and permeability to porosity ($K_g - \phi$) in Fig. 3.8c.

It is obvious that each loading resulted in a compression in all directions, but the axial compression was larger than radial compression due to the stress difference $\sigma_a - \sigma_r > 0$. Unloading resulted in an elastic expansion due to stress relief. At each stress level, the compaction progressed with time at decreasing strain rates. At a mean stress of σ_m

161

= 2.3 MPa $\dot{\varepsilon}_v$ decreased in four days from $8 \cdot 10^{-7}\,s^{-1}$ down to $2 \cdot 10^{-9}\,s^{-1}$ over 4 days, in 6 days at $\sigma_m = 8.8$ MPa to $\dot{\varepsilon}_v = 2 \cdot 10^{-9}\,s^{-1}$, and in 12 days $\dot{\varepsilon}_v =$ at $\sigma_r = 6$ MPa to $3 \cdot 10^{-10}\,s^{-1}$ (Fig. 3.8b), respectively. The unloading part of the $\sigma_m - \phi$ curve in Fig. 3.8c suggests the domination of the visco-plastic deformation of the backfill material. The pattern of the permeability – porosity relation is the same as the sample 1 with K_g decreasing from $\sim 10^{-12}\,m^2$ at $\phi = 25 - 33\,\%$ down to $5 \cdot 10^{-21}\,m^2$ at $\phi = 20.0\,\%$ (Fig. 3.8c). The very low permeability is about the same as that of intact clay rock.
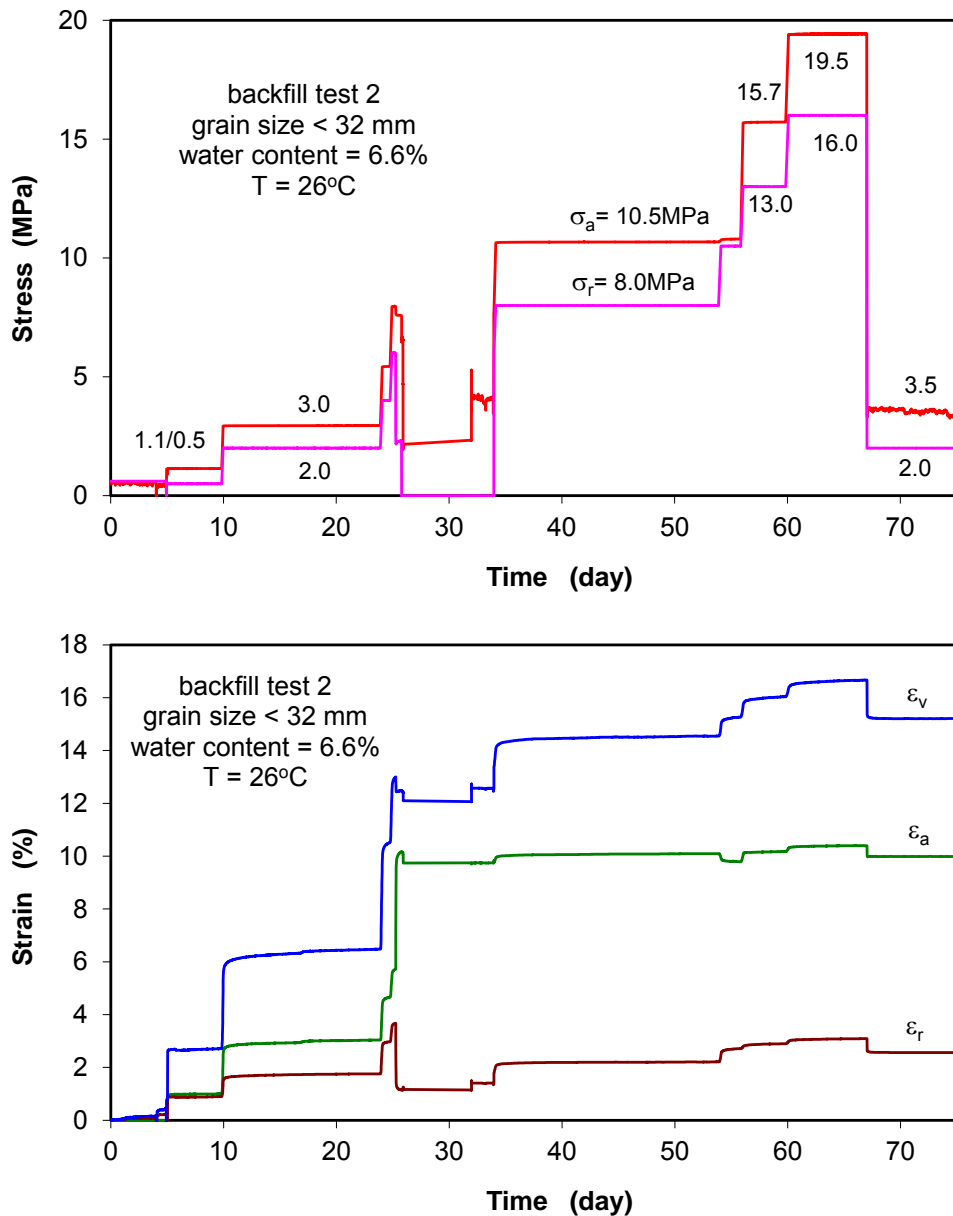
(a) Evolution of applied stresses and responses of axial/radial/volume strain
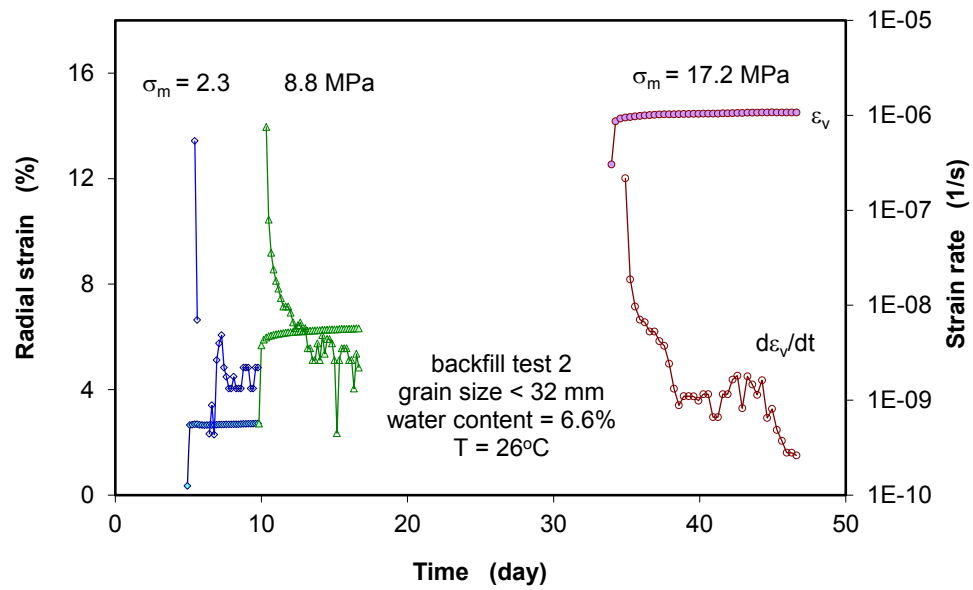
(b) Volumetric strain and strain rate
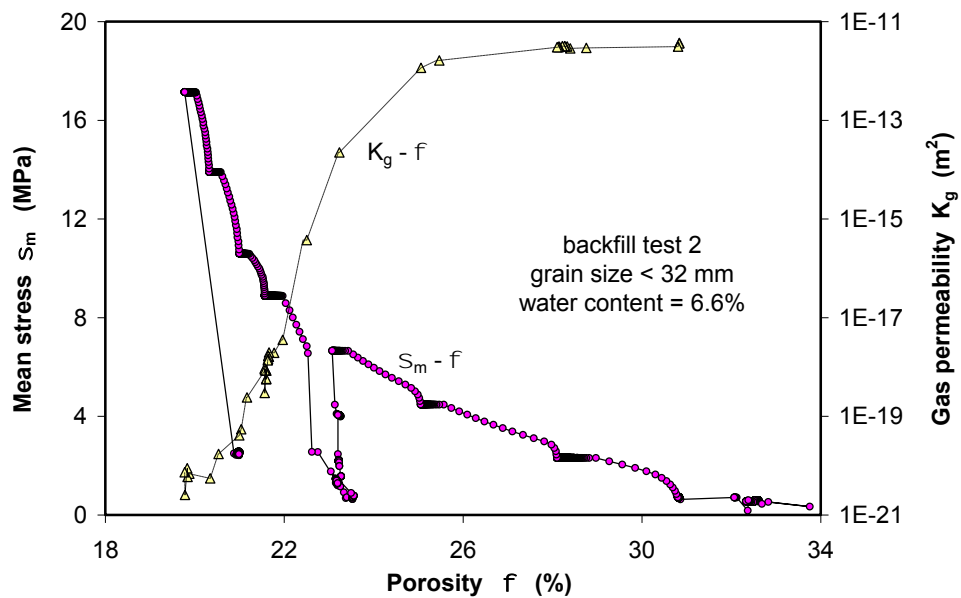
(c) Mean stress-porosity-permeability relation

Fig. 3.8   Results of the compaction and permeability test on clay backfill sample 2

The compacted sample with a porosity of ϕ = 21.0 % was examined with regard to the deviatoric deformation and strength behaviour under multiple confining stresses of σ_r = 2, 3, 5 and 7 MPa. For each confining stress, the axial stress was increased beyond the peak strength. The resulting stress-strain curves are plotted in Fig. 3.9. They show the typical elasto-plastic behaviour. From the linear part of each curve, the elastic parameters are determined and depicted in Fig. 3.10 as a function of the confining stress. Young's modulus varies from E = 430 to 1030 MPa, while the Poisson's ratio is

in a range between $v = 0.50$ and $v = 0.64$. The relatively large values of the Poisson's ratio v indicate dilatation of the compacted backfill due to the deviatoric stresses at each confining stress level, as shown by the volumetric strain curves in Fig. 3.9 (negative ε_v value).
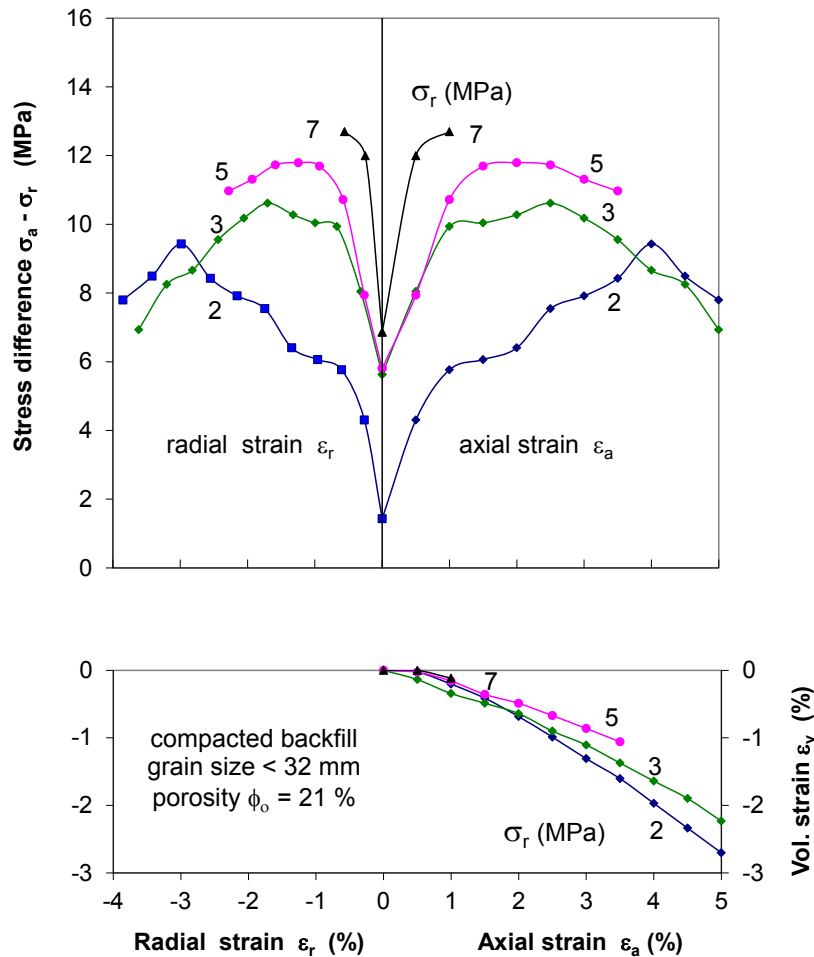
Fig. 3.9   Stress-strain curves obtained by deviatoric compression on compacted backfill at different confining stresses

Additionally, the peak strength was also determined for each confining stress. The values are illustrated in Fig. 3.11 as a function of the confining stress. The strength of the compacted backfill can be described by the Mohr-Coulomb's shear strength criterion:

$$\tau = \sigma_n \cdot \tan \varphi + c$$

or

$$\sigma_1 = 2 \cdot c \cdot \tan \left(45° + \frac{\varphi}{2}\right) + \sigma_3 \tan^2 \left(45° + \frac{\varphi}{2}\right) \tag{3.1}$$

where τ refers to the shear stress at failure on the failure plane, σ_n is the normal stress on the failure plane, c the cohesion, and φ the angle of internal friction. Based on the data, the strength parameters can be estimated to be c = 3.7 MPa and φ = 12°.
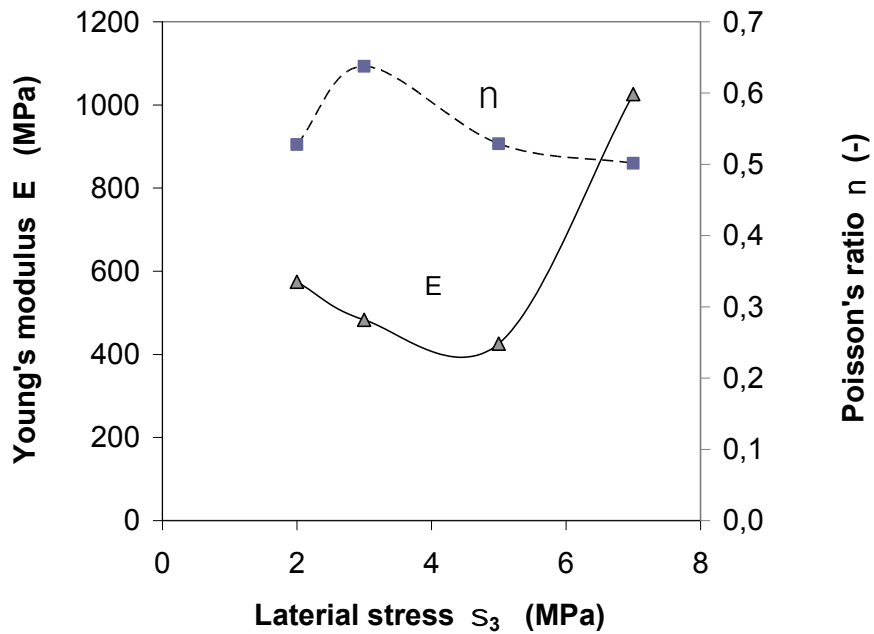
Fig. 3.10   Elastic parameters obtained on the compacted backfill at a porosity of 21 %
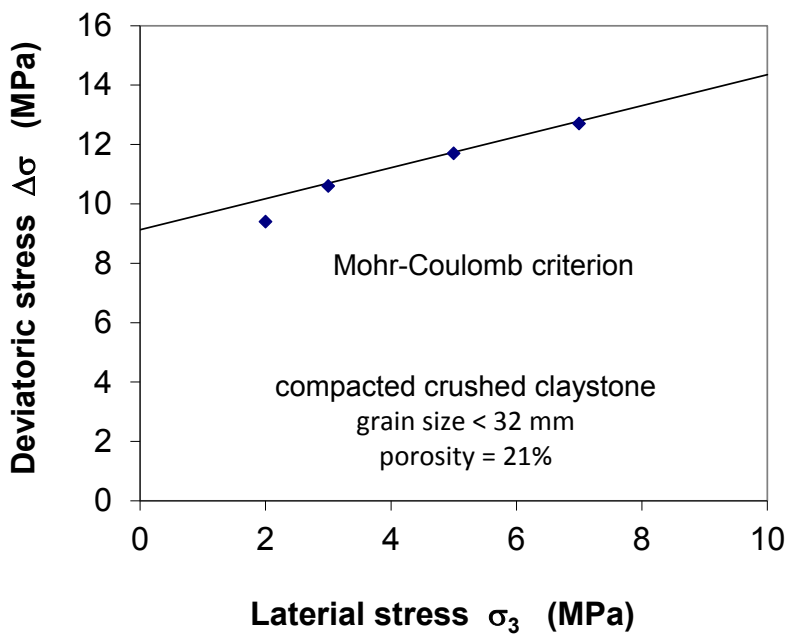
Fig. 3.11   Strength of the compacted backfill at a porosity of 21 %

Sample 3 was tested similar to sample 2 but with loading/unloading cycles to determine the elastic bulk modulus as a function of porosity. Additionally, a heating/cooling cycle was applied to examine thermal effects on the compaction of the backfill material. The results are illustrated in Fig. 3.12a depicting the evolution of applied stresses (σ_a/σ_r) and the response of deformation ($\varepsilon_a/\varepsilon_r/\varepsilon_v$), whereas the relationships of porosity to mean stress ($\phi - \sigma_m$) and volumetric bulk modulus to porosity ($K - \phi$) are shown in Fig. 3.12b, and the permeability-porosity relation ($K_g - \phi$) in Fig. 3.12c. The compaction behaviour of this sample is quite similar to that of sample 2. The elastic stiffness increases exponentially with the porosity reduction from K = 710 MPa at ϕ = 27.0 % up to K = 1,820 MPa at ϕ = 19.0 %. The permeability-porosity relation is comparable to that obtained on sample 2, with K_g decreasing from ~10^{-12} m^2 at $\phi \approx$ 27.0 % down to $10^{-20} - 10^{-21}$ m^2 at $\phi \approx$ 20.0 %.

During the last stage at σ_a/σ_r = 18/16 MPa, the sample at $\phi \approx$ 20.0 % was heated up to 60 °C for 4 days and 87 °C for 10 days, and then cooled down to 30 °C for 3 days. Each heating caused a volumetric expansion. The resulting mean thermal expansion coefficient amounts to α_v = 7.7·10^{-5} °C^{-1}. The temperature increase caused increasing creep rates (Fig. 3.12a). By contrast, cooling down from 90 °C to 30 °C produced an extremely large radial contraction of $\Delta\varepsilon_r$ = 3.0 % compared to the axial one $\Delta\varepsilon_1$ = 0.1 %. This phenomenon cannot be explained yet.

Post-testing was carried out on the compacted samples after dismantling. Fig. 3.13 shows pictures of the dismantled samples. From the measurements of mass and geometry, the initial state and the data recorded during the tests were calibrated. The inner structure of the compacted samples as shown in Fig. 3.14 was visually investigated. A cylindrical core was prepared from the sample. It had a size of D = 250 mm/L = 243 mm, a residual water content of w = 4.3 %, a bulk density of ρ_b = 2.34 g/cm^3, a dry density of ρ_d = 2.25 g/cm^3, and a porosity of ϕ = 17.5 %. The porosity of this core was lower than the value of ϕ = 19.0 % obtained from the whole sample. The difference may be attributed to the errors of the measurements of the geometry due to the rough surface of the sample (Fig. 3.13). Obviously, the final state of the crushed claystone after the compaction is very close to the intact rock. No macro-pores could be visually identified.
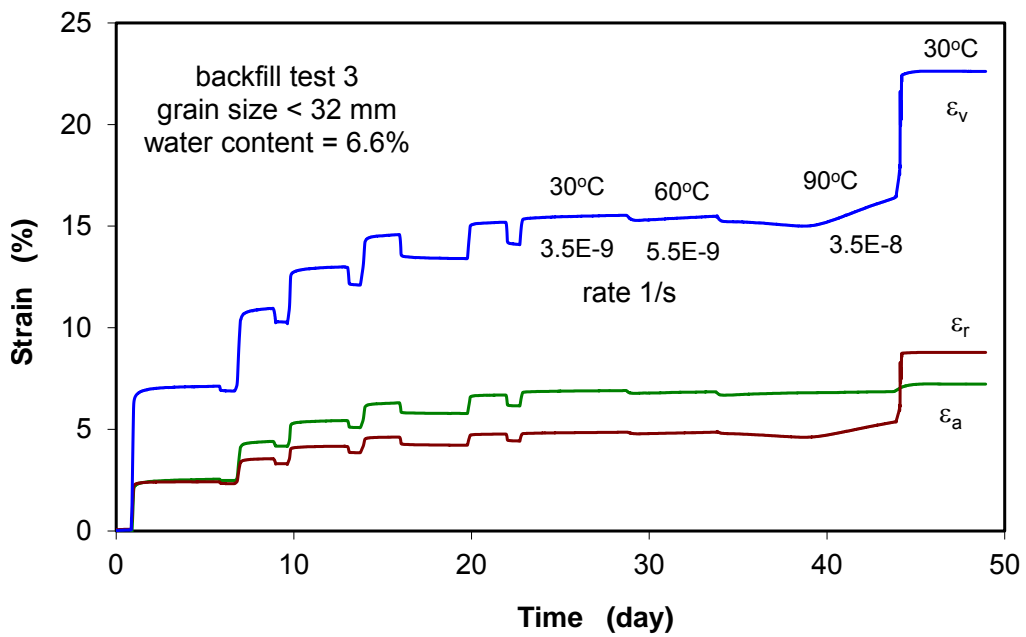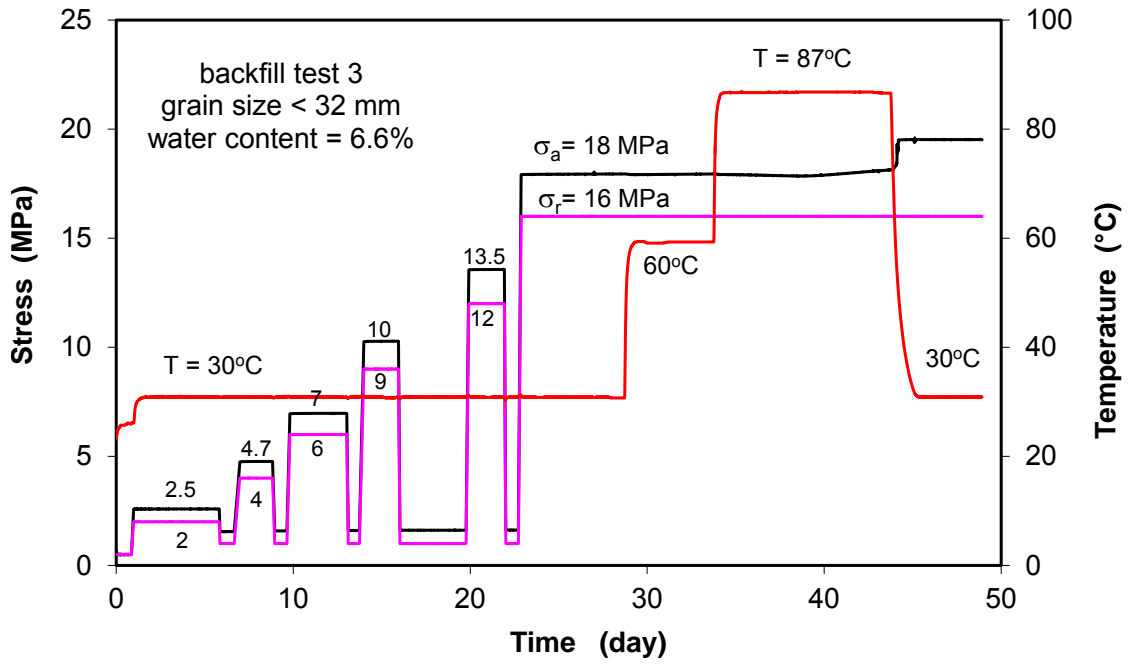
(a) Evolution of applied stresses and response of axial, radial and volume strain
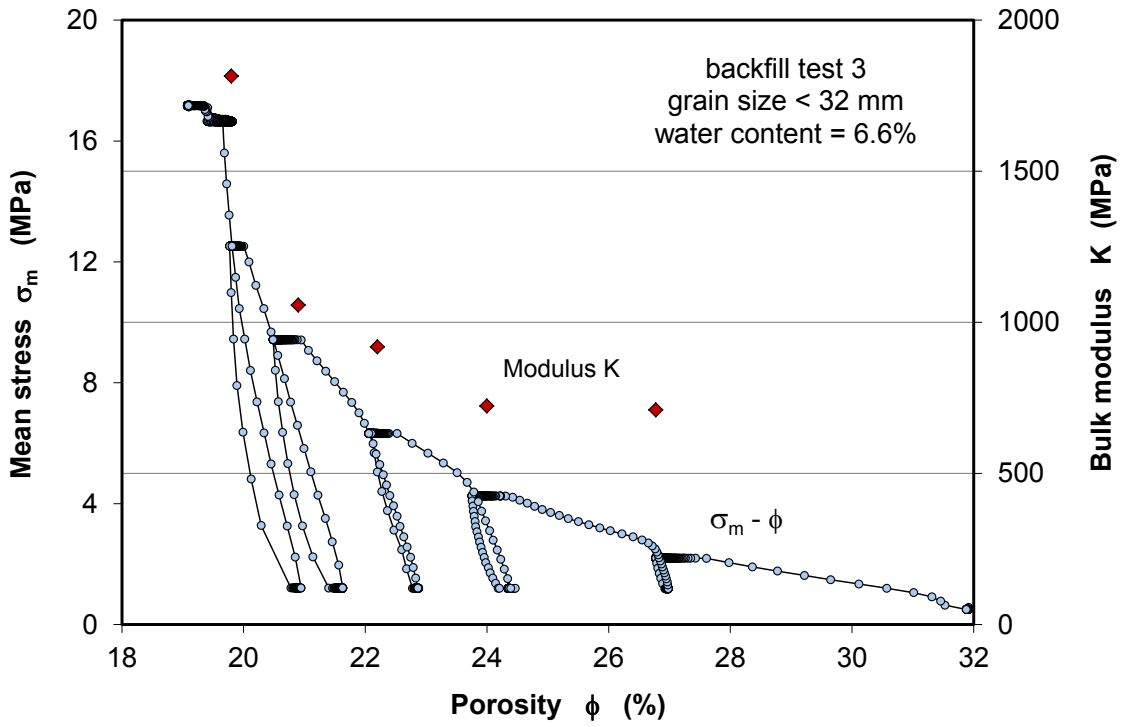
(b) Volumetric strain and bulk modulus
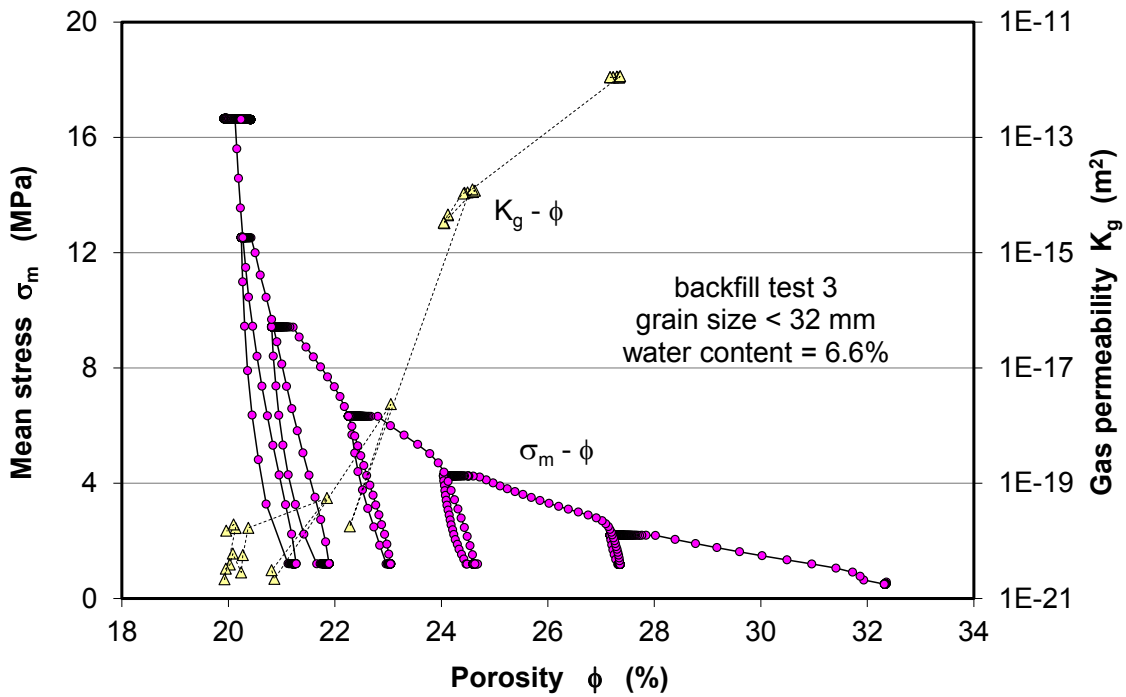
(c) Mean stress-porosity-permeability relation

Fig. 3.12 Results of the compaction and permeability test on clay backfill sample 3

(a) sample 1
  $\Delta\varepsilon_a = 0$
  $\sigma_r = 6$ MPa
  $\phi = 24.4$ %

(b) sample 2
  $\sigma_a = 12.7$ MPa
  $\sigma_r = 7.0$ MPa
  $\phi = 20.0$ %

(c) sample 3
  $\sigma_a = 19.5$ MPa
  $\sigma_r = 16.0$ MPa
  $\phi = 19.0$ %

Fig. 3.13   Pictures of the compacted backfill samples after testing

(a) Preparation of a cylinder of $D = 250$ mm / $L = 243$ mm from the compacted sample

(b) Inner structure of the compacted sample

Fig. 3.14   Photos of the compacted sample at a porosity of 17.5 %

3.3.3 Relationships of mean stress – porosity – permeability

Mean stress – porosity

Fig. 3.15 summarizes the mean stress-porosity curves obtained from the crushed clay-stone samples. As mentioned above, sample 1 (d < 20 mm) was compressed by increasing σ_r at $\Delta\varepsilon_a$ = 0 while the other two samples with coarse grains (d < 32 mm) were compressed quasi-hydrostatically. It shows that the three curves are close to each other indicating only little influence of the maximum grain sizes, the initial porosities and the load paths.

The mean stress-porosity relation is non-linear and may be expressed by an exponential function. For instance, the compaction model, which was originally proposed by Zhang /ZHA 93/ for the compaction of crushed salt in terms of compaction rate as function of mean stress, temperature and porosity, is applied here for the compaction of the crushed claystone:

$$\dot{\varepsilon}_v = A \,\exp\left(\frac{-Q}{RT}\right)\left(\frac{\sigma_m}{\sigma_o}\right)^n \left[\ln\left(\frac{\phi_o(1-\phi_e)}{\phi_e(1-\phi_o)}\right)\right]^{-m} \tag{3.2}$$

Where $\dot{\varepsilon}_v$ = volumetric strain rate (1/s), σ_m = mean effective stress (MPa), σ_o = reference stress (1 MPa), T = absolute temperature (K), R = universal gas constant (8.3143·10^{-3} kJ/(Kmole)), Q = activation energy (kJ/mole), ϕ_e = effective porosity (equal to the difference of the total porosity ϕ_t of the porous medium minus the porosity of the intact claystone ϕ_c, $\phi_e = \phi_t - \phi_c$, ϕ_o = effective initial porosity of the backfill loosely emplaced, A, n and m are the parameters depending on the material properties such as grain size, water content, mineral components, etc..

Equation (3.2) can be rewritten for fitting the data of mean stress in relation with porosity

$$\sigma_m = \left[\frac{\sigma_o\dot{\varepsilon}_v}{A\exp(-Q/RT)}\right]^{-n}\left[\ln\left(\frac{\phi_o(1-\phi_e)}{\phi_e(1-\phi_o)}\right)\right]^{\frac{m}{n}} \tag{3.3}$$

The parameters were preliminarily estimated for the tested material at room temperature: $A\exp(-Q/RT)$ = 1·10^{-14} 1/s, n = 10, m = 20, σ_o = 1 MPa, ϕ_{to} = 38 %, ϕ_c = 15 %, and $\phi_o = \phi_{to} - \phi_c$ = 23 %. Using two volumetric strain rates of $\dot{\varepsilon}_v$ = 1·10^{-8} and

$1 \cdot 10^{-9}$ 1/s, a reasonable agreement of the model with the data can be obtained. This suggests the suitability of the model for the compaction of claystone backfill.
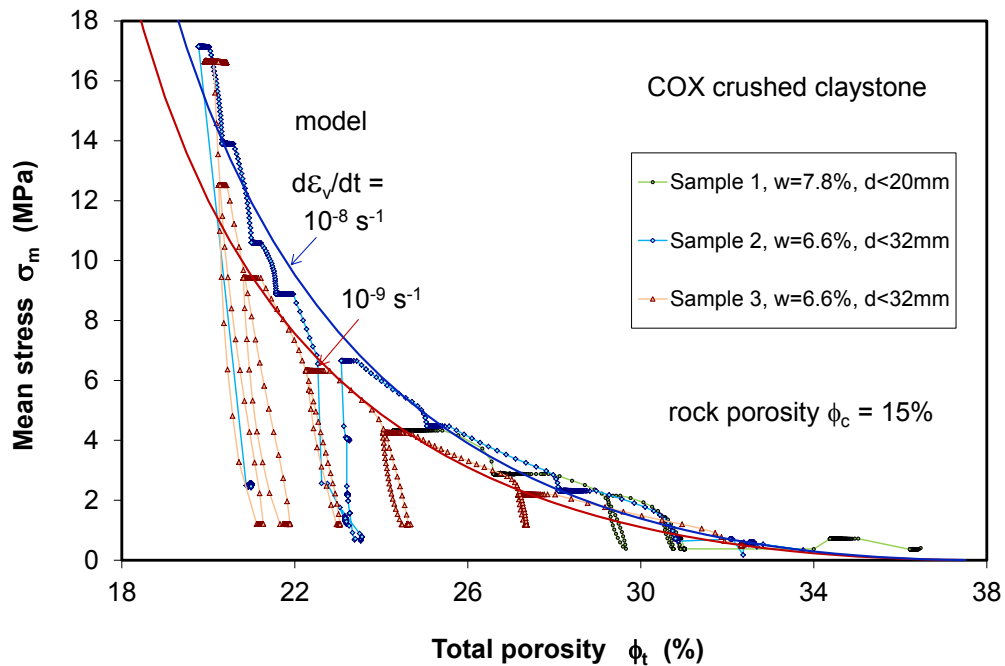
Fig. 3.15 Mean stress – porosity relation of crushed claystone with different grain sizes

Generally, the compressibility of the material is relatively high, i. e. its resistance against external load is relatively low. At mean stresses of 12 – 16 MPa, corresponding to the lithostatic stress at depths of 500 – 600 m, the backfill can be compacted to a low porosity of ~20 %. The stiffness and strength of the porous material increase with decreasing porosity.

Permeability – porosity

The gas permeability values obtained for the crushed claystone with grain sizes of $d < 20$ mm and $d < 32$ mm are plotted in Fig. 3.16 as a function of porosity and also compared to the water permeability of the aggregate with small grains of $d < 10$ mm. It is obvious that (a) the water permeability is much lower than the gas permeability and (b) the permeability of the coarse-grained aggregate is higher than that of the fine-grained material at a given porosity. The low water permeability is mainly attributed to the effects of water-induced swelling of the clay grains into the pores. The permeability decreases much faster at porosities below ~25 % for gas flow and below ~30 % for water

flow. Very low permeability values of less than 10^{-19} – 10^{-20} m^2 were measured for water flow at a porosity of ~27 % and for gas flow below porosities of 20 – 22 % depending on the grain size. The low water and gas permeabilities at the low porosities are close to the rock state.
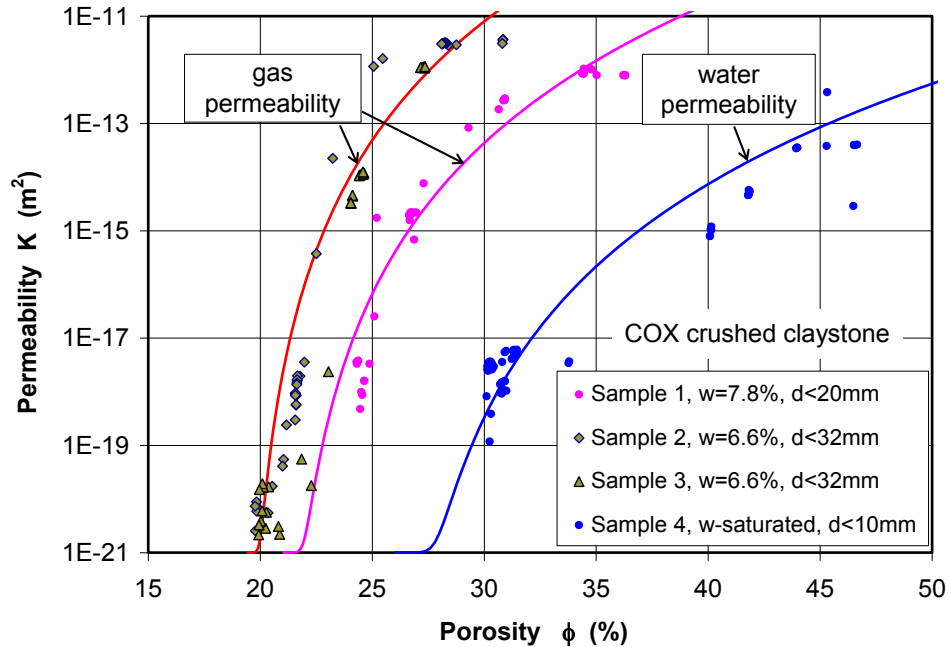
Fig. 3.16   Gas and water permeability of crushed claystone as a function of porosity

For describing this behaviour mathematically an effective porosity, ϕ_{eff}, is introduced here. It is defined as the difference between the total porosity ϕ and a threshold porosity ϕ_{min}. The threshold porosity characterises the compaction state at which the pore network becomes disconnected so that the pores become isolated and thus ineffective for fluid transport. The permeability-porosity relation can then be described by a power law

$$K = K_o \phi_{eff}{}^n \tag{3.4}$$

where K_o and n are parameters. Fitting these parameters to the measured data leads to the continuous curves that are also depicted in Fig. 3.16. A comparison shows a good agreement between model (Equation (3.4)) and measurements within the investigated data range.

Note that the crushed claystone is considered more suitable for backfilling the remaining void space in disposal boreholes and drifts. If a certain supporting capacity against

172

EDZ development is desired, the material has to be pre-compacted in situ to a certain degree to provide for a high density and hence a high stiffness. For the prediction of the long-term compaction behaviour of the backfill during the repository post-closure phase, adequate constitutive models need to be developed that involve all key factors such as stress, time or compaction rate, suction or water content, temperature, and chemical reactions with alkaline solutions that appear from the degradation of the concrete lining.

3.4 Sealing properties of compacted claystone-bentonite mixtures

Compacted bentonite and bentonite-sand mixtures are being widely investigated for sealing of underground repositories in crystalline rock and clay formations. Since natural claystone reacts with water similar to bentonite, it should be possible to use crushed claystone from the repository excavation as a main component of the EBS. According to the specific requirements for the sealing of boreholes, drifts and shafts, a mixture of crushed claystone and bentonite can be compacted to pre-defined densities for the construction of these seals. Generally a claystone-bentonite seal must have sufficient supporting capacity against damage propagation of the surrounding rock, low hydraulic conductivity against migration of radionuclides with fluids, and a certain swelling capacity for sealing of gaps and interfaces between compacted blocks and the surrounding rock. The hydro-mechanical properties of claystone-bentonite mixtures with various mixing ratios were determined by performing various kinds of experiments.

Fine-grained COX claystone powder with grain sizes of d < 0.5 mm and coarse-grained aggregate of $d < 10.0$ mm were used in the tests. A varying amount of MX80 bentonite powder of $d < 0.5$ mm was added to the crushed claystone to get different mixing ratios. The grain size distributions of the materials are shown in Fig. 3.4. Both fine- and coarse-grained COX aggregates had a water content of w = 4.3 %, while the delivered MX80 bentonite had a water content of w = 9.6 %.

3.4.1 Compressibility

The seals in the underground repositories are usally designed to consist of compacted blocks (bricks) of bentonite-based mineral mixtures and/or compacted bentonite pellets. To reach the designed densities (or porosities) of the sealing material a certain energy

is required for the compaction. This can be determined from the stress-compaction curves of the mixtures.

Test procedure

The compressibility of crushed claystone-bentonite mixtures was determined by axial compression in oedometer cells. The COX clay powder and the MX80 bentonite powder were mixed to various COX/MX80 ratios from pure bentonite to pure crushed claystone. Another mixture of consisted of the coarse-grained claystone of $d < 10\,mm$ and the bentonite in a COX/MX80 ratio of 50/50. Whereas the fine-grained mixtures were compacted in small cells of 46 mm diameter, the coarse-grained mixture was loaded in a large cell of 100 mm diameter. Fig. 3.17 shows the setup of the large oedometer test. The material was filled in the cell in three layers of 40 mm each to a total height of 120 mm. After each filling, the material was stamped by hand. The prepared samples were compacted at a strain rate of $1.5 \cdot 10^{-6}\,s^{-1}$ while the resulting increase in stress was measured. The test was terminated when a maximum load of 30 MPa was reached.

(a) Testing apparatus

(b) Oedometer cell

1 sample   2 oedometer cell
3 load piston 4 bottom plate
5 screw cap 6 sinter filter
7 load sensor   8 pressure sensor
9 LVDT-transducer   10 valves
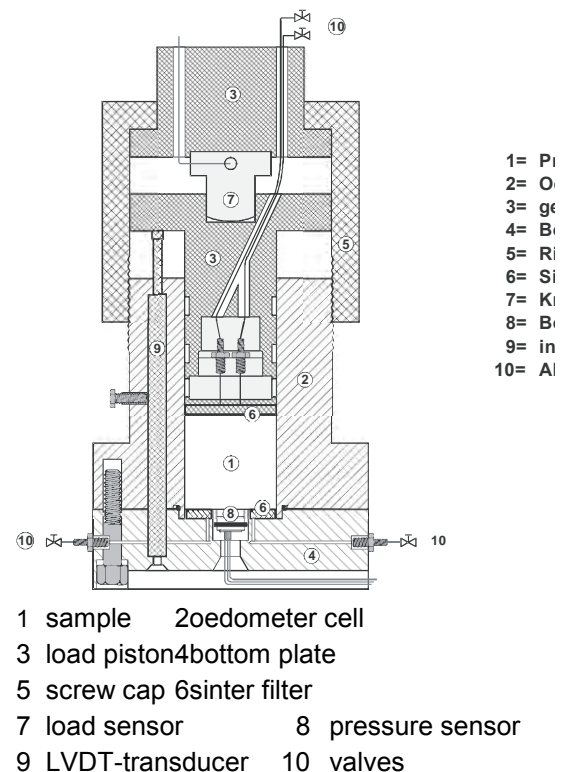
Fig. 3.17   Setup of oedometer compaction test on backfill material

Results

Fig. 3.18 illustrates the compaction process in terms of porosity as a function of stress. It can be recognized from the curves that

a) The initial porosities of the fine-grained mixtures after emplacement lay in a range of 70 – 75 % while a comparatively low porosity of ϕ = 41 % could be achieved by the coarse-grained mixture of 50 COX+50 MX80. This is due to a dense filling of the bentonite powder into the pores between the coarse claystone grains.

b) The porosity of each sample decreases with increasing stress. The compressibility decreases continuously with increasing stress and is significantly higher for loads below 5 MPa than above that value.

The $\phi - \sigma$ curves of all mixtures are nearly parallel and converge with increasing load to a constant porosity value. At high stresses of larger than 15 MPa, the porosity does not change significantly anymore.
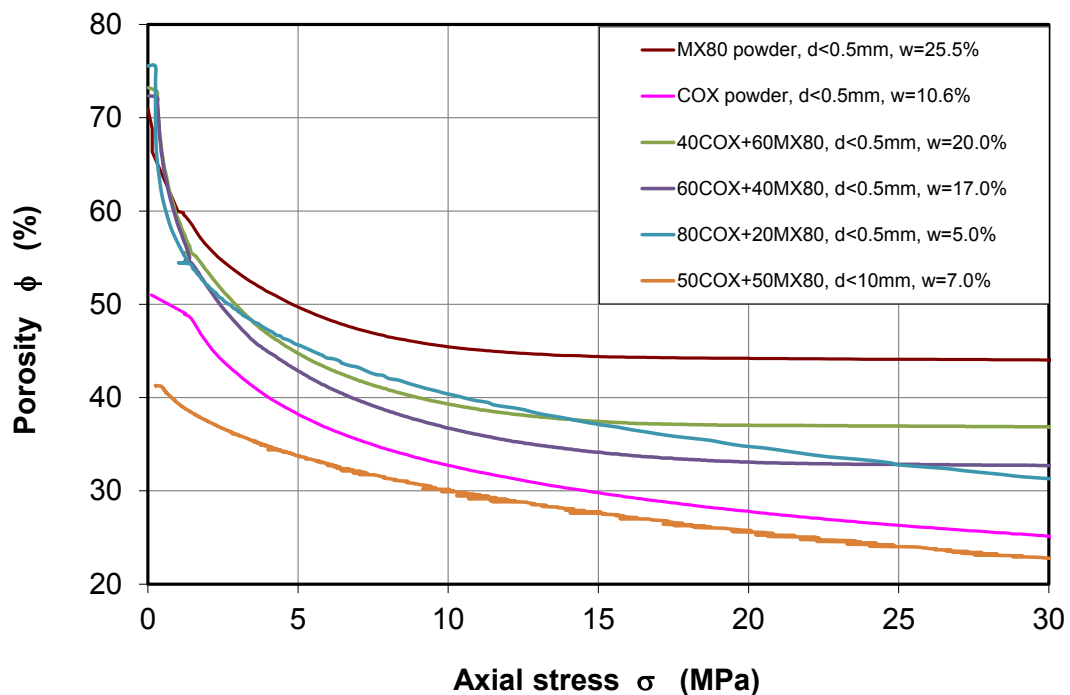
Fig. 3.18   Compaction behaviour of crushed claystone-bentonite mixtures

Tab. 3.2 Characteristics of claystone-bentonite mixtures compacted under 30 MPa

Property	COX powder	MX80 powder	40 COX+ 60 MX80	60 COX+ 40MX80	80 COX+ 20 MX80	50 COX+ 50 MX80
Diameter D [mm]	46.0	46.0	46.0	46.0	46.0	100.0
Height H [mm]	48.2	49.5	52.2	50.6	20.6	91.0
Grain size d [mm]	< 0.5	< 0.5	< 0.5	< 0.5	< 0.5	< 10.0
Water content w [%]	10.6	25.5	20.0	17.0	5.0	7.0
Bulk density ρ_b [g/cm^3]	2.25	1.95	2.08	2.14	1.97	1.91
Dry density ρ_d [g/cm^3]	2.02	1.56	1.67	1.79	1.86	1.79
Grain density ρ_s [g/cm^3]	2.70	2.78	2.75	2.73	2.72	2.74
Total porosity ϕ [%]	25.0	44.0	39.0	35.0	31.0	22.7
Water saturation S_w [%]	85.6	90.4	85.6	87.0	30.0	55.2
Swelling pressure [MPa]	3.0	> 7.6	6.0	6.0	6.5	9.5
Water permeability [m^2]	$1 \cdot 10^{-19}$	$3 \cdot 10^{-21}$	$2 \cdot 10^{-20}$	$3 \cdot 10^{-20}$	$2 \cdot 10^{-19}$	-

The characteristics of the samples compacted at 30 MPa are summarized in Tab. 3.2 Applying the same compaction energy, the achieved densities differ from one mixture to another. The dry density increases (and accordingly the porosity decreases) with an increasing fraction of claystone from ρ_d = 1.56 g/cm^3 (ϕ = 44 %) for pure bentonite to ρ_d = 2.02 g/cm^3 (ϕ = 25 %) for pure claystone powder. Using coarse claystone aggregate (d < 10 mm) instead of powder for the 50/50 mixture leads to a porosity of ϕ = 23 % which is lower than the porosities of the other fine-grained mixtures. As mentioned before, the reason for this effect lies in the structure of the pore space. A considerable amount of bentonite powder can fill up the pores between the coarse claystone grains.

3.4.2 Water retention

After installation of buffer and backfill in boreholes, drifts and shafts, the initially unsaturated sealing material will take up water due to the suction gradient between the saturated rock and the unsaturated seal from the humid air and liquid water in the pores. The resaturation process is mainly controlled by the relationship between water content and suction of the sealing material, (usually called water retention curve). The resaturation of the sealing material in turn governs the swelling of clay particles. The water retention curves of the compacted claystone-bentonite mixtures were determined for unconfined samples using the vapour equilibrium technique.

Test procedure

Four claystone-bentonite mixtures were prepared with COX aggregate ($d < 5$ mm) and MX80 bentonite powder ($d < 0.5$ mm) to the following ratios: COX, 80 COX+20 MX80, 60 COX+40 MX80, and MX 80. The mixtures were compacted in steel cells of 50 mm diameter and 33 mm height at an increasing load of up to 30 MPa. Seven samples were prepared for each mixture. Fig. 3.19 shows a picture of all the samples together. The major characteristics of the compacted mixtures are given in Tab. 3.4.
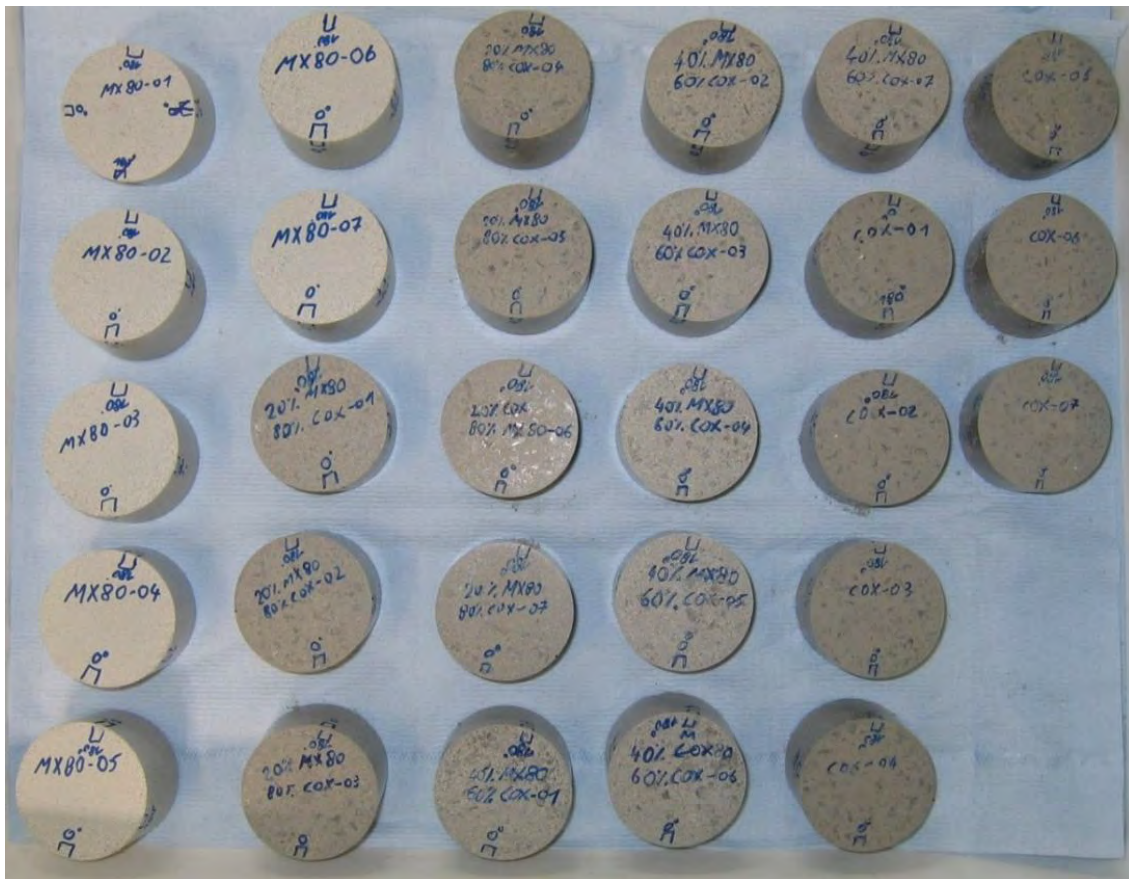
Fig. 3.19   Samples of compacted claystone-bentonite mixtures before testing

The samples were unconfined and placed in desiccators at different relative humidity values of RH = 15 % to 100 % and at ambient temperature of 25 °C. The corresponding suctions lie between 0.0 and 258 MPa. Each desiccator contained 4 samples, one per each mixture. The water content of the samples evolved with time towards an equilibrium with the preset humidity. Corresponding to the change in water content, the compacted claystone-bentonite mixtures expanded or contracted. While the relative humidity and temperature in each desiccator were continuously recorded by transistor psychrometer sensors, the water content and the deformation of each sample were

measured outside at different periods of time. Axial strains were measured at two op-posite positions at 0° and 180° and radial strains were recorded at two perpendicular directions. The results were taken as the average of the two values, from which the volumetric strain was calculated. The tests lasted for more than 6 months until equilibrium.

Tab. 3.3 Characteristics of compacted claystone-bentonite mixtures before water retention testing

Property	COX claystone	80 COX+ 20 MX80	60 COX+ 40 MX80	MX80 bentonite
Diameter D [mm]	50.0	50.0	50.0	50.0
Height H [mm]	33.0	33.0	33.0	33.0
Grain size d [mm]	< 5.0	< 5.0	< 5.0	< 0.5
Water content w [%]	3.0	4.50	5.45	9.67
Bulk density ρ_b [g/cm^3]	2.10	2.04	1.98	1.79
Dry density ρ_d [g/cm^3]	2.05	1.95	1.88	1.64
Grain density ρ_s [g/cm^3]	2.70	2.72	2.73	2.78
Total porosity ϕ [%]	24.2	28.2	31.2	41.1
Water saturation S_w [%]	25.6	31.1	32.8	38.4

Results

The measured data of water content, axial, radial, and volumetric strain are plotted in Fig. F.50 for compacted COX aggregate, Fig. F.51 for 80 COX + 20 MX80 mixture, Fig. F.52 for 60 COX + 40 MX80 mixture, and Fig. F.53 for MX80 bentonite. The initial water content of the samples was defined to be the water content which was determined at RH = 50 %. After changing to a lower humidity of RH = 15 %, all the mixtures were desaturated and shrank. This effect was most pronounced at the compacted bentonite with a water content reduction of Δw = 6 % and volumetric shrinkage of ε_v = 4. All other three samples showed only a reduction of Δw < 2 % and ε_v < 1 % under the same conditions. At RH > 50 %, the water content of each mixture increased with time, accompanied by swelling in all the directions. The higher the relative humidity was set and the higher the bentonite content was chosen, the more water was taken up and the larger was the volumetric increase. Whereas all samples at $RH \leq 96$ % reached equilibrium within 3 months, the water content still increased after 6 months at RH = 100 % at which time the related tests were terminated.

The measured equilibrium water contents for all the samples at all humidity conditions are depicted in Fig. 3.20 as a function of suction, which is related to the relative humidity by Kelvin's law /FRE 93/:

$$s = -\frac{RT}{v_{wo}\omega_v}\ln\left(\frac{p_v}{p_{vo}}\right) = -\frac{RT}{v_{wo}\omega_v}\ln(RH) \tag{3.5}$$

where s = soil suction (kPa)

R = universal gas constant (= 8.31432 J/mol K)

T = absolute temperature (K)

v_{wo} = specific volume of water or the inverse of density of water (= $1/\rho_w$, m³/kg)

ρ_w = density of water (= 998 kg/m³ at 20 °C)

ω_v = molecular mass of water vapour (= 18.016 kg/kmol)

p_v = partial pressure of pore-water vapour (kPa)

p_{vo} = saturation pressure of water vapour over a flat surface of pure water at the same temperature (kPa)

RH = relative humidity ($= \frac{p_v}{p_{vo}} \cdot 100, \%$).

Fig. 3.20 shows that a) the water content of each mixture increases with decreasing suction or increasing humidity, and b) moisture uptake at a given suction is proportional to the bentonite content of the mixture. Note that in the wet environment at zero suction or RH = 100 %, all the mixtures can take up large amounts of water. Measured were water contents up to w = 12 % for COX, w = 19 % for 80 COX+20 MX80, w = 28 % for 60 COX + 40 MX80, and w = 48 % for MX80 over 6 months during which equilibrium was not yet achieved.

The corresponding volumetric strains are illustrated in Fig. 3.21 as a function of suction and in Fig. 3.22 as a function of water content. At swelling the volume of each compacted mixture increases almost linearly with increasing water content. Under a high humidity of RH = 96 %, the compacted COX claystone expanded to ε_v = 12 %, while the others expanded even more to ε_v = 21 % (80 COX + 20 MX80), ε_v = 27 % (60 COX + 40 MX80), and ε_v = 38 % (MX80). Generally, all compacted claystone-bentonite mixtures exhibited significant swelling capacities which were proportional to the bentonite content to a certain extent.
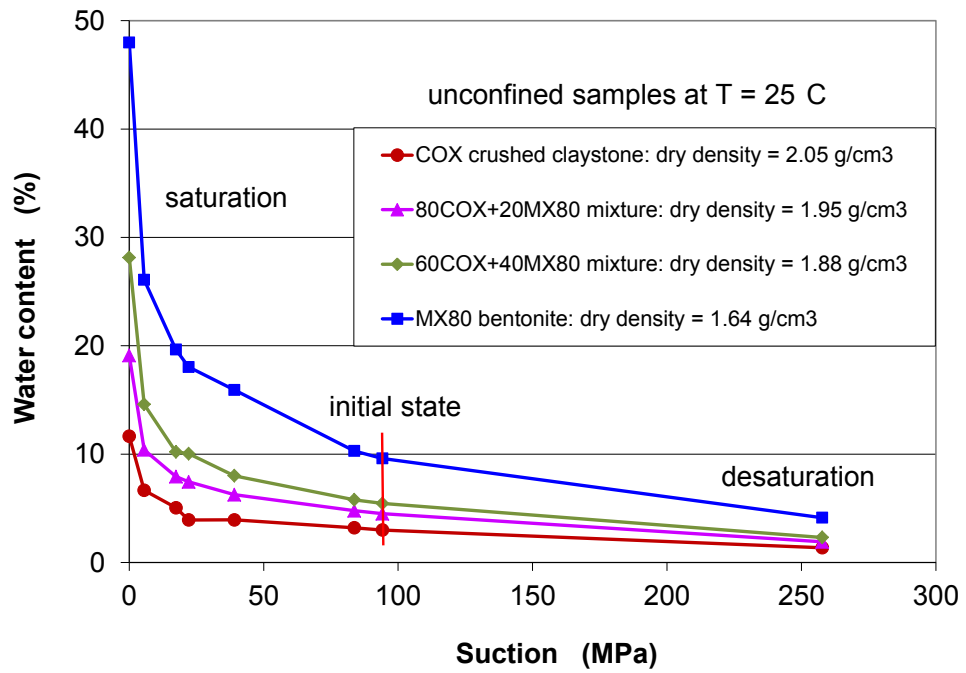
Fig. 3.20   Water retention curves of compacted claystone-bentonite mixtures
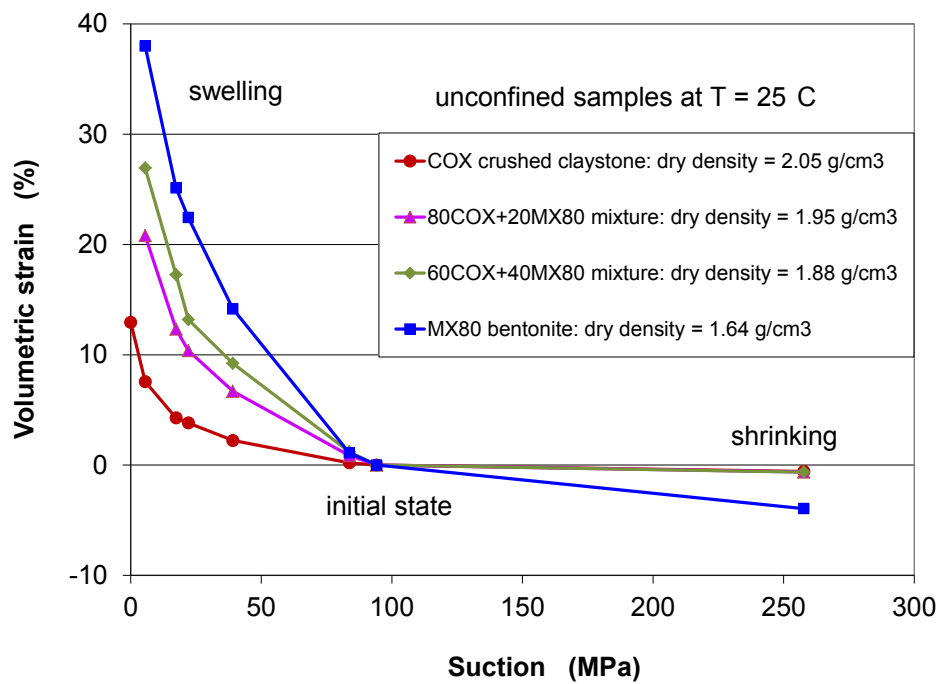
Fig. 3.21   Volumetric strain of compacted claystone-bentonite mixtures as function of applied suction
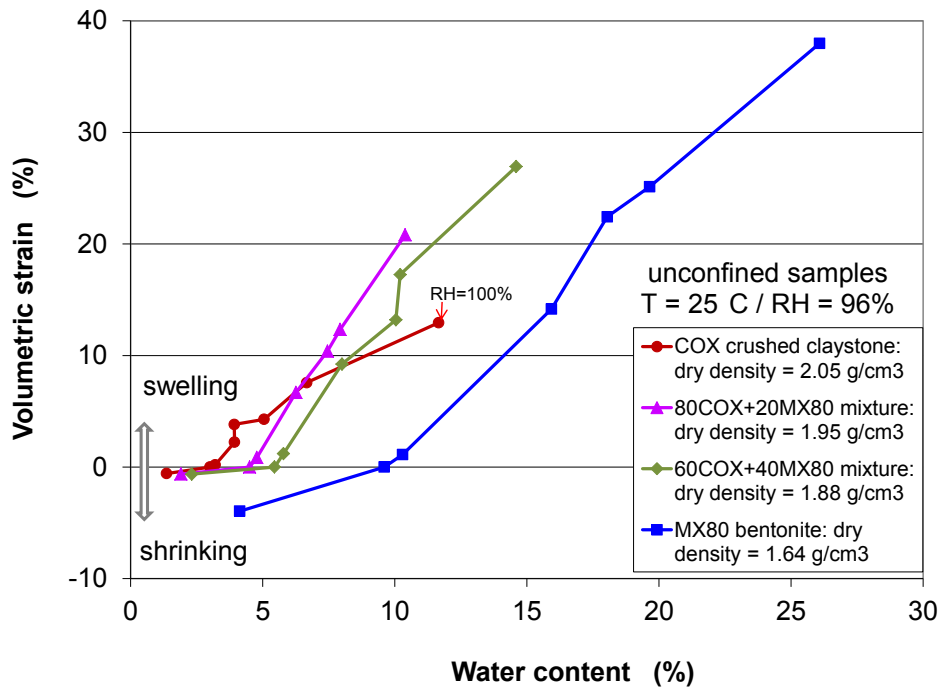
Fig. 3.22 Volumetric strain as a function of water content

3.4.3 Water saturation

Test procedure

For evaluation of the saturation process in the sealing materials, two series of tests were conducted with four samples of different mixtures in steel cylinders of 50 mm diameter and 100 mm length (Fig. 3.23). The initial states of the samples are summarized in Tab. 3.4. The saturation tests were carried out by bringing synthetic COX clay water in contact with the samples at one end face using a burette at atmospheric pressure. The opposite face was connected to the atmosphere via a porous plate.

Results

The recorded evolution of the water uptake is plotted in Fig. 3.24 for each sample. Due to the high initial suction in the relatively dry state, each sample took up water rapidly in the beginning and then the saturation process slowed down with time. The retardation of water migration is primarily caused by the increasing amount of water that is adsorbed in/on the clay minerals. As a consequence (a) suction decreases by increasing the chemical potential of the adsorbed water and (b) increasing swelling of the particles reduces the free pore space and thus the effective permeability.

Fig. 3.23   Test layout for saturation of compacted backfill in steel cylinder

Tab. 3.4   Characteristics of compacted mixtures before water saturation testing

Property	COX claystone	MX80 bentonite	50 COX+ 50 MX80	65 MX80+ 35 Sand
Diameter D [mm]	50.0	50.0	50.0	50.0
Height H [mm]	100.0	100.0	100.0	100.0
Grain size d [mm]	< 10.0	< 0.5	< 10.0	< 2.0
Water content w [%]	4.3	9.6	7.0	6.5
Bulk density ρ_b [g/cm^3]	1.90	1.55	1.90	1.64
Dry density ρ_d [g/cm^3]	1.82	1.42	1.78	1.54
Grain density ρ_s [g/cm^3]	2.70	2.78	2.74	2.72
Total porosity ϕ [%]	32.5	51.0	35.4	43.4
Water saturation S_w [%]	24.1	26.7	35.1	23.1

After saturation over 6 months, the COX sample was fully saturated. For the other three samples, 50 COX+50 MX80-mixture, 65 MX80-35 Sand-mixture and MX80 bentonite, the saturation lasted longer, over 9 to 15 months. After testing the samples were cut into slices of ~10 mm thickness to determine the distribution of water content and density. The data of bulk and dry density, water content and saturation degree obtained by this procedure are illustrated in Fig. 3.25 along with the sample length for each mixture. Because of the presence of some coarse grains the slices could not always be separated by a clean cut, leading to a relatively large scatter of the data. Even though, one can still recognize from the plots that:

a) looking at the water content distribution, the compacted claystone-bentonite mixture with 50/50-ratio seemed to be fully saturated;

b) the water distributed in the compacted bentonite-sand mixture with 65/35-ratio is relatively homogeneous along the total length, and the calculated saturation degrees are close to 100 %, indicating a full saturation over 15 months; and

c) the saturation degrees determined along the pure MX80 bentonite sample lie roughly at 100 % over the whole sample length, suggesting a full saturation over 15 months.
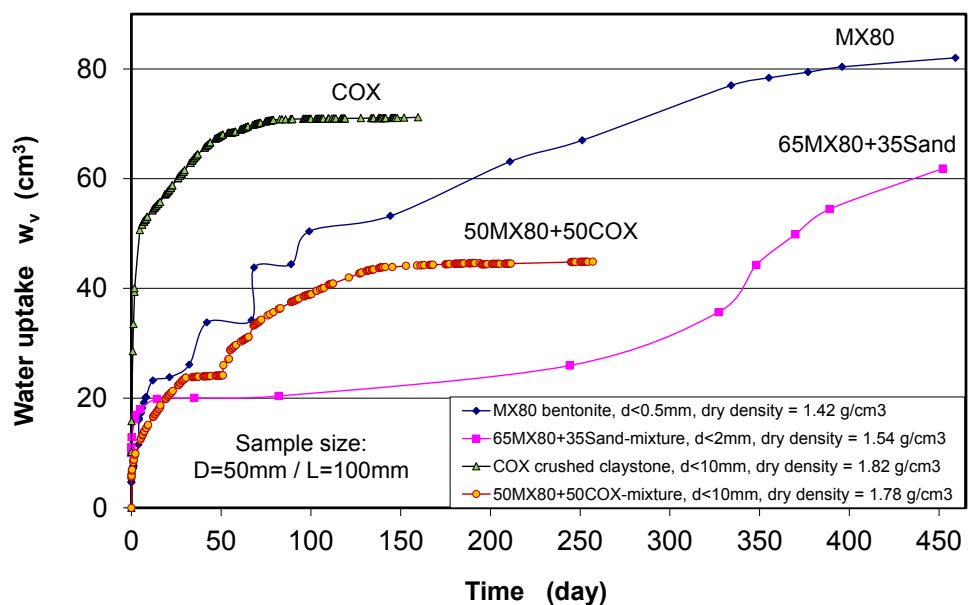
Fig. 3.24   Evolution of water uptake of compacted bentonite-claystone/sand mixtures in contact with synthetic clay water
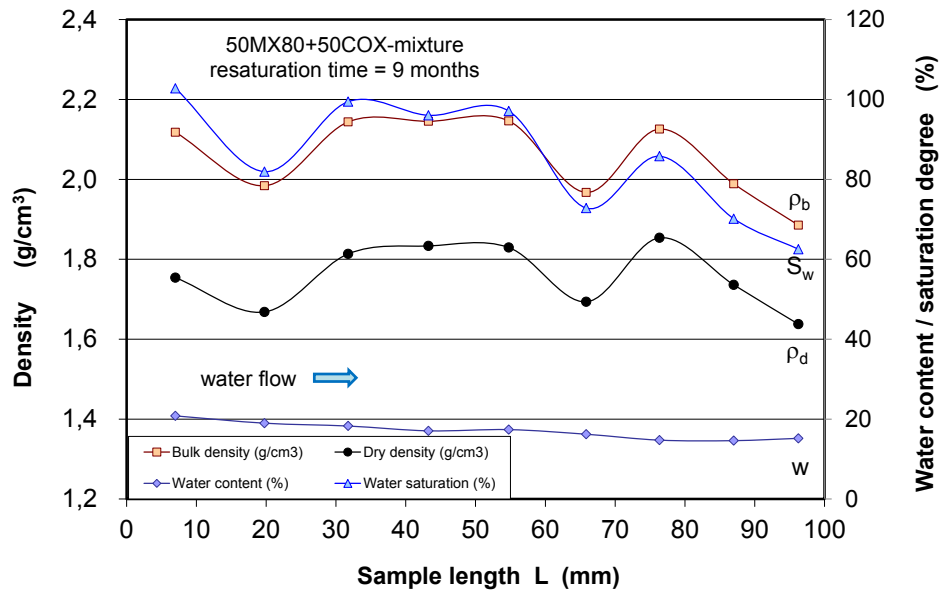
(a) compacted 50 MX80 + 50 COX-mixture after saturation time of 9 months
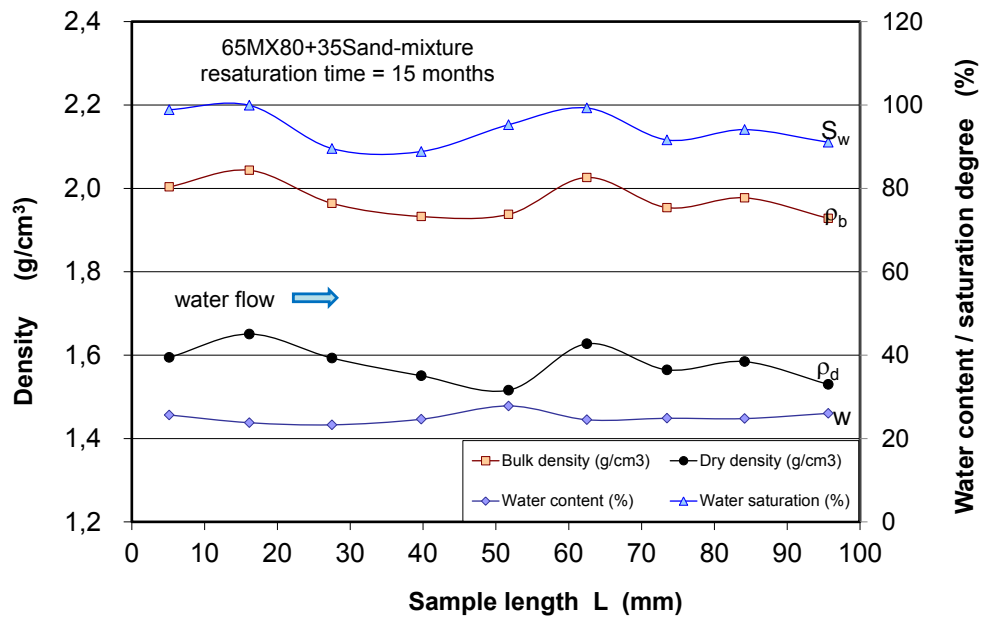
(b) compacted 65 MX80 + 35 Sand-mixture after saturation time of 15 months
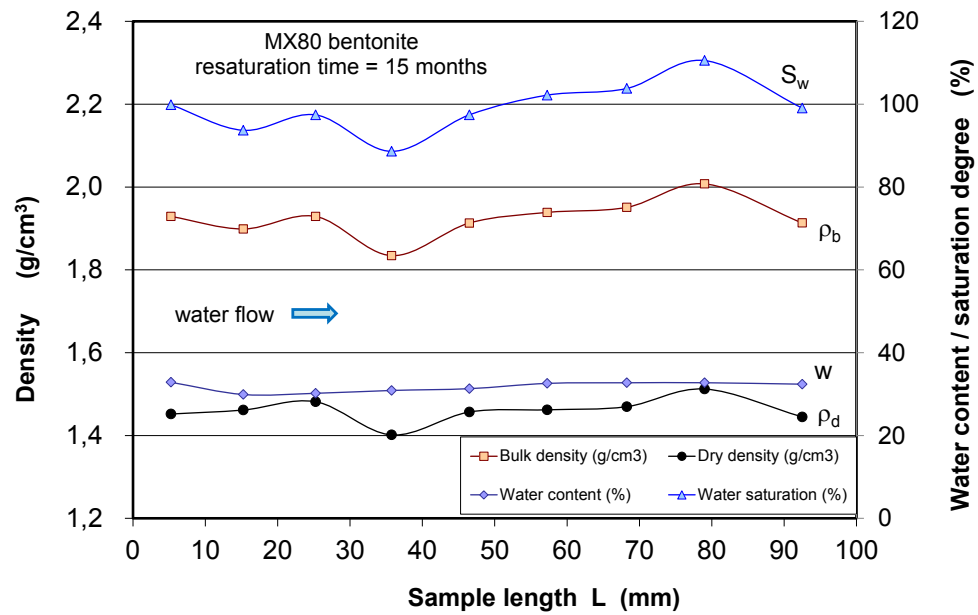
(c) compacted MX80 bentonite after saturation time of 15 months

Fig. 3.25 Distributions of bulk/dry density, water content and saturation in the bentonite-claystone/-sand mixtures after saturation (at different times)

Note: After dismantling it was recognized that corrosion occurred at the metal surface (see the pictures in Fig. 3.26). Corrosion of metal linings and waste containers in repositories will reduce their supporting capacity and can eventually lead to failure of the metallic structures. Additionally, corrosion produces gas whose fate must be known. Gas migration in the geological and engineered barrier system is an important issue for the safety assessment for repositories. This has to be investigated in the future.

(a) 65 MX80 + 35 Sand-mixture

(b) MX80 bentonite

Fig. 3.26 Corrosion of metal cell in contact with synthetic pore water over 15 months

3.4.4 Swelling capacity

Different swelling capacities of the backfill/sealing materials installed in boreholes, drifts and shafts are required to ensure complete hydraulic sealing and also to mechanically withstand ongoing EDZ development or even to support a healing process. The swelling pressure of buffer and backfill depends mainly on its dry density, mineralogy with a particular view to expansive clay minerals, initial water content, and the external boundary conditions such as inflow of water and rock deformation. The swelling pressures of the compacted claystone-bentonite mixtures were determined on the samples with different mixing ratios. The properties of the samples are given in Tab. 3.2.

Swelling pressure

The swelling pressure of the compacted samples with different mixtures was measured in specifically designed cells that are schematically shown in Fig. 3.27. The samples had a length of 50 mm and a diameter of 46 mm which was smaller than the inner cell diameter of 50 mm. The annulus between sample and cell was filled with fine-grained quartz sand with a grain diameter of $d < 0.5$ mm. After installation, the samples were axially pre-loaded to about 5 MPa and then fixed. Realistic conditions for the sealing material after installation implies that it is firstly wetted by humid air and later by liquid water from the surrounding rock Therefore, each sample was first ventilated by circulating air of controlled humidity through the surrounding sand layer and then flooded with synthetic clay water. Response in terms of axial stress was recorded by means of a pressure sensor installed at the top of the cell between load piston and cap. The variation of the axial stress with humidity is herein defined as the swelling pressure.
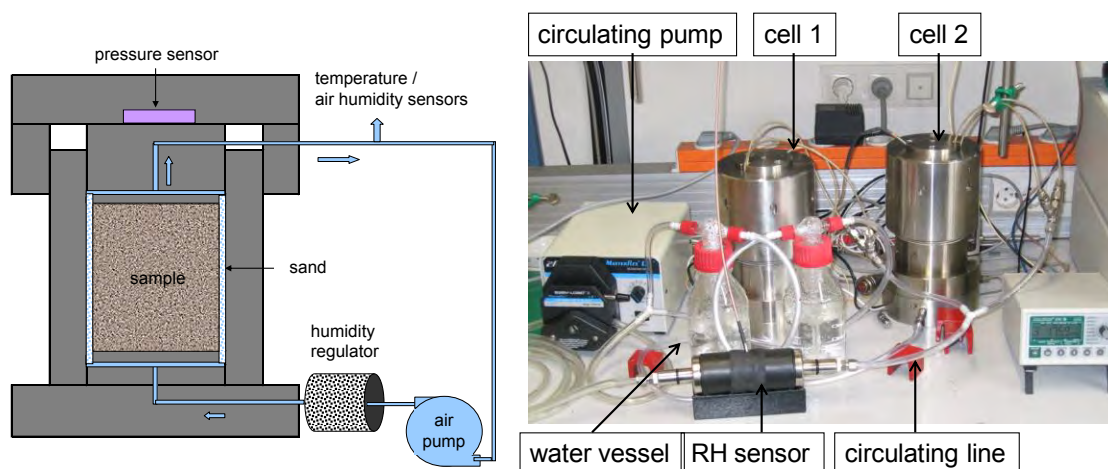
Fig. 3.27   Test setup for swelling pressure measurements on backfill samples

Fig. 3.28 depicts the measured swelling pressures for the samples with compacted pure claystone and with bentonite powder. The stressed samples were firstly dried by dry air leading to a drop of the axial stress from 4.5 MPa down to zero. The subsequent wetting by water vapour rapidly increased the stress to 7.6 MPa in the bentonite and to 3.0 MPa in the compacted claystone powder. Because of the soft lateral confinement represented by the loosely filled sand layer, the highly increased axial swelling pressure exceeded the strength of the compacted bentonite which lead to damage and to a residual strength of ~4 MPa. The lateral swelling of the bentonite consolidated the sand layer and increased the stiffness of the confinement for the sample, thus allowing further increase in the swelling pressure up to 6 MPa.

Finally, water flooding induced a further increase in swelling pressure in the bentonite to a value of 7 MPa due to swelling of remaining unsaturated particles. The swelling pressure obtained here on the compacted MX80 bentonite at a dry density of 1.56 g/cm^3 is comparable with those values reported in literature /DUE 11/, namely 6 to 8 MPa at dry densities of 1.55 to 1.60 g/cm^3. In contrast the stress in the claystone powder decreased down to 1.6 MPa due to wetting-induced weakness of particles and collapse of pore structures under the soft lateral confinement.
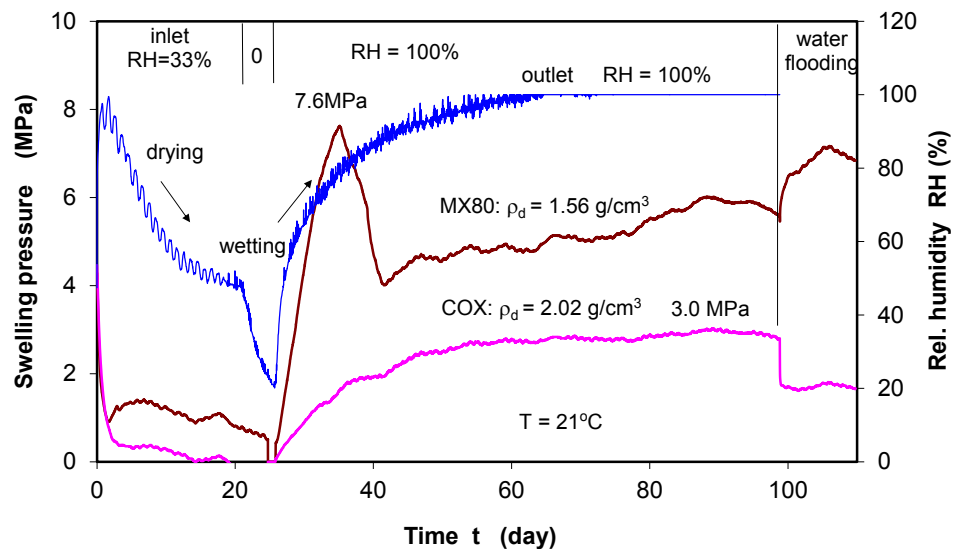
Fig. 3.28   Evolution of swelling pressures measured on compacted COX claystone and MX80 bentonite during air drying/wetting and water flooding

Fig. 3.29 illustrates the swelling pressures in the two samples with compacted claystone-bentonite mixtures (COX/MX80 ratios of 40/60 and 60/40) during air drying/wetting and water flooding. Both samples showed a very similar response of axial

stress to moisture change. After vapour wetting over a month, the increased swelling pressures in both mixtures stabilized at a level of 4.2 to 4.7 MPa. The additional water flooding caused a rapid increase in swelling pressure to 6.0 MPa in both mixtures which remained more or less constant for the remaining time.
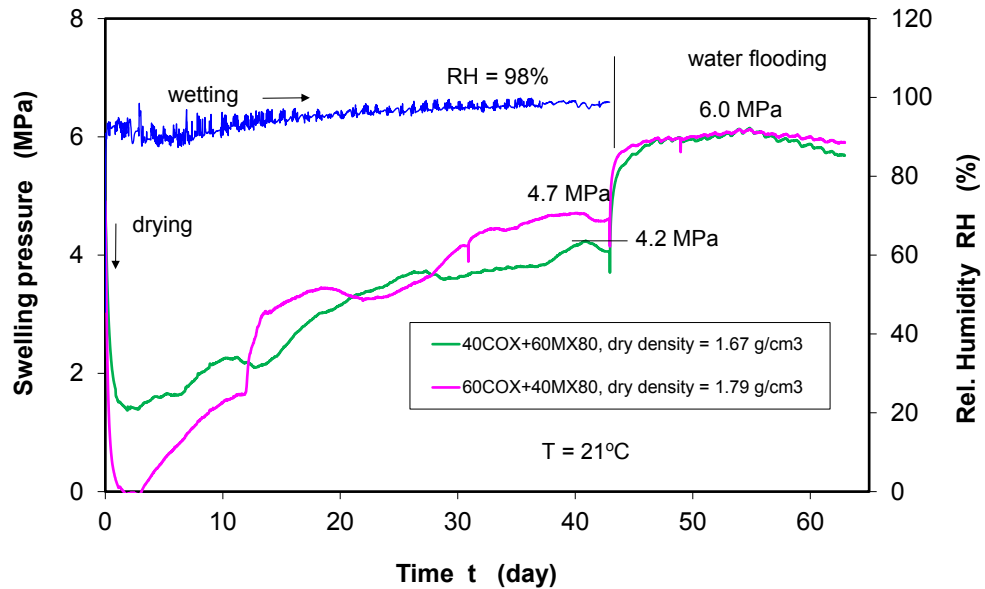
Fig. 3.29 Evolution of swelling pressures of compacted claystone-bentonite mixtures of 40/60 and 60/40 COX/MX80 during air drying/wetting and water flooding

Fig. 3.30 shows another test with another compacted 80 COX+20 MX80 mixture with a lower bentonite content and a water content of 5 %. Wetting with vapour caused an increase in axial stress from 4.5 to 6.5 MPa. The subsequent drying led to a rapid drop down to 1 MPa at RH = 23 %. Wetting again gave rise in the axial stress to 4.7 MPa. Flooding with synthetic pore water, however, resulted in a small drop down to 4 MPa.

In addition to the powdered claystone-bentonite mixtures, another mixture with coarse-grained COX aggregate of $d < 10$ mm and MX80 bentonite powder with a ratio of 50/50 was tested under confined conditions in a cell. One end face of the sample was brought into contact with synthetic clay water. Fig. 3.31 shows the water uptake and the buildup of swelling pressure versus time. Concurrent with water uptake, the swelling pressure increased gradually to the maximum value of 9.5 MPa after 6 months.
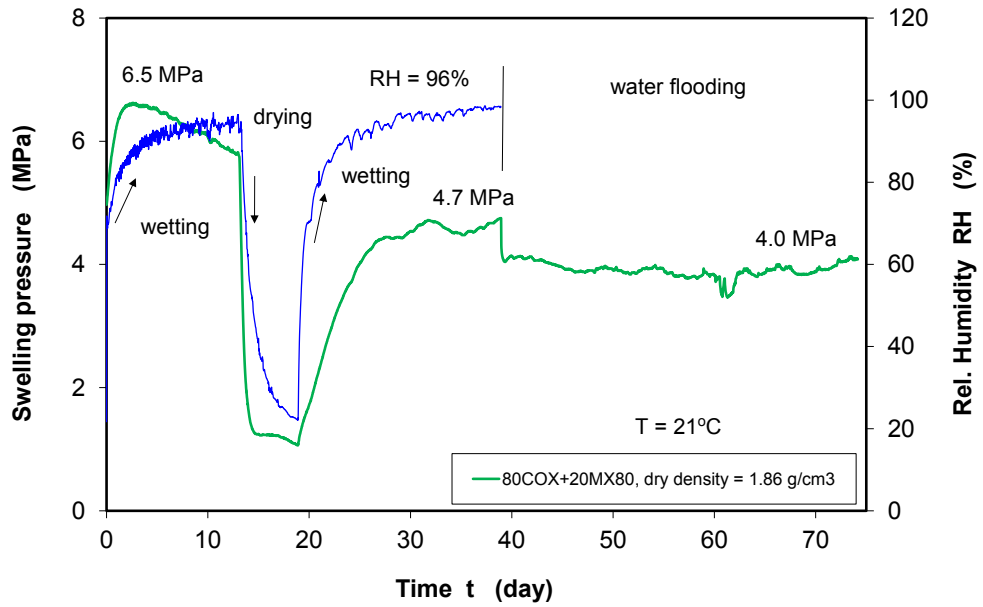
Fig. 3.30 Evolution of swelling pressure of a compacted claystone-bentonite mixture of 80 COX+20 MX80 during air drying/wetting and water flooding
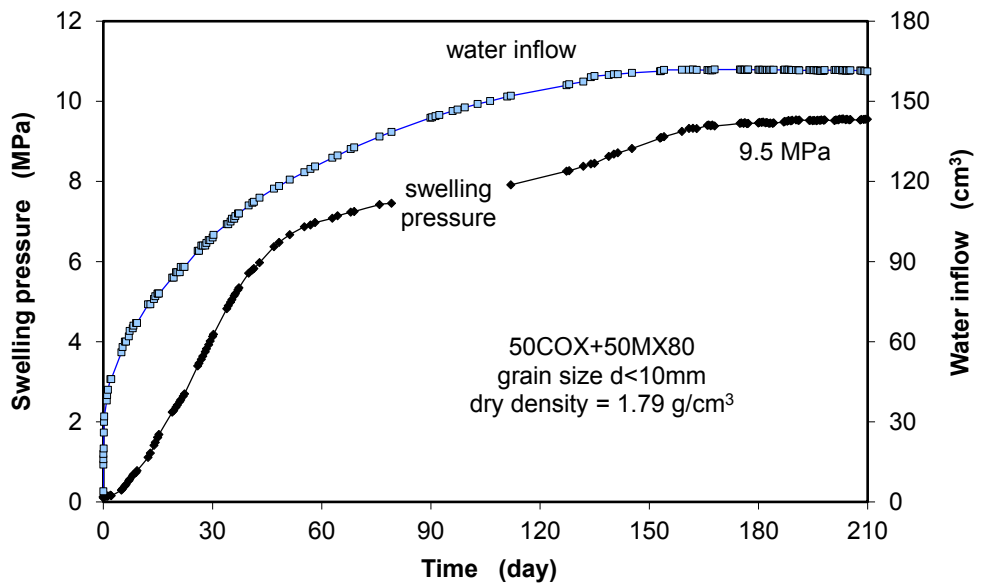
Fig. 3.31 Evolution of swelling pressure of a compacted 50 COX+50 MX80 mixture with coarse grains during water flooding

After 7 months, the swelling test was terminated. The dismantled sample was cut into small discs for the determination of water saturation distribution. Fig. 3.32 shows that the end part of the sample in a length of ~ 10 mm was not fully saturated yet. A picture of the tested sample in Fig. 3.33 indicates a very compact inner structure of the mixture.

189

The pores between COX coarse grains were completely filled with fine-grained bentonite.
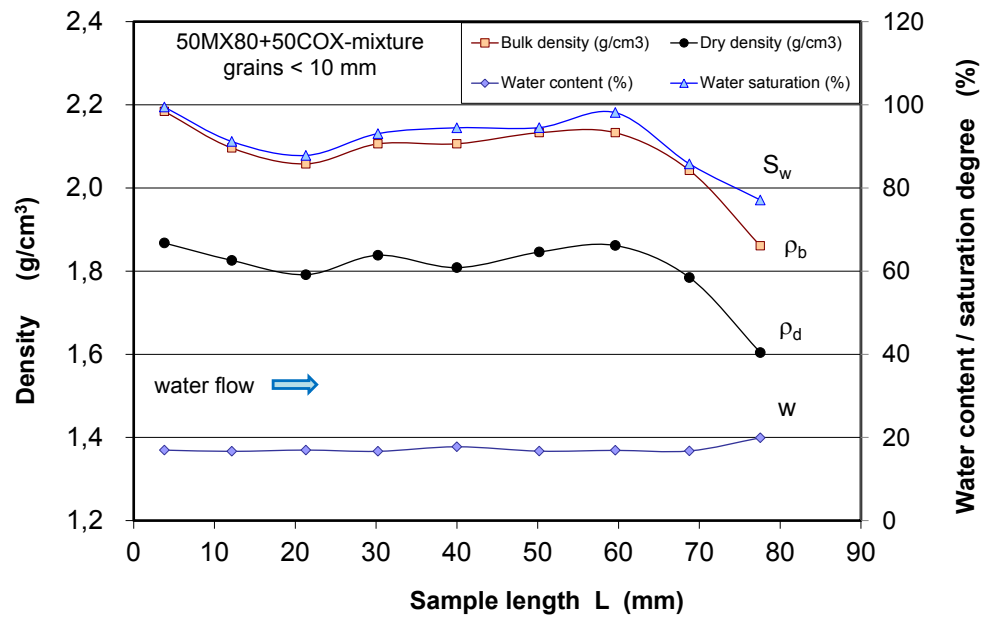
Fig. 3.32 Distributions of bulk/dry density, water content and saturation in the compacted 50 COX+50 MX80 mixture after water flooding over 7 months

Fig. 3.33 Inner structure of the compacted and resaturated 50 COX+50 MX80 mixture at dry density of 1.79 g/cm^3

The maximum swelling pressures of the compacted claystone-bentonite mixtures are given in Tab. 3.2. It is obvious that all the mixtures with claystone contents of 20 % to 80 % and compacted under the same load of 30 MPa exhibit significant and comparable swelling pressures ranging from 6 to 9.5 MPa. Even the pure compacted claystone

shows a swelling pressure of 3 MPa. An optimal mixture would therefore consist of coarse-grained claystone as main component and a fraction of fine-grained bentonite filling the pores in the aggregate, so that the resulting initial porosity is low and the swelling capacity of bentonite high.

Swelling strain

The swelling strain of the compacted mixtures was measured in oedometer cells under constant load. Fig. 3.34 demonstrates the swelling strain curves of two compacted claystone-bentonite mixtures with ratios of 50/50 and 80/20 in correspondence to the water uptake during saturation at an axial load of 1 MPa. Whereas the mixture of 80 % claystone and 20 % bentonite expanded immediately after contact with water and reached a maximum value of 0.34 % after about 3 weeks, the swelling of the mixture with more bentonite content was delayed by several days and reached a value of 2.57 % after 8 months.
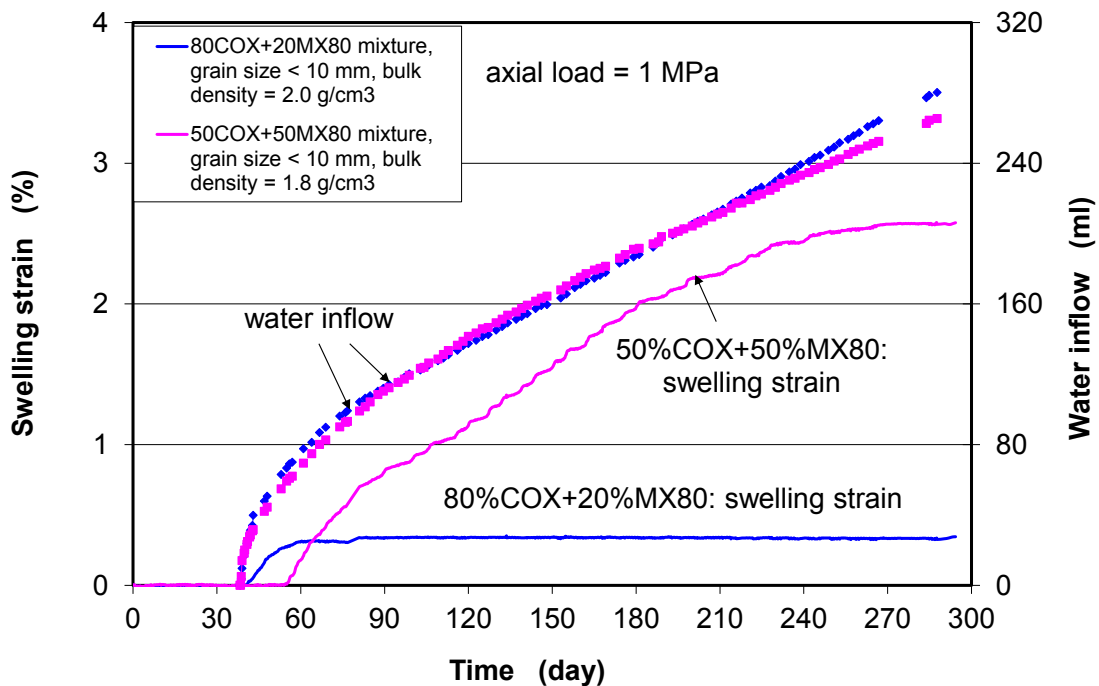
Fig. 3.34   Swelling strains of compacted claystone-bentonite mixtures in ratios of 50/50 and 80/20 during water saturation at an axial load of 1 MPa

3.4.5 Water permeability

Very low hydraulic conductivities are required for the seals, buffer and backfill in a repository since their purpose is to prevent fluid access to the repository and the release of radionuclides from it. This includes to a certain extent also flow through the EDZ. In order to limit the damage in the drift walls and thereby the permeability in the EDZ the swelling material must have the capacity to exert a certain mechanical pressure in the walls. However, volumetric swelling leads also to an increase of permeability in the swelling material itself. In an in situ drift sealing experiment (KEY) was therefore demonstrated that it is possible to achieve an overall seal permeability of less than $10^{-17}\,\text{m}^2$ by an appropriate choice of sealing material /DEL 07/. As a main component of the EBS, the compacted materials or blocks must exhibit lower permeabilities than that required on the whole EBS system.

Within this project, water permeabilities of crushed claystone and three compacted claystone-bentonite mixtures with COX/MX80 ratios of 80/20, 60/40 and 40/60 were determined. The characteristics of the compacted mixtures are given in Tab. 3.2. The compacted COX powder and MX80 bentonite with grains of $d < 0.5\,\text{mm}$ were confined in small oedometer cells of 50 mm diameter, while the coarse aggregate of $d < 10\,\text{mm}$ was tested in a large cell of 100 mm diameter as shown in Fig. 3.35. After a water uptake over two weeks, the measurement of water permeability was carried out for two months at a constant injection pressure of 1.0 MPa.

Fig. 3.35   Test setup for measurement of water permeability of backfill materials

The water permeability as a function of porosity obtained from samples with the coarse-grained claystone aggregate has been shown previously in Fig. 3.16 as well as the related gas permeability. The water permeability decreases with decreasing porosity from the initial value of $K_o = 1 \cdot 10^{-13}\,\text{m}^2$ at $\phi_o = 45\,\%$ down to $K_w = 2 \cdot 10^{-19}\,\text{m}^2$ at $\phi = 30\,\%$.

Fig. 3.36 shows the water permeability data for the three samples with the compacted mixtures versus time. It is obvious that the permeability values of all compacted mixtures are quite low and keep more or less constant at $K_w = 2 \cdot 10^{-19}\,\text{m}^2$ for 80 COX+20 MX80, $K_w = 3 \cdot 10^{-20}\,\text{m}^2$ for 60 COX+40 MX80, and $K_w = 2 \cdot 10^{-20}\,\text{m}^2$ for 40 COX+60 MX80. The very low water permeability values of the compacted mixtures are comparable with that of intact rock ($K_w < 10^{-20}\,\text{m}^2$). From the point of view of low hydraulic conductivity, all the tested mixtures are suitable as sealing materials. However, a bentonite content of 40 % or higher seems to increase the effectiveness of a claystone-bentonite mixture as a hydraulic barrier. Note, that this holds true despite the fact that the dry density for the mixture with only 20 % bentonite content was significantly higher than that of the other mixtures.
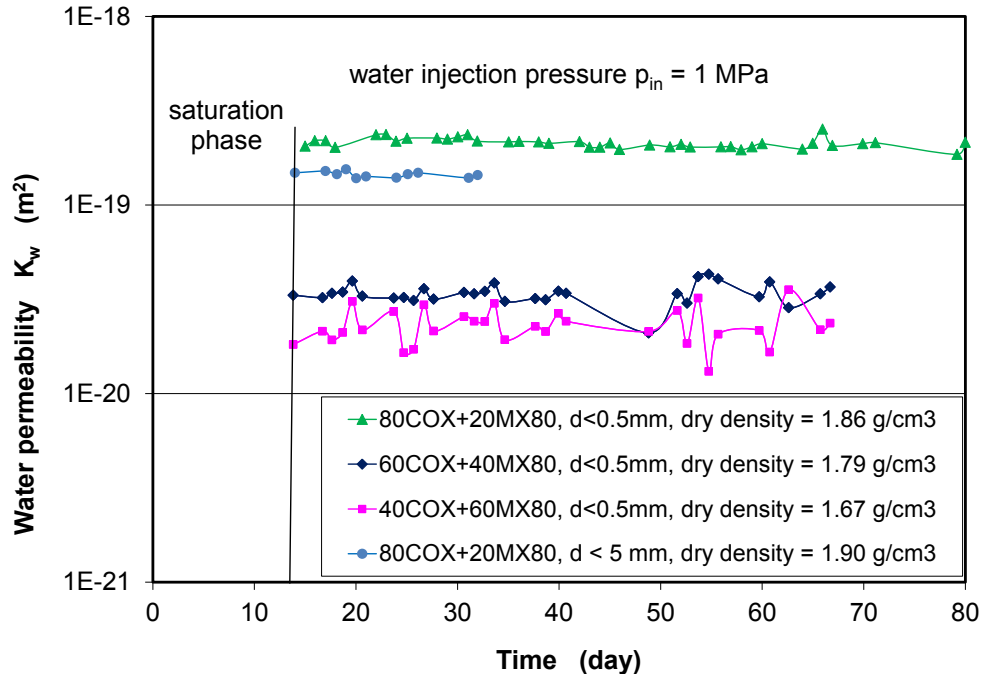
Fig. 3.36 Water permeability measured on compacted claystone-bentonite mixtures with COX/MX80 ratios of 80/20, 60/40 and 40/60

3.4.6 Thermal conductivity

As the excavated claystone and claystone-bentonite mixtures are considered to be used as buffer material surrounding high-level radioactive waste containers, knowledge of their thermal properties is required for analyses of the thermal processes in the buffer as well as in the nearfield of the repository. In the framework of this investigation programme, the thermal properties of crushed COX claystone with grain sizes of $d <$ 10 mm were characterized as a function of porosity and water saturation.

Heat capacity of a material is its capacity to store thermal energy which is defined by the first derivative of heat content of the material with respect to temperature:

$$C = \frac{dQ}{m\,dT} \approx \frac{\Delta Q}{m\,\Delta T} \qquad (3.6)$$

where
    C = specific heat capacity (J/kgK),
    ΔQ = increment of heat quantity (J),
    m = mass (kg),
    ΔT = temperature change (K).

Thermal conductivity is defined as the capacity of a material to conduct or transmit heat. This is the coefficient λ in Fourier's first law of heat conduction:

$$q = -\lambda\,\nabla T \qquad (3.7)$$

where
    q = heat flux (W/m^2),
    λ = thermal conductivity (W/mK),
    ∇ = differential operator, and
    ∇T = temperature gradient (K/m).

Thermal diffusivity is the coefficient κ in Fourier's second law – also called "diffusivity equation" – describing the transient heat transfer:

$$\nabla^2 q = -\frac{1}{\kappa}\frac{\partial T}{\partial t} \qquad (3.8)$$

where
    κ = thermal diffusivity (m^2/s), t = time (s).

Thermal diffusivity is related to other thermal properties as:

$$\kappa = \frac{\lambda}{C\,\rho} \qquad (3.9)$$

where

ρ = bulk density (kg/m^3).

Combining equations (3.6), (3.7) and (3.8), the heat conduction equation (3.7) can be expressed by

$$\nabla(\lambda\nabla\mathrm{T}) = C\,\rho\,\frac{\partial T}{\partial t} \qquad (3.10)$$

Test procedure

The coarse-grained aggregate with grain sizes of $d < 10\,\mathrm{mm}$ was tested under confined conditions. The initial water content was about 7.0 %. Cylindrical discs of 50 mm diameter and 20 mm height were prepared by compacting the crushed claystone to different dry densities of ρ_d = 1.82 to 1.93 g/cm^3. The corresponding porosities were calculated to amount to ϕ = 28.5 % to 32.5 %. Fig. 3.37 presents the photos of some moulded samples.

Fig. 3.37   Photos of moulded claystone aggregate for measurements

In order to investigate effects of water content on the thermal properties, the samples were de- and resaturated in desiccators at various constant humidity conditions adjust-

ed by means of different salt solutions over 7 days each. When equilibrium was achieved, the water content, bulk density and porosity were determined. Fig. 3.38 summarizes the bulk densities recorded at various water contents for the samples. The water contents of the samples wetted with water vapour at RH = 100 % reached values of w = 13 % to 16 %, about two times of the initial water content of the natural clay rock. This suggests a great water adsorption potential of the claystone. Under confined conditions the bulk density is linearly related with the water content: $\rho = \rho_d(1 - w)$, where ρ = bulk density, ρ_d = dry density and w = water content (-). Based on the obtained data, the degree of water saturation S_w can be calculated by

$$S_w = \frac{\rho_d w}{\rho_w \phi}$$

(3.11)

where
ρ_d = dry density,
ρ_w = water density,
w = water content,
ϕ = porosity.
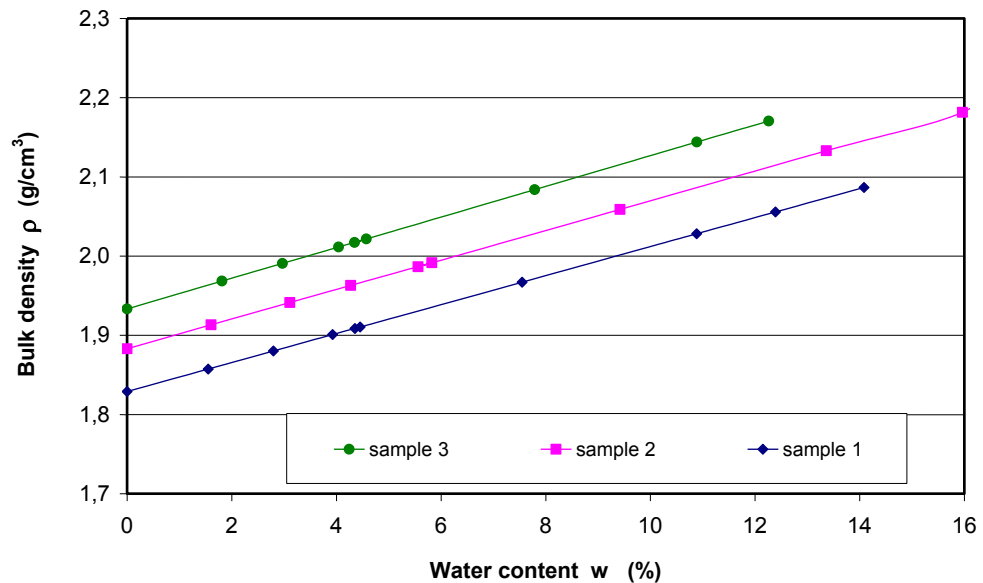
Fig. 3.38 Measured bulk densities at various water contents

Porosity as a function of water saturation due to the de-/resaturation procedure described above is depicted in Fig. 3.39. At a water saturation below $S_w \approx 30\%$ ($w < 4\%$), the porosity maintained more or less constant, while above this value the porosity increased non-linearly with increasing water saturation by $\Delta\phi = 1 - 2\%$ at $S_w \approx 80 - 90\%$. This indicates a certain swelling capacity of the compacted crushed claystone.
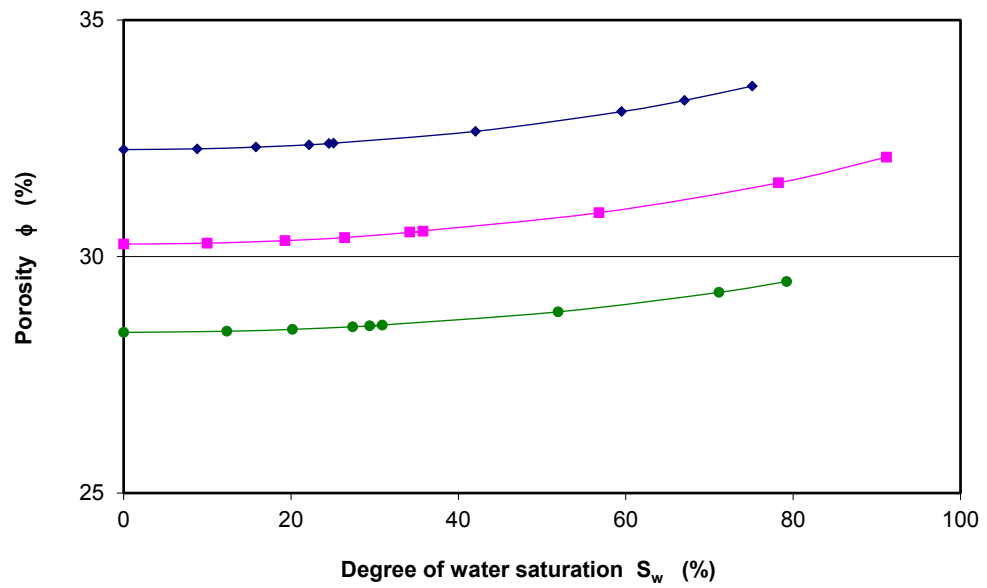
Fig. 3.39 Porosity variation in relation with water saturation

sensor position

heat input

sample installed
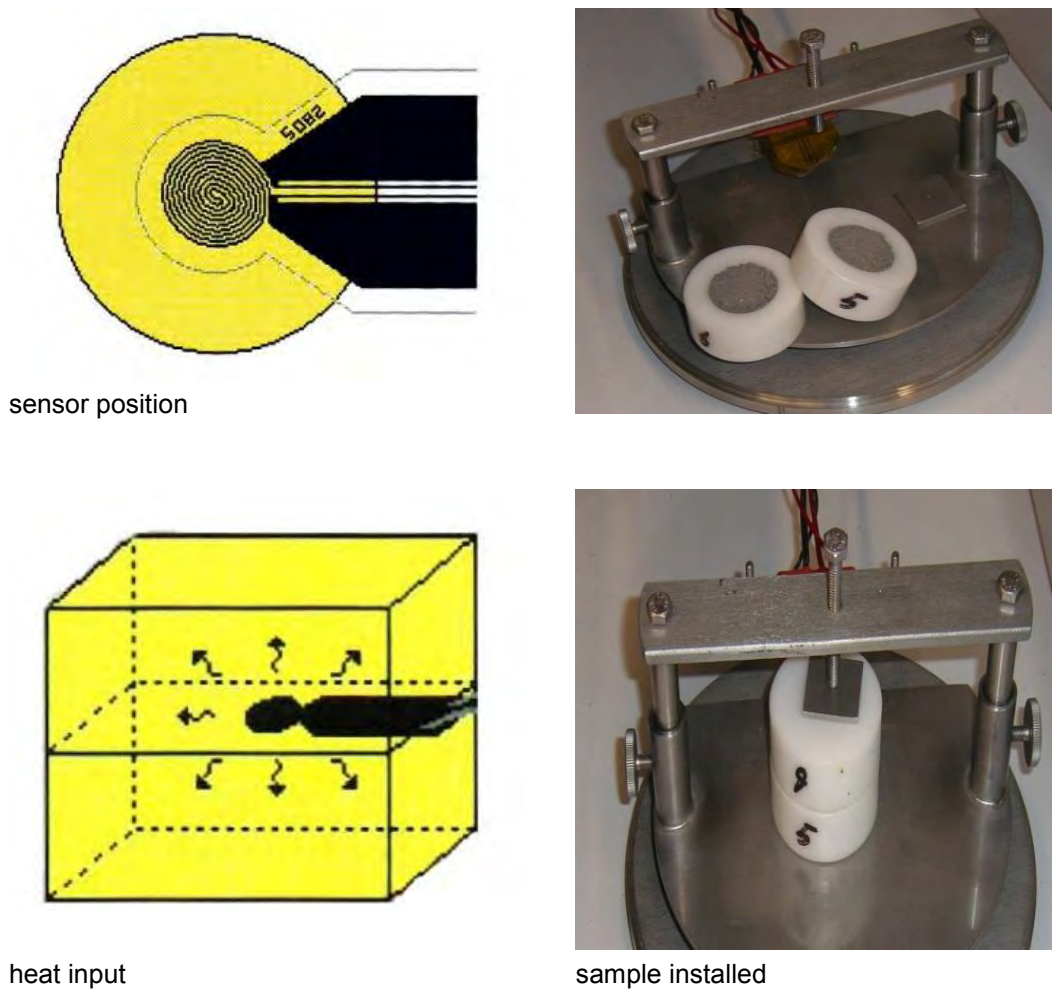
Fig. 3.40 Principle of Hot Disk measurement of thermal parameters

197

Thermal properties of the samples were measured with the Hot Disk Thermal Constants Analyser /HOT 07/. The testing method is based on the use of a heated sensor in the shape of a double spiral. The sensor is fitted between two pieces of a sample – each one with a plane surface facing the sensor, as shown in Fig. 3.40. The Hot Disk sensor acts as a heat source for increasing the temperature of the sample and at the same time as a "resistance thermometer" for recording the time dependent temperature increase. The heat conduction equation is solved assuming that the sensor consists of a certain number of concentric ring-like heat sources located in an infinitely large sample. Details of the experimental technique is given in /HOT 07/.

Results

Values of specific heat capacity measured on the samples with porosities of ϕ = 28.5 to 32.5 % are illustrated in Fig. 3.41 as a function of water saturation at different initial porosities ($n = \phi$). The resulting values for the specific heat capacity vary in a range between 800 and 1000 J/(kgK) from the dry to saturated state, without a noticeable dependency on the porosity and with only very little influence of saturation. The use of a mean value of C = 900 J/(kgK) would therefore be justified.
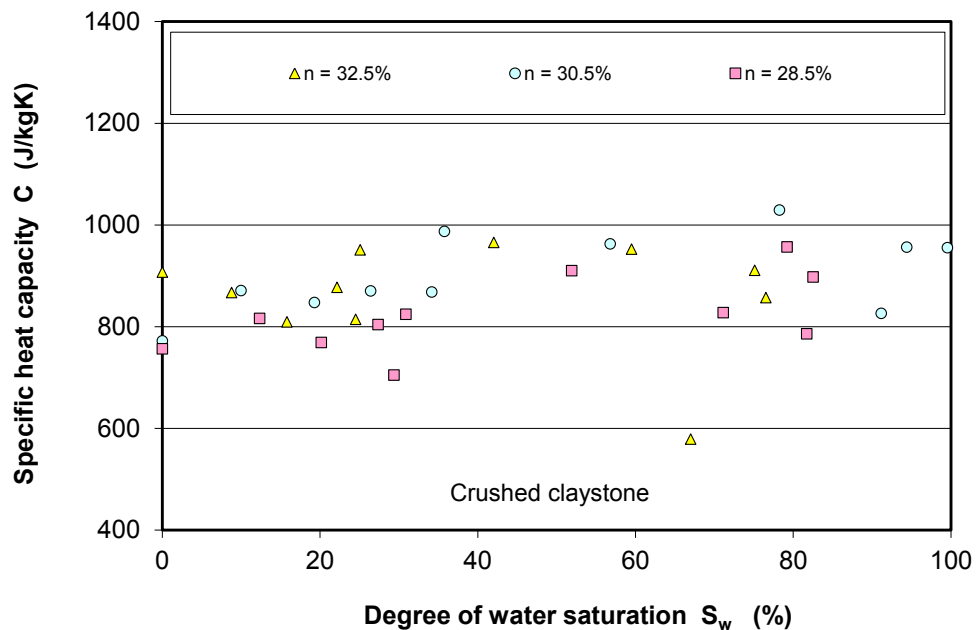
Fig. 3.41   Specific heat capacity in dependence on water saturation

The conductivity and diffusivity values are plotted vs. degree of water saturation in Fig. 3.42 and Fig. 3.43, respectively. Even though the data from each sample show a

relatively large scatter, a tendency of increase in both thermal conductivity and diffusivity with water saturation can be identified. These relationships may be approached by the geometric mean model

$$\lambda = \lambda_{sat}^{S_w} \cdot \lambda_{dry}^{(1-S_w)} \left(\frac{\phi_o}{\phi} \right)^{\beta} \qquad (3.12)$$

$$\kappa = \kappa_{sat}^{S_w} \cdot \kappa_{dry}^{(1-S_w)} \left(\frac{\phi_o}{\phi} \right)^{\beta} \qquad (3.13)$$

where λ, κ = thermal conductivity and diffusivity of an unsaturated soil, λ_{sat}, κ_{sat} = thermal conductivity and diffusivity of saturated claystone, λ_{dry}, κ_{dry} = thermal conductivity and diffusivity of dried claystone, ϕ_o, ϕ = porosity of intact claystone and porous aggregate, S_w = degree of water saturation, and β = fitting parameter. Parameter values determined for the intact claystone are ϕ_o = 15 %, λ_{dry} = 1.2 W/mK, λ_{sat} = 2.3 W/mK, κ_{dry} = 0.77·10⁻⁶ m²/s, κ_{sat} = 1.1·10⁻⁶ m²/s, and β = 0.5. With these parameters the thermal conductivity and diffusivity of the unsaturated aggregate are calculated according to Equations (3.12) and (3.13). The resulting curves are compared with the measured data in Fig. 3.42 and Fig. 3.43. Apparently, the data can be reasonably well represented by the mathematical models.
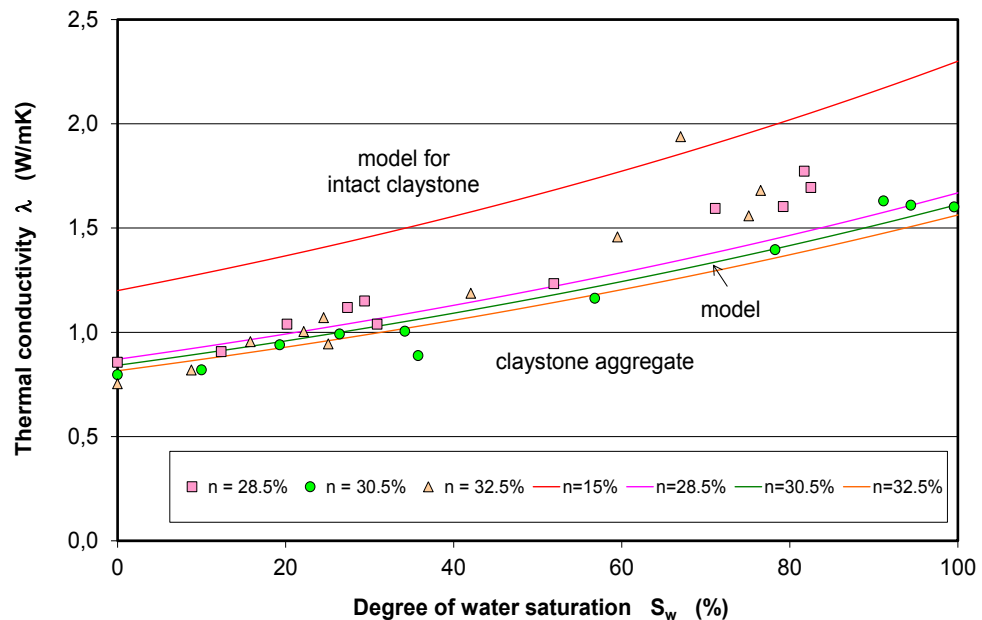
Fig. 3.42   Thermal conductivity of compacted claystone aggregate as a function of water saturation and porosity

199
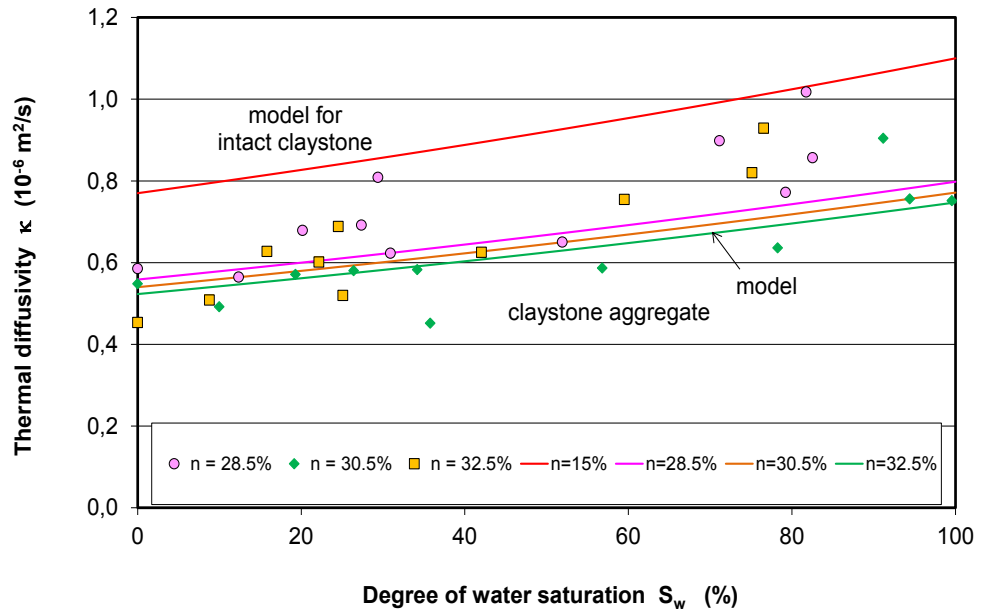
Fig. 3.43 Thermal diffusivity of compacted claystone aggregate as a function of water saturation and porosity

The thermal conductivities of the compacted claystone aggregate at a dry density of 1.80 to 1.93 g/cm^3 are somewhat higher than the 0.4 to 1.3 Wm^{-1}K^{-1} reported for FEBEX bentonite at a dry density of 1.57 to 1.72 g/cm^3 /HUE 00/ and the 0.4 to 1.0 Wm^{-1}K^{-1} found for MX80 bentonite at a dry density of 1.45 to 1.80 g/cm^3 /TAN 10b/. The data of both bentonites are represented in Fig. 3.44.

FEBEX bentonite; from /HUE 00/   MX80 bentonite; from /TAN 10a/
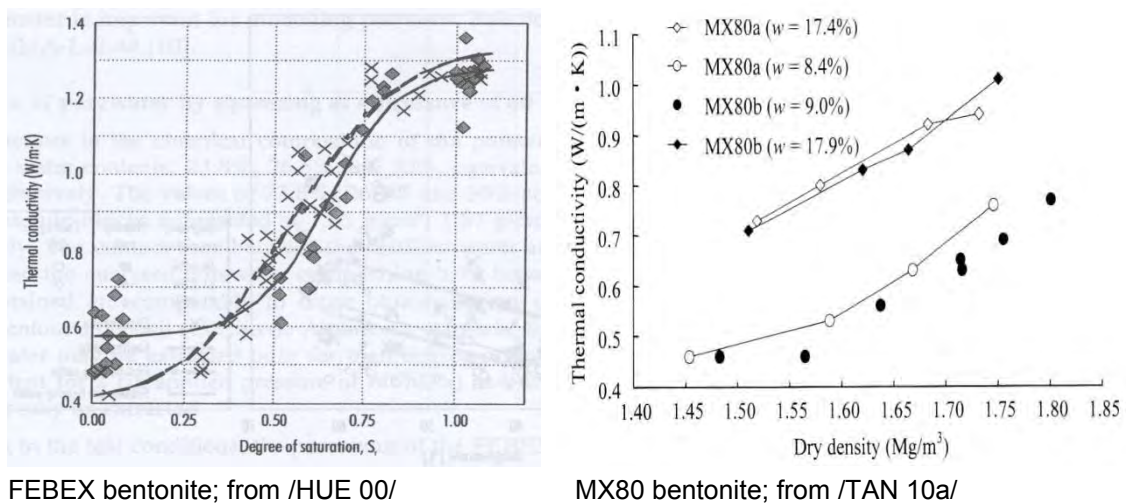
Fig. 3.44 Thermal conductivity of compacted FEBEX/MX80 bentonites as a function of water saturation /HUE 00/ and dry density /TAN 10/

200

3.5 Conclusions on claystone-based backfill/sealing materials

Excavated raw claystone as backfill material and compacted claystone-bentonite mixtures as sealing material have been comprehensively investigated. All materials exhibit favourable geotechnical properties with respect to their barrier function to prevent a release of radionuclides from a repository into the biosphere.

As backfill material, the coarse-grained claystone aggregate with grain sizes of less than 32 mm can be compacted from the initial porosities of 32 – 46 % to a low level of ~20 % as the applied stress increases to 12 – 16 MPa. The compaction of the material is mainly determined by applied mean stress, temperature, time or rate, water content, and grain size. The compaction leads to a decrease in permeability. It was found that (a) the water permeability is much lower than the gas permeability and (b) the permeability of the coarse-grained aggregate is higher than that of the fine-grained material at a given porosity. The low water permeability is mainly attributed to the effects of water-induced swelling of clay grains with a subsequent clogging of the pores. The permeability decreases much faster at porosities below ~25 % for gas flow and below ~30 % for water flow due to an increasing disconnection of the flow channels in the pore network. In the low porosity regions, the measured intrinsic permeability values of 10^{-19} to 10^{-21} m^2 are comparable with that of the intact rock (10^{-20} to 10^{-21} m^2).

As sealing material, compacted claystone-bentonite mixtures with different ratios of COX/MX80 = 0/100, 40/60, 50/50, 60/40, 80/20 and 100/0 were prepared by compaction at a pressure of 30 MPa. By application of the same energy, the dry density increases with increasing claystone content in the mixtures from 1.56 g/cm^3 for pure bentonite to 2.00 g/cm^3 for the claystone aggregate. The most important geotechnical properties of the compacted mixtures are characterized as follows:

- The water retention capacity of the claystone-bentonite mixtures increases with the fraction of bentonite. All the mixtures can take up large amounts of water from a humid environment ranging up from 12 % for the claystone aggregate and more than 50 % for pure bentonite under unconfined conditions.

- With water uptake, the unconfined mixtures expand from a volumetric increase of 12 % for the claystone aggregate up to 40 % for the pure bentonite. The swelling capacity is thus directly proportional to the bentonite content of the mixture.

- In axially-fixed and laterally-soft confined conditions, hydration causes a swelling pressure with a maximum in the rigid axial direction. The maximum swelling pres-

sures recorded vary between 3 MPa for the claystone aggregate and 8 MPa for the pure bentonite. Under constant-volume conditions, a rather high swelling pressure of 9.5 MPa was found for a compacted COX/MX80-mixture with a ratio of 50/50 and with coarse claystone grains up to 10 mm in size. All studied mixtures exhibit sufficiently high swelling capacities to meet the requirements for sealing materials.

- All compacted claystone-bentonite mixtures show very low water permeabilities. Determined was a range of 10^{-19} to 10^{-20} m^2 which is close to the values for intact clay rock. With regard to hydraulic conductivity, all the tested mixtures are suitable as sealing materials.

- Thermal properties of compacted claystone aggregate are dependent on the porosity and water saturation. On average, the specific heat capacity is about 900 Jkg^{-1}K^{-1}, the thermal conductivity increases with water saturation from 0.8 Wm^{-1}K^{-1} at dry conditions to 1.6 Wm^{-1}K^{-1} at saturated conditions. The thermal properties of compacted claystone are comparable with those of compacted bentonite.

These results encourage continuing the investigations on excavated claystone and claystone-bentonite mixtures as materials for engineered barrier systems with regard to the specific functional requirements. Further work should comprise the development of constitutive models describing the THM behaviour, and prediction of the long-term performance of the engineered barriers considering interactions with the openings support and the surrounding rock. This will be done in the framework of the newly launched EC project DOPAS – Full Scale Demonstration of Plugs and Seals /DOP 12/.

4 Summary and conclusions

4.1 Objectives and scope of the investigations

Clay formations are being investigated as a host medium for deep disposal of radioactive waste because of their favourable properties such as very low hydraulic conductivity against fluid transport, good sorption capacity for the retardation of radionuclides, and a high potential of self-sealing of excavation damaged zones. The construction of a repository, the disposal of heat-emitting high-level radioactive waste, the backfill and sealing of the rest of the cavities, however, will inevitably induce mechanical, hydraulic, thermal and chemical disturbances to the host formation over very long periods of time. The responses and resulting property changes of the clay host rock and engineered barriers are to be well understood, characterized, and predicted for assessing the long-term performance and safety of the repository.

In accordance with the R&D programme defined by the German Federal Ministry of Economics and Technology (BMWi), GRS has intensively performed site-independent research work on indurated clays during the last decade. Most of the investigations have been carried out on the Callovo-Oxfordian argillite and the Opalinus clay by participation in international research projects conducted at the underground research laboratories at Bure in France (MHM-URL) and Mont-Terri in Switzerland (MT-URL).

Within the THM-TON project i. e. the time period from May 2007 to May 2013, comprehensive laboratory investigations, in situ experiments and model simulations have been carried out:

- Laboratory investigations on the Callovo-Oxfordian and Opalinus clay rocks

    - Examination of effective stress and swelling pressure in indurated clay rock by taking bound porewater into account

    - Short-term deformation, damage and induced permeability change in the clay host rock, which will be produced by excavation of a repository

    - Long-term deformation of the clay host rock, which controls the closure process of the repository openings and the integrity of the geological and engineered barriers

- Swelling capability of the clay host rock, which will dominate the sealing process of the EDZ when water arrives

- Self-sealing of the EDZ, which is presently one of the highest concerns in the assessment of the long-term performance and safety of the repository because it has direct impact on the hydraulics and mechanics in the nearfield

- Thermal impact on the hydro-mechanical behaviour and the integrity of the clay host rock

- Laboratory investigations on excavated claystone and claystone-bentonite mixtures as backfill/sealing materials

  - Compaction behaviour of claystone aggregate as backfill material, which controls the mechanical interactions with support linings (if existing) and the surrounding rock, and also determines the evolution of the backfill porosity and hydraulic conductivity

  - Permeability–porosity-relation, which controls the fluid transport and thus the hydraulic long-term barrier function of the backfill

  - Water retention capacity, which influences the water saturation process and storage, water/gas two-phase flow, and build-up of swelling pressure in clay-based backfill/sealing materials

  - Swelling pressure in compacted claystone-bentonite mixtures is required for sealing of possibly remaining gaps within the seals and seal/rock interfaces and for supporting the surrounding rock against damage propagation

  - Thermal conductivity of buffer surrounding HLW containers, which controls the heat transfer and temperature distribution in the multi-barrier-system

- In situ investigation of hydro-mechanical responses of the Opalinus clay to the excavation of the gallery G08 within the mine-by (MB) experiment in the MT-URL

- Monitoring of long-term deformation of a borehole in the Opalinus clay at MT-URL (BD experiment)

- Numerical modelling and analysis of coupled HM processes in the Opalinus clay rock during the MB and BD experiments performed at the MT-URL and coupled THM processes in the Callovo-Oxfordian argillite during the TED heating experiments conducted at the MHM-URL

The most important results and conclusions from the laboratory investigations are summarized in the next subsections.

4.2　　　The THM behaviour of clay rocks

Comprehensive laboratory experiments have been performed to investigate the THM behaviour of the COX and OPA clay rocks under conditions to be expected in repositories.

Stress concept

In natural argillaceous rocks, a considerable fraction of the pore water is adsorbed on the internal and external surfaces of clay particles due to physico-chemical interactions. Stresses between clay particles must therefore at least partially be transferred through the adsorbed porewater rather than directly via solid-to-solid grain contacts. Based on the microstructure of the studied COX and OPA clay rocks, a stress concept has been established and experimentally validated. It suggests that the effective stress in a dense clay-water system is transferred through both interparticle bound porewater in narrow pores and solid-solid contacts between accessory minerals. The disjoining or swelling pressure exerted by the interparticle water-films due to physico-chemical interactions exceeds the pressure in large pores that are occupied by free water. The swelling pressure and the effective stress are related linearly to the effective degree of water saturation. The effective stress in clay rock consists of three parts: $\sigma_{eff} = \sigma_s + \pi_D S_e + \pi_o(\Delta w)$, a) the stress σ_s acting at solid-solid contact area, b) the swelling pressure $\pi_D S_e$ acting in the interparticle bound porewater and depending on the effective saturation S_e, and c) the swelling pressure $\pi_o(\Delta w)$ in saturated state depending on the water uptake Δw. In the very dense COX and OPA claystones, most of the porewater is adsorbed to the mineral surfaces and capable of bearing external loads as high as the lithostatic stresses and even bearing shear stresses as high as the material strength. This stress concept provides a reasonable view to the nature of the effective stress in argillaceous rocks and forms the fundamental basis for studying the coupled THMC processes such as the stress-strain behaviour, time-dependent deformation, moisture effects on the stiffness and strength, water and gas transport, sealing and healing of fractures, thermal and chemical impacts. However, further validation of this stress concept needs more information from investigations on the nano- to microscopic structures of the clay rocks.

Deformation, damage and permeability change

The short-term deformation of clay rock is typically characterized by elasto-plastic be-haviour. However, when yield stresses are reached, microcracks are initiated. Further growth and propagation of the microcracks with an increase of stress result in a transi-tion from the volume compaction to dilation at the dilatant threshold. Beyond that, the crack propagation becomes unstable until failure. As a fracture network is forming, the initially very low permeability of the clay rock jumps up over several orders of magni-tude, depending on the minimum confining stress. The yield, dilatant, and peak strengths increase with increasing the minimum principal stress. The peak strength can be reasonably well approached by the Hoek-Brown criterion: $\sigma_1 = \sigma_3 + (m \cdot \sigma_c \cdot \sigma_3 + s\sigma_c^2)^{1/2}$, where the uniaxial compression strength σ_c = 14 MPa, the parameter m = 9, and s = 1 are estimated for the COX clay rock. It was also found that the ratios of the yield stress σ_Y and dilatant stress σ_D to the peak strength σ_F are relatively constant: σ_Y/σ_F = 0.55 and σ_D/σ_F = 0.75. So the yield and dilatancy boundaries are defined. The residual strength is determined by the parameters m = 5 and s = 0 in the Hoek-Brown criterion.

Time-dependent deformation

The deformation of the COX and OPA clay rocks is time dependent. The samples creep already under extremely low stresses of less than 1 MPa, indicating negligible stress threshold for creep. The creep behaviour is also stress path dependent. Creep under increased load is characterized by a transient phase and a following stationary phase, while creep under decreased load leads to initially negative rates (expansion) with a subsequent phase of positive creep rates. Steady-state creep rates under low stresses below the damage threshold vary insignificantly with applied stresses. Above the damage boundary, creep is accelerated to rupture due to the propagation of mi-crocracks. The creep of saturated claystone is probably governed by slips and ruptures of interparticle bound water-films between mineral particles. The dependence of the stationary shear creep rate on deviatoric stress can be expressed by a hyperbolic sine equation proposed herein: $\dot{\varepsilon} = A \exp(-Q/RT) \cdot \sinh(\alpha\sigma)$, where $\dot{\varepsilon}$ = stationary shear creep rate, σ = shear stress, T = absolute temperature, R = universal gas constant, Q = activation energy, A and α = parameters. Based on the creep rate data obtained from the triaxial tests on the nearly-saturated samples in a temperature range of 20 to

100 °C, these parameters are preliminarily established for the saturated COX clay rock: A = 2.5·10^{-4} s^{-1}, α = 0.2 MPa^{-1}, and Q = 45 kJmol^{-1}.

Response to moisture change

Clay rocks exhibit a high adsorption potential. A large amount of water can be taken up from a humid environment up to water contents of 10 – 18 % under unconstrained conditions. The water uptake enlarges the distances between solid particles and the interlayers in clay minerals, causing macroscopic free swelling up to 7 – 13 %. Conversely, drying causes release of porewater and collapse of the pore structure to a macroscopic shrinkage of up to 1 – 2 %. Because of the sedimentary structure, the swelling/shrinking strain is more significant in the direction perpendicular to the bedding planes. Along the bedding planes fractures can appear as a consequence of shrinking. The significant influences of drying and wetting on the uniaxial creep and stress relaxation suggest that the adsorbed porewater plays the key role in the deformation of claystones. The mechanical properties such as elastic stiffness and strength increase with decreasing water content due to the increase in friction resistance between particles. The elastic stiffness, uniaxial dilatancy and failure strength of dried claystone samples are 4 to 5 times higher than those of saturated ones.

Thermal impact

The thermal impact on the COX claystone was experimentally studied with respect to thermal expansion and contraction under various confining stresses, temperature influences on creep deformation and strength, and thermal impact on borehole stability. Heating/cooling cycles covering the range between room temperature and maximum temperatures of 90 °C to 110 °C were applied to the samples. The following conclusions can be drawn:

- The saturated claystone under undrained conditions expands during heating and contracts during cooling. The thermal expansion and contraction are reversible and vary with temperature almost linearly, little or independent of an applied isostatic stress. The thermal expansion and contraction are predominantly controlled by the porewater because of its much higher expansion coefficient compared to that of the solid grains. The linear thermal expansion coefficient of the claystone can be approximated by the model: $\alpha_m = \alpha_s(1 - \phi) + \alpha_w/3 \cdot \phi$, where α_s = 2.0·10^{-6} K^{-1} is the expansion coefficient of clay minerals, and α_w = 4.2·10^{-4} K^{-1} is the expansion

coefficient of the porewater. A value of α_m = 2.5·10⁻⁵ K⁻¹ follows for a porosity of ϕ = 16.5 %.

- Temperature influence on the creep of the claystone was examined at temperatures of 25 °C to 110 °C. Under saturated and undrained conditions, the creep at a constant temperature below ~90 °C evolves linearly with time without or less transient phase. Creep is accelerated with temperature. The relationship of the stationary shear creep rate and temperature can be approximated by the Arrhenius equation: $\dot{\varepsilon} \sim \exp(-Q/RT)$, where the value of Q = 45 kJmol⁻¹ is estimated for the COX claystone. Under drained conditions, heating leads to mobilisation, evaporation and expulsion of the porewater from the claystone. The release of the porewater results in pore collapse and thus consolidation under confining stresses. The thermal consolidation increases the strength of the clay rock due to the increase of friction resistance between particles.

- The thermal impact on the mechanical stability of boreholes is significant. In case of the heating tests on large hollow cylinders under undrained conditions, the temperature increase accelerates the borehole convergence. When the boreholes are rigidly supported by steel liner, heating generates thermal stress on that. In case of backfilled boreholes, thermally-driven convergence consolidates the backfill material and the EDZ, and thus enhances the sealing process and the integrity of the natural and engineered barriers.

Self-sealing of fractures

Various laboratory sealing experiments were carried out with strongly cracked samples from the COX and OPA argillaceous formations under relevant repository conditions. The fractured samples were compacted and gas or synthetic porewater was injected under triaxial stresses and elevated temperatures. The sealing behaviour of the fractured claystones was investigated by means of deformation, permeability, and wave velocity measurements. From the experiments, the following conclusions can be drawn:

- The fracture aperture decreases non-linearly with increasing normal confining stress. The normal stress – fracture closure relationship can be approximated by an exponential equation: $\Delta b = b_m \left[1 - \exp\left(-\alpha \sigma_n^\beta\right)\right]$, where σ_n is the normal stress, Δb is the aperture decrease due to σ_n, b_m is the initial aperture of the individual sample (b_m = 0.1 – 1.7 mm for the tested samples), the parameters α = 0.3 and β =

0.5 are estimated for the damaged claystones. If the stress tends to infinity, $\sigma_n \to \infty$, the fractures will be fully closed, $\Delta b \to b_m$.

- The decrease in fracture permeability is related to the average aperture by a cubic law: $K_f = K_m + F\mathrm{b}^3/12$, where K_m is the gas permeability of the intact claystone ($K_m = 0$), b is the average fracture aperture, and the parameter F characterizes the fracture features and varies in a range of $1 \cdot 10^{-5} - 2 \cdot 10^{-2}$ m^{-1} for the tested samples. As the fracture aperture b decreases to null, K_f tends to zero.

- Wetting by water flow through fractures induces swelling of the clay matrix as well as filling and clogging of the interstices. This leads to a drastic decrease in perme-ability by several orders of magnitude compared to the initial gas permeability. At hydraulic gradients of less than 200 m/m, the advective Darcy's flow appears not to be dominating in the resealed clay rock.

- Heating from ambient temperature up to 90 °C has no remarkable impact on the water permeability of fractures, while cooling down decreases the permeability slightly. The thermally-induced changes in hydraulic conductivity are mainly due to the variations of water viscosity and density.

- Under relevant conditions for a repository (confining stresses of 2 to 18 MPa, tem-peratures of 20 °C to 90 °C, gas and water flow), the permeability of the fractured claystones decreases significantly to very low levels of 10^{-19} to 10^{-21} m^2, close to in-tact clay rock. The reduction takes time in the order of months or years. This is ra-ther quick in comparison to the long repository post-closure phase.

All the laboratory observations suggest the high sealing potential of the studied argilla-ceous rocks.

4.3   Geotechnical properties of claystone-based backfill/sealing materials

Crushed claystone produced by excavation of repository openings was investigated as backfill and sealing material. The raw aggregate with coarse grains can be used for backfilling repository openings and, mixed with bentonite, for sealing boreholes, drifts, and shafts. The geotechnical properties of the excavated COX claystone and the com-pacted claystone-bentonite mixtures were comprehensively characterized.

As backfill material, the coarse-grained claystone aggregate with grain sizes of less than 32 mm can be compacted from the initial porosities of 32 – 46 % to approximately 20 % as the applied stress increases to 12 – 16 MPa corresponding to the lithostatic stresses at a depth of ~500 m. The compaction of the backfill material is mainly determined by applied mean stress, temperature, load rate or time, water content, and grain size. The compaction leads to a decrease in gas permeability down to K_g = 10^{-19} – 10^{-21} m^2 at porosities of ϕ = 20 – 25 % and to a water permeability of K_w = 10^{-19} m^2 at ϕ = 30 %. The values are close to those of the undisturbed clay rock ($K < 10^{-20}$ – 10^{-21} m^2, at ϕ = 15 % – 17 %). The low water permeability is mainly attributed to the effects of water-induced swelling of clay grains and clogging of the pores.

As sealing material, fine-grained COX claystone powder with grains of $d < 0.5$ mm and coarse-grained aggregate of $d < 5.0$ and 10.0 mm were mixed with MX80 bentonite powder of $d < 0.5$ mm in different ratios. They were compacted by an axial load of 30 MPa. By application of the same energy, the dry density increases with the fraction of claystone in the mixture from 1.56 g/cm^3 for pure bentonite to 2.00 g/cm^3 for pure claystone aggregate. All the compacted mixtures exhibit favourable geotechnical properties with respect to their barrier functions:

- The water retention capacity of the claystone-bentonite mixtures increases with the fraction of bentonite. All the mixtures can take up large amounts of water from humid environment: pure claystone aggregate incorporates up to 12 % water and bentonite even 50 % under unconfined conditions.

- Due to hydration, the unconfined mixtures also expand. The volumetric increase of claystone amounts to 12 % and that of bentonite to 40 %, in other words the swelling capacity increases with the bentonite content of the mixture. Hydration leads furthermore to a buildup of swelling pressure. Maximum swelling pressure amounts to 3 MPa for pure claystone aggregate and to 8 MPa for bentonite. A rather high swelling pressure of 9.5 MPa was observed on a compacted COX/MX80-sample with a ratio of 50/50 and with coarse claystone grains up to 10 mm in size.

- All the compacted claystone-bentonite mixtures show very low water permeabilities in the range of 10^{-19} to 10^{-20} m^2, close to the intact clay rock.

- Thermal properties of compacted claystone aggregate are dependent on the porosity and water saturation. The mean specific heat capacity of 900 Jkg^{-1}K^{-1}, however, represents a rather good approximation for the whole range of water con-

tents. The thermal conductivity increases from $0.8\,Wm^{-1}K^{-1}$ for dry material to $1.6\,Wm^{-1}K^{-1}$ for saturated material. The thermal properties of compacted claystone are comparable to those of compacted bentonite.

All the studied claystone-bentonite mixtures show favourable geotechnical properties with respect to their barrier functions and appear to be able to prevent the release of radionuclides from a repository into the biosphere. The database provided from the experiments can be used for designing the engineered barrier system with regard to specific functional requirements. The investigations concerning excavated claystone and claystone-bentonite mixtures will be continued in the framework of the newly launched EC project DOPAS /DOP 12/.

Acknowledgement

References

/AND 05/   ANDRA: DOSSIER (2005): Synthesis – Evaluation of the feasibility of a geological repository in an argillaceous formation

/AND 06/   ANDRA (2006): Expression of need concerning coupled processes involved in the mechanical behaviour of repository structures, ANDRA internal report -CCCASMG060034

/AND 09/   ANDRA (2009): Note technique – Localisation des capteurs de temperature et de pression dans les forages peropheriques de l'experimentation TED, DNTAMFS090064

/BAN 83/   Bandis, S.C., Lumsden, A.C., Baron, N.R. (1983): Fundamentals of rock joint deformation, Int. J. Rock Mech. Min. Sci. & Geomech. Abstr., 20, 49-68

/BMU 09/   BMU (2009): Safety Requirements Governing the Final Disposal of Heat-Generating Radioactive Waste.- Bundesministerium für Umwelt, Naturschutz und Reaktorsicherheit (BMU), Berlin

/BMW 07/   Bundesministerium für Wirtschaft und Technologie (BMWi) – Referat III B 3 und PTKA-WTE (2007): Schwerpunkte zukünftiger FuE-Arbeiten bei der Endlagerung radioaktiver Abfälle (2007 – 2010) – Förderkonzept des Bundesministerium für Wirtschaft und Technologie

/BOC 10/   Bock, H., Dehandschutter, B., Martin, C.D., Mazurek, M., Haller, A.D., Skoczylas, F., Davy, C. (2010): Self-Sealing of Fractures in Argillaceous Formations in the Context of Geological Disposal of Radioactive Waste – Review and Synthesis, Clay Club Report, OECD, NEA No. 6184

/BOS 03/   Bossart, P., Wermeille, S. (2003): The Stress Field in the Mont Terri Region – Data Compilation. In: Heitzmann, P. & Tripet, J.-P. (ed.): Mont Terri Project – Geology, Paeohydrology and Stress Field of the Mont Terri Region – Reports of Federal Office for Water and Geology (FOWG), Geology Series 4, 65-92

/BRA 06/   Brady, B.H.G. and Brown, E.T. (2006): Rock Mechanics for underground mining, third edition, Springer

/BUM 12/   Bumbieler, F., Conil, N., Morel, J., Armond, G. (2012): Mechanical load applied on a stell casing in a 500 m deep clay formation – small scale and full scale in situ experiments, the 5th international clay meeting, Montpellier, Oct. 22-25, O/10A/4

/DAV 03/   Davies, C., Bernier, F. (2003): Impact of the Excavation Disturbed or Damaged Zone (EDZ) on the Performance of Radioactive Waste Geological Repositories. Proceedings of an European Commission Cluster Conference and Workshop Luxemburg, 3 to 5 November 2003, EUR 21028 EN

/DAV 07/   Davy, C.A., Skoczylas, F., Barnichon, F.-D., Lebon, P. (2007): Permeability of macro-cracked argillite under confinement: Gas and water testing. Physics and Chemistry of the Earth, 32, 667-680

/DEL 07/   Delay, J., Vinsot, A., Krieguer, J.M., Rebours, H., Armand, G. (2007): Making of the underground scientific experimental programme at Meuse/Haute-Marne underground research laboratory, north eastern France. Physics and Chemistry of the Earth 32, 2-18

/DEL 09/   Delay, J., Lebon, P., Rebours, H.: The Meuse/Haute-Marne Centre (2010): Next Steps towards a Deep Disposal Facility. Journal of Rock Mechanics & Geotechnical Engineering 2(1), 52-70.

/DEN 10/   Deneele, D., Cuisinier, O., Hallaire, V., Masrouri, F. (2010): Microstructural evolution and physic-chemical behaviour of compacted clayey soil submitted to an alkaline plume, Journal of Rock Mechanics and Geotechnical Engineering 2(2), 169-177

/DOP 12/   DOPAS – EC project: Full Scale Demonstration of Plugs and Seals, FP7-Fission-2012, Project number 323273

216

/DUE 11/   Dueck, A., Johannesson, L.-E., Kristensson, O., Olsson, S., Sjöland, A. (2011): Hydro-mechanical and chemical-mineralogical analyses of the bentonite buffer from a full-scale field experiment simulating a high-level waste repository, Clays and Clay Minerals, Vol. 59, No. 6, 595-607

/ESD 04/   ESDRED project – deliverable 1 (2004: Input data and functional requirements for buffer construction and monitoring equipment. F16W-CT-2004-508851, Mod1-WP1-D1

/FOR 13/   FORGE –Fate of Repository Gases Project (2013): Gas Generation and Migration, International Symposium and Workshop, 5-7 February 2013, Luxembourg

/FRE 93/   Fredlund, D.G., Rahardjo, H. (1993): Soil Mechanics for Unsaturated Soils. John Wiley & Sons, INC

/GOO 76/   Goodman, R.E. (1976): Methods of geological engineering in discontinuous rocks, West Publishing, New York

/HOR 96/   Horseman, S.T., Higgo, J.J.W., Alexander, J., Harrington, J.F. (1996): Water, Gas and Solute Movement through Argillaceous Media. Report CC-96/1

/HOT 07/   Hot Disk (2007): Hot Disk Thermal Constants Analyser – Instruction Manual (software version 5.9)

/HUE 00/   Huertas, F.; Fuentes-Cantillana, J.L.; Fullien, F.; Rivas, P.; Linares, J.; Farina, P.; Ghoreychi, M.; Jockwer, N.; Kickmaier, W.; Martinez, M.A.; Samper, J.; Alonso, E.; Elorza, F.J. (2000): Full-scale engineered barriers experiment for a deep geological repository for high-level radioactive waste in crystalline host rock (FEBEX project). Final report, EUR 19147 EN

/JOB 10/   Jobmann, M., Wilksnack, T.h., Voigt, H.-D. (2010): Investigation of damage-induced permeability of Opalinus clay, International journal of Rock Mechanics & Mining Sciences 47, 279-285

/KAR 08/   Karnland, O., Nilsson, U., Weber, H., Wersin, P. (2008): Sealing ability of Wyoming bentonite pellets foreseen as buffer material – Laboratory tests, Physics and Chemistry of the Earth 33, 472-475

/KEL 11/   Keller, L.M., Holzer, L., Wepf, R., Gasser, P., Münch, B., Marschall, P. (2011): On the application of focused ion beam nanotomography in characterizing the 3D pore space geometry of Opalinus clay, Physics and Chemistry of the Earth 36, 1539-1544

/LEB 10/   Lebon, P., Landais, P. (2010): On the Way to Siting and Licensing a Deep Disposal: What about the Research Programme on the Callovo-Oxfordian Formation, on the 4th international meeting – Clays in Natural & Engineered Barriers for Radioactive Waste Confinement, Nantes

/LEE 93/   Lee C.H., Farmer I. (1993): Fluid Flow in Discontinuous Rocks, Chapman & Hall

/LEV 10/   Levasseur, S., Charlier, R., Frieg, B., Collin, F. (2010): Hydro-mechanical modelling of the excavation damaged zone around an underground excavation at Mont Terri Rock Laboratory. International Journal of Rock Mechanics & Mining Sciences 47, 414-425

/LIU 10/   Liu, Y. (2010): Influence of heating and water-exposure on liquid limits of GMZ01 and MX80 bentonites, Journal of rock Mechanics and Geotechnical Engineering, 2(2), 188-192

/MAR 08/   Marschall, P., Cuss, R., Wieczorek, K., Popp, T. (2008): NF-PRO, Deliverable 4.4.1, State of the Art on Gas Transport in the Tunnel Nearfield/EDZ, Interim report, 66p

/MAR 97/   Martin, C.D. (1977): Seventeenth Canadian geotechnical colloquium: the effects of cohesion loss and stress path on brittle rock strength. Can Geotech J 34, 698-725

/MAZ 08/ Mazurek, M., Gautschi, A., Marschall, P., Vigneron, G., Lebon, P., Delay, J. (2008): Transferability of geoscientific information from various sources (study sites, underground rock laboratories, natural analogues) to support safety cases for radioactive waste repositories in argillaceous formations. Physics and Chemistry of the Earth, Vol. 33, 95-105

/MIT 76/ Mitchell, J.K. (1976): Fundamentals of soil Behavior. University of California, Berkeley, USA

/MIT 92/ Mitchell, J.K. (1992): Characteristics and Mechanisms of Clay Creep and Creep Rupture, in "Clay-water interface and its rheological implications, Clay Mineral society", Vol.4, 212-244

/NAG 02/ NAGRA (2002): Project Opalinus Clay, Models, Codes and Data for Safety Assessment – Demonstration of disposal feasibility for spent fuel, vitrified high-level waste and long-lived intermediate-level waste

/NAU 07/ Naumann, M., Hunsche, U., Schulze, O. (2007): Experimental investigations on anisotropy in dilatancy, failure and creep of Opalinus clay. Physics and Chemistry of the Earth, 32, 889-895

/NEA 11/ NEA CLAY CLUB Workshop (2011): Clay characterisation from nanoscopic to microscopic resolution, Karlsruhe, Germany, 6-8 September 2011

/NOY 00/ Noynaert, L. et al. (2000): Heat and radiation effects on the near field of a HLW or spent fuel repository in a clay formation (CERBERUS Project). EUR 19125EN, Contract No F14W-CT95-0008

/OLI 08/ Olivella, S., Alonso, E.E. (2008): Gas flow through clay barriers, Geotechnique, 58, No 3: 157-176

/PEA 03/ Pearson, F.J., Arcos, D., Bath, A. et al. (2003): Mont Terri Project – Geochemistry of Water in the Opalinus Clay formation at the Mont Terri Rock Laboratory, No 5, Bern

/POP 07/ Popp, T., Salzer, K. (2007): Anisotropy of seismic and mechanical properties of Opalinus clay during triaxial deformation in a multi-anvil apparatus. Physics and Chemistry of the Earth 32, 879-888

/PUS 01/ Pusch, R., Kasbohm, J. (2001): Can the Water Content of Highly Compacted Bentonite be Increased by Applying a High Water Pressure? SKB, Technical Report 01-33

/ROD 99/ Rodwell, W.R., Harris, A.W., Horseman, S.T., Lalieux, P., Müller, W., Ortiz Amaya, L., Pruess, K. (1999): Gas Migration and Two-Phase Flow through Engineered and Geological Barriers for a Deep Repository for Radioactive Waste. A Joint EC/NEA Status Report, European Commission, EUR 19122 EN

/RUT 03/ Rutqvist, J., Stephansson, O. (2003): The role of Hydromechanical Coupling in Fractured Rock Engineering. Hydrogeology Journal; 11(1), 7-40

/RUT 13/ Rutqvist, J., Leung, C., Hoch, A., Wang, Y., Wang Z. (2013): Linked multi-continuum and crack tensor approach for modelling of coupled geomechanics, fluid flow and transport in fractured rock. Journal of Rock Mechanics & Geotechnical Engineering 5, 18-31

/RUT 83/ Rutter, E.H. (1983): Pressure solution in nature, theory and experiment, Journal of Geological Society. London, Vol. 140, pp. 725-740

/SHA 08/ Shao, H., Schuster, K., Sönnke, J., Bräuer, V. (2008): EDZ development in indurated clay formations – In situ borehole measurements and coupled HM modelling, Physics and Chemistry of the Earth, Vol. 33, 388-395

/SRI 02/ Engineering behaviour of clays (2002): Influence of mineralogy, in the Proceedings of the Workshop on Chemo-Mechanical Coupling in clays: from nano-scale to engineering applications, Di Maio, Hueckel & Loret (eds), Swets & Zeitlinger, Lisse, ISBN 9058093840

/SU 07/ Su, K. (2007): Synthesis of the EC MODEX-REP project – Development and Validation of the Constitutive Hydro-mechanical Models for the Callovo-Oxfordian Argillites, FIKW-CT2000-00029

/TAN 10a/   Tang, C.S., Tang, A.M., Cui, Y.J., Delage, P., Shi, B. (2010): The coupled hydro-mechanical behaviour of compacted crushed Callovo-Oxfordian argillite, Journal of Rock Mechanics and Geotechnical Engineering 2(1) 86-90

/TAN 10b/   Tang, A.M. and Cui, Y.J. (2010): Effects of mineralogy on thermo-hydro-mechanical parameters of MX80 bentonite, Journal of Rock Mechanics and Geotechnical Engineering 2(1) 91-96

/TAN 11/   Tang, C.S., Tang, A.M., Cui, Y.J., Delage, P., Schroeder, C., Laure, E.D. (2011): Investigating the swelling pressure of compacted crushed Callovo-Oxfordian claystone, Physics and chemistry of the Earth 36 1857-1866

/TD 06/   Mont Terri Project: Extension of Rock Laboratory – Results and recommendation by rock mechanics analyses group, TD154, 7 Nov. 2006

/TER 96/   Terzaghi, K., Peck, R.B., Mesri, G. (1996): Soil Mechanics in Engineering Practice, Third Edition, John Wiley & Sons, INC

/THM 07/   THM-TON Projekt zur Untersuchung der THM-Prozesse im Nahfeld von Endlagern in Tonformationen, GRS – Vorhabensbeschreibung, Juli 2007

/TIM 10/   TIMODAZ project (2010): Thermal Impact on the Damaged Zone around a Radioactive Waste Disposal in Clay Host Rocks – Constitutive models development (Deliverable 10) & Simulation of lab and in situ tests (Deliverable 13), F16W-CT-036449

/TOU 07/   Tournassat C, Gaucher E C, Fattahi M, Grambow B.)2007): On the mobility and potential retention of iodine in the Callovian-Oxfordian formation. Physics and Chemistry of the Earth, Vol 32, 8-14, p. 539-551

/TSA 05/   Tsang, C.-F. , Bernier, F. (2005): Definitions of excavation disturbed zone and excavation damaged zone, in Davies, C. and Bernier, F. (eds.): Impact of the excavation disturbed zone (EDZ) on the performance of radioactive waste geological repositories, EUR 21028 EN: 5-8, Brussels

/TSA 12/   Tsang, C.F., Barnichon, J.D., Birkholzer, J., Li, X.L., Liu, H.H., Sillen, X. (2012): Coupled thermo-hydro-mechnical processes in the near field of a high-level radioactive waste repository in clay formations, International Journal of Rock Mechanics & Mining sciences 49, 31-44

/UPC 04/   UPC (2004): CODE-BRIGHT, A 3-D program for thermo-hydro-mechanical analysis in geological media

/VAN 80/   Van Genuchten, M.T. (1980): A Closed-Form Equation for predicting the hydraulic Conductivity of Unsaturated Soils. -Soil Sci. Soc. Am. J., 44:892-898

/WU 10/   Wu, F.Q, Wu, J., Qi, S.W. (2010): Phenomena and theoretical analysis for the failure of brittle rocks, Journal of Rock Mechanics & Geotechnical Engineering, 2(4): 331-337

/YON 12/   Yong, R.N., Nakano, M., Pusch. R. (2012): Environmental Soil Properties and Behaviour, CRC Press, Taylor & Francis Group

/ZHA 02/   Zhang, C.L., Dittrich, J., Müller, J., Rothfuchs, T. (2002): Experimental Study of the Hydro-mechanical Behaviour of the Callovo-Oxfordian Argillites – Part of the MODEX-REP Project., GRS-187

/ZHA 04a/   Zhang, C.L., Rothfuchs, T. (2004): Experimental Study of Hydro-mechanical Behaviour of the Callovo-Oxfordian Argillites. Applied Clay Science 26 325-336

/ZHA 04b/   Zhang, C.L., Rothfuchs, T., Moog, H., Dittrich, J., Müller, J. (2004): Thermo-Hydro-Mechanical and Geochemical Behaviour of the Callovo-Oxfordian Argillite and the Opalinus Clay. GRS-202

/ZHA 05/   Zhang, C.L., Wileveau, Y., Rothfuchs, T. (2005): A Heating Experiment in the Opalinus Clay at the Mont Terri Rock Laboratory. The 10th International Conference on Environmental Remediation and Radioactive Waste Management, September 4–8 2005, Glasgow, Scotland

/ZHA 06/   Zhang, C.L., Rothfuchs, T., Wieczorek, K., Jockwer, N., Wileveau, Y. (2006): Monitoring and Modelling of Responses of the Opalinus Clay to Heating. Chinese Journal of Rock Mechanics and Engineering, 25(4), 659-669

/ZHA 07a/ Zhang, C.L., Rothfuchs, T., Jockwer, N., Wieczorek, K., Dittrich, J., Müller, J., Hartwig, L., Komischke, M. (2007): Thermal Effects on the Opalinus Clay – A Joint Heating Experiment of ANDRA and GRS at the Mont Terri URL (HE-D Project), GRS-224

/ZHA 07b/ Zhang C.L, Rothfuchs T. (2007): Moisture Effects on Argillaceous Rocks, Proc. 2nd International Conference of Mechanics of Unsaturated Soils (ed. T. Schanz), Springer Proceedings in Physics 112, p. 319-326, Springer-Verlag Berlin Heidelberg

/ZHA 07c/ Zhang, C.L., Rothfuchs, T., Su, K., Hoteit, N. (2007): Experimental Study of the thermo-hydro-mechanical behaviour of indurated Clays, Physics and Chemistry of the Earth, Vol. 32, p. 957-965.

/ZHA 08a/ Zhang, C.L., Rothfuchs, T., Dittrich, J., Müller, J. (2008): Investigations on self-sealing of indurated clay – part of the EC NFPRO project, GRS-230

/ZHA 08b/ Zhang, C.L., Rothfuchs, T. (2008): Damage and sealing of clay rocks detected by measurements of gas permeability, Physics and Chemistry of the Earth, Vol. 33, 363-373

/ZHA 08c/ Zhang, C.L, Rothfuchs, T., Su, K. (2008): Laboratory Experiments on the Thermal Effects on Clay Rocks, The 3rd international conference on Coupled THMC processes in Geo-Systems, GEOPRO2008, Lille in France

/ZHA 09a/ Zhang, C.L., Wieczorek, K., Rothfuchs, T., Armand, G., Lebon, P. (2009): Responses of the Opalinus Clay to Heating during the HE-D Experiment at Mont Terri. The international conference and workshop in the framework of the EC TIMODAZ and THERESA projects, Luxembourg

/ZHA 09b/   Zhang C.L. (2009): Self-sealing of Fractures in Argillites under Repository conditions, The international conference and workshop in the framework of the EC TIMODAZ and THERESA projects, Sept. 2009, Luxembourg

/ZHA 10a/   Zhang, C. L, Wieczorek, K., Xie, M. L. (2010): Swelling experiments on mudstones, Journal of Rock Mechanics & Geotechnical Engineering, 2(1) 41-47

/ZHA 10b/   Zhang, C.L., Czaikowski, O., Rothfuchs, T. (2010): Thermo-Hydro-Mechanical Behaviour of the Callovo-Oxfordian Clay Rock – Final report of the BURE-HAUPT/EC-TIMODAZ project, GRS-266

/ZHA 10c/   Zhang C.L. (2010): Experimental Evidence for Self-sealing of Fractures in Claystone, The 4th international meeting – Clays in Natural & Engineered Barriers for Radioactive Waste Confinement, Nantes

/ZHA 93/   Zhang, C.L., Heemann, U., Schmidt, M.W., Staupendahl, G. (1993): A Constitutive Model for Description of Compaction Behavior of Crushed Salt Backfill, Proceedings of the 1993 ISRM International Symposium EUROCK'93, Lisbon, Portugal

List of Tables

List of Figures

227

237

238

Appendix

A Results of swelling pressure and strain tests on claystone

Tab. A.1 Fundamental properties of testing samples

Test No.	Sample ID	D/L [mm]	Grain density ρ_s [g/cm^3]	Bulk density ρ_b [g/cm^3]	Dry density ρ_d [g/cm^3]	Initial porosity ϕ_o [%]	Water content w [%]	Water saturation S_{lo} [%]	Pre-load σ_α [MPa]	Testing duration [day]	Measurement of parameters
1	EST27387A	40/40	2.70	2.39	2.24	16.95	6.58	87.1	14.3	265	axial stress, radial strain
	EST27387B	"	2.70	2.39	2.23	17.38	7.14	91.6	0	265	free swelling strain
2	EST40694A	40/40	2.70	2.44	2.28	15.45	6.80	94.0	15.5	110	axial stress, radial strain
	EST40694A	40/40	2.70	2.43	2.27	15.96	7.00	95.5	0	110	free swelling strain
3	OPA-EBT7A	40/40	2.70	2.46	2.33	13.70	5.70	94.0	2.2	110	axial stress, radial strain
	OPA-EBT7B	40/40	2.70	2.48	2.34	13.16	5.60	94.8	0	110	free swelling strain
4	EST40651A	40/40	2.70	2.36	2.23	17.54	6.50	82.5	7.0	110	axial stress, radial strain
	EST40651B	40/40	2.70	2.37	2.24	17.19	6.50	84.5	0	110	free swelling strain
5	EST40366A	40/40	2.70	2.41	2.25	16.58	7.00	95.1	5.0	50	axial stress, radial strain
	EST40366B	40/40	2.70	2.38	2.22	17.68	7.08	89.0	0	50	free swelling strain
6	EST33213A	40/40	2.70	2.41	2.29	15.30	5.38	80.4	1.0	120	axial stress, radial strain
	EST33213B	40/40	2.70	2.40	2.26	16.12	5.97	83.9	0	120	free swelling strain
7	EST27388A	40/40	2.70	2.40	2.26	16.30	7.22	0 at 105°C	1.0	165	axial stress, radial strain
	EST27388B	"	2.70	2.39	2.24	17.04	7.27	0 at 105°C	0	165	free swelling strain
8	EST27390A	40/40	2.70	2.36	2.24	17.04	7.00	92.0	1.0	40 d vapour	axial stress
	EST27390B	"	2.70	2.39	2.25	16.67	7.00	94.5	0	40 d syn. water	free swelling strain
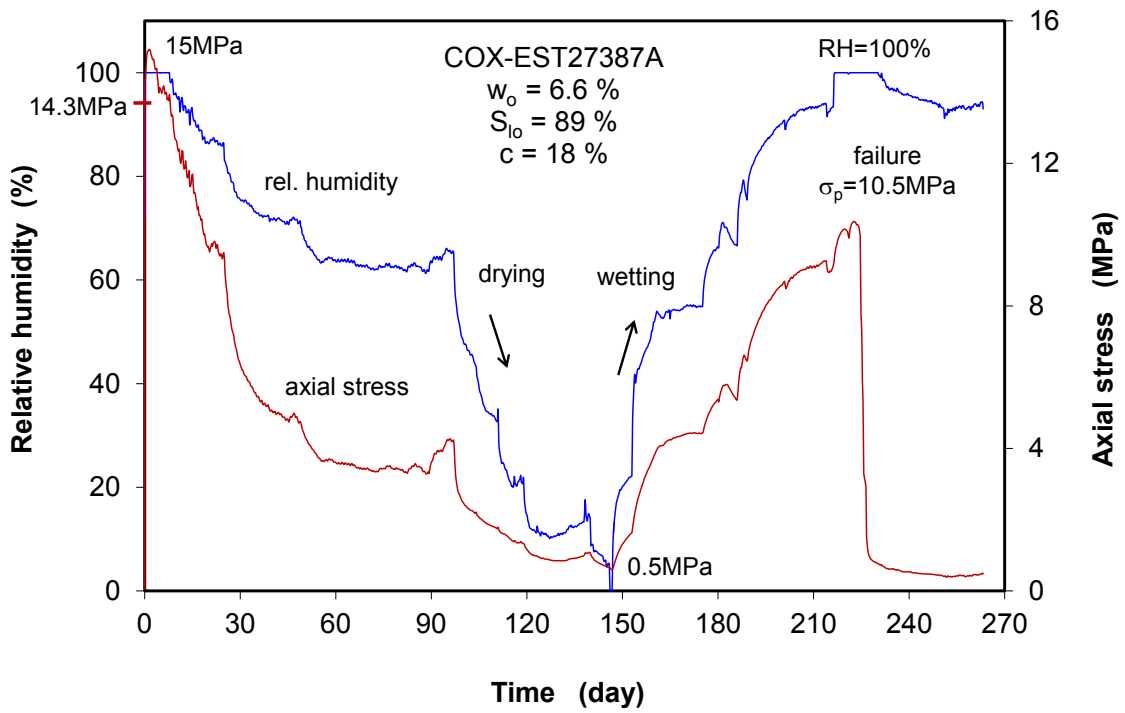
(a) Response of axial stress to humidity change
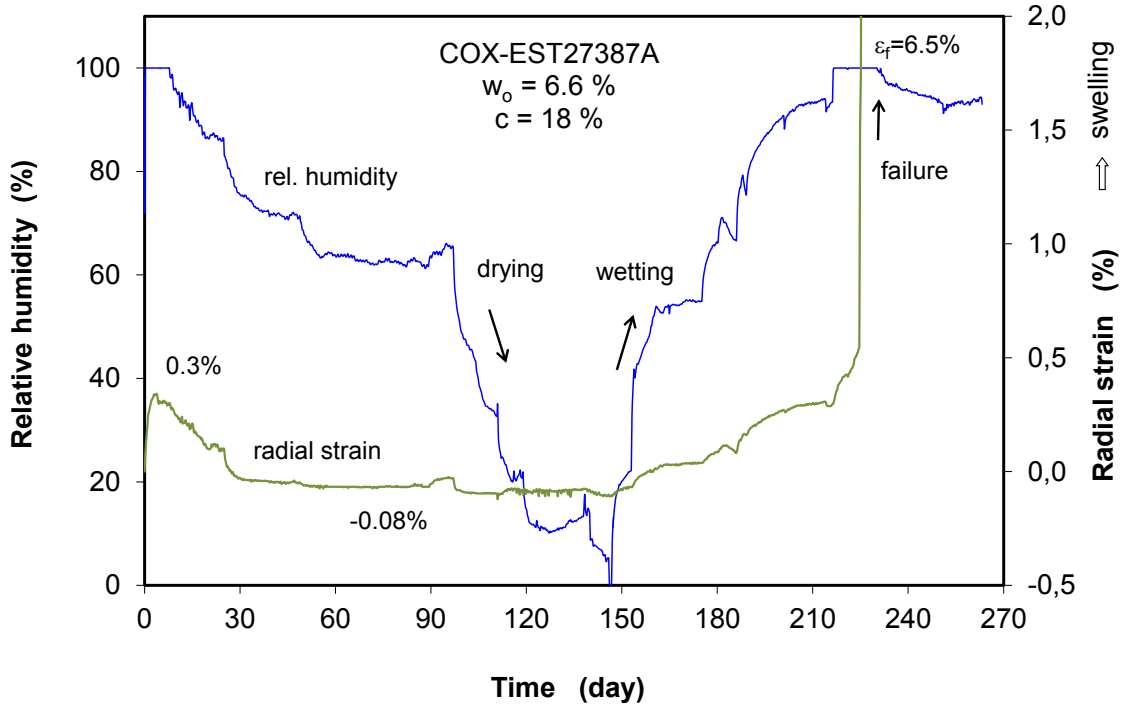
(b) Response of radial strain to humidity change

243
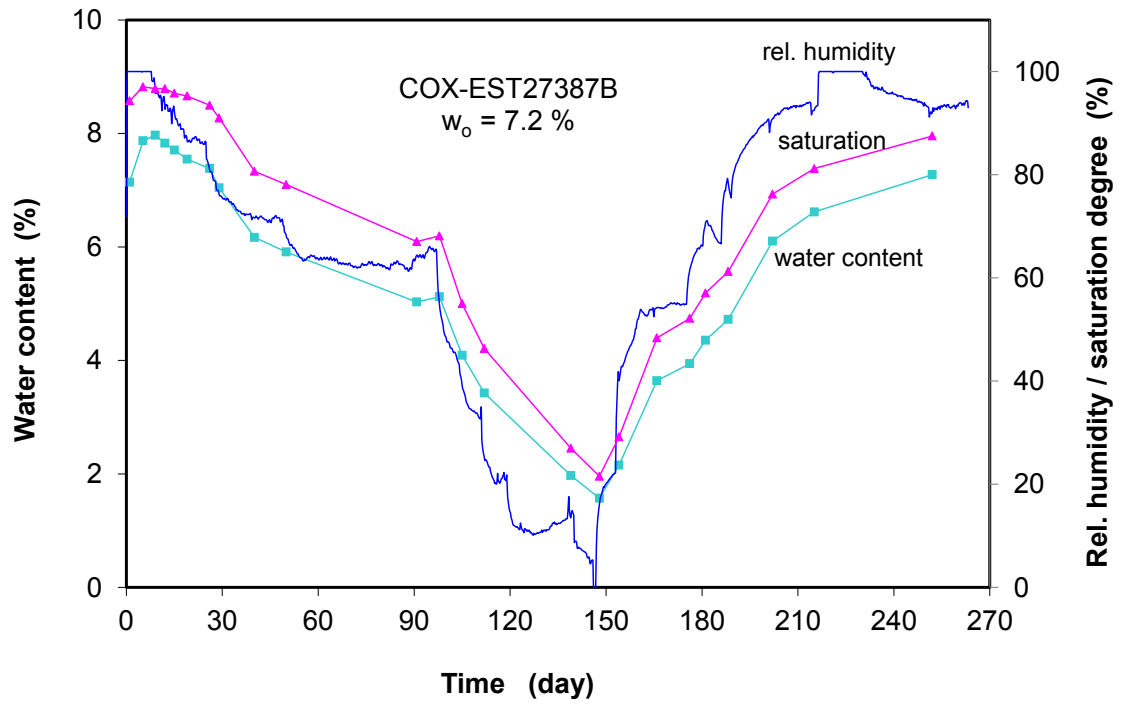
(c) Changes of water content and saturation
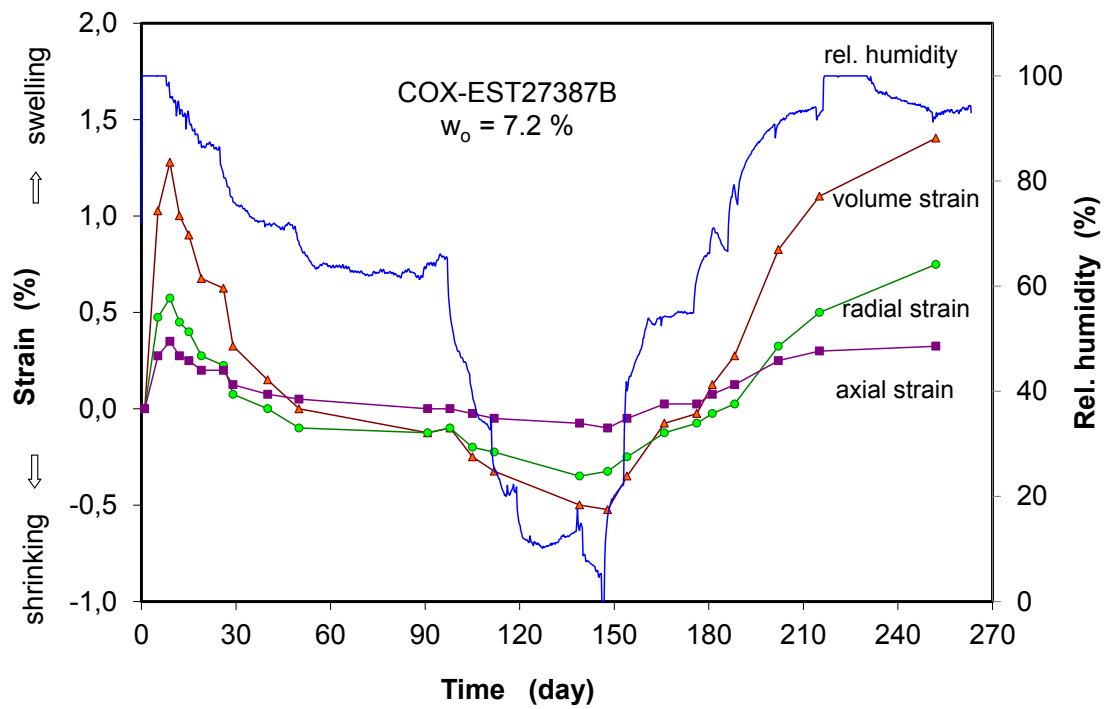
(d) Free swelling deformation

Fig. A.1 Results of swelling test 1 on COX sample EST27387
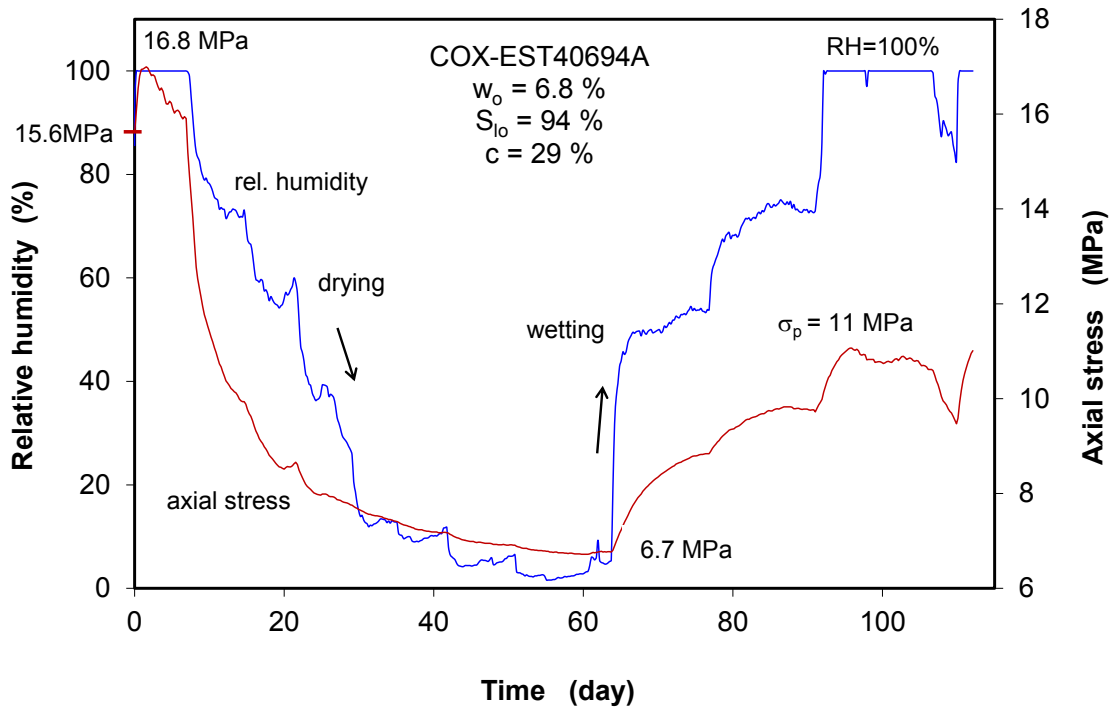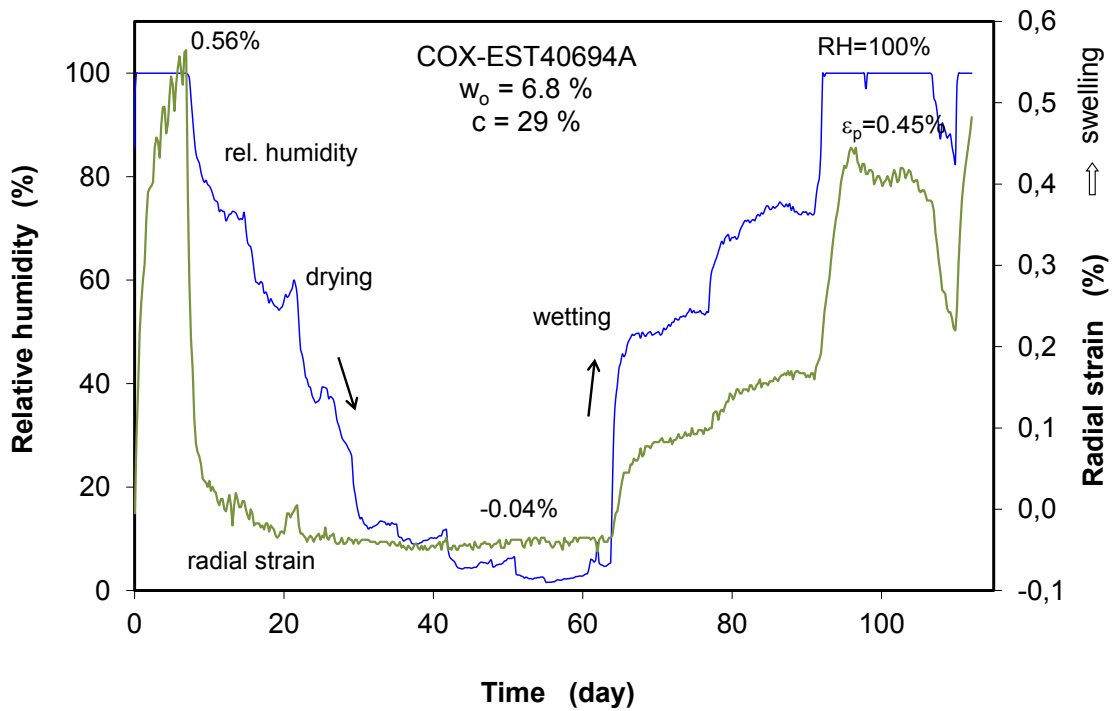
244

(a) Response of axial stress to humidity change

(b) Response of radial strain to humidity change

245
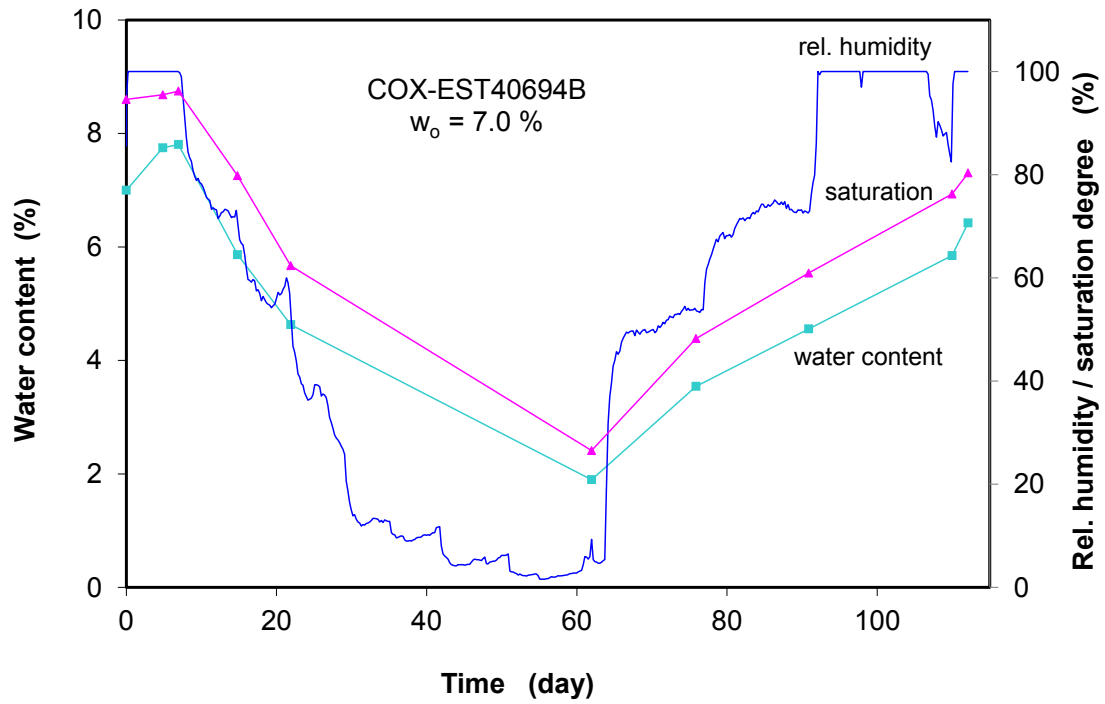
(c) Changes of water content and saturation
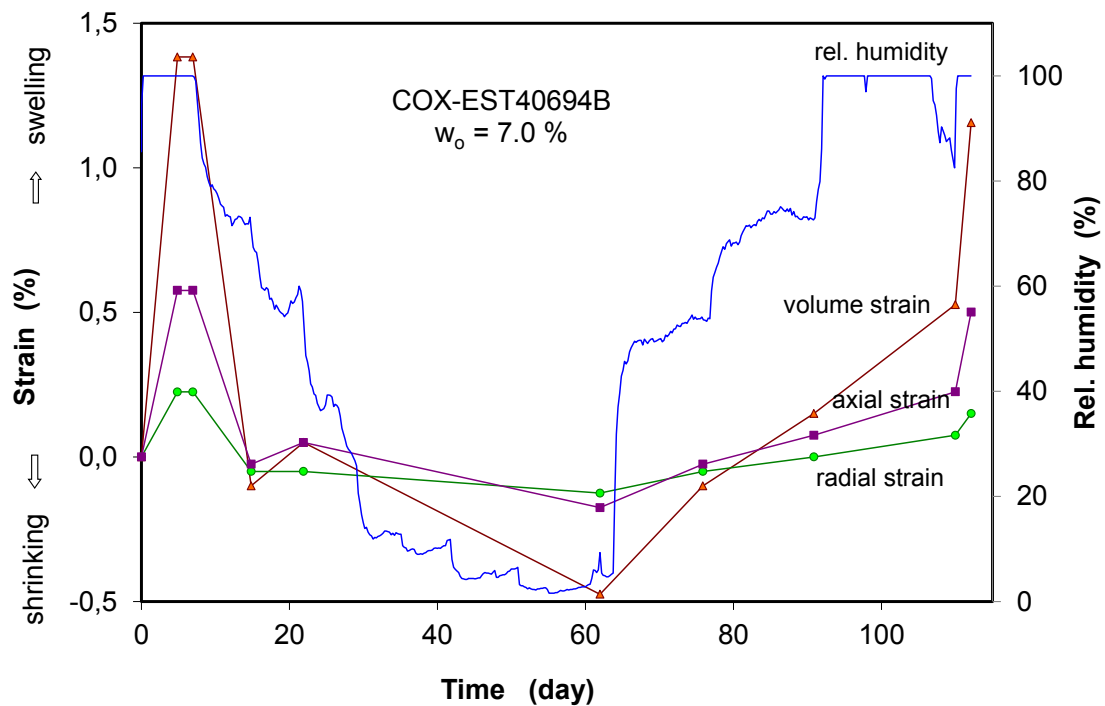
(d) Free swelling deformation

Fig. A.2 Results of swelling test 2 on COX sample EST40694B
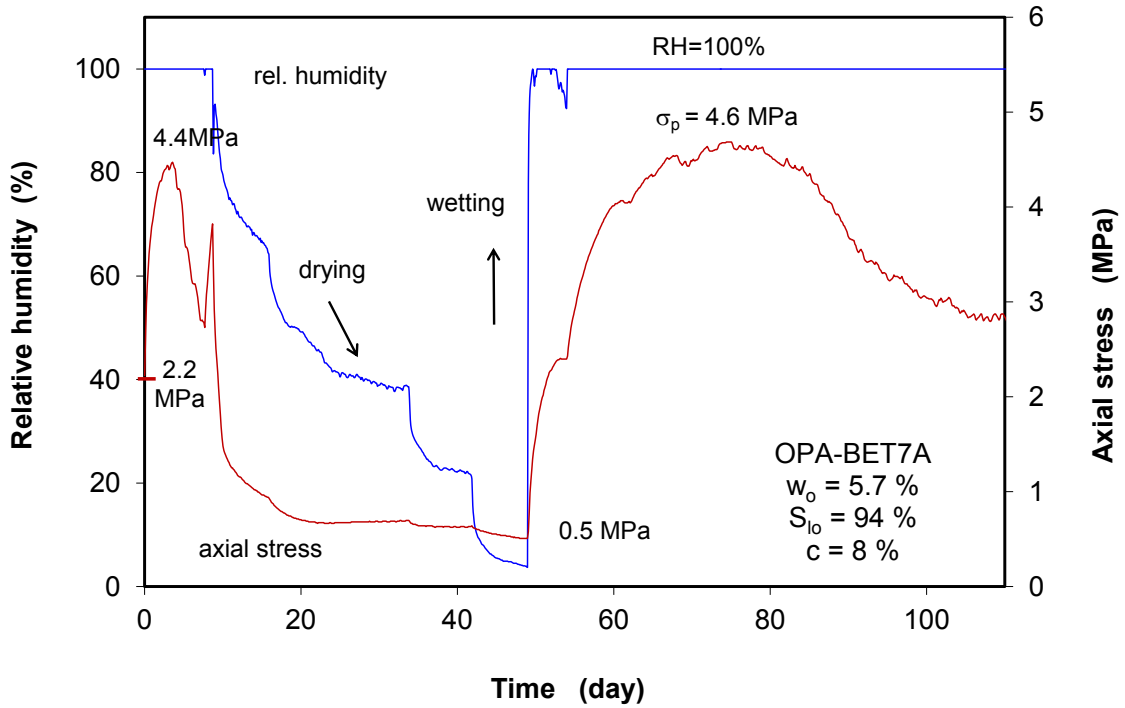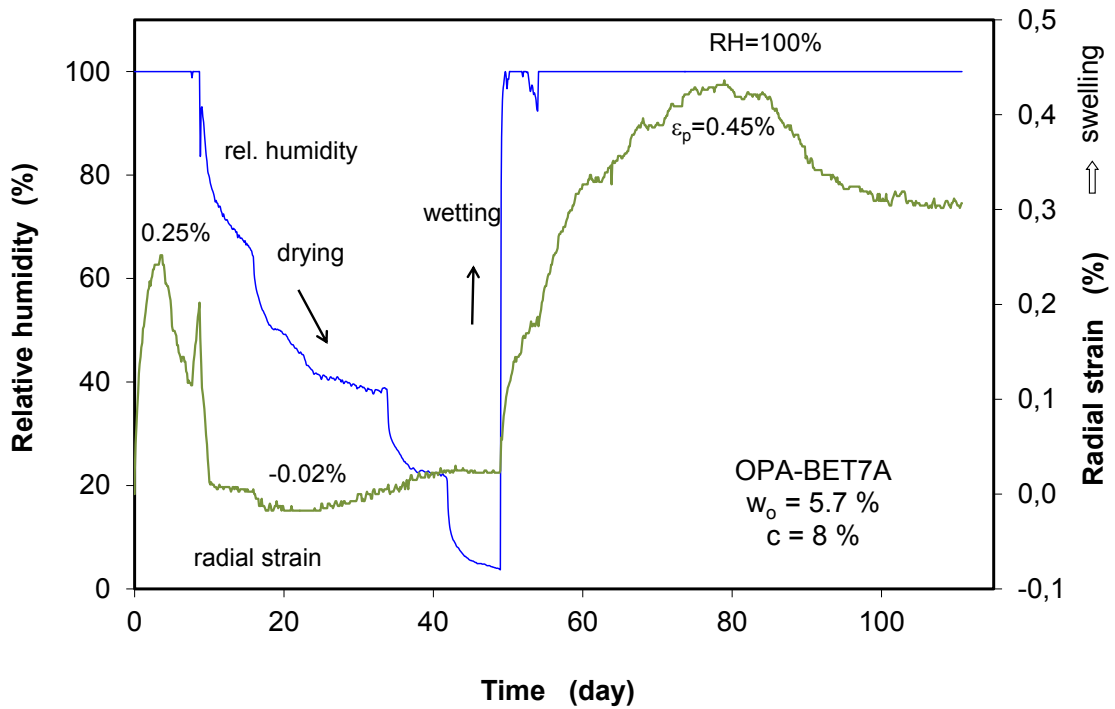
246

(a) Response of axial stress to humidity change

(b) Response of radial strain to humidity change
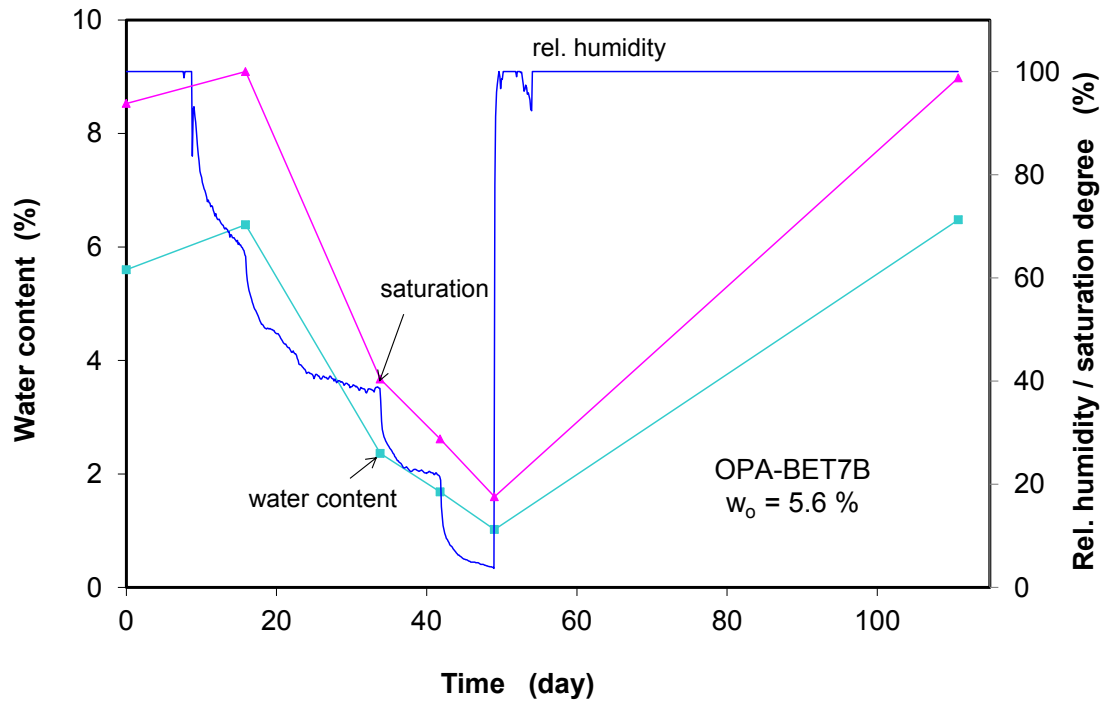
(c) Changes of water content and saturation
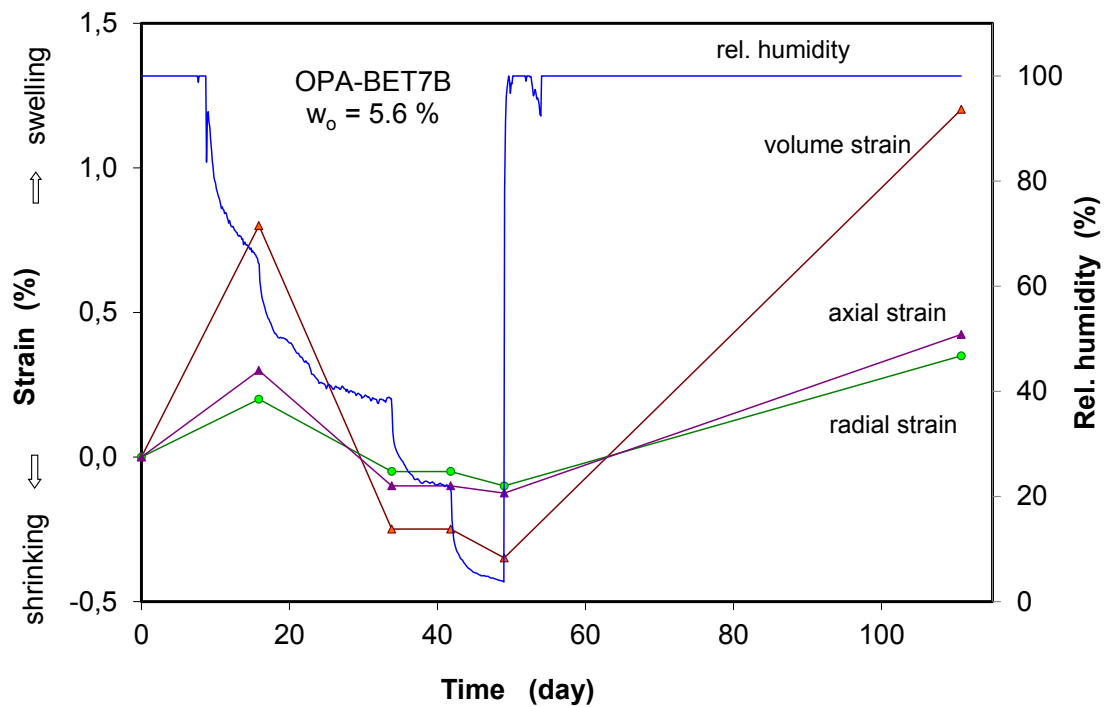
(d) Free swelling deformation

Fig. A.3 Results of swelling test 3 on OPA sample BET7
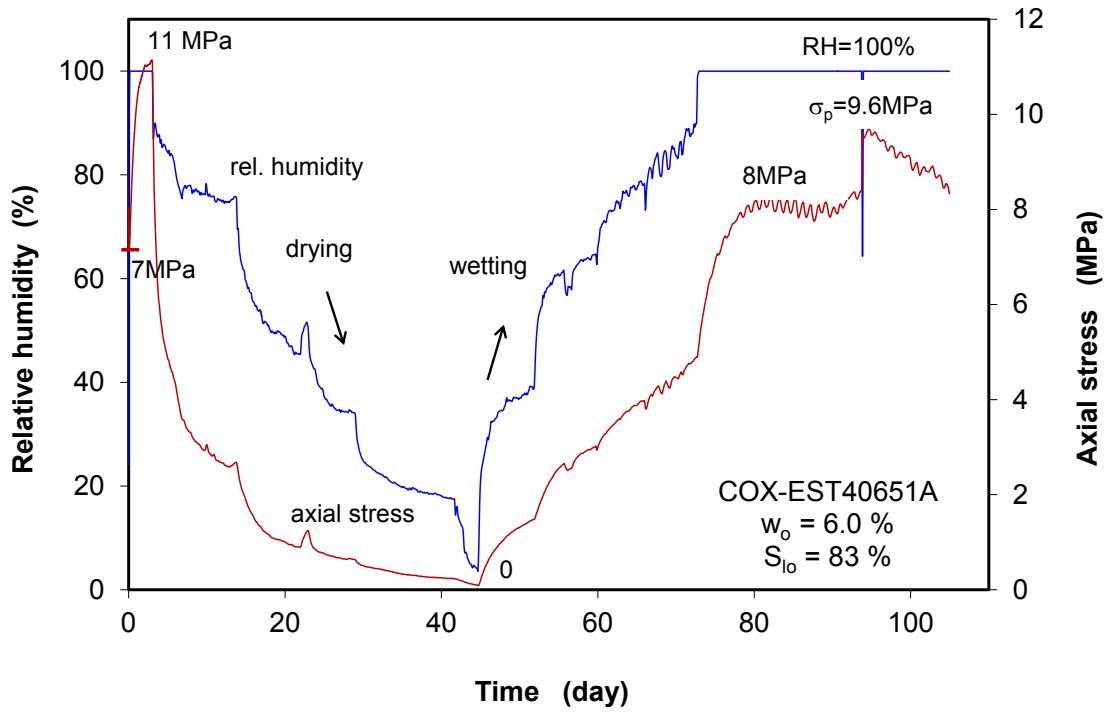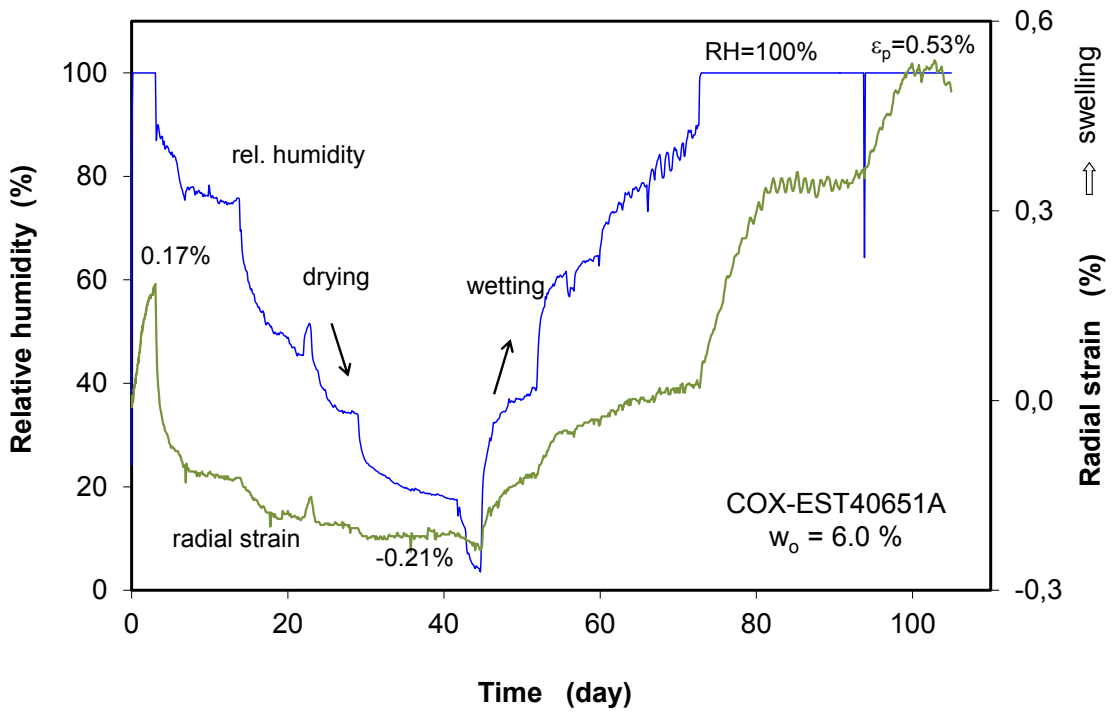
248

(a) Response of axial stress to humidity change

(b) Response of radial strain to humidity change
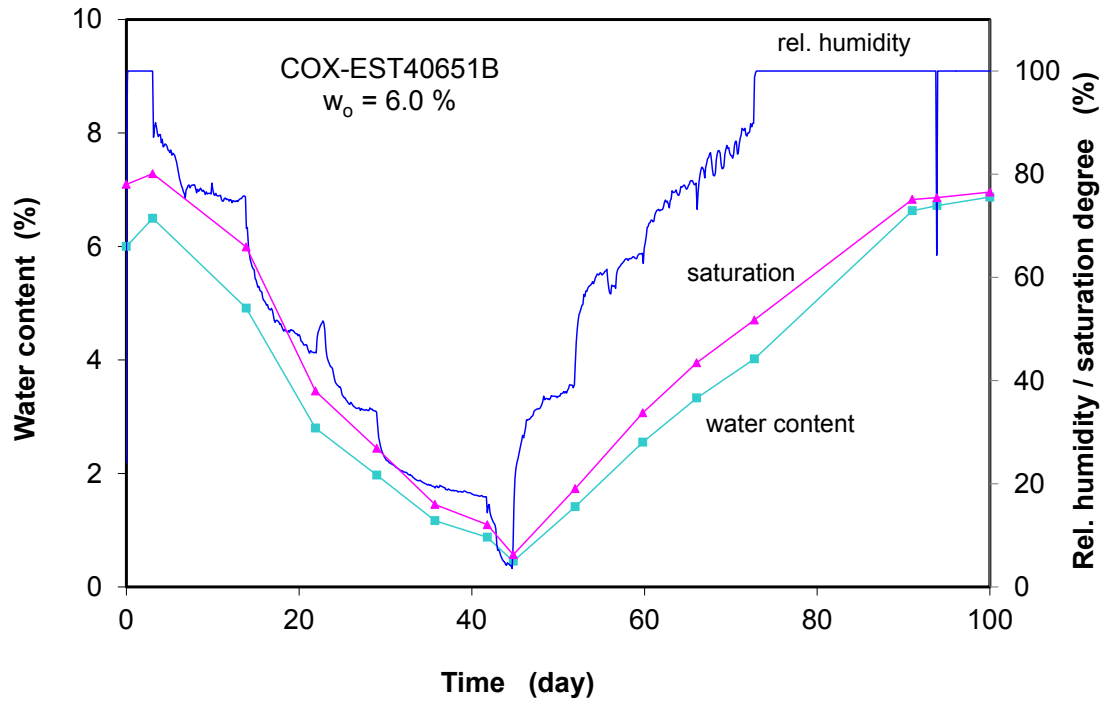
(c) Changes of water content and saturation
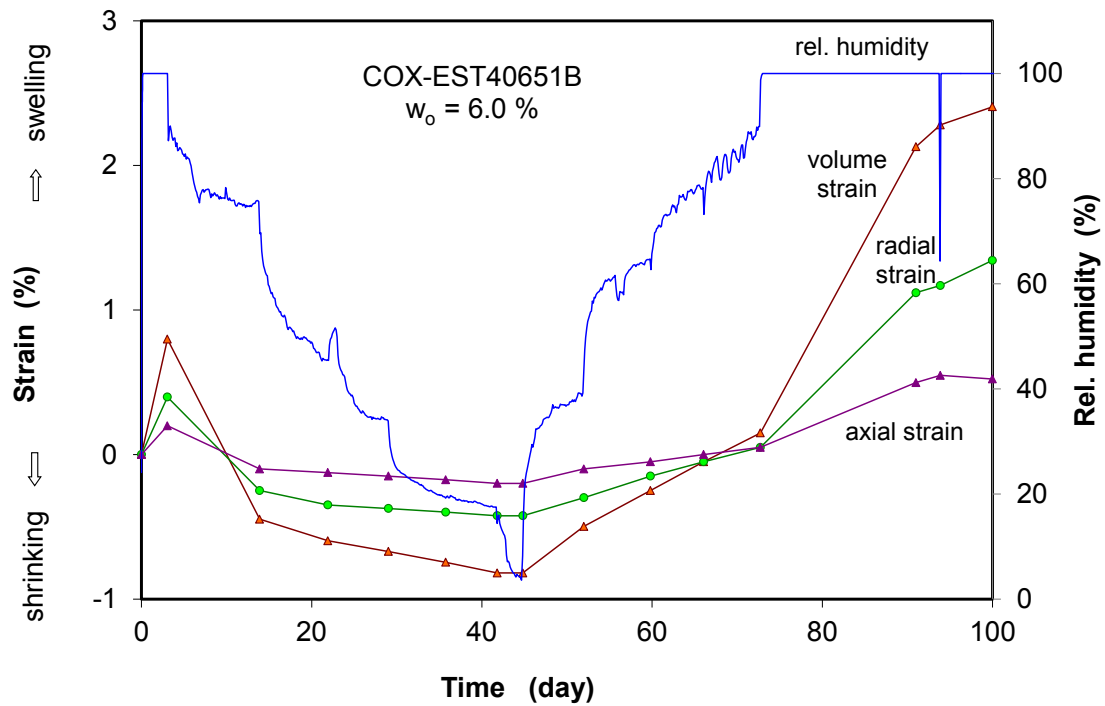
(d) Free swelling deformation

Fig. A.4   Results of swelling test 4 on COX sample EST40651
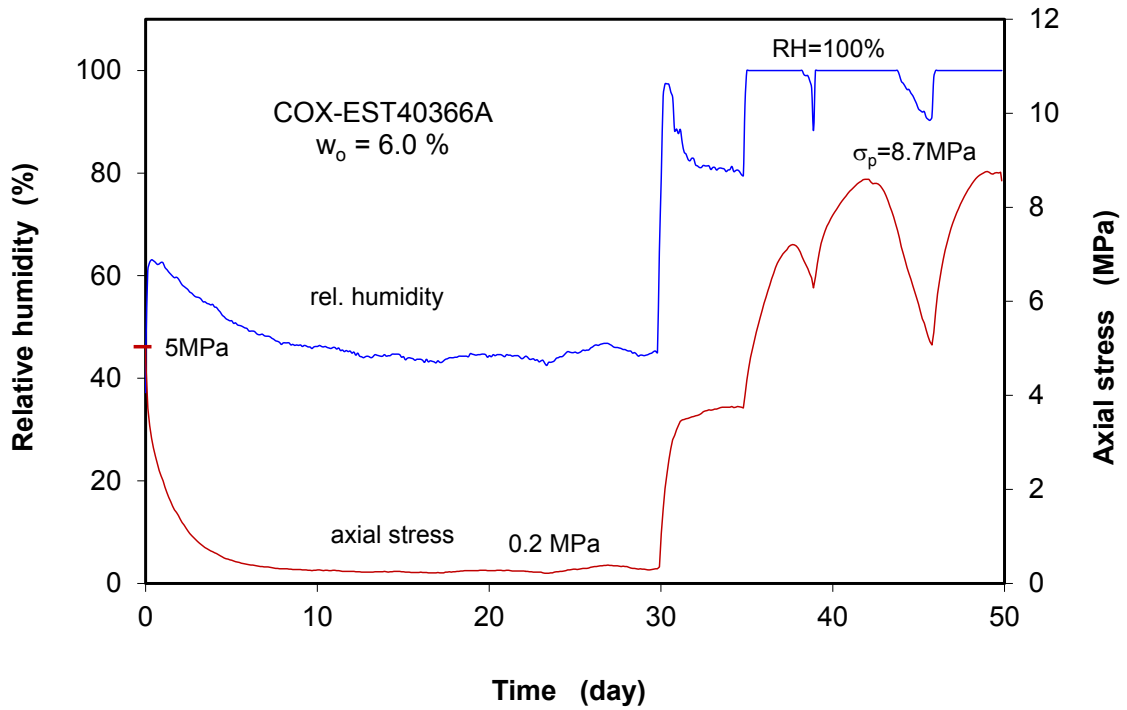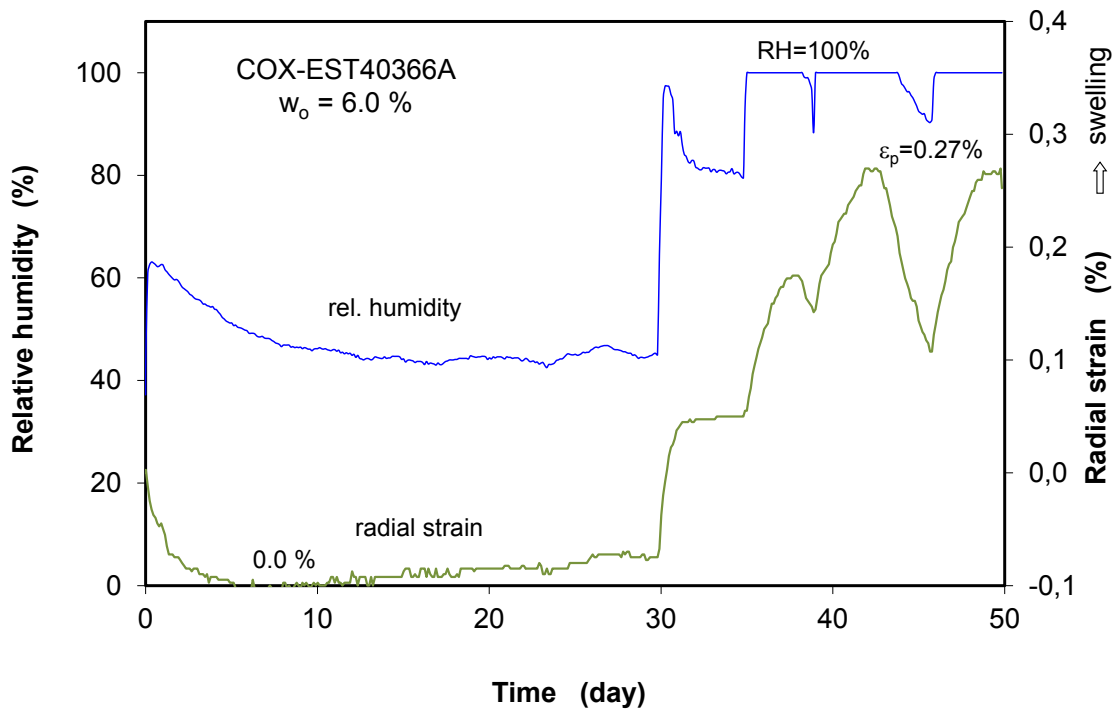
250

(a) Response of axial stress to humidity change

(b) Response of radial strain to humidity change
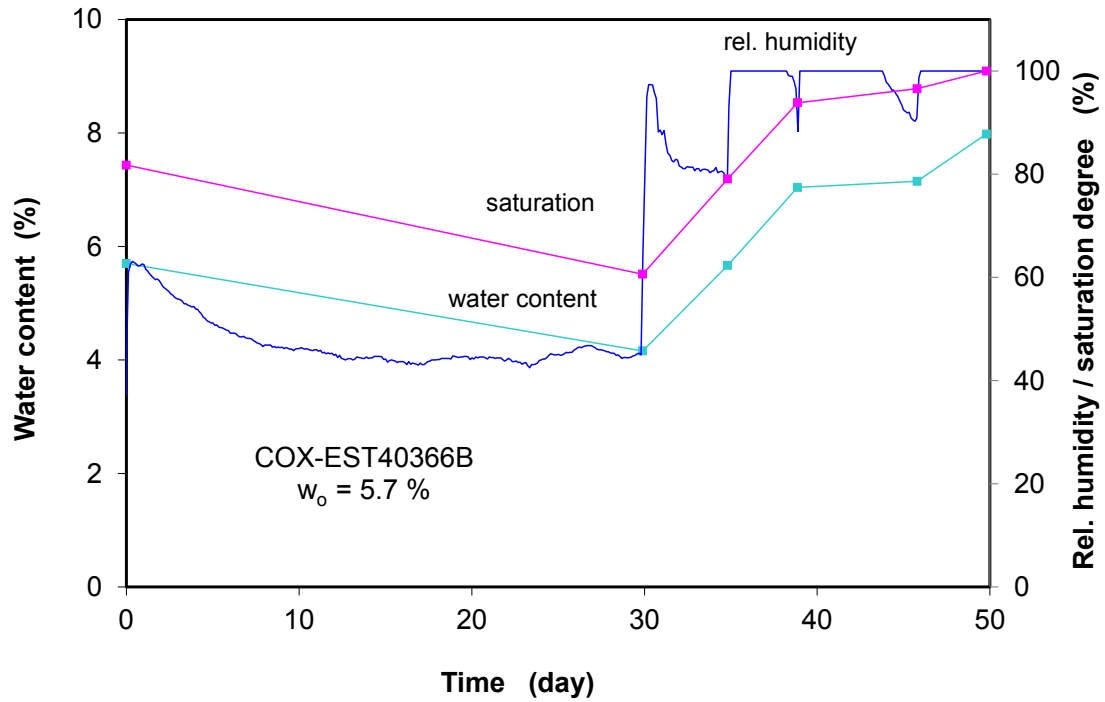
(c) Changes of water content and saturation
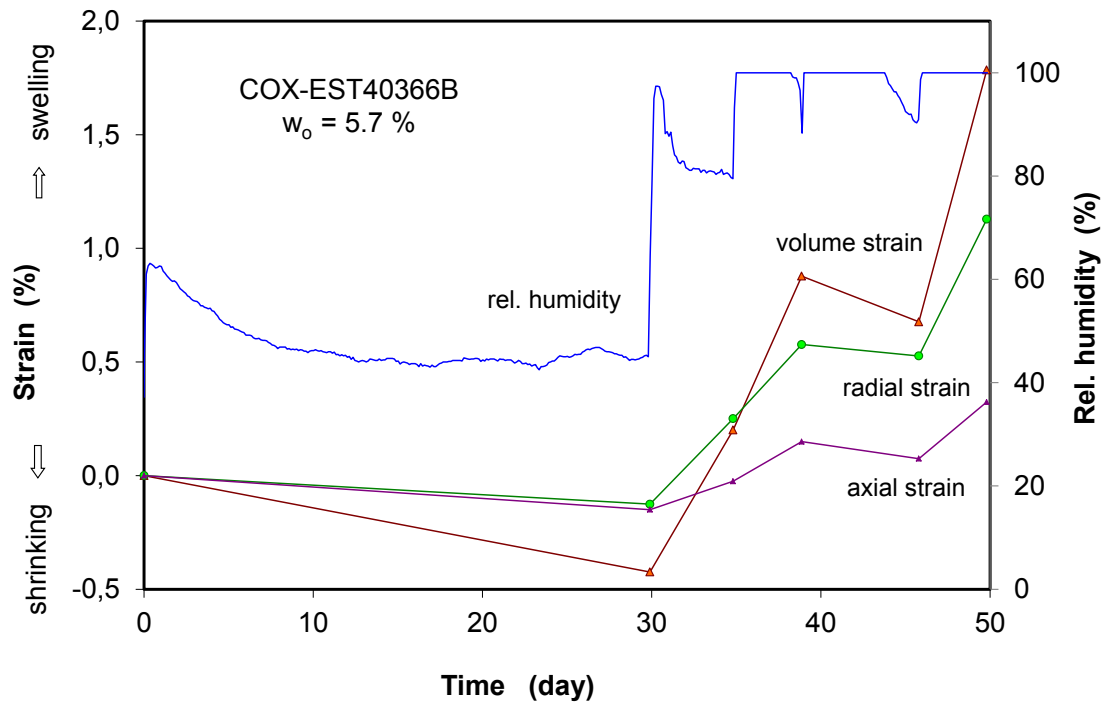
(d) Free swelling deformation

Fig. A.5   Results of swelling test 5 on COX sample EST40366
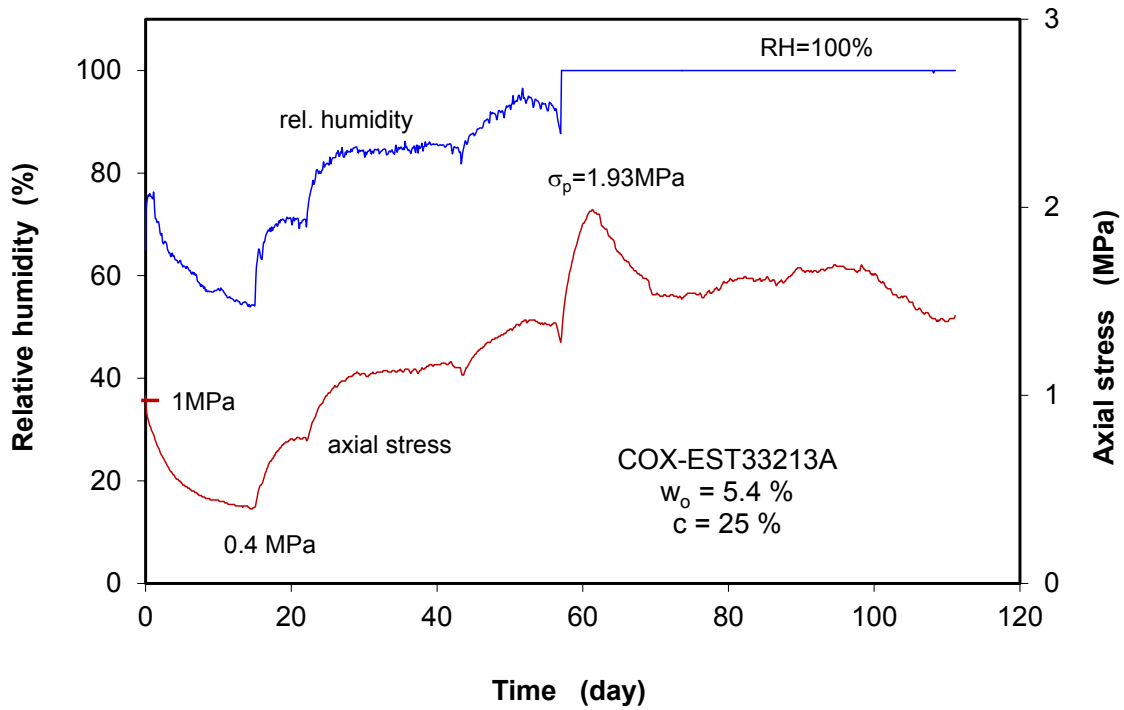
(a) Response of axial stress to humidity change
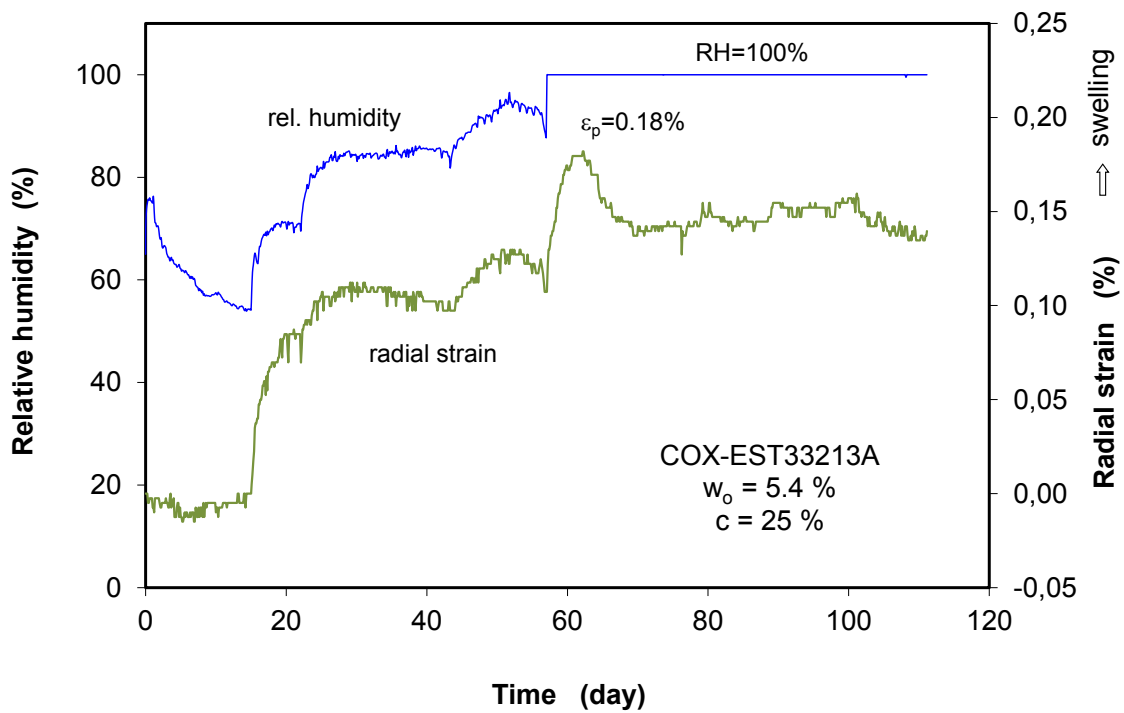
(b) Response of radial strain to humidity change
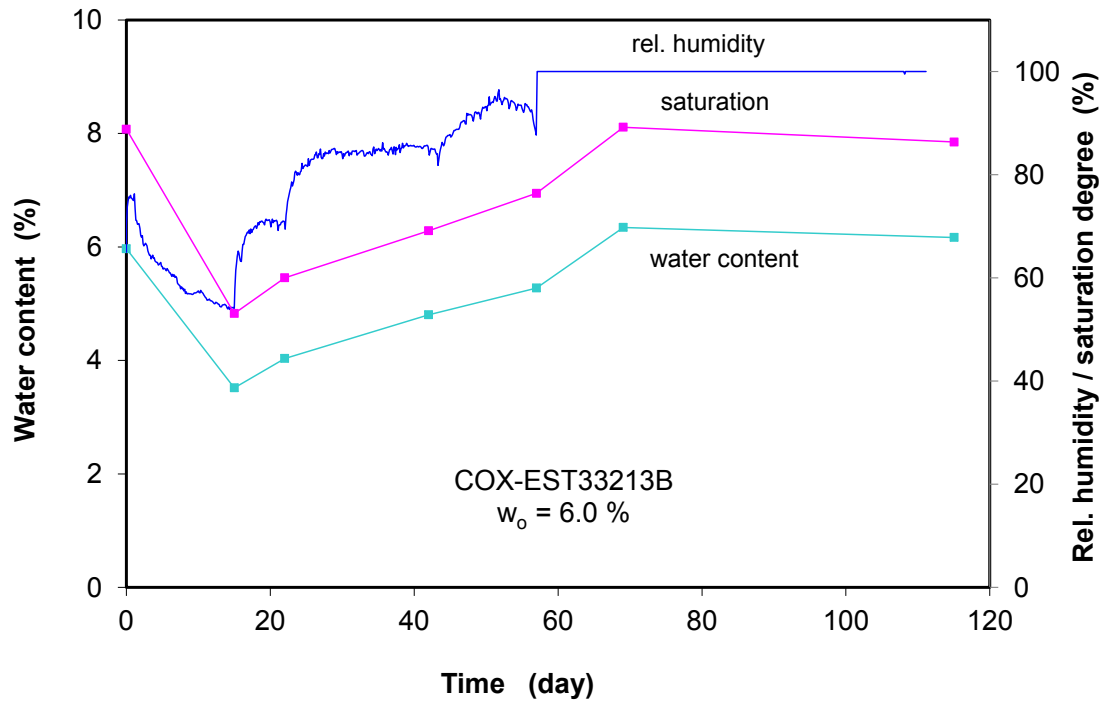
(c) Changes of water content and saturation
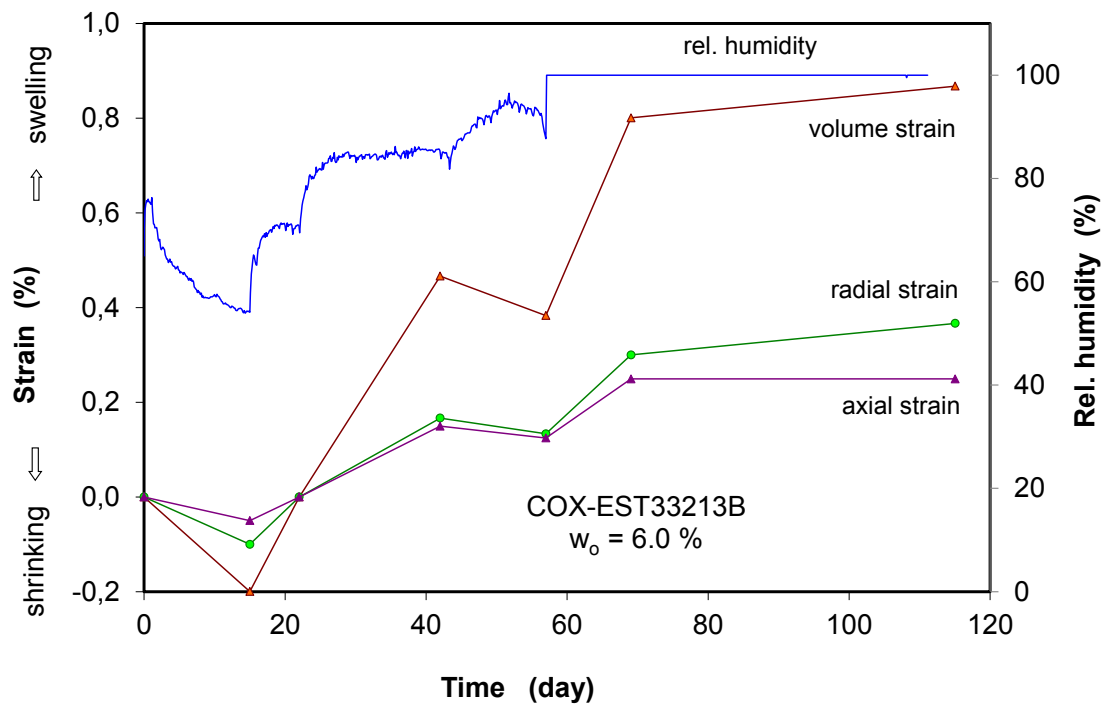
(d) Free swelling deformation

Fig. A.6 Results of swelling test 6 on COX sample EST33213
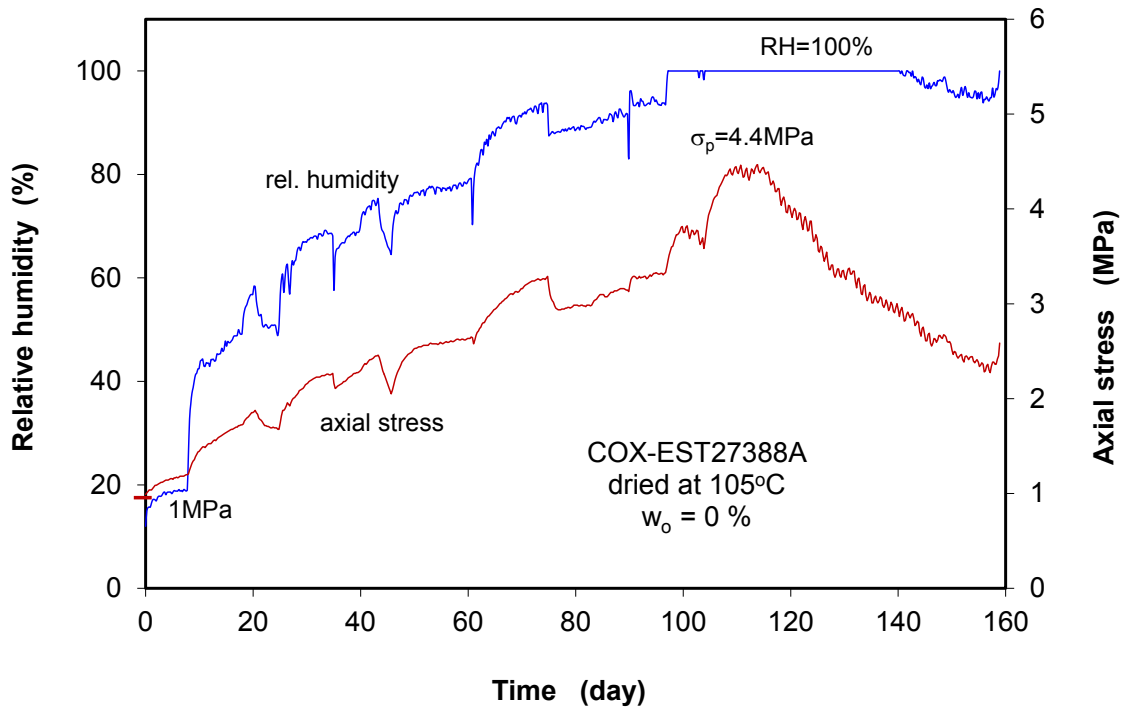
(a) Response of axial stress to humidity change
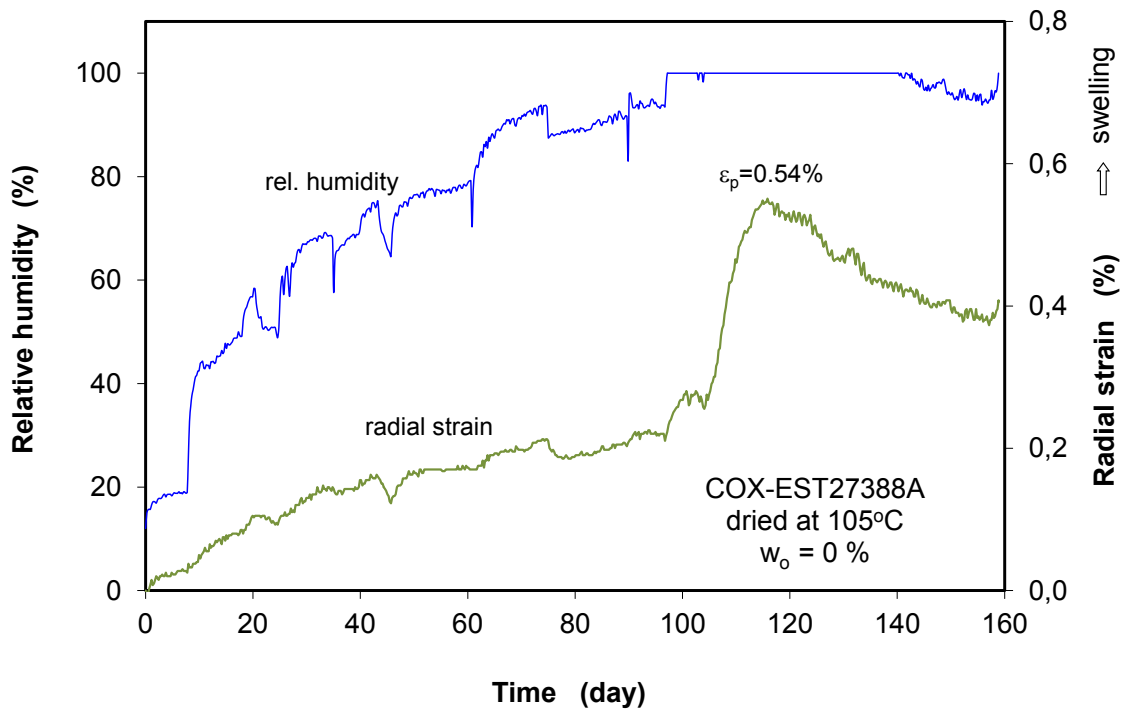
(b) Response of radial strain to humidity change
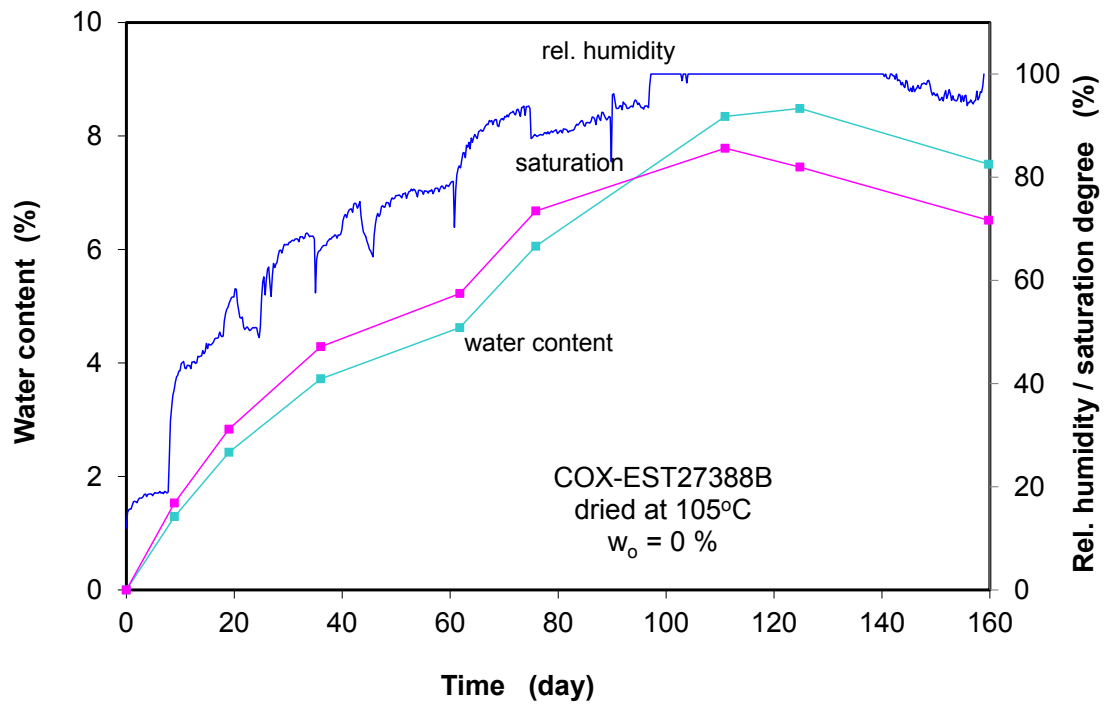
(c) Changes of water content and saturation
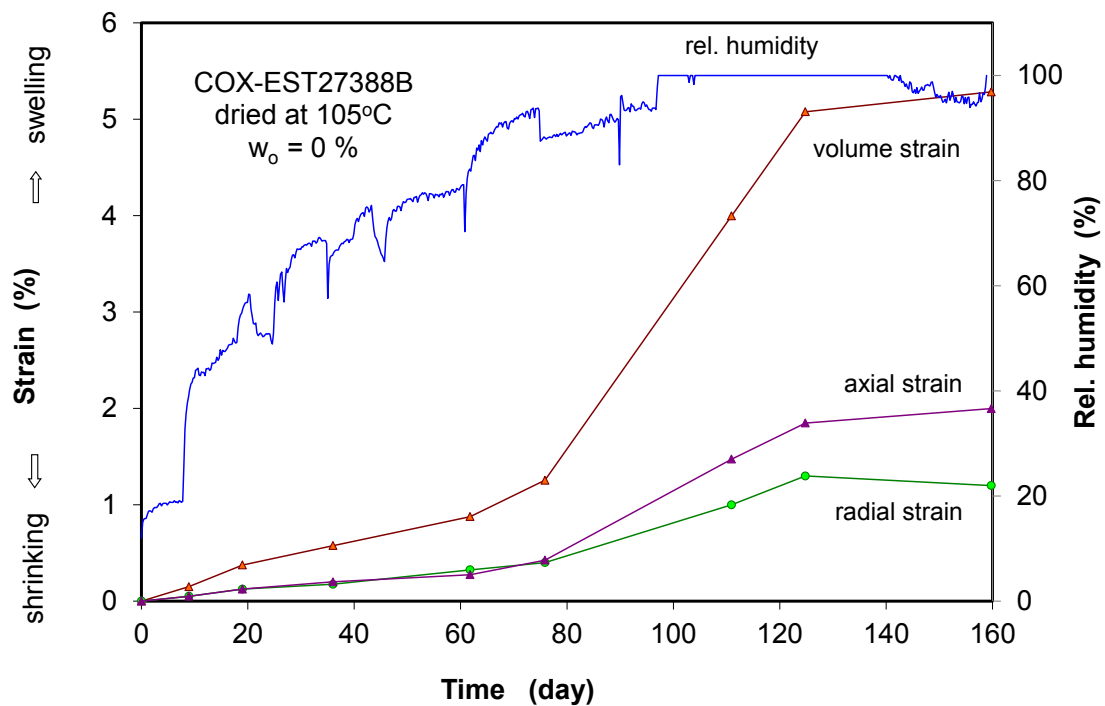
(d) Free swelling deformation

Fig. A.7   Results of swelling test 7 on COX sample EST27388
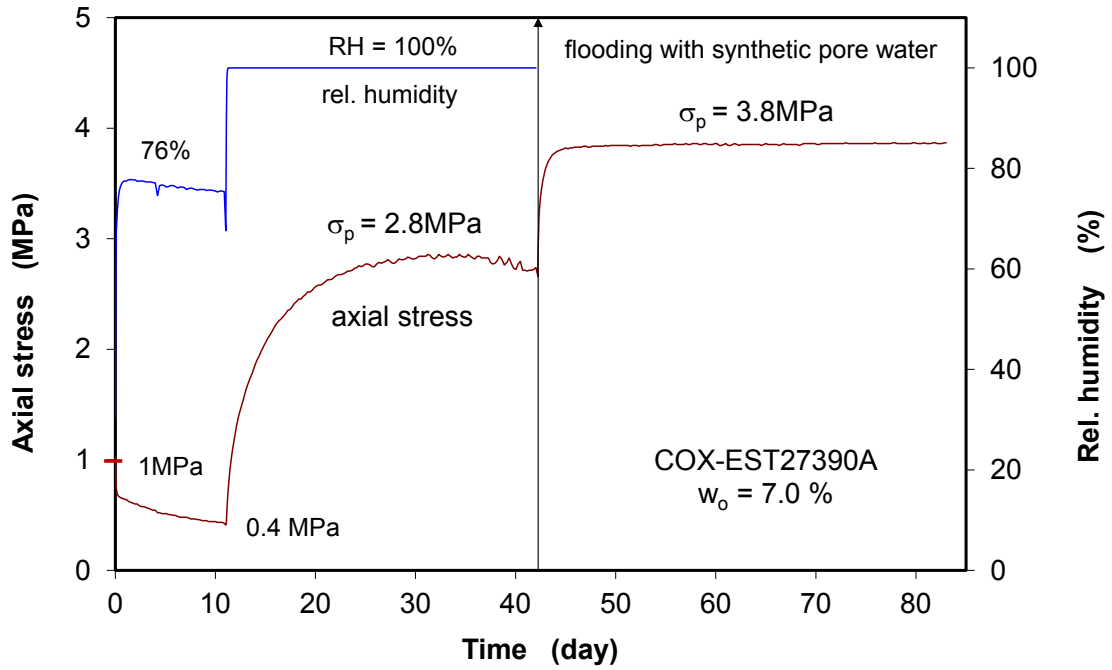
(a) Response of axial stress to humidity change
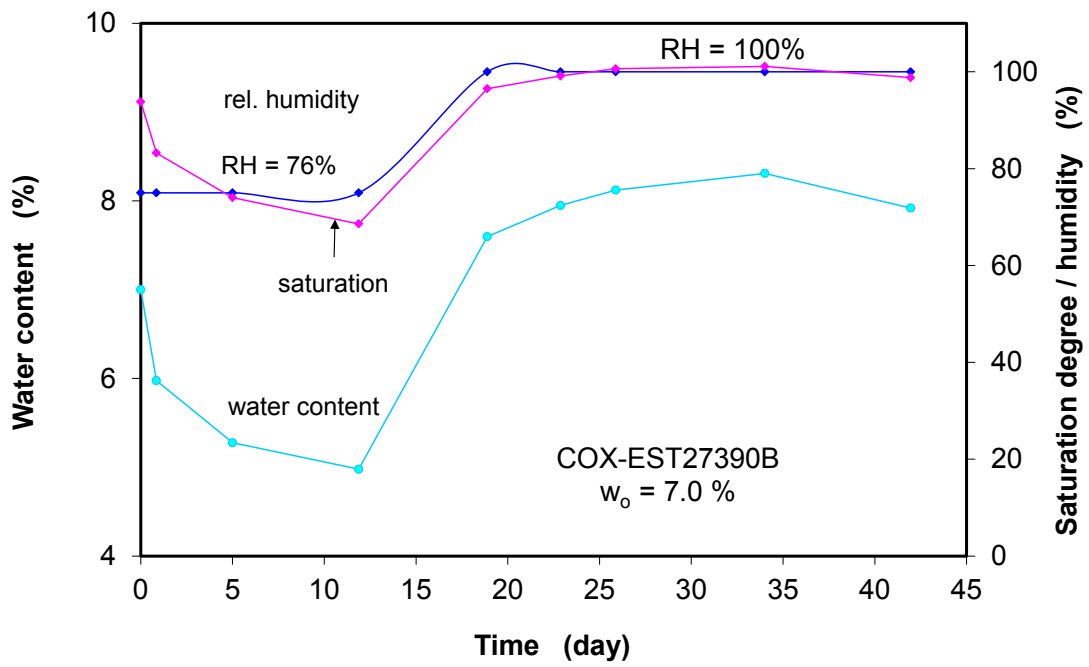
(b) Changes of water content and saturation
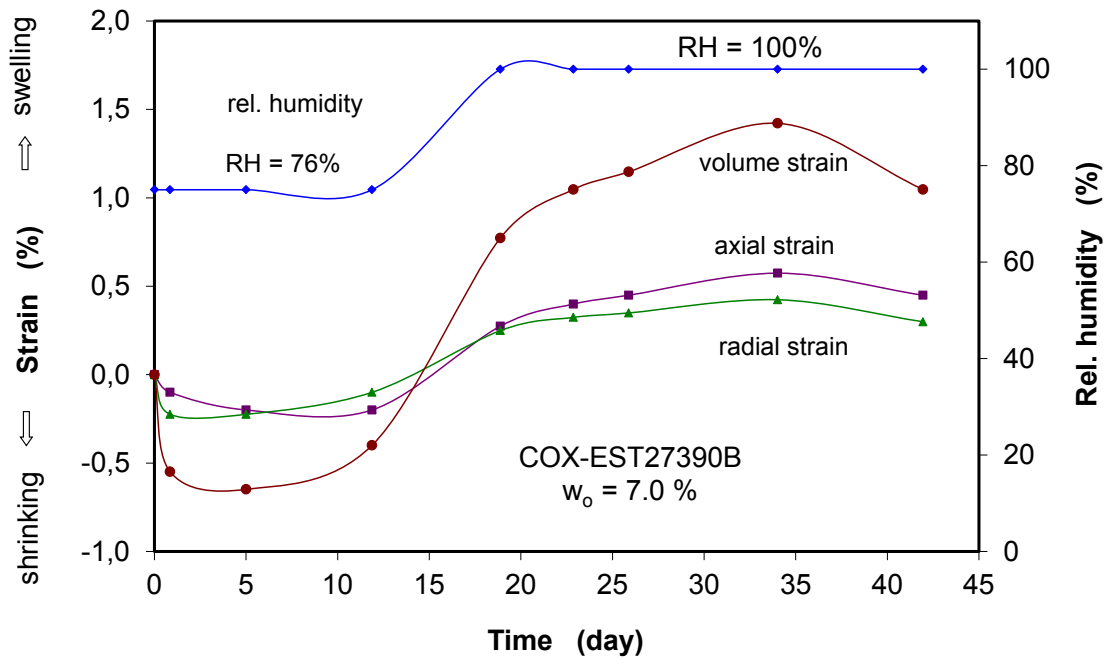
(c) Free swelling deformation

Fig. A.8   Results of swelling test 8 on COX sample EST27390
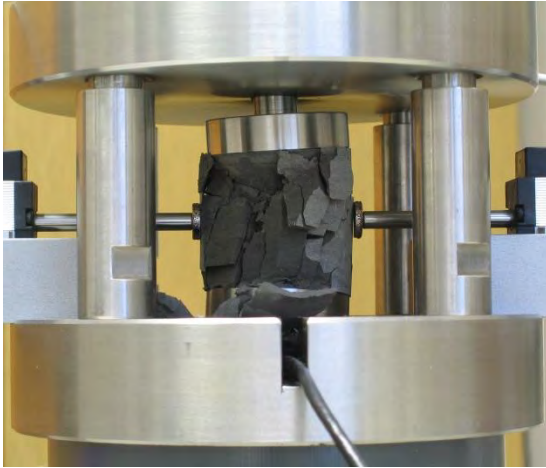
(d) OPA sample BET7 after wetting with water vapour
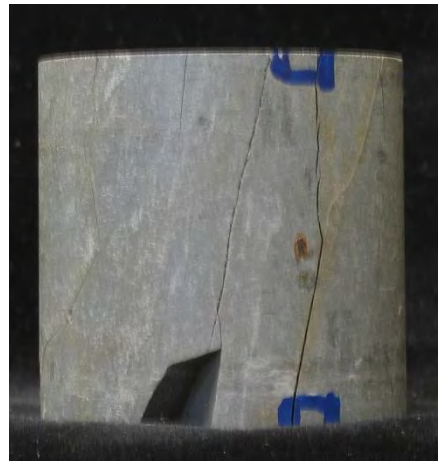
COX sample EST27387A after wetting with water vapour

(e) COX sample EST27390A pre-confined after exposing to synthetic porewater

(f) COX sample EST27390B unconfined after exposing to synthetic porewater

Fig. A.9 Photos of tested samples after wetting with vapour and liquid water

EST34693A σ_3 = 1 MPa	EST34717A σ_3 = 2 MPa	EST27347B σ_3 = 2.5 MPa	EST34713B σ_3 = 3 MPa
EST34689A σ_3 = 4 MPa	EST27347A σ_3 = 5 MPa	EST34717B σ_3 = 6 MPa	EST34711A σ_3 = 8 MPa
EST34711B σ_3 = 8 MPa	EST34721A σ_3 = 10 MPa	EST34713A σ_3 = 12 MPa	

Fig. B.10   Pictures of the first group COX samples before testing

B.1 Basic characteristic of the first group COX samples before triaxial compression testing

Tab. B.2   Basic characteristic of the first group COX samples before triaxial compression testing

Borehole	Sample ID	D/L [mm]	Grain density ρ_s [g/cm^3]	Bulk density ρ_b [g/cm^3]	Dry density ρ_d [g/cm^3]	Initial porosity ϕ_o [%]	Water content w [%]	Initial water saturation S_{wo} [%]	Porosity at 15MPa ϕ_e [%]	Water saturation at 15 MPa S_{we} [%]	Radial stress σ_3 [MPa]
TED1201	EST34689	70/140	2.702	2.375	2.211	18.2	6.89	83.9	16.3	95.6	4
	EST34693	"	2.675	2.403	2.271	15.1	5.51	82.8			1
TED1202	EST34711A	70/140	2.726	2.402	2.267	16.8	5.61	75.6			8
	EST34711B	"	2.726	2.400	2.265	16.9	5.61	75.2			8
	EST34713A	"	2.740	2.396	2.228	18.7	7.00	83.5	16.1	100.0	12
	EST34713B	"	2.747	2.394	2.241	18.4	6.40	77.8			3
	EST34717A	"	2.716	2.409	2.232	17.8	7.35	92.0	16.6	100.3	2
	EST34717B	"	2.716	2.405	2.228	18.0	7.35	91.2	16.6	100.3	6
	EST34721A	"	2.710	2.407	2.230	17.7	7.35	92.6	16.5	100.8	10
PAC1011	EST27347A	70/140	2.689	2.391	2.215	17.6	7.36	92.5			5
	EST27347B	"	2.689	2.397	2.221	17.4	7.36	93.8			2.5
	Mean value		**2.712**	**2.398**	**2.237**	**17.5**	**6.71**	**85.5**	**16.4**	**100.0**	

Measured data of deformation, gas permeability, ultrasonic wave am-plitude and velocity during triaxial compression tests
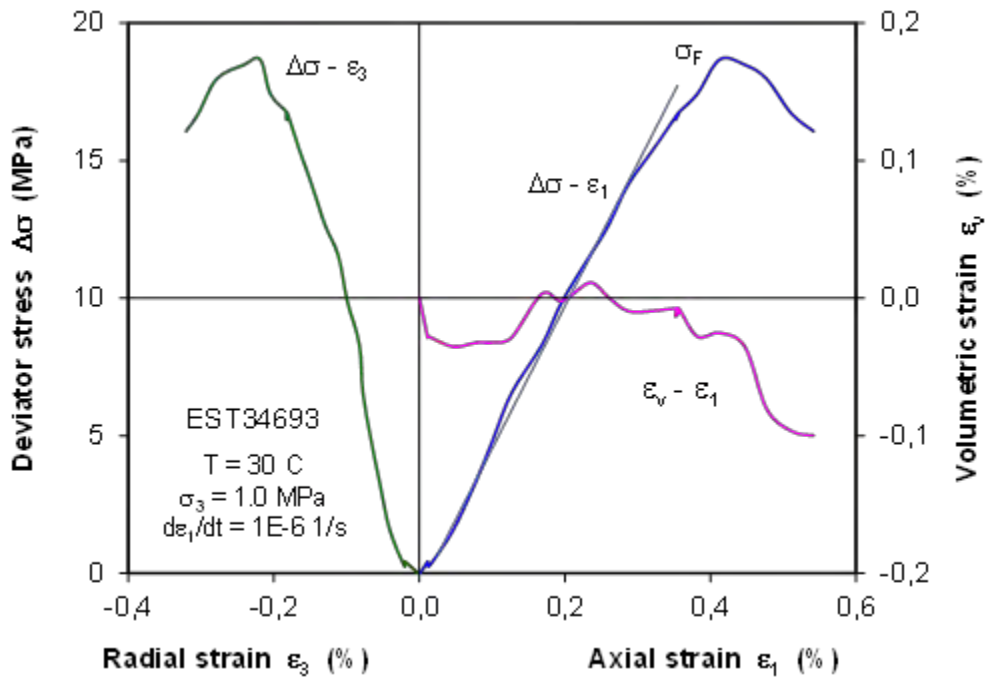
(a) Measured data of deformation
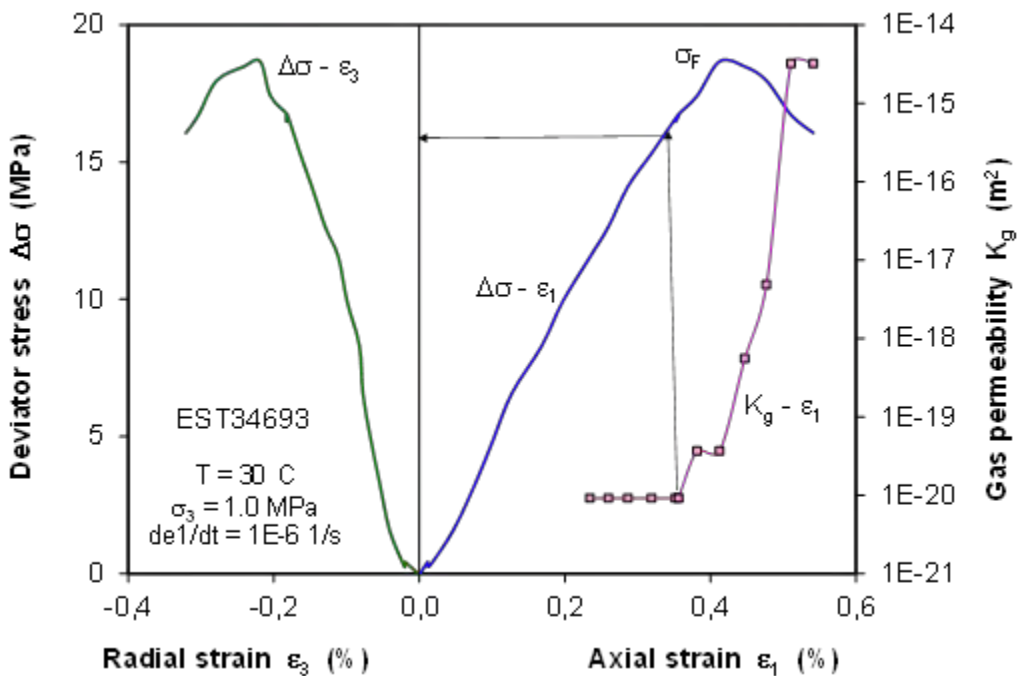
(b) Measured data of gas permeability
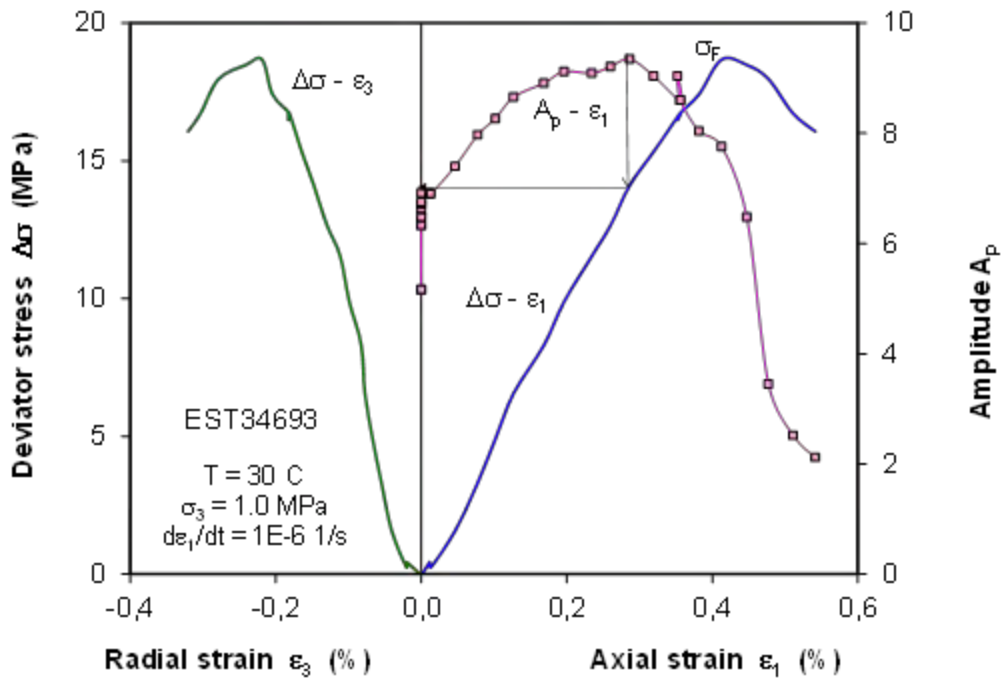
(c) Measured data of ultrasonic wave amplitude
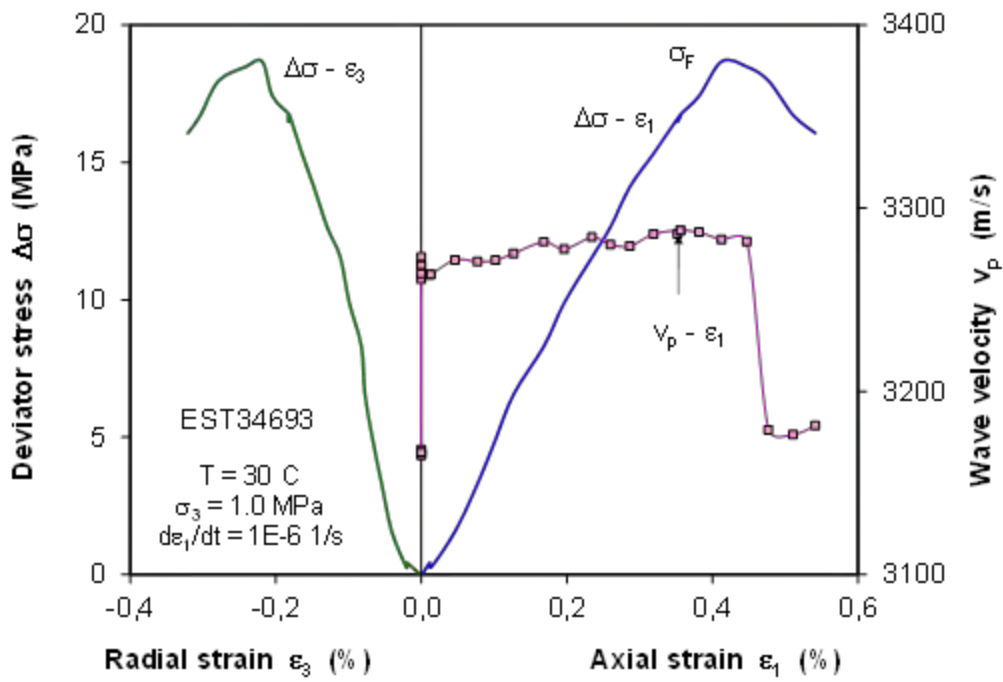
(d) Measured data of velocity

Fig. B.11 Results of deviatoric compression at lateral confining stress of 1 MPa
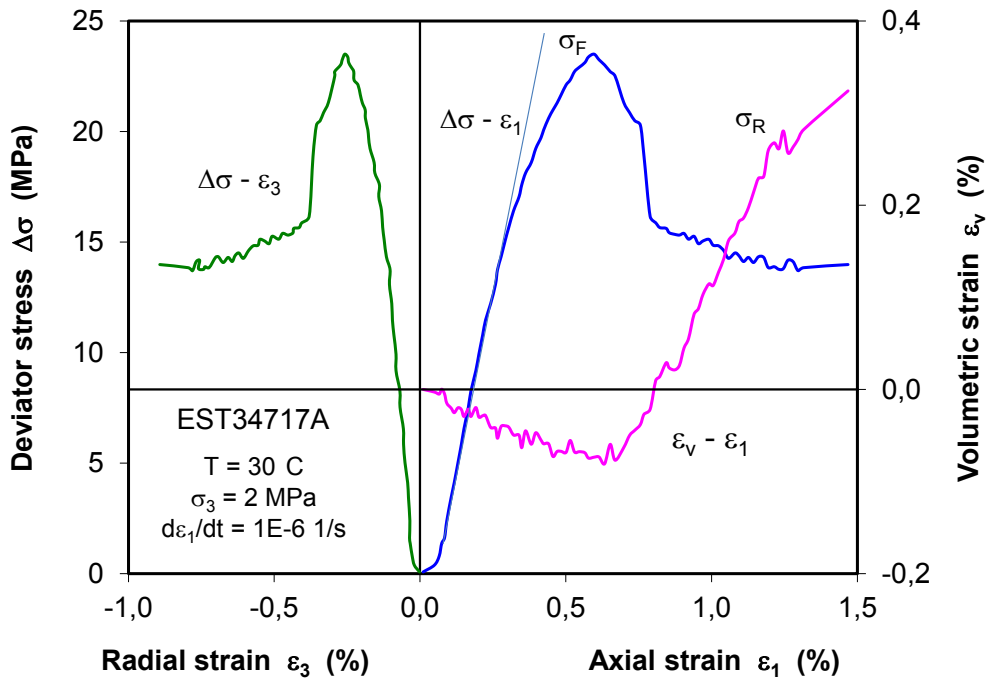
(a) Measured data of deformation
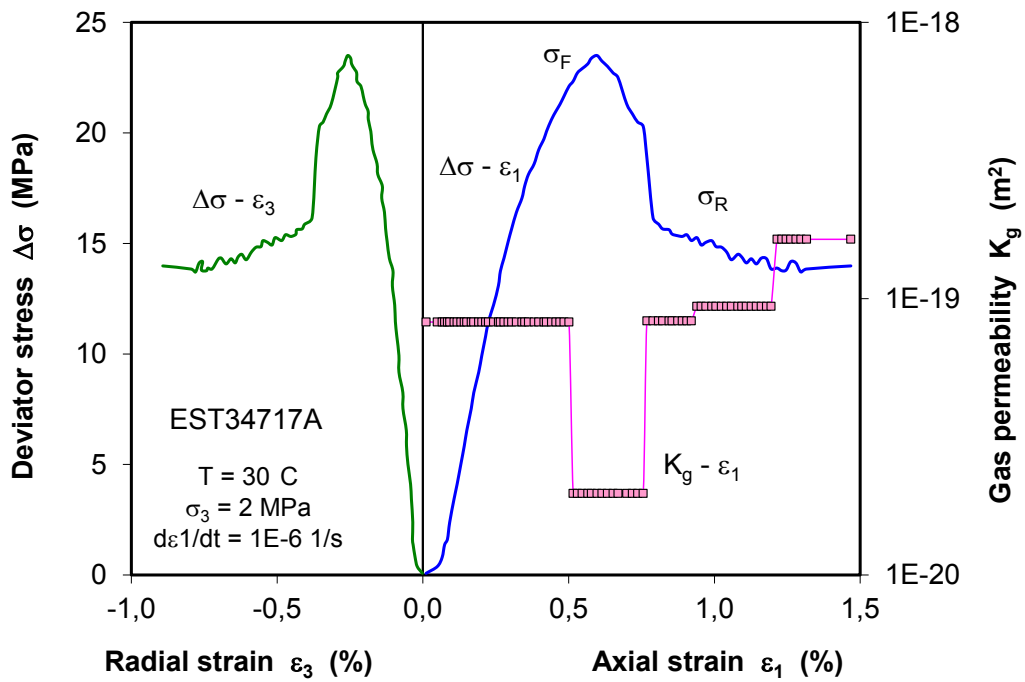
(b) Measured data of gas permeability
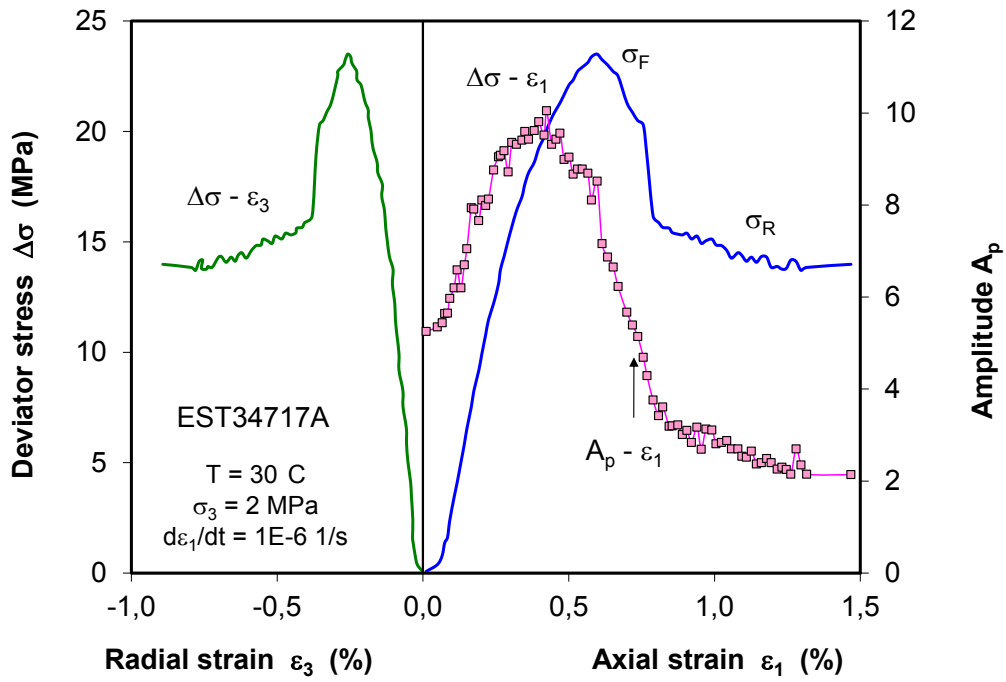
(c) Measured data of ultrasonic wave amplitude
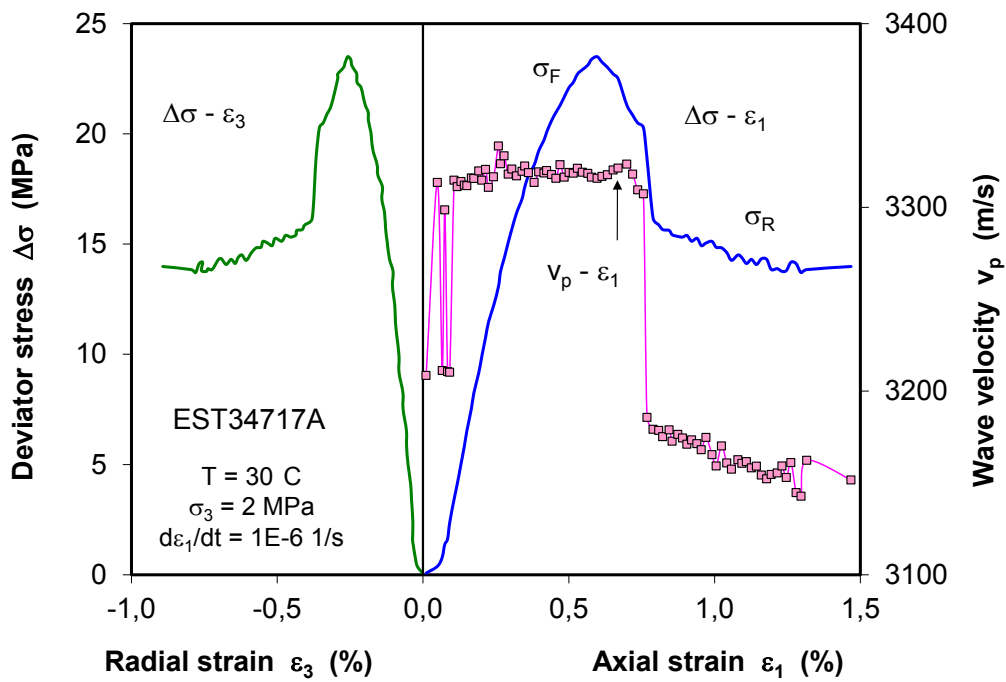
(d) Measured data of velocity

Fig. B.12   Results of deviatoric compression at lateral confining stress of 2 MPa
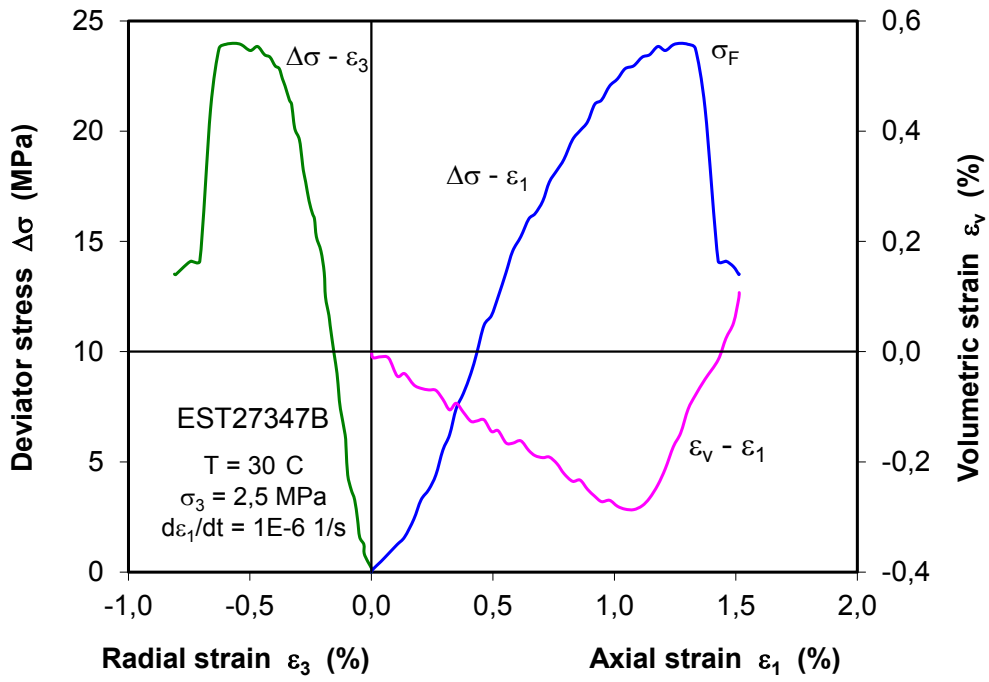
(a) Measured data of deformation
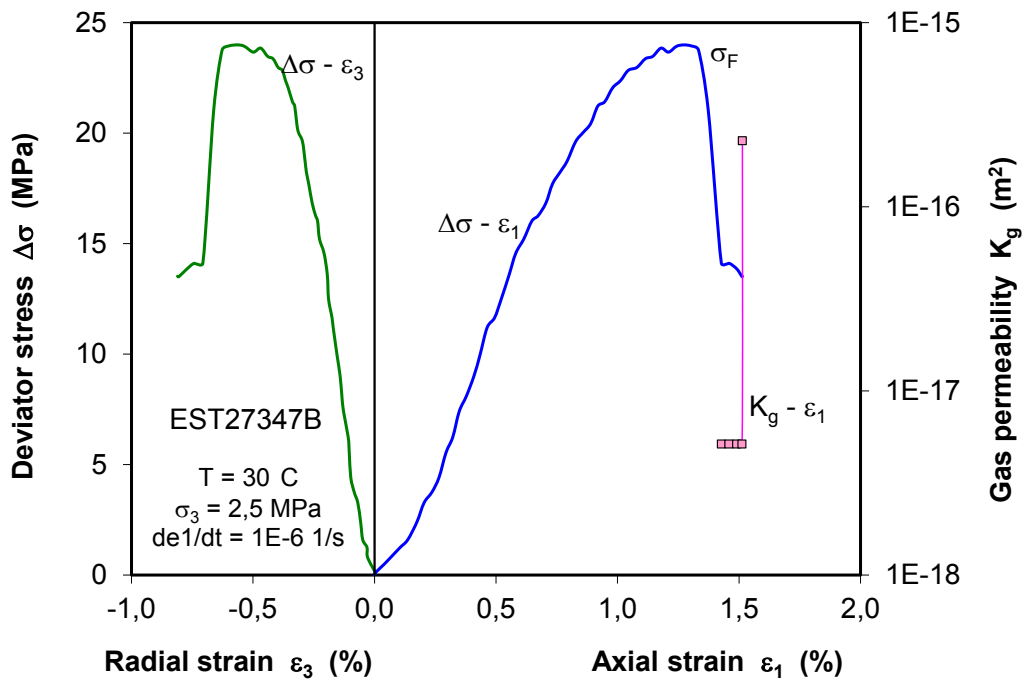
(b) Measured data of gas permeability
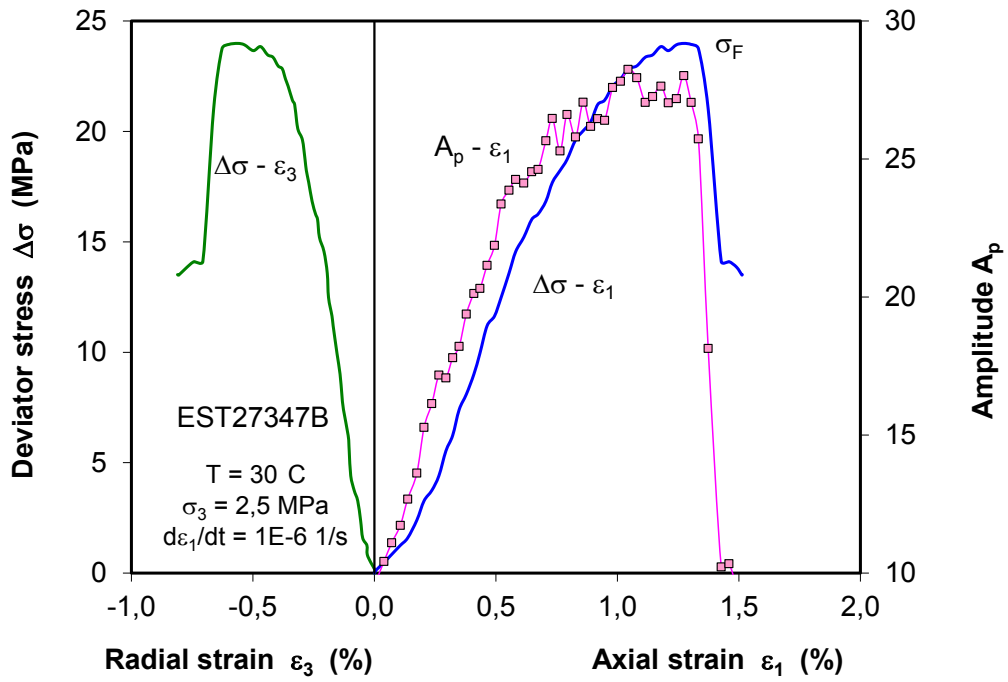
(c) Measured data of ultrasonic wave amplitude
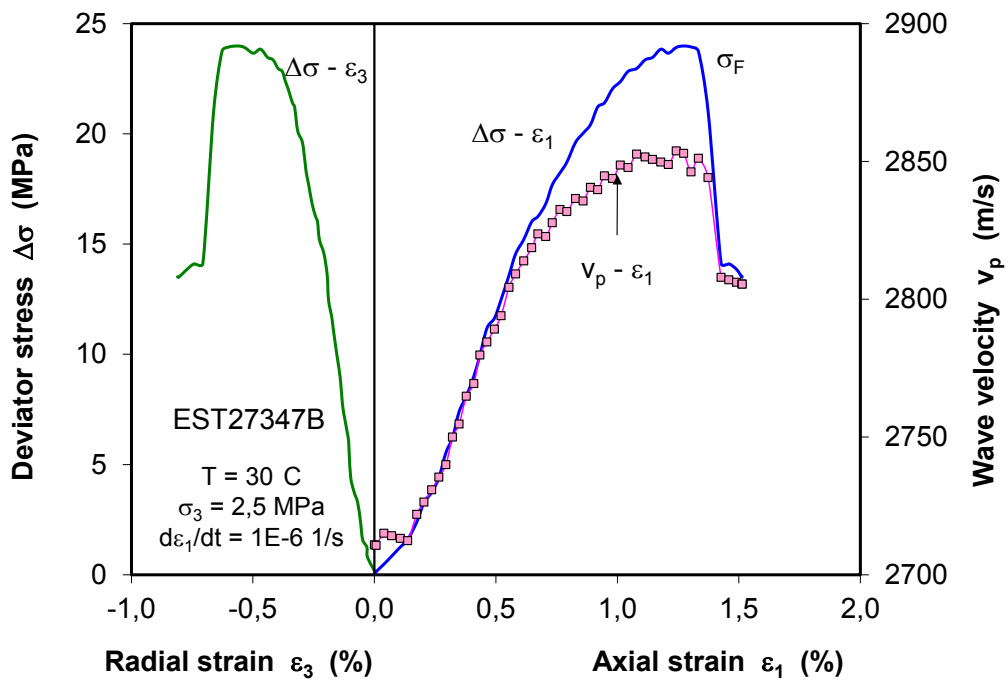
(d) Measured data of velocity

Fig. B.13 Results of deviatoric compression at lateral confining stress of 2.5 MPa
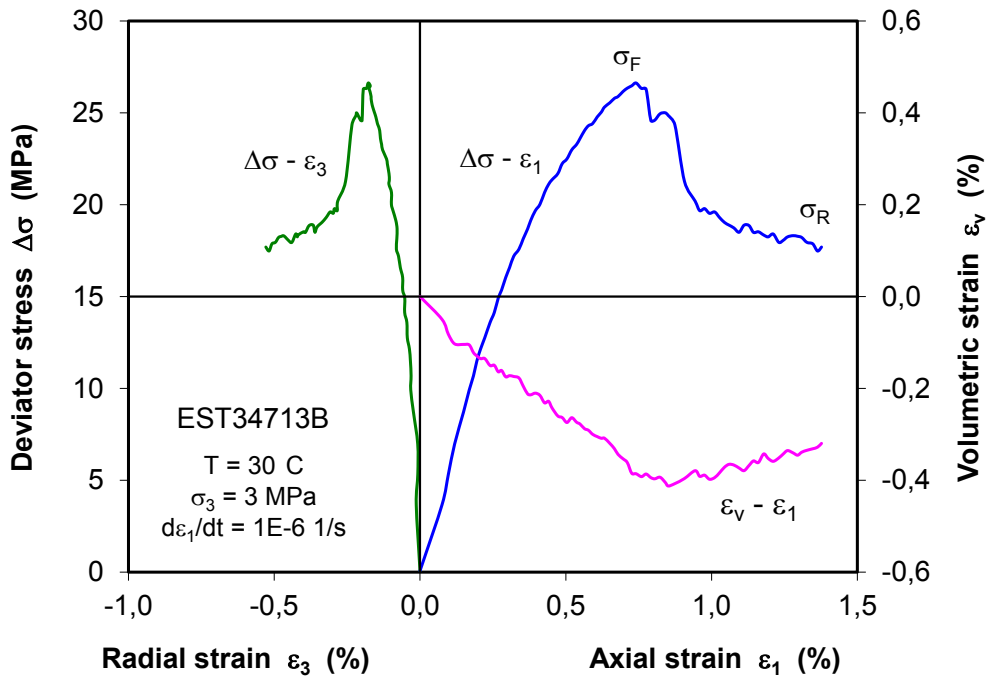
(a) Measured data of deformation
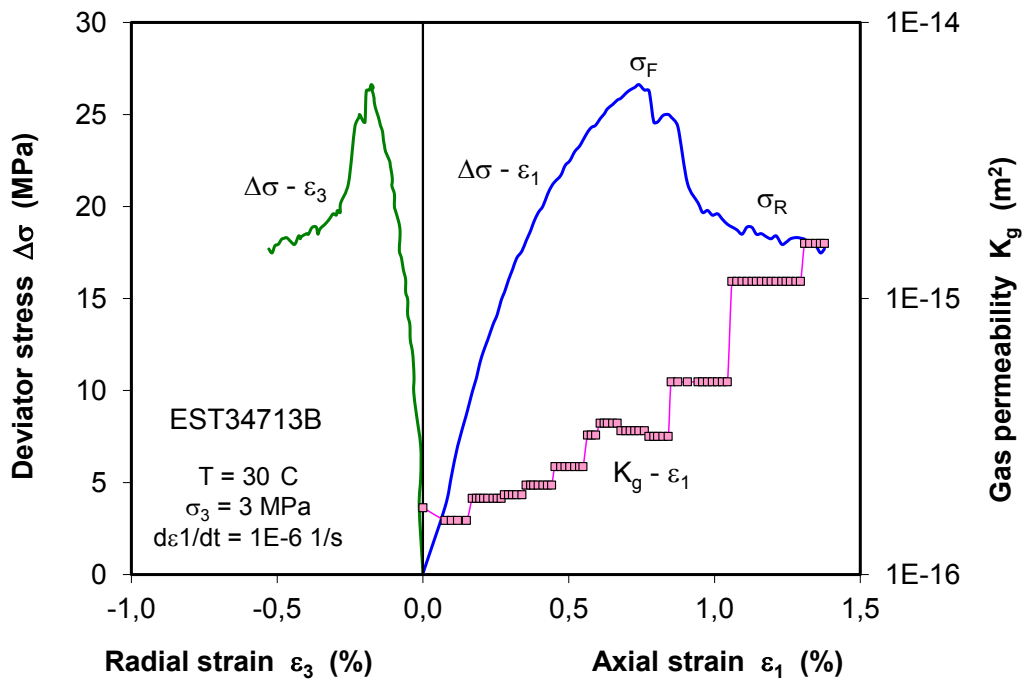
(b) Measured data of gas permeability
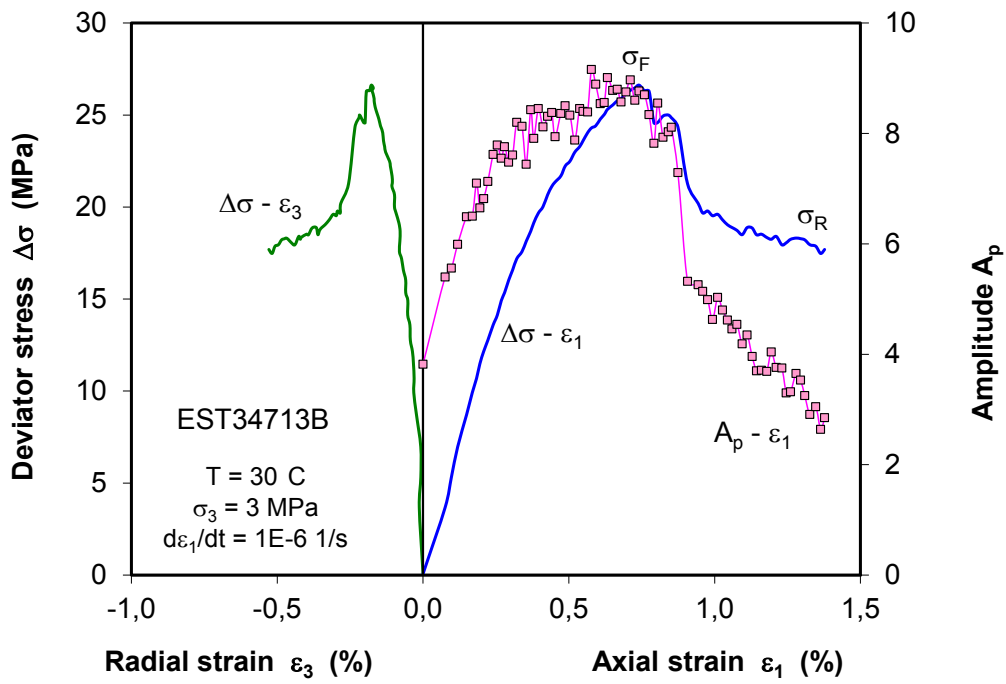
(c) Measured data of ultrasonic wave amplitude
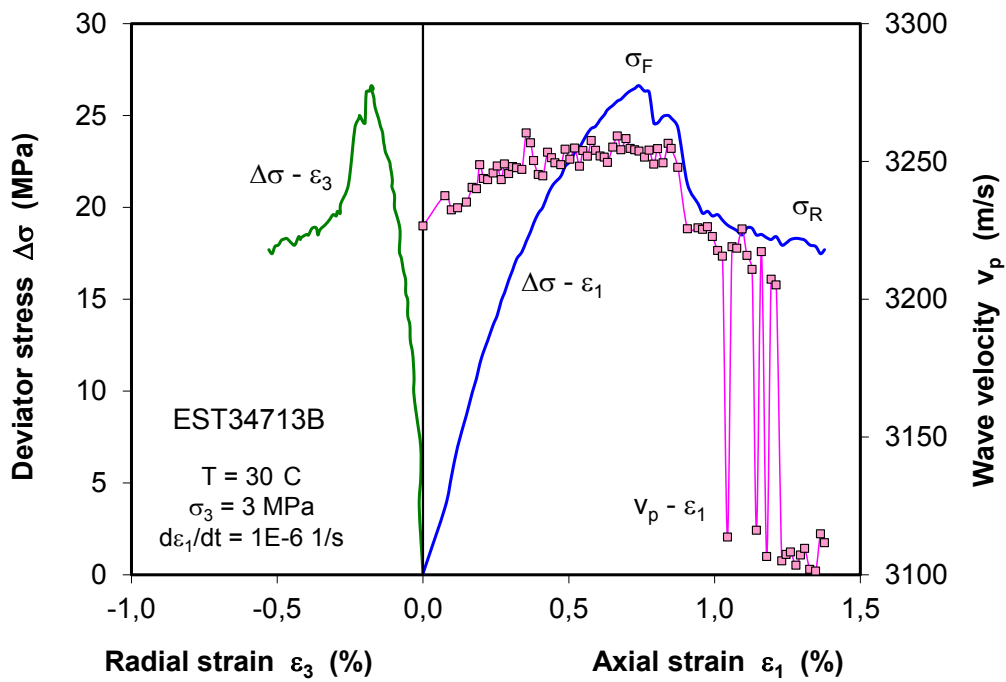
(d) Measured data of velocity

Fig. B.14 Results of deviatoric compression at lateral confining stress of 3 MPa
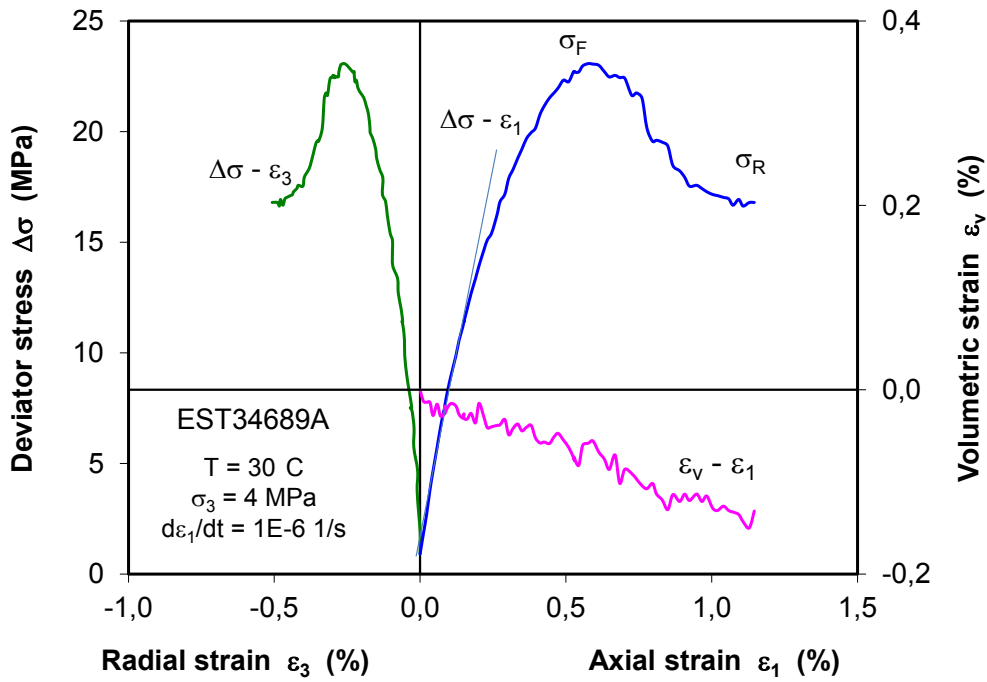
(a) Measured data of deformation
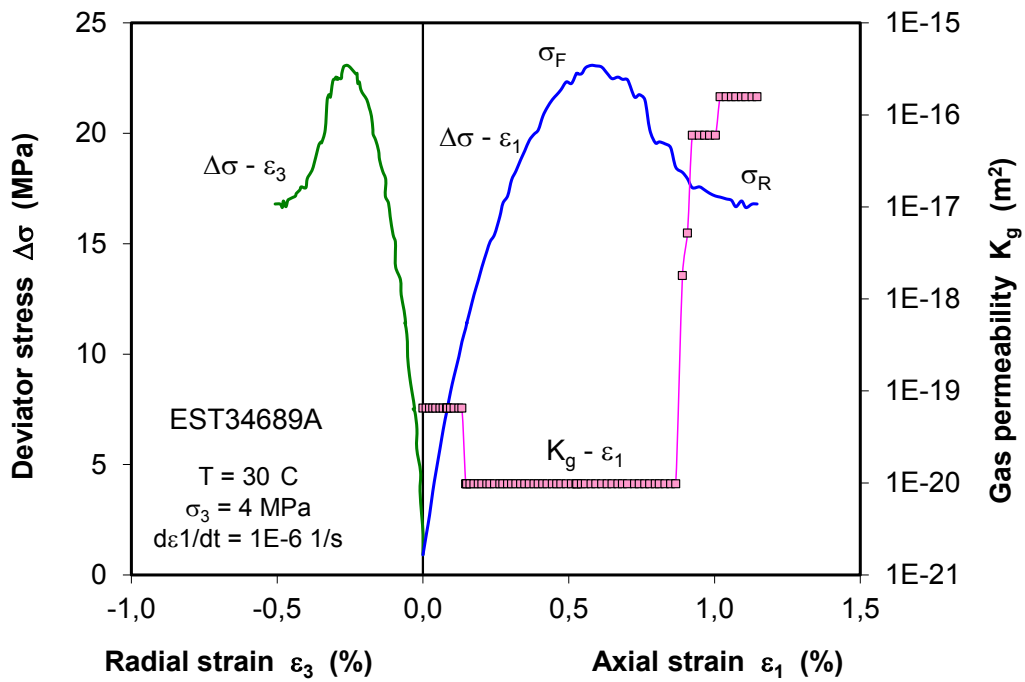
(b) Measured data of gas permeability
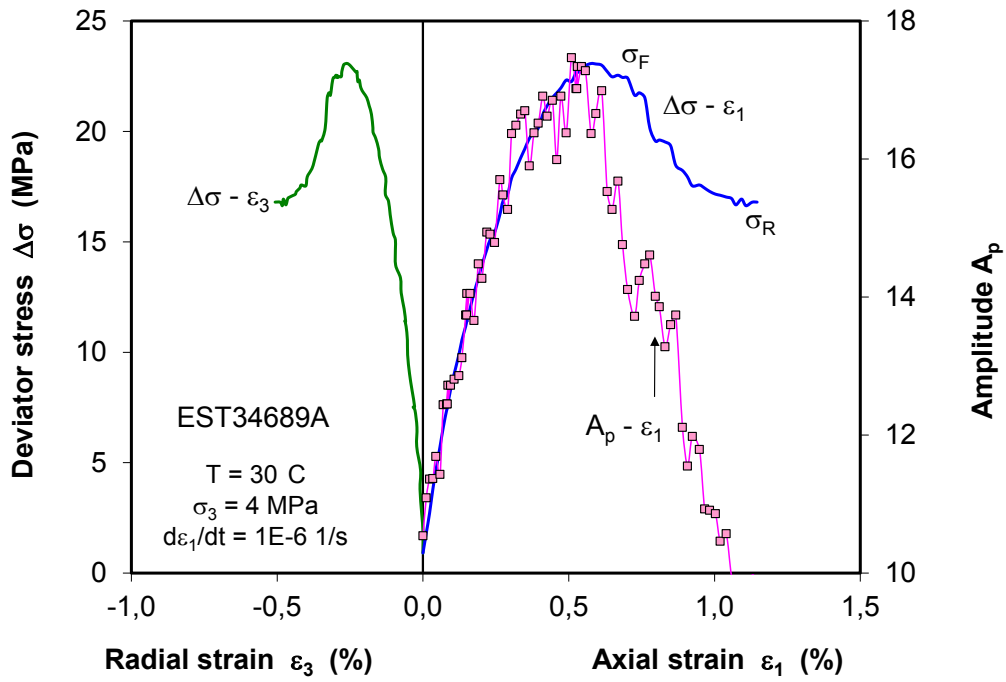
(c) Measured data of ultrasonic wave amplitude
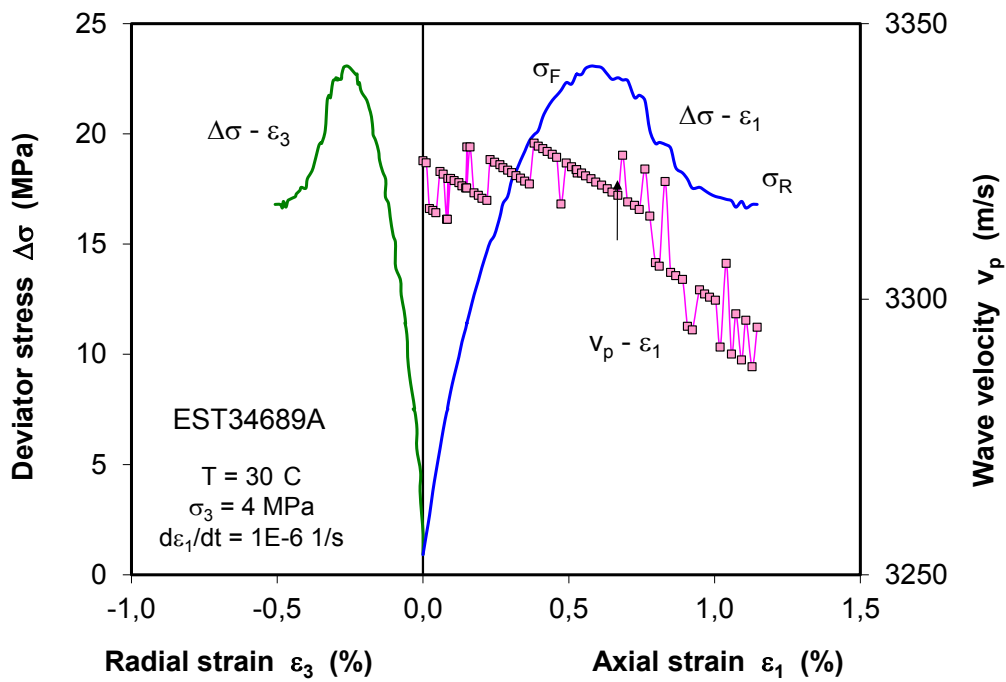
(d) Measured data of velocity

Fig. B.15 Results of deviatoric compression at lateral confining stress of 4 MPa
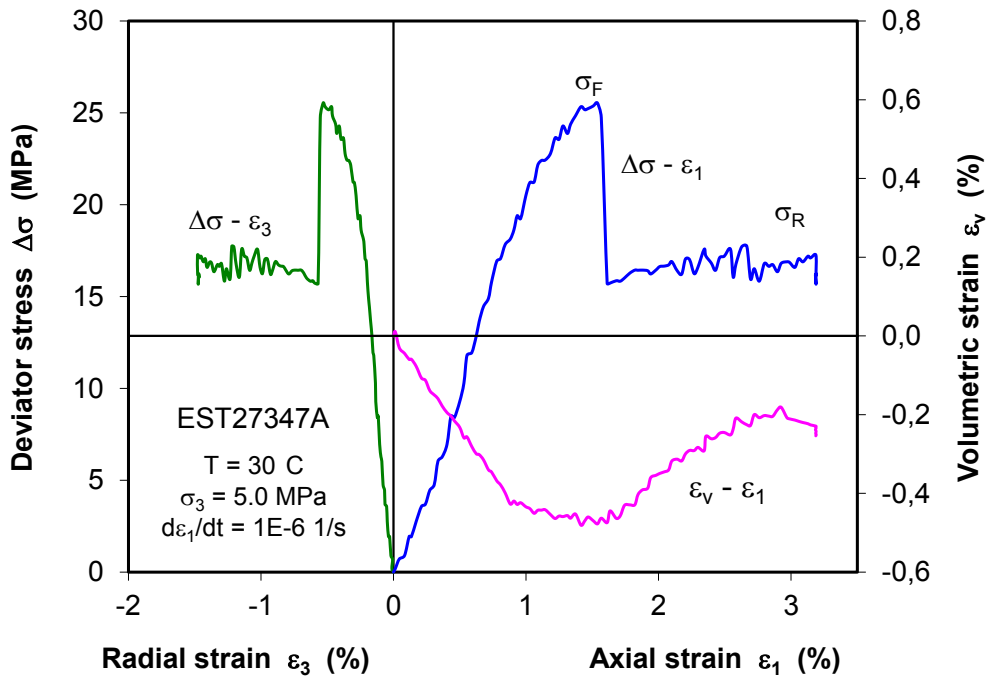
(a) Measured data of deformation
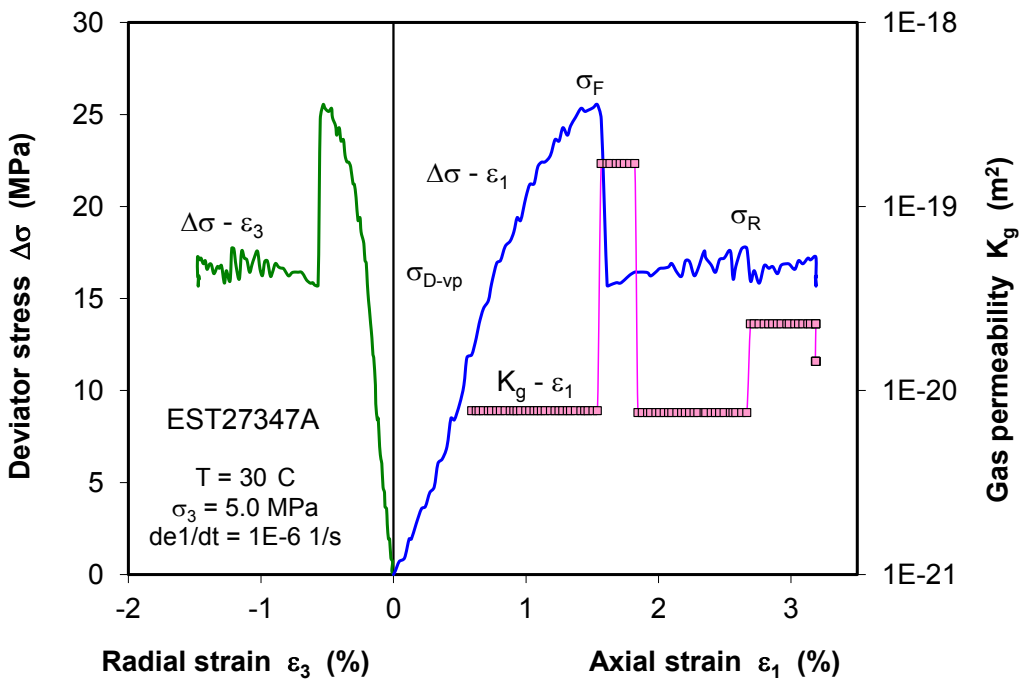
(b) Measured data of gas permeability
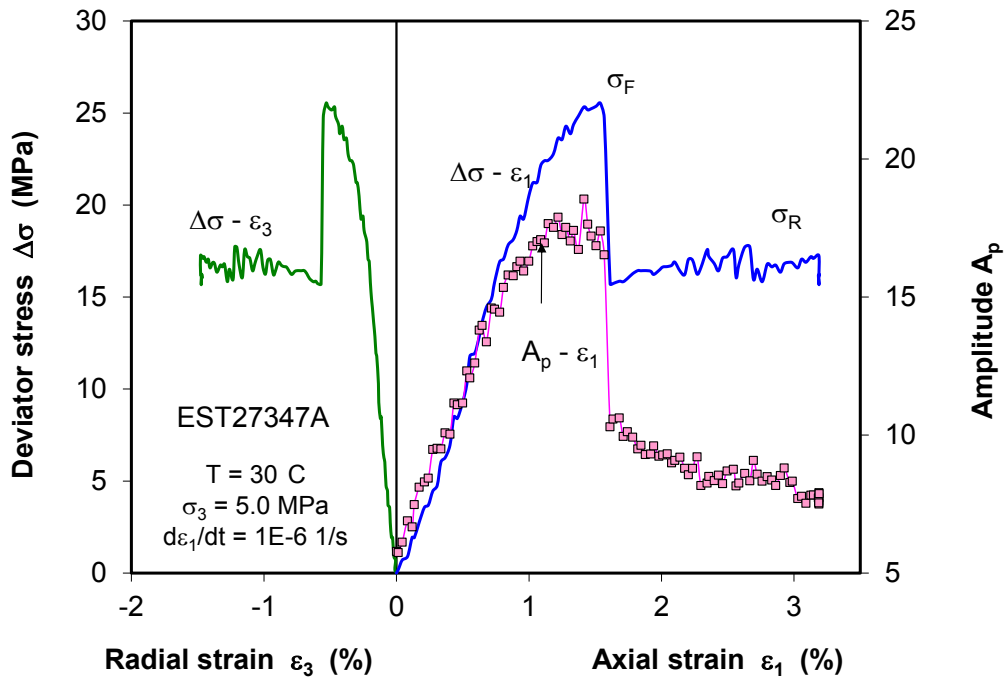
(c) Measured data of ultrasonic wave amplitude
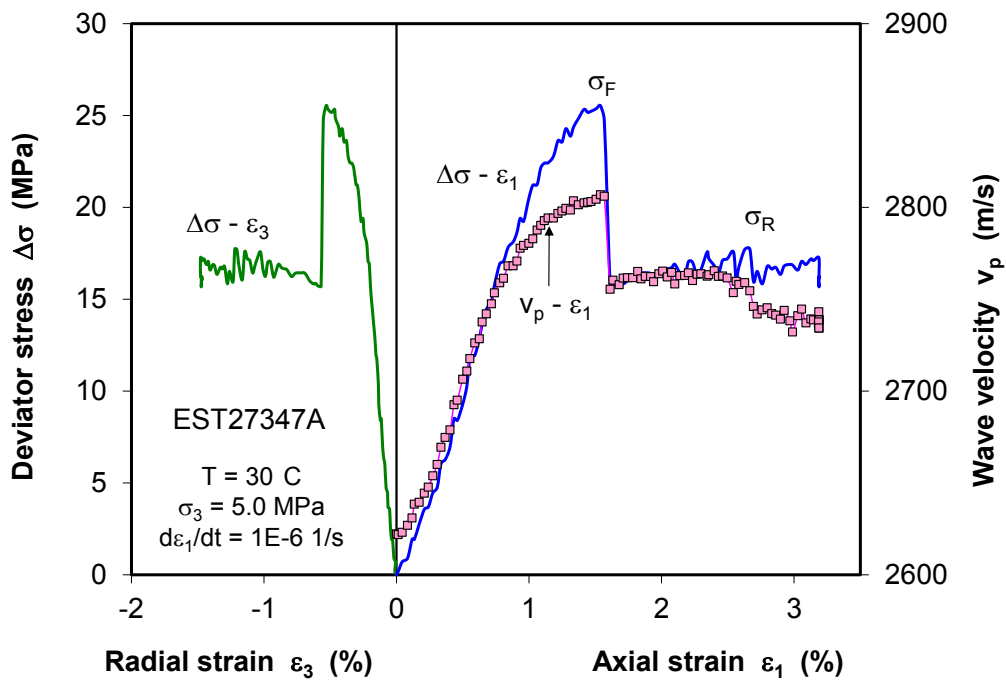
(d) Measured data of velocity

Fig. B.16 Results of deviatoric compression at lateral confining stress of 5 MPa
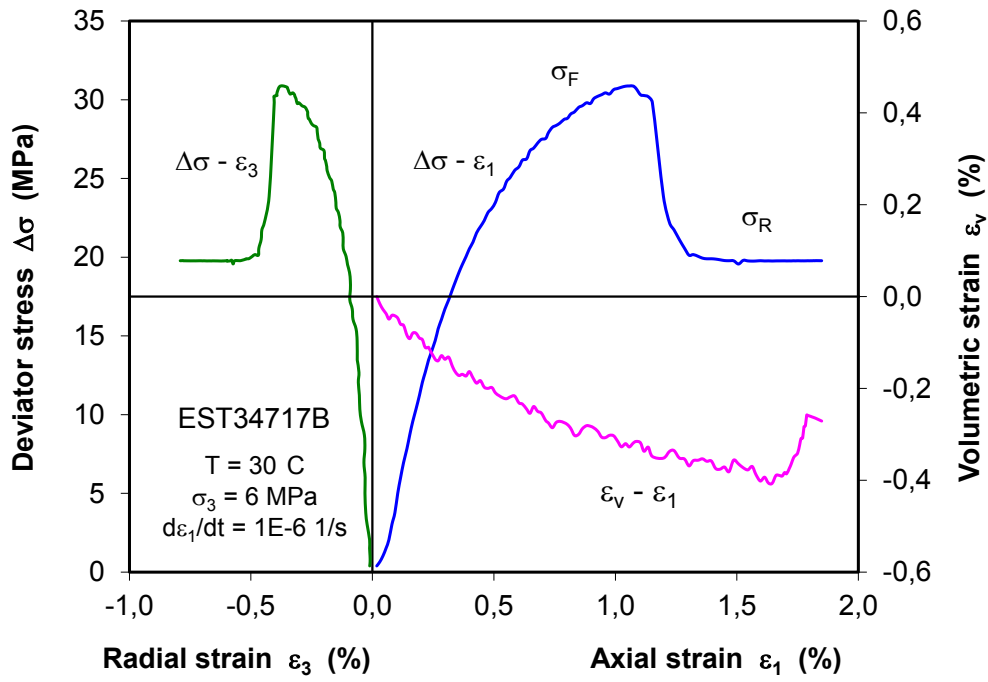
(a) Measured data of deformation
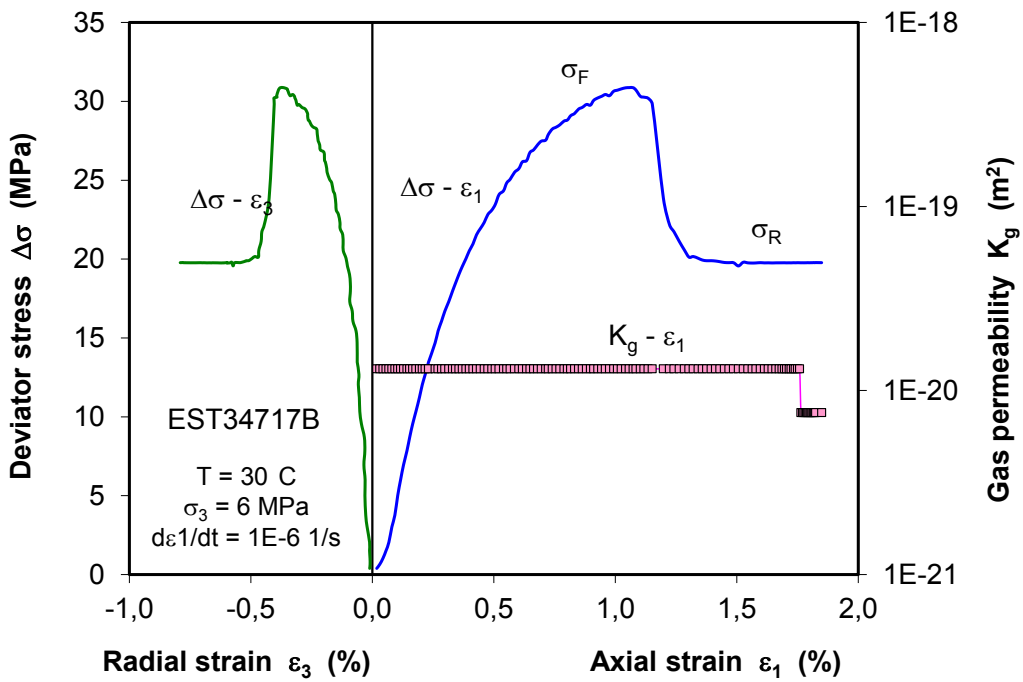
(b) Measured data of gas permeability
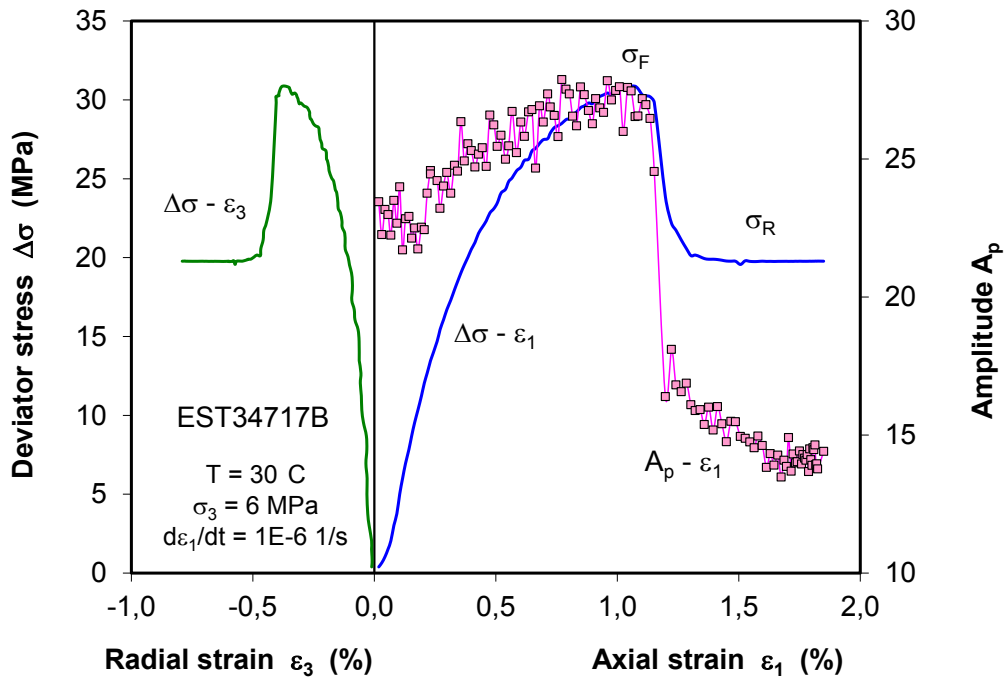
(c) Measured data of ultrasonic wave amplitude
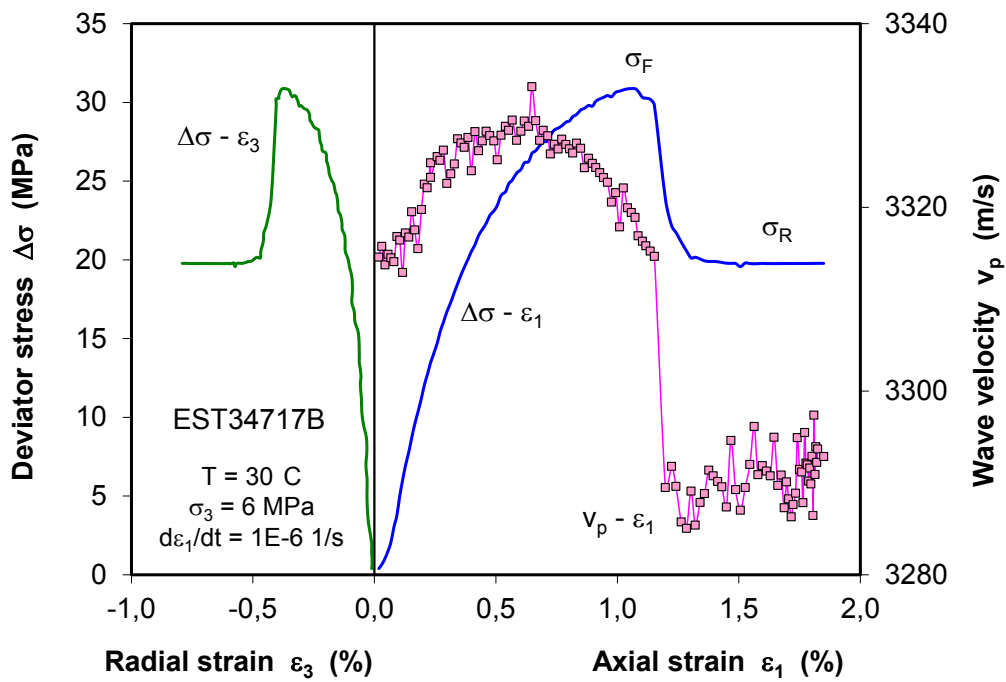
(d) Measured data of velocity

Fig. B.17 Results of deviatoric compression at lateral confining stress of 6 MPa
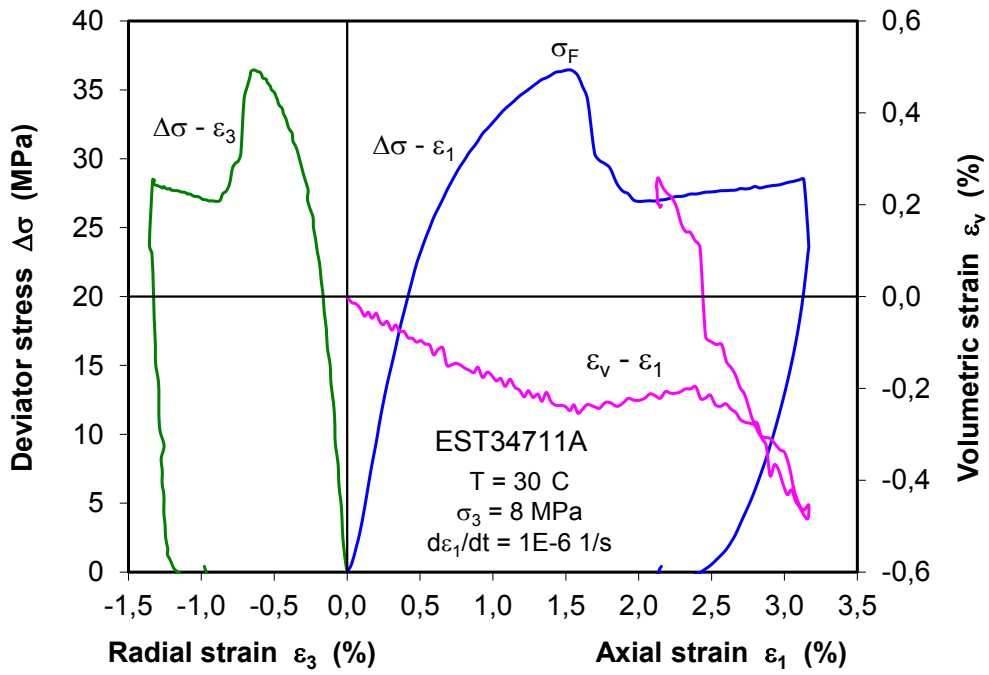
(a) Measured data of deformation
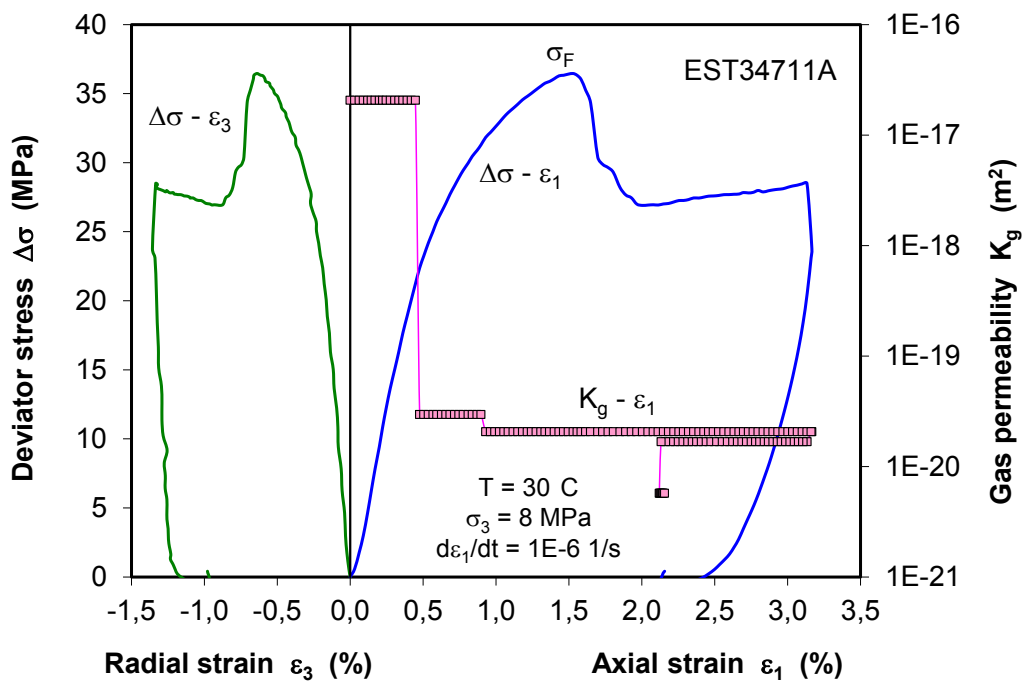
(b) Measured data of gas permeability
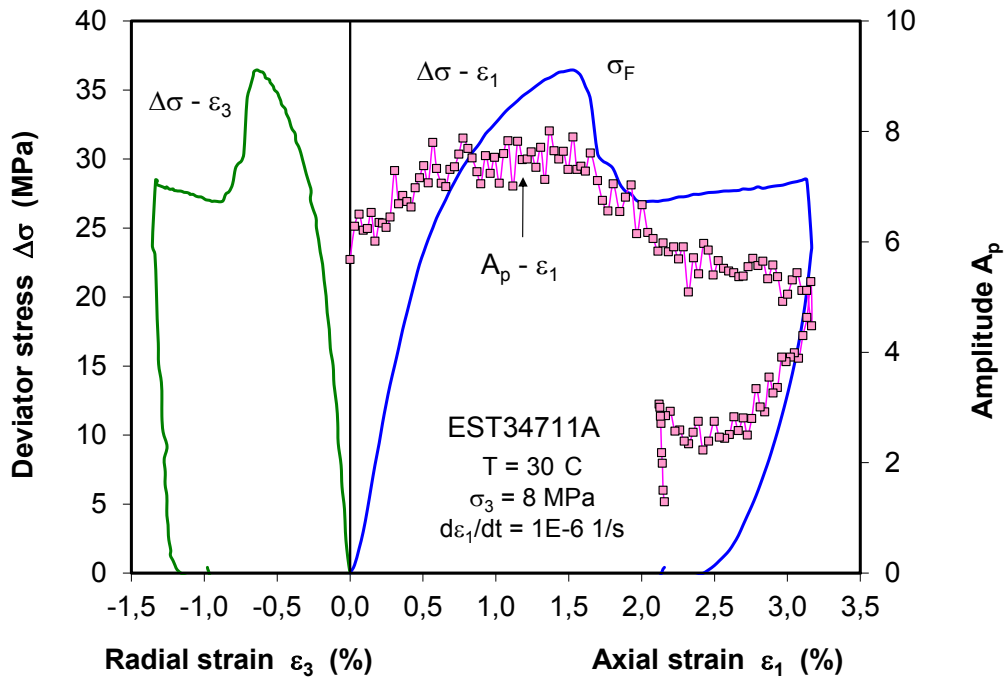
(c) Measured data of ultrasonic wave amplitude
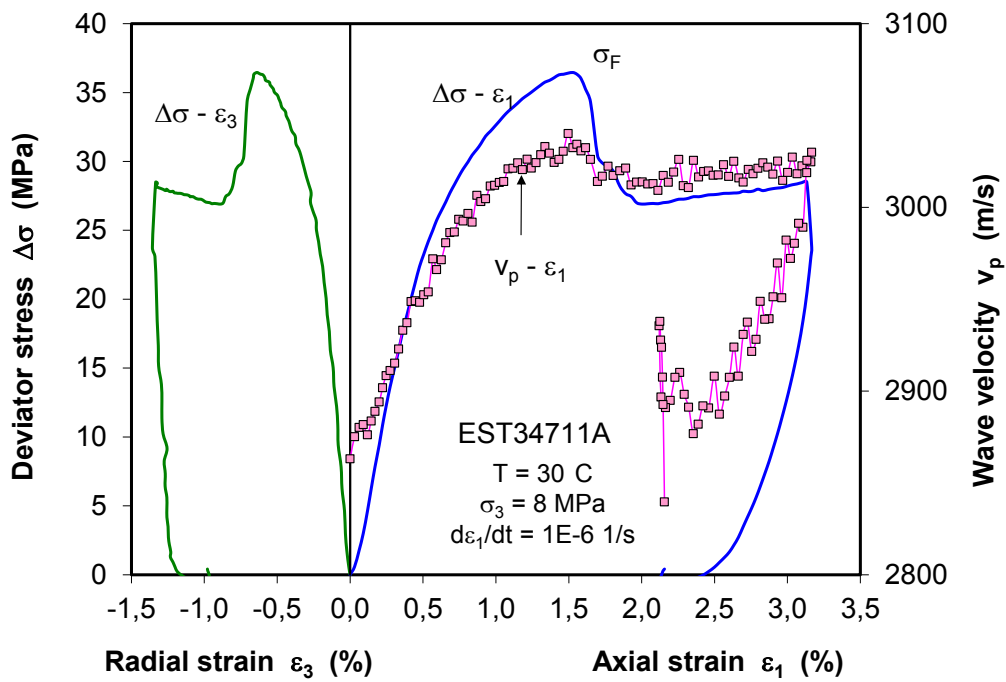
(d) Measured data of velocity

Fig. B.18 Results of deviatoric compression at lateral confining stress of 8 MPa
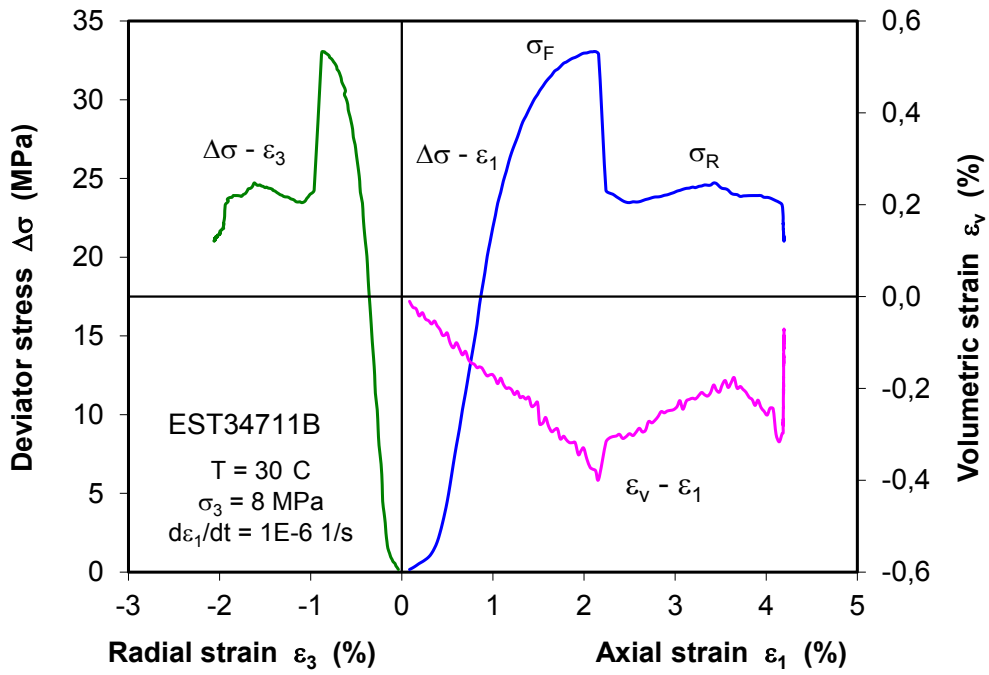
(a) Measured data of deformation
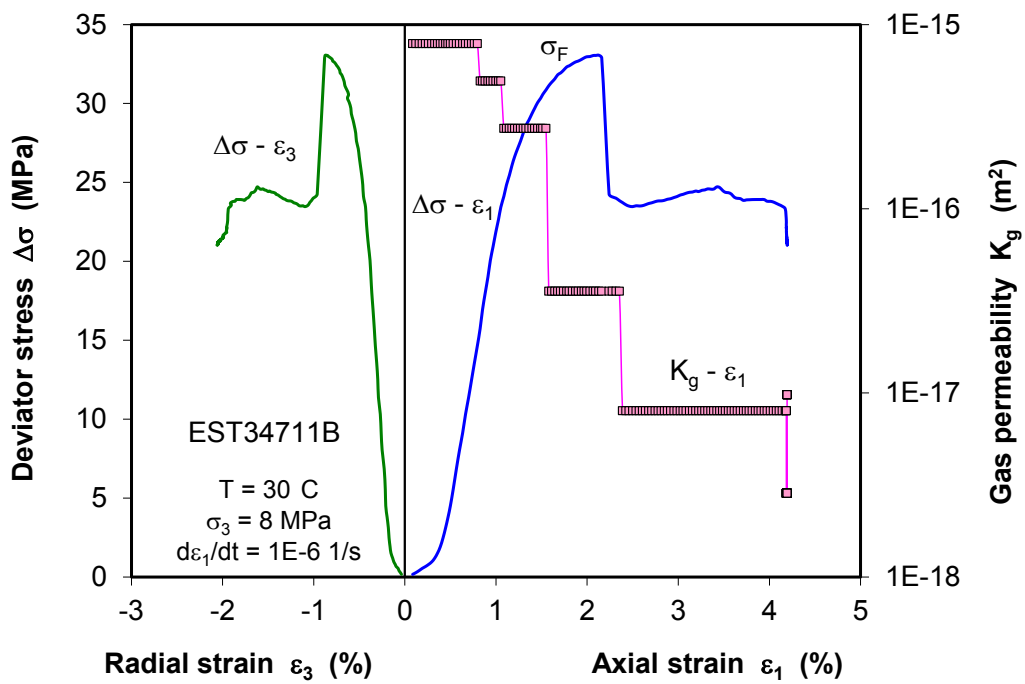
(b) Measured data of gas permeability
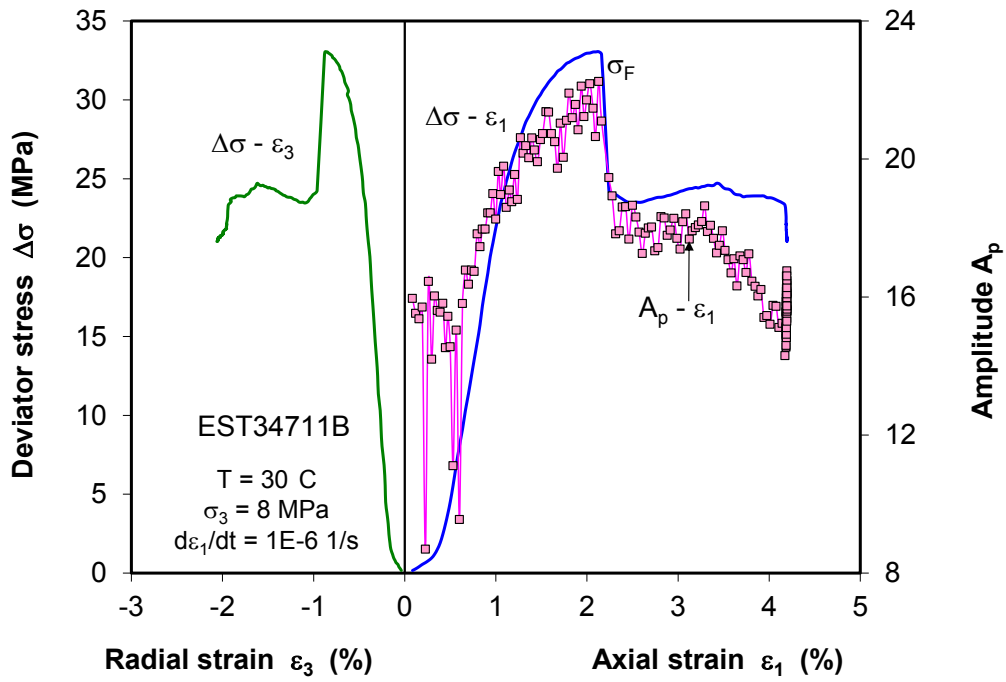
(c) Measured data of ultrasonic wave amplitude
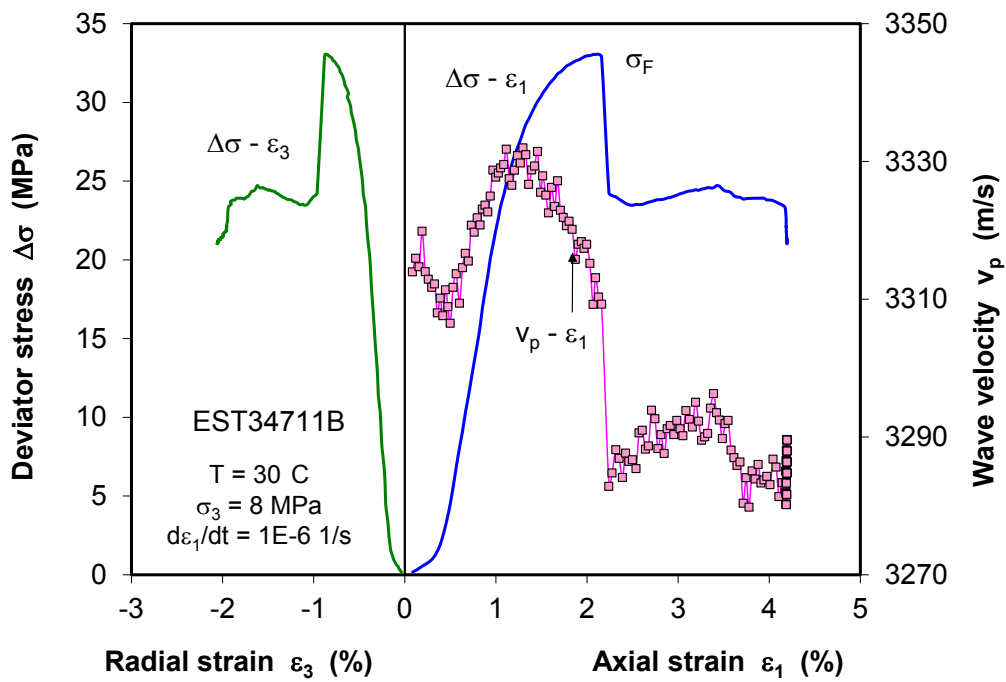
(d) Measured data of velocity

Fig. B.19 Results of deviatoric compression at lateral confining stress of 8 MPa
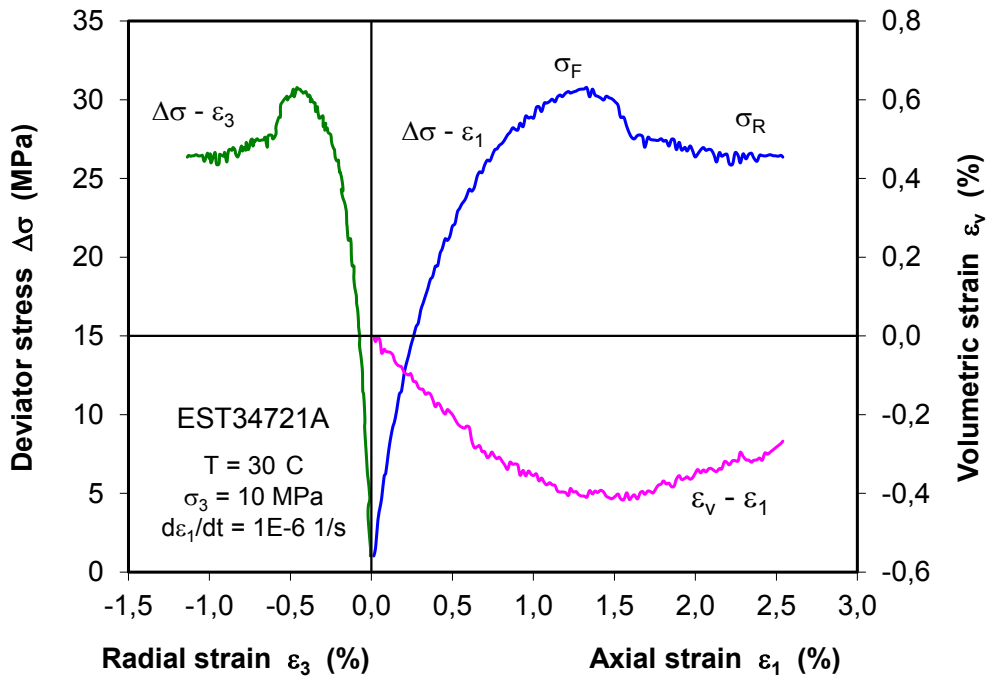
(a) Measured data of deformation
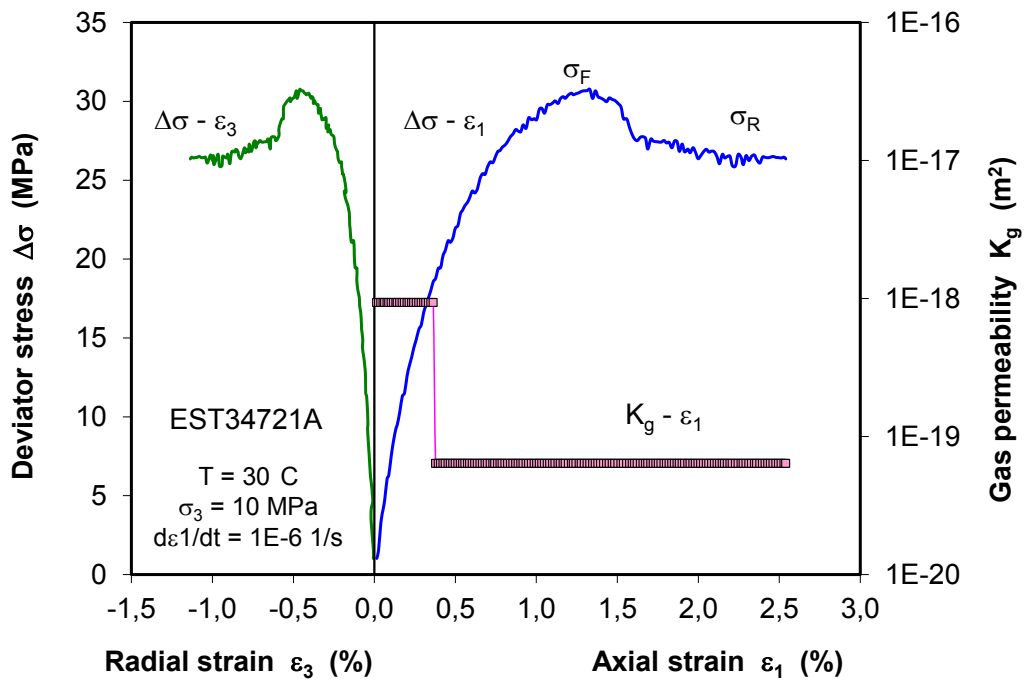
(b) Measured data of gas permeability
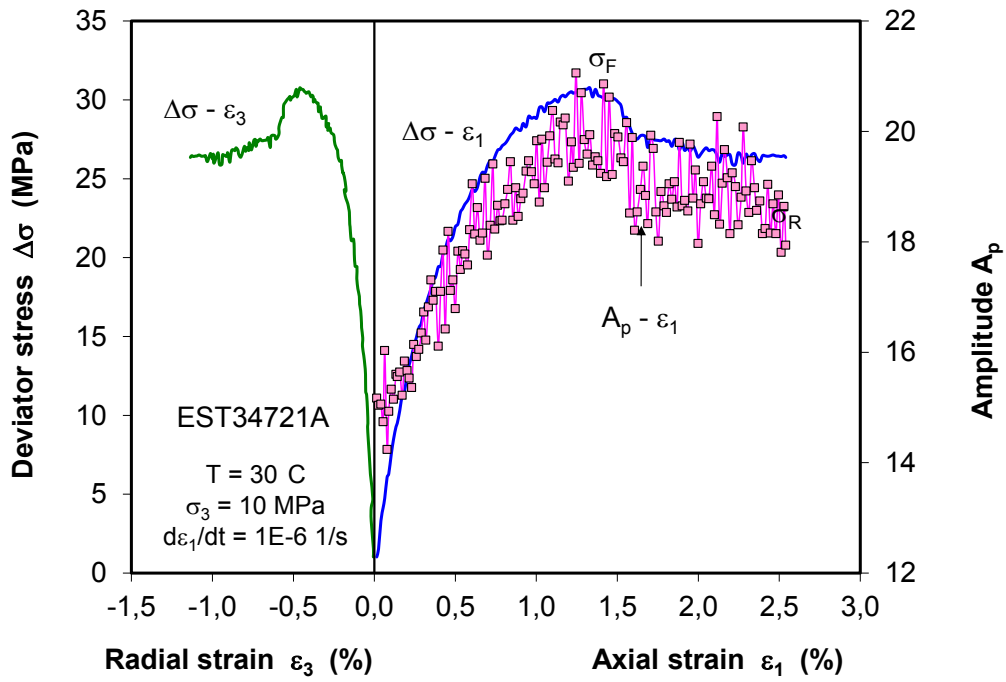
(c) Measured data of ultrasonic wave amplitude
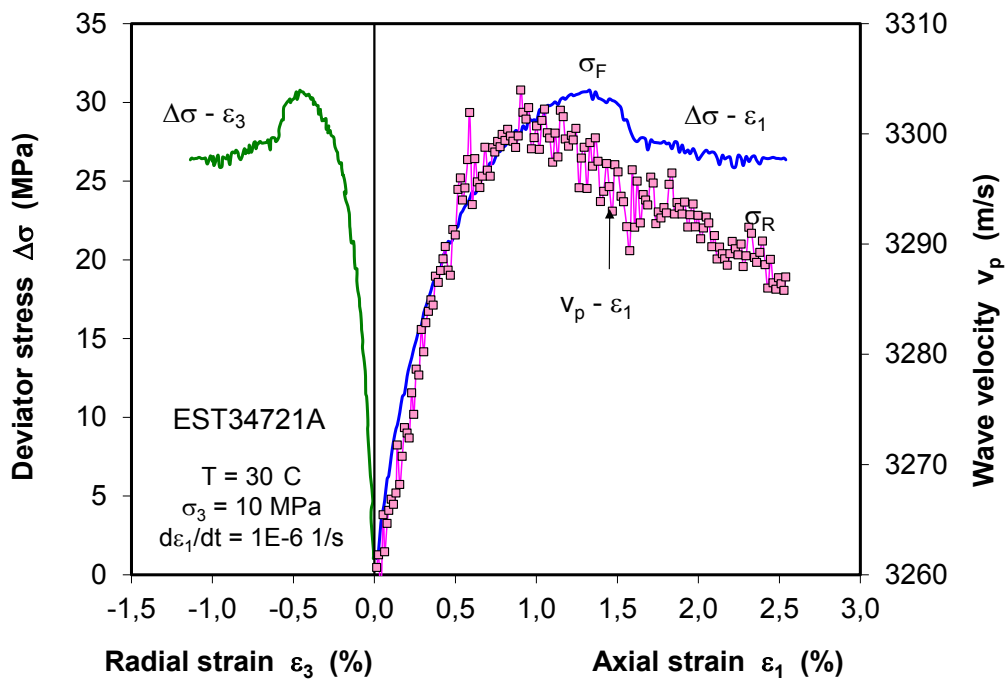
(d) Measured data of velocity

Fig. B.20   Results of deviatoric compression at lateral confining stress of 10 MPa
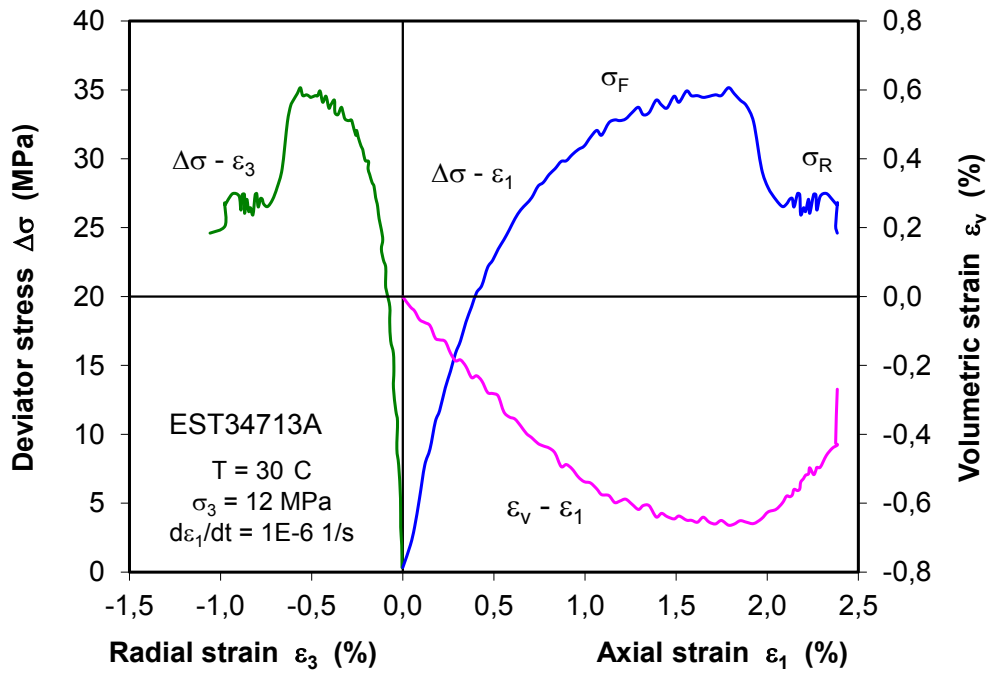
(a) Measured data of deformation
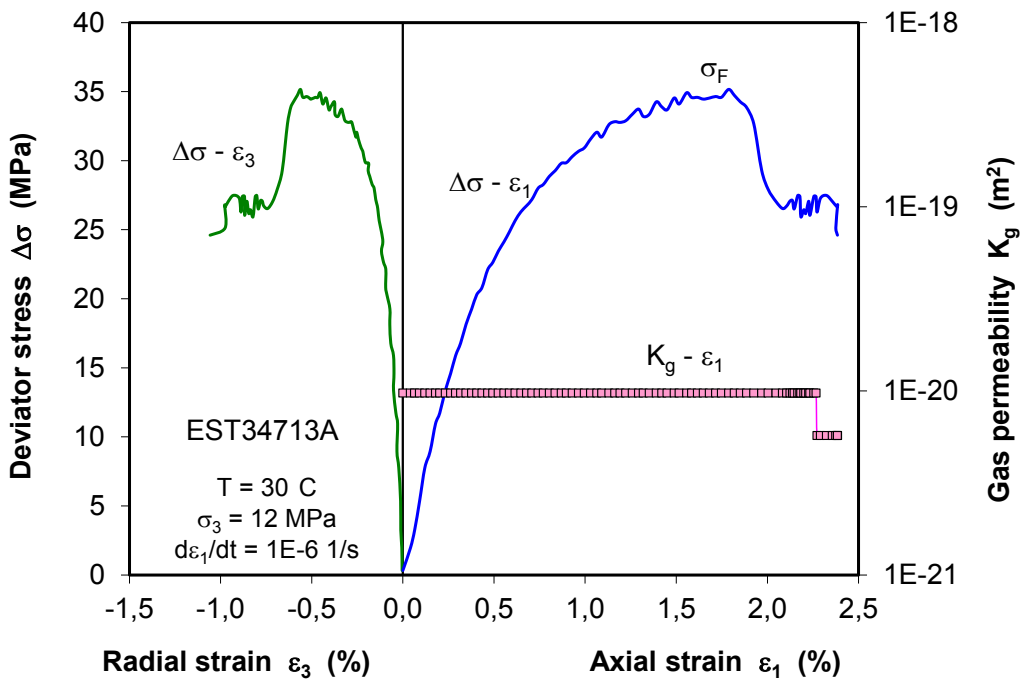
(b) Measured data of gas permeability
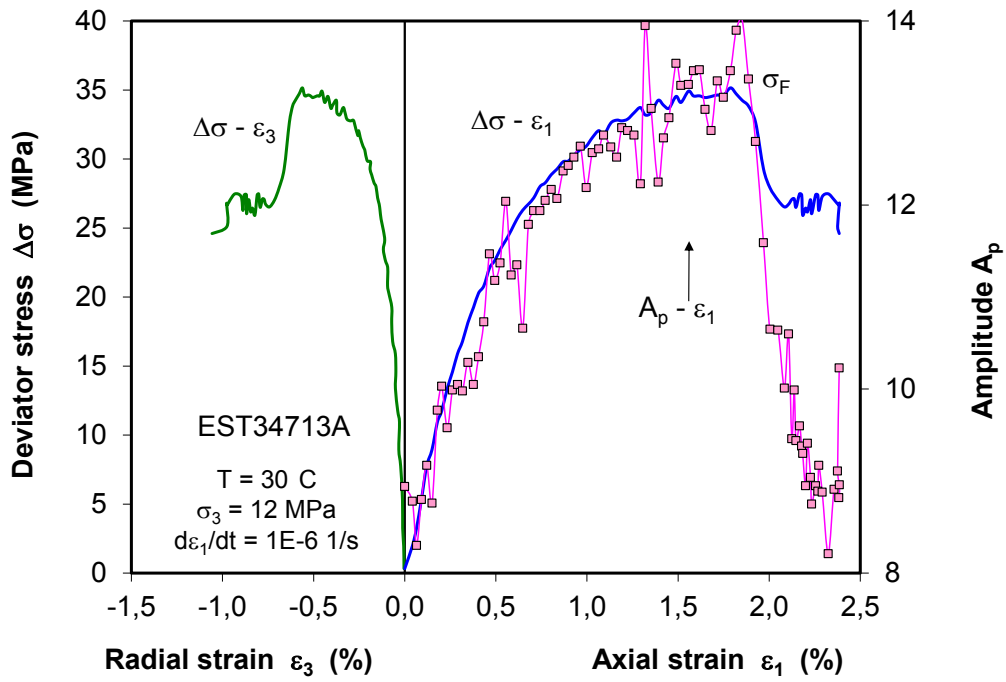
(c) Measured data of ultrasonic wave amplitude
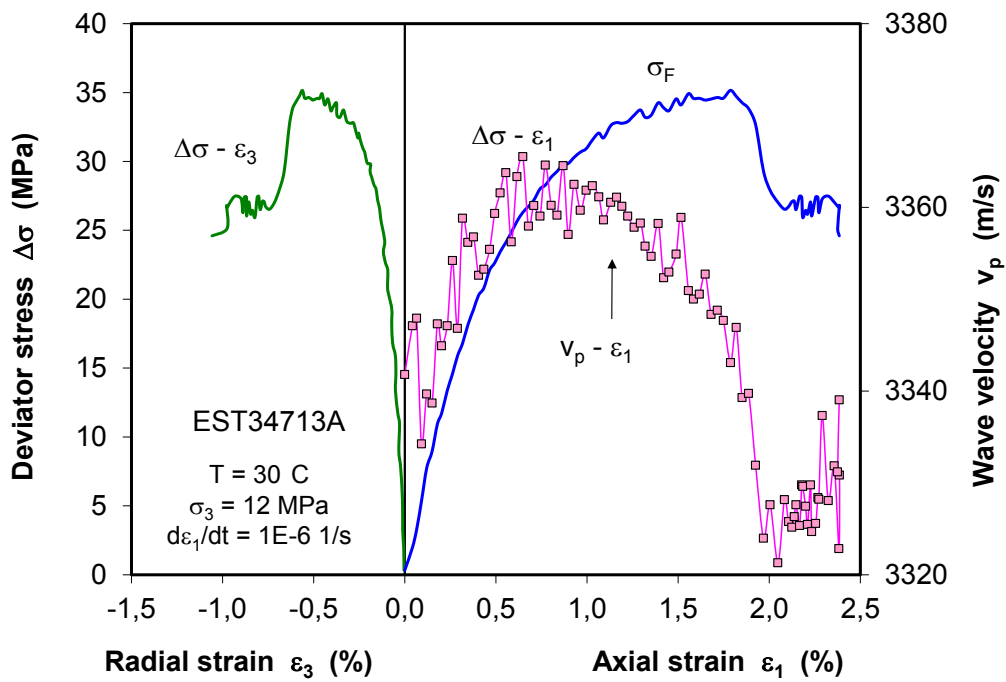
(d) Measured data of velocity

Fig. B.21 Results of deviatoric compression at lateral confining stress of 12 MPa

EST34693A
σ_3 = 1 MPa
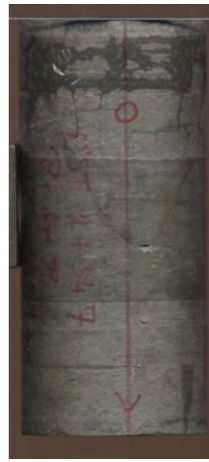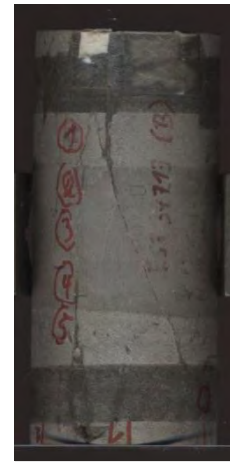
EST34717A
σ_3 = 2 MPa

EST27347B
σ_3 = 2.5 MPa

EST34713B
σ_3 = 3 MPa

EST34689A
σ_3 = 4 MPa

EST27347A
σ_3 = 5 MPa

EST34717B
σ_3 = 6 MPa

EST34711A
σ_3 = 8 MPa

EST34717B
σ_3 = 8 MPa

EST34721A
σ_3 = 10 MPa

EST34713A
σ_3 = 12 MPa

Fig. B.22   Fractures developed in COX samples after deviatoric loading

285

B.3 Elastic parameters, strengths and permeability values determined on the COX samples by deviatoric loading

Tab. B.3 Elastic parameters, strengths and permeability values determined on the COX samples by deviatoric loading

Sample ID	Radial stress σ_3 [MPa]	Young's modulus E [GPa]	Poisson ratio ν [-]	Yield strength σ_Y [MPa]	σ_Y/σ_F ratio	Dilatancy strength σ_D [MPa]	σ_D/σ_F ratio	Peak strength σ_F [MPa]	Residual strength σ_R [MPa]	σ_R/σ_F ratio	Fracture angle ß [°]	Initial permeability Kg-o [m²]	Final permeability Kg-e [m²]
EST34693A	1	5.66	0.38	11.6	0.63	14.2	0.77	18.5			25.0	$9 \cdot 10^{-21}$	$3 \cdot 10^{-15}$
EST34717A	2	7.00	0.40	13.8	0.59	20.6	0.88	23.4	14.0	0.60	30.0	$2 \cdot 10^{-20}$	$2 \cdot 10^{-19}$
EST27347B	2.5	3.41	0.38	16.0	0.67	22.0	0.92	23.9	13.9	0.58	30.0	$5 \cdot 10^{-18}$	$2 \cdot 10^{-16}$
EST34713B	3	4.50	0.42	17.2	0.65	25.0	0.94	26.5	17.4	0.66	25.0	$1 \cdot 10^{-16}$	$1 \cdot 10^{-15}$
EST34689A	4	5.99	0.42	12.7	0.55	19.5	0.85	23.0	16.8	0.73	27.0	$9 \cdot 10^{-21}$	$1 \cdot 10^{-16}$
EST27347A	5	2.80	0.28	16.9	0.67	22.0	0.87	25.4	16.5	0.65	25.0	$8 \cdot 10^{-21}$	$1 \cdot 10^{-19}$
EST34717B	6	6.62	0.28	16.5	0.53	25.5	0.83	30.9	19.8	0.64	35.0	$2 \cdot 10^{-20}$	$1 \cdot 10^{-20}$
EST34711A	8	4.47	0.15	21.0	0.58	30.0	0.82	36.4	27.0	0.74	25.0	$2 \cdot 10^{-17}$	$2 \cdot 10^{-20}$
EST34711B	8	5.43	0.20	22.6	0.68	26.0	0.79	33.0	23.7	0.72	35.0	$8 \cdot 10^{-16}$	$8 \cdot 10^{-18}$
EST34721A	10	4.43	0.20	18.0	0.59	28.2	0.92	30.7	26.4	0.86	32.0	$9 \cdot 10^{-19}$	$6 \cdot 10^{-20}$
EST34713A	12	4.04	0.24	20.2	0.58	28.9	0.83	34.9	27.0	0.77	27.0	$1 \cdot 10^{-20}$	$6 \cdot 10^{-21}$
mean value		4.94	0.30		0.60		0.83			0.65	28.8		

B.4 **Results of Brazilian tensile tests on COX samples**

(a) Test 1
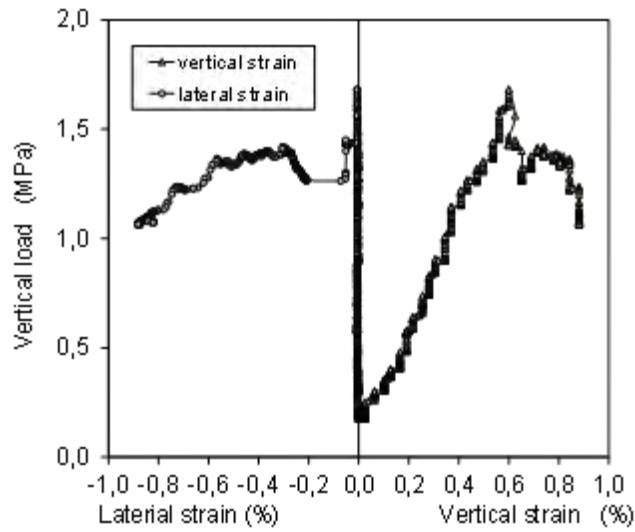
(b) Test 1
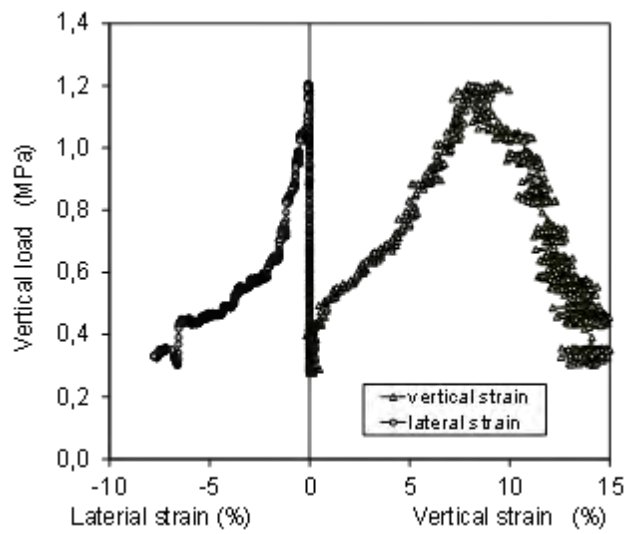
(c) Test 2

Fig. B.23 Results of Brazilian tensile tests on COX samples

B.5 Results of post-failure tests on COX samples
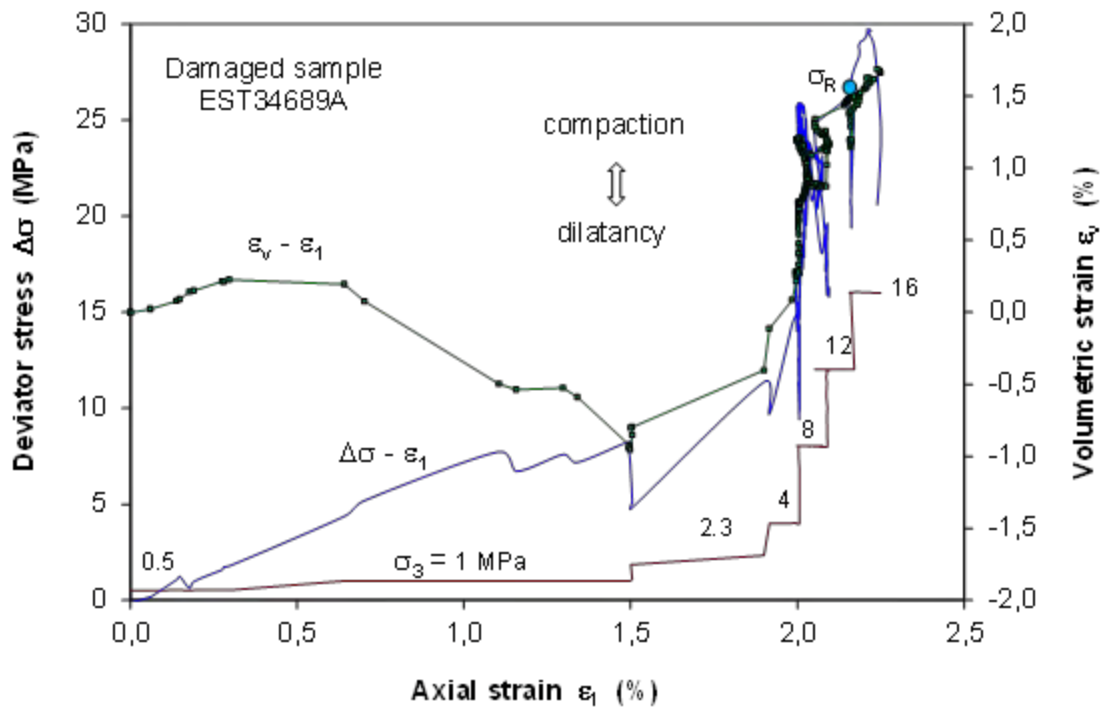
(a) Measured data of deformation
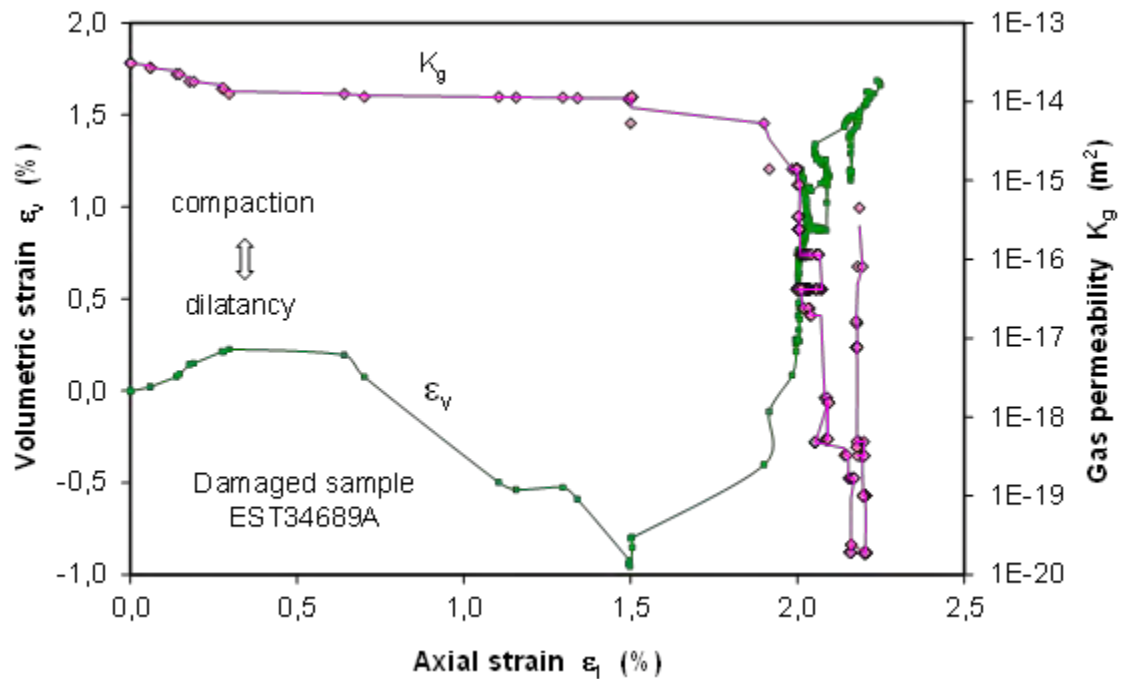
(b) Measured data of gas permeability

Fig. B.24 COX sample EST34689A
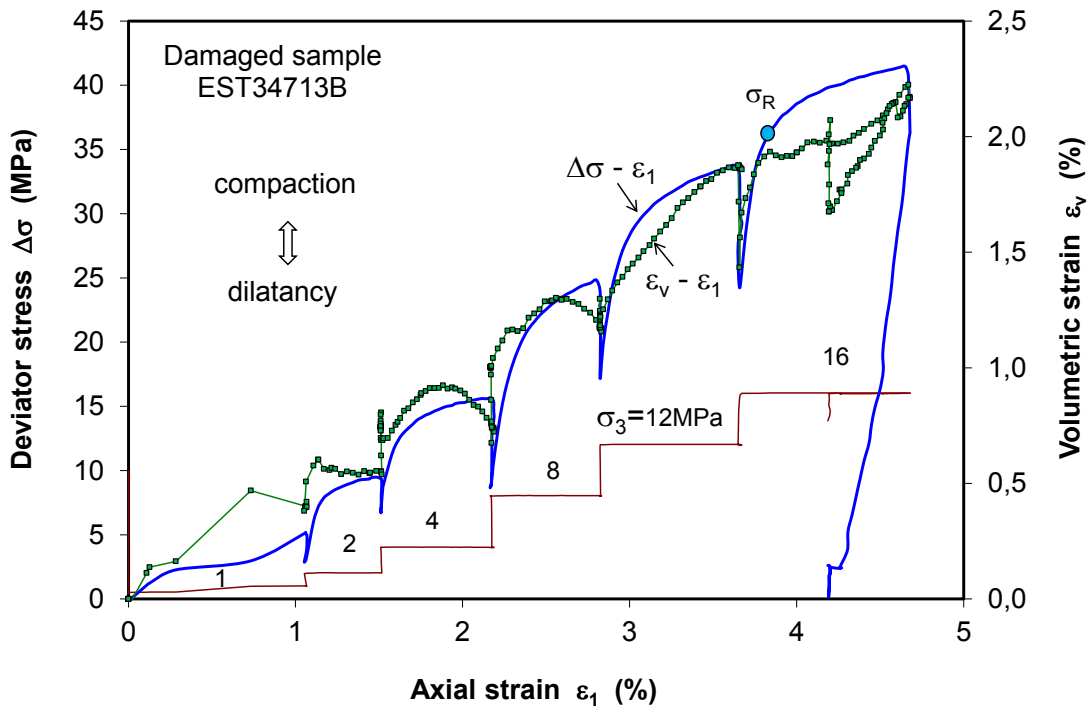
(a) Measured data of deformation
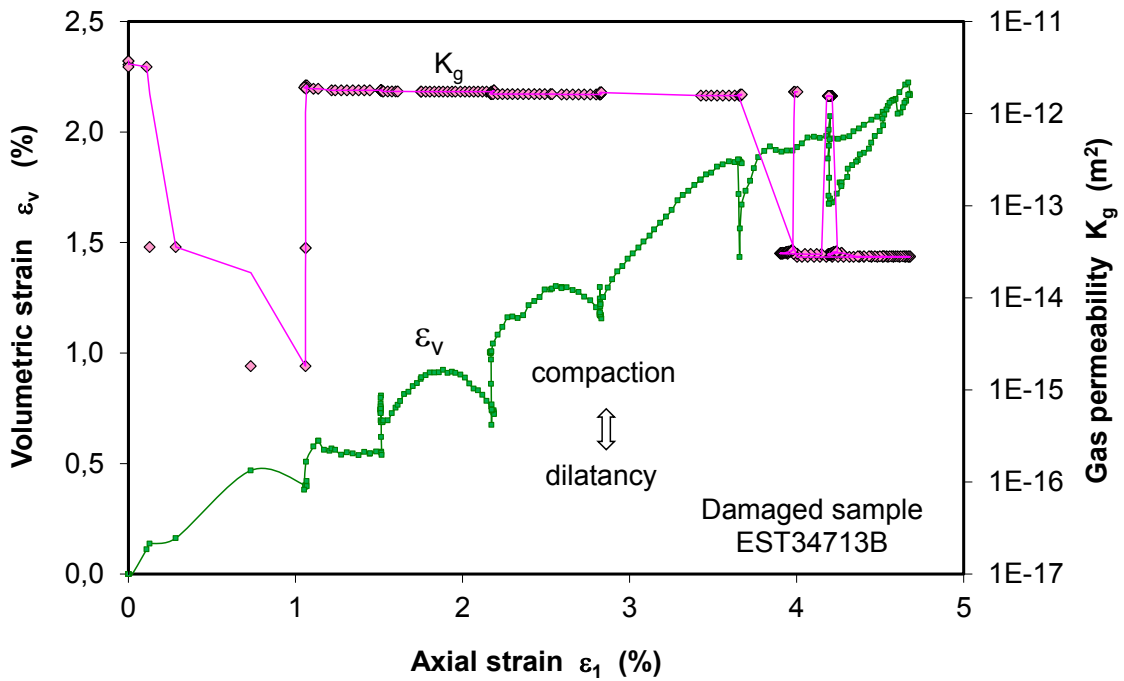
(b) Measured data of gas permeability

Fig. B.25   COX sample EST34713B
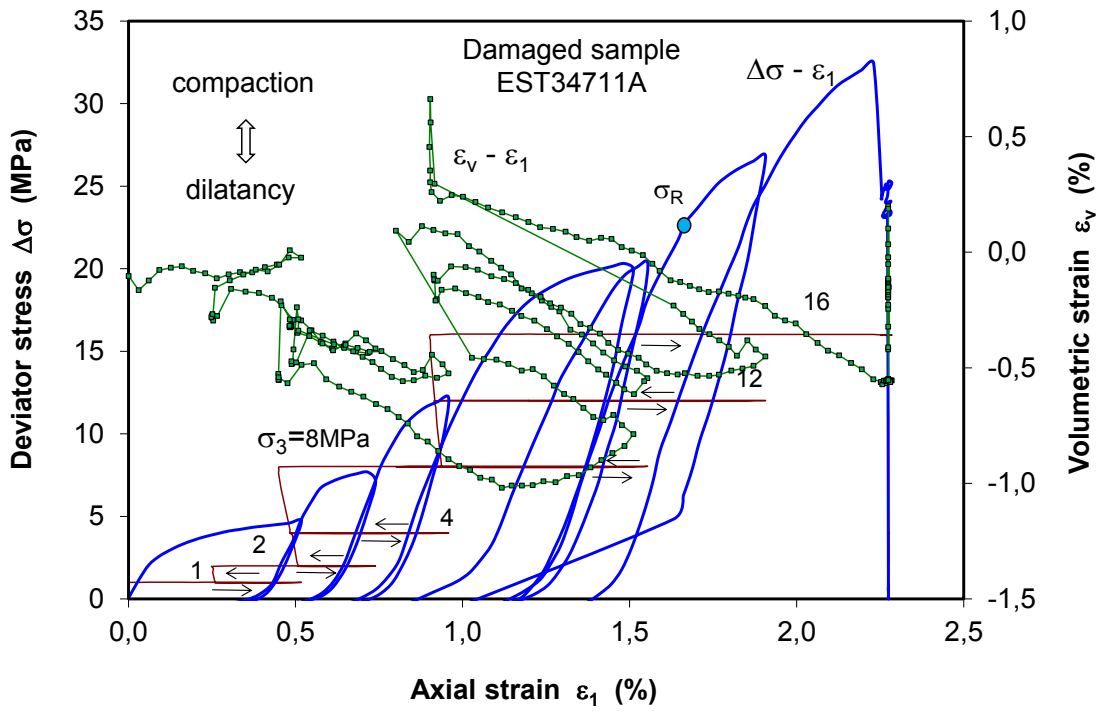
(a) Measured data of deformation
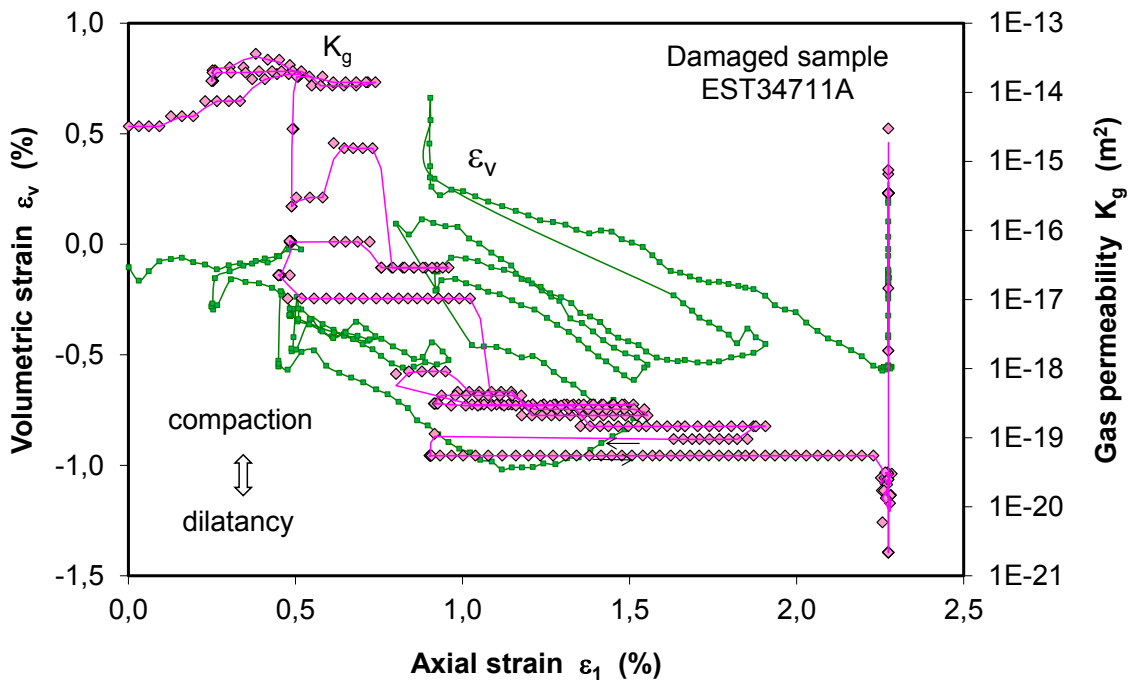
(b) Measured data of gas permeability

Fig. B.26 COX sample EST34711A

C Results of long-term creep tests on claystone

C.1 Fundamental properties and Pictures of COX and OPA samples
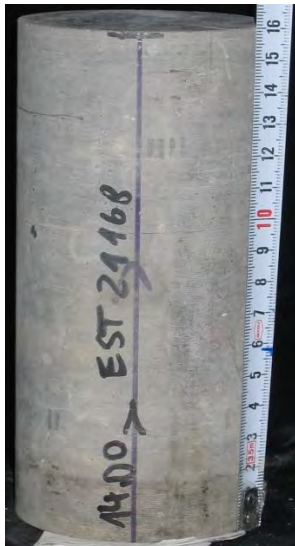
(a) EST21168

(b) EST21173

(c) EST21171
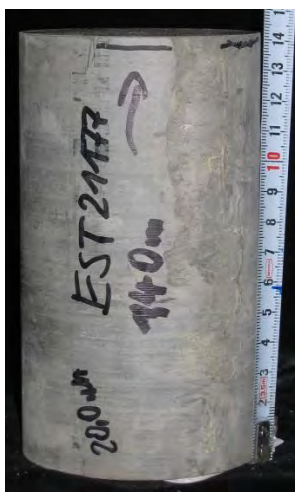
(d) EST21177

(e) EST34695

(f) EOPA-DVB1

Fig. C.27 Pictures of some COX and OPA samples prepared before testing

Tab. C.4   Fundamental properties of the COX and OPA samples before creep testing

Sample COX	Diameter [mm]	Length [mm]	Axis direction to bedding	Water content w [%]	Grain density ρ_s [g/cm^3]	Bulk density ρ_b [g/cm^3]	Dry density ρ_d [g/cm^3]	Porosity ϕ [%]	Water saturation S_w [%]	Testing type
EST27342-1	78.5	157	parallel	5.20	2.710	2.417	2.329	14.1	86	uniaxial creep
EST27342-2	78.5	157	parallel	5.20	2.710	2.417	2.329	14.1	86	uniaxial creep
EST27345-1	78.5	157	parallel	5.05	2.710	2.402	2.287	15.6	74	uniaxial creep
EST34695-1	108	143	parallel	5.77	2.710	2.373	2.244	16.7	78	uniaxial creep
EST34695-2	108	151	parallel	5.77	2.710	2.377	2.247	17.3	75	uniaxial creep
EST21168	78.5	160	perpendicular	5.33	2.694	2.393	2.272	15.7	77	uniaxial creep
EST21171	78.5	160	perpendicular	5.34	2.681	2.363	2.243	16.3	73	uniaxial creep
EST21173	78.5	160	perpendicular	5.40	2.684	2.399	2.276	15.2	81	uniaxial creep
EST21177	78.5	160	perpendicular	5.33	2.694	2.393	2.272	15.7	77	uniaxial creep
EST25321	78.5	161	parallel	5.70	2.687	2.417	2.286	15.2	86	uniaxial creep
EST27345-2	70.0	140	parallel	5.70	2.700	2.370	2.281	15.5	87	triaxial creep
EST34687-2	100	190	parallel	5.90	2.700	2.413	2.279	15.6	90	triaxial creep
OPA										
OPA-DVB1	87.1	180	parallel	6.30	2.700	2.460	2.315	14.2	100	uniaxial creep
OPA-DVB2	87.1	180	parallel	6.30	2.700	2.457	2.311	14.3	100	uniaxial creep
OPA-DVB3	87.1	180	parallel	6.30	2.700	2.457	2.311	14.3	100	uniaxial creep
OPA-DVB4	70.0	140	parallel	5.92	2.700	2.439	2.302	14.7	93	triaxial creep

C.2 Uniaxial creep curves of the COX and OPA samples
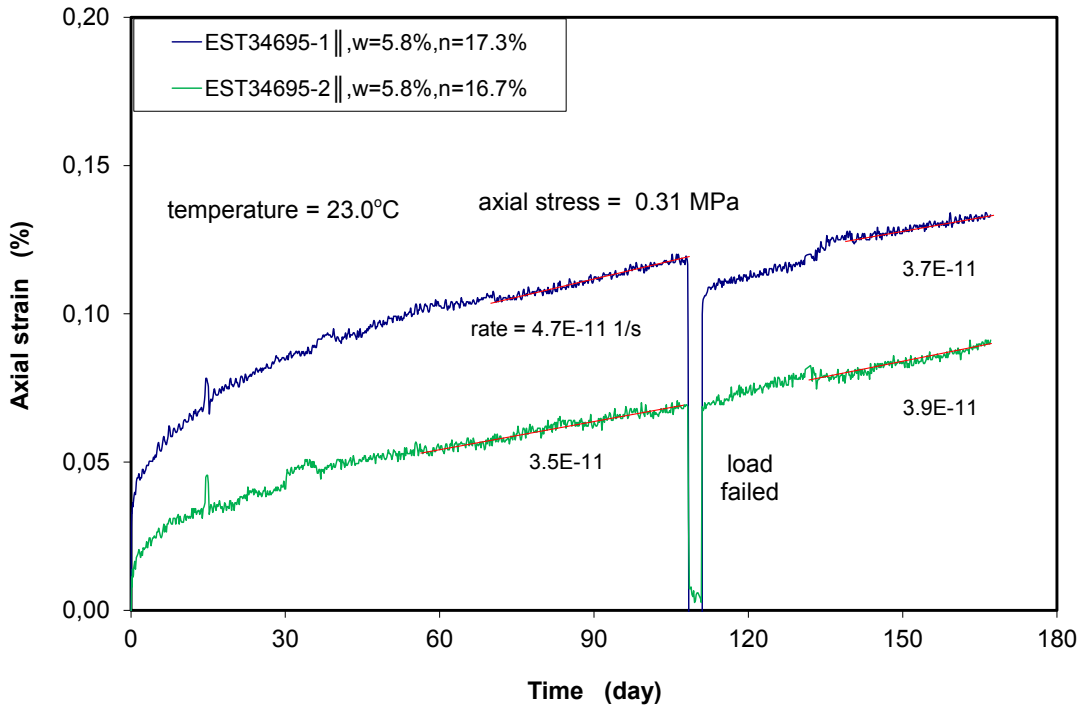
Fig. C.28 Creep curves of COX samples under low uniaxial stress of 0.3 MPa
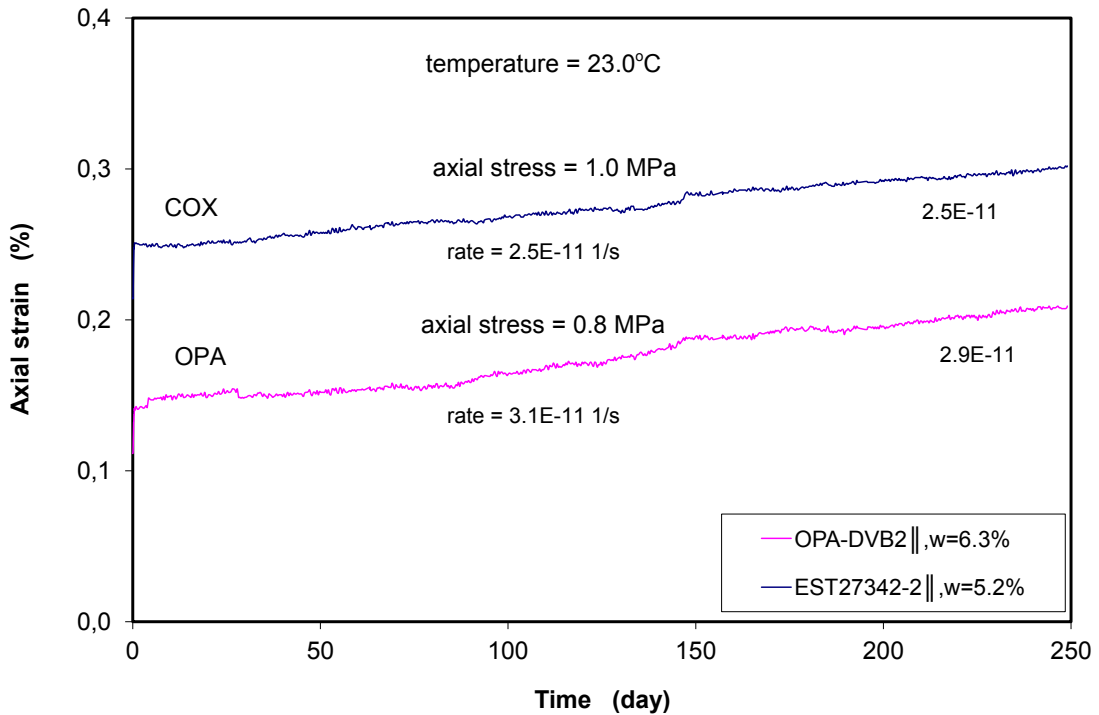
Fig. C.29 Creep curves of COX-EST27342-2‖ at 1 MPa and OPA-DVB2‖ at 0.8 MPa

293
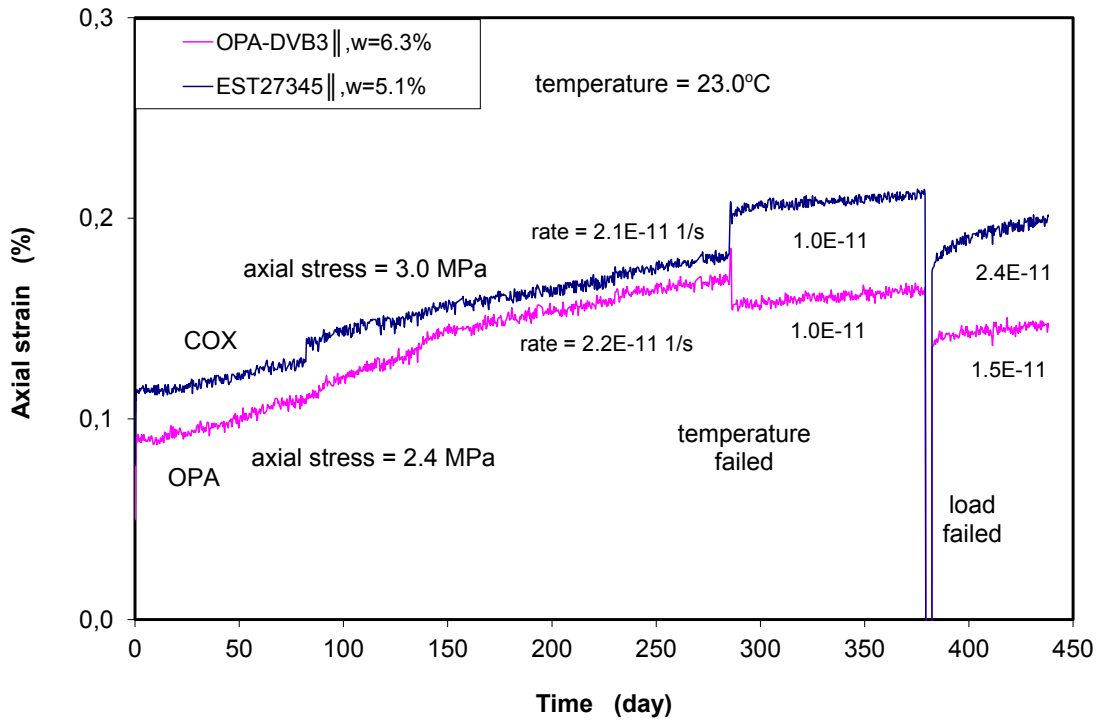
Fig. C.30 Creep curves of COX-EST27345-1‖ at 3 MPa and OPA-DVB3‖ at 2.4 MPa
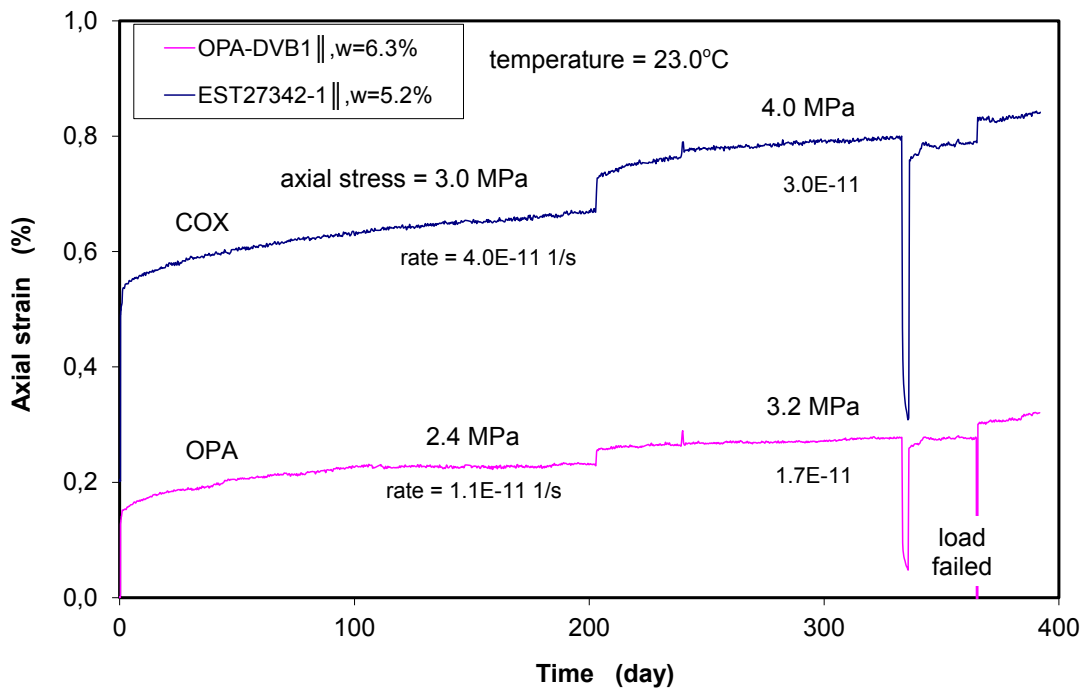
Fig. C.31 Creep curves of COX-EST27342-1‖ at 3 & 4 MPa and OPA-DVB1‖ at 2.4 & 3.2 MPa

294
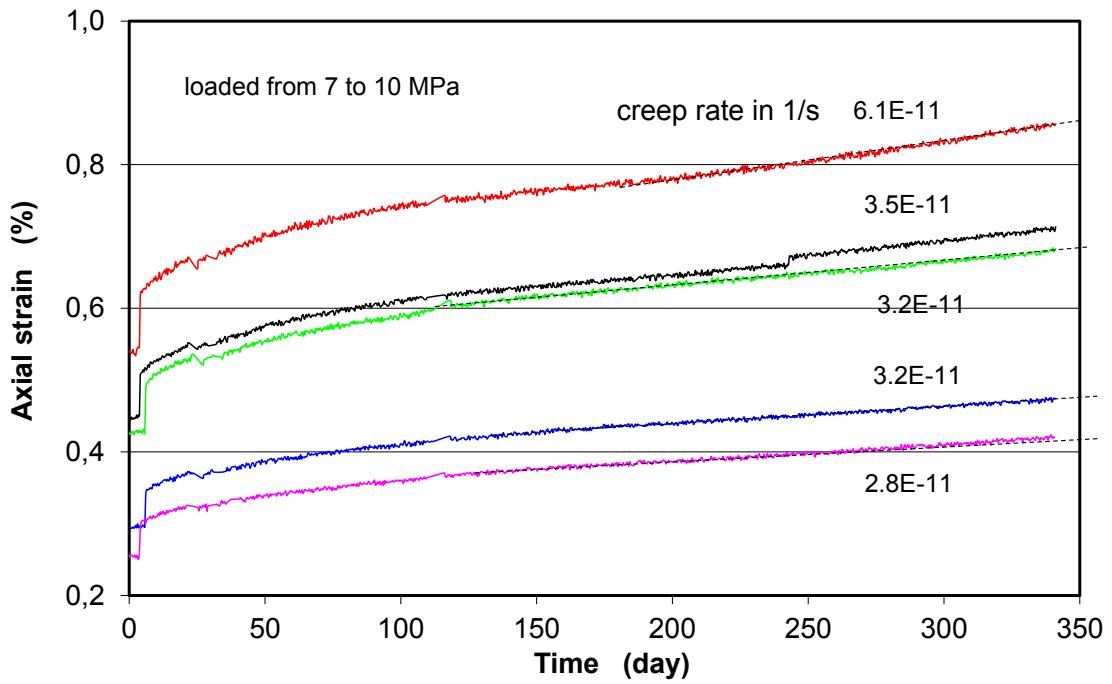
(a) loaded from 7 to 10 MPa
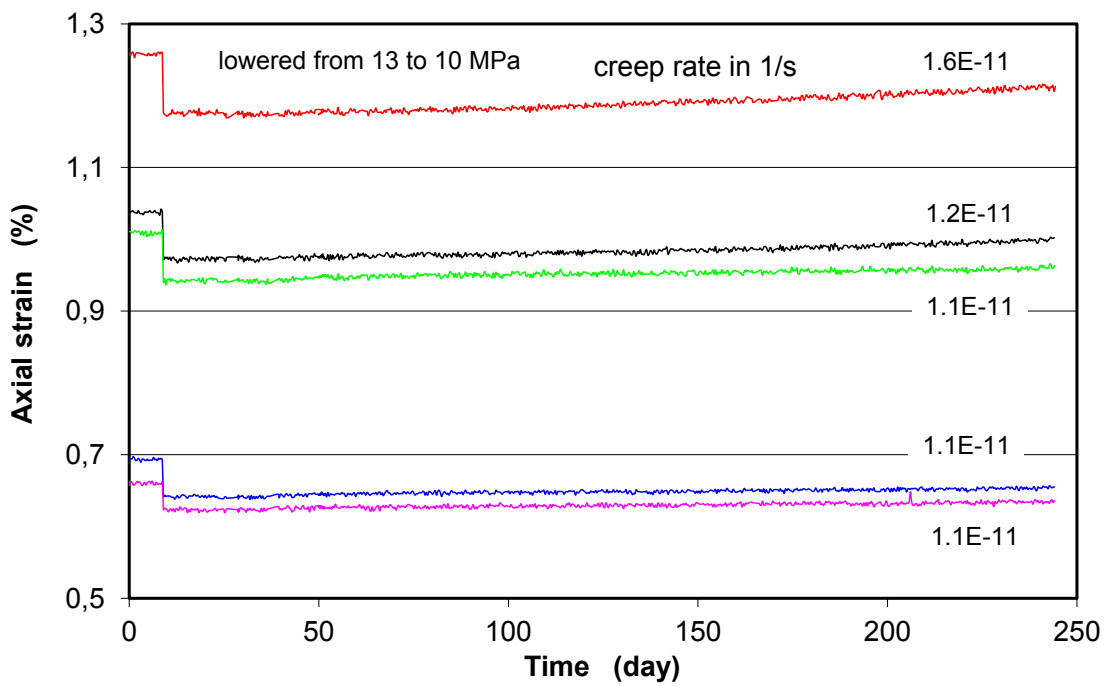
(b) unloaded from 13 to 10 MPa

Fig. C.32 Effects of loading paths on the creep behaviour at uniaxial load of 10 MPa
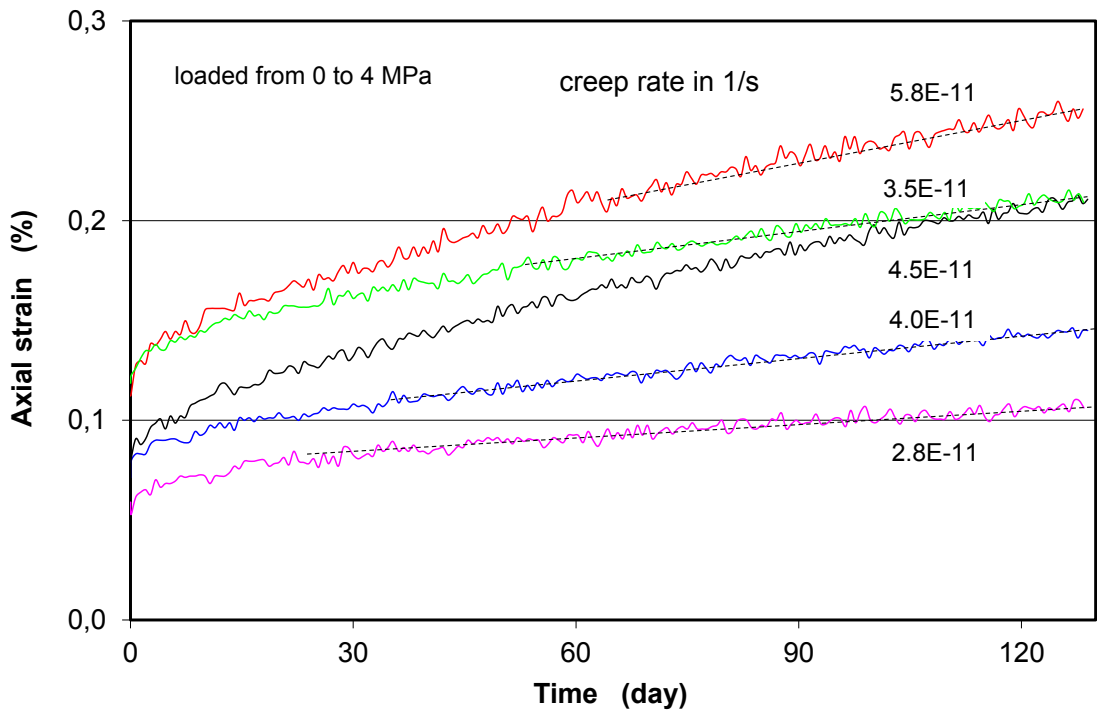
(a) loaded from 0 to 4 MPa
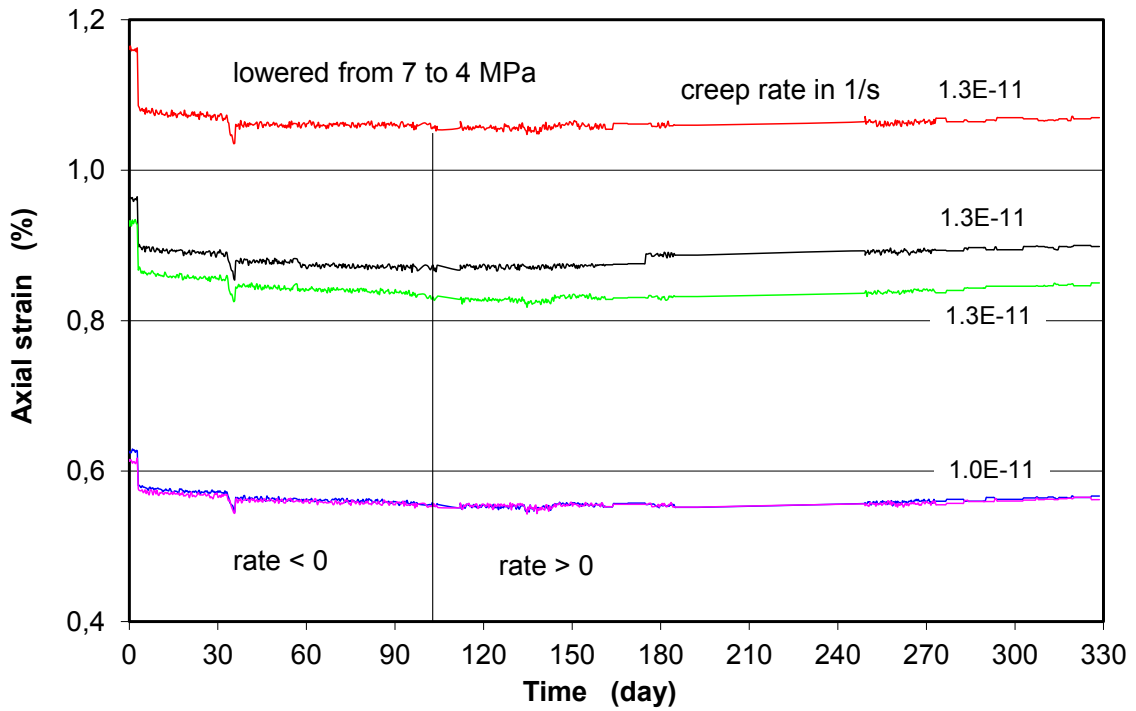
(b) unloaded from 7 to 4 MPa

Fig. C.33 Effects of loading paths on the creep behaviour at uniaxial load of 4 MPa
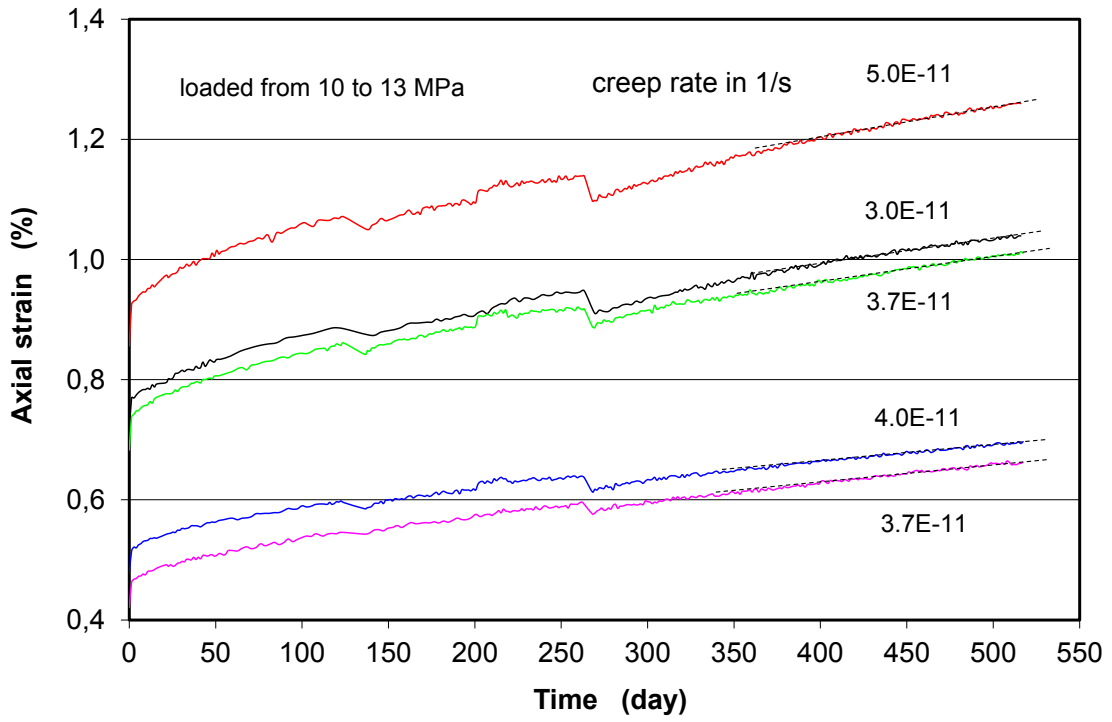
(a) stepwise increased uniaxial loads from 10 to 13 MPa
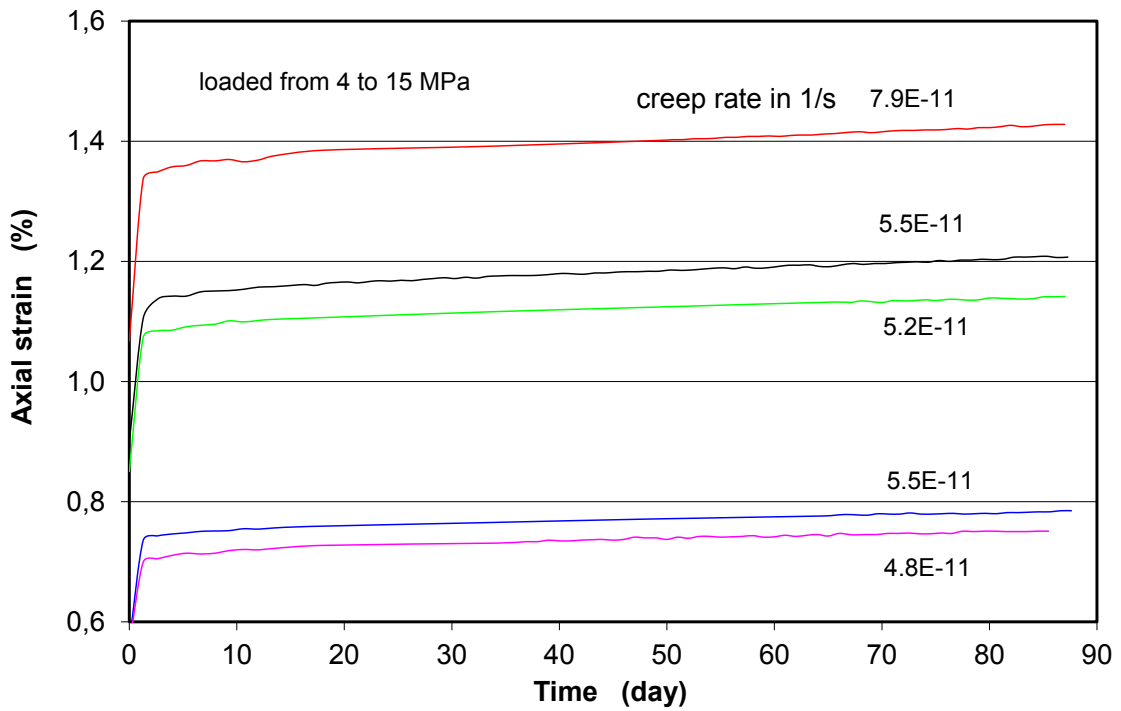
(b) stepwise increased uniaxial loads from 4 to 15 MPa

297
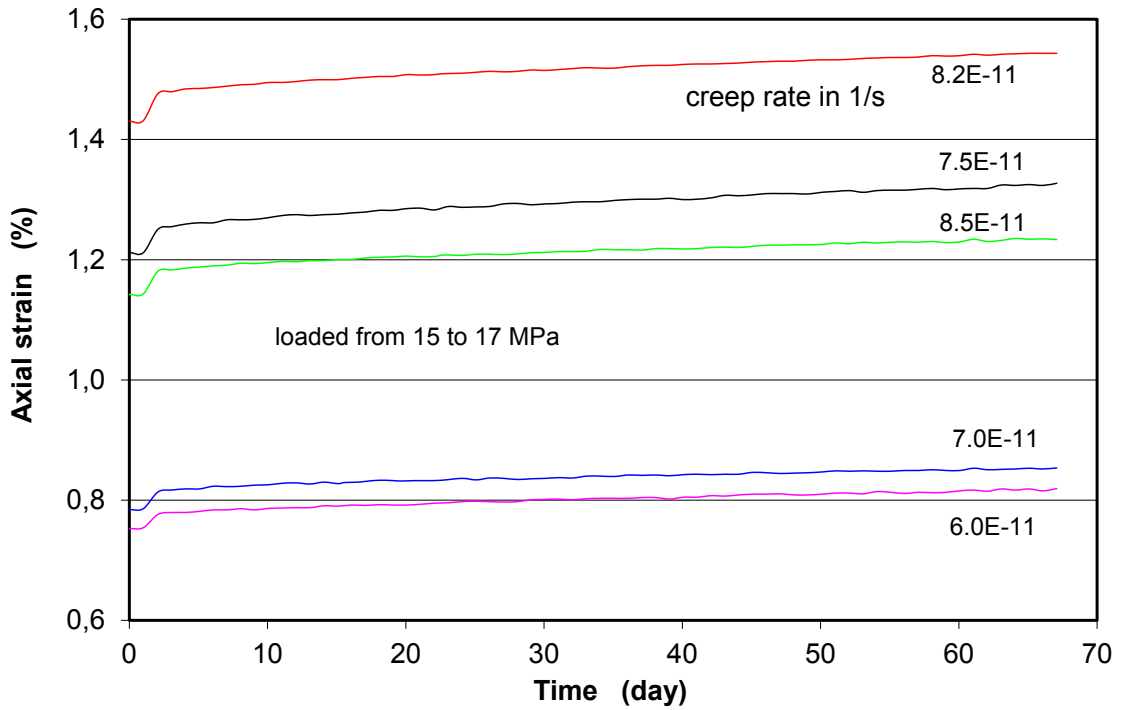
(c) stepwise increased uniaxial loads from 15 to 17 MPa
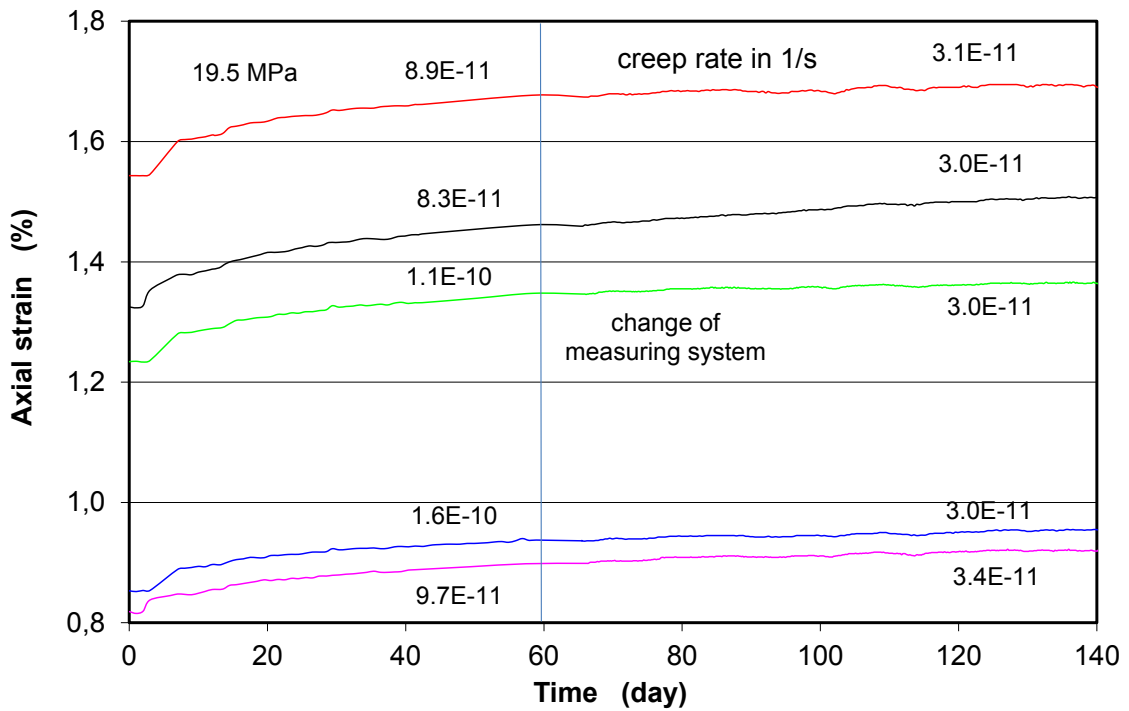
(d) stepwise increased uniaxial loads of 19.5 MPa

Fig. C.34   Creep behaviour under stepwise increased uniaxial loads of 13, 15, 17 and 19.5 MPa
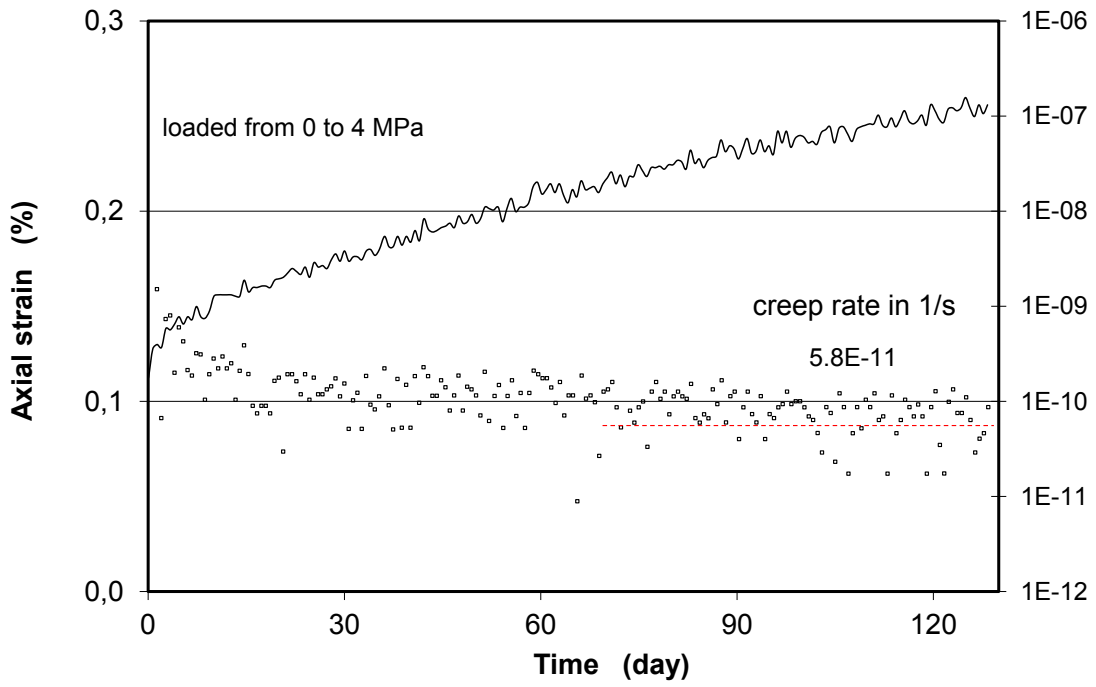
(a) Loaded from 0 to 4 MPa
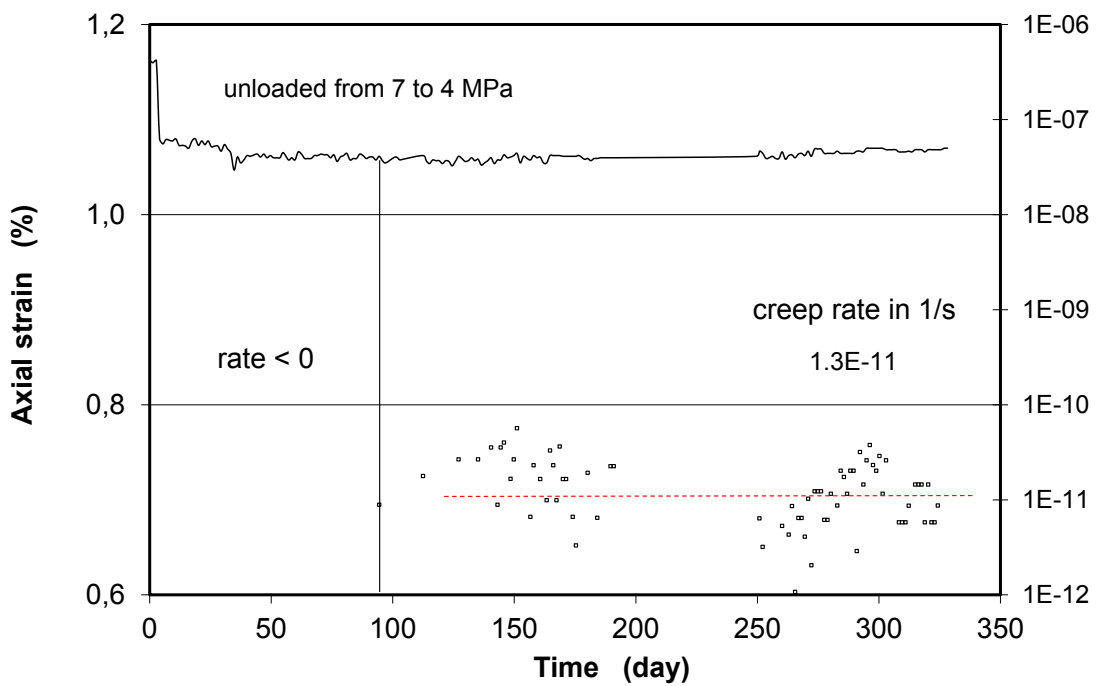
(b) Unloaded from 7 to 4 MPa
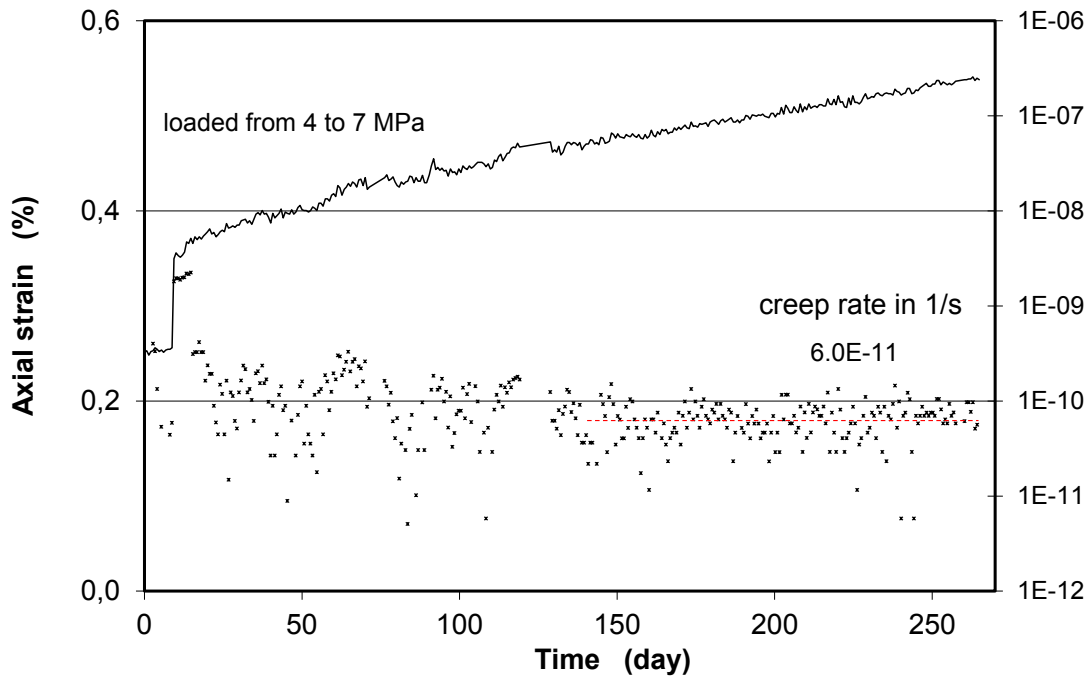
(c) Loaded from 4 to 7 MPa
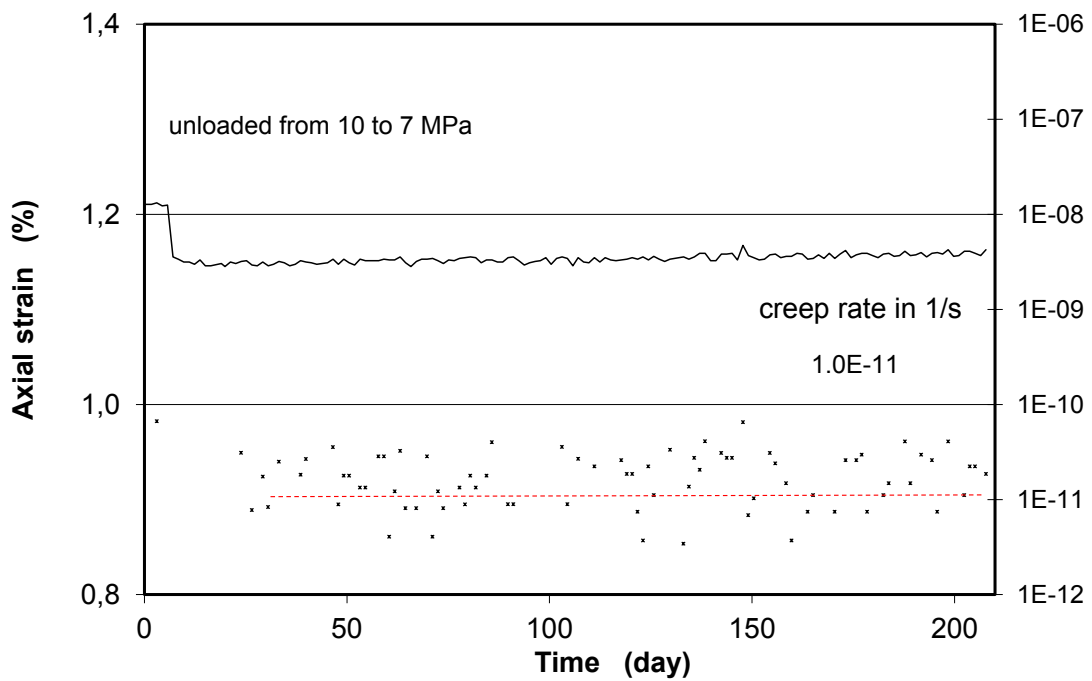
(d) Unloaded from 10 to 7 MPa
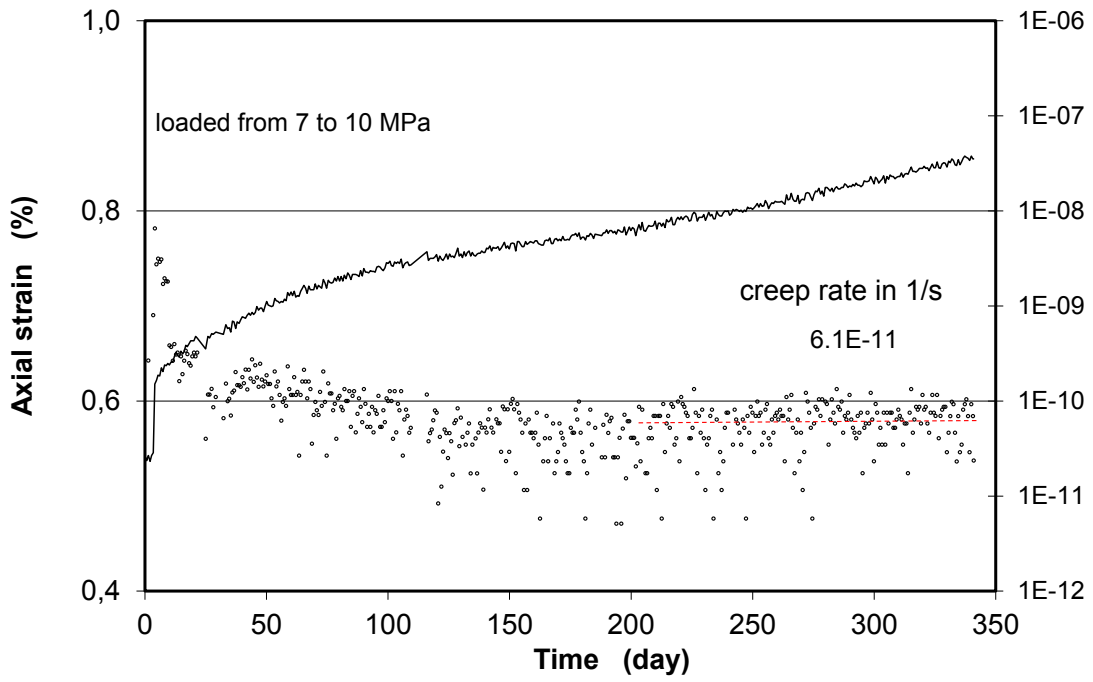
(e) Loaded from 7 to 10 MPa
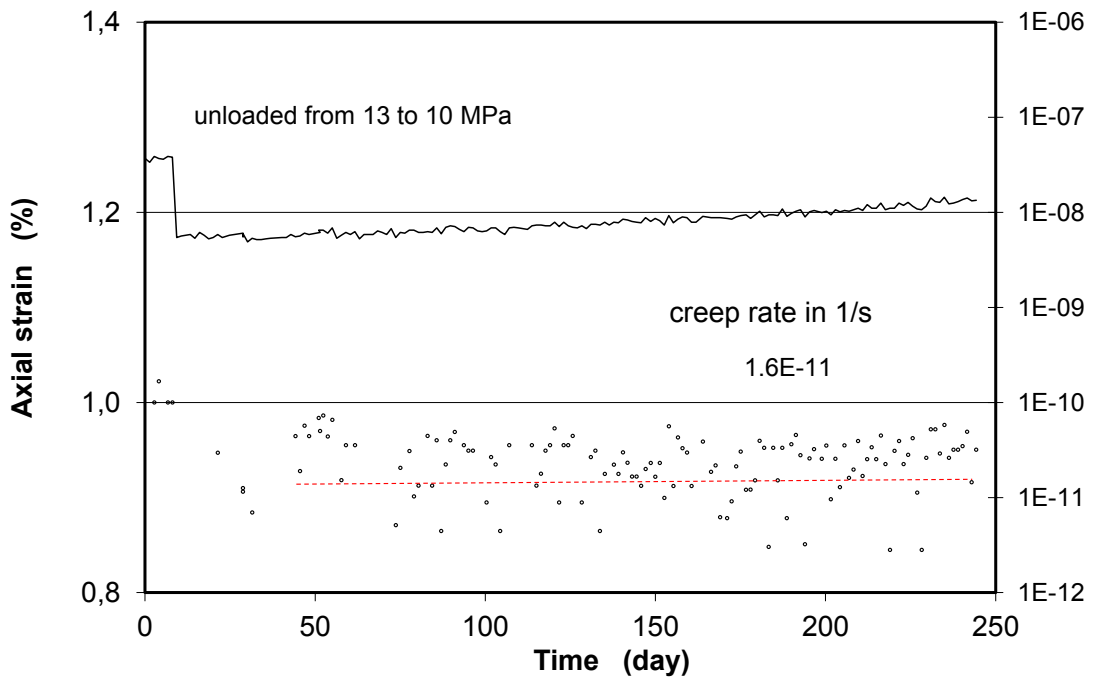
(f) Unloaded from 13 to 10 MPa
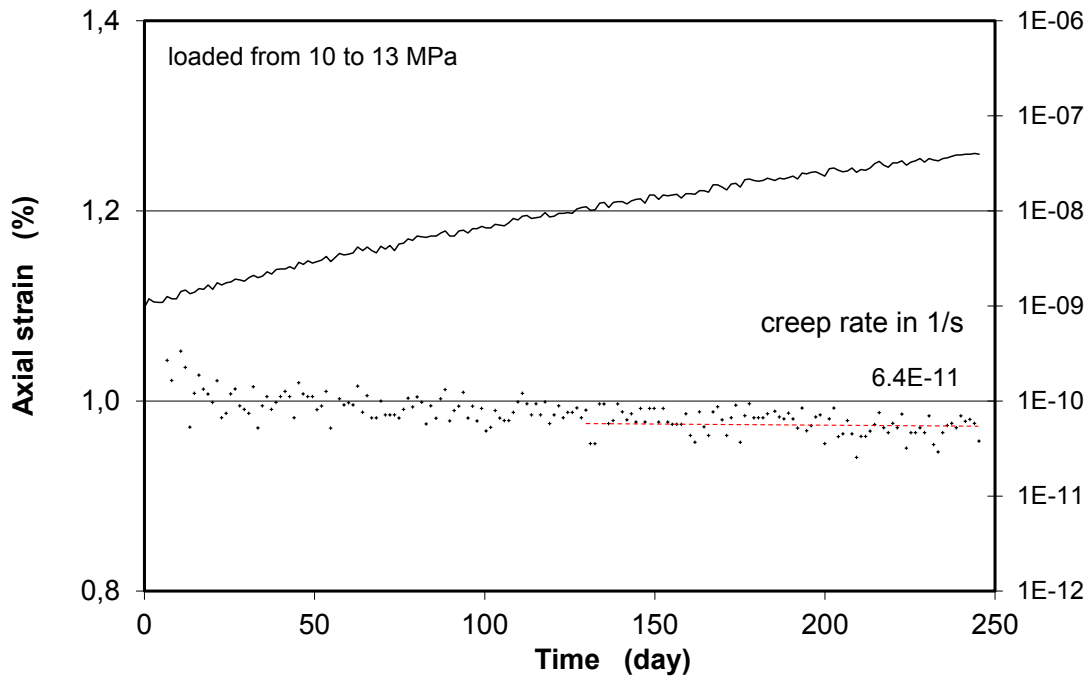
(g) Loaded from 10 to 13 MPa
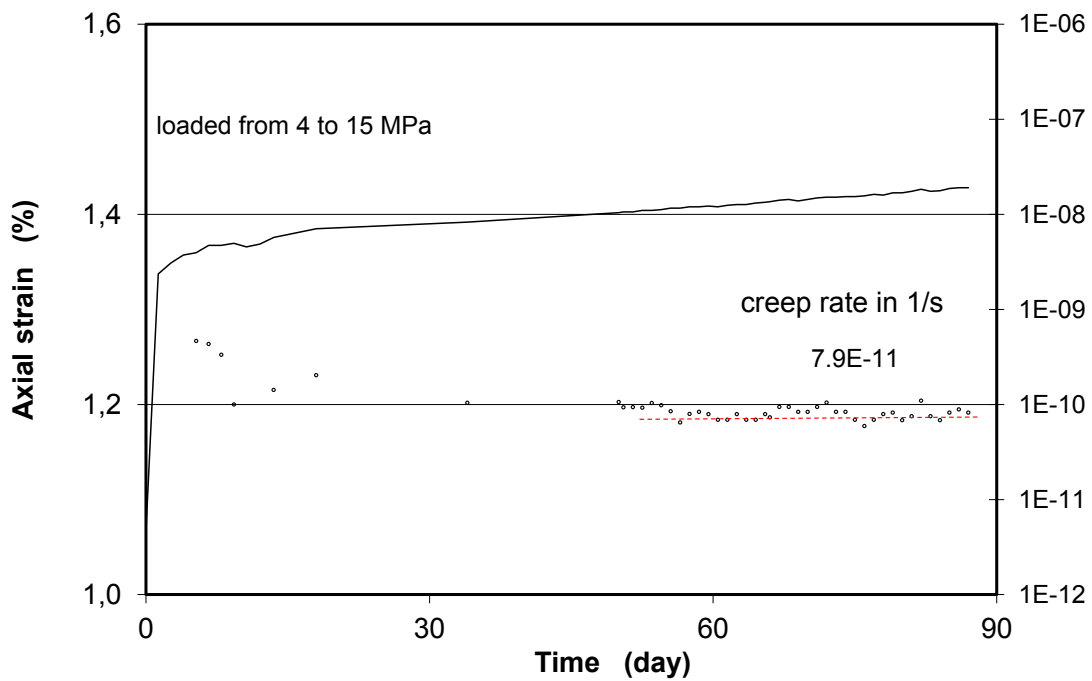
(h) Loaded from 4 to 15 MPa
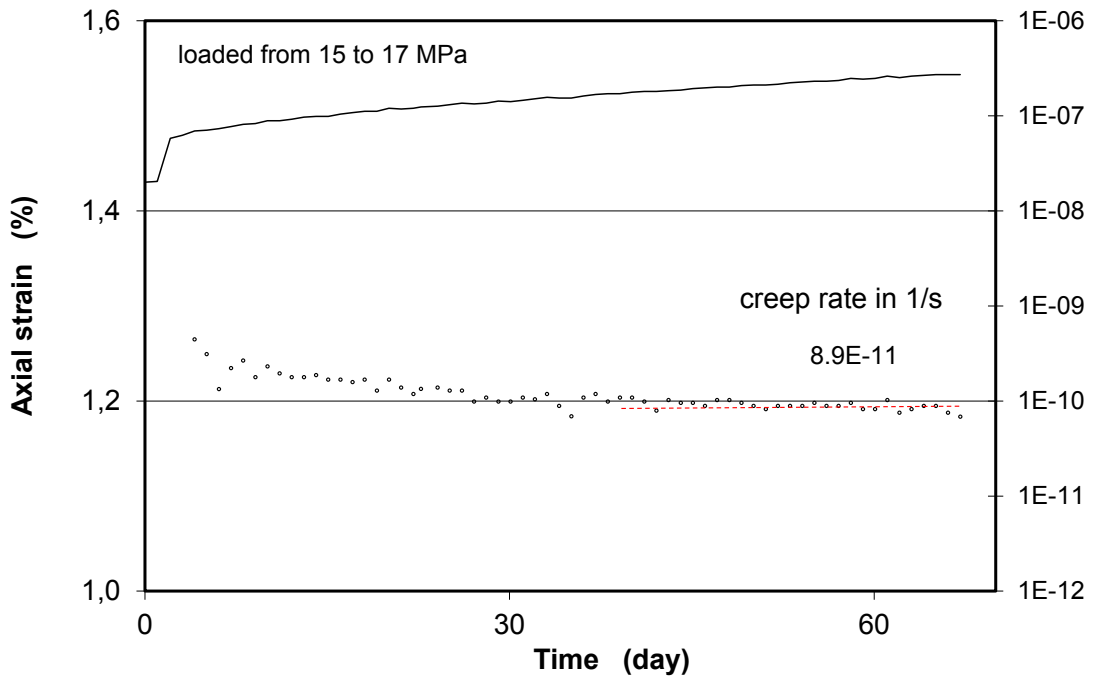
(i) Loaded from 15 to 17 MPa
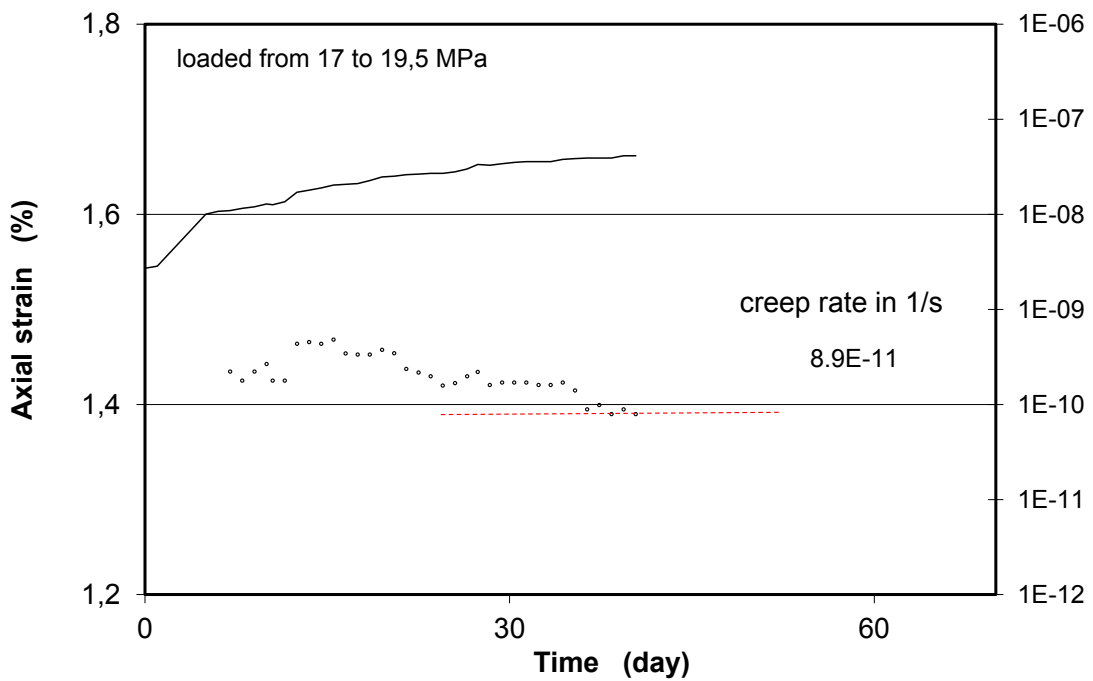
(j) Loaded from 17 to 19.5 MPa

Fig. C.35 Evolution of uniaxial creep strain and creep rate of a COX clay sample at different stress levels
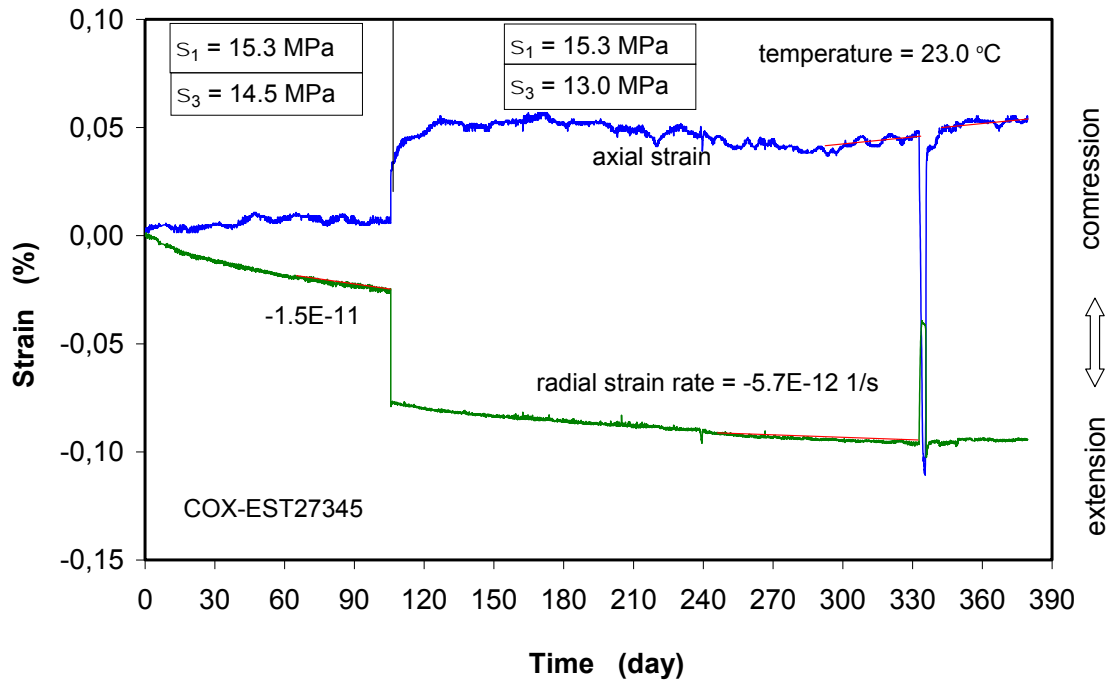
(a) strain-time curves of a COX sample (ϕ = 15.0 %, $S_w \approx 90$ %)
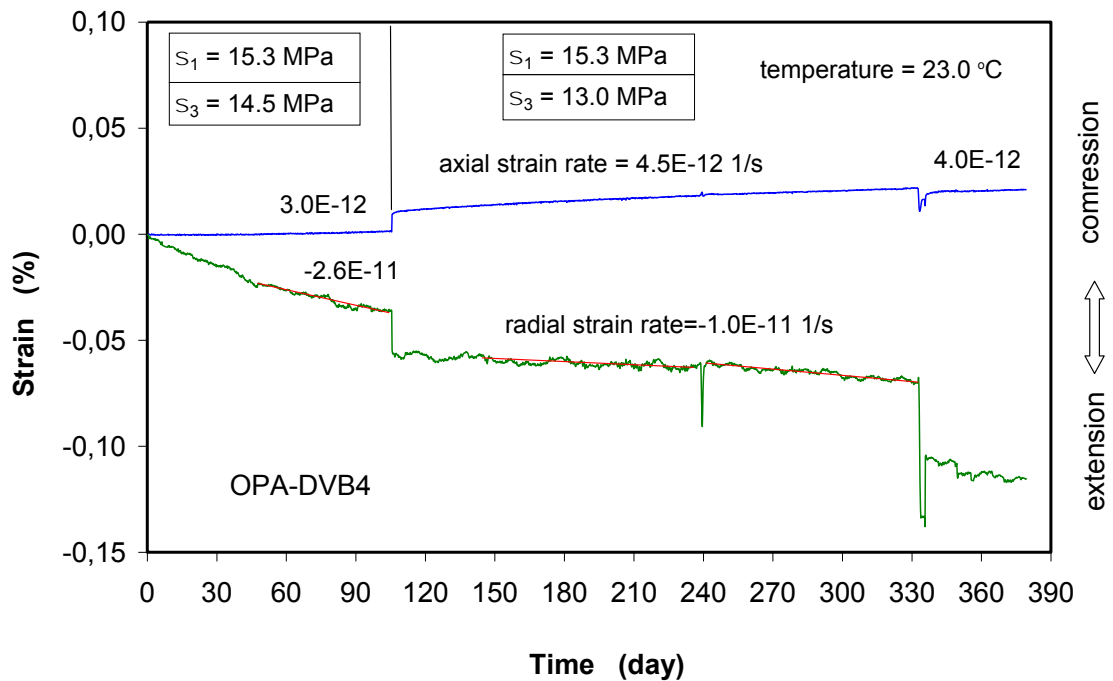
(b) strain-time curves of a OPA sample (ϕ = 13.2 %, Sw $\approx$ 100 %)

Fig. C.36 Results of triaxial creep tests on the COX and OPA claystones at high confining stresses but low deviatoric stresses

D Results of uniaxial compression tests on claystone as a function of water content

Tab. D.5 Results of uniaxial compression tests on dried claystone

Sample ID	Sample size D/L [mm]	Relative humidity RH [%]	Drying/ wetting duration [day]	Bulk density ρ_b [g/cm^3]	Water content w [%]	Water saturation S_{lo} [%]	Dilatancy strength σ_D [MPa]	Peak strength σ_F [MPa]	Young's modulus E [MPa]	Poisson ratio ν [-]
EST40478A	50/100	12	40	2.378	1.4	18.0	29.0	49.2	4787	0.02
EST40478B	50/100	54	40	2.406	3.2	41.5	20.0	34.5	3387	0.13
EST40478C	50/100	75	40	2.429	4.5	58.8	12.0	24.5	3824	0.15
EST40376A	50/100	90	40	2.425	6.2	81.4	12.0	25.6	3486	0.14
EST40648A	50/100	98	40	2.371	7.4	97.2	6.5	13.5	2140	0.25
EST40376B	50/100	100	40	2.399	7.7	101.4	5.0	10.0	1228	0.67

(a) EST40376B, w = 7.7 %
    before testing

(b) EST40376B, w = 7.7 %
    after testing

(c) EST40376A, w = 6.2 %
    after testing

(d) EST40478C, w = 4.5 %
    after testing

(e) EST40478B, w = 3.2 %
    after testing

(f) EST40478A, w = 1.4 %
    after testing

Fig. D.37   Results of uniaxial compression tests on claystone as a function of water content
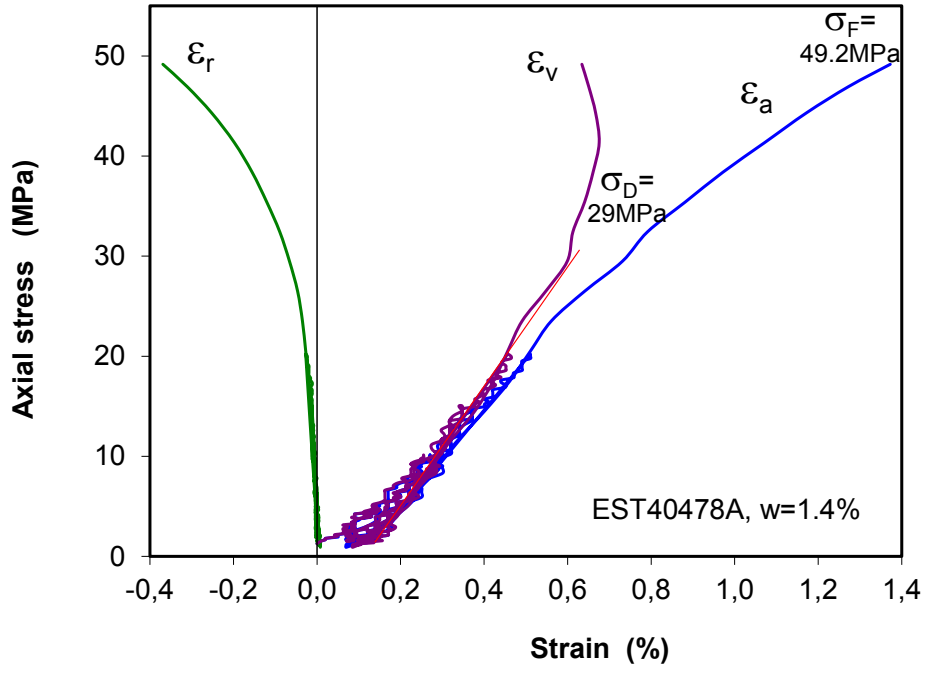
(a) EST40478A, W = 1.4 %
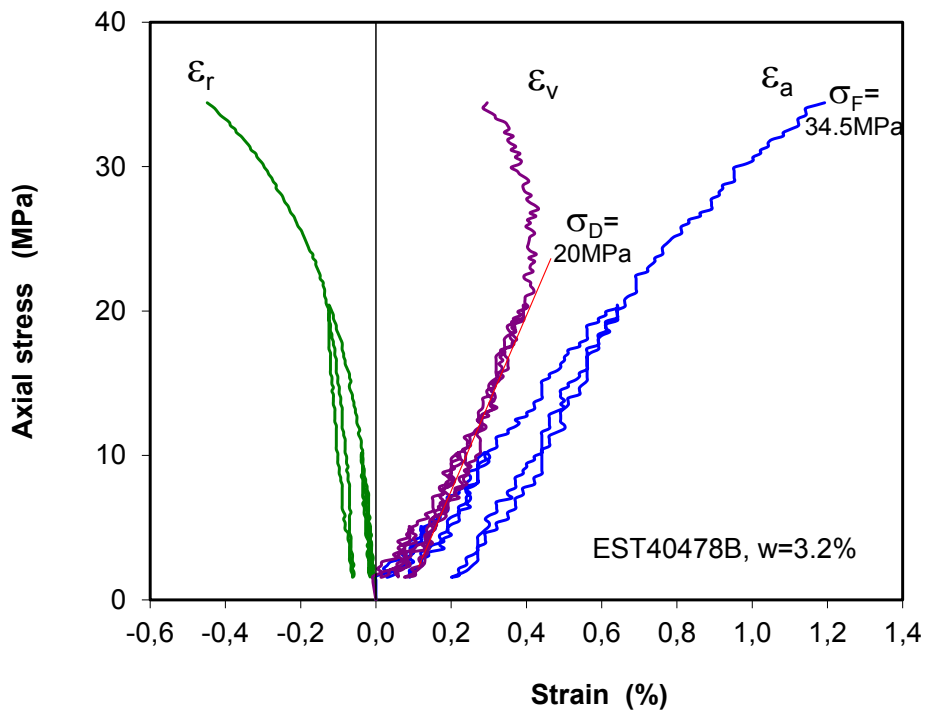
(b) EST40478B, W = 3.2 %
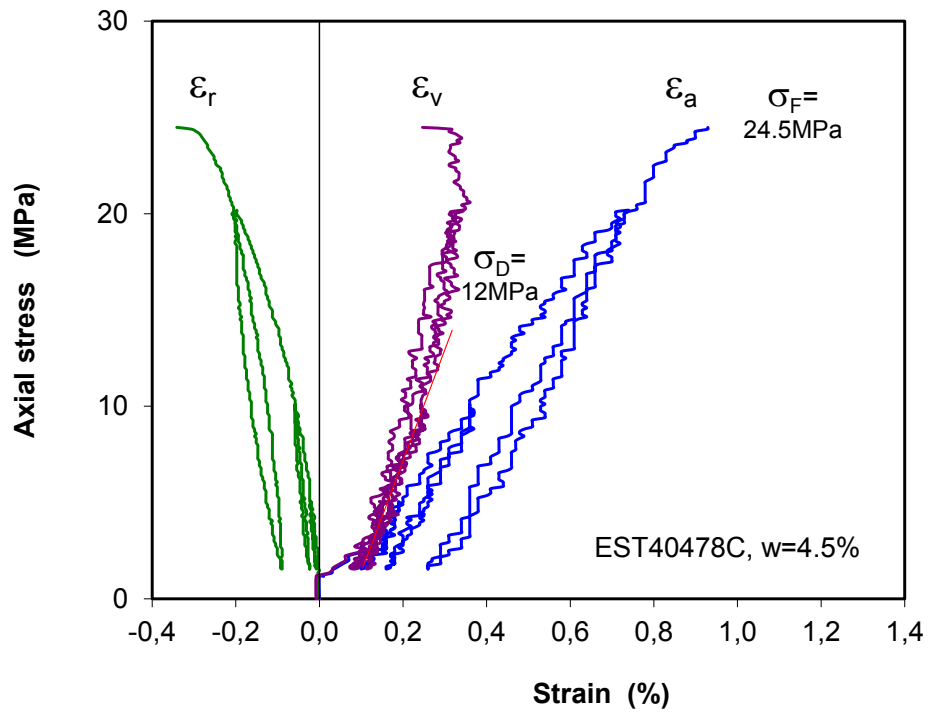
(c) EST40478C, W = 4.5 %
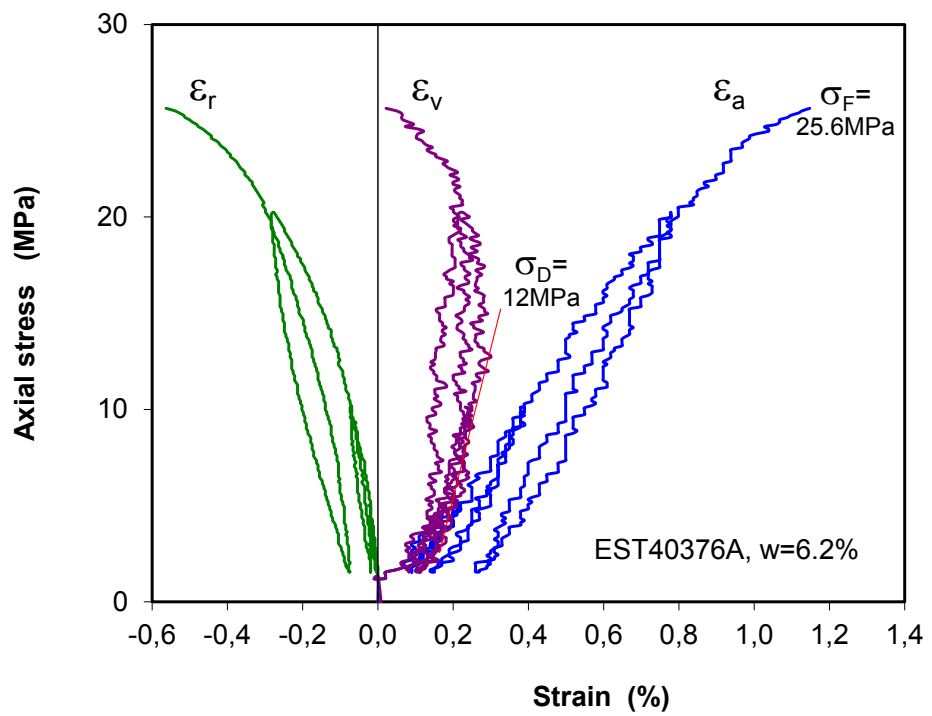
(d) EST40376A, W = 6.2 %
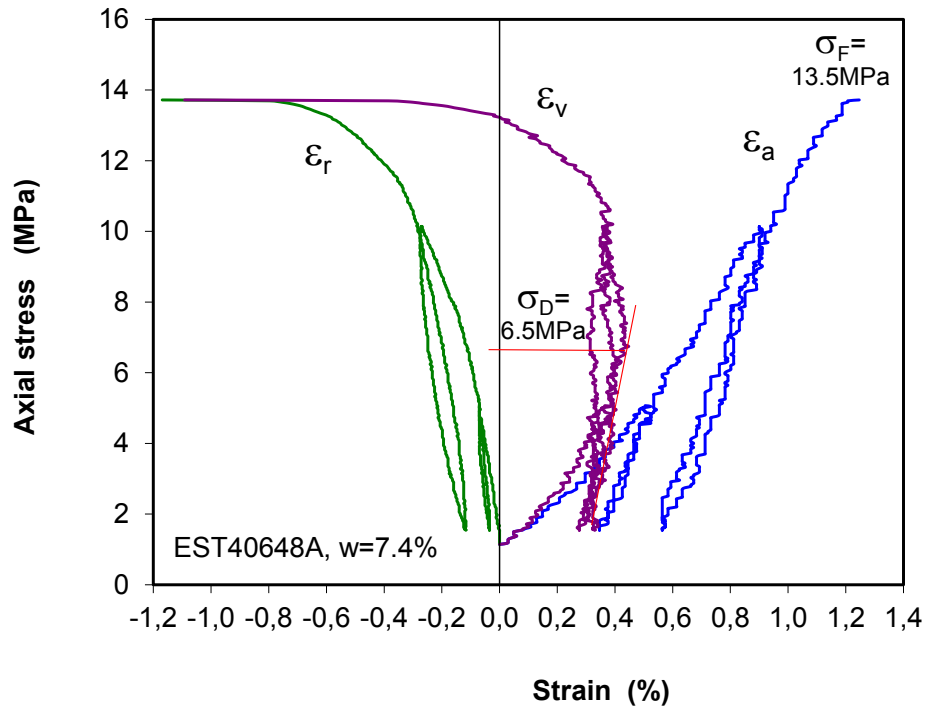
(e) EST40648A, W = 7.4 %
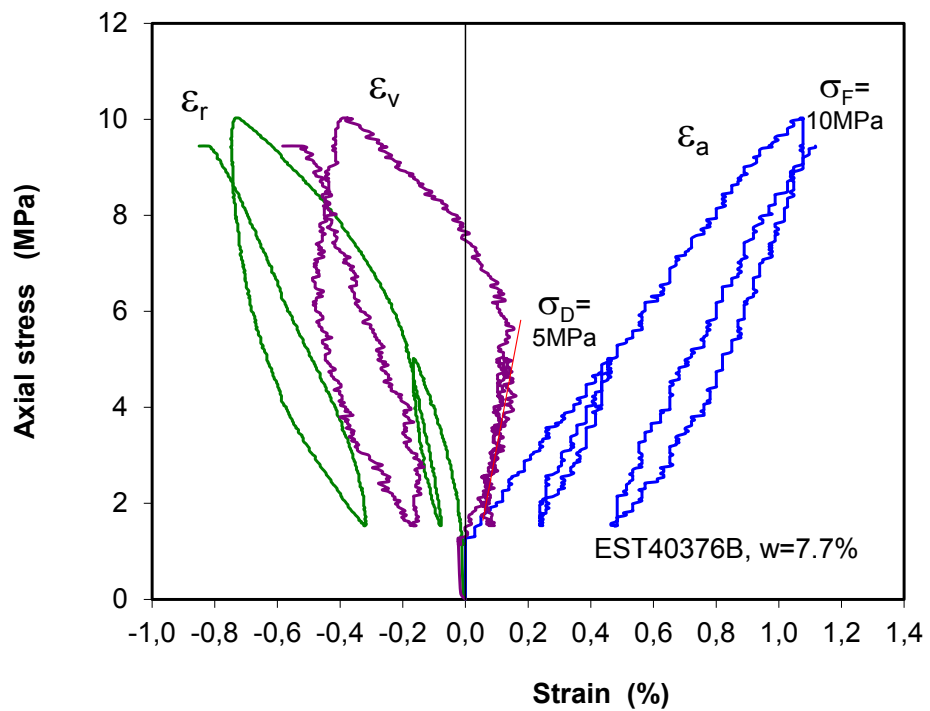
(f) EST40376B, W = 7.7 %

Fig. D.38   Results of uniaxial compression tests on COX samples with different water contents

E   Results of thermal-mechanical tests on claystone

Tab. E.6   Fundamental properties of testing samples

Sample ID	D/L [mm]	Grain density [g/cm^3]	Bulk density [g/cm^3]	Dry density [g/cm^3]	Initial porosity [%]	Water content [%]	Water saturation [%]
EST34678	98/200	2.700	2.413	2.241	17.0	7.11	93.8
EST33204A	50/95	2.700	2.409	2.264	16.1	6.00	84.2
EST33204B	50/92	2.700	2.400	2.256	16.4	6.00	82.3
EST33213A	50/95	2.700	2.423	2.277	15.7	6.04	87.7
EST33213B	50/95	2.700	2.473	2.328	13.8	5.86	99.0
EST33211A	50/95	2.700	2.452	2.310	14.4	5.70	91.8
EST33211B	50/95	2.700	2.457	2.316	14.2	5.75	93.6

Sample ID	Conf. stress $\sigma_\rho/\sigma_\alpha$ [MPa]	Max. temperature [°C]	Test duration [day]	Water content after test [%]	Water loss [%]
EST34678	15/15-1/1	68	35.0	6.8	0.31
EST33204A	3/15	50	6.0	x	x
EST33204B	3/15	110	45.0	x	x
EST33213A	1/15	110	55.0	x	x
EST33213B	0.5/15	110	45.0	x	x
EST33211A	0.5/15	120	20.0	x	x
EST33211B	3/15	60	362.0	3.9	1.85

(a) EST33204A, w=6.0%   (b) EST33204B, w=6.0%   (c) EST33213A, w=6.0%

(d) EST33213B, w=5.9%   (e) EST33211A,w=3.9%   (f) EST33211A,w=5.8%

Fig. E.39   Testing samples

Tab. E.7   Characters of large COX hollow cylinders for borehole stability tests

Test No.	Sample	Size D/d/L [mm]	Grain density [g/cm³]	Bulk density [g/cm³]	Dry density [g/cm³]	Porosity [%]	Water content [%]	Degree of saturation [%]
MTS1	EST45590 -490m ⊥	D280 d103 L518	2.70	2.43	2.29	15.3	6.0	90.0
MTS2	EST45592 -490m ⊥	D280 d103 L520	2.70	2.41	2.25	16.5	7.1	97.0

(a) unpacked core EST45590

(b) unpacked core EST45592

(c) planishing the end face

(d) drilled borehole

Fig. E.40   Large COX hollow cylinders for borehole stability tests

Results of thermal expansion tests on a COX sample under isostatic confining stresses
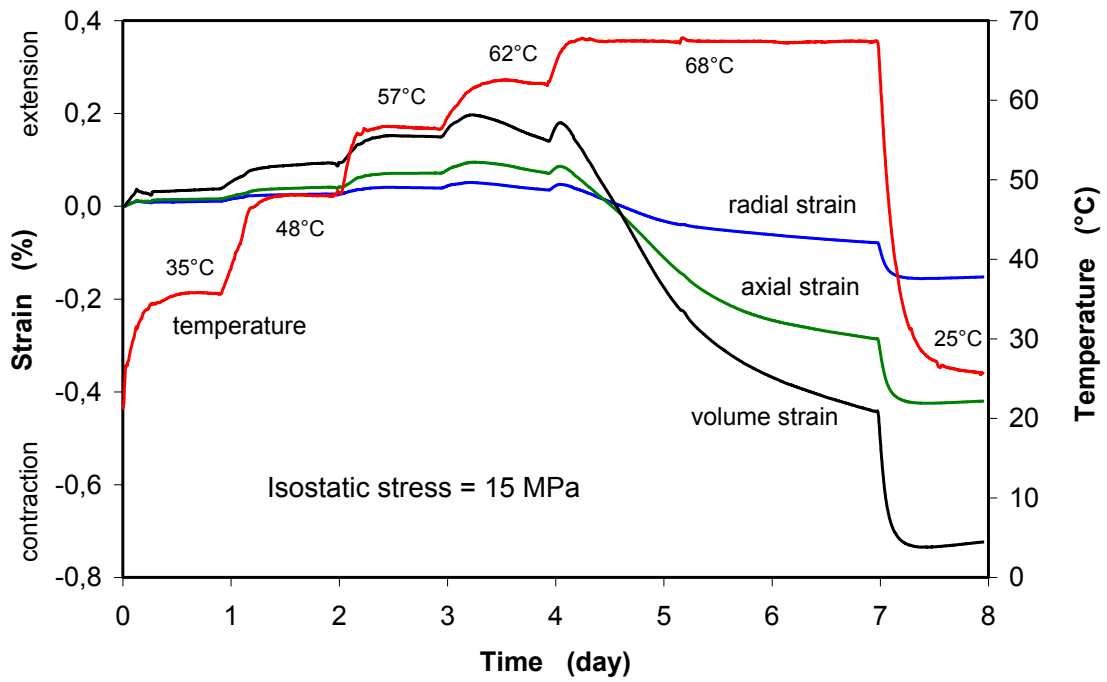
(a) under isostatic stress of 15 MPa
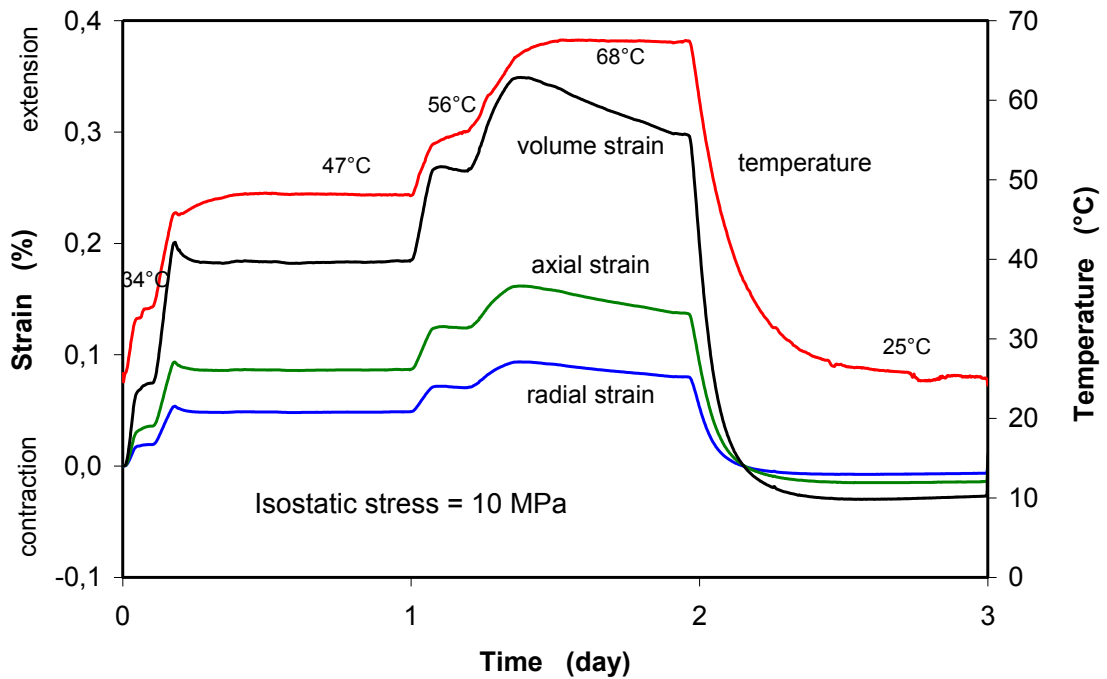
(b) under isostatic stress of 10 MPa
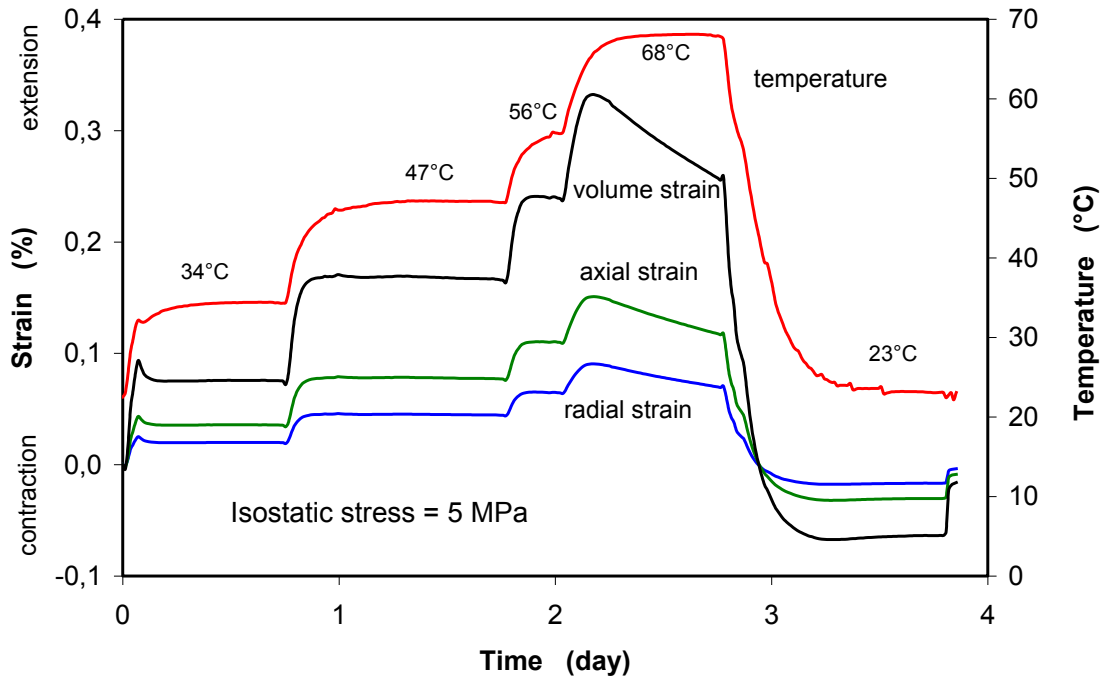
(c) under isostatic stress of 5 MPa
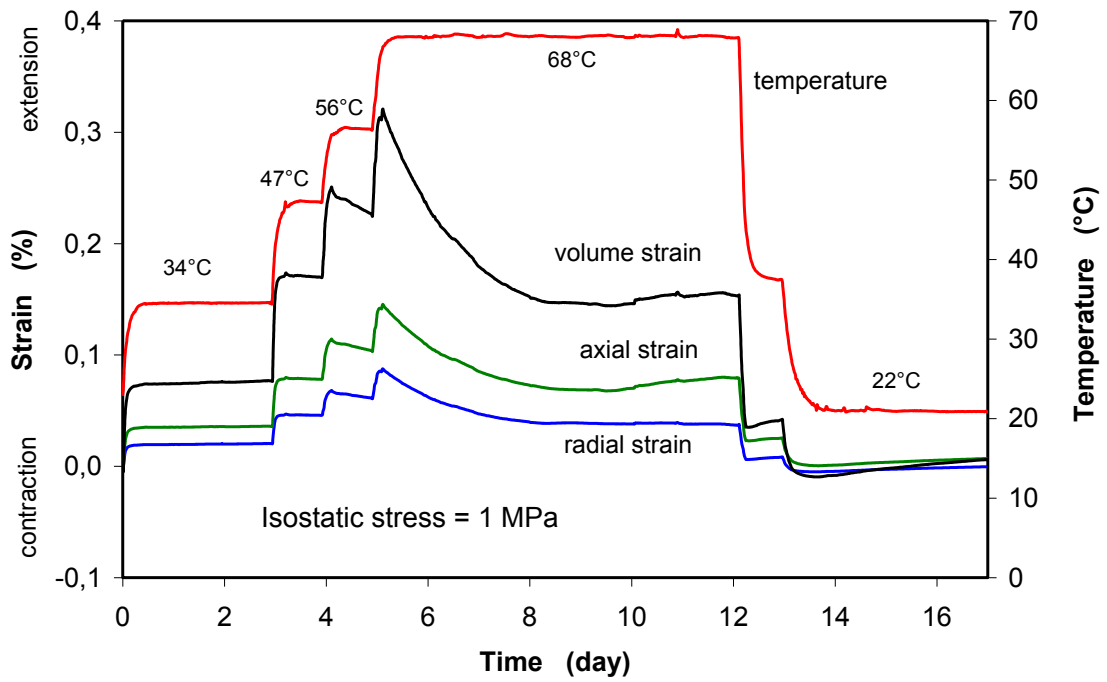
(d) under isostatic stress of 1 MPa

Fig. E.41   Evolution of thermal expansion of COX claystone during heating and cooling cycles under confining stresses of 15, 10, 5 and 1 MPa
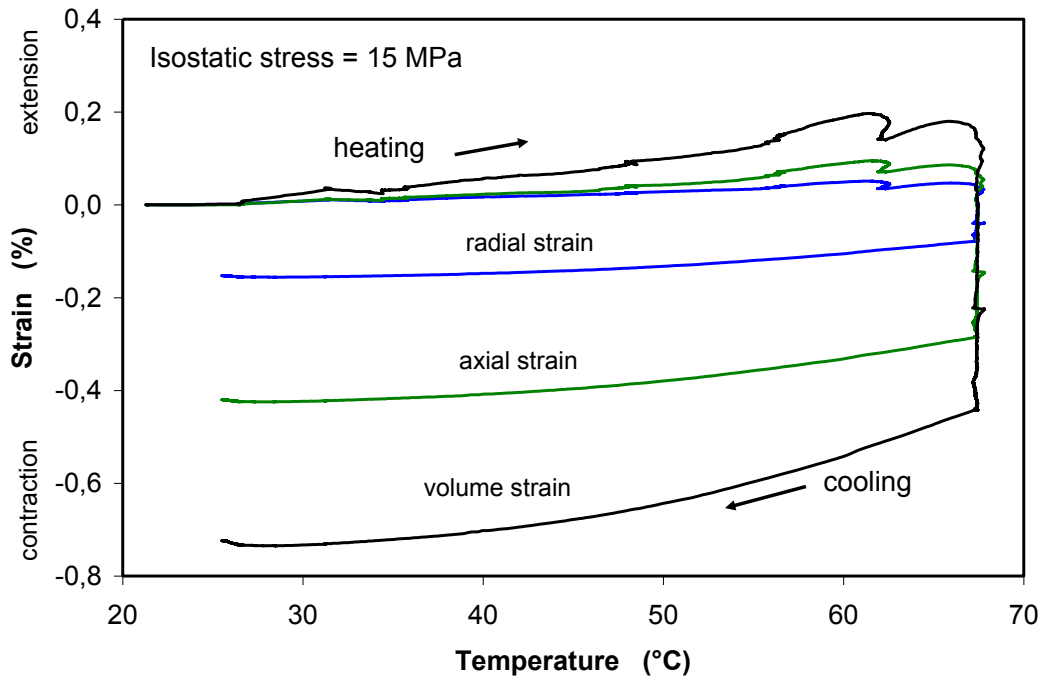
(a)   under isostatic stress of 15 MPa
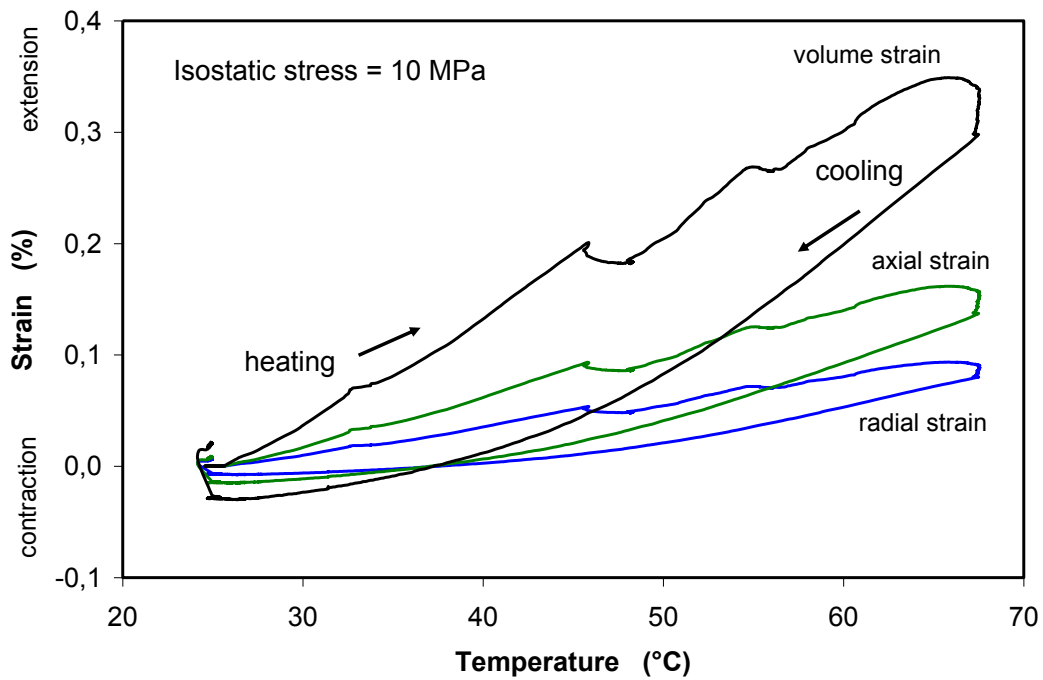
(b)   under isostatic stress of 10 MPa
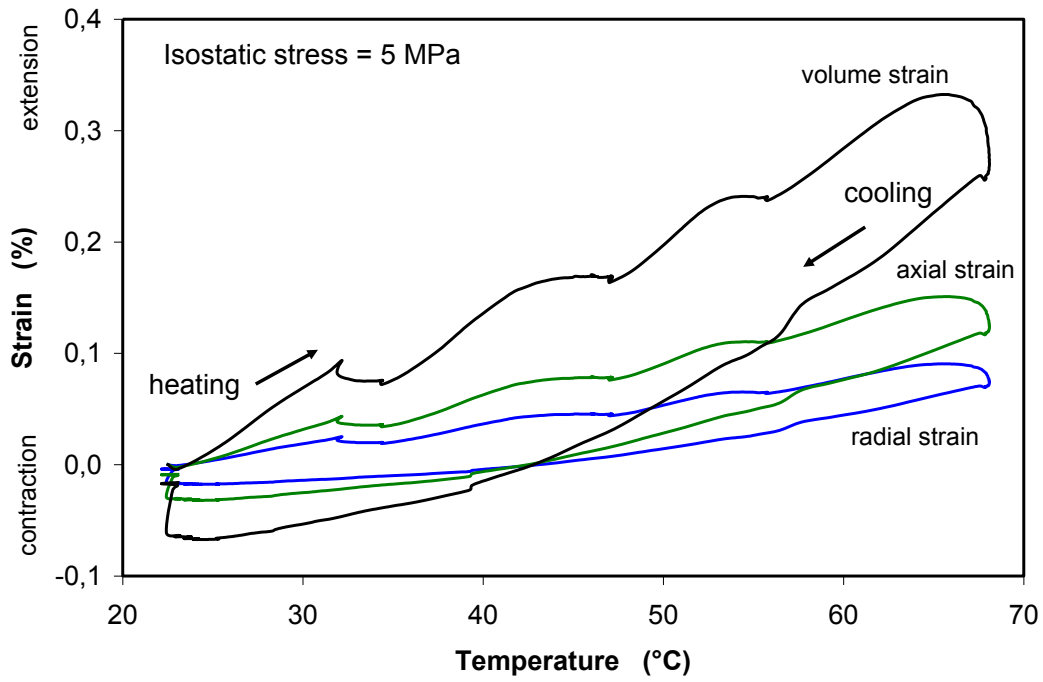
(c)   under isostatic stress of 5 MPa
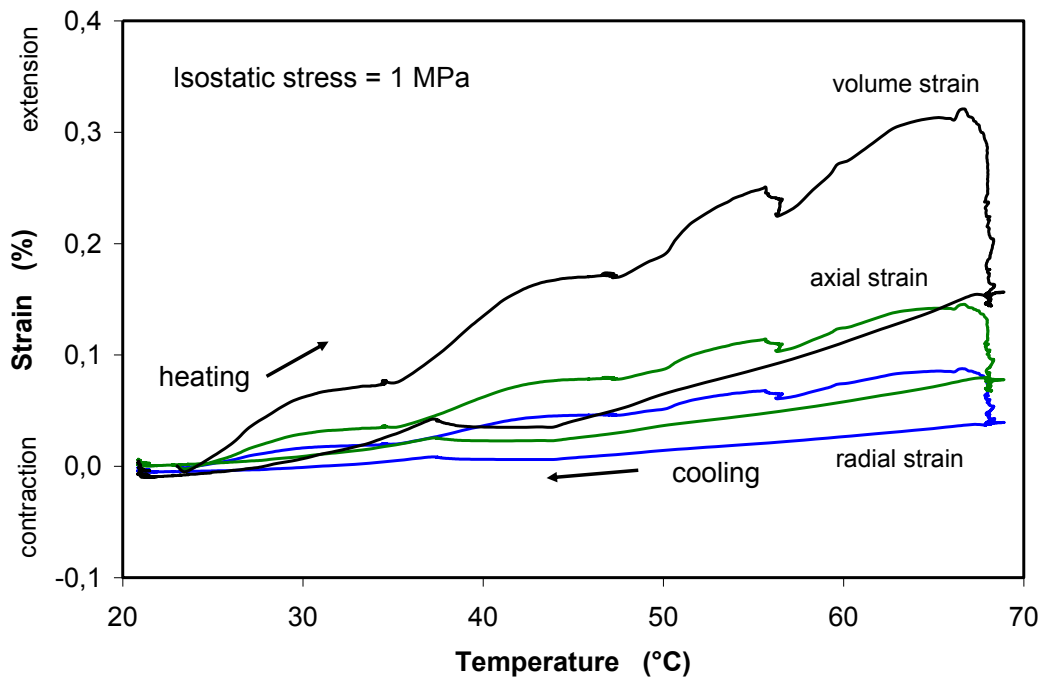
(d)   under isostatic stress of 1 MPa

Fig. E.42   Thermal expansion of COX claystone in dependence of applied tempera-
ture under confining stresses of 15, 10, 5 and 1 MPa
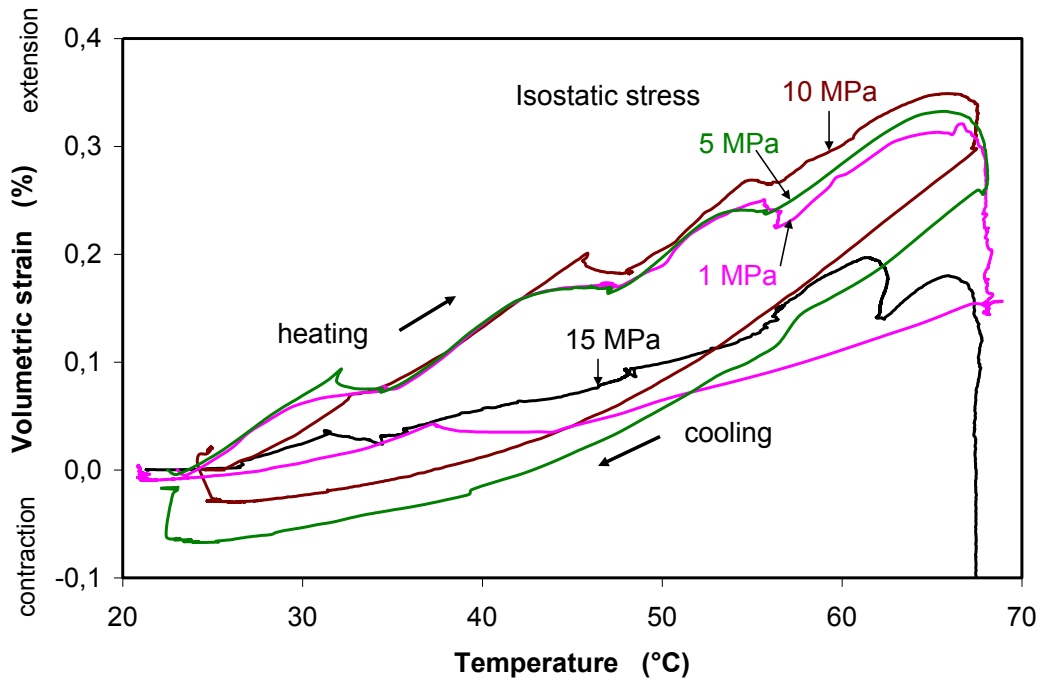
Fig. E.43 Thermal expansion of synthetic COX and OPA water as a function of temperature
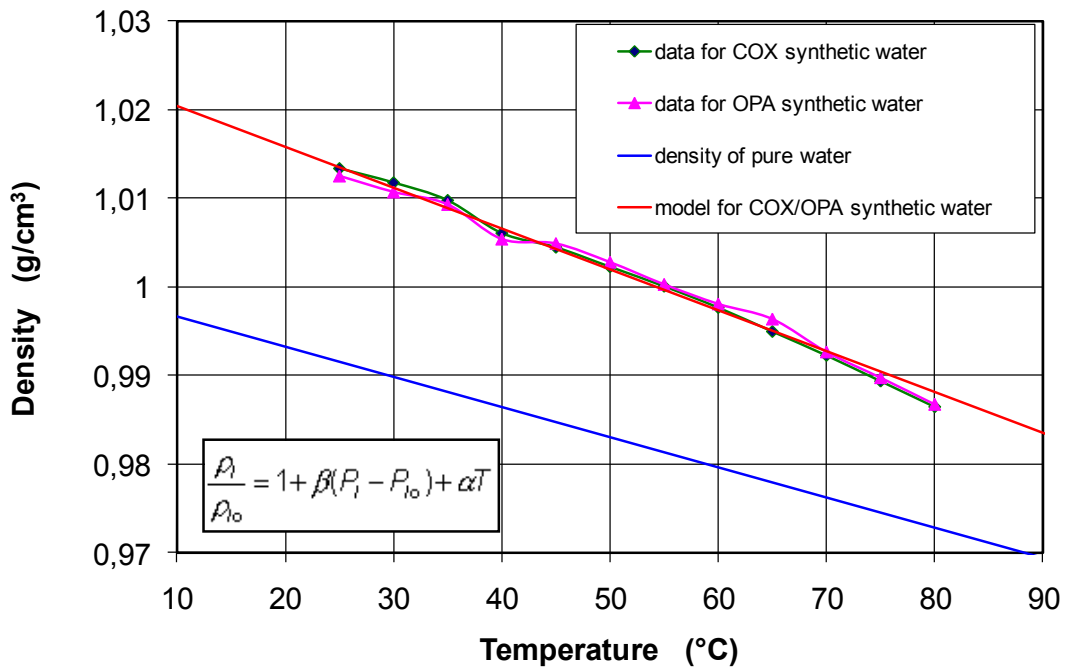
Fig. E.44 Comparison of thermal volume expansions under different confining stresses

E.2   Results of thermal deformation tests on COX samples under deviatoric confining stresses
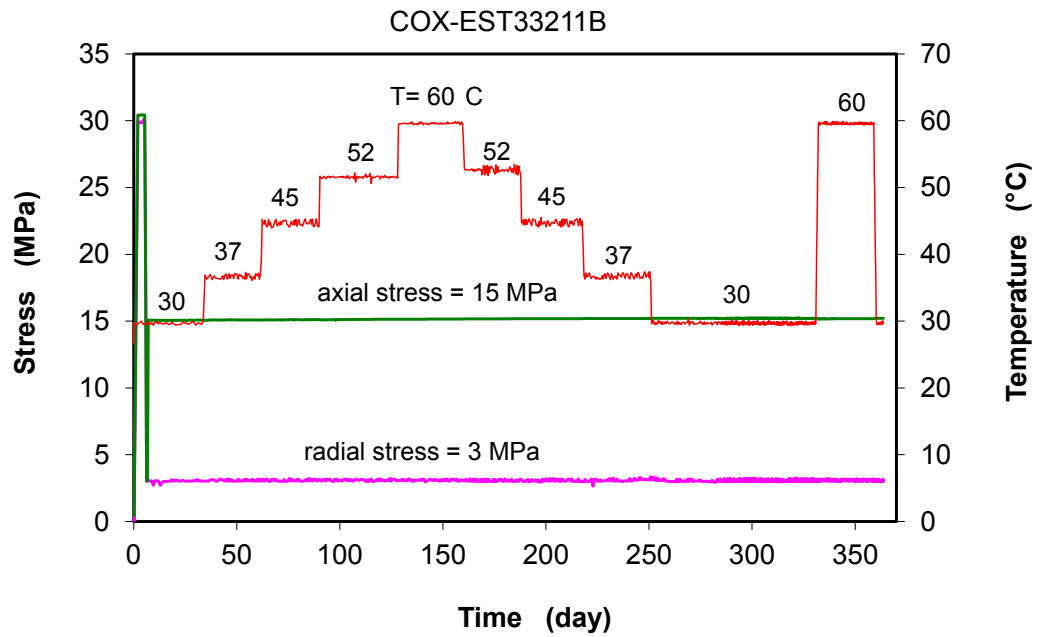
(a) Axial/radial stress
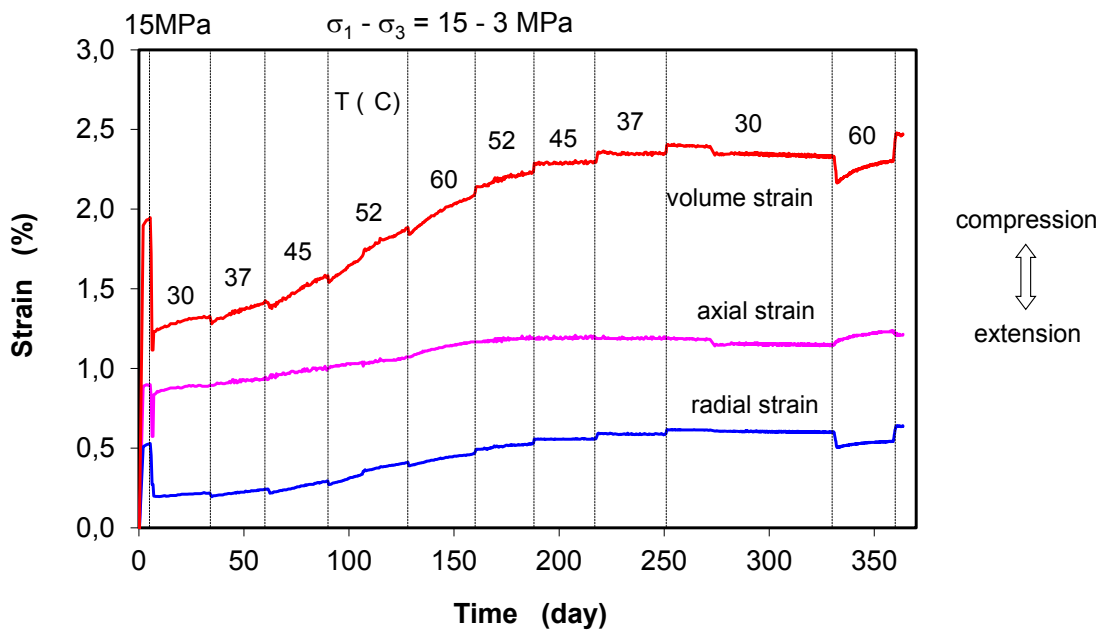
(b) Axial/radial/volumetric strain

Fig. E.45   Long-term creep test on EXT33211B
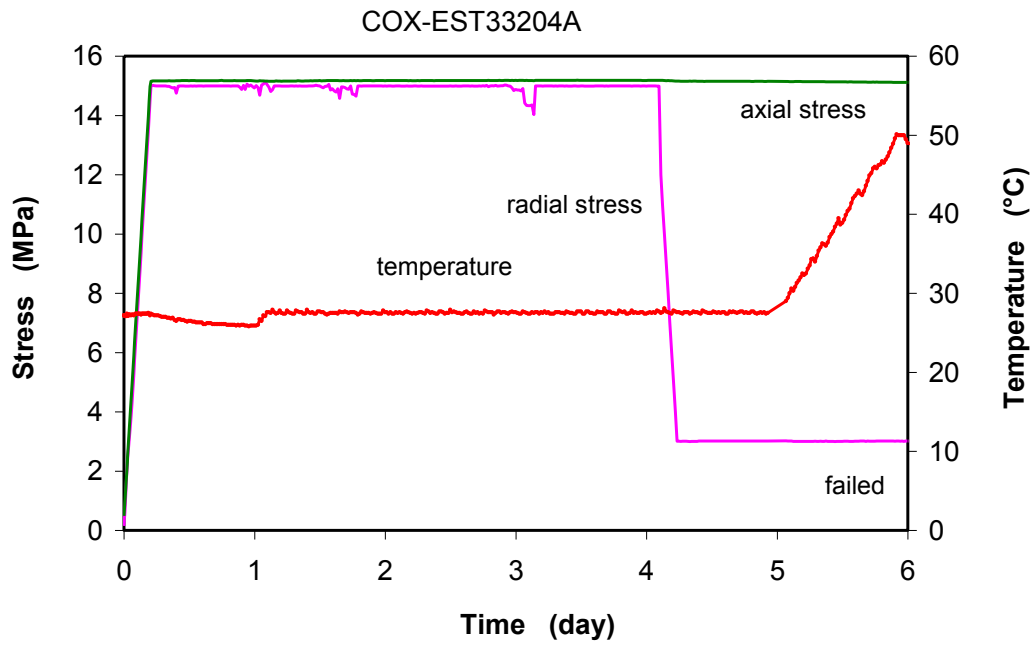
(a) Axial/radial stress
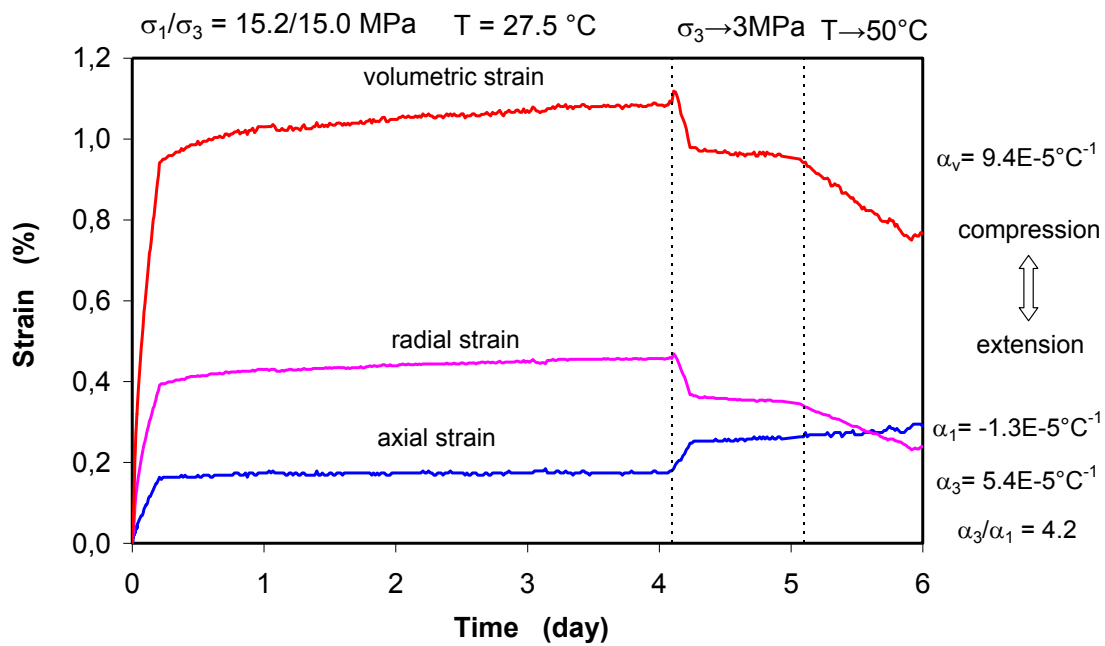
(b) Axial/radial/volumetric strain

Fig. E.46   Test on EXT33204A
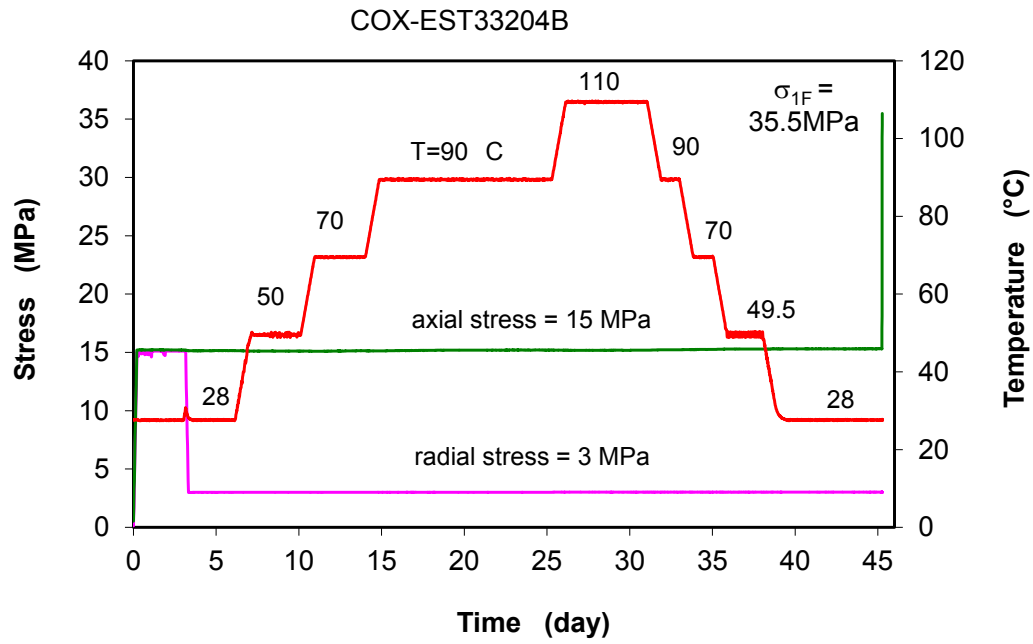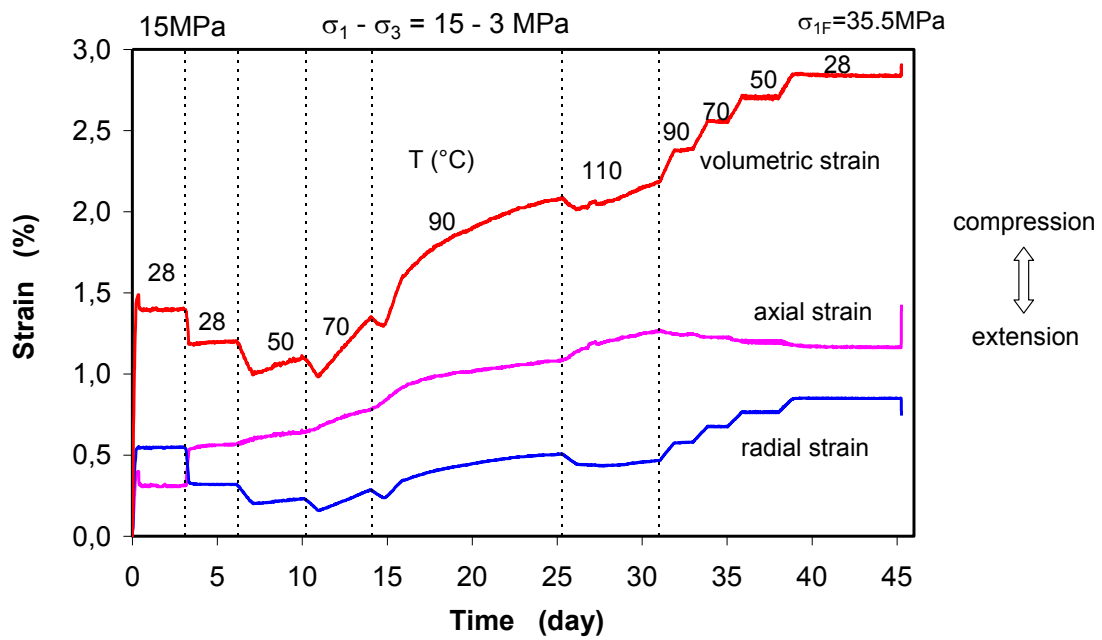
319

COX-EST33204B

(a) Axial/radial stress

(b) Axial/radial/volumetric strain
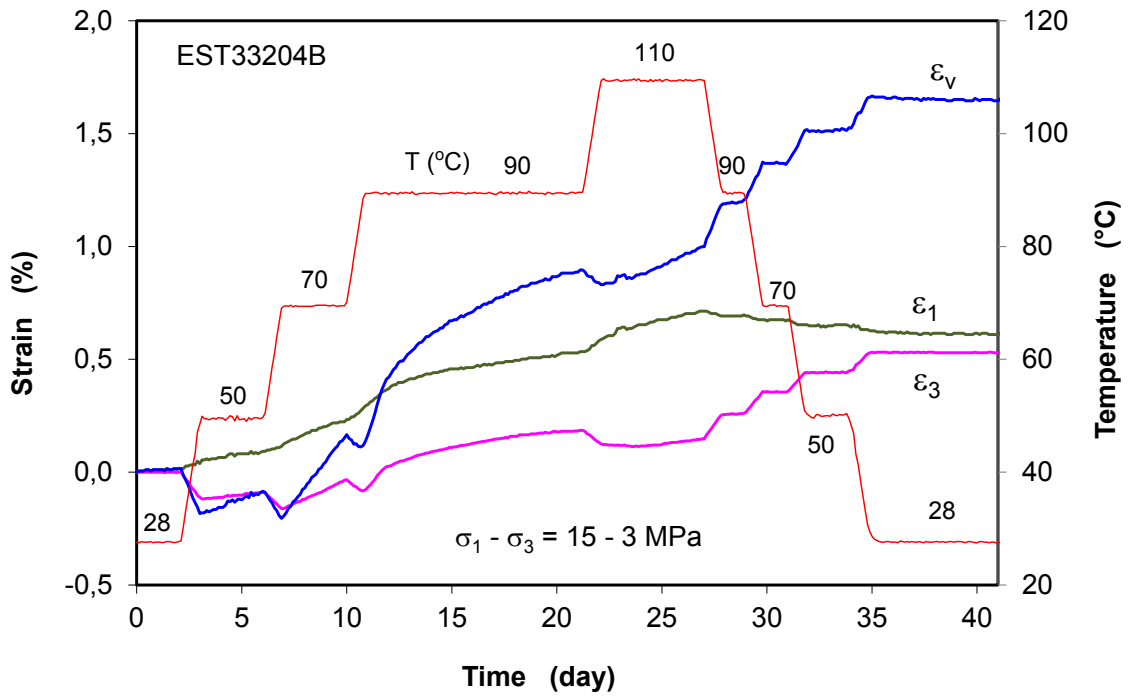
(c) Axial/radial/volumetric strain
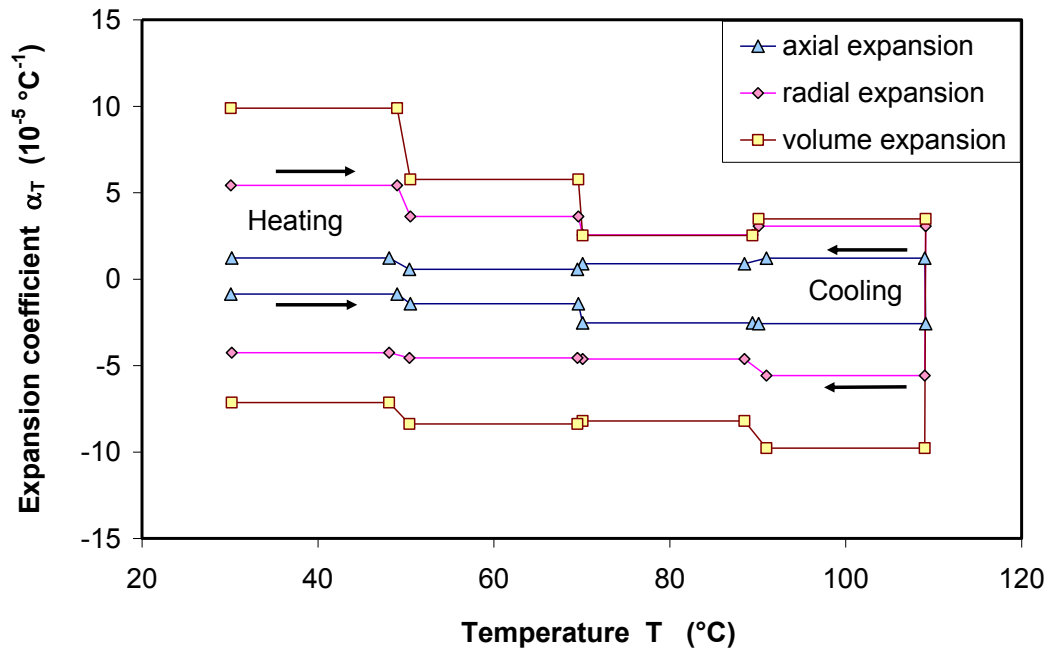
(d) Thermal expansion coefficients

Fig. E.47 Test on EXT33204B
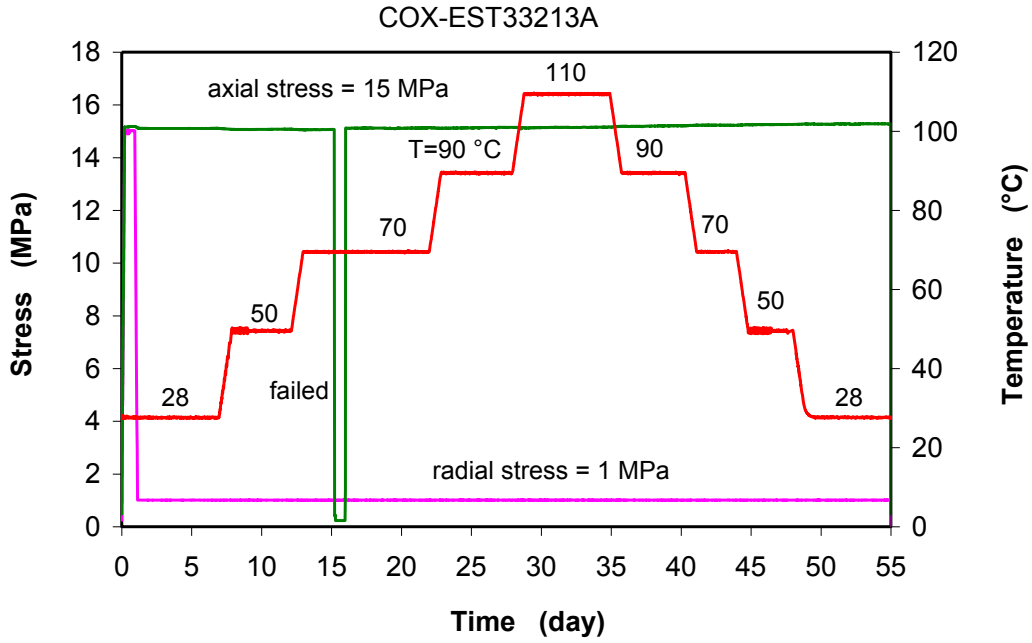
(a) Axial/radial stress
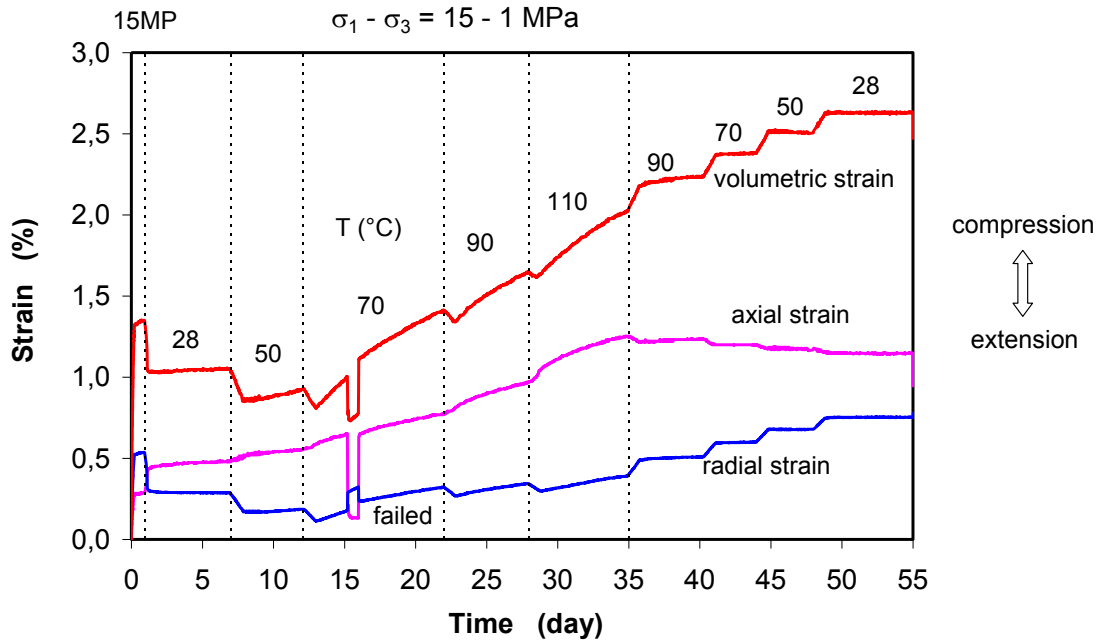
(b) Axial/radial/volumetric strain
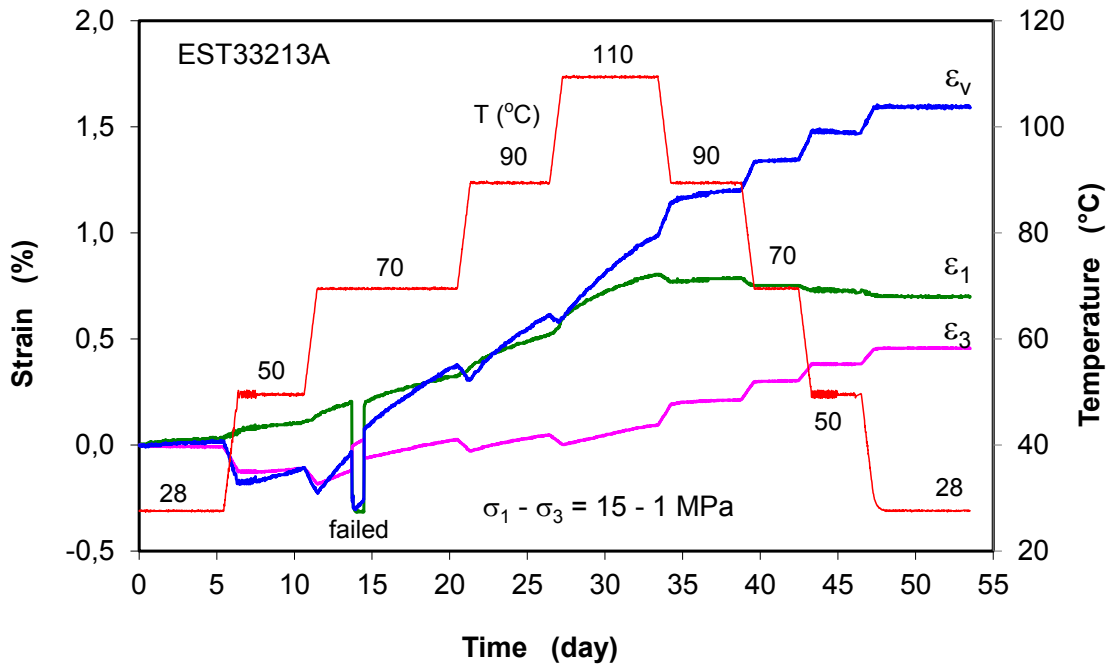
(c) Axial/radial/volumetric strain
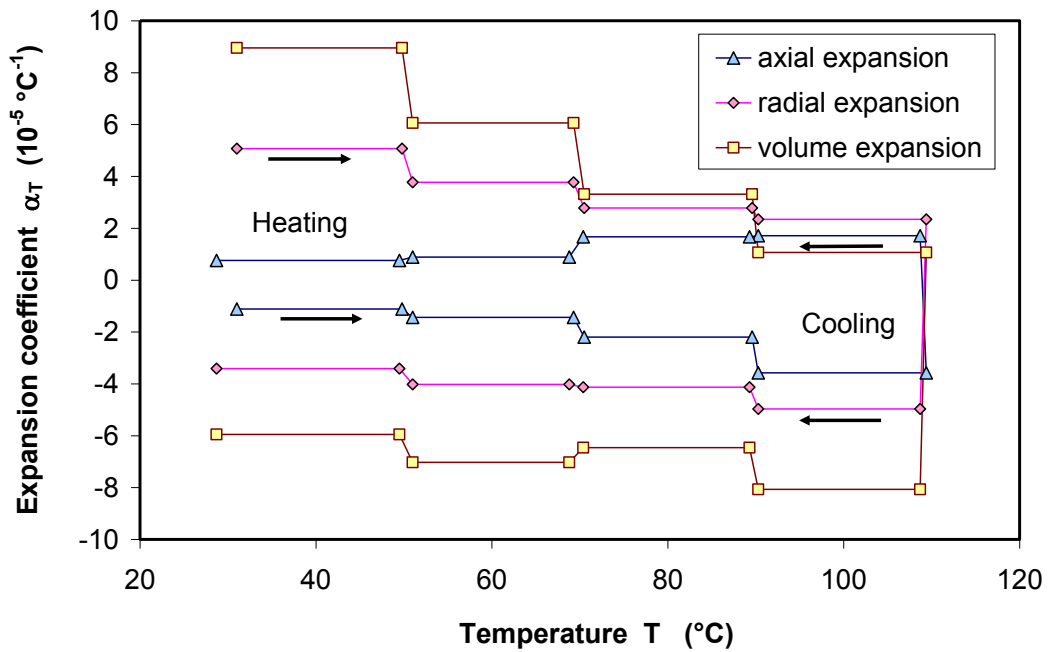
(d) Thermal expansion coefficients

Fig. E.48   Test on EXT33213A
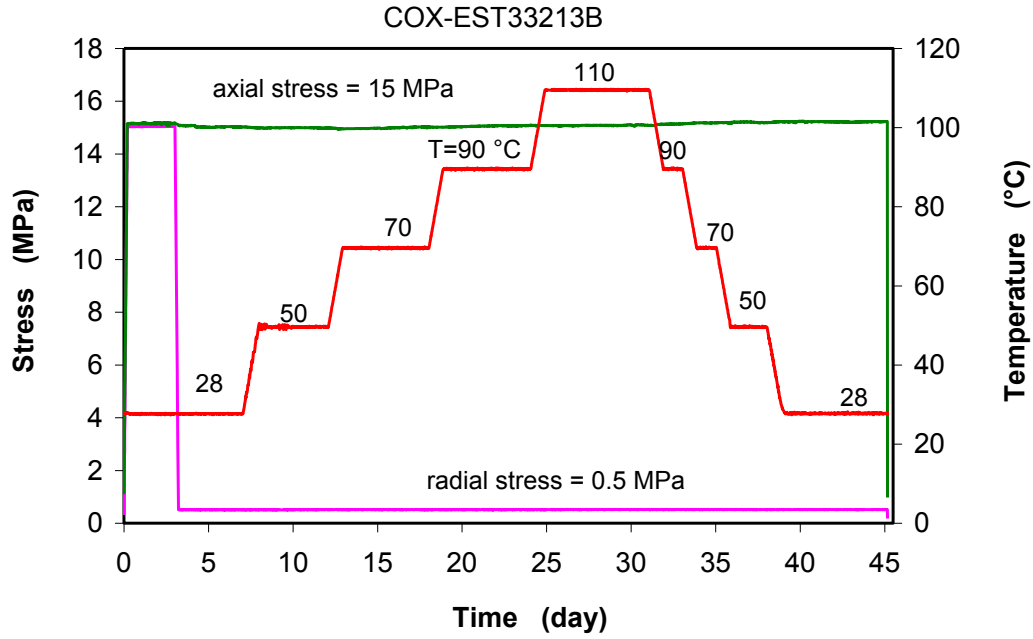
(a) Axial/radial stress
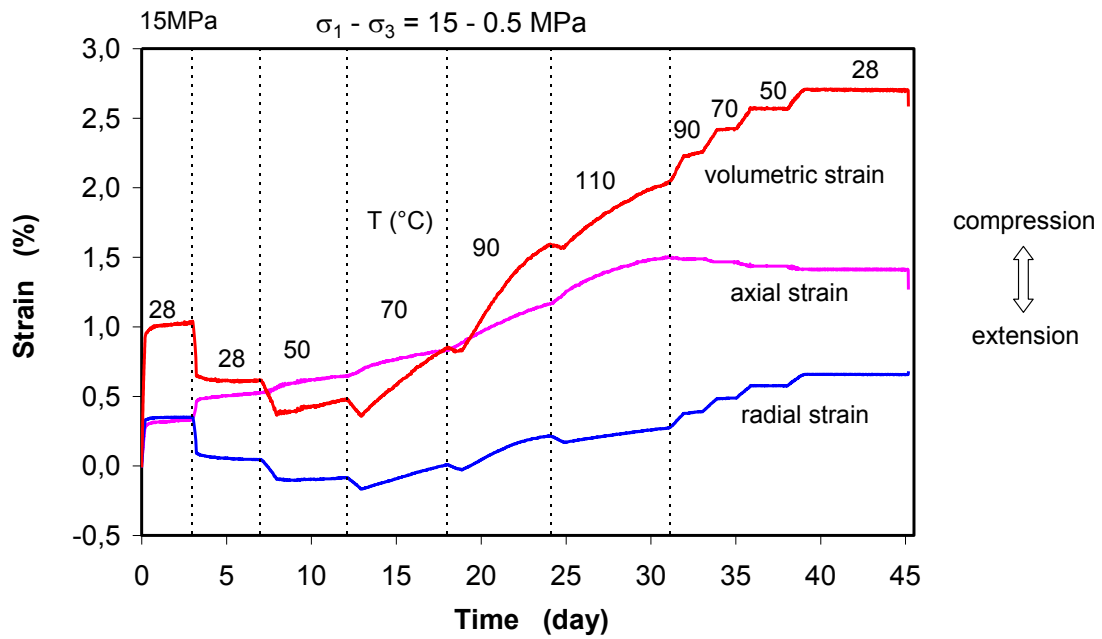
(b) Axial/radial/volumetric strain
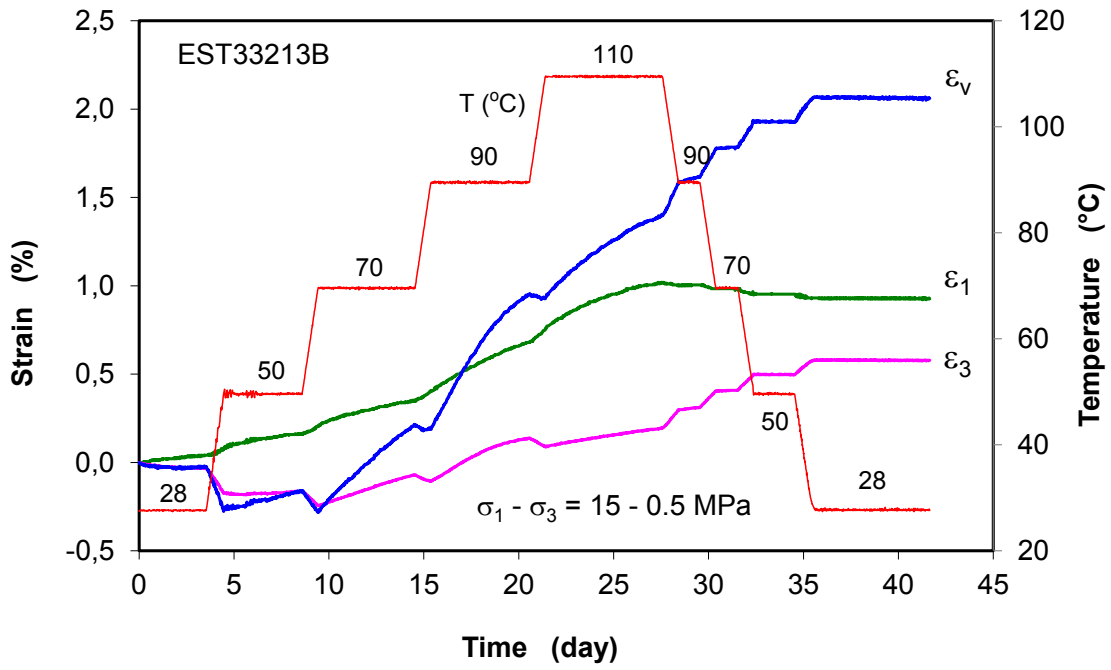
(c) Axial/radial/volumetric strain
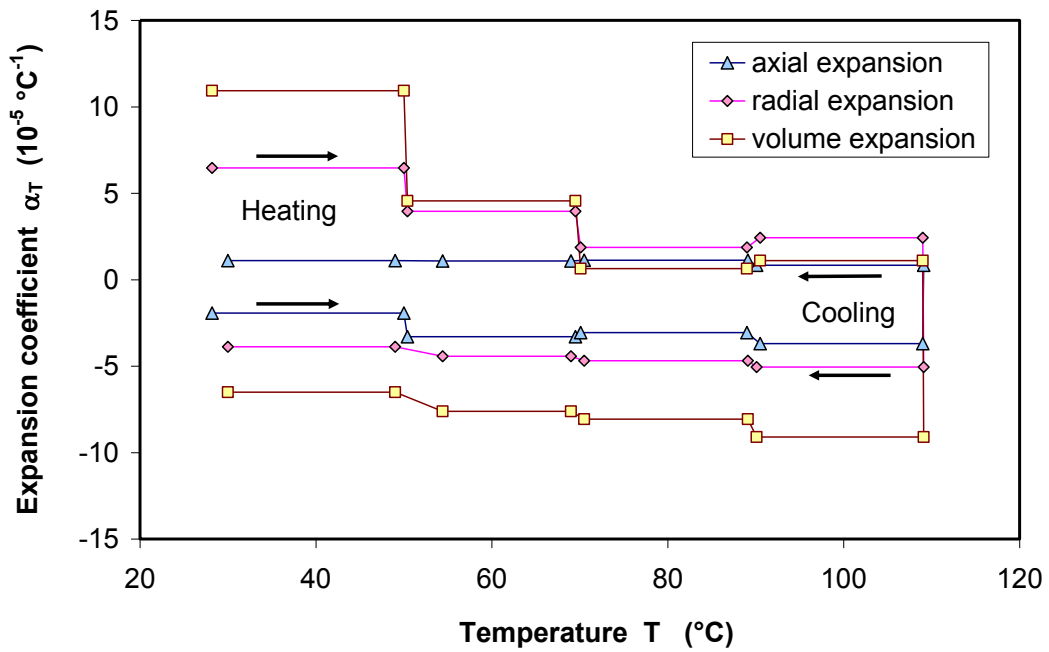
(d) Thermal expansion coefficients

Fig. E.49 Test on EXT33213B
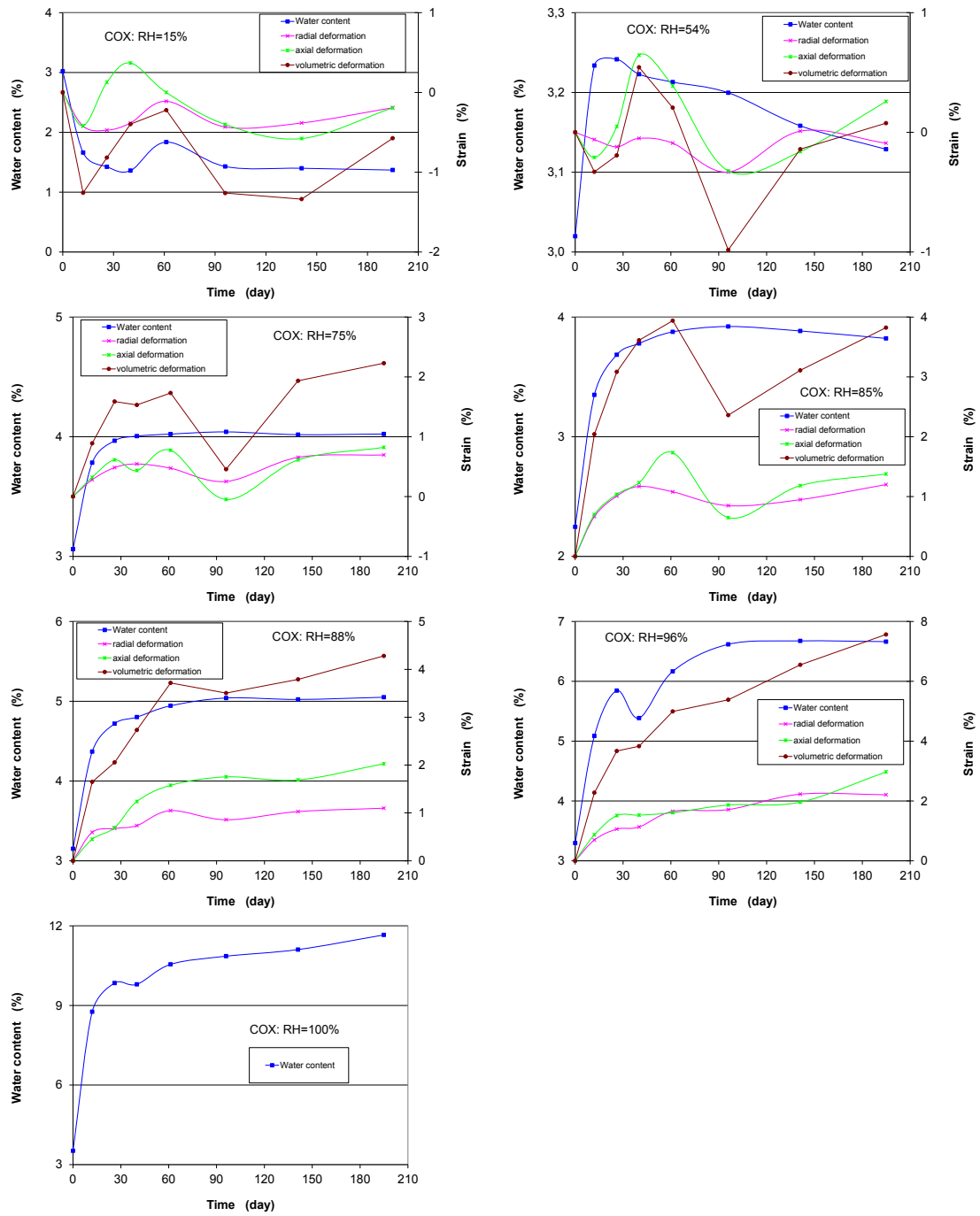
Fig. F.50   Water uptake and induced deformation of compacted COX aggregate in a humid environment
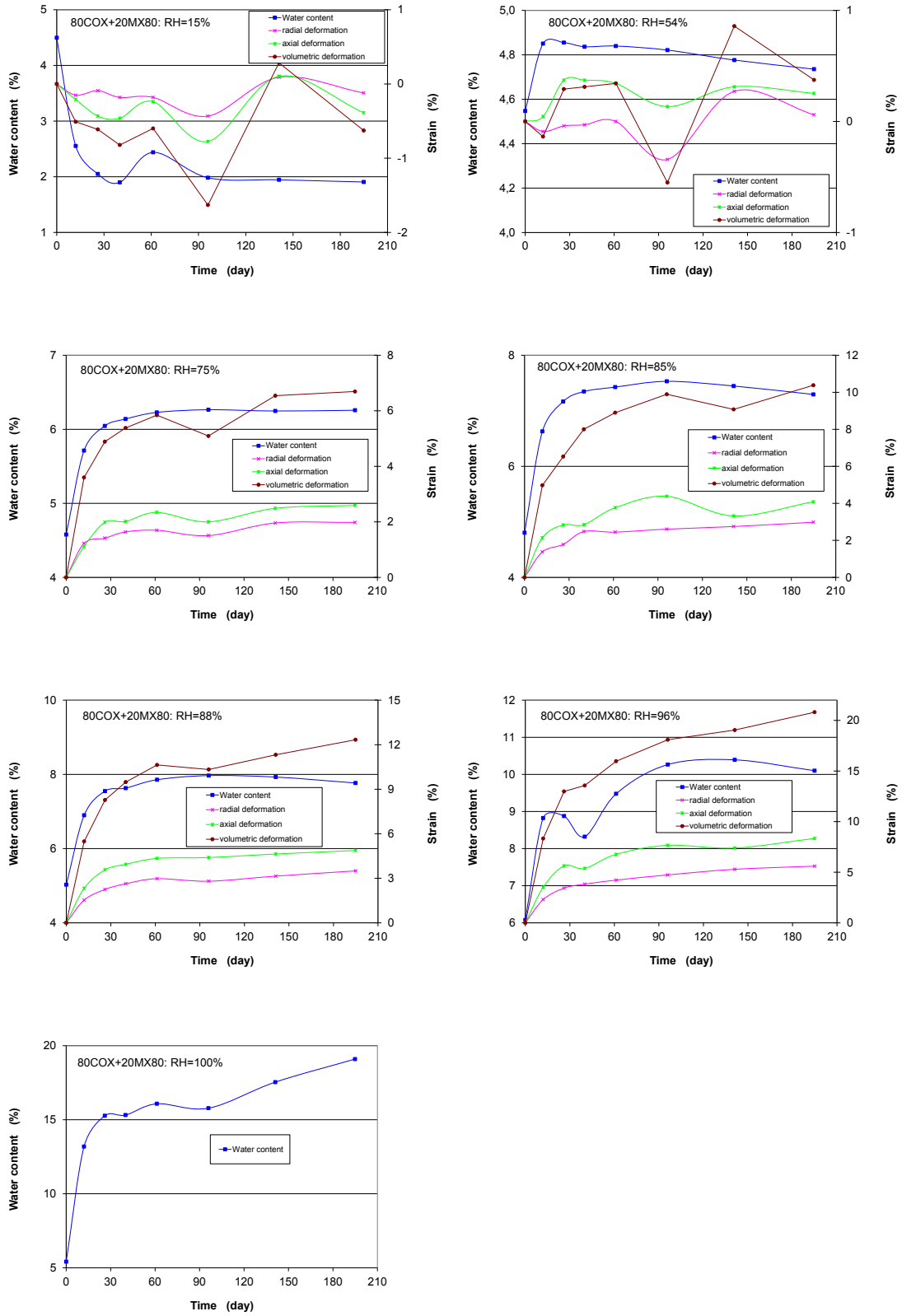
Fig. F.51 Water uptake and induced deformation of compacted 80COX+20MX80 mixture in a humid environment
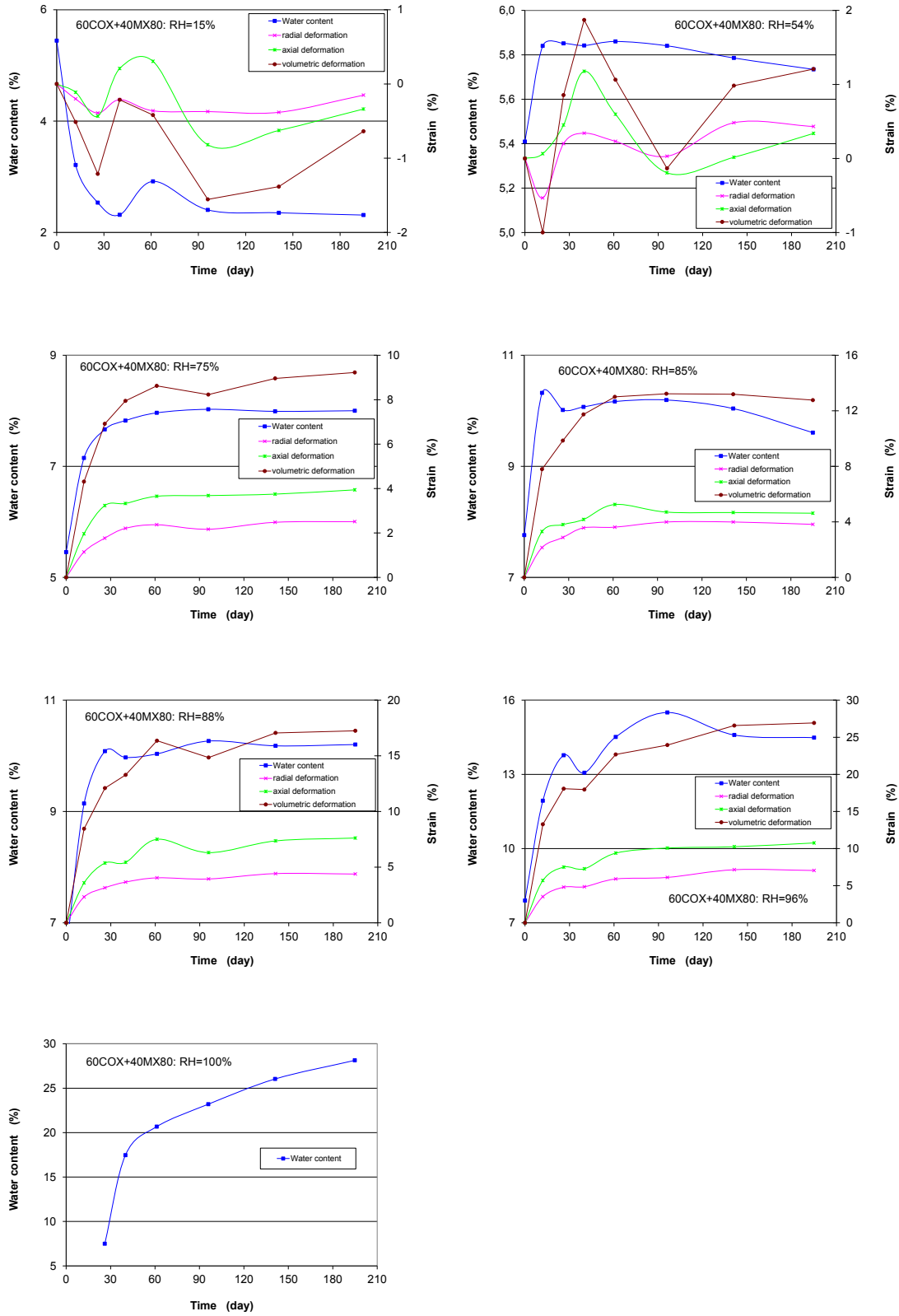
Fig. F.52 Water uptake and induced deformation of compacted 60COX+40MX80 mixture in a humid environment
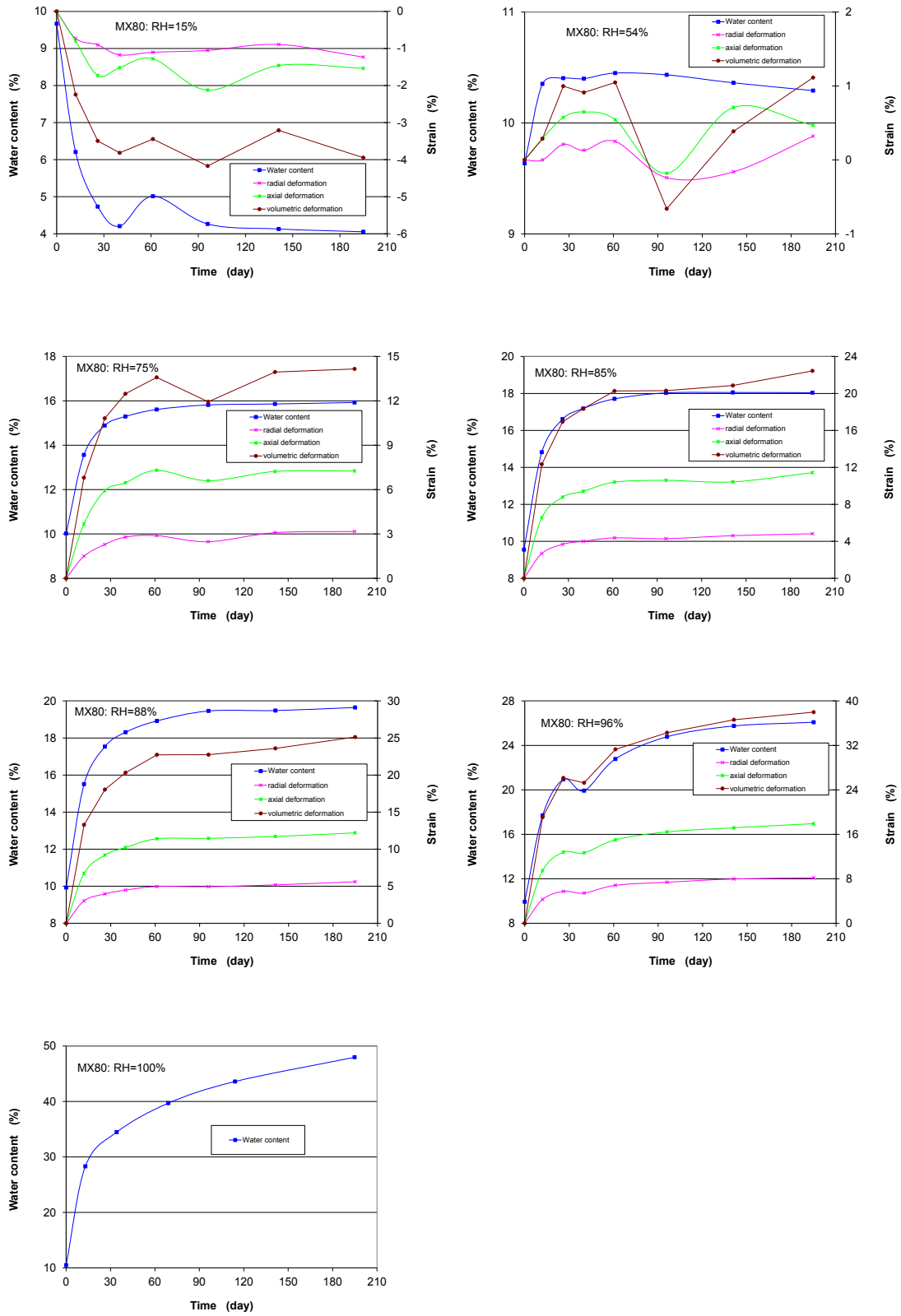
Fig. F.53 Water uptake and induced deformation of compacted MX80 bentonite in a humid environment
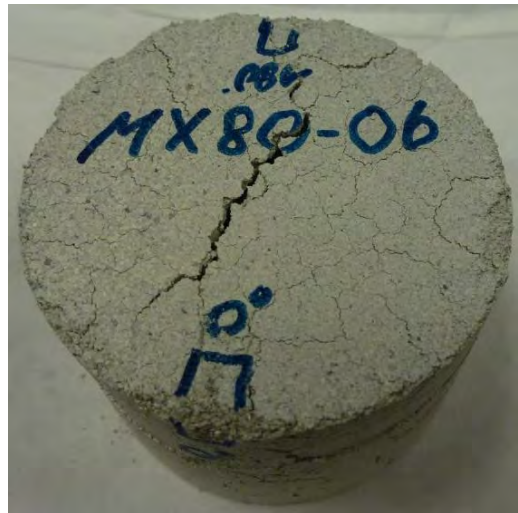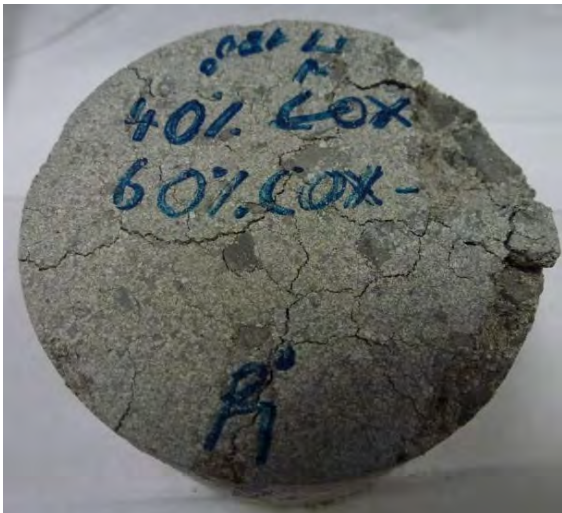
Fig. F.54   Samples of the compacted claystone-bentonite mixtures after water saturation at RH = 96 % over 6 months